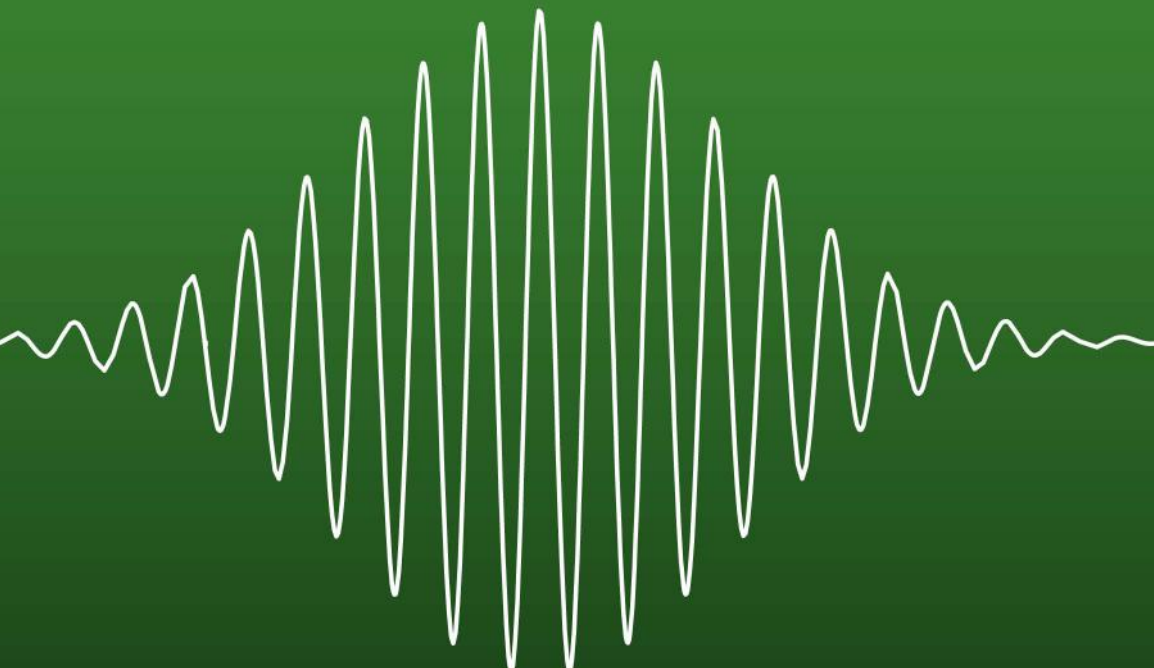


SERIES IN OPTICS AND OPTOELECTRONICS

# An Introduction to Quantum Optics

## Photon and Biphoton Physics



Yanhua Shih



CRC Press  
Taylor & Francis Group

A TAYLOR & FRANCIS BOOK

# An Introduction to Quantum Optics

# **SERIES IN OPTICS AND OPTOELECTRONICS**

---

Series Editors: **E Roy Pike**, Kings College, London, UK

**Robert G W Brown**, University of California, Irvine

*Recent titles in the series*

**Principles of Adaptive Optics**

Robert K Tyson

**Thin-Film Optical Filters, Fourth Edition**

H Angus Macleod

**Optical Tweezers: Methods and Applications**

Miles J Padgett, Justin Molloy, David McGloin (Eds.)

**Principles of Nanophotonics**

Motoichi Ohtsu, Kiyoshi Kobayashi, Tadashi Kawazoe

Tadashi Yatsui, Makoto Naruse

**The Quantum Phase Operator: A Review**

Stephen M Barnett, John A Vaccaro (Eds.)

**An Introduction to Biomedical Optics**

R Splinter, B A Hooper

**High-Speed Photonic Devices**

Nadir Dagli

**Lasers in the Preservation of Cultural Heritage:**

**Principles and Applications**

C Fotakis, D Anglos, V Zafiroopoulos, S Georgiou, V Tornari

**Modeling Fluctuations in Scattered Waves**

E Jakeman, K D Ridley

**Fast Light, Slow Light and Left-Handed Light**

P W Milonni

**Diode Lasers**

D Sands

**Diffractive Optics of Millimetre Waves**

I V Minin, O V Minin

**Handbook of Electroluminescent Materials**

D R Vij

**Handbook of Moire Measurement**

C A Walker

**Next Generation Photovoltaics**

A Martí, A Luque

# An Introduction to Quantum Optics

## Photon and Biphoton Physics

**Yanhua Shih**

*University of Maryland  
Baltimore County, USA*



CRC Press

Taylor & Francis Group  
Boca Raton London New York

---

CRC Press is an imprint of the  
Taylor & Francis Group, an **informa** business

A TAYLOR & FRANCIS BOOK

MATLAB® is a trademark of The MathWorks, Inc. and is used with permission. The MathWorks does not warrant the accuracy of the text or exercises in this book. This book's use or discussion of MATLAB® software or related products does not constitute endorsement or sponsorship by The MathWorks of a particular pedagogical approach or particular use of the MATLAB® software.

Taylor & Francis  
6000 Broken Sound Parkway NW, Suite 300  
Boca Raton, FL 33487-2742

© 2011 by Taylor and Francis Group, LLC  
Taylor & Francis is an Informa business

No claim to original U.S. Government works

Printed in the United States of America on acid-free paper  
10 9 8 7 6 5 4 3 2 1

International Standard Book Number-13: 978-1-4200-1248-4 (Ebook-PDF)

This book contains information obtained from authentic and highly regarded sources. Reasonable efforts have been made to publish reliable data and information, but the author and publisher cannot assume responsibility for the validity of all materials or the consequences of their use. The authors and publishers have attempted to trace the copyright holders of all material reproduced in this publication and apologize to copyright holders if permission to publish in this form has not been obtained. If any copyright material has not been acknowledged please write and let us know so we may rectify in any future reprint.

Except as permitted under U.S. Copyright Law, no part of this book may be reprinted, reproduced, transmitted, or utilized in any form by any electronic, mechanical, or other means, now known or hereafter invented, including photocopying, microfilming, and recording, or in any information storage or retrieval system, without written permission from the publishers.

For permission to photocopy or use material electronically from this work, please access [www.copyright.com](http://www.copyright.com) (<http://www.copyright.com/>) or contact the Copyright Clearance Center, Inc. (CCC), 222 Rosewood Drive, Danvers, MA 01923, 978-750-8400. CCC is a not-for-profit organization that provides licenses and registration for a variety of users. For organizations that have been granted a photocopy license by the CCC, a separate system of payment has been arranged.

**Trademark Notice:** Product or corporate names may be trademarks or registered trademarks, and are used only for identification and explanation without intent to infringe.

Visit the Taylor & Francis Web site at  
<http://www.taylorandfrancis.com>

and the CRC Press Web site at  
<http://www.crcpress.com>

*To my family*



---

# *Contents*

---

|  |           |
|--|-----------|
| Preface.....   | xiii      |
| Acknowledgments .....  | xvii      |
| Author.....  | xix       |
| <br>   |           |
| <b>1. Electromagnetic Wave Theory and Measurement of Light.....</b>                                  | <b>1</b>  |
| 1.1 Electromagnetic Wave Theory of Light.....  | 1         |
| 1.2 Classical Superposition .....  | 4         |
| 1.3 Measurement of Light.....  | 9         |
| 1.4 Intensity of Light: Expectation and Fluctuation .....  | 13        |
| 1.4.1 Chaotic-Thermal Light .....  | 14        |
| 1.4.2 Coherent Light .....   | 15        |
| 1.5 Measurement of Intensity: Ensemble Average<br>and Time Average .....                             | 16        |
| 1.5.1 Unavoidable Time Average Caused by the Finite<br>Response Time of the Measurement Device ..... | 18        |
| 1.5.2 Timely Accumulative Measurement.....   | 20        |
| Summary .....  | 24        |
| Suggested Reading .....  | 24        |
| <br>   |           |
| <b>2. Coherence Property of Light—The State of the Radiation .....</b>                               | <b>25</b> |
| 2.1 Coherence Property of Light .....  | 25        |
| 2.1.1 Incoherent Sub-Source and Incoherent<br>Fourier-Mode: Chaotic Light.....                       | 25        |
| 2.1.2 Coherent Sub-Sources and Coherent Fourier-Modes ...  | 26        |
| 2.1.3 Incoherent Sub-Sources and Coherent<br>Fourier-Modes .....                                     | 27        |
| 2.1.4 Coherent Sub-Sources and Incoherent<br>Fourier-Modes .....                                     | 30        |
| 2.2 Temporal Coherence .....   | 32        |
| 2.3 Spatial Coherence .....  | 34        |
| Summary .....  | 40        |
| Suggested Reading .....  | 40        |
| <br>   |           |
| <b>3. Diffraction and Propagation .....</b>  | <b>41</b> |
| 3.1 Diffraction .....  | 41        |
| 3.2 Field Propagation .....  | 45        |
| Summary .....  | 50        |
| Suggested Reading .....  | 51        |

|   |            |
|---|------------|
| <b>4. Optical Imaging .....</b>   | <b>53</b>  |
| 4.1 A Classic Imaging System .....  | 55         |
| 4.2 Fourier Transform via a Lens .....  | 60         |
| Summary .....   | 61         |
| Suggested Reading .....   | 61         |
| <b>5. First-Order Coherence of Light .....</b>  | <b>63</b>  |
| 5.1 First-Order Temporal Coherence .....  | 67         |
| 5.1.1 $\Gamma(\mathbf{r}_1, t_1; \mathbf{r}_2, t_2)$ : Chaotic-Thermal Light .....  | 67         |
| 5.1.2 $\Gamma(\mathbf{r}_1, t_1; \mathbf{r}_2, t_2)$ : A Large Number of Overlapped and<br>Partially Overlapped Wavepackets ..... | 70         |
| 5.1.3 $\Gamma(\mathbf{r}_1, t_1; \mathbf{r}_2, t_2)$ : A Wavepacket .....   | 72         |
| 5.1.4 $\Gamma(\mathbf{r}_1, t_1; \mathbf{r}_2, t_2)$ : Two Wavepackets .....  | 76         |
| 5.1.5 $\Gamma(\mathbf{r}_1, t_1; \mathbf{r}_2, t_2)$ : CW Laser Radiation .....   | 78         |
| 5.2 First-Order Spatial Coherence .....   | 79         |
| 5.2.1 Chaotic-Thermal Source .....  | 80         |
| 5.2.2 Coherent Radiation Source .....   | 83         |
| Summary .....   | 84         |
| Suggested Reading .....   | 84         |
| <b>6. Second-Order Coherence of Light .....</b>   | <b>85</b>  |
| 6.1 Second-Order Coherence of Coherent Light .....  | 87         |
| 6.2 Second-Order Correlation of Chaotic-Thermal Radiation<br>and the HBT Interferometer .....                                     | 90         |
| 6.2.1 HBT Interferometer I: Second-Order Temporal<br>Coherence .....  | 93         |
| 6.2.2 HBT Interferometer II: Second-Order Spatial<br>Coherence .....  | 97         |
| 6.2.3 HBT Correlation and the Detection-Time Average .....  | 99         |
| 6.3 The Physical Cause of the HBT Phenomenon .....  | 103        |
| 6.4 Near-Field Second-Order Spatial Coherence of Thermal<br>Light .....   | 111        |
| 6.5 Nth-Order Coherence of Light .....  | 115        |
| 6.6 Nth-Order Near-Field Spatial Coherence of Thermal Light .....   | 120        |
| Summary .....   | 122        |
| Appendix 6.A .....  | 123        |
| Suggested Reading .....   | 124        |
| <b>7. Homodyne Detection and Heterodyne Detection of Light .....</b>  | <b>127</b> |
| 7.1 Optical Homodyne and Heterodyne Detection .....   | 127        |
| 7.2 Balanced Homodyne and Heterodyne Detection .....  | 129        |
| 7.3 Balanced Homodyne Detection of Independent and<br>Coupled Thermal Fields .....  | 135        |
| Summary .....   | 138        |
| Suggested Reading .....   | 139        |

|   |            |
|---|------------|
| <b>8. Quantum Theory of Light: Field Quantization and Measurement.....</b>              | <b>141</b> |
| 8.1 The Experimental Foundation—Part I: Blackbody Radiation .....                       | 142        |
| 8.2 The Experimental Foundation—Part II: Photoelectric Effect ...                       | 147        |
| 8.3 The Light Quantum and the Field Quantization .....                                  | 151        |
| 8.4 Photon Number State of Radiation Field .....  | 161        |
| 8.5 Coherent State of Radiation Field .....   | 166        |
| 8.6 Density Operator and Density Matrix .....   | 170        |
| 8.7 Composite System and Two-Photon State of Radiation Field .....                      | 175        |
| 8.8 A Simple Model of Incoherent and Coherent Radiation Source .....                    | 178        |
| 8.9 Pure State and Mixed State .....  | 185        |
| 8.10 Product State, Entangled State, and Mixed State of Photon Pairs .....              | 196        |
| 8.11 Time-Dependent Perturbation Theory.....  | 203        |
| 8.12 Measurement of Light: Photon Counting .....  | 205        |
| 8.13 Measurement of Light: Joint Detection of Photons .....                             | 207        |
| 8.14 Field Propagation in Space-Time .....  | 210        |
| Summary .....   | 214        |
| Suggested Reading .....   | 214        |
| <b>9. Quantum Theory of Optical Coherence.....</b>                                      | <b>217</b> |
| 9.1 Quantum Degree of First-Order Coherence .....                                       | 220        |
| 9.2 Photon and Effective Wavefunction .....   | 233        |
| 9.3 Measurement of the First-Order Coherence or Correlation .....                       | 236        |
| 9.4 Interference between Independent Radiations .....                                   | 239        |
| 9.5 Quantum Degree of Second-Order Coherence .....                                      | 242        |
| 9.6 Two-Photon Interference vs. Statistical Correlation of Intensity Fluctuations ..... | 259        |
| 9.7 Second-Order Spatial Correlation of Thermal Light.....                              | 261        |
| 9.8 Photon Counting and Measurement of $G^{(2)}$ .....                                  | 267        |
| 9.9 Quantum Degree of Nth-Order Coherence .....   | 271        |
| Summary .....   | 272        |
| Suggested Reading .....   | 274        |
| <b>10. Quantum Entanglement .....</b>   | <b>275</b> |
| 10.1 EPR Experiment and EPR State .....   | 276        |
| 10.2 Product State, Entangled State, and Classically Correlated State .....             | 282        |
| 10.2.1 Product State .....  | 282        |

|   |            |
|---|------------|
| 10.2.2 Entangled State.....   | 283        |
| 10.2.3 Classically Correlated State .....   | 284        |
| 10.3 Entangled States in Spin Variables .....   | 284        |
| 10.4 Entangled Biphoton State.....  | 285        |
| 10.5 EPR Correlation of Entangled Biphoton System .....   | 291        |
| 10.6 Subsystem in an Entangled Two-Photon State .....   | 299        |
| 10.7 Biphoton in Dispersive Media .....   | 303        |
| Summary .....   | 307        |
| Suggested Reading .....   | 307        |
| <br>  |            |
| <b>11. Quantum Imaging.....</b>   | <b>309</b> |
| 11.1 Biphoton Imaging.....  | 309        |
| 11.2 Ghost Imaging.....   | 317        |
| 11.3 Ghost Imaging and Uncertainty Relation .....   | 326        |
| 11.4 Thermal Light Ghost Imaging .....  | 334        |
| 11.5 Classical Simulation of Ghost Imaging .....  | 341        |
| 11.6 Turbulence-Free Ghost Imaging .....  | 344        |
| Summary .....   | 347        |
| Suggested Reading .....   | 348        |
| <br>  |            |
| <b>12. Two-Photon Interferometry—I: Biphoton Interference .....</b>                                     | <b>351</b> |
| 12.1 Is Two-Photon Interference the Interference of Two<br>Photons? .....                               | 353        |
| 12.2 Two-Photon Interference with Orthogonal Polarization.....  | 363        |
| 12.3 Franson Interferometer.....  | 367        |
| 12.4 Two-Photon Ghost Interference .....  | 371        |
| 12.5 Delayed Choice Quantum Eraser.....   | 376        |
| Summary .....   | 384        |
| Suggested Reading .....   | 384        |
| <br>  |            |
| <b>13. Two-Photon Interferometry—II: Quantum Interference of<br/>    Chaotic-Thermal Light .....</b>    | <b>387</b> |
| 13.1 Two-Photon Young's Interference.....   | 388        |
| 13.2 Two-Photon Anti-Correlation of Incoherent<br>Chaotic-Thermal Light .....                           | 396        |
| 13.3 Two-Photon Interference with Incoherent Orthogonal<br>Polarized Chaotic-Thermal Light.....         | 408        |
| Summary .....   | 420        |
| Suggested Reading .....   | 420        |
| <br>  |            |
| <b>14. Bell's Theorem and Bell's Inequality Measurement.....</b>  | <b>421</b> |
| 14.1 Hidden Variable Theory and Quantum Calculation for the<br>Measurement of Spin 1/2 Bohm State ..... | 426        |
| 14.2 Bell's Theorem and Bell's Inequality .....   | 429        |

|                                  |            |
|----------------------------------|------------|
| 14.3 Bell States.....            | 434        |
| 14.4 Bell State Preparation..... | 438        |
| Summary .....                    | 446        |
| Suggested Reading .....          | 447        |
| <b>Index .....</b>               | <b>449</b> |



---

## Preface

---

This book is a selected collection of my lecture notes on quantum optics for my PhD thesis students and for an introductory-level graduate course at the University of Maryland.

My students and colleagues encouraged me to publish these lecture notes as a textbook or reference book that might be helpful in understanding the quantum theory of light from a relatively elementary, introductory level. The successful introduction of the concept of photon, or quantum of light, stimulated a new foundation of physics, namely, quantum theory. Today, quantum theory has turned out to be the overarching principle of modern physics. A quotation from John Archibald Wheeler: "It would be difficult to find a single subject among the physical sciences that is not affected in its foundations or in its applications by quantum theory." After a century of wondering, what do we know about the photon itself? The photon is a wave: it has no mass, it travels at the highest speed in the universe, and it interferes with itself. The photon is a particle: it has a well-defined value of momentum and energy, and it even "spins" like a particle. The photon is neither a wave nor a particle, because whichever we think it is, we would have difficulty in explaining the other part of its behavior. The photon is a wave-like particle and/or a particle-like wave: a photon can never be divided into parts, but interference of a single photon can be easily observed in a modern optics laboratory. It seems that a photon passes both paths of an interferometer when interference patterns are observed; however, if the interferometer is set in such a way that its two paths are "distinguishable," the photon "knows" which path to follow and never passes through both paths. Apparently, a photon has to make a choice when facing an interferometer: a choice of "both-path" like a wave or "which-path" like a particle. Surprisingly, the choice is not necessary before passing through the interferometer. It has been experimentally demonstrated that the choice of which path and/or both paths can be delayed until after the photon has passed through the interferometer. More surprisingly, the which-path information can even be "erased" (Scully's quantum eraser) after the annihilation of the photon itself. In light of new technology, many historical *gedankenexperiments* became testable. In the past two decades, we have at least experimentally proved the existence of a biphoton system that behaves exactly as Einstein–Podolsky–Rosen (EPR) expected in 1935. In this biphoton system, the value of the momentum and the position for neither single subsystem is determinate. However, if one of the subsystems is measured with a certain momentum and/or position, the momentum and/or position of the other one is determined with certainty despite the distance between them. More exciting results have come from recent multiphoton interference experiments dealing with "classical"

chaotic-thermal light. Similar nonlocal superpositions between two-photon amplitudes and three-photon amplitudes have been observed in the joint photodetection of chaotic radiation, and the resulting nonlocal point-to-point correlation of a randomly distributed photon pair has been utilized to reproduce turbulence-free “ghost” images.

The behavior of a photon, or a pair of photons, apparently does not follow any of the basic criteria, reality, causality, and locality of our everyday life. From the point of view of quantum theory, however, all of these surprises are predictable and explainable. The nonclassical behaviors of light quanta are the result of quantum interference, involving the superposition of single-photon or multiphoton amplitudes, a nonclassical entity corresponding to different yet indistinguishable alternative ways of producing a photodetection event or a joint-photodetection event. The superposition of quantum amplitudes is a common phenomenon in the quantum world. It occurs between either single-photon amplitudes or multiphoton amplitudes in the measurement of either “quantum light” or “classical light.” Although questions regarding the fundamental issues about the concept of the photon still exist, the quantum theory of light has perhaps had the most influence on quantum mechanics.

This book aims to introduce these and many other exciting developments in quantum optics together with the basic theory and concepts of quantum optics to students and scientists in a simple and straightforward way. Different from most traditional textbooks on this subject, it places more emphasis on the experimental part of the analysis. All fundamental concepts are introduced in the process of analyzing typical experimental measurements and observations. The basic methods of classical and quantum mechanical measurements in quantum optics are explored through the analysis of typical experiments. This attempt is aimed at (1) helping students and young scientists analyze, summarize, and resolve quantum optical problems; and (2) encouraging students and young researchers to be more open minded in looking for the truth and improving their ability in making new discoveries in the field of physics.

In this regard, this book attempts to provide a number of nontraditional interpolations to certain historical and recent experimental discoveries in the field of quantum optics. The readers may find the following differences between this book and other traditional books on this subject: (1) this book introduces the concept of atomic transition and the resulting radiation from the transition as sub-sources and sub-radiations at the very beginning of the classical theory of light. Although no quantization is involved, this attempt is aimed at providing a general physical picture and background to introduce the concept of photon and the quantum theory of light; (2) it attempts to connect the interference phenomenon among a large number of sub-radiations with the concept of a statistical ensemble average in the classical treatment of optical measurements and optical coherence. What is

the physical cause of the measured intensity fluctuations? This book gives a nontraditional but perhaps more reasonable answer; (3) it attempts to distinguish quantum mechanical multiphoton interference from classical statistical correlation of intensity fluctuations. From the point of view of classical theory, the joint detection of two or more photodetectors measures the statistical correlation of intensities. Any nontrivial second order or higher-order correlation of light is caused by the nontrivial correlation of intensity fluctuations. From the point of view of quantum theory, the joint detection of two or more photodetectors measures the probability of jointly having two or more photons contribute to the joint-photodetection event. If more than one multiphoton amplitude contributes to the event, the superposition between these quantum amplitudes results in a multiphoton constructive or destructive interference effect, which may not be considered or explainable in the classical statistical theory of intensity fluctuation correlation. It does not seem difficult to distinguish multiphoton interference from statistical correlation in the measurement of entangled photon pairs. However, it is definitely not easy to appreciate the quantum interference picture in the measurement of “classical” thermal light, even if the measurement is at the single-photon level. This book gives much experimental evidence and theoretical analysis in supporting the viewpoint of quantum mechanics. I hope that this effort will help readers see a general quantum interference picture of light, which perhaps reflects the physical truth behind all optical observations. To this end, the last chapter provides a detailed analysis of Bell’s theorem and Bell’s inequality.

Introducing the basic concepts, tools, and exciting developments of quantum optics to the readers, this book starts from the Maxwell equations, providing a general overview of the optical coherence of light without quantization. However, all concepts and tools are introduced in the process of analyzing the superposition between a large number of the very basic sub-radiations, each created from an atomic transition. After having such a picture in mind, it would be only natural to introduce the concept of field quantization and the concepts and tools of quantum optics based on the principles and rules of quantum mechanics. The similarity and differences between classical and quantum coherence are then analyzed and discussed in detail. The last five chapters contain five different categories of recent research topics in quantum optics and quantum information. I hope not only to introduce these exciting developments to the readers, but also to give them a chance to put into practice the concepts and tools they have learned from this book.

I hope that this book, which has been written to the best of my ability and knowledge, can be of help to students, researchers, and all readers, in general, in their efforts to understand, develop, and advance the field of optical science, which is undergoing tremendous change.

For MATLAB® and Simulink® product information, please contact

The MathWorks, Inc.  
3 Apple Hill Drive  
Natick, MA, 01760-2098 USA  
Tel: 508-647-7000  
Fax: 508-647-7001  
E-mail: [info@mathworks.com](mailto:info@mathworks.com)  
Web: [www.mathworks.com](http://www.mathworks.com)

---

## *Acknowledgments*

---

I would first like to thank my wonderful teachers Carroll O. Alley, David N. Klyshko, Morton H. Rubin, and John A. Wheeler, not only for teaching me physics but also for passing the ethos of physicists to me: seeking for the truth and only the truth. My thanks also go to my students, postdocs, and coworkers for their impressive experimental and theoretical research works, which have provided great support to this book. At the same time, my apologies to them for not having cited their research findings due to limited space and time. Only those experiments and theories that directly support the contents and discussion points have been selected. I would also like to apologize to all other researchers in the field of quantum optics, for not using or citing their works. Finally, I would like to thank Ling-An Wu, Jason Simon, and Liang Shih for helping me with language issues.



---

## *Author*

---

**Yanhua Shih**, professor of physics, received his PhD in 1987 from the Department of Physics, University of Maryland, College Park. He started the Quantum Optics Laboratory at the University of Maryland Baltimore County (UMBC) in the fall of 1989. His group has been recognized as one of those leading in the field of quantum optics that attempts to probe the foundations of quantum theory. His pioneering researches on multiphoton entanglement, multiphoton interferometry, and quantum imaging have been highly appreciated by the physics and engineering community, and attracted a great deal of attention.



# 1

---

## *Electromagnetic Wave Theory and Measurement of Light*

---

### 1.1 Electromagnetic Wave Theory of Light

To introduce the basic concepts on the coherence property of light, we begin with the Maxwell equations—the foundation of the classical electromagnetic (EM) wave theory of light. The set of four Maxwell equations forms the basis of the theory for classical electromagnetic phenomena and electromagnetic wave phenomena. In free space, the Maxwell equations have the form

$$\nabla \times \mathbf{E} = -\frac{\partial \mathbf{B}}{\partial t}, \quad (1.1)$$

$$\nabla \times \mathbf{H} = \frac{\partial \mathbf{D}}{\partial t}, \quad (1.2)$$

$$\nabla \cdot \mathbf{D} = 0, \quad (1.3)$$

$$\nabla \cdot \mathbf{B} = 0, \quad (1.4)$$

where

$\mathbf{E}$  and  $\mathbf{H}$  are the electric and magnetic field vectors

$\mathbf{D}$  and  $\mathbf{B}$  are the electric displacement and magnetic induction vectors, respectively

We also have the relations

$$\begin{aligned} \mathbf{D} &= \epsilon_0 \mathbf{E}, \\ \mathbf{B} &= \mu_0 \mathbf{H}, \end{aligned} \quad (1.5)$$

where  $\epsilon_0$  and  $\mu_0$  are the free-space electric permittivity and magnetic permeability, respectively.

Taking the curl of Equation 1.1, using Equations 1.2, 1.3, 1.5, as well as the identity

$$\nabla \times \nabla \times \mathbf{E} = \nabla(\nabla \cdot \mathbf{E}) - \nabla^2 \mathbf{E}, \quad (1.6)$$

the electric field vector  $\mathbf{E}(\mathbf{r}, t)$  can be shown to satisfy the wave equation

$$\nabla^2 \mathbf{E} - \frac{1}{c^2} \frac{\partial^2 \mathbf{E}}{\partial t^2} = 0. \quad (1.7)$$

Similarly, the magnetic field vector  $\mathbf{H}(\mathbf{r}, t)$ , or the magnetic induction vector  $\mathbf{B}(\mathbf{r}, t)$ , can be shown to satisfy the same wave equation

$$\nabla^2 \mathbf{H} - \frac{1}{c^2} \frac{\partial^2 \mathbf{H}}{\partial t^2} = 0 \quad (1.8)$$

where  $c \equiv 1/\sqrt{\epsilon_0 \mu_0}$  is the speed of light in free space.

Equations 1.7 and 1.8 both contain the basic wave equation structure (for a variable  $v$ ):

$$\nabla^2 v - \frac{1}{c^2} \frac{\partial^2 v}{\partial t^2} = 0. \quad (1.9)$$

Now, suppose  $v(\mathbf{r}, t)$  has a Fourier integral representation

$$v(\mathbf{r}, t) = \int_{-\infty}^{\infty} d\omega v(\mathbf{r}, \omega) e^{-i\omega t} \quad (1.10)$$

with the inverse transform

$$v(\mathbf{r}, \omega) = \frac{1}{2\pi} \int_{-\infty}^{\infty} dt v(\mathbf{r}, t) e^{i\omega t}. \quad (1.11)$$

Substituting Equation 1.10 into Equation 1.9, it is straightforward to find that the Fourier transform  $v(\mathbf{r}, \omega)$  also satisfies the Helmholtz wave equation

$$\nabla^2 v(\mathbf{r}, \omega) + k^2 v(\mathbf{r}, \omega) = 0 \quad (1.12)$$

where  $k = \omega/c$  is the wave number. The wave number takes either a set of discrete or continuous values determined by the boundary conditions. Equation 1.12 has well-known plane-wave solutions

$$v_k(\mathbf{r}) = v_k e^{i\mathbf{k} \cdot \mathbf{r}} \quad (1.13)$$

and thus we have

$$v_k(\mathbf{r}, t) = v_k e^{-i(\omega t - \mathbf{k} \cdot \mathbf{r})} + \text{c.c.} \quad (1.14)$$

where

$v_k$  is the complex amplitude associated with mode  $\mathbf{k}$

c.c. stands for the complex conjugate

To simplify the mathematics, we will neglect writing c.c. in the following discussions unless otherwise specified.

Due to the linear nature of the differential equation, any linear superposition of the plane-wave is also a solution of Equation 1.9. Therefore, we can, in principle, find a set of transforms of  $v_k(\mathbf{r}, t)$  for the wave function  $v(\mathbf{r}, t)$ . This property may be considered as the “classical superposition principle.”

With the convention that the physical fields are the real parts of the complex solutions, we may write the plane-wave electric and magnetic fields in the form

$$\begin{aligned}\mathbf{E}(\mathbf{r}, t) &= \mathbf{E} e^{-i(\omega t - \mathbf{k} \cdot \mathbf{r})} \\ \mathbf{H}(\mathbf{r}, t) &= \mathbf{H} e^{-i(\omega t - \mathbf{k} \cdot \mathbf{r})},\end{aligned}\tag{1.15}$$

where  $\mathbf{E}$  and  $\mathbf{H}$  are vectors that are constant in space-time, usually named field strengths.

To satisfy the divergence equations (Equations 1.3 and 1.4) of the Maxwell equations requires that both the  $\mathbf{E}$  and  $\mathbf{H}$  vector fields be purely transverse, i.e., perpendicular to the wavevector  $\mathbf{k}$ . The curl equations (Equations 1.1 and 1.2) require even further restrictions on the  $\mathbf{E}$  and  $\mathbf{H}$  vector fields: (1)  $\mathbf{E} \perp \mathbf{H}$ ; (2) in free space,  $\mathbf{E}$  and  $\mathbf{H}$  are in phase at all points of space-time, with their magnitudes related by  $|\mathbf{E}| = \sqrt{\mu_0/\epsilon_0}|\mathbf{H}|$ .

It is then useful to define a set of orthogonal unit vectors  $(\hat{\mathbf{e}}_1, \hat{\mathbf{e}}_2, \hat{\mathbf{k}})$  and rewrite the field strengths as

$$\mathbf{E} = \hat{\mathbf{e}}_1 E_0, \quad \mathbf{H} = \hat{\mathbf{e}}_2 \sqrt{\frac{\epsilon_0}{\mu_0}} E_0\tag{1.16}$$

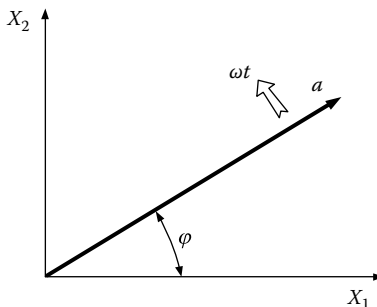
or

$$\mathbf{E} = \hat{\mathbf{e}}_2 E'_0, \quad \mathbf{H} = -\hat{\mathbf{e}}_1 \sqrt{\frac{\epsilon_0}{\mu_0}} E'_0,\tag{1.17}$$

where  $E_0$  and  $E'_0$  are complex constants. It is easy to see that there are two independent polarization directions of  $\hat{\mathbf{e}}_1$  and  $\hat{\mathbf{e}}_2$  for the plane-wave field of frequency  $(\omega, \mathbf{k})$ . In certain types of problems, it is convenient to write the field strength  $E_0$  as a product of the amplitude  $a$  and phase term  $e^{i\phi}$ , or as quadratures in the complex amplitude plane:

$$\begin{aligned}E_0 &= a e^{i\phi} \\ &= a \cos \phi + i a \sin \phi,\end{aligned}\tag{1.18}$$

where the amplitude  $a$  is real and positive. The physical picture of the amplitude-phase-quadrature concept is schematically shown in Figure 1.1. It is interesting to see that the plane-wave solution of the electromagnetic field corresponds to a classical harmonic oscillator.

**FIGURE 1.1**

A harmonic oscillator picture of a plane-wave solution with frequency  $\omega$ . The real and positive amplitude  $a$  rotates at angular speed  $\omega$  starting from initial phase  $\varphi$ . The  $X_1$ - and  $X_2$ -axes indicate the two quadratures.

## 1.2 Classical Superposition

Since the electromagnetic wave equation is a linear differential equation, it is elementary to draw the following two corollaries:

1. If each  $\mathbf{E}_j(\mathbf{r}, t)$  is a solution of the wave equation, then the linear superposition

$$\mathbf{E}(\mathbf{r}, t) = \sum_j \mathbf{E}_j(\mathbf{r}, t) \quad (1.19)$$

is also a solution of the wave equation. We may refer to Equation 1.19 as the principle of classical superposition. A wide range of optical coherent phenomena can be formulated in the form of Equation 1.19. As a simple example, we consider a radiation source that contains a large number of independent sub-sources. If each sub-source gives rise to a subfield  $\mathbf{E}_j(\mathbf{r}, t)$  at space-time point  $(\mathbf{r}, t)$ , the measured field  $\mathbf{E}(\mathbf{r}, t)$  must be the result of the superposition of all the subfields.

2. It is possible, in principle, to decompose a radiation field  $\mathbf{E}(\mathbf{r}, t)$  into an appropriate linear superposition of a set of solutions of the wave equation. This is from a different approach, or a different view point, to define the classical superposition. For example, we may find a set of plane waves to write the field  $\mathbf{E}(\mathbf{r}, t)$  as the following superposition:

$$\mathbf{E}(\mathbf{r}, t) = \sum_{\mathbf{k}} \hat{\mathbf{e}}_{\mathbf{k}} E(\mathbf{k}) e^{-i(\omega t - \mathbf{k} \cdot \mathbf{r})} \quad (1.20)$$

or

$$\mathbf{E}(\mathbf{r}, t) = \int d\mathbf{k} \hat{\mathbf{e}}_{\mathbf{k}} E(\mathbf{k}) e^{-i(\omega t - \mathbf{k} \cdot \mathbf{r})}. \quad (1.21)$$

Note, as we have discussed in Section 1.1, there are two independent polarizations of  $\hat{\mathbf{e}}_{\mathbf{k}}$  for each plane-wave solution of  $\mathbf{k}$ . A coherent superposition of the two independent polarizations results in a polarized field (vector), otherwise, the field is unpolarized with a random relationship between the two independent polarizations. We will focus our attention onto one of the polarization of the field in the following discussions unless otherwise specified. The polarization state of the field will be discussed in Chapters 12 through 14.

To further simplify the mathematics, we consider a 1D approximation of Equation 1.21 and focus our discussion on the longitudinal behavior of the field along one selected propagation direction. Our goal is to learn the temporal behavior of the field through the measurement at a point photodetector. For a point radiation source, in the far-field approximation, the field can be written as

$$E(r, t) = \int_0^{\infty} d\omega E(\omega) e^{-i[\omega t - k(\omega)r]} \quad (1.22)$$

where

$r$  is the distance between the point source and the point of observation

$E(\omega) = a(\omega)e^{i\varphi(\omega)}$  is the complex spectrum amplitude density (or spectrum amplitude for short) for the plane-wave mode of frequency  $\omega$

The dispersion relation  $k = k(\omega)$  allows us to express the wave number through the frequency detuning  $\nu$ ,

$$\omega \equiv \omega_0 + \nu.$$

Therefore, Equation 1.22 can be formally integrated:

$$\begin{aligned} E(r, t) &= e^{-i[\omega_0 t - k(\omega_0)r]} \int_{-\infty}^{\infty} d\nu E(\nu) e^{-i\nu\tau} \\ &= e^{-i[\omega_0 t - k(\omega_0)r]} \mathcal{F}_\tau \{E(\nu)\} \end{aligned} \quad (1.23)$$

where  $\mathcal{F}_\tau \{E(\nu)\}$  is the Fourier transform of the complex spectrum amplitude  $E(\nu)$ . In Equation 1.23, a first order approximation in dispersion has been applied:

$$k(\omega) \simeq k(\omega_0) + \frac{dk}{d\omega} \Big|_{\omega_0} \nu.$$

We have also defined

$$\tau \equiv t - \frac{r}{u(\omega_0)}$$

where the inverse of the first order dispersion

$$u(\omega_0) = \frac{1}{\left. \frac{dk}{d\omega} \right|_{\omega_0}}$$

is named the group velocity of the wavepacket if there exists a wavepacket. In a vacuum, the phase speed of the carrier frequency and the group speed of the wavepacket (envelope) are both equal to  $c$ ,

$$\frac{\omega}{k} = \frac{d\omega}{dk} = c,$$

since  $\omega = kc$ . Equation 1.23 is then simplified to

$$E(r, t) = e^{-i\omega_0\tau} \mathcal{F}_\tau \{E(v)\} \quad (1.24)$$

where  $\tau \equiv t - r/c$ . In most of the following discussions, we will assume light propagates in a vacuum and use the simplified notation of Equation 1.24.

The field  $E(r, t)$  is now formally written in terms of the Fourier transform of  $E(\omega)$  in Equation 1.24. The resulting function of the Fourier integral  $\mathcal{F}_\tau \{E(\omega)\}$  is determined by the complex spectrum amplitude  $E(\omega) = a(\omega)e^{i\varphi(\omega)}$ . Both the real-positive amplitude  $a(\omega)$  and the phase  $\varphi(\omega)$  play important roles. If  $a(\omega)$  and  $\varphi(\omega)$  are well-defined functions of  $\omega$ , the resulting field  $E(r, t)$  will be a well-defined function of space-time, and vice versa. On the other hand, if  $a(\omega)$  and/or  $\varphi(\omega)$  vary rapidly and randomly from time to time, no deterministic function of  $E(r, t)$  is expected.

In classical optics, both  $a(\omega)$  and  $\varphi(\omega)$  can be simultaneously defined precisely. Consequently,  $E(r, t)$  will also be a precisely defined function in space-time. The uncertainty relation between  $\Delta a(\omega)$  and  $\Delta\varphi(\omega)$  is not the subject of this chapter. In the following discussions, we will assume a well-defined distribution function of  $a(\omega)$  and give freedom to the phase  $\varphi(\omega)$ . The variations or uncertainties of the phase  $\varphi(\omega)$  will determine the coherent property of the radiation.

We discuss two cases in the following: (I) coherent superposition and (II) incoherent superposition.

Case (I): Coherent superposition

1.  $\varphi(\omega) = \varphi_0 = \text{constant}$

With a constant phase of  $\varphi(\omega) = \varphi_0$ , if  $a(v)$  is a well-defined function of the detuning frequency  $v$  then the Fourier integral of Equation 1.23 defines a wavepacket in space-time given by

$$E(r, t) = e^{-i[\omega_0 t - k(\omega_0)r - \varphi_0]} \mathcal{F}_\tau \{a(v)\}. \quad (1.25)$$

The envelope of the wavepacket, which is the Fourier transform of the spectrum amplitude  $a(\nu)$ , propagates with group velocity  $u(\omega_0)$ . When the wavepacket is centered at  $t = 0, r = 0$ , all its superposed plane waves, each defined as a “Fourier-mode,” exhibit a common initial phase  $\varphi_0$ . Under the envelope is the carrier harmonic wave of frequency  $\omega_0$ , which propagates at phase velocity  $\omega_0/k(\omega_0)$ . In vacuum, the phase velocity and group velocity have the same value of  $c$ . The group velocity, however, could be quite different from the phase velocity in dispersive media. In a dispersive medium, each plane-wave mode of  $\omega$  may have different phase velocities depending on the dispersion of the medium. In special circumstances, the superposition of these modes results in an interesting effect wherein the group velocity could be greater than the phase velocity or greater than  $c$ , even if all the phase velocities of the modes are less than  $c$ . The value of the group velocity, whether less than or greater than the phase velocity, is determined by the first order dispersion of the medium. The wavepacket defined in Equation 1.25 is the result of a coherent superposition of the electromagnetic field.

For certain amplitude distribution functions of  $a(\nu)$ , the Fourier integral in Equation 1.23 can be easily evaluated. For example, a Gaussian distribution function in terms of the detuning frequency  $\nu$

$$E(\nu) = E_0 e^{-\sigma^2 \nu^2} e^{i\varphi_0}, \quad (1.26)$$

where  $\sigma$  is a constant, results in a Gaussian wavepacket in space-time:

$$E(r, t) = E_0 e^{-t^2/4\sigma^2} e^{-i[\omega_0 t - k(\omega_0)r - \varphi_0]} \quad (1.27)$$

where all constants have been absorbed into  $E_0$ . Figure 1.2 illustrates a classical Gaussian wavepacket. The wavepacket has a well-defined envelope, which propagates with group velocity  $u(\omega_0)$ . Under the envelope is the carrier wave of frequency  $\omega_0$ , which propagates at phase velocity  $\omega_0/k(\omega_0)$ .

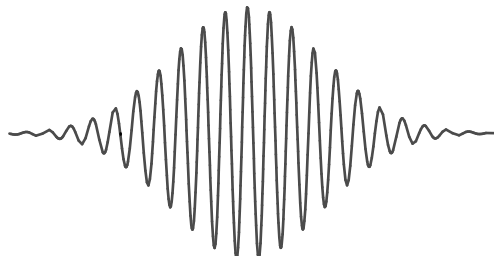


**FIGURE 1.2**

Schematic of a Gaussian wavepacket. The envelope of the wavepacket propagates with group velocity  $u(\omega_0)$ . Under the envelope is the carrier wave of frequency  $\omega_0$ . The carrier propagates with phase velocity  $\omega_0/k(\omega_0)$ . When the wavepacket is centered at  $t = 0, r = 0$ , all its “Fourier-modes” exhibit a common initial phase  $\varphi(\omega) = \varphi_0$ .

Another useful example is for a constant distribution

$$E(\nu) = E_0 e^{i\varphi_0}, \quad (1.28)$$

where  $E_0$  is a constant. The envelope of the wavepacket in space-time turns to be a  $\delta$ -function

$$\mathcal{F}_\tau\{E(\nu)\} = E_0 \delta(\tau), \quad (1.29)$$

where, again, all constants have been absorbed into  $E_0$ . In reality, we may assume a constant  $E(\nu)$  within a certain bandwidth  $\Delta\nu$

$$E(\nu) = \begin{cases} E_0 & -\Delta\nu/2 \leq \nu \leq \Delta\nu/2 \\ 0 & \text{otherwise.} \end{cases}$$

In this case, the Fourier transform gives a sinc-function, which is defined as  $\text{sinc}(x) \equiv \sin(x)/x$ ,

$$E(r, t) = E_0 \text{sinc}\left(\frac{\Delta\nu \tau}{2}\right) e^{-i[\omega_0 t - k(\omega_0)r - \varphi_0]}. \quad (1.30)$$

## 2. $\varphi(\omega) = \omega t_0$ with $t_0 = \text{constant}$

With  $\varphi(\omega) = \omega t_0$ , if  $a(\nu)$  is a well-defined function of the detuning frequency  $\nu$ , the Fourier integral of Equation 1.23 also defines a wavepacket in space-time:

$$E(r, t) = e^{-i[\omega_0(t-t_0) - k(\omega_0)r]} \mathcal{F}_{(\tau-t_0)}\{a(\nu)\}. \quad (1.31)$$

This wavepacket is the same as that of Equation 1.25 except all its Fourier-modes exhibit a common initial phase  $\varphi_0=0$  when the wavepacket is centered at  $t=t_0$ ,  $r=0$ . This wavepacket is the result of a superposition among a set of Fourier-modes that are excited coherently by the source at time  $t = t_0$ . We will have more discussions about this wavepacket in Section 1.4.

Case (II): Incoherent superposition,  $\varphi(\omega) = \text{random number}$

The phases of the complex spectral amplitude are completely random. There is no defined phase relationship between different harmonic modes. The Fourier transform of Equation 1.23 consequently results in a random function even if the real-positive amplitude  $a(\omega)$  may have a well defined distribution. In this situation we may model each Fourier component or each plane-wave mode of  $\omega$  as an independent harmonic oscillator. Light with this characteristic belongs to the category of chaotic-thermal radiation. These kinds of radiations, usually named Gaussian light, are produced from stochastic processes with complete randomly distributions in phase space. Thermal light is a typical example, except it has a well-defined Planck distribution in terms of its spectrum, or amplitude  $a(\omega)$ . We will follow the tradition to call these kinds of light as chaotic-thermal light.

In the above discussion, we have treated the field  $E(r, t)$  as a superposition of a large number of chaotic or coherent harmonic modes. This superposition determines the properties of the field. Mathematically, the space-time function of  $E(r, t)$  is the Fourier transform of  $E(\omega)$  and vice versa. The physics behind the mathematics is the classical EM wave theory of light.

Now we consider a more complicated superposition, which involves a large number of sub-sources. Assume the field  $E(r, t)$  is created by the excitation of a large number of sub-sources, such as trillions of atomic transitions, of a distant point star. The resultant field can be modeled as the superposition of subfields in terms of the sub-sources and their harmonic modes of frequency  $\omega$ :

$$E(r, t) = \sum_{\omega} \sum_{j=1}^N a_j(\omega) e^{i\varphi_j(\omega)} e^{-i[\omega t - k(\omega)r]}, \quad (1.32)$$

where the real-positive amplitude  $a_j$  and the phase  $\varphi_j$  belong to the  $j$ th sub-source. The formally integrated electric field of Equation 1.32 is thus

$$\begin{aligned} E(r, t) &\cong e^{-i[\omega_0 t - k(\omega_0)r]} \int_{-\infty}^{\infty} dv \left( \sum_{j=1}^N a_j(v) e^{i\varphi_j(v)} \right) e^{-iv\tau} \\ &= e^{-i[\omega_0 t - k(\omega_0)r]} \mathcal{F}_{\tau} \left\{ \sum_{j=1}^N a_j(v) e^{i\varphi_j(v)} \right\}. \end{aligned} \quad (1.33)$$

The space-time property of the field  $E(r, t)$  is clearly related to the amplitudes and phases of the sub-sources and the harmonic modes under the Fourier integral, namely, the Fourier-modes. The coherent property of light is thus determined by two mechanisms: (1) the coherent or incoherent superposition of the subfields radiated from the sub-sources and (2) the coherent or incoherent superposition of the Fourier-modes.

In summary, the physics behind all of the above discussions is the Maxwell EM wave theory of light. Mathematically, the electromagnetic wave equation is a linear differential equation. If each  $E_j(r, t)$  is a solution of the wave equation, the linear superposition of  $E(r, t) = \sum_j E_j(r, t)$  is also a solution. It is worth noticing that the superposition, or the interference, of the subfields, must physically occur at a given space-time point. In the framework of Maxwell EM wave theory of light, the fields can never be superposed nonlocally at different space-time points.

### 1.3 Measurement of Light

The field  $E(r, t)$  is not the physical quantity directly measurable by a photodetector. Roughly speaking, a photoelectron event involves the annihilation of

a photon and the release of a photoelectron contributing to the output current of a photodetector. The output current of the photodetector is proportional to the energy carried by the annihilated photons per unit time. The detailed quantum process of photodetection and the quantization of the electromagnetic field will be discussed in Chapter 8. Classically, the photoelectron current of a photodetector measures the intensity of light, which is defined as the amount of energy crossing a unit area per unit of time, and is given by the Poynting vector of the electromagnetic field

$$\mathbf{S} = \frac{1}{\mu_0} \mathbf{E} \times \mathbf{B},$$

where  $\mathbf{E}$  and  $\mathbf{B}$  are the electric and magnetic fields (real functions). At optical frequencies, the Poynting vector is an extremely rapid varying function of time, twice as rapid as the field. Unfortunately, there is no photodetector that is able to resolve these fast vibrations (on the order of  $10^{-15}$  s). This suggests that at least practically, a time average is occurring in the process of photodetection. The photocurrent is a measure of the magnitude of the cycle-averaged Poynting vector. Thus, we define the “instantaneous” intensity, or simply the intensity, of light as

$$I(\mathbf{r}, t) = \frac{\epsilon_0 c}{2} |\mathbf{E}(\mathbf{r}, t)|^2, \quad (1.34)$$

where we have considered the effect that  $\mathbf{B}$  is at right angles to  $\mathbf{E}$ . The “cycle-average theorem” is also applied:

$$\overline{[Re \mathbf{E}(\mathbf{r}, t)]^2} = \frac{1}{2} Re |\mathbf{E}(\mathbf{r}, t)|^2. \quad (1.35)$$

For convenience, we will absorb the constant  $\epsilon_0 c / 2$  of Equation 1.34 into the field, except for certain necessary quantitative discussions.

In the case of far-field measurements for a point radiation source, substituting Equation 1.22 into Equation 1.34, the intensity of the radiation can be written as

$$I(r, t) = \iint d\omega d\omega' E^*(\omega) E(\omega') e^{-i[(\omega' - \omega)t - (k' - k)r]}. \quad (1.36)$$

Using the formally integrated result of Equation 1.23, Equation 1.36 can be written as the modular square of the Fourier transform of the fields

$$I(r, t) = |\mathcal{F}_\tau \{E(v)\}|^2, \quad (1.37)$$

where  $E(v) = a(v) e^{i\varphi(v)}$  is the complex spectrum amplitude. Thus, if the Fourier transform of the complex spectrum amplitude is a well-defined

wavepacket in space-time, the instantaneous intensity will be a well-defined pulse in space-time. For example, the intensity of a Gaussian wavepacket in the form of Equation 1.27 is a well-defined Gaussian pulse in space-time:

$$I(r, t) = I_0 e^{-\tau^2/2\sigma^2}.$$

It is interesting to see that the intensity follows the “slow” envelope function of the wavepacket; however it loses the high-frequency harmonic modulation in the “cycle-average” of Equation 1.35.

In the case of multi-sub-sources, substituting Equation 1.33 into Equation 1.34, the intensity of the formally integrated field of Equation 1.33 is thus

$$I(r, t) = \int d\omega d\omega' \left\{ \sum_{j,k} a_j(\omega) a_k(\omega') e^{i[\varphi_j(\omega) - \varphi_k(\omega')]} \right\} e^{i(\omega - \omega')\tau}. \quad (1.38)$$

Equation 1.38 can be formally integrated

$$I(r, t) = \left| \mathcal{F}_\tau \left\{ \sum_{j=1}^N a_j(v) e^{i\varphi_j(v)} \right\} \right|^2. \quad (1.39)$$

Now we examine the formally integrated intensity in detail. We will first examine the simple case of a single-sub-source, i.e., Equation 1.36 or Equation 1.37 and then examine Equation 1.38 or Equation 1.39 for multi-sub-sources.

### Case (I): Single-sub-source

In the case of a single-sub-source, Equation 1.36 can be separated into two integrals:

$$I(r, t) = \int_{\omega=\omega'} d\omega |E(\omega)|^2 + \int_{\omega \neq \omega'} d\omega d\omega' E^*(\omega) E(\omega') e^{i(\omega-\omega')\tau} \quad (1.40)$$

where  $E(\omega) = a(\omega)e^{-i\varphi(\omega)}$ . The first integral contributes a constant to the intensity. The second integral, which contains all “cross terms” among different modes, is the contribution to interference. The interference term may contribute significantly or trivially, depending on the coherent property of light. If  $\varphi(\omega)$  is a constant, i.e., the Fourier-modes superpose coherently, the interference term will be the dominant part; however, if  $\varphi(\omega)$  takes random values, i.e., the Fourier-modes superpose incoherently, the interference term will contribute trivially due to destructive interference. The second term in Equation 1.40 may vanish completely if  $\varphi_j(\omega) - \varphi_k(\omega')$  takes *all possible values*

in the integral. In reality, the phase factor of  $\varphi_j(\omega) - \varphi_k(\omega')$  may not take *all possible values* and the interference cancellation may not be complete. This term will have a random value from time to time in a nondeterministic manner. In this situation, the integral contributes to variations in the intensity  $\delta I$ . The relative contribution between the two integrals in Equation 1.40 can be roughly estimated. Suppose we have  $N$  modes in terms of  $\omega$  and all modes contribute to the observation. It is easy to see that the first sum contributes  $N$  terms while the second sum contributes  $N^2$  terms. If each term in the summation has roughly the same contribution, then for a large number of  $N$ , the difference between  $N$  and  $N^2$  is significant when there is no destructive interference cancellation in the superposition.

### Case (II): Multi-sub-sources

In the case of multi-sub-sources, we may rewrite Equations 1.38 and 1.39 into four groups:

$$\begin{aligned} I(r, t) = & \int_{\omega=\omega'} d\omega \sum_{j=k} a_j^2(\omega) + \int_{\omega=\omega'} d\omega \left\{ \sum_{j \neq k} a_j(\omega) a_k(\omega) e^{i[\varphi_j(\omega) - \varphi_k(\omega)]} \right\} \\ & + \int_{\omega \neq \omega'} d\omega d\omega' \left\{ \sum_{j=k} a_j(\omega) a_j(\omega') e^{i[\varphi_j(\omega) - \varphi_j(\omega')]} \right\} e^{i(\omega - \omega')\tau} \\ & + \int_{\omega \neq \omega'} d\omega d\omega' \left\{ \sum_{j \neq k} a_j(\omega) a_k(\omega') e^{i[\varphi_j(\omega) - \varphi_k(\omega')]} \right\} e^{i(\omega - \omega')\tau}. \end{aligned} \quad (1.41)$$

The first integral contributes a constant. The second integral is interesting. It will be a nonzero constant if all the sub-sources radiate coherently with a constant phase  $\varphi_j(\omega)$ . In the case of chaotic-thermal radiation, this term may vanish if  $\varphi_j(\omega) - \varphi_k(\omega')$  takes *all possible values*. In reality, the phase factor of  $\varphi_j(\omega) - \varphi_k(\omega')$  may not take *all possible values* and the interference cancellation may not be complete. This term will take a random value from time to time in a nondeterministic manner, and will contribute to the variations of the intensity  $\delta I$ . Similarly, the contribution of the third and the fourth integral are determined by the coherent or incoherent nature of the superposition, see detailed discussions in next section. Let us estimate the relative magnitude of the four terms in Equation 1.41. Suppose there are  $M$  sub-sources and  $N$  modes of  $\omega$  in the superposition and all contribute to the measurement. The first sum contributes  $M \cdot N$  terms, the second contributes  $M^2 \cdot N$  terms, the third contributes  $M \cdot N^2$  terms, and the fourth contributes  $M^2 \cdot N^2$  terms. If each term in the sums has roughly the same contribution without interference cancellation, for a large number of  $M$  and  $N$  the differences between the first sum and the other three sums are significant. Therefore, if in any way we can obtain coherent radiation from the sub-sources and/or

the Fourier-modes; constructive interference of the second, third, and fourth terms of the superposition will enhance the instantaneous intensity,  $I(r, t)$ , by many orders of magnitude compared with that of chaotic-thermal radiation.

---

## 1.4 Intensity of Light: Expectation and Fluctuation

In the classical EM wave theory of light, the expectation value of intensity at a space-time coordinate is calculated from Equation 1.41 by *taking into account all possible realizations of the field in the superposition in terms of the complex amplitudes of the sub-sources and the Fourier-modes*. In general, we define the expectation value of intensity as

$$\langle I(\mathbf{r}, t) \rangle = \left\langle |E(\mathbf{r}, t)|^2 \right\rangle = \left\langle \sum_j E_j^*(\mathbf{r}, t) \sum_k E_k(\mathbf{r}, t) \right\rangle, \quad (1.42)$$

where  $j$  and  $k$  label the  $j$ th and  $k$ th subfields within the superposition. The notation  $\langle \dots \rangle$ , which is adapted from statistics, denotes the mathematical expectation of the measurement. In the probability theory, the expectation value of a measurement equals the mean value of an ensemble measurement. It is not difficult to show the result of *taking into account all possible realizations of the field* is equivalent to an ensemble average. The expectation value  $\langle I(\mathbf{r}, t) \rangle$  is a number that depends on the space-time coordinates of the measurement event. To emphasize the dependence or independence as either a nontrivial distribution or a constant distribution of space-time coordinates,  $\langle I(\mathbf{r}, t) \rangle$  is also called expectation function.

A single measurement of intensity at a space-time point yields the expectation value, if and only if the measured subfields take *all possible values* of their complex amplitudes in the superposition. Realistically, the subfields may not be able to take *all possible realizations* in a measurement and therefore the measured intensity at a space-time coordinate or the observed intensity as a function of space-time,  $I(\mathbf{r}, t)$ , may differ from  $\langle I(\mathbf{r}, t) \rangle$ . We may write  $I(\mathbf{r}, t)$  into the sum of its expectation value or function  $\langle I(\mathbf{r}, t) \rangle$  and its variation  $\delta I(\mathbf{r}, t)$

$$I(\mathbf{r}, t) = \langle I(\mathbf{r}, t) \rangle + \delta I(\mathbf{r}, t). \quad (1.43)$$

In our simplified model of the radiation source, the expectation value or expectation function of the intensity  $I(r, t)$  is then calculated from

$$\langle I(r, t) \rangle = \left\langle \int d\omega d\omega' \sum_{j,k} a_j(\omega) a_k(\omega') e^{i[\varphi_j(\omega) - \varphi_k(\omega')] \tau} e^{i(\omega - \omega')\tau} \right\rangle, \quad (1.44)$$

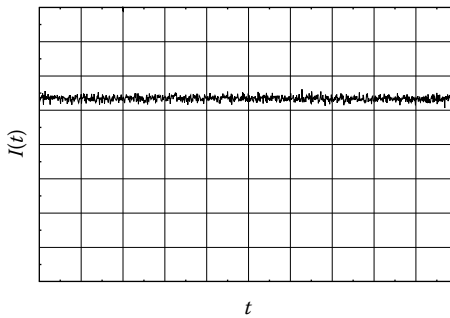
by taking into account all possible values of the complex amplitudes ( $a$  and  $\varphi$ ) in terms of the sub-sources as well as the Fourier-modes. Following Equation 1.41, Equation 1.44 can be rewritten into four terms:

$$\begin{aligned} \langle I(r, t) \rangle = & \left\langle \int_{\omega=\omega'} d\omega \sum_{j=k} a_j^2(\omega) \right\rangle + \left\langle \int_{\omega=\omega'} d\omega \left\{ \sum_{j \neq k} a_j(\omega) a_k(\omega) e^{i[\varphi_j(\omega) - \varphi_k(\omega)]} \right\} \right\rangle \\ & + \left\langle \int_{\omega \neq \omega'} d\omega d\omega' \left\{ \sum_{j=k} a_j(\omega) a_j(\omega') e^{i[\varphi_j(\omega) - \varphi_j(\omega')]} \right\} e^{i(\omega - \omega')\tau} \right\rangle \\ & + \left\langle \int_{\omega \neq \omega'} d\omega d\omega' \left\{ \sum_{j \neq k} a_j(\omega) a_k(\omega') e^{i[\varphi_j(\omega) - \varphi_k(\omega')]} \right\} e^{i(\omega - \omega')\tau} \right\rangle. \quad (1.45) \end{aligned}$$

The first term of Equation 1.45 contributes a constant value to  $\langle I(r, t) \rangle$ . The other three terms may have a zero or a nonzero contribution depending on how the subfields achieve their superposition. It is easy to see that the phase  $\varphi$  will play an extremely important role. In the following, we analyze two extreme cases: (1) randomly distributed  $\varphi_j(\omega) - \varphi_k(\omega')$  and (2) a constant  $\varphi_j(\omega) - \varphi_k(\omega')$ . The subfields are superposed incoherently in case (1) but coherently in case (2). In modern language, we usually divide light into roughly two categories: incoherent and coherent. A discharge tube radiates incoherent light and a laser beam is considered as coherent. Either incoherent or coherent, the property of light is determined intrinsically by the radiation source. The subfields are emitted incoherently in a chaotic-thermal radiation source and coherently in a coherent radiation source.

#### 1.4.1 Chaotic-Thermal Light

In the early days, the only light sources available for optical observations and measurements were thermal light that is prepared in the stochastic process of radiation. A thermal source contains a large number of independent sub-sources, such as trillions of atoms or molecules. Either identical or different, these atomic transitions, or sub-sources, emit light independently and randomly. Each individual emitter may radiate light into any or all physically allowable states from time to time. If the subfields take all possible complex amplitudes in their superposition, the contributions of the second, the third, and the fourth terms in Equation 1.45 are all negligible due to the interference cancellation.  $\langle I(t) \rangle$  turns to be a constant and therefore invariant under the displacements of time variables, i.e., invariant for any time  $t$ . This is the characteristic of stationary fields. Thermal light is typically stationary. Realistically, the subfields may not be able to take all possible complex

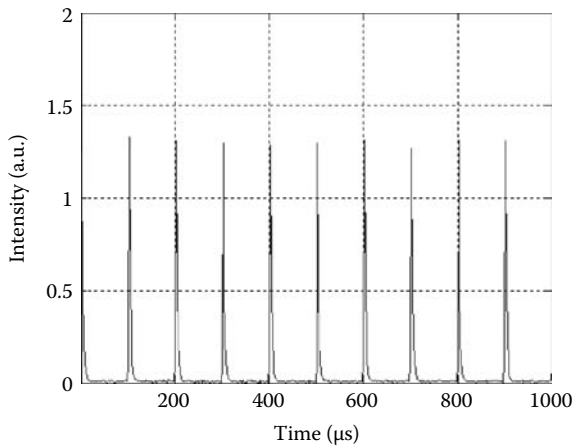
**FIGURE 1.3**

A typical measured intensity of chaotic-thermal light by a fast point photodetector.  $I(t)$  fluctuated randomly in the neighborhood of a constant value.

amplitudes in a measurement and consequently the measured instantaneous intensity  $I(\mathbf{r}, t)$  at time  $t$  may differ from its expectation value  $\langle I(\mathbf{r}, t) \rangle$  for that chosen time  $t$  and differ from time to time. The variation  $\delta I(\mathbf{r}, t)$  turns to be a random function of time  $t$ , and the measured  $I(\mathbf{r}, t)$  fluctuate randomly from time to time in the neighborhood of  $\langle I(\mathbf{r}, t) \rangle$  nondeterministically. Figure 1.3 illustrates an experimentally measured intensity,  $I(t)$ , of chaotic-thermal light by a point photodetector placed at a chosen coordinate  $\mathbf{r}$ .

#### 1.4.2 Coherent Light

Since the invention of lasers, coherent light has become the most popular light sources in modern optical measurements. These sources not only produce light coherently but also, in certain cases, nonstationary. For example, a pulsed laser, either Q-switched or mode-locked, generates well-defined wavepackets in  $E(\mathbf{r}, t)$  or pulses in  $I(\mathbf{r}, t)$ . The intensity,  $I(\mathbf{r}, t)$ , no longer fluctuates randomly in the neighborhood of a constant value from time to time nondeterministically, but becomes a well-defined function of time deterministically. In this extreme case, the subfields in Equation 1.44 are superposed at each space-time coordinate with a constant phase  $\varphi_j(\omega) - \varphi_k(\omega') = \varphi_0$ . The expectation value of the intensity is calculated from Equation 1.45 by taking a constant phase in terms of the sub-source and Fourier-mode. In a measurement, however, the subfields may not be able to take the same constant phase from the radiation source and thus produce a wavepacket slightly differ from its expectation. Consequently, the measured intensity distribution function  $I(\mathbf{r}, t)$  may fluctuate in the neighborhood of its expectation function  $\langle I(\mathbf{r}, t) \rangle$  from pulse to pulse randomly in a nondeterministic manner. Figure 1.4 shows a laser pulse train measured by a fast photodetector. The pulse is a well-defined Gaussian-like function of time  $t$  deterministically, but fluctuates from pulse to pulse nondeterministically.

**FIGURE 1.4**

Measured laser pulse train. The intensity is a function of time  $t$  deterministically, but fluctuates from pulse to pulse.

## 1.5 Measurement of Intensity: Ensemble Average and Time Average

In classical theory of light, an idealized point photodetector measures the instantaneous intensity of radiation  $I(\mathbf{r}, t)$  at space-time coordinate  $(\mathbf{r}, t)$ . Assuming a point photodetector that is placed at a chosen coordinate  $\mathbf{r}$  reads a value of  $I$  at time  $t$ , we may find the measured value  $I$  slightly differ from the expectation value  $\langle I \rangle$

$$I = \langle I \rangle + \delta I, \quad (1.46)$$

where  $\delta I$  denotes the difference. Note, the coordinate  $(\mathbf{r}, t)$  has been dropped from  $I(\mathbf{r}, t)$  since  $\mathbf{r}$  and  $t$  are both fixed in this measurement. Suppose we are not making one measurement but a large number of independent measurements simultaneously on a set of identical radiation fields under the same experimental condition. We may find each measured value  $I_j$  slightly differ from  $\langle I \rangle$  and differ from each other. The statistical mean intensity is defined as

$$\bar{I} = \frac{1}{N} \sum_{j=1}^N I_j = \langle I \rangle + \frac{1}{N} \sum_{j=1}^N \delta I_j, \quad (1.47)$$

where  $I_j$  is the measured instantaneous intensity of the  $j$ th member of the ensemble. The mean value  $\bar{I}$  equals the expectation value  $\langle I \rangle$  when  $N \sim \infty$ ,

$$\langle I \rangle = \bar{I} = \lim_{N \sim \infty} \frac{1}{N} \sum_{j=1}^N I_j, \quad (1.48)$$

since statistically

$$\lim_{N \sim \infty} \frac{1}{N} \sum_{j=1}^N \delta I_j = 0 \quad (1.49)$$

for a large set of randomly distributed values of  $\delta I_j$ . Besides, Equation 1.48 is physically reasonable. The expectation value is calculated by taking into account all possible realizations of the subfields. In a real measurement, however, the subfields may not be able to take all possible realizations but a particular set of complex amplitudes in the superposition. When a large number of measurements contribute to the statistical averaging, especially when  $N \sim \infty$ , the subfields will definitely have a chance to take all possible complex amplitudes and consequently give an averaged value equal to  $\langle I \rangle$ . Equation 1.48, in general, connects the expectation value  $\langle I \rangle$  with the concept of ensemble average. In certain observations, such as the measurement of a bright thermal source, a measurement may involve more than enough number of subfields for taking account all possible phases randomly distributed between 0 and  $2\pi$ . In this case, the measured instantaneous intensity could be indistinguishable from its expectation value within the finite response time of the photodetector.

We now introduce the concept of time-averaged intensity  $\langle I(t) \rangle_T$ . In Figure 1.3, we have shown that the measured intensity  $I(t)$  of chaotic-thermal light fluctuates randomly from time to time in the neighborhood of a constant value

$$\langle I(t) \rangle_T \equiv \frac{1}{T} \int_{t-\frac{T}{2}}^{t+\frac{T}{2}} dt I(t) \quad (1.50)$$

where  $T$  is the integral period. What is the relationship between  $\langle I(t) \rangle$  and  $\langle I(t) \rangle_T$ ? For chaotic-thermal radiation, it is easy to show that

$$\langle I(t) \rangle_{T \sim \infty} = \langle I(t) \rangle. \quad (1.51)$$

Since the ensemble-averaged intensity equals the time-averaged intensity when  $T \sim \infty$ , chaotic-thermal radiation is considered as stationary and ergodic. In statistics, ergodic implies that the ensemble average is equivalent to the time average of a typical member of the ensemble; stationary implies that the ensemble-averaged mean value is independent of time. Since time average and ensemble average are equivalent for chaotic-thermal light, we may take a large number of  $I(t_j)$ , each at a different time  $t_j$ , to evaluate the statistical mean intensity of thermal light

$$\bar{I} = \frac{1}{N} \sum_j^N I(t_j).$$

It is obvious that  $\bar{I} = \langle I(t) \rangle_T$  when  $N \sim \infty$ .

Equation 1.51 is valid for chaotic-thermal light. The situation is different in the measurement of coherent radiation. For instance, in a pulsed laser, the coherent superposition of the cavity modes produces a wavepacket, which is a function of  $t$  deterministically. The result of the time average will be different from that of the ensemble average. We discuss two types of time averages in the following.

### 1.5.1 Unavoidable Time Average Caused by the Finite Response Time of the Measurement Device

In a real measurement, the finite response time of the photodetector and the associated electronics may physically impose a time average on  $I(\mathbf{r}, t)$ . The resolving time, or response time,  $t_c$ , of a measurement device is usually much longer than a few cycles of the light wave. For example, a fast photodetector may have a response time on the order of nanoseconds, which differs from the femtosecond cycle period of a visible light wave by a factor of  $10^6$ . The output current of a photodetector,  $i(t)$ , cannot follow any fast variations of the intensity beyond the timescale of  $t_c$ . Unavoidable time averaging within that timescale occurs during the detection process. Hence, a much longer time average other than the “cycle-average” is always present during an experimental measurement. The output current of the photodetector with finite response time  $t_c$  is thus

$$i(\mathbf{r}, \tilde{t}) \propto \langle I(\mathbf{r}, t) \rangle_{t_c} = \int_{t_c} dt |E(\mathbf{r}, t)|^2, \quad (1.52)$$

where we have introduced a “mean” time  $\tilde{t}$  (or “slow” time), which has a minimum basic timescale of  $t_c$ . Any meaningful physics we learn from the measurement cannot go beyond that timescale. This unavoidable resolving time limit,  $t_c$ , is usually referred to as the characteristic time of the measurement device. Considering a particular response function of the detection system, we usually write the time average as a convolution

$$i(\mathbf{r}, \tilde{t}) \propto \int dt |E(\mathbf{r}, t)|^2 \mathcal{D}(\tilde{t} - t). \quad (1.53)$$

We have used a generic normalized function  $\mathcal{D}(\tilde{t} - t)$  to simulate the response distribution function of the photodetector, where  $\tilde{t}$  represents the mean time of a photodetection event.  $\mathcal{D}(\tilde{t} - t)$  is usually taken to be a Gaussian. To simplify the mathematics, it is also common to use a square-function, which

turns Equation 1.53 into Equation 1.52. Either use a Gaussian or a square-function, the result of the convolution of Equation 1.53 will be different for  $t_c <$  pulse-width and for  $t_c >$  pulse-width, if  $I(\mathbf{r}, t)$  is a well-defined function of time, such as a Gaussian-like pulse. When  $t_c \ll$  pulse-width  $\mathcal{D}(\tilde{t} - t)$  can be approximated as a  $\delta$ -function. The output of the convolution will be the Gaussian-like pulse itself, perhaps broadened slightly. On the other hand, if  $t_c \gg$  pulse-width, for instance in the measurement of femtosecond laser pulse, the pulse itself can be approximated as a  $\delta$ -function. The output of the convolution will be the response function of the photodetector,

$$i(\tilde{t}) \propto \int dt \delta(t - t_0) \mathcal{D}(\tilde{t} - t) = \mathcal{D}(\tilde{t} - t_0). \quad (1.54)$$

In either case, the convolution yields a time averaged function of  $\tilde{t}$ .

Assuming a square response function, following Equation 1.52, the output photocurrent of a photodetector is formally calculated as follows:

$$\begin{aligned} i(r, \tilde{t}) &\propto \langle I(r, t) \rangle_{t_c} \\ &= \iint d\omega d\omega' E^*(\omega) E(\omega') \left[ \int_{t_c} dt e^{i(\omega-\omega')t} \right] e^{-i(k-k')r} \\ &= \iint d\omega d\omega' E^*(\omega) E(\omega') \text{sinc} \frac{(\omega - \omega')t_c}{2} e^{i[(\omega - \omega')\tilde{t} - (k - k')r]}, \end{aligned} \quad (1.55)$$

where

$$E(\omega) = \sum_j a_j(\omega) e^{iq_j(\omega)}$$

when sub-sources are taken into account. Compared with the instantaneous intensity of Equation 1.38,  $i(r, \tilde{t})$  has cut off all beat frequencies that the slow photodetector may not be able to follow. The addition of the surviving beat modes of  $\omega - \omega' < 2\pi/t_c$  yields a much smoother function for the measured  $i(r, \tilde{t})$ . The response time, or characteristic time of the photodetector,  $t_c$ , is a critical physical parameter, which must be carefully chosen for certain experimental expectations.

In the early days, the most popular measurement device for light was the human eye, which has a response time of  $\sim 1/15$  s. For a time average of  $t_c \sim 1/15$  s, the sinc-function in Equation 1.55 can be approximately treated as a delta function  $\delta(\omega - \omega')$ . We thus effectively have a time average of  $T \sim \infty$ :

$$\begin{aligned} \langle I(r, t) \rangle_{T \sim \infty} &= \iint d\omega d\omega' E^*(\omega) E(\omega') \delta(\omega - \omega') e^{i[(\omega - \omega')\tilde{t} - (k - k')r]} \\ &= \int_0^\infty d\omega |E(\omega)|^2. \end{aligned} \quad (1.56)$$

Notice the second integral in Equation 1.40 (or the third and the fourth terms in Equation 1.45) has vanished in the time average of Equation 1.56, indicating that even if  $\mathcal{F}_\tau\{E(v)\}$  is in the form of a well-defined wavepacket, or  $|\mathcal{F}_\tau\{E(v)\}|^2$  is a well-defined pulse, the result of its time-averaged intensity is a constant when  $T \sim \infty$ . This result is consistent with the Parseval theorem:

$$\int_{T \sim \infty} dt |E(\omega)|^2 = \int_0^\infty d\omega |E(\omega)|^2. \quad (1.57)$$

It should be emphasized that Equation 1.56 has included all cross terms of the subfields associated with the sub-sources. Taking into account the sub-sources, we may rewrite Equation 1.56 into the following form:

$$\langle I(r, t) \rangle_{T \sim \infty} = \int_0^\infty d\omega \left[ \sum_j E_j^*(\omega) \sum_k E_k(\omega) \right], \quad (1.58)$$

which differs from the integral of  $\sum_j |E_j(\omega)|^2$ . The cross terms vanish only in the measurement of chaotic-thermal light when taking into account the random relative phases of  $\varphi_j - \varphi_k$ . In the measurement of coherent light, especially when  $\varphi_j - \varphi_k$  takes a constant value, the time average has a null effect on the second term of Equation 1.45, although the third and the fourth terms may vanish completely.

The unavoidable time average caused by the slow response time of a measurement device may yield the same constant value as the expectation value of chaotic-thermal light, however, the physics behind these two types of “averaging” is very different. The time average is physically imposed by the slow time-resolving ability of the measurement device. The constant obtained from the expectation operation is the result of a superposition, which may not be simply treated as an “averaging,” especially in the case of coherent superposition. In a coherent superposition, the expectation calculation yields a well-defined pulse. The time average will broaden the pulse significantly if the response time of the photodetector is much greater than the pulse width,  $t_c \gg \Delta t$ . For instance, as we have mentioned earlier that a photodetector with nanosecond response time will broaden a femtosecond laser pulse to nanosecond in  $i(\tilde{t})$ . When  $t_c \sim \infty$ , the time average yields a constant photocurrent in any circumstances.

### 1.5.2 Timely Accumulative Measurement

Another type of time integral may apply if a measurement has to be taken accumulatively in time. The time-integrated expectation value of intensity is defined as

$$Q(\mathbf{r}) = \int_{T_1}^{T_2} dt \langle I(\mathbf{r}, t) \rangle, \quad (1.59)$$

where we have assumed that the accumulative measurement starts from  $t = T_1$  and ends at  $t = T_2$ . It is easy to see that  $Q(\mathbf{r})$  will be a constant in time for the above simple measurement of intensity, if the accumulative time period is long enough to be treated as infinity,  $T_2 - T_1 \sim \infty$ , even if the expectation function is a well-defined pulse.

The time-averaged intensity measured in timely accumulative measurement is defined as follows:

$$\langle I(\mathbf{r}) \rangle_T = \frac{1}{T_2 - T_1} \int_{T_1}^{T_2} dt I(\mathbf{r}, t). \quad (1.60)$$

It is easy to find that

$$\langle I(\mathbf{r}) \rangle_T = \frac{Q(\mathbf{r})}{T_2 - T_1}$$

when  $T_2 - T_1 \sim \infty$ .

In general, due to interference and/or diffraction, it is quite possible that the expectation value  $\langle I(\mathbf{r}, t) \rangle$ , the statistical mean value  $\bar{I}(\mathbf{r}, t)$ , and the time averaged value  $\langle I(\mathbf{r}, t) \rangle_T$  of a radiation all turn to be nontrivial functions of space-time variables. For instance, considering a pulsed laser beam, we may set up a 2D CCD array in the transverse plane to monitor the intensity distribution spatially and temporally. First, let us focus on the transverse spatial distribution function  $I(\vec{\rho})$ , where  $\vec{\rho}$  is the transverse coordinate vector. We may observe a symmetrical Gaussian-like function centered on the optical axis of the laser beam. The measured  $I(\vec{\rho})$  function may differ slightly from  $\langle I(\vec{\rho}) \rangle$  in a measurement at a chosen time  $t$ . If we are not making one measurement but a large number of independent measurements simultaneously, which involves a large number of identical laser beams and CCD arrays in the same experimental condition, we may observe (1) a large number of symmetrical Gaussian-like functions each centered on the optical axis of a laser beam and (2) each observed Gaussian-like function may differ slightly from  $\langle I(\vec{\rho}) \rangle$  and differ from each other.

$$I_j(\vec{\rho}) = \langle I(\vec{\rho}) \rangle + \delta I_j(\vec{\rho}), \quad (1.61)$$

where  $I_j(\vec{\rho})$  corresponds to the measurement on the  $j$ th member of the ensemble. The statistical mean function is defined as follows:

$$\bar{I}(\vec{\rho}) = \frac{1}{N} \sum_{j=1}^N I_j(\vec{\rho}), \quad (1.62)$$

The statistical mean function  $\bar{I}(\vec{\rho})$  equals the expectation function  $\langle I(\vec{\rho}) \rangle$  when  $N \sim \infty$  as usual

$$\langle I(\vec{\rho}) \rangle = \bar{I}(\vec{\rho}) = \lim_{N \sim \infty} \frac{1}{N} \sum_{j=1}^N I_j(\vec{\rho}), \quad (1.63)$$

since

$$\lim_{N \sim \infty} \frac{1}{N} \sum_{j=1}^N \delta I_j(\vec{\rho}) = 0. \quad (1.64)$$

Now we turn the measurement to temporal distribution function by recording the output current of each CCD element continuously as a function of time  $t$ . This is equivalent to measure the intensity at each transverse coordinate  $\vec{\rho}$  as a function of time  $t$ ,  $I(\vec{\rho}, t)$ . We may find (1) each CCD element observes a well-defined Gaussian-like function of  $t - t_0$ , where  $t_0$  is the time coordinate of the maximum amplitude of the Gaussian-like function; and (2) each observed Gaussian-like function may differ from pulse to pulse in the neighborhood of  $\langle I(\vec{\rho}, t - t_0) \rangle$ . The statistical mean function averaged from pulse to pulse is defined as follows:

$$\bar{I}(\vec{\rho}, t - t_0) = \frac{1}{N} \sum_{j=1}^N I_j(\vec{\rho}, t - t_{0j}), \quad (1.65)$$

where

$I_j(\vec{\rho}, t - t_{0j})$  corresponds to the  $j$ th pulse

$t_{0j}$  is the time coordinate of the maximum amplitude of the  $j$ th pulse

The statistical mean function  $\bar{I}(\vec{\rho}, t - t_0)$  equals the expectation function  $\langle I(\vec{\rho}, t - t_0) \rangle$  when  $N \sim \infty$

$$\langle I(\vec{\rho}, t - t_0) \rangle = \bar{I}(\vec{\rho}, t - t_0) = \lim_{N \sim \infty} \frac{1}{N} \sum_{j=1}^N I_j(\vec{\rho}, t - t_{0j}). \quad (1.66)$$

It should be emphasized that the mean function obtained in Equation 1.66 is different from time average, although the ensemble average involves time-based measurements from pulse to pulse.

In summary, the expectation value or function  $\langle I(\mathbf{r}, t) \rangle$ , the statistical mean value or function  $\bar{I}(\mathbf{r}, t)$ , the time averaged value  $\langle I(\mathbf{r}, t) \rangle_T$ , and the fluctuation  $\delta I(\mathbf{r}, t)$  are defined as follows:

1.  $\langle I(\mathbf{r}, t) \rangle$  is defined as

$$\langle I(\mathbf{r}, t) \rangle = \left\langle \sum_j E_j^*(\mathbf{r}, t) \sum_k E_k(\mathbf{r}, t) \right\rangle$$

by means of taking into account all possible complex amplitudes of the subfields.

2.  $\bar{I}(\mathbf{r}, t)$  is defined as

$$\bar{I}(\mathbf{r}, t) = \frac{1}{N} \sum_{j=1}^N I_j(\mathbf{r}, t),$$

where  $I_j(\mathbf{r}, t)$  is the measured intensity of the  $j$ th member of the ensemble.

3.  $\langle I(\mathbf{r}, t) \rangle_T$  is defined as

$$\langle I(\mathbf{r}, t) \rangle_T = \frac{1}{T} \int_{t-\frac{T}{2}}^{t+\frac{T}{2}} dt I(\mathbf{r}, t),$$

where  $I(\mathbf{r}, t)$  is the measured intensity at time  $t$ .

4.  $\delta I(\mathbf{r}, t)$  is defined as

$$\delta I(\mathbf{r}, t) = I(\mathbf{r}, t) - \langle I(\mathbf{r}, t) \rangle.$$

With regard to the intensity fluctuations, it is necessary to emphasize the following two points:

- In the measurement of coherent radiation, we may observe a well-defined wavepacket or pulse that is a function of time  $t$ , such as a Gaussian. Can the Gaussian function itself be considered as intensity fluctuation? The answer is negative. The well-defined function of time is usually predictable from the expectation evaluation. The intensity fluctuations should be statistically random and nondeterministic. In this case, it is the variations of the Gaussian function from pulse to pulse that correspond to the intensity fluctuations.
- Even if the measured instantaneous intensity  $I(\mathbf{r}, t)$  can be written into two parts such as an interference pattern  $I(\mathbf{r}, t) = I_0 + I \cos \omega \tau$ , where  $\tau$  is a function of  $(\mathbf{r}, t)$ ,  $I_0$  and  $I$  are constants, the second term  $I \cos \omega \tau$  is definitely not the variation  $\delta I(\mathbf{r}, t)$ , although the measured function itself sinusoidally "fluctuates" in the neighborhood of a constant  $I_0$  deterministically.

---

## Summary

In this chapter we introduced the following theory and concepts:

1. The Maxwell equations and the electromagnetic wave equation: the foundation of the classical EM wave theory of light.
  2. The classical superposition.
  3. The measurement of light: the Poynting vector and the concept of intensity; the expectation value and fluctuations of intensity; the expectation value and the ensemble measurement; the time averaged intensity.
  4. We have started to build a simple model of radiation with multi-sub-sources and multimode.
- 

## Suggested Reading

- Born, M. and E. Wolf, *Principle of Optics*, Cambridge University Press, Cambridge, U.K., 2002.  
Jackson, J.D., *Classical Electrodynamics*, John Wiley & Sons, New York, 1998.

# 2

---

## *Coherence Property of Light—The State of the Radiation*

---

### 2.1 Coherence Property of Light

In this section, we introduce the concept of coherence. What do we mean when we name a radiation coherent or incoherent? For instance, what is the physical reason for us to consider a discharge tube radiates incoherent light, but a laser radiates coherent light? We will start our discussion from the simple model of radiation we have introduced in Chapter 1. To simplify the discussion, we consider far-field measurements on a radiation, which comes from a point source that contains a large number of point sub-sources, such as trillions of atomic transitions. Focusing on the coherent and incoherent superposition in terms of the sub-sources and Fourier modes, we analyze the following four extreme cases:

- (I) Incoherent sub-sources and incoherent Fourier-modes
- (II) Coherent sub-sources and coherent Fourier-mode
- (III) Incoherent sub-sources and coherent Fourier-mode
- (IV) Coherent sub-sources and incoherent Fourier-mode

#### 2.1.1 Incoherent Sub-Source and Incoherent Fourier-Mode: Chaotic Light

For chaotic light, the sub-sources and the Fourier-modes are all independent, thus exhibiting random relative phases  $\varphi_j(\omega) - \varphi_k(\omega')$ . As a result of the chaotic sum, the only surviving terms in Equation 1.44 are those amplitudes (and their conjugates) that belong to the same sub-source and the same mode of frequency  $\omega$ , i.e.,  $j = k$  and  $\omega = \omega'$ , when taking into account *all possible* values of  $\varphi_j(\omega) - \varphi_k(\omega')$ . These surviving terms are known as the “diagonal-terms” of the matrix elements

$$\langle I(r, t) \rangle = \int d\omega \sum_j a_j^2(\omega), \quad (2.1)$$

corresponding to the first term of Equation 1.45. If  $a_j(\omega)$  is a well-defined distribution function in terms of  $\omega$ , Equation 2.1 can be written in the following

form:

$$\langle I(r, t) \rangle = \int d\omega \sum_j |E_j(\omega)|^2 = \int_0^\infty d\omega \sum_j I_j(\omega), \quad (2.2)$$

which indicates that the expectation value of the total intensity is the sum of the expectation value of the sub-intensities in terms of the sub-sources. Note that in Equation 2.1, the expectation evaluation is only partial, we have left out the evaluation for the real-positive amplitudes. The coherence property of light is determined by the relative phases between the sub-radiations. In certain measurements, we may need to take into account *all possible* values of  $a_j^2(\omega)$  in terms of the sub-sources and the Fourier-modes.

Examining Equations 1.41 and 1.45, the second, third, and fourth integrals may all contribute to the variation of the intensity  $\delta I$ , if the interference cancellation is incomplete. These contributions may vary from time to time causing random fluctuations of the intensity in the neighborhood of its expectation value. The incomplete cancellations are the major contributions to  $\delta I$  compared with the variations of the  $a_j^2(\omega)$ 's in Equation 2.1. The ratio between these two types of contributions could be on the order of  $M \times N$ , where  $M \sim \infty$  is the number of modes and  $N \sim \infty$  is the number of sub-sources.

In summary, we have given a simply classical model of incoherent chaotic light, in which the complex amplitudes of the chaotic field have randomly distributed relative phases  $\varphi_j(\omega) - \varphi_k(\omega')$  with regards to the sub-sources as well as the Fourier-modes. It is the randomness of the phases that distinguishes an *incoherent chaotic sum* from a *coherent superposition*. The stochastic nature of an incoherent chaotic light, however, does not exclude the following possibilities: (1) the real and positive amplitude  $a(\omega)$  may have a well-defined distribution function in terms of frequency  $\omega$ , such as thermal light; (2) the intensity itself may have a certain distribution function  $p(I)$ , such as a Gaussian, in the neighborhood of its mean value  $\bar{I}$ .

### 2.1.2 Coherent Sub-Sources and Coherent Fourier-Modes

The second extreme case of the classical model of radiation concerns coherent sub-sources and coherent Fourier-modes. A Q-switched laser pulse is a good example. All terms of the superposition in Equations 1.44 and 1.45 survive. The expectation function of intensity is thus

$$\begin{aligned} \langle I(r, t) \rangle &= \left\langle \int dv \sum_j a_j(v) e^{iv\tau} \int dv' \sum_k a_k(v') e^{-iv'\tau} \right\rangle \\ &= \left| \mathcal{F}_\tau \{ A(v) \} \right|^2. \end{aligned} \quad (2.3)$$

where we have defined  $A(\nu) = \sum_j a_j(\nu)$  as the total amplitude of the mode of frequency  $\omega$ . The intensity expectation turns out to be a well-defined pulse in Equation 2.3.

Differing from chaotic-thermal field, here, we assume a constant phase relationship between the subfields. The calculated wavepacket, or pulse, is the result of constructive interference or coherent superposition of the subfields. With regard to the fluctuations, chaotic-thermal field and coherent wavepacket take two extremes. In chaotic-thermal case, the subfields may not take all possible relative phases, and in coherent light, the subfields may not take an identical constant phase. The incomplete destructive interference in chaotic radiation and the incomplete constructive interference in coherent light between sub-sources are the major causes of the intensity fluctuation.

We have shown in Figure 1.4 a laser pulse train measured by a fast photodetector. The pulse is a well-defined function of time  $t$  deterministically, but fluctuates from pulse to pulse in a nondeterministic manner.

### 2.1.3 Incoherent Sub-Sources and Coherent Fourier-Modes

In the third simplified model, we assume each of the sub-sources emits independently with random relative phases. The Fourier-modes, however, are coherently excited at time  $t_{0j}$ . Under the assumption of incoherent sub-sources, the only surviving terms in Equation 1.44 are those with  $j = k$ , which includes the first and third sums of Equation 1.45,

$$\begin{aligned} \langle I(r, t) \rangle &= \int d\omega d\omega' \sum_j a_j(\omega) e^{-i\omega t_{0j}} a_j(\omega') e^{i\omega' t_{0j}} e^{i(\omega - \omega')\tau} \\ &= \sum_j \left\{ \int d\nu [a_j(\nu) e^{-i\nu t_{0j}}] e^{i\nu\tau} \right\} \left\{ \int d\nu' [a_j(\nu') e^{i\nu' t_{0j}}] e^{-i\nu'\tau} \right\} \\ &= \sum_j |\mathcal{F}_{(\tau - t_{0j})}\{a_j(\nu)\}|^2. \end{aligned} \quad (2.4)$$

This result reflects explicitly the incoherent nature of the sub-sources and the coherent nature of the Fourier-modes. The expectation value of intensity,  $\langle I(r, t) \rangle$ , is the sum of all possible sub-pulses excited by all possible independent sub-sources. It is clear that each of the sub-pulses is in the form of a well-defined function in space-time due to the coherent superposition of its Fourier-modes.

Equation 2.4 is formulated as a summation of a set of sub-pulses. Each sub-pulse corresponds to the Fourier transforms of  $a_j(\nu)$  of the  $j$ th sub-source. Each Fourier transform yields a well defined wavepacket in space-time if  $a_j(\nu)$  is well defined. The expectation value, or expectation function,  $\langle I(r, t) \rangle$  is now determined by the summation of these well-defined sub-pulses. We examine the following simplified cases:

1. *Single wavepacket or pulse*

We assume the field is weak enough so only one wavepacket, or one pulse, is involved in the measurement of  $I(r, t)$ , we may keep Equation 2.4 as the expectation value, except only one nonzero  $a_j$ . For identical sub-sources, such as a large number of possible identical atomic transitions, we may simplify Equation 2.4 to

$$\langle I(r, t) \rangle = |\mathcal{F}_{(\tau-t_0)}\{a(v)\}|^2. \quad (2.5)$$

The expectation value, or expectation function, is obviously a well-defined function of time.

2. *A few wavepackets or pulses*

If a few wavepackets, or pulses, are involved in the measurement of  $I(r, t)$ , Equation 2.4 has only a few terms in the summation. The expectation value, or expectation function, is mainly determined by the distribution of  $t_{0j}$ . If all the  $t_{0j}$  are closer together, i.e., the separations between the  $t_{0j}$ 's are much smaller than the width of the wavepacket, the addition of these pulses simply yields a broadened pulse with a larger amplitude. Otherwise, if  $t_{0j}$  has a rather uniform distribution,  $\langle I(r, t) \rangle$  may turn out to be a smoother function in space-time, or close to a constant.

3. A large number of overlapped–partially overlapped wave packets or pulses.

The summation could be complicated. Here, we study a simplified model in which we assume the wavepackets or pulses all have the same function of  $t - t_{0j}$ , and are distributed randomly and continuously. The summation can be simplified to an integral over  $t_0$  from  $-\infty$  to  $+\infty$ ,

$$\begin{aligned} \langle I(r, t) \rangle &\cong \int dt_0 |\mathcal{F}_{(\tau-t_0)}\{a_j(v)\}|^2 \\ &= \int dv dv' a(v) a(v') \left[ \int dt_0 e^{i(v-v')t_0} \right] e^{-i(v-v')\tau} \\ &\cong N \int dv a^2(v), \end{aligned} \quad (2.6)$$

where we have approximated the integral for  $t_0$  to infinity. Due to the assumption of a random and continuous distribution of pulses, the number of pulses included in the summation is proportional to the width of the integral of  $t_0$ ,  $N \propto T$ . To compare with the earlier results, we rewrite Equation 2.6 as

$$\langle I(r, t) \rangle = \int dv \sum_j a_j^2(v).$$

It is interesting to see that the expectation value of the intensity of a large number of *randomly* distributed wavepackets is the same as that of chaotic light.

Mathematically, integrating over parameter  $t_0$  is equivalent to integrating over time  $t$ . Physically, the two types of summation correspond to the following two pictures: (1) a measurement at time  $t$  deals with a large number of randomly distributed overlapped–partially-overlapped wavepackets and (2) a large number of accumulated measurements happen randomly at different time.

To have a better understanding of the physics behind this observation, we examine Equation 1.32 and write the field as the superposition of a large number of wavepackets

$$E(r, t) = \sum_j e^{-i\omega_0(\tau-t_{0j})} \mathcal{F}_{(\tau-t_{0j})}\{a(v)\}, \quad (2.7)$$

where  $t_{0j}$  labels the  $j$ th wavepacket. The  $j$ th classical wavepacket is the result of coherent superposition of the  $j$ th group of Fourier-modes. The wavepacket propagates in space-time with a well-defined envelope initiated at  $r = 0$  and  $t = t_{0j}$ .

Following Equation 2.7, we first examine the superposition of two wavepackets

$$E(r, t) = e^{-i\omega_0(\tau-t_{01})} \mathcal{F}_{(\tau-t_{01})}\{a(v)\} + e^{-i\omega_0(\tau-t_{02})} \mathcal{F}_{(\tau-t_{02})}\{a(v)\}, \quad (2.8)$$

where the  $j$ th ( $j=1, 2$ ) wavepacket is centered at time  $t=r/c + t_{0j}$ , i.e., the  $j$ th group of Fourier-modes have a common phase at  $r=0$ ,  $t=t_{0j}$ . The instantaneous intensity is thus:

$$\begin{aligned} I(r, t) &= |\mathcal{F}_{(\tau-t_{01})}\{a(v)\}|^2 + |\mathcal{F}_{(\tau-t_{02})}\{a(v)\}|^2 \\ &\quad + 2\text{Re} [e^{-i\omega_0(t_{02}-t_{01})} \mathcal{F}_{(\tau-t_{01})}^*\{a(v)\} \cdot \mathcal{F}_{(\tau-t_{02})}\{a(v)\}]. \end{aligned} \quad (2.9)$$

The third term of Equation 2.9 is the interference term. Either observable or unobservable, it will contribute to the resulting light intensity. The visibility of the interference is determined by the following two factors: (1) the overlapping or nonoverlapping of the wavepacket and (2) the phase difference of  $\omega_0(t_{02} - t_{01})$ .

Now we consider a large number of overlapped–partially overlapped wavepackets. The measured intensity is:

$$\begin{aligned} I(r, t) &= \sum_j |\mathcal{F}_{(\tau-t_{0j})}\{a(v)\}|^2 \\ &\quad + \sum_{j \neq k} [e^{-i\omega_0(t_{0k}-t_{0j})} \mathcal{F}_{(\tau-t_{0j})}^*\{a(v)\} \cdot \mathcal{F}_{(\tau-t_{0k})}\{a(v)\}]. \end{aligned} \quad (2.10)$$

If  $t_{0j}$  takes *all possible* values leading to a set of *random* relative phases of  $\omega_0(t_{0j} - t_{0k})$ , the second sum in Equation 2.10 vanishes. The expectation intensity is thus

$$\langle I(r, t) \rangle = \left\langle \sum_j |\mathcal{F}_{(\tau - t_{0j})}\{a(v)\}|^2 \right\rangle. \quad (2.11)$$

Equation 2.11 can be further simplified for an integral over  $t_0$  from  $-\infty$  to  $+\infty$  similar to that of Equation 2.6, becoming

$$\langle I(r, t) \rangle = \int dv \sum_j a_j^2(v),$$

which is the result of a destructive interference when taking into account all possible values of  $e^{-i\omega_0(t_{01} - t_{02})}$ .

#### 2.1.4 Coherent Sub-Sources and Incoherent Fourier-Modes

We shall now consider the classical model of another type of light where the sub-sources radiate coherently. The Fourier-modes, however, are independent with random relative phases. Continuous wave (CW) laser light is a closer example, except that the cavity-modes of the laser are usually discrete rather than continuous. Since the Fourier-modes are assumed incoherent, the only surviving terms in Equation 1.44 are those with  $\omega = \omega'$ . The expectation value of the intensity is thus

$$\langle I(r, t) \rangle = \int d\omega \sum_{j,k} a_j(\omega) a_k(\omega) \quad (2.12)$$

which includes to the first and second sums of Equation 1.45. Equation 2.12 reflects the incoherent nature of the Fourier-modes and the coherent nature of the sub-sources: the measured intensity is the sum of the sub-intensities of the Fourier modes; however, the amplitudes corresponding to the sub-sources add coherently with all cross-terms of the sub-sources. Equation 2.12 can be further evaluated by assuming  $a(v)$  to be a well-defined function for all sub-sources:

$$\langle I(r, t) \rangle \cong N^2 \int d\omega a^2(\omega) = \int dv A^2(\omega), \quad (2.13)$$

where  $A(\omega) = \sum_j a_j(\omega) \simeq N a(\omega)$ .

Comparing with Equation 2.1, we see that  $\langle I(r, t) \rangle$  is  $N$  times greater. We thus have a “super radiator,” a result of coherent superposition or constructive interference in terms of the sub-sources.

In summary, an intensity measurement may involve the physics of both the coherence behavior and the statistical behavior of the radiation. The

expectation value or the expectation function of intensity is calculated by taking into account all possible realizations of the field in the superposition. For a particular measurement, the measured value or measured function may differ from the expectation value or the expectation function from time to time. The intensity fluctuations of light are mainly caused by the uncontrollable constructive-destructive interference between the subfields. After a large number of measurements, the statistical mean of the measured values of intensity, or the measured functions of intensity, approaches the calculated expectation value or expectation function of the intensity. We say that the expectation operation is equivalent to an ensemble average. By this means we may treat the uncontrollable randomly fluctuated radiation as a statistically stochastic process.

*Coherence property:* We may roughly classify light into two types— incoherent chaotic-thermal light and coherent light. Gas discharge lamps emit typical incoherent chaotic-thermal light, and laser radiation is typically coherent. As we have learned from the above discussion, the coherence property of radiation is mainly determined by the coherent or incoherent superposition of its subfields, either in terms of sub-sources or Fourier harmonic modes. Phenomenologically, the laser light fields are superposed coherently within certain selected temporal and spatial modes. The intensity of these modes is thus enhanced by many orders of magnitude compared with that of chaotic-thermal radiation. For instance, a single-mode CW laser may put several watts of power into a single longitudinal cavity mode (realistically, perhaps with a few megahertz bandwidth of spectrum) and a  $\text{TEM}_{00}$  transverse spatial mode. Compared with a thermal light source of several watts, which radiates light into a  $4\pi$  angle in space and over a wide spectral range, the light intensity per mode (within a few megahertz bandwidth of diffraction limited single spatial mode) may differ by a factor of up to  $\sim 10^{12}$ . It is much easier to observe, or to demonstrate, interference and other wave phenomena of light by using laser light. However, this does not mean that the interference properties of laser light and thermal light of the same bandwidth with regards to temporal and spatial modes are different. We will discuss this in the following section.

*Statistical properties of intensity fluctuations:* The instantaneous intensity  $I(r, t)$  may exhibit a well-defined distribution function  $p(I)$  in the neighborhood of its expectation value or expectation function of  $\langle I(r, t) \rangle$ . A typical distribution is Gaussian, which in general indicating a complete random stochastic process of light creation.

Both the coherence and the statistical characteristics are intrinsic properties of light and are predetermined in the light source, i.e., they depend on how the light is generated. In the language of quantum optics, the coherence as well as the statistical properties of light are determined by the state of the field.

## 2.2 Temporal Coherence

The concept of temporal coherence implies two aspects of physics: (1) the coherent and incoherent superposition of subfields in terms of their temporal relationship and (2) the superposition or interference between temporally delayed fields. Temporal coherence is an intrinsic property of the radiation. In this section, we will focus our discussion on the physics of (1) and leave (2) to Section 5.1.

So far, we have restricted our discussion to point radiation sources. A point source may consist of a large number of sub-sources such as trillions of atomic transitions that radiate a large number of spherical harmonic waves, labeled by different modes of frequency and different sub-sources within the point source. In the Maxwell electromagnetic wave theory, each spherical harmonic wave is a solution of the Maxwell wave equation, and thus the superposition of all or part of these spherical harmonic subfields at a space-time point of observation is also a solution of the Maxwell wave equation

$$\mathbf{E}(\mathbf{r}, t) = \sum_{\omega} \sum_{j=1}^N \hat{\mathbf{e}} \frac{E_{0j}(\omega)}{r} e^{-i[\omega t - k(\omega)r]}, \quad (2.14)$$

where  $E_{0j}(\omega) = a_{0j}(\omega)e^{i\varphi_{0j}(\omega)}$  is the complex amplitude for the mode  $\omega$  excited by the  $j$ th sub-source. The amplitude distribution of the field is described by  $a_{0j}(\omega)$ , while the phase variation, or the relative temporal relationship, among the harmonic subfields is represented by  $\varphi_{0j}(\omega)$ , and the polarization is indicated by an unit vector  $\hat{\mathbf{e}}$ . To simplify the notation we select one polarization of the field, and the vector notation will be dropped in the following discussions. These harmonic waves, or subfields, are thus superposed at a space-time point either incoherently or coherently depending on their relative initial phases  $e^{i\varphi_j(\omega)}$ , or say by the nature of their temporal relationship.

Equation 2.14 shows that each subfield has a spherical symmetry, which is reasonable for a point source and a spherical boundary condition of infinity. The superposition of these spherical harmonic subfields, either incoherent, partial coherent, or coherent, has no effect on the transverse spatial distribution of the field, but may lead to different temporal behavior of the radiation. For example, constructive-destructive interference among a large number of Fourier-modes of different frequencies results in a wavepacket with longitudinal propagation, and the temporal distribution (width and shape) of the wavepacket is determined by the spectral distribution of the subfields.

In the previous section, we have suggested four classical models to classify the radiation field:

- (I) Incoherent sub-sources and incoherent Fourier-modes
- (II) Coherent sub-sources and coherent Fourier-mode
- (III) Incoherent sub-sources and coherent Fourier-mode
- (IV) Coherent sub-sources and incoherent Fourier-mode

In terms of the concept of coherence, radiation (I) is definitely temporally incoherent; radiation (II) is definitely temporally coherent. Radiation (III) is interesting since in the weak light condition, the measurement at a space-time point may reveal that the radiation behaves like a wavepacket from time to time, caused by the coherent constructive-destructive interference among many Fourier-modes excited by each individual sub-source. In this situation, we may classify radiation (III) as temporally coherent. When the light intensity gets stronger, however, the incoherent superposition of a large number of overlapped or partially overlapped wavepackets turns the radiation temporally incoherent. Radiation (IV) is very special. On one hand, the coherent superposition among sub-sources involves constructive interference of harmonic waves, which builds up an enhanced Fourier-mode; on the other hand, the incoherent superposition of Fourier-modes prohibits the formation of a wavepacket. If the radiation source excites a single-frequency mode, or if a single frequency is isolated from the multimodes for observation, we may classify radiation (IV) as temporally coherent. However, if multimodes cannot be avoided in the measurement, we may have to take into account the incoherent nature of radiation (IV).

For a point source and free propagation, the subfields excited by all sub-sources take the same optical path when reaching a space-time point of observation. It is the constructive-destructive interference among different frequency modes that results in a wavepacket (field) or a pulse (intensity). For example, the coherent superposition of radiation (II) excites a wavepacket

$$\begin{aligned}
 E(r, t) &= \frac{e^{-i(\omega_0 t - k_0 r)}}{r} \int d\nu \sum_j a_j(\nu) e^{-i\nu\tau} \\
 &= \mathcal{F}_\tau \left\{ \sum_j a_j(\nu) \right\} \frac{e^{-i(\omega_0 t - k_0 r)}}{r},
 \end{aligned} \tag{2.15}$$

representing a spherical harmonic wave propagating together within an envelope. The envelope is the Fourier transform of the spectral distribution function of the field, and propagates with the same speed as that of the phase of the spherical harmonic wave in free space. It is interesting to see that the constructive-destructive interference turns continuous waves (or modes) into a pulse and enhances the intensity significantly within the pulse. Of course, the energy of the radiation must be conserved. The enhancement

of the energy within the pulse (constructive interference) is at the price of losing energy outside the pulse (destructive interference).

In far-field observations, the wavepacket of a spherical wave can be approximated as a wavepacket of a plane wave at the space points of interest:

$$E(\mathbf{r}, t) \simeq \mathcal{F}_\tau \left\{ \sum_j a_{0j}(\nu) \right\} e^{-i(\omega_0 t - \mathbf{k}_0 \cdot \mathbf{r})}, \quad (2.16)$$

where we have written the field as a polarized vector field and treated  $a_{0j}(\nu) = a_j/r \simeq \text{constant}$  in the neighborhood of  $r \sim \infty$ .

The plane-wave approximation of Equation 2.16 has been applied in the previous sections.

### 2.3 Spatial Coherence

Similar to that of temporal coherence, the concept of spatial coherence involves two aspects of physics: (1) the coherent or incoherent superposition of subfields that are excited from spatially separated sub-sources and (2) the superposition or interference between spatially separated fields. Spatial coherence is also an intrinsic property of the radiation. In this section, we will focus our discussion on the physics of (1) and leave (2) to Section 5.2.

Instead of point sources we now consider radiation sources with finite dimensions, e.g., the 1D source shown in Figure 2.1, and turn our attention to the spatial behavior of the radiation. More precisely, we are interested

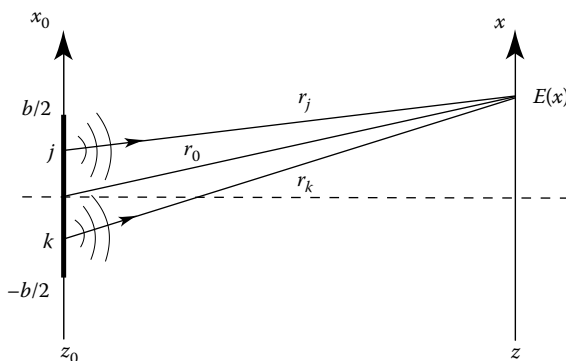


**FIGURE 2.1**

A 1D radiation source of finite dimensions consists of a large number of sub-sources distributed along the  $x_0$ -axis.

in knowing the radiation distribution at an arbitrary transverse observation plane based on earlier knowledge either at the source or at another transverse plane in which the distribution is known. Compared with point sources, the geometry of spatially extended sources complicates the physics and mathematics. For a point radiation source and free propagation (direct point-to-point propagation), the subfields originated from all sub-sources take the same optical path length when reaching a space-time point of observation. For a radiation source of finite dimension, however, the superposed subfields may not experience the same optical path length to reach the observer. The superposition is more complicated in this case.

To make the physics and mathematics of spatial coherence easily understandable, we divide our discussion into three steps: (1) the study of the spatial coherent property of the source, which involves the superposition of subfields excited from a large number of coherent or incoherent sub-sources (Section 2.3); (2) the study of diffraction of a spatial mode when passing through an aperture, which involves the superposition of a large number of secondary wavelets originating from each point of the primary wave front of the mode (Section 3.1); and (3) the propagation of a known field from one plane to another plane, which combines the physics and mathematics of both (1) and (2) (Section 3.2).

Assume the 1D radiation source of Figure 2.1 consists of a large number of randomly distributed sub-sources along the  $x_0$ -axis from  $x_0 = -b/2$  to  $x_0 = b/2$ . To simplify the mathematics, we assume single frequency radiation ( $\omega = \text{constant}$ ) and limit our discussion to one polarization.\* The source plane is assigned as  $z_0 = 0$ . The observation plane of  $z = \text{constant}$  is parallel to the source plane and located at a distance  $z$ . We are interested in knowing where and how the light is arriving on the plane of  $z = \text{constant}$ . Basically, we need to calculate the intensity distribution, or the expectation value  $\langle I(x, t) \rangle$  along the  $x$ -axis. Different from a point source, here each subfield excited by a sub-source corresponding to one point of the  $x_0$ -axis takes a different optical path to reach a point on the  $x$ -axis. The field  $E(x, t)$  is the result of the superposition of these subfields:

$$E(x, t) = \int_{-b/2}^{b/2} dx_0 \frac{E(x_0)}{r} e^{-i(\omega t - kr)}, \quad (2.17)$$

where  $E(x_0) = a(x_0)e^{i\varphi(x_0)}$  is the complex amplitude of the field excited at the sub-source of  $x_0$ . In Equation 2.17 we have treated each subfield spherical wave centered at each sub-source using

$$r = \sqrt{z^2 + (x - x_0)^2}.$$

---

\* We will keep this assumption in the next several sections unless otherwise specified.

The expectation value of the intensity  $\langle I(x, t) \rangle$  is thus written as

$$\langle I(x, t) \rangle = \left\langle \int_{-b/2}^{b/2} dx_0 dx'_0 \frac{a(x_0)}{r} \frac{a(x'_0)}{r'} e^{-i[\varphi(x_0) - \varphi(x'_0)]} e^{-ik[r - r']} \right\rangle \quad (2.18)$$

where

$$r = \sqrt{z^2 + (x - x_0)^2}$$

$$r' = \sqrt{z^2 + (x - x'_0)^2}$$

We will analyze two extreme cases: chaotic sub-sources and coherent sub-sources. Due to the single-frequency approximation,  $\langle I(x, t) \rangle$  will be a constant in time. One should keep in mind that if multifrequencies are involved, interference among different frequency modes and consequently temporal coherence must be taken into account.

### Case I: Chaotic sub-sources

In the case of chaotic sub-sources, the only surviving terms under the integral of Equation 2.18 are those terms with  $x_0 = x'_0$  when taking into account all possible realizations of the field with random values of  $\varphi(x_0) - \varphi(x'_0)$ . The expectation value of the intensity at  $x$ ,  $\langle I(x, t) \rangle$ , turns out to be a trivial sum of the sub-intensities from each sub-source at  $x_0$ :

$$\langle I(x, t) \rangle = \int_{-b/2}^{b/2} dx_0 \frac{a^2(x_0)}{r^2} \simeq \int_{-b/2}^{b/2} dx_0 I_{x_0}(x). \quad (2.19)$$

Therefore, in the case of chaotic sub-sources, we expect to observe smoothly distributed light along the entire  $x$ -axis, i.e.,  $\langle I(x, t) \rangle \sim \text{constant}$  (in space and in time) when  $x$  is not too far from the optical axis.

In certain cases, Equation 2.19 is also written in terms of the angular diameter of the radiation source that is defined from the viewpoint of the observer. For example, the angular size of the 1D aperture in Figure 2.1,  $\Delta\theta$ , is defined as the angle between two lines that connect the observation point of  $x$  with the source points of  $x_0 = b/2$  and  $x_0 = -b/2$ . Equation 2.19 may be written in terms of the angular variable  $\theta$  as

$$\langle I(x, t) \rangle = \int_{-\Delta\theta/2}^{\Delta\theta/2} d\theta I(\theta) \sim I_0, \quad (2.20)$$

where  $I_0$  is a constant, if  $x$  is not too far from the optical axis, or if  $I(\theta) \sim \text{constant}$ .

In the discussion of the temporal behavior of radiation, we found that chaotic-thermal sub-sources produce temporal randomly distributed radiation. Now we have discovered similar behavior for chaotic sub-sources with transverse spatial distribution. The physics is very simple: for a chaotic source, each sub-source radiates *independently*. The sub-intensities, instead of the subfields, excited from these chaotic sub-sources are then simply added at any space-time point of observation.

### Case II: Coherent sub-sources

In the case of coherent sub-sources we analyze the following two special situations:

#### A. $\varphi(x_0) = \varphi_0 = \text{constant}$

While  $\varphi(x_0) = \text{constant}$  for all subfields distributed along the  $x_0$ -axis, the field at space point  $x$  is the result of a coherent superposition of a large number of spherical harmonic waves each centered at  $x_0$ . Equation 2.18 becomes

$$\langle I(x, t) \rangle = \left| \int_{-b/2}^{b/2} dx_0 \frac{a(x_0)}{r} e^{-i(\omega t - kr)} \right|^2, \quad (2.21)$$

where  $r = \sqrt{z^2 + (x - x_0)^2}$  is a function of  $x$  and  $x_0$  for a chosen  $z$ . The coherent superposition indicated in Equation 2.21 results in a diffraction pattern on the observation plane, implying a constructive-destructive interference. The diffraction pattern is easy to calculate numerically for any observation plane, either far field or near field. To have an analytical solution, however, is never easy for an arbitrary plane. We now consider far-field observation by applying the far-field Fraunhofer approximation

$$r = \sqrt{z^2 + (x - x_0)^2} \simeq r_0 - \vartheta x_0, \quad (2.22)$$

where angle  $\vartheta$  is defined in Figure 2.1 with  $\vartheta \simeq x/r_0 \simeq x/(z-z_0)$ . Substituting Equation 2.22 into Equation 2.21, the diffraction pattern is approximated as

$$\langle I(x, t) \rangle \simeq \left| \frac{e^{-i[\omega t - kr_0(x)]}}{r_0} \int_{-b/2}^{b/2} dx_0 a_0 e^{-ik\vartheta x_0} \right|^2 = I_0 \text{sinc}^2 \frac{k\vartheta b}{2}, \quad (2.23)$$

where  $b$  is the width of the 1D source, and we have treated  $a(x_0) \simeq a_0$  as a constant, which is reasonable for a random distribution.

Equation 2.23 indicates a standard Fraunhofer diffraction pattern of a 1D aperture, which is the result of coherent superposition of a large number of subfields each excited by a point sub-source distributed along the  $x_0$ -axis. The subfields are superposed *constructively* within the pattern and *destructively* outside the pattern. It is interesting to see that although each sub-source radiates spherical waves in all directions, when the sub-sources radiate coherently, we can only observe light within a certain limited angular region,  $\Delta\vartheta \sim \lambda/b$ . For visible light, a coherent source of a few millimeters in transverse dimension only radiates nearly collimated light with a diverging angle on the order of  $\Delta\vartheta \sim 10^{-3}$  rad, which can be effectively treated as collimated radiation.

$$\text{B. } \varphi(x_0) = k_{x_0} x_0$$

In certain experimental conditions, the complex amplitude of the subfield may have a phase factor of  $e^{ik_{x_0}x_0}$ , where  $k_{x_0}$  is a constant. This phase factor implies that any sub-source located at an arbitrary coordinate  $x_0$  radiates with a constant relative phase,  $\Delta\varphi = k_{x_0}\Delta x_0$ , with respect to the sub-source at  $x_0 + \Delta x_0$ . Equation 2.23 becomes

$$\begin{aligned} \langle I(x, t) \rangle &\simeq \left| \frac{e^{-i[\omega t - kr_0(x)]}}{r_0} \int_{-b/2}^{b/2} dx_0 a_0 e^{ik_{x_0}x_0} e^{-ik\vartheta x_0} \right|^2 \\ &= I_0 \operatorname{sinc}^2 \frac{(k_{x_0} - k\vartheta)b}{2}. \end{aligned} \quad (2.24)$$

Equation 2.24 implies a similar far-field Fraunhofer diffraction pattern as shown in Equation 2.23, except with a constant angular shift in the propagation direction  $\theta_0 = k_{x_0}/k$ .

Equations 2.23 and 2.24 have defined a wavepacket in the transverse dimension, which is the Fourier transform of the aperture function

$$\begin{aligned} E(x, t) &\simeq \frac{e^{-i[\omega t - kr_0(x)]}}{r_0(x)} \int_{-\infty}^{\infty} dx_0 A(x_0) e^{ik_x x_0} \\ &= \mathcal{F}_{k_x} \{A(x_0)\} \frac{e^{-i[\omega t - kr_0(x)]}}{r_0(x)}, \end{aligned} \quad (2.25)$$

where

$A(x_0)$  is named the “aperture function”

$k_x \sim k\vartheta$  is the transverse wavevector along the  $x$ -direction also known as the “spatial frequency”

The aperture function  $A(x_0)$  of the 1D source in Figure 2.1 is usually written as

$$A(x_0) = \begin{cases} a_0 e^{i\varphi(x_0)} & -b/2 \leq x_0 \leq b/2 \\ 0 & \text{otherwise} \end{cases}$$

where

$$\varphi(x_0) = \varphi_0 = \text{constant in Equation 2.23}$$

$$\varphi(x_0) = k_x x_0 \text{ in Equation 2.24}$$

The real-positive amplitude of the field along the 1D aperture is described by  $a(x_0)$ , while the phase variation along the 1D aperture is represented by  $e^{i\varphi(x_0)}$ . The wavepacket consists of a “carrier” spherical wave and a 1D “envelope”  $\mathcal{F}_{k_x}\{A(x_0)\}$  in the transverse dimension. The envelope restricts the values of  $k_x$  within a certain limit, which implies a restricted propagation direction. The formation of the wavepacket is the result of a constructive-destructive interference among a large number of coherent subfields excited by the spatially coherent sub-sources.

In Equation 2.25, the transverse coordinate  $x_0$  and the transverse wavevector  $k_x$  are Fourier conjugate variables, and obviously, the far-field observation plane is effectively the Fourier transform plane of the aperture function. Based on the Fourier transform, we may introduce a classical “uncertainty relation” between spatial variables  $x_0$  and  $k_x$  (or  $p_x$ )

$$\Delta x_0 \Delta k_x \geq 2\pi \quad \text{or} \quad \Delta x_0 \Delta p_x \geq h, \quad (2.26)$$

where

$p_x$  is the transverse momentum

$h$  is the Planck constant

Equation 2.26 defines a “diffraction limit” for a spatially coherent radiation source. Laser beams with a TEM<sub>00</sub> mode are typically spatially coherent. An idealized laser beam propagates under its “diffraction limit”: the greater the size of the laser beam, the smaller the diverging angle.

It is interesting to see the similarities between the temporal wavepacket in the longitudinal dimension and the spatial wavepacket in the transverse dimension. The temporal coherence of the radiation produces temporal wavepackets, implying temporal constructive-destructive interference; and the spatial coherence of the radiation results in spatial wavepackets, implying spatial constructive-destructive interference. In both cases, the energy of the radiation is enhanced significantly in the region of constructive interference, at the price of losing energy in the region of destructive interference.

---

## Summary

In this chapter, we first classified the concept of coherence. In fact, there have been two different types of coherence in optics: (1) an optical property based on which a radiation or a radiation source is named coherent or incoherent and (2) the observable or unobservable interference between temporally delayed or spatially separated electromagnetic fields. In this section, we restricted all discussion on (1).

To specify the coherence property, or the state of a radiation field, we introduced a simple model of radiation with multi-sub-source and multimode. Assuming a far-field pointradiation source, based on this simple model, the coherence property of radiation is classified into four extreme cases:

- (I) Incoherent sub-sources and incoherent Fourier-modes
- (II) Coherent sub-sources and coherent Fourier-mode
- (III) Incoherent sub-sources and coherent Fourier-mode
- (IV) Coherent sub-sources and incoherent Fourier-mode

In the discussion of case (III), we introduced the concepts of single wavepacket, a few wavepackets, and a large number of overlapped–partially overlapped wavepackets, each created from a sub-source. Although we did not introduce the concept of photon and formulate each subfield with a specific atomic transition, the purpose is obvious.

The optical coherence is then generalized to non–point-like sources. The concepts of spatial coherence and spatial wavepacket are introduced. The concepts of temporal coherence and spatial coherence are distinguished.

---

## Suggested Reading

Goodman, J.W., *Introduction to Fourier Optics*, Roberts & Company, Englewood, CO, 2005.

# 3

---

## *Diffraction and Propagation*

---

### 3.1 Diffraction

To demonstrate the minimum-width diffraction pattern, we need a spatially coherent radiation source such as that in Figure 2.1 with either  $\varphi(x_0) = \varphi_0$  or  $\varphi(x_0) = k_{x0}x_0$ . A laser beam with TEM<sub>00</sub> mode is definitely a better choice. Before the invention of the laser, optical collimators were widely used to simulate such a source. A collimator consists of a pin hole, or a line aperture (1D), and a lens system, as shown in Figure 3.1. The pin hole is placed at the principal focus of the lens system and is illuminated by a discharged light tube. The use of the pin hole is to simulate a point radiation source. The lens system introduces appropriate phase delays to the spherical wavefront originating from the point source and turns it into a “flat” wavefront. The spherical radiation then becomes a well-collimated light beam. Figure 3.1 is a schematic setup of such a collimated radiation source for observing the minimum-width diffraction pattern of a 1D aperture with a finite dimension of  $b$ . The well-collimated beam normally incident on the 1D aperture, passes the aperture, and propagates to an arbitrary observation plane of  $z = \text{constant}$ . What intensity distribution do we expect to observe on this plane?

The radiation field at the aperture can be approximated as a plane wave. According to Huygens’s principle, every point on a primary wavefront serves as the source of spherical secondary wavelets. Therefore, in the plane of the 1D aperture, each point on the primary plane wavefront can be treated as a sub-source with a constant phase  $\varphi(x_0) = \varphi_0$ . The secondary wavelets are thus superposed coherently on the observation plane

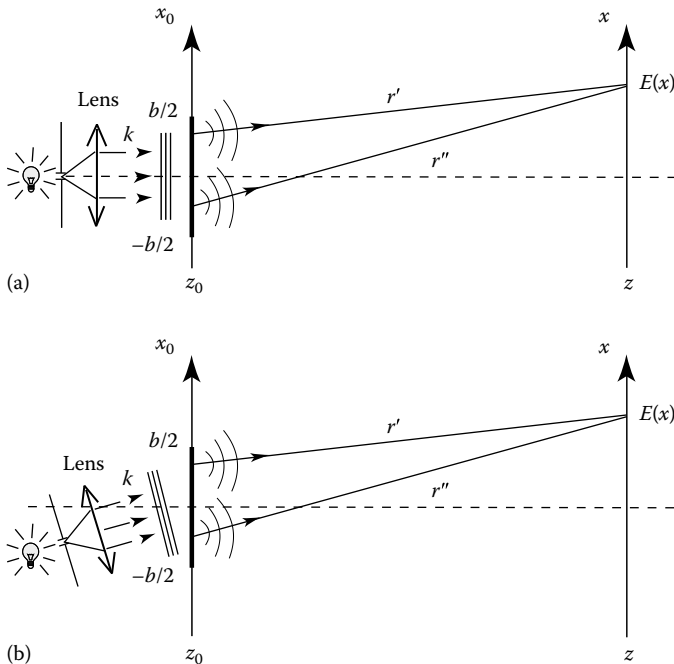
$$E(x, t) = \int_{-b/2}^{b/2} dx_0 \frac{E_0}{r} e^{-i(\omega t - kr)}, \quad (3.1)$$

where

$E_0 = a_0 e^{i\varphi_0} = A(x_0)$  is a complex amplitude

$$r = \sqrt{z^2 + (x - x_0)^2}$$

The constructive–destructive interference of the secondary wavelets results in a diffraction pattern on the observation plane. The diffraction can

**FIGURE 3.1**

Schematic experimental setup of single-slit diffraction. (a) The normally incident light passes the 1D aperture, propagates to and arrives at an arbitrary observation plane, either far field or near field. (b) The incident radiation illuminates the 1D aperture from a non-normal incident angle  $\theta_0 \neq 0$ . In both setups, the coherent superposition of the secondary wavelets results in a diffraction pattern. The far-field diffraction is named Fraunhofer while the near-field diffraction is called Fresnel.

be easily estimated numerically from Equation 3.1 for an arbitrary observation plane. The far-field diffraction is named Fraunhofer diffraction to distinguish it from the near-field Fresnel diffraction. Under the Fraunhofer far-field approximation, substituting Equation 2.22 into Equation 3.1 and following the same procedure as that for the coherent sub-sources of Figure 2.1, we obtain the same Fraunhofer diffraction pattern of Equation 2.23:

$$\begin{aligned} \langle I(x, t) \rangle &\simeq \left| \frac{e^{-i[\omega t - kr_0(x)]}}{r_0} \int_{-b/2}^{b/2} dx_0 A(x_0) e^{-ik_x x_0} \right|^2 \\ &= I_0 \operatorname{sinc}^2 \frac{k \vartheta b}{2}, \\ &= I_0 \operatorname{sinc}^2 \frac{\pi b x}{\lambda(z - z_0)}, \end{aligned} \quad (3.2)$$

where, again,  $\vartheta \simeq x/(z - z_0)$ .

Figure 3.1b is another example of such a collimated radiation source for observing the minimum-width diffraction pattern of a 1D aperture. Different from Figure 3.1a, in this setup, the wavevector of the collimated radiation does not pass normally through the 1D aperture plane but at an angle of  $\theta_0 \neq 0$ . Along the  $x_0$ -axis of the 1D aperture, the amplitude of each secondary wavelet gains a relative phase factor  $\varphi(x_0) = k_{x_0}x_0$ , where  $k_{x_0} = k\theta_0$  is the  $x$  component of the incident wavevector. Obviously, this phase factor makes a contribution to the integral of  $x_0$ . The secondary wavelets are thus superposed coherently, as described in Equation 3.1, on the observation plane with the complex amplitude of  $E_0 = a_0 e^{ik_{x_0}x_0} = A(x_0)$ . Under the Fraunhofer far-field approximation, following the same procedure as that for the coherent sub-sources of Figure 2.1, we obtain the same Fraunhofer diffraction pattern of Equation 2.24:

$$\begin{aligned}\langle I(x, t) \rangle &\simeq \left| \frac{e^{-i[\omega t - kr_0(x)]}}{r_0} \int_{-b/2}^{b/2} dx_0 A(x_0) e^{-ik_x x_0} \right|^2 \\ &= I_0 \operatorname{sinc}^2 \frac{(k_{x_0} - k_x)b}{2}, \\ &= I_0 \operatorname{sinc}^2 \frac{\pi b}{\lambda} \left( \frac{x}{z - z_0} - \theta_0 \right),\end{aligned}\quad (3.3)$$

where

$$k_x = k\vartheta \simeq kx/(z - z_0)$$

$\theta_0 = k_{x_0}/k$  is the incident angle of the collimated radiation

We now conclude that the far-field Fraunhofer diffraction pattern represents the Fourier transform of the aperture function

$$E(x, t) = \frac{e^{-i[\omega t - kr_0(x)]}}{r_0(x)} \mathcal{F}_{k_x} \{A(x_0)\} \quad (3.4)$$

with  $A(x_0) = a(x_0)e^{i\varphi(x_0)}$  in general. The aperture function  $A(x_0)$  corresponding to Figure 3.1a, in which  $\varphi(x_0) = \varphi_0$ , and Figure 3.1b, in which  $\varphi(x_0) = k_{x_0}x_0$ , are the same as those of the coherent sub-sources (A) and (B). It is interesting to compare the physical situation of Figure 2.1 with that of Figure 3.1. In Figure 2.1, we have a large number of spatially separated sub-sources each radiating spherical waves within a  $4\pi$  solid angle. In Figure 3.1, we assume only one point source and the radiation is well collimated by the use of a collimator. Although the physical situations are quite different, for both setups we observe the same diffraction pattern indicating the same constructive-destructive interference. It is clear that the primary wavefront of a point radiation source serves as a large number of spatially separated coherent

sub-sources. We may consider the radiation excited by a point source to be spatially coherent, although the source may be temporally incoherent.

The Fraunhofer diffraction pattern is treated as a Fourier transform of the aperture function under the far-field approximation. We may turn this approximation into an exact Fourier transform with the help of an optical converging lens. Figure 3.2 is a schematic setup of such a Fourier transformer. We assume an aperture function of  $\tilde{A}(\vec{\rho}_0) = A(\vec{\rho}_0)e^{i\varphi(\vec{\rho}_0)}$ , where  $\vec{\rho}_0$  is the 2D transverse coordinate on the aperture plane,  $A(\vec{\rho}_0)$  and  $e^{i\varphi(\vec{\rho}_0)}$  are the amplitude and the phase of the field at coordinate  $\vec{\rho}_0$  of the aperture, respectively. The field on the observation plane, which is the back focal plane of the lens in this setup, is the result of a coherent superposition of the secondary wavelets excited by each point of the primary wavefront at the aperture. The observed diffraction pattern represents the Fourier transform of the aperture function

$$E(\vec{\rho}) \propto \mathcal{F}_{\frac{\omega}{c} \frac{\vec{\rho}}{f}} \{ \tilde{A}(\vec{\rho}_0) \} \quad (3.5)$$

where  $(\omega/c)(\vec{\rho}/f)$  and  $\vec{\rho}_0$  are the conjugate variables of the Fourier transform. Equation 3.5 reveals the constructive-destructive nature of diffraction. It is easy to find that any plane wave, formed by a collection of parallel bundles of rays selected from the secondary wavelets, is brought to convergence at a unique point on the back focal plane of the lens: the parallel bundles of rays travel exactly the same optical path lengths to that unique point and superpose *constructively*. In other words, the field at each point on the Fourier transform plane represents a unique constructive interference of a plane wave excited by the secondary wavelets in the plane of the aperture. We will have a detailed calculation to support the above observation in Chapter 4 on imaging.

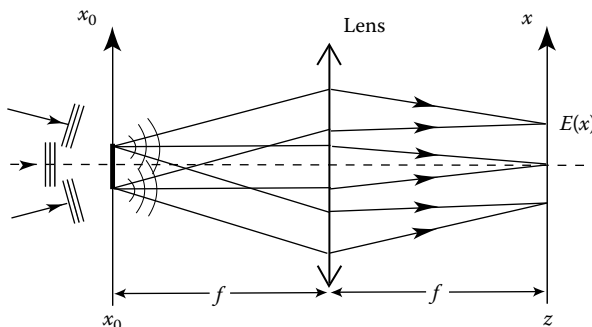


**FIGURE 3.2**

Schematic setup of a Fourier transformer. Light passing through the aperture at the front focal plane of a lens converges to form a far-field diffraction pattern on the back focal point of the lens, which is called the Fourier transform plane. The observed diffraction pattern represents the Fourier transform of the aperture function.

---

### 3.2 Field Propagation

In this section, we continue our discussion on the transverse behavior of radiation with regard to its propagation. Precisely, we are interested in determining  $E(\mathbf{r}, t)$  on a transverse plane of  $z = \text{constant}$  from a known distribution of the field  $E(\mathbf{r}_0, t_0)$  on a plane of  $z_0 = 0$ . We assume the field  $E(\mathbf{r}_0, t_0)$  is generated by an arbitrary source, either point-like or spatially extended. The observation plane at  $z = \text{constant}$  is located at an arbitrary distance from plane  $z_0 = 0$ , either far field or near field. The goal is to find a general solution  $E(\mathbf{r}, t)$ , or  $I(\mathbf{r}, t)$ , on the observation plane, based on the knowledge of  $E(\mathbf{r}_0, t_0)$  and the Maxwell electromagnetic wave theory. The use of Green's function or the field propagator, which describes the propagation of each mode of the field from the plane  $z_0 = 0$  to the observation plane  $z = \text{constant}$ , makes this goal formally achievable.

Unless  $E(\mathbf{r}_0, t_0)$  is a nonanalytic function in the space-time region of interest, there must exist a Fourier integral representation for  $E(\mathbf{r}_0, t_0)$ :

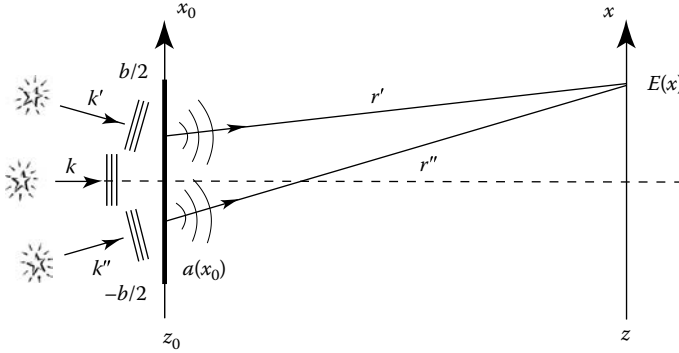
$$E(\mathbf{r}_0, t_0) = \int d\mathbf{k} E(\mathbf{k}) v_{\mathbf{k}}(\mathbf{r}_0, t_0) e^{-i\omega t_0}, \quad (3.6)$$

where  $v_{\mathbf{k}}(\mathbf{r}_0, t_0)$  is a solution of the Helmholtz wave equation under appropriate boundary conditions. The solution of the Maxwell wave equation  $v_{\mathbf{k}}(\mathbf{r}_0, t_0) e^{-i\omega t_0}$ , namely, the Fourier mode, can be chosen as a set of plane waves or spherical-waves, for example, depending on the boundary conditions. In Equation 3.6,  $E(\mathbf{k}) = a(\mathbf{k}) e^{i\phi(\mathbf{k})}$  is the complex amplitude of the Fourier-mode  $\mathbf{k}$ . In principle, we should be able to find an appropriate Green's function corresponding to the propagation of each mode under the Fourier integral point by point from the plane  $z_0 = 0$  to the plane of observation,

$$\begin{aligned} E(\mathbf{r}, t) &= \int d\mathbf{k} E(\mathbf{k}) g(\mathbf{k}, \mathbf{r} - \mathbf{r}_0, t - t_0) v_{\mathbf{k}}(\mathbf{r}_0, t_0) e^{-i\omega t_0} \\ &= \int d\mathbf{k} E(\mathbf{k}, \mathbf{r}_0, t_0) g(\mathbf{k}, \mathbf{r} - \mathbf{r}_0, t - t_0), \end{aligned} \quad (3.7)$$

where  $E(\mathbf{k}, \mathbf{r}_0, t_0) = E(\mathbf{k}) v_{\mathbf{k}}(\mathbf{r}_0, t_0) e^{-i\omega t_0}$ . The observed field  $E(\mathbf{r}, t)$  is the result of the superposition of these modes, which are propagated from the plane  $z_0 = 0$  to the plane  $z = \text{constant}$  mode by mode.

A simple example to introduce the concept of Green's function is illustrated in Figure 3.3. The radiation passes through a 1D aperture along the  $x_0$ -axis and then propagates and arrives at the observation plane. We assume a known field distribution function on the  $z_0$ -plane (or  $x_0$ -axis in 1D), and intend to calculate the field distribution on a *far-field* plane of  $z = \text{constant}$  (or along the  $x$ -axis in 1D). To simplify the mathematics, we further assume the radiation on the plane  $z_0 = 0$  is the result of a superposition among a

**FIGURE 3.3**

A simple example to introduce the concept of Green's function. The field on the plane  $z_0 = 0$  is the result of a superposition, either coherent or incoherent, of a large number of plane waves, each emitted from a distant point star and with a different  $\mathbf{k}$  vector. The observation plane  $z = \text{constant}$  is in the far-field zone. We are interested in Green's function that propagates each mode, point by point, from the plane  $z_0 = 0$  to the far-field observation plane  $z = \text{constant}$ .

large set of discrete plane waves, as shown in Figure 3.3. Although the field  $E(x_0, z_0, t_0)$  in the  $z_0$ -plane is the result of the superposition, either coherent or incoherent, according to the Maxwell wave theory of light, we may treat the propagation of each plane wave independently from plane  $z_0$  to plane  $z$ . The propagation or diffraction of a plane wave has been studied in Section 3.1. Let us consider that each plane wave contributes an amplitude  $a_j e^{i(\varphi_j + k_{jx_0} x_0)}$  along the  $x_0$ -axis, where  $a_j e^{i\varphi_j}$  is the constant complex amplitude of the  $j$ th mode, and  $e^{ik_{jx_0} x_0}$  represents the relative phase delay introduced by the  $x_0$  component of the  $j$ th incident wavevector,  $k_{jx_0}$ . The radiation field  $E(x, t)$  along the  $x$ -axis is thus

$$\begin{aligned} E(x, z, t) &= \sum_{\vec{k}_j} \frac{e^{-i[\omega_j t - k_j r_0(x)]}}{r_0(x)} \int_{-b/2}^{b/2} dx_0 a_j e^{i(\varphi_j + k_{jx_0} x_0)} e^{-ik_x x_0} \\ &= \sum_{\vec{k}_j} a_j e^{i\varphi_j} \left\{ \frac{e^{-i[\omega_j t - k_j r_0(x)]}}{r_0(x)} \int_{-b/2}^{b/2} dx_0 e^{i(k_{jx_0} - k_x)x_0} \right\} \\ &= \sum_{\vec{k}_j} g(\vec{k}_j; z - z_0, t - t_0) E(\vec{k}_j; x_0, z_0, t_0) \end{aligned} \quad (3.8)$$

where

$$g(\vec{k}_j; z - z_0, t - t_0) = \frac{e^{-i[\omega_j(t-t_0) - k_j r_0(x)]}}{r_0(x)} \int_{-b/2}^{b/2} dx_0 e^{i(k_{jx_0} - k_x)x_0} \quad (3.9)$$

is Green's function, which propagates the  $j$ th mode of the radiation field from plane  $z_0 = 0$  to the plane of observation. As we have discussed earlier, the spatial wavepacket represents a far-field Fraunhofer diffraction pattern produced by the 1D aperture from  $-b/2$  to  $b/2$  on the  $x_0$ -axis.

The physical picture of this simple example is clear: the  $j$ th mode of plane wave is diffracted by the 1D aperture to the far-field observation plane of  $z = \text{constant}$  as a spatial wavepacket. For a smaller (larger) sized aperture, the propagation direction of the  $j$ th mode is diffracted with a larger (smaller) diverging angle. When  $b \sim 0$ , the plane wave becomes spherical centered at the point-like aperture; when  $b \sim \infty$ , Green's function determines a unique propagation direction  $\vartheta = k_{jx_0}/k$ , corresponding to an undisturbed plane wave. It is worth mentioning that the approximations we have made are valid for far field only. One should not apply the above result to near field. The near-field Fresnel approximation will be given in the following.

For certain experimental setups, the propagation may have to be broken into a few steps,  $g = g_1 \times g_2 \times \dots \times g_N$ , in these cases

$$E(\mathbf{r}, t) = \int d\mathbf{k} E(\mathbf{k}, \mathbf{r}_0, t_0) g_1(\mathbf{k}, \mathbf{r}_1 - \mathbf{r}_0, t_1 - t_0) \times g_2(\mathbf{k}, \mathbf{r}_2 - \mathbf{r}_1, t_2 - t_1) \times \dots \times g_N(\mathbf{k}, \mathbf{r} - \mathbf{r}_{N-1}, t - t_{N-1}), \quad (3.10)$$

where  $N$  represents the number of steps. The final  $g(\mathbf{k}, \mathbf{r} - \mathbf{r}_0, t - t_0)$  can be quite different for different setups. No matter how complicated it is, Green's function plays the same role in the propagation of each Fourier-mode from space-time point  $(\mathbf{r}_0, t_0)$  to  $(\mathbf{r}, t)$ .

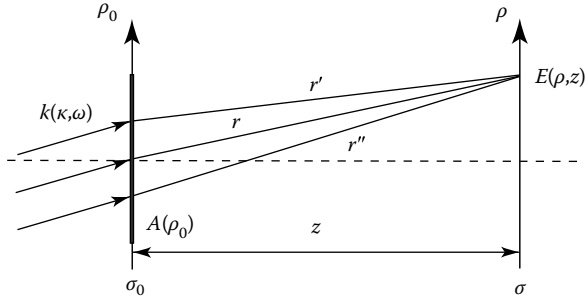
In certain experimental setups, it is convenient to write Equation 3.7 in the following form

$$E(\vec{\rho}, z, t) = \int d\omega d\vec{\kappa} g(\vec{\kappa}, \omega; \vec{\rho} - \vec{\rho}_0, z - z_0, t - t_0) E(\vec{\kappa}, \omega; \vec{\rho}_0, z_0, t_0), \quad (3.11)$$

where we have used the transverse-longitudinal coordinates in space-time ( $\vec{\rho}$  and  $z$ ) and in momentum ( $\vec{\kappa}$ ,  $\omega$ ). Green's function in Equation 3.11 propagates each mode of the field from plane  $\sigma_0$  of  $z_0 = 0$  to plane  $\sigma$  of  $z = \text{constant}$ . To simplify the mathematics in Equation 3.11, we have assumed one polarization. This simplification is reasonable for certain types of experimental setups; if not, we need to include the superposition of different polarizations and follow the sum rule of vectors.

Figure 3.4 illustrates an experimental setup in which the field travels freely from a finite size aperture  $A$  on the plane  $\sigma_0$  to the observation plane  $\sigma$ . Based on Figure 3.4, we evaluate  $g(\vec{\kappa}, \omega; \vec{\rho}, z)$ , namely, Green's function for free-space Fresnel propagation and diffraction.

According to the Huygens–Fresnel principle, the field at a space-time point  $(\vec{\rho}, z, t)$  is the result of a superposition of the spherical secondary wavelets that originated from each point on the  $\sigma_0$  plane, see Figure 3.4,

**FIGURE 3.4**

Schematic of free-space Fresnel propagation. The complex amplitude  $\tilde{A}(\vec{\rho}_0)$  is composed of a real function  $A(\vec{\rho}_0)$  and a phase  $e^{-i\vec{k}\cdot\vec{\rho}_0}$  associated with each of the transverse wavevectors  $\vec{k}$  on the plane of  $\sigma_0$ . Note: only one mode of wavevector  $\mathbf{k}(\vec{k}, \omega)$  is shown in the figure.

$$E(\vec{\rho}, z, t) = \int d\omega d\vec{k} E(\vec{k}, \omega; 0, 0) \int d\vec{\rho}_0 \frac{\tilde{A}(\vec{\rho}_0)}{r} e^{-i(\omega t - kr)}, \quad (3.12)$$

where we have set  $z_0 = 0$  and  $t_0 = 0$  at plane  $\sigma_0$ , and defined  $r = \sqrt{z^2 + |\vec{\rho} - \vec{\rho}_0|^2}$ . In Equation 3.12,  $\tilde{A}(\vec{\rho}_0)$  is the complex amplitude, or relative distribution of the field on the plane of  $\sigma_0$ , which may be written as a simple aperture function in terms of the transverse coordinate  $\vec{\rho}_0$ , as we have discussed earlier.

In the near-field Fresnel paraxial approximation, when  $|\vec{\rho} - \vec{\rho}_0|^2 \ll z^2$ , we take the first-order expansion of  $r$  in terms of  $z$  and  $\vec{\rho}$ :

$$r = \sqrt{z^2 + |\vec{\rho} - \vec{\rho}_0|^2} \simeq z \left( 1 + \frac{|\vec{\rho} - \vec{\rho}_0|^2}{2z^2} \right). \quad (3.13)$$

Thus  $E(\vec{\rho}, z, t)$  can be approximated as

$$E(\vec{\rho}, z, t) \simeq \int d\omega d\vec{k} E(\vec{k}, \omega; 0, 0) \int d\vec{\rho}_0 \frac{\tilde{A}(\vec{\rho}_0)}{z} e^{i\frac{\omega}{c}z} e^{i\frac{\omega}{2cz}|\vec{\rho} - \vec{\rho}_0|^2} e^{-i\omega t},$$

where  $e^{i\frac{\omega}{2cz}|\vec{\rho} - \vec{\rho}_0|^2}$  is known as the Fresnel phase factor.

Assuming the complex amplitude  $\tilde{A}(\vec{\rho}_0)$  is composed of a real function  $A(\vec{\rho}_0)$  and a phase  $e^{i\vec{k}\cdot\vec{\rho}_0}$ ,  $\tilde{A}(\vec{\rho}_0) = A(\vec{\rho}_0)e^{i\vec{k}\cdot\vec{\rho}_0}$ , associated with the transverse wavevector and the transverse coordinate in the plane of  $\sigma_0$ , which is reasonable for the setup of Figure 3.4, we can then write  $E(\vec{\rho}, z, t)$  in the following form:

$$E(\vec{\rho}, z, t) = \int d\omega d\vec{k} E(\vec{k}, \omega; 0, 0) e^{-i\omega t} \frac{e^{i\frac{\omega}{c}z}}{z} \int d\vec{\rho}_0 A(\vec{\rho}_0) e^{i\vec{k}\cdot\vec{\rho}_0} e^{i\frac{\omega}{2cz}|\vec{\rho} - \vec{\rho}_0|^2}. \quad (3.14)$$

Neglecting the temporal phase factor  $e^{-i\omega t}$ , the spatial Green's function  $g(\vec{\kappa}, \omega; \vec{\rho}, z)$  for free-space Fresnel propagation is thus

$$g(\vec{\kappa}, \omega; \vec{\rho}, z) = \frac{e^{i\frac{\omega}{c}z}}{z} \int_{\sigma_0} d\vec{\rho}_0 A(\vec{\rho}_0) e^{i\vec{\kappa} \cdot \vec{\rho}_0} G\left(|\vec{\rho} - \vec{\rho}_0|, \frac{\omega}{cz}\right), \quad (3.15)$$

where we have defined a Gaussian function  $G(|\vec{\alpha}|, \beta) = e^{i(\beta/2)|\alpha|^2}$ , namely, the Fresnel phase factor. It is straightforward to find that the Gaussian function  $G(|\vec{\alpha}|, \beta)$  has the following properties:

$$\begin{aligned} G^*(|\vec{\alpha}|, \beta) &= G(|\vec{\alpha}|, -\beta), \\ G(|\vec{\alpha}|, \beta_1 + \beta_2) &= G(|\vec{\alpha}|, \beta_1) G(|\vec{\alpha}|, \beta_2), \\ G(|\vec{\alpha}_1 + \vec{\alpha}_2|, \beta) &= G(|\vec{\alpha}_1|, \beta) G(|\vec{\alpha}_2|, \beta) e^{i\beta \vec{\alpha}_1 \cdot \vec{\alpha}_2}, \\ \int d\vec{\alpha} G(|\vec{\alpha}|, \beta) e^{i\vec{\gamma} \cdot \vec{\alpha}} &= i \frac{2\pi}{\beta} G\left(|\vec{\gamma}|, -\frac{1}{\beta}\right). \end{aligned} \quad (3.16)$$

Note that the last equation in Equation 3.16 is the Fourier transform of the  $G(|\vec{\alpha}|, \beta)$  function. As we shall see in the following, these properties are very useful in simplifying the calculations of Green's function  $g(\vec{\kappa}, \omega; \vec{\rho}, z)$ .

Now, we imagine inserting a plane  $\sigma'$ , which has an transverse dimension of infinity, between  $\sigma_0$  and  $\sigma$ . This is equivalent having two consecutive Fresnel propagations over a distance of  $d_1$  and  $d_2$ . Thus, the calculation of these consecutive Fresnel propagations should yield the same Green's function as that of the above direct Fresnel propagation shown in Equation 3.15:

$$\begin{aligned} g(\omega, \vec{\kappa}; \vec{\rho}, z) &= C^2 \frac{e^{i\frac{\omega}{c}(d_1+d_2)}}{d_1 d_2} \int_{\sigma'} d\vec{\rho}' \int_{\sigma_0} d\vec{\rho}_0 \tilde{A}(\vec{\rho}_0) G\left(|\vec{\rho}' - \vec{\rho}_0|, \frac{\omega}{cd_1}\right) G\left(|\vec{\rho} - \vec{\rho}'|, \frac{\omega}{cd_2}\right) \\ &= C \frac{e^{i\frac{\omega}{c}z}}{z} \int_{\sigma_0} d\vec{\rho}_0 \tilde{A}(\vec{\rho}_0) G\left(|\vec{\rho} - \vec{\rho}_0|, \frac{\omega}{cz}\right) \end{aligned} \quad (3.17)$$

where  $C$  is a necessary normalization constant. The double integral of  $d\vec{\rho}_0$  and  $d\vec{\rho}'$  in Equation 3.17 can be evaluated as

$$\begin{aligned} &\int_{\sigma'} d\vec{\rho}' \int_{\sigma_0} d\vec{\rho}_0 \tilde{A}(\vec{\rho}_0) G\left(|\vec{\rho}' - \vec{\rho}_0|, \frac{\omega}{cd_1}\right) G\left(|\vec{\rho} - \vec{\rho}'|, \frac{\omega}{cd_2}\right) \\ &= \int_{\sigma_0} d\vec{\rho}_0 \tilde{A}(\vec{\rho}_0) G\left(\vec{\rho}_0, \frac{\omega}{cd_1}\right) G\left(\vec{\rho}, \frac{\omega}{cd_2}\right) \\ &\times \int_{\sigma'} d\vec{\rho}' G\left(\vec{\rho}', \frac{\omega}{c} \left(\frac{1}{d_1} + \frac{1}{d_2}\right)\right) e^{-i\frac{\omega}{c} \left(\frac{\vec{\rho}_0}{d_1} + \frac{\vec{\rho}'}{d_2}\right) \cdot \vec{\rho}'} \end{aligned}$$

$$\begin{aligned}
&= \frac{i2\pi c}{\omega} \frac{d_1 d_2}{d_1 + d_2} \int_{\sigma_0} d\vec{\rho}_0 \tilde{A}(\vec{\rho}_0) G\left(\vec{\rho}_0, \frac{\omega}{cd_1}\right) G\left(\vec{\rho}, \frac{\omega}{cd_2}\right) \\
&\quad \times G\left(\left|\frac{\vec{\rho}_0}{d_1} + \frac{\vec{\rho}}{d_2}\right|, \frac{\omega}{c} \left(\frac{d_1 d_2}{d_1 + d_2}\right)\right) \\
&= \frac{i2\pi c}{\omega} \frac{d_1 d_2}{d_1 + d_2} \int_{\sigma_0} d\vec{\rho}_0 \tilde{A}(\vec{\rho}_0) G\left(|\vec{\rho} - \vec{\rho}_0|, \frac{\omega}{c(d_1 + d_2)}\right)
\end{aligned}$$

where we have applied Equation 3.16, and the integral of  $d\vec{\rho}'$  has been taken to infinity. Substituting this result into Equation 3.17, we have

$$\begin{aligned}
g(\vec{k}, \omega; \vec{\rho}, z) &= C^2 \frac{i2\pi c}{\omega} \frac{e^{i\frac{\omega}{c}(d_1+d_2)}}{d_1 + d_2} \int_{\sigma_0} d\vec{\rho}_0 \tilde{A}(\vec{\rho}_0) G\left(|\vec{\rho} - \vec{\rho}_0|, \frac{\omega}{c(d_1 + d_2)}\right) \\
&= C \frac{e^{i\frac{\omega}{c}z}}{z} \int_{\sigma_0} d\vec{\rho}_0 \tilde{A}(\vec{\rho}_0) G\left(|\vec{\rho} - \vec{\rho}_0|, \frac{\omega}{cz}\right).
\end{aligned}$$

Therefore, the normalization constant  $C$  must take the value of  $C = -i\omega/2\pi c$ . The normalized Green's function for free-space Fresnel propagation is thus

$$g(\vec{k}, \omega; \vec{\rho}, z) = \frac{-i\omega}{2\pi c} \frac{e^{i\frac{\omega}{c}z}}{z} \int_{\sigma_0} d\vec{\rho}_0 \tilde{A}(\vec{\rho}_0) G\left(|\vec{\rho} - \vec{\rho}_0|, \frac{\omega}{cz}\right). \quad (3.18)$$

## Summary

A radiation source at a space-time region radiates coherent or incoherent light. An optical measurement is set up at a separate space-time region, which can be in far field or near field. We are interested in determining  $E(\mathbf{r}, t)$  for the observation. This chapter serves two purposes: (1) it introduces the concepts of diffraction and Green's function and (2) provides exercises of classical superposition of EM waves, especially the superposition of a large number of spatial modes.

The most important results obtained from the above exercise are as follows:

1. The far-field Fraunhofer diffraction pattern represents the Fourier transform of the aperture function

$$E(x, t) = \frac{e^{-i[\omega t - kr_0(x)]}}{r_0(x)} \mathcal{F}_{k_x}\{A(x_0)\}.$$

2. The normalized Green's function for free-space Fresnel near-field propagation

$$g(\vec{\kappa}, \omega; \vec{\rho}, z) = \frac{-i\omega}{2\pi c} \frac{e^{i\frac{\omega}{c}z}}{z} \int_{\sigma_0} d\vec{\rho}_0 \tilde{A}(\vec{\rho}_0) G\left(|\vec{\rho} - \vec{\rho}_0|, \frac{\omega}{cz}\right).$$

---

### Suggested Reading

Goodman, J.W., *Introduction to Fourier Optics*, Roberts & Company, Englewood, Co, 2005.  
Hecht, E., *Optics*, Addison-Wesley, Reading, MA, 2001.



# 4

---

## *Optical Imaging*

---

The concept of classical imaging was well developed in optics prior to the electromagnetic wave theory of light. The early theories of geometric optics provided quite a few phenomenological explanations of the point-to-point relationship between an object plane and an image plane. In these theories, light is treated as a bundle of rays and the image is explained as the result of the peculiar way of their propagation. A later theory of classical imaging, namely, the theory of physical optics, is based on the concept of waves. Light is treated as waves that propagate to and interfere at a space-time point. The image is considered to be the result of constructive-destructive interference among these wavelike bundle rays, or bundle ray-like waves.

Figure 4.1 schematically illustrates a standard imaging setup. An object that is either self-luminous or externally illuminated by a radiation source. An imaging lens is used to image the randomly radiated or scattered radiations from the object onto an image plane, which is defined by the “Gaussian thin lens equation”

$$\frac{1}{s_i} + \frac{1}{s_o} = \frac{1}{f}, \quad (4.1)$$

where

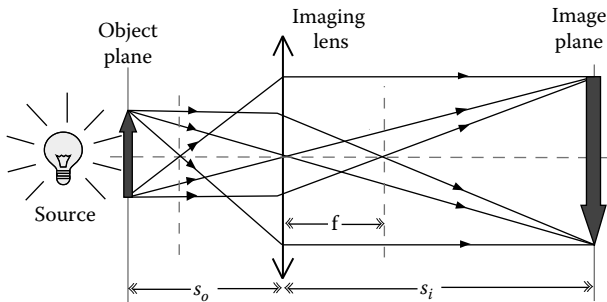
$s_o$  is the distance between the object and the imaging lens

$s_i$  is the distance between the imaging lens and the image plane

$f$  is the focal length of the imaging lens

Basically, this equation defines two planes with a point-to-point relationship, namely the object plane and the image plane: any radiation starting from a point on the object plane will impinge at a unique point on the image plane. It is not difficult to see from Figure 4.1 that the point-to-point relationship is the result of *constructive-destructive interference*. All radiation fields starting from a point on the object plane, which experience equal distance propagation, will superpose constructively to arrive at one unique point on the image plane, while those that experience unequal distance propagation will superpose destructively at all other points on the image plane. The use of the imaging lens makes this constructive-destructive interference possible.

A perfect point-to-point image-forming relationship between the object and image planes produces a perfect image. The observed image is a reproduction, either magnified or demagnified, of the illuminated object, mathematically corresponding to a convolution between the object

**FIGURE 4.1**

Imaging: a lens produces an *image* of an object in the plane defined by the Gaussian thin-lens equation  $1/s_i + 1/s_o = 1/f$ . The concept of an image is based on the existence of a point-to-point relationship between the object plane and the image plane.

distribution function  $|A(\vec{\rho}_o)|^2$  (aperture function) and a  $\delta$ -function, which characterizes the perfect point-to-point relationship between the object and image planes:

$$I(\vec{\rho}_i) = \int_{\text{obj}} d\vec{\rho}_o |A(\vec{\rho}_o)|^2 \delta\left(\vec{\rho}_o + \frac{\vec{\rho}_i}{m}\right) \quad (4.2)$$

where

$I(\vec{\rho}_i)$  is the intensity in the image plane

$\vec{\rho}_o$  and  $\vec{\rho}_i$  are 2D vectors of the transverse coordinates in the object and image planes, respectively

$m = s_i/s_o$  is the image magnification factor

In reality, limited by the finite size of the imaging system, we may never obtain a perfect point-to-point correspondence. The incomplete constructive-destructive interference turns the point-to-point correspondence into a point-to-“spot” relationship. The  $\delta$ -function in the convolution of Equation 4.2 will be replaced by a point-spread function:

$$I(\vec{\rho}_i) = \int_{\text{obj}} d\vec{\rho}_o |A(\vec{\rho}_o)|^2 \text{somb}^2\left[\frac{R}{s_o} \frac{\omega}{c} \left|\vec{\rho}_o + \frac{\vec{\rho}_i}{m}\right|\right], \quad (4.3)$$

where the sombrero-like function, or the Airy disk, is defined as

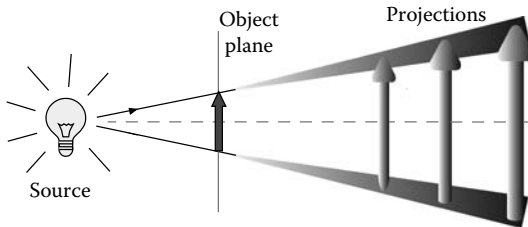
$$\text{somb}(x) = \frac{2J_1(x)}{x},$$

and

$J_1(x)$  is the first-order Bessel function

$R$  the radius of the imaging lens

$R/s_o$  is known as the numerical aperture of the imaging system

**FIGURE 4.2**

Projection: a light source illuminates an object and no image-forming system is present, no image plane is defined, and only projections, or shadows, of the object can be observed.

The sombrero-like point-spread function, or the Airy disk, defines the spot size on the image plane that is produced by the radiation coming from point  $\vec{p}_o$ . It is clear from Equation 4.3 that a larger imaging lens and shorter wavelength will result in a narrower point-spread function, and thus a higher spatial resolution of the image. The finite size of the spot determines the spatial resolution of the imaging system.

It should be emphasized that we must not confuse a trivial “projection” with an image. Similar to an x-ray photograph, projection makes a shadow of an object, instead of an image of the object. Figure 4.2 distinguishes a projection shadow from an image. The object–shadow correspondence is essentially defined by the propagation direction of the light rays, and there is no unique imaging plane. The shadow can be found in any plane behind the object. A projection shadow is the result of the simple “blocked–unblocked” effect of light, which is very different from an imaged image, both from a fundamental and from a practical viewpoint. There is no spatial resolution defined in terms of the Rayleigh criterion for a projection shadow.

## 4.1 A Classic Imaging System

We now calculate the point-to-spot function and analyze the imaging mechanism within the framework of Maxwell’s electromagnetic wave theory. As we have discussed in Section 3.2, the field  $E(\vec{p}_i, z_i, t)$  at the image plane can be written as

$$E(\vec{p}_i, z_i, t) = \int d\omega d\vec{\kappa} E(\vec{\kappa}, \omega; \vec{p}_o, z_0 = 0, t_0 = 0) g(\vec{\kappa}, \omega; \vec{p}_i, z_i, t), \quad (4.4)$$

where

$E(\vec{\kappa}, \omega, \vec{\rho}_o, z_0 = 0, t_0 = 0)$  is the complex amplitude of the mode with transverse wavevector  $\vec{\kappa}$  and frequency  $\omega$  in the object plane

$g(\vec{\kappa}, \omega; \vec{\rho}_i, z_i, t)$  is the Green's function

In Equation 4.4, we have taken  $z_0 = 0$  and  $t_0 = 0$  at the object plane as usual. To simplify the mathematics, we will assume  $\omega = \text{constant}$  and focus on one polarization of the field in the following analysis and calculation, unless certain circumstances are specified.

Based on the simple experimental setup of Figure 4.3,  $g(\vec{\kappa}, \omega; \vec{\rho}, z)$  is found to be

$$\begin{aligned} g(\vec{\kappa}, \omega; \vec{\rho}_i, s_o + s_i) &= \int_{\text{obj}} d\vec{\rho}_o \int_{\text{lens}} d\vec{\rho}_l \left\{ A(\vec{\rho}_o) e^{i\vec{\kappa} \cdot \vec{\rho}_o} \right\} \left\{ \frac{-i\omega}{2\pi c} \frac{e^{i\frac{\omega}{c}s_o}}{s_o} G\left(|\vec{\rho}_l - \vec{\rho}_o|, \frac{\omega}{cs_o}\right) \right\} \\ &\quad \times \left\{ G\left(|\vec{\rho}_l|, -\frac{\omega}{cf}\right) \right\} \left\{ \frac{-i\omega}{2\pi c} \frac{e^{i\frac{\omega}{c}s_i}}{s_i} G\left(|\vec{\rho}_i - \vec{\rho}_l|, \frac{\omega}{cs_i}\right) \right\} \end{aligned} \quad (4.5)$$

where  $\vec{\rho}_o$ ,  $\vec{\rho}_l$ , and  $\vec{\rho}_i$  are two-dimensional vectors defined, respectively, in the object, lens, and image planes. The first curly bracket includes the object-aperture function  $A(\vec{\rho}_o)$  and the phase factor  $e^{i\vec{\kappa} \cdot \vec{\rho}_o}$  contributed to the object plane by each transverse mode  $\vec{\kappa}$ , as illustrated in Figure 3.4. The terms in the second and fourth curly brackets describe free-space Fresnel propagation-diffraction from the source/object plane to the imaging lens, and from the imaging lens to the detection plane, respectively. The Fresnel propagator includes a spherical wave function  $e^{i\frac{\omega}{c}(z_j - z_k)} / (z_j - z_k)$  and a Fresnel phase factor  $G(|\vec{\alpha}|, \beta) = e^{i(\beta/2)|\vec{\alpha}|^2} = e^{i\omega|\vec{\rho}_j - \vec{\rho}_k|^2/2c(z_j - z_k)}$ . The third curly bracket adds a phase factor,  $G\left(|\vec{\rho}_l|, -\frac{\omega}{cf}\right) = e^{-i\frac{\omega}{2cf}|\vec{\rho}_l|^2}$ , which is introduced by the imaging lens.

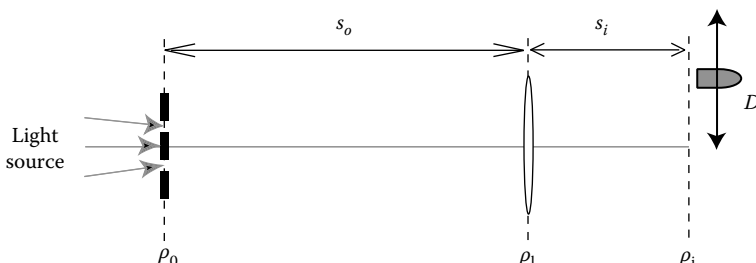


FIGURE 4.3

A typical imaging system. A lens of finite size is used to produce a demagnified image of an object with limited spatial resolution.

Applying the properties of the Gaussian function, Equation 4.5 can be simplified into the following form:

$$\begin{aligned} g(\vec{\kappa}, \omega; \vec{\rho}_i, z = s_o + s_i) &= \frac{-\omega^2}{(2\pi c)^2 s_o s_i} e^{i\frac{\omega}{c}(s_o + s_i)} G\left(|\vec{\rho}_i|, \frac{\omega}{cs_i}\right) \int_{obj} d\vec{\rho}_o A(\vec{\rho}_o) G\left(|\vec{\rho}_o|, \frac{\omega}{cs_o}\right) e^{i\vec{\kappa} \cdot \vec{\rho}_o} \\ &\times \int_{lens} d\vec{\rho}_l G\left(|\vec{\rho}_l|, \frac{\omega}{c} \left[ \frac{1}{s_o} + \frac{1}{s_i} - \frac{1}{f} \right]\right) e^{-i\frac{\omega}{c} \left( \frac{\vec{\rho}_o}{s_o} + \frac{\vec{\rho}_i}{s_i} \right) \cdot \vec{\rho}_l}. \end{aligned} \quad (4.6)$$

The image plane is defined by the Gaussian thin-lens equation of Equation 4.1. Hence, the second integral in Equation 4.6 simplifies and gives, for a finite sized lens of radius  $R$ , the so-called point-spread function of the imaging system:

$$\text{somb}(x) = \frac{2J_1(x)}{x} \quad \text{with } x = \left[ \frac{R}{s_o} \frac{\omega}{c} \left| \vec{\rho}_o + \frac{\vec{\rho}_i}{m} \right| \right]$$

where

$J_1(x)$  is the first-order Bessel function

$m = s_i/s_o$  is the magnification of the imaging system

Substituting the result of Equation 4.6 into Equation 4.4 enables us to obtain the classical self-correlation of the field, or, equivalently, the intensity at the image plane.

$$I(\vec{\rho}_i, z_i, t) = \langle E^*(\vec{\rho}_i, z_i, t) E(\vec{\rho}_i, z_i, t) \rangle \quad (4.7)$$

where  $\langle \dots \rangle$  denotes an ensemble average. We assume monochromatic light for classical imaging as usual.

Case (I): Incoherent imaging

The ensemble average  $\langle E^*(\vec{\kappa}, \omega) E(\vec{\kappa}', \omega) \rangle$  yields zeros except when  $\vec{\kappa} = \vec{\kappa}'$ . Taking  $\vec{\kappa} = \vec{\kappa}'$  and  $E(\vec{\kappa}) \sim \text{constant}$ , the integral on  $d\vec{\kappa}$  yields

$$\int d\vec{\kappa} e^{i\vec{\kappa} \cdot (\vec{\rho}_o - \vec{\rho}'_o)} \simeq \delta(\vec{\rho}_o - \vec{\rho}'_o).$$

The image is thus

$$I(\vec{\rho}_i) \propto \int_{obj} d\vec{\rho}_o |A(\vec{\rho}_o)|^2 \text{somb}^2 \left[ \frac{R}{s_o} \frac{\omega}{c} \left| \vec{\rho}_o + \frac{\vec{\rho}_i}{m} \right| \right]. \quad (4.8)$$

An incoherent image, magnified by a factor of  $m$ , is thus given by the convolution between the squared moduli of the object aperture function and the point-spread function. The spatial resolution of the image is thus determined by the finite width of the somb<sup>2</sup>-function.

### Case (II): Coherent imaging

Assuming the object is illuminated by a coherent wavepacket, which is the result of a superposition of a large number of coherent plane-wave modes. We write the wavevector of each mode into a vector sum:  $\mathbf{k} = k_z \hat{z}_0 + \vec{k}$ , where, again,  $k_z \hat{z}_0$  and  $\vec{k}$  are the longitudinal and transverse wavevectors. The transverse part of the wavepacket is approximately

$$\int d\vec{k} E(\vec{k}) e^{i\vec{k} \cdot \vec{\rho}_o} \simeq \mathcal{F}_{\vec{\rho}_o}\{E(\vec{k})\}.$$

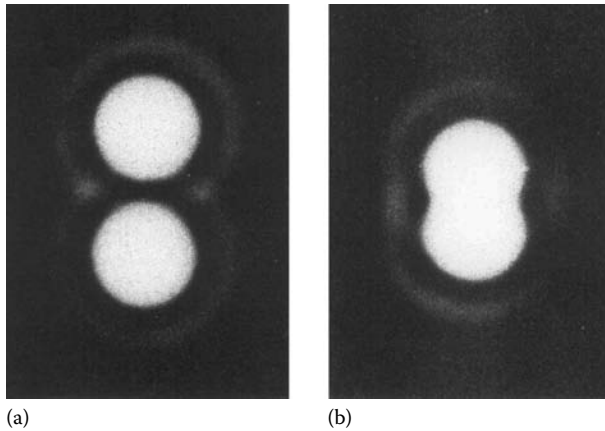
We further assume  $\mathcal{F}_{\vec{\rho}_o}\{E(\vec{k})\} \sim \text{constant}$ , i.e., a smooth and uniform illumination on the entire object-aperture. The image, or the intensity distribution on the image plane, is thus

$$I(\vec{\rho}_i) \propto \left| \int_{obj} d\vec{\rho}_o A(\vec{\rho}_o) e^{i\frac{\omega}{2cs_0} |\vec{\rho}_o|^2} \text{somb} \left[ \frac{R}{s_o} \frac{\omega}{c} \left| \vec{\rho}_o + \frac{\vec{\rho}_i}{m} \right| \right] \right|^2. \quad (4.9)$$

A coherent image, magnified by a factor of  $m$ , is thus given by the modulus square of the convolution between the object aperture function (multiplied by a Fresnel phase factor) and the point-spread function.

For  $s_i < s_o$  and  $s_o > f$ , both Equations 4.8 and 4.9 describe a real demagnified inverted image. In both cases, a narrower sombrero-function yields a higher spatial resolution. Thus, the use of shorter wavelengths allows for improvement of the spatial resolution of an imaging system.

The finite size of the image spot, which is defined by the point-spread function, determines the *spatial resolution* of the imaging setup, and thus limits the ability of making demagnified images. The most popular definition of the spatial resolution of imaging is perhaps Rayleigh's criterion: the images of two nearby point objects are said to be *unresolvable* when the center of one point-spread function falls on the first minimum of the point-spread function of the other. Figure 4.4 qualitatively depicts this situation, in which the two point-spread functions have just become unresolvable. To quantify this situation, we consider a point object located at  $\vec{\rho}_o = 0$  of the object plane. For an idealized imaging system, this point would have a unique corresponding image point on the image plane at  $\vec{\rho}_i = 0$ , which means a point-to-point relationship. Realistically, however, we have to take into account the point-to-spot relationship that is determined by the size of the point-spread function. Rayleigh's criterion defines the size of the point-spread function by taking its first minimum, i.e.,

**FIGURE 4.4**

(a) Nonoverlapped images. The images of two nearby point objects are spatially resolvable.  
 (b) Overlapped images. The center of one point-spread function falls on the first minimum of the point-spread function of the other. This situation is defined as *unresolvable* by Rayleigh's criterion.

$$\frac{R\omega}{c s_i} \Delta |\vec{\rho}_i| \simeq 3.83 \quad \text{or} \quad \Delta |\vec{\rho}_i| \simeq 1.22 \frac{\pi c s_i}{R\omega} \quad (4.10)$$

Now, we consider another nearby point on the object plane  $\vec{\rho}_o = \vec{a}$ . In order to distinguish the image of  $\vec{\rho}_o = \vec{a}$  from that of  $\vec{\rho}_o = 0$ , the value of  $m|\vec{a}|$  cannot be smaller than  $\Delta|\vec{\rho}_i|$ . Therefore, we must have

$$m|\vec{a}| \geq \frac{\pi c s_i}{R\omega},$$

where again  $m = |\vec{\rho}_i|/|\vec{\rho}_o| = s_i/s_o$  is the magnification factor of the image. We thus have a minimum resolvable angular separation, or angular limit of resolution,

$$\Delta\theta_{min} \simeq \frac{|\vec{a}|}{s_o} \simeq 1.22 \frac{\pi c}{R\omega} = 1.22 \frac{\lambda}{D}, \quad (4.11)$$

where  $D$  is the diameter of the lens system. It is clear from Equations 4.3 and 4.11 that the use of large-size imaging lenses and shorter-wavelength radiation sources will result in narrower point-spread functions and smaller minimum resolvable angles, i.e., higher spatial resolution. To improve the spatial resolution, one of the efforts in the lithography industry is the use of shorter wavelengths. This effort is, however, limited to a certain level because of the inability of lenses to effectively work beyond a certain "cutoff" wavelength.

Equations 4.3 and 4.11 impose a diffraction-limited spatial resolution on an imaging system when the diameter of the imaging system and the

wavelength of the light source are both fixed. This limit is fundamental in both classical optics and in quantum mechanics. Any violation would be considered a violation of the uncertainty principle.

---

## 4.2 Fourier Transform via a Lens

We continue a similar calculation for the Fourier transformer described in Section 3.1. Figure 3.2 schematically illustrates this simple Fourier transformer, which consists of an object-aperture and a converging lens. The object aperture is located in the front focal plane of the converging lens, and is illuminated by a well-collimated light beam. The diffracted plane waves are collected and converged by the lens to form a far-field diffraction pattern at its back focal plane. We will show that this diffraction pattern is the Fourier transform of the aperture function  $A(\vec{\rho}_o)$ . Comparing the setup of Figure 3.2 with that of Figure 4.1, what we need is to assign  $s_o = f$  and  $s_i = f$ , and to complete the integrals of Equation 4.6. We will first evaluate the integral over the lens. To simplify the mathematics, we approximate the integral to infinity. Differing from the calculation for imaging resolution, the purpose of this evaluation is to find the Fourier transform. Thus, the approximation of an infinite lens is appropriate. By applying the properties of the Gaussian function listed in Equation 3.16, the integral over the lens contributes the following function of  $\vec{\rho}_o$  to the integral of  $d\vec{\rho}_o$  in Equation 4.6:

$$\int_{\text{lens}} d\vec{\rho}_l G\left(|\vec{\rho}_l|, \frac{\omega}{cf}\right) e^{-i\frac{\omega}{c}(\frac{\vec{\rho}_o}{f} + \frac{\vec{\rho}}{f}) \cdot \vec{\rho}_l} \propto C G\left(|\vec{\rho}_o|, -\frac{\omega}{cf}\right) e^{-i\frac{\omega}{cf}\vec{\rho}_o \cdot \vec{\rho}},$$

where  $C$  absorbs all constants including a phase factor  $G\left(|\vec{\rho}|, -\frac{\omega}{cf}\right)$ . Replacing this result with the integral of  $d\vec{\rho}_l$  in Equation 4.6, under the condition of a well-collimated light illumination of  $\vec{\kappa} = 0$ , we obtain:

$$E(\vec{\rho}) \propto \int_{\text{obj}} d\vec{\rho}_o A(\vec{\rho}_o) e^{-i\frac{\omega}{cf}\vec{\rho} \cdot \vec{\rho}_o} = \mathcal{F}_{\left(\frac{\omega}{c}\frac{\vec{\rho}}{f}\right)} \{A(\vec{\rho}_o)\}, \quad (4.12)$$

which is the Fourier transform of the object-aperture function  $A(\vec{\rho}_o)$  with conjugate variable  $(\omega/c)(\vec{\rho}/f)$ . In fact,  $(\omega/c)(\vec{\rho}/f)$  is the transverse wavevector on the back focal plane of the lens. For a well-collimated light illumination of  $\vec{\kappa} \neq 0$ , the far-field diffraction pattern will be shifted:

$$E(\vec{\rho}) \propto \int_{\text{obj}} d\vec{\rho}_o A(\vec{\rho}_o) e^{i\vec{\kappa} \cdot \vec{\rho}_o} e^{-i\frac{\omega}{cf}\vec{\rho} \cdot \vec{\rho}_o} = \mathcal{F}_{\left(\frac{\omega}{c}\frac{\vec{\rho}}{f} - \vec{\kappa}\right)} \{A(\vec{\rho}_o)\}. \quad (4.13)$$

## Summary

Classical imaging implies a unique point-to-point relationship between the object plane and the image plane: any radiation starting from a point on the object plane will “collapse” to a unique point on the image plane. This point-to-point image-forming relationship is the result of *constructive-destructive interference*. The radiation fields coming from a point on the object plane will experience equal distance propagation to superpose constructively at one unique point on the image plane, and experience unequal distance propagations to superpose destructively at all other points on the image plane. The use of the imaging lens makes this constructive-destructive interference possible.

This chapter is another good exercise for practicing the classical superposition principle. This exercise is not restricted to imaging. In principle, we can calculate the distributions of the radiation field or intensity on any plane that is parallel to the object plane. In fact, we have given a solution for the radiation field on the Fourier transform plane,  $E(\vec{\rho})$ , which is simply a Fourier transform of the aperture function.

The most important results derived from the imaging excise are as follows:

$$\frac{1}{s_i} + \frac{1}{s_o} = \frac{1}{f'}$$

$$I(\vec{\rho}_i) \propto \int_{obj} d\vec{\rho}_o |A(\vec{\rho}_o)|^2 \text{somb}^2 \left[ \frac{R}{s_o} \frac{\omega}{c} \left| \vec{\rho}_o + \frac{\vec{\rho}_i}{m} \right| \right],$$

and

$$I(\vec{\rho}_i) \propto \left| \int_{obj} d\vec{\rho}_o A(\vec{\rho}_o) e^{j \frac{\omega}{2cs_0} |\vec{\rho}_o|^2} \text{somb} \left[ \frac{R}{s_o} \frac{\omega}{c} \left| \vec{\rho}_o + \frac{\vec{\rho}_i}{m} \right| \right] \right|^2.$$

## Suggested Reading

Goodman, J.W., *Introduction to Fourier Optics*, Roberts & Company, Englewood, Co,

2005.

Hecht, E., *Optics*, Addison-Wesley, Reading, MA, 2001.



# 5

---

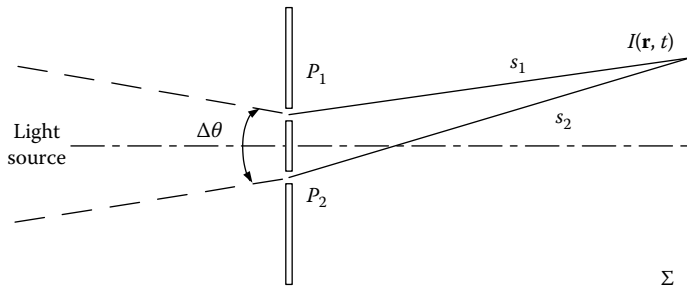
## *First-Order Coherence of Light*

---

The concept of first-order coherence was introduced in classical theory of light to quantify the interference between temporally delayed or spatially separated electromagnetic waves. The superposed radiations are defined as first-order coherent if the interference fringes exhibit 100% modulation, or first-order incoherent if no interference fringes are observable. The radiation fields are considered as partial coherent if the modulation is less than 100%, however, greater than zero. The higher the degree of first-order coherence, the higher interference visibility we could observe. Although it is named “coherence” and is an intrinsic property of the radiation itself, either temporal or spatial, the concept is very different from the coherence property of light that we have discussed in the early sections. For a certain spectral bandwidth  $\Delta\omega$  and spatial frequency  $\Delta\vec{k}$  or  $\Delta k_x$  ( $\Delta k_y$ ), the interference observed in an interferometer is the same for laser light and thermal light. The measurement cannot distinguish a laser beam from thermal radiation by means of the degree of first-order coherence. Although laser radiation is named coherent, this does not mean we can observe interference for a temporal delay beyond certain limits. Similarly, thermal light is considered incoherent radiation, but this does not prevent us to observe interference fringes under the “white-light” condition, i.e., in the neighborhood of equal optical paths of an interferometer. One should pay special attention to this.

To introduce the concepts of the degree of first-order coherence, we consider a typical Young’s interference experiment shown in Figure 5.1. The upper and the lower pinholes  $P_1$  and  $P_2$  are located at coordinates  $\mathbf{r}_1$  and  $\mathbf{r}_2$ , respectively. The observation is made by scanning a point photodetector on the far-field observation plane  $\Sigma$ , or with a point photodetector array. The light source, a bright distant star that is treated as either a point source or an extended source with a certain angular size, the pinholes, and the observation plane are arranged symmetrically with respect to the optical axis, as shown in Figure 5.1.

The radiation field at space-time coordinates  $P_1(\mathbf{r}_1, t_1)$  and  $P_2(\mathbf{r}_2, t_2)$  are superposed in a later time at each point on the transverse plane  $\Sigma$  for the observation of interference. Either observable or unobservable, the interference is determined by the intrinsic property of the radiation: (1) the maximum allowable optical delay for observing interference is determined by the spectral bandwidth of the field, the greater the bandwidth  $\Delta\omega$  the shorter the allowable temporal delay between the superposed

**FIGURE 5.1**

Schematic of Young's double-slit interference experiment. The interference pattern is observed by scanning a point photodetector on the observation plane  $\Sigma$ .

fields; (2) the maximum allowable transverse spatial separation between the two superposed fields is determined by the bandwidth of the spatial frequency  $|\Delta\vec{k}|$ , the greater the bandwidth of  $|\Delta\vec{k}|$  the smaller the allowable separation between the two fields. Observations (1) and (2) are considered as the temporal coherence and spatial coherence of the radiation field, respectively, by definition. Although thermal light and laser radiation are distinguished as incoherent light and coherent radiation, the concepts of temporal coherence and spatial coherence may apply to both.

The expectation value of the intensity,  $I(\mathbf{r}, t)$ , at space-time point  $(\mathbf{r}, t)$  is

$$\begin{aligned}\langle I(\mathbf{r}, t) \rangle &= \left\langle |E(\mathbf{r}, t)|^2 \right\rangle = \left\langle \left| E\left(\mathbf{r}_1, t - \frac{s_1}{c} \right) + E\left(\mathbf{r}_2, t - \frac{s_2}{c} \right) \right|^2 \right\rangle \\ &= \langle E^*(\mathbf{r}_1, t_1)E(\mathbf{r}_1, t_1) \rangle + \langle E^*(\mathbf{r}_2, t_2)E(\mathbf{r}_2, t_2) \rangle \\ &\quad + \langle E^*(\mathbf{r}_1, t_1)E(\mathbf{r}_2, t_2) \rangle + \langle E(\mathbf{r}_1, t_1)E^*(\mathbf{r}_2, t_2) \rangle \end{aligned}\quad (5.1)$$

where  $t_1 = t - s_1/c$ ,  $t_2 = t - s_2/c$ , referring to the earlier times of the fields at the upper and the lower pinholes  $\mathbf{r}_1$  and  $\mathbf{r}_2$ , respectively. It is recognized that the first two terms in Equation 5.1 correspond to the light intensity passing through the upper and lower pinholes at space-time points  $(\mathbf{r}_1, t_1)$  and  $(\mathbf{r}_2, t_2)$ , respectively. The third and fourth terms, which involves the cross product of the field at space-time point  $(\mathbf{r}_2, t_2)$  (or  $(\mathbf{r}_1, t_1)$ ) and its conjugate at space-time point  $(\mathbf{r}_1, t_1)$  (or  $(\mathbf{r}_2, t_2)$ ), gives rise to an interference pattern at the observation plane and results in a sinusoidal modulation of the photocurrent as a function of the position of the scanning photodetector.

The instantaneous interference pattern  $I(\mathbf{r}, t)$  may fluctuate from time to time in the neighborhood of the expectation function  $\langle I(\mathbf{r}, t) \rangle$  of Equation 5.1. As we have discussed in Section 1.4,  $\langle I(\mathbf{r}, t) \rangle$  is calculated by "taking

into account all possible realizations of the fields." We break  $\langle I(\mathbf{r}, t) \rangle$  of Equation 5.1 into two groups:

1.  $\langle E^*(\mathbf{r}_1, t_1) E(\mathbf{r}_1, t_1) \rangle$  and  $\langle E^*(\mathbf{r}_2, t_2) E(\mathbf{r}_2, t_2) \rangle$ ;
2.  $\langle E^*(\mathbf{r}_1, t_1) E(\mathbf{r}_2, t_2) \rangle$  and  $\langle E(\mathbf{r}_1, t_1) E^*(\mathbf{r}_2, t_2) \rangle$ .

We define

$$\begin{aligned}\Gamma(\mathbf{r}_1, t_1; \mathbf{r}_1, t_1) &\equiv \langle E^*(\mathbf{r}_1, t_1) E(\mathbf{r}_1, t_1) \rangle \\ \Gamma(\mathbf{r}_2, t_2; \mathbf{r}_2, t_2) &\equiv \langle E^*(\mathbf{r}_2, t_2) E(\mathbf{r}_2, t_2) \rangle\end{aligned}\quad (5.2)$$

and

$$\begin{aligned}\Gamma(\mathbf{r}_1, t_1; \mathbf{r}_2, t_2) &\equiv \langle E^*(\mathbf{r}_1, t_1) E(\mathbf{r}_2, t_2) \rangle \\ \Gamma(\mathbf{r}_2, t_2; \mathbf{r}_1, t_1) &\equiv \langle E(\mathbf{r}_1, t_1) E^*(\mathbf{r}_2, t_2) \rangle\end{aligned}\quad (5.3)$$

as the self-coherence function and the mutual-coherence function, respectively. It is obvious that

$$\Gamma(\mathbf{r}_1, t_1; \mathbf{r}_2, t_2) = \Gamma^*(\mathbf{r}_2, t_2; \mathbf{r}_1, t_1). \quad (5.4)$$

In connection with the concepts of classical statistics, the self-coherence function of Equation 5.2 and the mutual-coherence function of Equation 5.3 are recognized as the self-correlation function and the cross-correlation function, respectively, of the fields. Physically,  $\Gamma(\mathbf{r}_1, t_1; \mathbf{r}_2, t_2)$  determines the visibility of the interference, which will be quantified in the following. The self-coherence function  $\Gamma(\mathbf{r}_j, t_j; \mathbf{r}_j, t_j)$ ,  $j = 1, 2$ , defined in Equation 5.2 represents the expectation value, or expectation function of intensity, which has been discussed in Section 1.4. Applying the mutual-coherence function and the self-coherence function, the expectation value of  $I(\mathbf{r}, t)$  in Equation 5.1 is written as

$$\langle I(\mathbf{r}, t) \rangle = \Gamma_{11} + \Gamma_{22} + \Gamma_{12} + \Gamma_{21}. \quad (5.5)$$

where we have used the shortened notation  $\Gamma_{11} = \Gamma(\mathbf{r}_1, t_1; \mathbf{r}_1, t_1)$ ,  $\Gamma_{22} = \Gamma(\mathbf{r}_2, t_2; \mathbf{r}_2, t_2)$ ,  $\Gamma_{12} = \Gamma(\mathbf{r}_1, t_1; \mathbf{r}_2, t_2)$ , and  $\Gamma_{21} = \Gamma(\mathbf{r}_2, t_2; \mathbf{r}_1, t_1)$ .

Now, we introduce the normalized complex degree of first-order coherence by writing Equation 5.5 in the following form

$$\begin{aligned}\langle I(\mathbf{r}, t) \rangle &= \Gamma_{11} + \Gamma_{22} + 2\sqrt{\Gamma_{11} \Gamma_{22}} \operatorname{Re} \gamma_{12} \\ &= \langle I_1 \rangle + \langle I_2 \rangle + 2\sqrt{\langle I_1 \rangle \langle I_2 \rangle} |\gamma_{12}| \cos(\omega\tau)\end{aligned}\quad (5.6)$$

where  $\tau = \tau_1 - \tau_2 = (t_1 - t_2) + (z_2 - z_1)/c = (s_2 - s_1)/c + (z_2 - z_1)/c$ . In Equation 5.6, we have defined the normalized complex degree of first-order coherence

$$\begin{aligned}\gamma(\mathbf{r}_1, t_1; \mathbf{r}_2, t_2) &\equiv \frac{\Gamma(\mathbf{r}_1, t_1; \mathbf{r}_2, t_2)}{\sqrt{\Gamma(\mathbf{r}_1, t_1; \mathbf{r}_1, t_1) \Gamma(\mathbf{r}_2, t_2; \mathbf{r}_2, t_2)}} \\ &= \frac{\langle E^*(\mathbf{r}_1, t_1) E(\mathbf{r}_2, t_2) \rangle}{\sqrt{\langle |E(\mathbf{r}_1, t_1)|^2 \rangle \langle |E(\mathbf{r}_2, t_2)|^2 \rangle}},\end{aligned}\quad (5.7)$$

for  $\Gamma(\mathbf{r}_1, t_1; \mathbf{r}_1, t_1) \neq 0$  and  $\Gamma(\mathbf{r}_2, t_2; \mathbf{r}_2, t_2) \neq 0$ . It is easy to find that

$$0 \leq |\gamma_{12}| \leq 1. \quad (5.8)$$

$|\gamma_{12}|$  is thus related to the visibility of the interference fringe modulation

$$V \equiv \frac{I_{MAX} - I_{MIN}}{I_{MAX} + I_{MIN}} = \frac{2\sqrt{\langle I_1 \rangle \langle I_2 \rangle}}{\langle I_1 \rangle + \langle I_2 \rangle} |\gamma_{12}|. \quad (5.9)$$

If  $\langle I_1 \rangle = \langle I_2 \rangle = I_0/2$ , which is perhaps the most common arrangement for an optimized interferometer,  $|\gamma_{12}|$  is identical to the visibility of the interference modulation:

$$V = |\gamma_{12}|.$$

The expectation function of the intensity on the observation plane is thus

$$\langle I(\mathbf{r}, t) \rangle = I_0 [1 + V \cos(\omega\tau)]. \quad (5.10)$$

The radiation fields at space-time points  $(\mathbf{r}_1, t_1)$  and  $(\mathbf{r}_2, t_2)$  are named coherent, partially coherent, and incoherent in terms of the value of  $|\gamma_{12}|$ :

|                           |   |
|---------------------------|---|
| Coherent fields           | if $ \gamma(\mathbf{r}_1, t_1; \mathbf{r}_2, t_2)  = 1$     |
| Partially coherent fields | if $0 <  \gamma(\mathbf{r}_1, t_1; \mathbf{r}_2, t_2)  < 1$ |
| Incoherent fields         | if $ \gamma(\mathbf{r}_1, t_1; \mathbf{r}_2, t_2)  = 0$ .   |

In Sections 5.1 and 5.2, we calculate and discuss the mutual-coherence function  $\Gamma(\mathbf{r}_1, t_1; \mathbf{r}_2, t_2)$  and the complex degree of first-order coherence  $\gamma(\mathbf{r}_1, t_1; \mathbf{r}_2, t_2)$  for a few simplified models of radiation in terms of the concepts of temporal and spatial coherence.

---

## 5.1 First-Order Temporal Coherence

We discuss first-order temporal coherence of light in this section. Considering Young's double-slit experimental setup of Figure 5.2 with a distant point light source at  $\mathbf{r} = 0$ , which contains a large number of incoherent or coherent sub-sources.

### 5.1.1 $\Gamma(\mathbf{r}_1, t_1; \mathbf{r}_2, t_2)$ : Chaotic-Thermal Light

Similar to the model of thermal radiation in Section 1.4, we assume  $E(\mathbf{r}_1, t_1)$  and  $E(\mathbf{r}_2, t_2)$  both contain a large number of incoherent subfields originated from a large number of independent and randomly radiating point sub-sources. The mutual-coherence function of  $E(\mathbf{r}_1, t_1)$  and  $E(\mathbf{r}_2, t_2)$  is expected to be

$$\begin{aligned} & \Gamma(\mathbf{r}_1, t_1; \mathbf{r}_2, t_2) \\ &= \left\langle \sum_{j,k} \int d\omega d\omega' a_j(\omega) a_k(\omega') e^{-i(\varphi_j(\omega) - \varphi_k(\omega'))} e^{i[(\omega t_1 - \omega' t_2) - (k(\omega)z_1 - k'(\omega')z_2)]} \right\rangle \\ &\simeq \sum_j \int d\omega a_j^2(\omega) e^{i[\omega(t_1 - t_2) - k(\omega)(z_1 - z_2)]} \\ &\simeq e^{i\omega_0\tau} \mathcal{F}_\tau \left\{ \sum_j a_j^2(\nu) \right\}, \end{aligned} \quad (5.11)$$

where the expectation operation or ensemble average has taken into account all possible realizations of the phases in the sum of the subfields. In

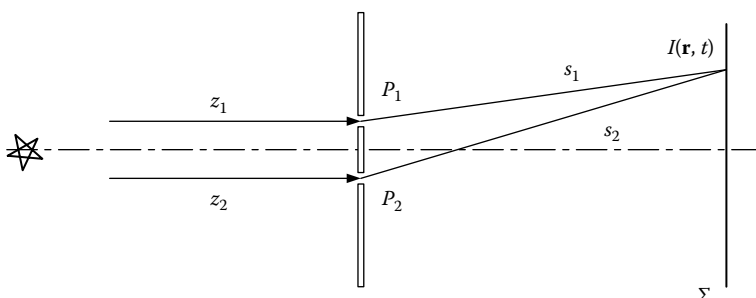


**FIGURE 5.2**

Schematic of Young's double-slit interference experiment, which measures the temporal coherence of radiation originated from a distant point source.

Equation 5.11, we have defined  $\tau = t_1 - t_2 = (s_2 - s_1)/c + (z_2 - z_1)/c$ . In the simplified situation in which all the subfields hold identical spectrum distribution  $a^2(\omega)$ , it is easy to find that the optical delay of  $\tau$  and the spectral bandwidth  $\Delta\omega$  are restricted by the relation of  $\Delta\omega\tau = 2\pi$  for a nonzero mutual coherence function of  $\Gamma_{12}$ , and consequently for an observable interference.

The mutual coherence function  $\Gamma(\mathbf{r}_1, t_1; \mathbf{r}_2, t_2)$  can be calculated directly by substituting Equation 1.33, the formally integrated Fourier transform of the fields for  $E^*(\mathbf{r}_1, t_1)$  and  $E(\mathbf{r}_2, t_2)$ , into Equation 5.3,

$$\begin{aligned} & \Gamma(\mathbf{r}_1, t_1; \mathbf{r}_2, t_2) \\ &= e^{i[\omega_0(t_1-t_2)-k_0(z_1-z_2)]} \left\langle \mathcal{F}_{\tau_1}^* \left\{ \sum_j a_j(\nu) e^{-i\varphi_j(\nu)} \right\} \mathcal{F}_{\tau_2} \left\{ \sum_j a_j(\nu') e^{i\varphi_j(\nu')} \right\} \right\rangle \\ &= e^{i[\omega_0(t_1-t_2)-k_0(z_1-z_2)]} \left\langle \int \int d\nu d\nu' \sum_{j,k} a_j(\nu) a_k(\nu') e^{-i[\varphi_j(\nu) - \varphi_k(\nu')]} e^{i(\nu\tau_1 - \nu'\tau_2)} \right\rangle \\ &= e^{i\omega_0\tau} \mathcal{F}_\tau \left\{ \sum_j a_j^2(\nu) \right\}, \end{aligned} \quad (5.12)$$

where, again, the expectation operation is partially completed by taking into account all possible values of the random relative phases  $\varphi_j(\nu) - \varphi_k(\nu')$ . The only surviving terms in the integral are the diagonal terms of  $\nu = \nu'$  and  $j = k$ . Again, we find that the optical delay of  $\tau$  and the spectral bandwidth  $\Delta\omega$  are restricted by  $\Delta\omega\tau = 2\pi$  for a nonzero mutual coherence function of  $\Gamma_{12}$ , and consequently an observable interference.

Taking the result of Equation 5.11 or Equation 5.12, keeping only the nonzero contributions, the expectation value of  $\langle I(\mathbf{r}, t) \rangle$ , can be written into the following form by taking into account the chaotic nature of the radiation field,

$$\langle I(\mathbf{r}, t) \rangle \simeq \sum_j \int d\omega |E_j(\omega; z_1, t_1) + E_j(\omega; z_2, t_2)|^2. \quad (5.13)$$

Equation 5.13 indicates that the expected interference pattern is the sum of a large number of individual sub-interference patterns,  $I_j(\omega; \mathbf{r}, t)$ , each is produced by a Fourier-mode of  $\omega$  associated with a sub-source of  $j$ th. In the neighborhood of  $\tau = 0$ , these individual sub-patterns coincide so that the intensity modulation can be easily observed ( $V(0) \cong 100\%$ ). When the detector moves away from  $\tau = 0$ , i.e., the value of  $|\tau|$  increases, the relative phase shifts between the sub-patterns increase. The spread of the sub-patterns

smooths the light intensity distribution on the observation plane, and the interference visibility is then reduced from 100% to 0%, which means a constant distribution. The interference visibility,  $V(\tau)$ , is determined by the maximum relative phase shift  $\Delta\omega\tau$ , where  $\Delta\omega = \omega_{max} - \omega_{min}$  is the bandwidth of the field. If  $\Delta\omega\tau \ll 2\pi$ , i.e., the relative phase shifts are not large enough to produce noticeable separation between these sub-patterns for the value of  $\tau$ , then the interference modulation will be observable. When the relative phase shifts increase, however, the sub-patterns are significantly separated at the value of  $\tau$ . The interference modulation visibility is then reduced to zero. In other words, for a certain spectral bandwidth of  $\Delta\omega$ , if the time delay  $\tau \ll 2\pi/\Delta\omega$ , the fields at  $t$  and  $t + \tau$  are considered temporally coherent by definition. Otherwise, the fields are considered temporally incoherent by definition, which means no interference can be observed.

From Equation 5.13 we may conclude that each Fourier-mode associated with a sub-source only interferes with itself. However, we should not ignore that Equation 5.13 is the result of a destructive interference cancellation between all possible different Fourier-modes associated with all possible different sub-sources. It is the interference between different modes associated with different sub-sources that leads to Equation 5.11, or Equation 5.12, and consequently makes “each Fourier-mode associated with a sub-source only interfere with itself.” We should keep this in mind in the following discussions for different measurements and models.

The complete destructive interference, cancellation happens only when “taking into account all possible realizations of the field.” In one measurement, the cancellation may not be complete, therefore, the interference pattern may randomly fluctuate in the neighborhood of its expectation of Equation 5.13 in a nondeterministic manner. In a perfect interferometer, this fluctuation may be the major contribution to the observation.

In summary, for a far-field point thermal source,  $\Gamma(\mathbf{r}_1, t_1; \mathbf{r}_2, t_2)$  is a function of the temporal delay  $\tau = \tau_1 - \tau_2 = (s_2 - s_1)/c + (z_2 - z_1)/c$  only, which implies that the temporal correlation function of a chaotic-thermal field is invariant under the displacements of time variables, i.e., invariant for any time  $t$ . This is the characteristic of stationary fields. For stationary fields, the temporal mutual-correlation function  $\Gamma(\mathbf{r}_1, t_1; \mathbf{r}_2, t_2)$  is usually written as  $\Gamma_{12}(\tau)$ . Compared with the expectation value of the intensity of chaotic-thermal radiation in Equation 2.1, we find  $\langle I(\mathbf{r}_1, t_1) \rangle = \Gamma_{11}(0)$  and  $\langle I(\mathbf{r}_2, t_2) \rangle = \Gamma_{22}(0)$ . The expectation function of the intensity on the observation plane of Young’s double-slit experiment illustrated in Figure 5.1 is thus

$$\begin{aligned}\langle I(\mathbf{r}, t) \rangle &= \Gamma_{11}(0) + \Gamma_{22}(0) + 2 \operatorname{Re} \Gamma_{12}(\tau) \\ &= \Gamma_{11}(0) + \Gamma_{22}(0) + 2\sqrt{\Gamma_{11}(0) \Gamma_{22}(0)} \operatorname{Re} \gamma_{12}(\tau),\end{aligned}\quad (5.14)$$

where

$\Gamma_{11}(0)$  [ $\Gamma_{22}(0)$ ] is calculated in Equation 2.1

$\Gamma_{12}(\tau)$  is calculated in Equation 5.12

It can be seen from Equations 5.14 and 5.12 that the maximum interference occurs in the neighborhood of  $\tau = 0$ . The interference starts to be invisible at  $\tau = 2\pi/\Delta\omega$ . In Equation 5.14, the normalized complex degree of first-order temporal coherence is defined by

$$\gamma_{12}(\tau) \equiv \frac{\Gamma_{12}(\tau)}{[\Gamma_{11}(0)]^{\frac{1}{2}} [\Gamma_{22}(0)]^{\frac{1}{2}}}.$$

The time delay

$$\tau = \frac{2\pi}{\Delta\omega} \equiv \tau_c \quad (5.15)$$

is defined as the coherence time of the field and consequently  $c\tau_c$  is defined as the coherence length of the field. The fields with separation  $\tau$  are named temporally coherent when  $|\gamma(\tau)| = 1$ , corresponding to  $\tau \ll \tau_c$ ; temporally partially coherent when  $0 < |\gamma(\tau)| < 1$ , corresponding to  $0 < \tau < \tau_c$ ; and temporally incoherent when  $|\gamma(\tau)| = 0$ , corresponding to  $\tau \geq \tau_c$ . Therefore, when we say a thermal radiation source has a coherence time  $\tau_c$  or a coherence length  $c\tau_c$  we mean that first-order interference is observable between any fields with a temporal separation of  $\tau < \tau_c$ .

### 5.1.2 $\Gamma(\mathbf{r}_1, t_1; \mathbf{r}_2, t_2)$ : A Large Number of Overlapped and Partially Overlapped Wavepackets

Similar to the model of thermal radiation in Section 1.4, we assume the measured radiation field is the result of a superposition of a large number of wavepackets radiated from a large number of sub-sources. In this model, the sub-sources radiate independently; however, the  $j$ th group of Fourier-modes are created coherently at time  $t_{0j}$  from the  $j$ th sub-source. The coherent superposition of the Fourier-modes of the  $j$ th sub-source yields a well-defined wavepacket in space-time when  $a_j(v)$  is a well-defined function in terms of frequency. We label the wavepacket associated with the  $j$ th sub-source with parameter  $t_{0j}$ . We assume the photodetection event at space-time point  $(\mathbf{r}, t)$  involves a large number of randomly distributed wavepackets and the fields  $E(\mathbf{r}_1, t_1)$  and  $E(\mathbf{r}_2, t_2)$  are the results of a superposition of  $N$  overlapped–partially overlapped wavepackets. Substituting Equation 1.25, the formally integrated wavepackets of  $E(\mathbf{r}_1, t_1)$  and  $E(\mathbf{r}_2, t_2)$ , into  $\langle E^*(\mathbf{r}_1, t_1)E(\mathbf{r}_2, t_2) \rangle$ , the mutual coherence function  $\Gamma(\mathbf{r}_1, t_1; \mathbf{r}_2, t_2)$  is written as

$$\begin{aligned}
\Gamma(\mathbf{r}_1, t_1; \mathbf{r}_2, t_2) &= \left\langle \sum_{j=1}^N e^{i\omega_0 \tau_{j1}} \mathcal{F}_{\tau_{j1}}^* \{a(v)\} \sum_{k=1}^N e^{-i\omega_0 \tau_{k2}} \mathcal{F}_{\tau_{k2}} \{a(v)\} \right\rangle \\
&= \left\langle \sum_j e^{i\omega_0 (\tau_{j1} - \tau_{j2})} \mathcal{F}_{\tau_{j1}}^* \{a(v)\} \mathcal{F}_{\tau_{j2}} \{a(v)\} \right\rangle \\
&\quad + \left\langle \sum_{j \neq k} e^{i\omega_0 (\tau_{j1} - \tau_{k2})} \mathcal{F}_{\tau_{j1}}^* \{a(v)\} \mathcal{F}_{\tau_{k2}} \{a(v)\} \right\rangle
\end{aligned} \tag{5.16}$$

where  $j$  and  $k$  label the  $j$ th and  $k$ th wavepacket. We have also defined  $\tau_{j1} = (t - t_{0j}) - s_1/c - z_1/c$  and  $\tau_{k2} = (t - t_{0k}) - s_2/c - z_2/c$ . It is convenient to break up the sum into two groups. If we consider a random distribution of the wavepackets, i.e., arbitrary initial time of  $t_{0j}$  and  $t_{0k}$ , the second group ( $j \neq k$ ) of the sum vanishes when taking into account all possible values of  $t_{0j} - t_{0k}$  in the superposition. This result indicates that *the only observable interference is the interference of the wavepacket with itself*. Interference between two different wavepackets becomes unobservable when taking into account all possible realizations of the wavepacket.

Now we approximate the sum into an integral of  $t_0$ , similar to what we have done in Section 1.4. The mutual coherence function  $\Gamma(\mathbf{r}_1, t_1; \mathbf{r}_2, t_2)$  is calculated as

$$\begin{aligned}
\Gamma(\mathbf{r}_1, t_1; \mathbf{r}_2, t_2) &= \left\langle e^{i\omega_0 \tau} \sum_j \mathcal{F}_{\tau_{j1}}^* \{a(v)\} \mathcal{F}_{\tau_{j2}} \{a(v)\} \right\rangle \\
&\simeq e^{i\omega_0 \tau} \int_{-\infty}^{\infty} dt_0 \mathcal{F}_{\tau_1}^* \{a(v)\} \mathcal{F}_{\tau_2} \{a(v)\} \\
&= e^{i\omega_0 \tau} \mathcal{F}_\tau \{a^2(v)\}
\end{aligned} \tag{5.17}$$

where

$$\begin{aligned}
\tau_1 &= (t - t_0) - (z_1 + s_1)/c \\
\tau_2 &= (t - t_0) - (z_2 + s_2)/c \\
\tau &= \tau_1 - \tau_2 = (s_2 - s_1)/c + (z_2 - z_1)/c
\end{aligned}$$

The mutual-coherence function, and consequently the interference visibility, is quantitatively determined by how much the two wavepackets,  $\mathcal{F}_{\tau_{j1}} \{a(v)\}$  and its delayed conjugate  $\mathcal{F}_{\tau_{j2}}^* \{a(v)\}$ , are overlapped in space-time. The integral has a maximum value when  $\tau = \tau_1 - \tau_2 = 0$ . The radiation fields become first-order incoherent when  $\tau \geq 2\pi/\Delta\omega$ . Again,

$$\tau_c = 2\pi/\Delta\omega$$

is called the coherence time of the field, which is nothing but the temporal width of the wavepackets.

Substituting Equations 2.11 and 5.17 into  $\langle I(\mathbf{r}, t) \rangle$ , the expectation function of the intensity in the observation plane is thus

$$\begin{aligned} \langle I(\mathbf{r}, t) \rangle \simeq & \int dt_0 \left\{ |\mathcal{F}_{\tau_1-t_0}\{a(v)\}|^2 + |\mathcal{F}_{\tau_2-t_0}\{a(v)\}|^2 \right. \\ & \left. + 2\text{Re}[\mathcal{F}_{\tau_1-t_0}^*\{a(v)\} \mathcal{F}_{\tau_2-t_0}\{a(v)\} e^{i\omega_0\tau}] \right\} \end{aligned} \quad (5.18)$$

Equation 5.18 indicates a summation of a large number of individual sub-interference-patterns each associated with an individual wavepackets. One may conclude from Equation 5.18, again, that each wavepacket only interferes with itself. Due to the common relative delay  $\tau$ , all the sub-interference patterns comprise the same sinusoidal function. The identical sub-interference patterns  $I_j(\mathbf{r}, t - t_{0j})$  add at the observation plane. For a large number of randomly and continuously distributed sub-patterns in terms of  $t_{0j}$ , the measured interference pattern is the same as that of the thermal light.

The integral over  $t_0$  in Equation 5.17 is mathematically equivalent to a time integral and, consequently, an autocorrelation or a self-convolution of the wavepacket:

$$\begin{aligned} \Gamma(\mathbf{r}_1, t_1; \mathbf{r}_2, t_2) &= e^{-i\omega_0\tau} \int_{-\infty}^{\infty} dt \mathcal{F}_{\tau_1}^*\{E(v)\} \mathcal{F}_{\tau_2}\{E(v)\} \\ &= \int_{-\infty}^{\infty} dt' E^*(t') E(t' - \tau) \end{aligned} \quad (5.19)$$

Applying the Wiener–Khintchine theorem, we have

$$\Gamma(\mathbf{r}_1, t_1; \mathbf{r}_2, t_2) = \int_{-\infty}^{\infty} dt E^*(t) E(t - \tau) = \int_{-\infty}^{\infty} dv |E(v)|^2 e^{-iv\tau}$$

### 5.1.3 $\Gamma(\mathbf{r}_1, t_1; \mathbf{r}_2, t_2)$ : A Wavepacket

We assume the measurement involves only one wavepacket at a time period of  $\Delta t \geq \tau_c$ . This experimental condition is achievable by using a weak light source at the single-photon level or a laser pulse. In either case, the wavepacket may split into two by taking path  $s_1$  (passing through pinhole  $P_1$ ) and/or path  $s_2$  (passing through pinhole  $P_2$ ) to be superposed at  $(\mathbf{r}, t)$ . We further assume an idealized point photodetector is used to monitor the intensity  $I(\mathbf{r}, t)$ . Classical theory does not prevent a photodetector from responding to any energy level of light even if it carries energy less than that of a photon. The instantaneous intensity of  $(\mathbf{r}, t)$  is calculated as

$$\begin{aligned} I(\mathbf{r}, t) &= |\mathcal{F}_{(\tau_1-t_0)}\{a(v)\} e^{-i\omega_0(\tau_1-t_0)} + \mathcal{F}_{(\tau_2-t_0)}\{a(v)\} e^{-i\omega_0(\tau_2-t_0)}|^2 \\ &= |\mathcal{F}_{(\tau_1-t_0)}\{a(v)\}|^2 + |\mathcal{F}_{(\tau_2-t_0)}\{a(v)\}|^2 \\ &\quad + 2\text{Re}[\mathcal{F}_{(\tau_1-t_0)}^*\{a(v)\} \mathcal{F}_{(\tau_2-t_0)}\{a(v)\} e^{i\omega_0\tau}] \end{aligned} \quad (5.20)$$

where, again,  $a(\nu)$  is the amplitude for the Fourier mode of frequency  $\omega$  of the wavepacket,  $\tau_1 = t_1 - z_1/c$ ,  $\tau_2 = t_2 - z_2/c$ ,  $t_0$  is the initial creation time of the wavepacket. It is easy to see from Equation 5.20 that an interference pattern is potentially observable when the two wavepackets overlap at the observation points  $(\mathbf{r}, t)$ . The maximum interference occurs in the neighborhood of  $\tau = \tau_1 - \tau_2 \sim 0$  when the two wavepackets completely overlap. For  $\tau > 2\pi/\Delta\omega$ , the two Fourier transforms cannot have nonzero values simultaneously, the third term of Equation 5.20 vanishes, and consequently no interference is observable when the temporal delay is greater than the temporal width of the wavepacket. Obviously, the coherence time of the field equals the width of the wavepacket,  $\tau_c = 2\pi/\Delta\omega$ .

Next, we consider a measurement that involves a large number of wavepackets. We will separate the calculation for single-photon wavepackets from that of coherent laser pulses.

#### Case I: Wavepackets at the single-photon's level

Although Maxwell electromagnetic wave theory of light does not prevent the interference of a wavepacket at the single-photon level, if only one photon is involved in the measurement, the measurement may not give us any meaningful information, except a photoelectron event occurring at a space-time coordinate  $(\mathbf{r}, t)$ . Therefore, a timely accumulative measurement on a large number of wavepacksts is always necessary in this case. Assuming a large number of nonoverlapped wavepackets are excited from a large number of individual atomic transitions, and each wavepacket is created at a different initial time  $t_{0j}$ . Each wavepacket produces photocurrent  $i_j(t)$  to charge an electronic integrator continuously. From wavepacket to wavepacket, the photocurrents keep charging the integrator until achieving an observable level. The first-order temporal mutual-coherence function is expected to be

$$\begin{aligned}\Gamma(\mathbf{r}_1, t_1; \mathbf{r}_2, t_2) &= \left\langle \sum_j \int_{\Delta T} dt \mathcal{F}_{\tau_{1j}}^* \{a(\nu)\} \mathcal{F}_{\tau_{2j}} \{a(\nu)\} e^{i\omega_0 \tau} \right\rangle \\ &\simeq N \int_{\Delta T} dt [\mathcal{F}_{\tau_1}^* \{a(\nu)\} \mathcal{F}_{\tau_2} \{a(\nu)\} e^{i\omega_0 \tau}] \end{aligned}\quad (5.21)$$

where

$a_j(\nu)$  is the amplitude for the Fourier mode of frequency  $\omega$  of the  $j$ th wavepacket

$$\tau_{1j} = \tau_1 - t_{0j} = (t - t_{0j}) - (z_1 + z_1)/c$$

$$\tau_{2j} = \tau_2 - t_{0j} = (t - t_{0j}) - (z_2 + z_2)/c$$

$$\tau = \tau_{1j} - \tau_{2j} = (z_2 - z_1)/c + (z_2 - z_1)/c$$

$t_{0j}$  is the initial creation time of the  $j$ th wavepacket

In Equation 5.21, as usual, we have modeled an “identical” distribution of  $a(\omega)$  for all the wavepackets involved in the measurement. When  $\Delta T$  is long enough, the degree of first-order temporal coherence can be approximated as

$$\gamma_{12}(\tau) \simeq \mathcal{F}_\tau \{a^2(\nu)\} e^{i\omega_0\tau} \quad (5.22)$$

In Equation 5.22, we have completed the time integrals either in a similar approach as shown in Equation 2.6 or by applying the Wiener–Khintchine theorem.

It is interesting to see that the first-order coherence time or coherence length of the field in this case is the same as that of thermal light

$$\tau_c = 2\pi/\Delta\omega$$

although the mechanism of interference is the overlapping–nonoverlapping of the wavepackets, which is very different from that of the thermal light.

The measured intensity on the observation plane is expected to be

$$\begin{aligned} \langle I(\mathbf{r}, t) \rangle &= \left\langle \sum_j \int_{\Delta T} dt \left\{ |\mathcal{F}_{\tau_{1j}}\{a(\nu)\}|^2 + |\mathcal{F}_{\tau_{2j}}\{a(\nu)\}|^2 \right. \right. \\ &\quad \left. \left. + 2\text{Re}[\mathcal{F}_{\tau_{1j}}^*\{a(\nu)\} \mathcal{F}_{\tau_{2j}}\{a(\nu)\} e^{i\omega_0\tau}] \right\} \right\rangle \\ &\simeq I_0 [1 + \mathcal{F}_\tau \{a^2(\nu)\} \cos(\omega_0\tau)], \end{aligned} \quad (5.23)$$

where  $I_0$  is a constant corresponding to the averaged intensity on the observation plane. Equation 5.23 indicates an observable interference pattern from a physically realizable measurement process. It is easy to see that the final observable interference pattern is the sum of a large number of identical sub-interference patterns, each produced by a wavepacket. There is no surprise in classical theory for a wavepacket of a single photon to interfere with itself. Classical electromagnetic wave theory does not prevent any wavepacket physically passing through both the upper and the lower slits of an Young’s double-slit interferometer simultaneously, even if the wavepacket itself only carries the energy of a single-photon.

A question naturally arises: what do we mean “each wavepacket produces a sub-interference pattern”? As we have mentioned that if only one photon is involved in the measurement, the measurement may not give us any meaningful information, except a photoelectron event occurring at a space-time coordinate  $(\mathbf{r}, t)$ . The confusion comes from the use of mixed language and concepts of classical theory and quantum theory. In classical theory, as we have emphasized earlier, there is no lower energy limit for a wavepacket to carry, and there is no lower energy limit for producing a photoelectron event. There is no problem in classical theory to have a sub-interference pattern by means of an intensity distribution  $I_j(\mathbf{r}, t)$  in

space-time, even if the  $j$ th wavepacket only carries the energy of a single photon. Of course, this is inconsistent with the experimental observation. Although classical electromagnetic wave theory of light successfully predicted the interference of a wavepacket at the single-photon level, quantum theory is always necessary for characterizing the physics of the measurement of a photon. From the measurement point of view, the sub-interference pattern means nothing but a probability distribution function  $P_j(\mathbf{r}, t)$ : the probability of observing a photodetection event at space-time coordinate  $(\mathbf{r}, t)$  for the measurement of the  $j$ th wavepacket. In an accumulative measurement involving a large number of  $N$  wavepackets, there will be  $NP_j(\mathbf{r})$  photodetection events occurring at coordinate  $\mathbf{r}$ , where  $P_j(\mathbf{r})$  is the time averaged probability, corresponding to the time averaged intensity  $\langle I_j(\mathbf{r}, t) \rangle_{\Delta T}$  of the  $j$ th wavepacket. The probability interpretation is consistent with quantum mechanics. It seems a “semiclassical” or “semi-quantum” theory, in which the field is treated as classical wave and the measurement is treated as a quantum process of photodetection, is quite possible for characterizing the interference phenomenon of a single-photon wavepacket.

### Case II: A laser pulse

A laser pulse is the result of coherent superposition among a large number of subfields associated with a large number of coherently radiating sub-sources. An idealized modern photodetector is able to monitor the instantaneous intensity  $I(\mathbf{r}, t)$  of a laser pulse with observable photocurrent  $i(t)$ . Ensemble average is physically meaningful for the measurement of a laser pulse. In Chapter 1, we have discussed the measurement and statistics on intensity, or self-coherence function, of a coherent wavepacket. The measurement of the first-order coherence of a laser wavepacket has no difference in terms of the measurement statistics, except the measurement physically occurs at space-time  $(\mathbf{r}, t)$ , however, the mutual-coherence function  $\Gamma(\mathbf{r}_1, t_1; \mathbf{r}_2, t_2)$  refers the fields  $E(\mathbf{r}_1, t_1)$  and  $E(\mathbf{r}_2, t_2)$  at early times  $t_1 = t - s_1/c$  and  $t_2 = t - s_2/c$ , respectively. Taking into account all possible realizations of the fields  $E(\mathbf{r}_1, t_1)$  and  $E(\mathbf{r}_2, t_2)$ , the mutual-coherence function  $\langle E^*(\mathbf{r}_1, t_1)E(\mathbf{r}_2, t_2) \rangle$  is found to be

$$\begin{aligned} \Gamma(\mathbf{r}_1, t_1; \mathbf{r}_2, t_2) &= \langle E^*(\mathbf{r}_1, t_1)E(\mathbf{r}_2, t_2) \rangle \\ &= \mathcal{F}_{\tau_1}^* \{A(\nu)\} \mathcal{F}_{\tau_2} \{A(\nu)\} e^{i\omega_0\tau} \end{aligned} \quad (5.24)$$

where, again,  $A(\nu) = \sum_j a_j(\nu)$  is the total amplitude for the mode of frequency  $\omega$ , and  $\tau_1 = t_1 - z_1/c$ ,  $\tau_2 = t_2 - z_2/c$ ,  $\tau = \tau_1 - \tau_2 = (z_2 - z_1)/c + (t_2 - t_1)/c$ . We have also defined  $t_0 = 0$  as the initial increation time of the pulse. The expectation function is calculated by taking into account a constant phase for all subfields associated with a large number of sub-sources. Similar to the wavepacket at the single-photon level, the degree of first-order coherence is determined by the overlapping–nonoverlapping of the wavepackets.

At the neighborhood of  $\tau \sim 0$ ,  $\Gamma(\mathbf{r}_1, t_1; \mathbf{r}_2, t_2)$  achieves its maximum value, we consider the fields  $E(\mathbf{r}_1, t_1)$  and  $E(\mathbf{r}_2, t_2)$  first-order coherent; however, when  $\tau > 2\pi/\Delta\omega$  the two wavepackets cannot have nonzero values simultaneously,  $\Gamma(\mathbf{r}_1, t_1; \mathbf{r}_2, t_2) = 0$ , we define the fields of  $E(\mathbf{r}_1, t_1)$  and  $E(\mathbf{r}_2, t_2)$  first-order incoherent, although the laser pulse itself is considered as coherent radiation. It is interesting to see that  $\Gamma(\mathbf{r}_1, t_1; \mathbf{r}_2, t_2)$  indicates a nonstationary field, which is consistent with the nature of a laser pulse.

Due to the nonstationary nature, we need to pay attention to the normalized degree of first-order coherence function  $\gamma_{12}(\tau_1, \tau_2)$ ,

$$\gamma_{12}(\tau_1, \tau_2) = \frac{\mathcal{F}_{\tau_1}^* \{A(v)\} \mathcal{F}_{\tau_2} \{A(v)\} e^{i\omega_0 \tau}}{\sqrt{|\mathcal{F}_{\tau_1} \{A(v)\}|^2 |\mathcal{F}_{\tau_2} \{A(v)\}|^2}} \quad (5.25)$$

under the condition of

$$|\mathcal{F}_{\tau_1} \{A(v)\}|^2 |\mathcal{F}_{\tau_2} \{A(v)\}|^2 \neq 0$$

One may find that Equation 5.25 leads to  $|\gamma_{12}(\tau_1, \tau_2)| = 1$  for real functions of the Fourier transforms, such as Gaussian, even if the two wavepackets only slightly overlap. This is because the product of the self-coherence functions  $\Gamma_{11}(\tau_1)$  and  $\Gamma_{22}(\tau_2)$ , which is used for normalization, functions the same as that of the mutual-coherence function  $\Gamma_{12}(\tau_1, \tau_2)$ . Examine Equation 5.9, we find the visibility of the interference fringe modulation is very different from the degree of fist-order coherence  $|\gamma_{12}(\tau_1, \tau_2)|$ . In this case, the interference visibility has to be estimated from its definition of Equation 5.9.

#### 5.1.4 $\Gamma(\mathbf{r}_1, t_1; \mathbf{r}_2, t_2)$ : Two Wavepackets

Suppose the input radiation at the upper and the lower pinholes of Young's interferometer, respectively, are in the form of wavepackets, either produced from two independent atomic transitions or from two independent laser systems. The two wavepackets are superposed on the observation plane producing an interference pattern by means of the instantaneous intensity

$$\begin{aligned} I(\mathbf{r}, t) &= |\mathcal{F}_{(\tau_1-t_01)} \{a_1(v)\} e^{-i\omega_0(\tau_1-t_01)} + \mathcal{F}_{(\tau_2-t_02)} \{a_2(v)\} e^{-i\omega_0(\tau_2-t_02)}|^2 \\ &= |\mathcal{F}_{(\tau_1-t_01)} \{a_1(v)\}|^2 + |\mathcal{F}_{(\tau_2-t_02)} \{a_2(v)\}|^2 \\ &\quad + 2\text{Re}[\mathcal{F}_{(\tau_1-t_01)}^* \{a_1(v)\} \mathcal{F}_{(\tau_2-t_02)} \{a_2(v)\} e^{i\omega_0[(t_02-t_01)+\tau]}] \end{aligned} \quad (5.26)$$

where 1 denotes wavepacket 1, which passes the upper pinhole along path  $s_1$ , and 2 denotes wavepacket 2, which passes the lower pinhole along

path  $s_2$ ,  $t_{01}$  and  $t_{02}$  are the initial creation times of the two wavepackets at the two independent sources. It is easy to see from Equation 5.26 that an instantaneous interference pattern is potentially observable when the two wavepackets are overlapped at  $(\mathbf{r}, t)$ .

To calculate the mutual-coherence function  $\Gamma(\mathbf{r}_1, t_1; \mathbf{r}_2, t_2)$ , we separate the discussion for pairs of single-photon wavepackets from that of coherent laser pulse.

### Case I: Two wavepacks at the single-photon level

A timely accumulative measurement is always necessary in this case. Using the same measurement scheme described in last section, we assume each pair of wavepacket produces photocurrent  $i_j(t)$  to charge an electronic integrator continuously. From pair to pair, the photocurrents keep charging the integrator until achieving an observable level. The first-order temporal mutual-coherence function is expected to be

$$\begin{aligned}\Gamma(\mathbf{r}_1, t_1; \mathbf{r}_2, t_2) &= \left\langle \sum_j \int_{\Delta T} dt \mathcal{F}_{\tau_{1j}}^* \{a(v)\} \mathcal{F}_{\tau_{2j}} \{a(v)\} e^{i\omega_0 \tau_j} \right\rangle \\ &= \left\langle \sum_j e^{i\omega_0(t_{02j}-t_{01j})} \int_{\Delta T} dt [\mathcal{F}_{\tau_{1j}}^* \{a(v)\} \mathcal{F}_{\tau_{2j}} \{a(v)\} e^{i\omega_0 \tau}] \right\rangle \\ &\simeq 0\end{aligned}\quad (5.27)$$

where the  $j$ th pair of wavepackets, labeled by  $1j$  and  $2j$ , are created at initial times  $t_{0j}$  and  $t_{02j}$ , randomly, independently, and respectively,  $\tau_{1j} = \tau_1 - t_{01j} = (t - t_{01j}) - (s_1 + z_1)/c$ ,  $\tau_{2j} = \tau_2 - t_{02j} = (t - t_{02j}) - (s_2 + z_2)/c$ ,  $\tau_j = \tau_{1j} - \tau_{2j} = (t_{02j} - t_{01j}) + \tau$ , and  $\tau = (s_2 - s_1)/c + (z_2 - z_1)/c$ .

It is not difficult to see that  $\Gamma(\mathbf{r}_1, t_1; \mathbf{r}_2, t_2) \simeq 0$  comes from the averaging of  $(t_{01j} - t_{02j})$ : each  $j$ th pair of wavepackets produces an “instantaneous” interference pattern with a special initial phase  $\omega_0(t_{02j} - t_{01j})$ ; due to the randomness of  $t_{01j}$  and  $t_{02j}$  from wavepacket pair to wavepacket pair, the averaged sinusoidal function of  $\cos\{\omega_0[(t_{02j} - t_{01j}) + \tau]\}$  results in a value of zero. Based on Equation 5.27, we may conclude that the interference between independent wavepackets at the single-photon level is practically non-observable.

### Case II: Two independent laser pulses

Again, an idealized modern photodetector is able to monitor the instantaneous intensity  $I(\mathbf{r}, t)$  of a pair of laser wavepackets. Ensemble average is physically meaningful for the measurement of a pair of laser wavepackets. Taking into account all possible realizations of the fields  $E(\mathbf{r}_1, t_1)$  and  $E(\mathbf{r}_2, t_2)$  from a pair of laser wavepackets, the mutual-coherence function  $\langle E^*(\mathbf{r}_1, t_1)E(\mathbf{r}_2, t_2) \rangle$  is found to be

$$\begin{aligned}\Gamma(\mathbf{r}_1, t_1; \mathbf{r}_2, t_2) &= \langle E^*(\mathbf{r}_1, t_1) E(\mathbf{r}_2, t_2) \rangle \\ &= \mathcal{F}_{(t_1-t_{01})}^* \{A(v)\} \mathcal{F}_{(t_2-t_{02})} \{A(v)\} e^{i\omega_0[(t_{02}-t_{01})+\tau]} \quad (5.28)\end{aligned}$$

where

$A(v) = \sum_j a_j(v)$  is the total amplitude for the mode of frequency  $\omega$   
 $t_{01}$  and  $t_{02}$  are the initial creation times of the two laser pulses

It is easy to see that within a selected pair of laser wavepackets,  $(t_{02} - t_{01})$  holds a well-defined value. If the measurement is completed within a pair of laser wavepackets, the interference will be observable. In fact, the interference between two independent lasers was experimentally demonstrated by Mandel during the years of the 1960s to 1970s just a few years after the invention of the laser.\*

What will happen if the measurement involves a large number of individual wavepacket pairs accumulatively? Can we still observe interference? As we have discussed earlier, in this kind of measurement, the finally measured interference pattern on the observation plane is the sum of a large number of time-averaged sub-interference patterns, each is produced by a wavepacket pair

$$\begin{aligned}\langle I(\mathbf{r}, t) \rangle_{\Delta T} &\simeq \sum_j \int_{\Delta T} dt \left\{ |\mathcal{F}_{\tau_{1j}} \{a_1(v)\}|^2 + |\mathcal{F}_{\tau_{2j}} \{a_2(v)\}|^2 \right. \\ &\quad \left. + 2 \operatorname{Re} \mathcal{F}_{\tau_{1j}}^* \{a_1(v)\} \mathcal{F}_{\tau_{2j}} \{a_2(v)\} e^{i\omega_0[(t_{02j}-t_{01j})+\tau]} \right\} \quad (5.29)\end{aligned}$$

where  $j$  labels the  $j$ th wavepacket pair, we have also assumed no overlapping between wavepackets in pass one (upper pinhole) and pass two (lower pinhole), respectively. If the wavepacket pairs are “phase-locked,” where “phase-lock” means forcing the two lasers to generate their wavepackets at  $t_{02j} - t_{01j} = \text{constant}$  for all  $j$  to have  $\tau_j = \text{constant} + \tau$ , which is independent of  $j$ , the sub-interference patterns would be identical from wavepacket pair to wavepacket pair, and consequently, the timely accumulative observation would be the sum of these identical sub-interference patterns. In this case the timely accumulative interference, which involves a large number of wavepackets, is observable.

### 5.1.5 $\Gamma(\mathbf{r}_1, t_1; \mathbf{r}_2, t_2)$ : CW Laser Radiation

Continuous wave (CW) laser radiation may contain one cavity mode, a few cavity modes, or a number of cavity modes, each centered at frequency  $\omega_0$

---

\* These experiments stimulated a great deal of attention on a fundamental issue: can interference take place between two different photons? The debate was partially provoked from a statement of Dirac: “...photon... only interferes with itself. Interference between two different photons never occurs.”

with finite bandwidth  $\Delta\omega_j$ , where  $j$  labels the  $j$ th cavity mode. Each cavity mode can be treated as either a coherent wavepacket of temporal width  $2\pi/\Delta\omega_j$  or a single frequency mode of  $\Delta\omega_j \sim 0$ . In principle, our earlier treatment of  $\Gamma(\mathbf{r}_1, t_1; \mathbf{r}_2, t_2)$  for a wavepacket, a few wavepackets, or a number of overlapped–partially overlapped wavepackets may apply to CW laser radiation, except each wavepacket has a different center frequency  $\omega_{0j}$ .

In the following, we estimate the first-order coherence function of CW laser radiation by approximating the fields  $E(\mathbf{r}_1, t_1)$  and  $E(\mathbf{r}_2, t_2)$  as a set of overlapped–partially overlapped wavepackets each centered at  $\omega_{0j}$  with spectral bandwidth  $\Delta\omega_j$ ,

$$\begin{aligned}\Gamma(\mathbf{r}_1, t_1; \mathbf{r}_2, t_2) &= \sum_j \mathcal{F}_{\tau_1-t_{0j}}^* \{A_{1j}^2(\nu)\} e^{i\omega_{0j}(\tau_1-t_{0j})} \sum_k \mathcal{F}_{\tau_2-t_{0k}} \{A_{2k}^2(\nu)\} e^{-i\omega_{0k}(\tau_2-t_{0k})} \\ &= \sum_{j=k} \mathcal{F}_{\tau_1-t_{0j}}^* \{A_{1j}^2(\nu)\} \mathcal{F}_{\tau_2-t_{0j}} \{A_{2j}^2(\nu)\} e^{i\omega_{0j}\tau} \\ &\quad + \sum_{j \neq k} \mathcal{F}_{\tau_1-t_{0j}}^* \{A_{1j}^2(\nu)\} \mathcal{F}_{\tau_2-t_{0k}} \{A_{2k}^2(\nu)\} e^{i[\omega_{0j}(\tau_1-t_{0j}) - \omega_{0k}(\tau_2-t_{0k})]}\end{aligned}\quad (5.30)$$

where  $A_{1j}(\nu)$  and  $A_{2j}(\nu)$  are the amplitude distribution function of the  $j$ th cavity mode along pass one and pass two, respectively, with  $\nu = \omega_j - \omega_{0j}$ .

The result of Equation 5.30 depends on the number of cavity modes in the summation. For a single-mode CW laser system, Equation 5.30 has only one term:

$$\Gamma(\mathbf{r}_1, t_1; \mathbf{r}_2, t_2) = \mathcal{F}_{\tau_1-t_0}^* \{A_1^2(\nu)\} \mathcal{F}_{\tau_2-t_0} \{A_2^2(\nu)\} e^{i\omega_0\tau}$$

The degree of first-order temporal coherence is determined by the overlapping or nonoverlapping of the two superposed wavepackets. The coherent length of a single-mode modern CW laser system may achieve a few hundred meters. For a CW laser system with a few cavity modes or a number of cavity modes, the overlapping–nonoverlapping of each cavity mode and the spreading of the sinusoidal modulations of different  $\omega_{0j}$  in the first sum both need to be taken into account. The second sum may not give a null contribution if the interference cancelation is incomplete. The beating frequencies between cavity modes will be observable in this case.

## 5.2 First-Order Spatial Coherence

The finite bandwidth of the spectrum is not the only factor determining the degree of first-order coherence and consequently the interference visibility. The finite transverse dimension, or the finite angular size, of the

source is another important factor we have to take into account regarding the interference between spatially separated radiation fields. This concern leads to the concepts of spatial coherence and the degree of first-order spatial coherence.

### 5.2.1 Chaotic-Thermal Source

Assume a distant star of finite size consists of a large number of independent point sub-sources of radiation. From the view point of Young's double-slit interferometer, which is schematically illustrated in Figure 5.3, each point sub-source is identified by an angular coordinate  $\theta$  (1D). To simplify the mathematics and to focus on the physics of spatial coherence, we assume the fields received from each of  $N$  independent point sub-sources of the distant star,  $E_j(\mathbf{r}, t)$ , are monochromatic plane waves with a different transverse wavevector along the  $x$ -axis,  $k_x \sim k\theta$ , which is also called the spatial frequency. The fields  $E(\mathbf{r}_1, t_1)$  at pinhole  $P_1$  and  $E(\mathbf{r}_2, t_2)$  at pinhole  $P_2$ , respectively, are treated as a superposition of the  $N$  independent subfields. The mutual coherence function  $\Gamma(\mathbf{r}_1, t_1; \mathbf{r}_2, t_2)$  is then written as

$$\begin{aligned}\Gamma(\mathbf{r}_1, t_1; \mathbf{r}_2, t_2) &= \left\langle \sum_{j=1}^N E_j^*(\mathbf{r}_1, t_1) \sum_{k=1}^N E_k(\mathbf{r}_2, t_2) \right\rangle \\ &= \left\langle \sum_j E_j^*(\mathbf{r}_1, t_1) E_j(\mathbf{r}_2, t_2) \right\rangle + \left\langle \sum_{j \neq k} E_j^*(\mathbf{r}_1, t_1) E_k(\mathbf{r}_2, t_2) \right\rangle \quad (5.31)\end{aligned}$$

where  $j$  and  $k$  label each of the independent contributions of a point sub-source. It is convenient to break up the sum into two groups.

Since the independent point sub-sources have random phases, the second group ( $j \neq k$ ) of the sum vanishes in the expectation calculation when taking

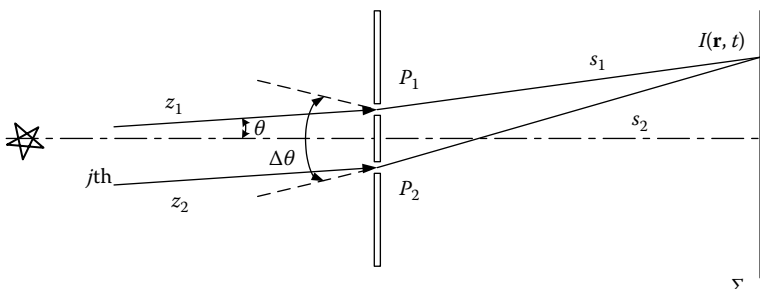


**FIGURE 5.3**

Schematic of Young's interference experiment. The source is a distant star of finite angular size ( $\Delta\theta \neq 0$ ) consisting of a large number of independent point sub-sources.

into account all possible values of the relative phase differences  $\varphi_j - \varphi_k$ . Thus  $\Gamma(\mathbf{r}_1, t_1; \mathbf{r}_2, t_2)$  becomes

$$\Gamma(\mathbf{r}_1, t_1; \mathbf{r}_2, t_2) = \sum_{j=1}^N E_j^*(\mathbf{r}_1, t_1) E_j(\mathbf{r}_2, t_2). \quad (5.32)$$

Equation 5.32 indicates that the only observable interference is the interference of the subfield with itself.

We can transfer Equation 5.32 into a simple integral by assuming a uniform distribution of the sub-sources on the distant star

$$\begin{aligned} \Gamma(\mathbf{r}_1, t_1; \mathbf{r}_2, t_2) &= \sum_{j=1}^N E_{j1}^* e^{i[\omega(t-\frac{s_1}{c})-k(z_{j1})]} E_{j2} e^{-i[\omega(t-\frac{s_2}{c})-k(z_{j2})]} \\ &= e^{i\omega\tau_s} \sum_{j=1}^N a_{j1} a_{j2} e^{ik(z_{j2}-z_{j1})} \\ &\cong e^{i\omega\tau_s} \int_{-\Delta\theta/2}^{\Delta\theta/2} \left( \frac{I_0}{\Delta\theta} \right) d\theta e^{ikb\theta} \\ &= I_0 \operatorname{sinc} \left( \frac{\pi b \Delta\theta}{\lambda} \right) e^{i\omega\tau_s}, \end{aligned} \quad (5.33)$$

where

$$\begin{aligned} \tau_s &= (s_2 - s_1)/c \\ I_0 &\sim \sum_{j=1}^N a_{j1} a_{j2} \sim \text{constant} \end{aligned}$$

We have simplified the mathematics to 1D. The integral is taken over the entire angular diameter of the star from  $-\Delta\theta/2$  to  $\Delta\theta/2$  by considering  $N \rightarrow \infty$ .

The normalized degree of first-order spatial coherence of the two fields at the upper and lower pinholes is thus

$$\gamma(\mathbf{r}_1, t_1; \mathbf{r}_2, t_2) = \operatorname{sinc} \left( \frac{\pi b \Delta\theta}{\lambda} \right) e^{i\omega\tau_s} = \operatorname{sinc}(\Delta k_x b) e^{i\omega\tau_s}. \quad (5.34)$$

Here,  $\gamma(\mathbf{r}_1, t_1; \mathbf{r}_2, t_2)$  is a function of the separation  $b$  between the upper and the lower pinholes and the angular size  $\Delta\theta$  of the distant star. The two fields at the upper and lower pinholes are said to be spatially coherent when  $b \ll \lambda/\Delta\theta$ , or  $b \ll 2\pi/\Delta k_x$ , ( $|\gamma(\mathbf{r}_1, t_1; \mathbf{r}_2, t_2)| \cong 1$ ), and the two fields are said to be spatially incoherent when  $b \geq \lambda/\Delta\theta$ , or  $b \geq 2\pi/\Delta k_x$ , ( $|\gamma(\mathbf{r}_1, t_1; \mathbf{r}_2, t_2)| \cong 0$ ). For a point source,  $\Delta\theta \sim 0$ , and consequently  $|\gamma_{12}| \cong 1$  for any value of  $b$ . This means the radiation fields excited by a point radiation source are spatially coherent despite the spatial separation between the fields.

The interference pattern on the observation plane can be written as

$$\langle I(\mathbf{r}, t) \rangle = I_0 \left[ 1 + \operatorname{sinc} \left( \frac{\pi b \Delta \theta}{\lambda} \right) \cos(\omega \tau_s) \right], \quad (5.35)$$

with an interference visibility

$$V = |\gamma_{12}| = \operatorname{sinc} \left( \frac{\pi b \Delta \theta}{\lambda} \right) = \operatorname{sinc} (\Delta k_x b). \quad (5.36)$$

Notice we have simplified the calculation of the  $\gamma$  function by assuming a monochromatic plane wave of single wavelength  $\lambda$ , so that  $V = |\gamma_{12}|$  is independent of  $\tau_s$ .

Similar to temporal coherence, we may find the following physical picture useful for understanding the concept of spatial coherence. In the classical chaotic light model of a finite size distant star, see Figure 5.3, the  $N \sim \infty$  point sub-sources are considered independent by means of exciting fields with completely random phases. The only observable interference is the self-interference of the fields emitted from the same sub-source. The cross-interference between fields excited from different sub-sources cancels completely while taking into account all possible values of the relative phases between sub-fields. The measured intensity on the observation plane is thus

$$\begin{aligned} \langle I(\mathbf{r}, t) \rangle &= \sum_{j=1}^N I_j(\mathbf{r}, t) \\ &= \sum_{j=1}^N \left[ |E_j(\mathbf{r}_1, t_1)|^2 + |E_j(\mathbf{r}_1, t_1)|^2 + 2 \operatorname{Re} E_j^*(\mathbf{r}_1, t_1) E_j(\mathbf{r}_2, t_2) \right]. \end{aligned} \quad (5.37)$$

We may consider that each point sub-source on the distant star, identified by angle  $\theta$ , produces a Young's double-slit sinusoidal interference pattern on the observation plane with a different initial phase at point  $s_1 = s_2$ , which is determined by  $k(z_{i2} - z_{i1}) \sim kb\theta \sim k_x b$ . The maximum relative phase separation between these individual patterns is  $k(\Delta\theta b)$ , or  $\Delta k_x b$ , corresponding to the phase difference between the interference patterns excited by the sub-sources of  $\Delta\theta$  and  $-\Delta\theta$ . Therefore, when  $2\pi \Delta\theta b / \lambda \ll 2\pi$ , i.e.,  $b \ll \lambda / \Delta\theta$ , or  $b \ll 2\pi / \Delta k_x$ , the relative phase shifts are not large enough to produce noticeable separation between the sub-interference-patterns and so the interference modulation is observable. However, when the relative phase shifts increase to a certain value of  $2\pi \Delta\theta b / \lambda \sim 2\pi$ , i.e.,  $b \sim \lambda / \Delta\theta$  or  $b \sim 2\pi / \Delta k_x$ , the individual patterns become significantly separated. The spread of the patterns smooths the light intensity distribution on the observation plane so the interference pattern can no longer be identified, and the interference modulation visibility is reduced from 100% to 0%. Based on the above observation,

we introduce the concept of spatial coherence of the field. For a given light source with angular size  $\Delta\theta$ , the fields  $E(\mathbf{r}_1, t)$  and  $E(\mathbf{r}_2, t)$  are considered as spatially coherent if their transverse spatial separation is less than

$$b_c = \frac{\lambda}{\Delta\theta} = \frac{2\pi}{\Delta k_x}, \quad (5.38)$$

where  $b_c$  is called the transverse coherence length of the radiation. Any fields with spatial separation beyond  $b_c$  are considered as spatially incoherent, which implies no observable interference. The degree of first-order spatial coherence, defined in Equation 5.7 and calculated in Equation 5.34, is a quantitative measure of Young's double-slit interference for a radiation source of finite angular size  $\Delta\theta$ .

Taking up an early suggestion by Fizeau Michelson designed a stellar interferometer based on the mechanism of Young's double-pinhole interference. One important application of the Michelson stellar interferometer is the measurement of the angular size of a star or the angular separation between double stars. The principle and operation of this stellar interferometer is simple. What one needs to do is to manipulate the separation between the two pinholes from  $b = 0$ , point by point, to a critical value  $b = b_c$ . If one can make an accurate judgment at the critical value of  $b = b_c$  at which the interference pattern becomes invisible, this value of  $b_c$  can be used to estimate of the angular size of the distant star. According to Equation 5.35, the double-slit interferometer starts to lose its interference at  $b_c = \lambda/\Delta\theta$ . The angular size of the distant star,  $\Delta\theta = \lambda/b_c$ , is thus measured with certain accuracy. Of course, making an accurate judgment is never easy, as there are too many physical parameters that contribute to the instability of an interference pattern.

### 5.2.2 Coherent Radiation Source

For coherent radiation sources, the condition of having an observable Young's double-pinhole interference pattern is obvious: both pinholes must be illuminated by the radiation simultaneously. We have discussed the propagation of spatially coherent radiation, such as a laser beam, in Sections 2.3 and 3.2. The coherent radiation propagates in a collimated manner with diffraction-limited diverging angle  $\Delta\vartheta = \lambda/b$  in 1D, or  $\Delta\vartheta = 1.22\lambda/D$  in 2D, where  $D$  is the diameter of the source. If the spatially coherent radiation is regarded as a wavepacket in the transverse dimension, the above condition indicates that the distance between the two pinholes must be less than the transverse width of the spatial wavepacket. In other words, the spatial separation between the fields  $E(\mathbf{r}_1, t_1)$  and  $E(\mathbf{r}_2, t_2)$  must be within the spatial coherence of the field, which is the transverse width of the spatial wavepacket in this case, in order to have observable interference.

## Summary

In this chapter, we introduced the concept of first-order coherence of light to qualify and quantify the interference ability between temporally delayed or spatially separated radiation fields. In general, the normalized degree of first-order coherence is defined and calculated as

$$\begin{aligned}\gamma(\mathbf{r}_1, t_1; \mathbf{r}_2, t_2) &\equiv \frac{\Gamma(\mathbf{r}_1, t_1; \mathbf{r}_2, t_2)}{\sqrt{\Gamma(\mathbf{r}_1, t_1; \mathbf{r}_1, t_1) \Gamma(\mathbf{r}_2, t_2; \mathbf{r}_2, t_2)}} \\ &= \frac{\langle E^*(\mathbf{r}_1, t_1) E(\mathbf{r}_2, t_2) \rangle}{\sqrt{\langle |E(\mathbf{r}_1, t_1)|^2 \rangle \langle |E(\mathbf{r}_2, t_2)|^2 \rangle}}.\end{aligned}$$

The degree of first-order coherence is usually measured through an interferometer, which produces either a temporal delay or a spatial separation between the interfered radiation fields at space-time point  $(\mathbf{r}, t)$ .

The first-order coherence of light and the coherence property of light are two different concepts.

In this chapter, a few detailed analysis on temporal and spatial coherence are given. These excises are helpful in understanding the physics of first-order interference phenomena in terms of chaotic light and coherent light.

## Suggested Reading

- Born, M. and E. Wolf, *Principle of Optics*, Cambridge University Press, Cambridge, U.K., 2002.
- Loudon, R., *The Quantum Theory of Light*, Oxford Science Publications, Oxford, U.K., 2000.

# 6

## Second-Order Coherence of Light

The first-order coherence (correlation) function  $\Gamma(\mathbf{r}_1, t_1; \mathbf{r}_2, t_2)$  and the degree of first-order coherence  $\gamma(\mathbf{r}_1, t_1; \mathbf{r}_2, t_2)$  are not directly measured at space-time points  $(\mathbf{r}_1, t_1)$  and  $(\mathbf{r}_2, t_2)$ . A photodetection event can never happen at two different space-time coordinates. As we have learned in Section 5.1, the fields  $E(\mathbf{r}_1, t_1)$  and  $E(\mathbf{r}_2, t_2)$  at  $(\mathbf{r}_1, t_1)$  and  $(\mathbf{r}_2, t_2)$  are superposed at space point  $\mathbf{r}$  and measured at a later time  $t$ ,  $t = t_1 + s_1/c = t_2 + s_2/c$ , by a photodetector. The second-order coherence (correlation) function  $\Gamma^{(2)}(\mathbf{r}_1, t_1; \mathbf{r}_2, t_2)$  and the normalized degree of second-order coherence  $\gamma^{(2)}(\mathbf{r}_1, t_1; \mathbf{r}_2, t_2)$ , however, are measured by two photodetectors at space-time points  $(\mathbf{r}_1, t_1)$  and  $(\mathbf{r}_2, t_2)$  directly. Figure 6.1 is a schematic illustration of a Hanbury Brown and Twiss (HBT) interferometer, which measures the second-order coherence (correlation) function  $\Gamma^{(2)}(\mathbf{r}_1, t_1; \mathbf{r}_2, t_2)$  as well as the normalized degree of second-order coherence  $\gamma^{(2)}(\mathbf{r}_1, t_1; \mathbf{r}_2, t_2)$  of the input radiation. Comparing with Figure 5.3, in Figure 6.1 we place two photodetectors behind the double-pinhole for the joint-detection of two individual photodetection events at  $(\mathbf{r}_1, t_1)$  and  $(\mathbf{r}_2, t_2)$ . Different from the first-order coherence measurement, in Figure 6.1 the observation is based on the joint-photocurrent  $i_1(t) \times i_2(t)$  at the electronic linear multiplier (or RF mixer),

$$\begin{aligned} V_{12}(t) &\propto i_1(t) i_2(t) \\ &\propto I_1(\mathbf{r}_1, t_1) I_2(\mathbf{r}_2, t_2) \\ &= E^*(\mathbf{r}_1, t_1) E(\mathbf{r}_1, t_1) E^*(\mathbf{r}_2, t_2) E(\mathbf{r}_2, t_2) \end{aligned} \quad (6.1)$$

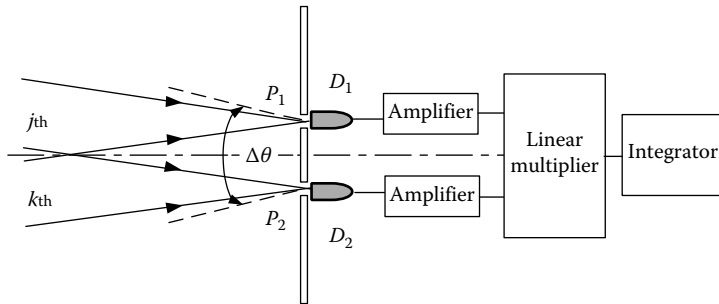
where

$V_{12}(t)$  is the output voltage of the linear multiplier

$i_1(t)$  and  $i_2(t)$  are the electronically amplified photocurrent of  $D_1$  and  $D_2$ , respectively, at time  $t$  of the multiplication

$t_1 = t - \tau_1^e$ ,  $t_2 = t - \tau_2^e$  are the early times that are defined by the electronic time delays  $\tau_1^e$  and  $\tau_2^e$ , including the delays of the detectors, the amplifiers and the adjustable delay-line cables

We have assumed idealized photodetectors by neglecting the time averages over  $t_1$  and  $t_2$ . The instantaneous intensities  $I_1(\mathbf{r}_1, t_1)$  and  $I_2(\mathbf{r}_2, t_2)$  are identified by the electronic delays. Note that  $t_1$ ,  $t_2$ , and the relative time delay  $t_1 - t_2 = \tau_1^e - \tau_2^e$  are all defined by the electronics in this setup.

**FIGURE 6.1**

Schematic of a Hanbury Brown and Twiss interferometer. The interferometer is similar to Young's double-pinhole interferometer and the Michelson stellar interferometer, except that two photodetectors are placed behind the pinholes for joint-detection of the radiations at space-time coordinates \$P\_1(\mathbf{r}\_1, t\_1)\$ and \$P\_2(\mathbf{r}\_2, t\_2)\$.

The second-order coherence function, or correlation function, is defined as

$$\begin{aligned}\Gamma^{(2)}(\mathbf{r}_1, t_1; \mathbf{r}_2, t_2) &= \langle I(\mathbf{r}_1, t_1) I(\mathbf{r}_2, t_2) \rangle \\ &= \langle E^*(\mathbf{r}_1, t_1) E(\mathbf{r}_1, t_1) E^*(\mathbf{r}_2, t_2) E(\mathbf{r}_2, t_2) \rangle\end{aligned}\quad (6.2)$$

and the degree of second-order coherence is defined as

$$\gamma^{(2)}(\mathbf{r}_1, t_1; \mathbf{r}_2, t_2) = \frac{\langle E^*(\mathbf{r}_1, t_1) E(\mathbf{r}_1, t_1) E^*(\mathbf{r}_2, t_2) E(\mathbf{r}_2, t_2) \rangle}{\langle E^*(\mathbf{r}_1, t_1) E(\mathbf{r}_1, t_1) \rangle \langle E^*(\mathbf{r}_2, t_2) E(\mathbf{r}_2, t_2) \rangle} \quad (6.3)$$

where the ensemble average, \$\langle \dots \rangle\$ denotes, again, *taking into account all possible realizations of the field*.

The second-order coherence or correlation is defined as the expectation value of the product of the two measured intensities at space-time points \$(\mathbf{r}\_1, t\_1)\$ and \$(\mathbf{r}\_2, t\_2)\$. Perhaps, the easiest expectation is a factorizable \$\Gamma^{(2)}(\mathbf{r}\_1, t\_1; \mathbf{r}\_2, t\_2)\$

$$\begin{aligned}\Gamma^{(2)}(\mathbf{r}_1, t_1; \mathbf{r}_2, t_2) &= \langle I(\mathbf{r}_1, t_1) \rangle \langle I(\mathbf{r}_2, t_2) \rangle \\ &= \Gamma^{(1)}(\mathbf{r}_1, t_1; \mathbf{r}_1, t_1) \Gamma^{(1)}(\mathbf{r}_2, t_2; \mathbf{r}_2, t_2),\end{aligned}\quad (6.4)$$

with the corresponding degree of second-order coherence

$$\gamma^{(2)}(\mathbf{r}_1, t_1; \mathbf{r}_2, t_2) = 1. \quad (6.5)$$

The physics behind a factorizable (non-factorizable) \$\Gamma^{(2)}(\mathbf{r}\_1, t\_1; \mathbf{r}\_2, t\_2)\$ with \$\gamma^{(2)} = 1\$ (\$\gamma^{(2)} \neq 1\$) will be given in later discussions. Statistically, a factorizable \$\Gamma^{(2)}(\mathbf{r}\_1, t\_1; \mathbf{r}\_2, t\_2)\$ with \$\gamma^{(2)} = 1\$ means the two measured intensities

$I(\mathbf{r}_1, t_1)$  and  $I(\mathbf{r}_2, t_2)$  are independent with no correlation. The nontrivial second-order *correlation* and *anti-correlation*, respectively, are defined with

$$\gamma^{(2)}(\mathbf{r}_1, t_1; \mathbf{r}_2, t_2) > 1, \quad (6.6)$$

and

$$\gamma^{(2)}(\mathbf{r}_1, t_1; \mathbf{r}_2, t_2) < 1. \quad (6.7)$$

Now we are ready to calculate and analyze the second-order correlation function and the degree of second-order coherence of light. We will focus on two extreme cases: (1)  $\Gamma^{(2)}$  and  $\gamma^{(2)}$  for coherent light; (2)  $\Gamma^{(2)}$  and  $\gamma^{(2)}$  for chaotic-thermal radiation. The HBT effect and thermal light ghost imaging will be introduced in case (2).

## 6.1 Second-Order Coherence of Coherent Light

In this section, we study the second-order coherence of coherent light. We start from the measurement of the second-order temporal coherence of a coherent radiation. A schematic experimental setup is illustrated in Figure 6.2. A well-collimated laser beam is divided by a 50/50 beamsplitter. Photodetectors  $D_1$  and  $D_2$  are scanned in the far-field zones of the transmitted and the reflected arms for the joint-detection of the radiation. The joint-detection circuit contains a current-current linear multiplier, which has been described earlier. The output of the current-current linear multiplier, which is proportional to  $\Gamma^{(2)}(z_1, t_1; z_2, t_2)$ , is recorded as the function of  $\tau_1 = t_1 - z_1/c$  and  $\tau_2 = t_2 - z_2/c$ , by scanning either the electronic delays,

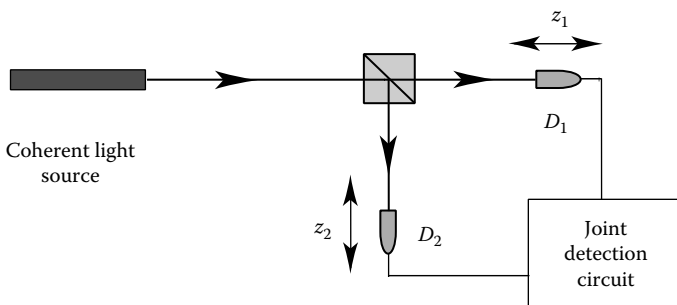


**FIGURE 6.2**

A schematic measurement of the second-order temporal coherence function  $\Gamma^{(2)}(z_1, t_1; z_2, t_2)$  of a coherent radiation. A well-collimated laser beam can be approximated as a point light source at infinity that contains a large number of point coherent sub-sources and coherent Fourier modes.

or the optical delays, as shown in Figure 6.2. In Section 1.4 we have given four simplified models of radiation to clarify four different types of superposition among a large number of subfields. A well-collimated laser beam can be approximately treated as a point light source of model (II) at infinity that contains a large number of point coherent sub-sources and coherent Fourier modes. Based on the analysis of Chapter 1, we may assume the coherent superposition produces coherent Gaussian wavepackets as given in Equation 1.27,

$$E(z, t) = E_0 e^{-\tau^2/4\sigma^2} e^{-i[\omega_0 t - k(\omega_0)z - \varphi_0]},$$

where, as usual, we have chosen  $t_0 = 0$  as the initial radiation time of the wavepacket at the source of  $z_0 = 0$ . In this case,  $D_1$  and  $D_2$  measure two identical but independent Gaussian pulses, respectively. It is easy to see that the second-order temporal coherence function  $\Gamma^{(2)}(z_1, t_1; z_2, t_2)$  becomes a factorizable function of  $\Gamma^{(1)}(z_1, t_1; z_1, t_1)$  and  $\Gamma^{(1)}(z_2, t_2; z_2, t_2)$

$$\begin{aligned} \Gamma^{(2)}(z_1, t_1; z_2, t_2) &= \langle E^*(z_1, t_1)E(z_1, t_1)E^*(z_2, t_2)E(z_2, t_2) \rangle \\ &= I_{01}e^{-\tau_1^2/2\sigma^2} I_{02}e^{-\tau_2^2/2\sigma^2} \\ &= \Gamma^{(1)}(z_1, t_1; z_1, t_1) \Gamma^{(1)}(z_2, t_2; z_2, t_2) \end{aligned} \quad (6.8)$$

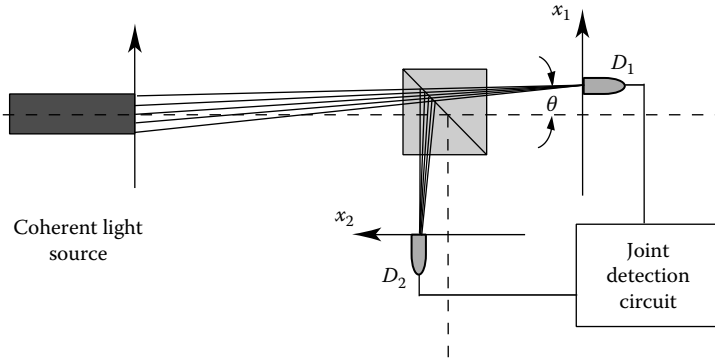
and consequently,

$$\gamma^{(2)}(z_1, t_1; z_2, t_2) = 1.$$

We may find four straightforward consequences from Equation 6.8:

1. The factorizable  $\Gamma^{(2)}$  is a product of two independent local intensity  $\langle I(z_1, t_1) \rangle$  and  $\langle I(z_2, t_2) \rangle$ .
2. The factorizable  $\Gamma^{(2)}$  means no statistical correlation between the measured intensities  $I(z_1, t_1)$  and  $I(z_2, t_2)$ , although the two pulses are “fluctuated” synchronically in a deterministic manner.
3.  $\Gamma^{(2)}$  is a function of time. This property comes from the time-dependent nature of the wavepackets or pulses. Moreover,  $\gamma^{(2)}$  is defined only when  $\Gamma^{(1)}(z_1, t_1; z_1, t_1) \neq 0$  and  $\Gamma^{(1)}(z_2, t_2; z_2, t_2) \neq 0$ .
4. The value of  $\Gamma^{(2)}(z_1, t_1; z_2, t_2)$  is not only determined by the relative delay  $\tau_1 - \tau_2$  between the two pulses but also by the absolute delays  $\tau_1$  and  $\tau_2$  of each independent wavepacket. This property is different from that of the stationary radiation.

Next, we consider the measurement of the second-order transverse coherence of a coherent radiation. The schematic experimental setup is shown in

**FIGURE 6.3**

A schematic measurement of the second-order spatial coherence of a coherent radiation. The transmitted and the reflected laser beam each produces a diffraction pattern, resulting in a factorizable  $\Gamma^{(2)}(x_1, x_2) = \Gamma^{(1)}(x_1, x_1)\Gamma^{(1)}(x_2, x_2)$ . Imagine the measurement is in the far-field zone of a laser.

Figure 6.3. The setup looks similar to that of Figure 6.2 except the scanning of  $D_1$  and  $D_2$  are in the transverse planes, instead of longitudinally. The transverse scanning is chosen with a set of electronic and optical delays in which the second-order temporal correlation achieves its maximum. To simplify the mathematics, we calculate the second-order coherence in far-field and in 1D. Taking the results of Section 3.1, we find

$$\begin{aligned}\Gamma^{(2)}(x_1, x_2) &= \langle E^*(x_1)E(x_1)E^*(x_2)E(x_2) \rangle \\ &= I_{01} \operatorname{sinc}^2 \frac{\pi D x_1}{\lambda z_1} I_{02} \operatorname{sinc}^2 \frac{\pi D x_2}{\lambda z_2} \\ &= \Gamma^{(1)}(x_1, x_1)\Gamma^{(1)}(x_2, x_2)\end{aligned}\quad (6.9)$$

where

$D$  is the diameter of the laser beam (transverse size of the source)

$\lambda$  is the wavelength of the radiation

and consequently,

$$\gamma^{(2)}(x_1, x_2) = 1.$$

The physics of Equation 6.9 is very clear: the transmitted and the reflected laser beam each produces a diffraction pattern on the observation planes, independently, resulting in a factorizable  $\Gamma^{(2)}(x_1, x_2) = \Gamma^{(1)}(x_1, x_1)\Gamma^{(1)}(x_2, x_2)$ .

It is not difficult to generalize the 1D solution  $\Gamma^{(2)}(x_1, x_2)$  to 2D  $\Gamma^{(2)}(\vec{\rho}_1, \vec{\rho}_2)$

$$\begin{aligned}\Gamma^{(2)}(\vec{\rho}_1, \vec{\rho}_2) &= \langle E^*(\vec{\rho}_1)E(\vec{\rho}_1)E^*(\vec{\rho}_2)E(\vec{\rho}_2) \rangle \\ &= I_{01} \left[ \text{somb}^2 \frac{D\omega}{z_1 c} |\vec{\rho}_1| \right] I_{02} \left[ \text{somb}^2 \frac{D\omega}{z_2 c} |\vec{\rho}_2| \right] \\ &= \Gamma^{(1)}(\vec{\rho}_1, \vec{\rho}_1) \Gamma^{(1)}(\vec{\rho}_2, \vec{\rho}_2).\end{aligned}\quad (6.10)$$

and consequently,

$$\gamma^{(2)}(\vec{\rho}_1, \vec{\rho}_2) = 1.$$

In general, the second-order coherence function  $\Gamma^{(2)}(\mathbf{r}_1, t_1; \mathbf{r}_2, t_2)$  of coherent radiation is simply a factorizable function of two expected intensities measured by  $D_1$  and  $D_2$  at coordinates  $(\mathbf{r}_1, t_1)$  and  $(\mathbf{r}_2, t_2)$ , respectively:

$$\begin{aligned}\Gamma^{(2)}(\mathbf{r}_1, t_1; \mathbf{r}_2, t_2) &= \langle E^*(\mathbf{r}_1, t_1)E(\mathbf{r}_1, t_1)E^*(\mathbf{r}_2, t_2)E(\mathbf{r}_2, t_2) \rangle \\ &= \Gamma^{(1)}(\mathbf{r}_1, t_1; \mathbf{r}_1, t_1) \Gamma^{(1)}(\mathbf{r}_2, t_2; \mathbf{r}_2, t_2),\end{aligned}\quad (6.11)$$

and consequently the normalized degree of second-order coherence of coherent radiation turns out to be

$$\gamma^{(2)}(\mathbf{r}_1, t_1; \mathbf{r}_2, t_2) = 1.\quad (6.12)$$

## 6.2 Second-Order Correlation of Chaotic-Thermal Radiation and the HBT Interferometer

The second-order coherence function of chaotic-thermal light is different from that of the coherent radiation, which cannot be factorized into a product of two first-order self-correlation functions. This means that the two measured intensities are no longer independent. The nontrivial second-order coherence, or correlation of thermal radiation was experimentally discovered by Hanbury Brown and Twiss in 1956. In their experimental setup, now known as the Hanbury Brown and Twiss (HBT) intensity interferometer, the randomly radiated thermal light is observed to have twice the chance of being captured by two independent photodetectors placed within a transverse area that equals the coherence area of the radiation, and within a short time window, which equals the coherence time of the radiation. The observation of HBT surprised the physics community. As we have learned in Section 6.1, the local superpositions of electromagnetic waves at space-time points  $(\mathbf{r}_1, t_1)$  and  $(\mathbf{r}_2, t_2)$ , respectively, are independent of each other. Where does the nontrivial second-order correlation come from? Is it caused by the quantum nature of light? Even if we reexamine the physics from the point of

quantum mechanics, we may still be puzzled by the question: what is the physical cause for the randomly radiated photons to be bunched in pairs? Thermal radiation process is supposed to be stochastic! The history has been interesting: although the discovery of HBT initiated a number of key concepts of modern quantum optics, the HBT phenomenon itself was commonly accepted as the classical statistical correlation of intensity fluctuations.

The goal of this section is aimed at the physics behind this nontrivial second-order coherence function. We will first derive the non-factorizable second-order correlation function of thermal light in terms of its first-order coherence. Questions and concerns about the non-factorizable correlation will be given in connection with the temporal and spatial HBT interferometers.

Consider a radiation source that contains a large number of independent point sub-sources. The radiation fields  $E(\mathbf{r}_1, t_1)$  and  $E(\mathbf{r}_2, t_2)$  are the result of the superposition of the subfields that are excited by each of the independent sub-sources. The sub-fields are labeled as  $E_j(\mathbf{r}_1, t_1)$  and  $E_j(\mathbf{r}_2, t_2)$  in terms of the sub-sources and the photodetectors  $D_1$  and  $D_2$ . We thus have

$$\begin{aligned} \Gamma^{(2)}(\mathbf{r}_1, t_1; \mathbf{r}_2, t_2) &= \langle E^*(\mathbf{r}_1, t_1) E(\mathbf{r}_1, t_1) E^*(\mathbf{r}_2, t_2) E(\mathbf{r}_2, t_2) \rangle \\ &= \left\langle \sum_{j,k,l,m} E_j^*(\mathbf{r}_1, t_1) E_k(\mathbf{r}_1, t_1) E_l^*(\mathbf{r}_2, t_2) E_m(\mathbf{r}_2, t_2) \right\rangle, \end{aligned} \quad (6.13)$$

where  $j, k, l, m$  label the independent sub-fields coming from the corresponding independent point sub-sources. Considering the random phases of the independent subfields, taking into account all possible realizations of the subfields, the only surviving terms in the summation are the following: (1)  $j = k, l = m$ , (2)  $j = m, k = l$ . We can then rewrite  $\Gamma^{(2)}(\mathbf{r}_1, t_1; \mathbf{r}_2, t_2)$  as the sum of the following two groups corresponding to the above two cases:

$$\begin{aligned} \Gamma^{(2)}(\mathbf{r}_1, t_1; \mathbf{r}_2, t_2) &= \sum_j E_j^*(\mathbf{r}_1, t_1) E_j(\mathbf{r}_1, t_1) \sum_l E_l^*(\mathbf{r}_2, t_2) E_l(\mathbf{r}_2, t_2) \\ &\quad + \sum_j E_j^*(\mathbf{r}_1, t_1) E_j(\mathbf{r}_2, t_2) \sum_l E_l^*(\mathbf{r}_2, t_2) E_l(\mathbf{r}_1, t_1) \\ &= \sum_j \sum_l \left| \frac{1}{\sqrt{2}} [E_j(\mathbf{r}_1, t_1) E_l(\mathbf{r}_2, t_2) + E_l(\mathbf{r}_1, t_1) E_j(\mathbf{r}_2, t_2)] \right|^2, \end{aligned} \quad (6.14)$$

where the ensemble average has been partially completed by taking into account all possible phases associated with each of the independent sub-fields. Equation 6.14 indicates that  $\Gamma^{(2)}(\mathbf{r}_1, t_1; \mathbf{r}_2, t_2)$  is the sum of a large set of superposition between “joint-fields”  $E_j(\mathbf{r}_1, t_1) E_l(\mathbf{r}_2, t_2)$  and  $E_l(\mathbf{r}_1, t_1) E_j(\mathbf{r}_2, t_2)$ , which are survived from the interference cancelation.

Before examining the physics of this peculiar superposition, we calculate and relate the second-order coherence function  $\Gamma^{(2)}(\mathbf{r}_1, t_1; \mathbf{r}_2, t_2)$  with the first-order coherence functions:

$$\begin{aligned} & \Gamma^{(2)}(\mathbf{r}_1, t_1; \mathbf{r}_2, t_2) \\ &= \sum_j \sum_l \left| \frac{1}{\sqrt{2}} [E_j(\mathbf{r}_1, t_1)E_l(\mathbf{r}_2, t_2) + E_l(\mathbf{r}_1, t_1)E_j(\mathbf{r}_2, t_2)] \right|^2 \\ &= \Gamma^{(1)}(\mathbf{r}_1, t_1; \mathbf{r}_1, t_1)\Gamma^{(1)}(\mathbf{r}_2, t_2; \mathbf{r}_2, t_2) + |\Gamma^{(1)}(\mathbf{r}_1, t_1; \mathbf{r}_2, t_2)|^2 \\ &= \Gamma_{11}^{(1)}\Gamma_{22}^{(1)} + \Gamma_{12}^{(1)}\Gamma_{21}^{(1)}, \end{aligned} \quad (6.15)$$

where  $\Gamma_{ij}^{(1)}$ ,  $i, j = 1, 2$ , is defined as

$$\begin{aligned} \Gamma_{11}^{(1)} &= \sum_j |E_j(\mathbf{r}_1, t_1)|^2, \quad \Gamma_{22}^{(1)} = \sum_l |E_l(\mathbf{r}_1, t_1)|^2 \\ \Gamma_{12}^{(1)} &= \sum_j E_j^*(\mathbf{r}_1, t_1)E_j(\mathbf{r}_2, t_2), \quad \Gamma_{21}^{(1)} = \sum_l E_l(\mathbf{r}_1, t_1)E_l^*(\mathbf{r}_2, t_2). \end{aligned}$$

Different from the factorizable second-order coherence function of coherent light, we have obtained a nontrivial second-order coherence function, which is no longer factorizable. In Equation 6.15, the first term  $\Gamma_{11}^{(1)}\Gamma_{22}^{(1)}$  represents the product of the mean intensities measured respectively by  $D_1$  and  $D_2$  at space-time coordinates  $(\mathbf{r}_1, t_1)$  and  $(\mathbf{r}_2, t_2)$ . The second term  $|\Gamma_{12}^{(1)}|^2$ , corresponding to the cross (interference) term of the superposition, is the nontrivial contribution to the second-order coherence function. The normalized non-factorizable degree of second-order coherence  $\gamma^{(2)}(\mathbf{r}_1, t_1; \mathbf{r}_2, t_2)$  is thus related to the degree of first-order coherence

$$\gamma^{(2)}(\mathbf{r}_1, t_1; \mathbf{r}_2, t_2) = 1 + |\gamma^{(1)}(\mathbf{r}_1, t_1; \mathbf{r}_2, t_2)|^2 = 1 + |\gamma_{12}^{(1)}|^2. \quad (6.16)$$

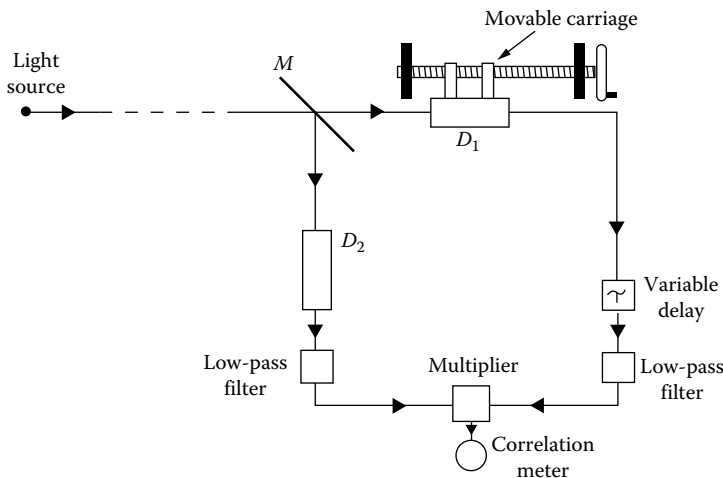
Equations 6.15 and 6.16 are valid for both the temporal and the spatial coherence of chaotic-thermal light. For chaotic-thermal radiation,  $\gamma^{(2)}(\mathbf{r}_1, t_1; \mathbf{r}_2, t_2)$  has a maximum value of 2.

The nontrivial second-order coherence is the result of Equation 6.14, which is derived from Equation 6.13 by taking into account the random phases of the thermal radiation. The random phases of the sub-sources result in an interference cancellation and turn Equation 6.13 into Equation 6.14. The nontrivial second-order coherence is the result of the superposition among these surviving terms that are left out from the interference cancellation. It is interesting to see from Equation 6.14 that  $\Gamma^{(2)}(\mathbf{r}_1, t_1; \mathbf{r}_2, t_2)$  of thermal light is the sum of a large set of interference patterns resulted from the

superposition between “joint-fields”  $E_j(\mathbf{r}_1, t_1)E_l(\mathbf{r}_2, t_2)$  and  $E_l(\mathbf{r}_1, t_1)E_j(\mathbf{r}_2, t_2)$ . The first term in the superposition corresponds to the situation in which the field at  $D_1$  is excited by the  $j$ th sub-source, and the field at  $D_2$  is excited by the  $l$ th sub-source. The second term in the superposition corresponding to a different but indistinguishable situation in which the field at  $D_1$  is excited by the  $l$ th sub-source, and field at  $D_2$  is excited by the  $j$ th sub-source. These two terms of superposition are illustrated in Figure 6.1. Equation 6.14 indicates an interference phenomenon concealed in the joint measurement of  $D_1$  and  $D_2$ . The physics behind this peculiar superposition seems beyond the framework of the classical electromagnetic theory of light. The classical superposition, as we have discussed in previous sections, physically happens at a space-time point  $(\mathbf{r}, t)$  and results in a local field  $E(\mathbf{r}, t)$ . The intensity of  $|E(\mathbf{r}, t)|^2$  is measured locally by a photodetector at that space-time point. The superposition in Equation 6.14, however, occurs physically at two space-time points  $(\mathbf{r}_1, t_1)$  and  $(\mathbf{r}_2, t_2)$  and results in a joint detection event of  $D_1$  and  $D_2$  at space-time points  $(\mathbf{r}_1, t_1)$  and  $(\mathbf{r}_2, t_2)$ , respectively.

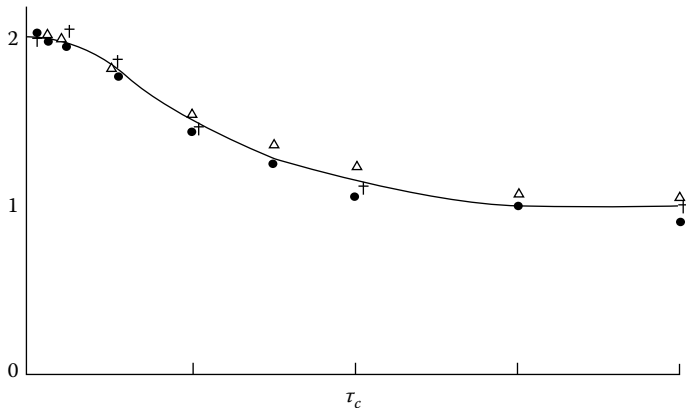
### 6.2.1 HBT Interferometer I: Second-Order Temporal Coherence

One of the laboratory demonstrations of Hanbury Brown and Twiss that was published in 1956 was a nontrivial second-order temporal correlation measurement of thermal light. The schematic diagram of the experimental setup is shown in Figure 6.4. Radiation from a distant thermal source (such as a bright star) is divided at a beamsplitter into two equal beams to be detected



**FIGURE 6.4**

Schematic of the historical Hanbury Brown and Twiss experiment. The HBT interferometer measures the second-order temporal coherence of radiation in the joint-detection of two distant photodetectors  $D_1$  and  $D_2$ .

**FIGURE 6.5**

Historical measurements of the second-order temporal coherence function of thermal light. For a balanced optical and electronic delay, thermal radiation has almost twice the chance of being captured by two individual photodetectors at  $t_1 - t_2 \sim 0$ , although the thermal radiation is randomly radiated from the source.

at two photodetectors  $D_1$  and  $D_2$ , one of which can be scanned longitudinally along the optical path. The output photocurrents are then multiplied electronically in the linear multiplier (RF mixer).

Figure 6.5 is a collection of historically measured temporal correlation function of thermal light by using similar experimental setups of the HBT interferometer. To simplify the discussion, we assume a balanced optical and electronic delay. In these measurements, the two distant photodetectors  $D_1$  and  $D_2$  have almost twice the chance to be triggered at  $t_1 - t_2 \sim 0$  than that of  $t_1 - t_2 > \tau_c$ , where  $\tau_c$  is the coherence time of the thermal field.

Apparently, this observation explored a paradoxical behavior of thermal light. Analogous to the language of Einstein–Podolsky–Rosen (EPR), although  $D_1$  and  $D_2$  are triggered randomly from time to time at any time  $t_1$  and  $t_2$ , if one of them is triggered at a certain time, the other one has double the chance of being triggered at  $t_1 = t_2$ . It seems that the randomly distributed “thermal photons” are nonrandomly “bunched” in joint measurement between two distant photodetectors. Comparing with the EPR paradox for entangled particles, one may feel even more uncomfortable because of the independent and random stochastic nature of thermal radiation.

What is the physical cause of the nontrivial HBT correlation? The HBT phenomenon was historically interpreted as a statistical correlation of intensity fluctuations. We will show in Section 6.3 that the phenomenological theory of statistical intensity fluctuation correlation may not be able to give adequate interpretation under certain experimental conditions. Following our early discussions, it seems natural and easy to treat the HBT

correlation as an interference phenomenon, except this interference is not caused by the classic superposition of  $|E(\mathbf{r}_1, t_1) + E(\mathbf{r}_2, t_2)|^2$ . This interference is indeed beyond the local superposition principle of the Maxwell EM wave theory of light. To explore the physics behind this phenomenon, perhaps, it is necessary to introduce the quantum mechanical concept of multi-photon interference. We will leave this introduction to Chapter 8. At this moment, let us simply treat this peculiar interference as a nonlocal interference between paired fields of joint-detection and consider the nontrivial temporal HBT correlation as the result of Equation 6.14, which is the key equation to see the interference nature of the observation. To calculate the temporal correlation, we may apply the results of Equations 6.15 and 6.16 directly. However, in order to have a better seeing of the physics, in the following, we will repeat part of the calculations that has been included in Equations 6.14 and 6.15.

Assuming a point light source at  $z = 0$  contains a large number of independent and randomly radiating sub-sources, the radiation fields  $E(z_1, t_1)$  and  $E(z_2, t_2)$  at photodetectors  $D_1$  and  $D_2$ , respectively, are the results of superposition among a large number of subfields, labeled by  $E_j(z_1, t_1)$  and  $E_j(z_2, t_2)$ , originated from each of these independent sub-sources. The temporal coherence  $\Gamma^{(2)}(z_1, t_1; z_2, t_2)$  is therefore

$$\begin{aligned}\Gamma^{(2)}(z_1, t_1; z_2, t_2) &= \langle E^*(z_1, t_1) E(z_1, t_1) E^*(z_2, t_2) E(z_2, t_2) \rangle \\ &= \left\langle \sum_{j,k,l,m} E_j^*(z_1, t_1) E_k(z_1, t_1) E_l^*(z_2, t_2) E_m(z_2, t_2) \right\rangle,\end{aligned}$$

where  $j, k, l, m$  label the independent subfields and the corresponding point sub-source. Considering the random phases of the independent subfields, as the result of an interference cancelation when tanking into account all possible phases of the sub-fields, the only surviving terms in the summation are the following: (1)  $j = k, l = m$  and (2)  $j = m, k = l$ . We can then write  $\Gamma^{(2)}(z_1, t_1; z_2, t_2)$  as the sum of the following two groups corresponding to the above two cases:

$$\begin{aligned}\Gamma^{(2)}(z_1, t_1; z_2, t_2) &= \sum_j E_j^*(z_1, t_1) E_j(z_1, t_1) \sum_l E_l^*(z_2, t_2) E_l(z_2, t_2) \\ &\quad + \sum_j E_j^*(z_1, t_1) E_j(z_2, t_2) \sum_l E_l^*(z_2, t_2) E_l(z_1, t_1) \\ &= \sum_j \sum_l \left| \frac{1}{\sqrt{2}} [E_j(z_1, t_1) E_l(z_2, t_2) + E_l(z_1, t_1) E_j(z_2, t_2)] \right|^2,\end{aligned}\tag{6.17}$$

which is a simplified version of Equation 6.14 restricted to longitudinal coordinates. We now apply the wavepacket model defined in earlier sections where each sub-source emits a wavepacket at time  $t_{0j}$ . Equation 6.17 is thus formally written as

$$\begin{aligned} \Gamma^{(2)}(z_1, t_1; z_2, t_2) &= \sum_j \sum_l \frac{1}{2} \left| e^{-i\omega_0 \tau_{1j}} \mathcal{F}_{\tau_{1j}}\{a_j(v)\} e^{-i\omega_0 \tau_{2l}} \mathcal{F}_{\tau_{2l}}\{a_l(v)\} \right. \\ &\quad \left. + e^{-i\omega_0 \tau_{1l}} \mathcal{F}_{\tau_{1l}}\{a_l(v)\} e^{-i\omega_0 \tau_{2j}} \mathcal{F}_{\tau_{2j}}\{a_j(v)\} \right|^2, \end{aligned} \quad (6.18)$$

where  $\mathcal{F}_{\tau_{1j}}\{a_j(v)\}$  and  $\mathcal{F}_{\tau_{2j}}\{a_j(v)\}$  are the Fourier transforms of the measured fields  $\tau_{1j} = (t_1 - t_{0j}) - z_1/c = \tau_1 - t_{0j}$  and  $\tau_{2j} = (t_2 - t_{0j}) - z_2/c = \tau_2 - t_{0j}$ . The physics behind Equation 6.18 is very clear. Two independent wavepackets, excited by the  $j$ th and the  $l$ th sub-sources, result in a joint detection event between  $D_1$  and  $D_2$  with two probabilities: (1) the  $j$ th and the  $l$ th wavepackets are detected by  $D_1$  and  $D_2$ , respectively; and (2) the  $j$ th and the  $l$ th wavepackets are detected by  $D_2$  and  $D_1$ , respectively. As we have discussed earlier, Equation 6.18 indicates an interference concealed in the joint measurement of  $D_1$  and  $D_2$ .\* Equation 6.18 can be written in terms of the first-order coherence function:

$$\begin{aligned} \Gamma^{(2)}(z_1, t_1; z_2, t_2) &= \sum_j |\mathcal{F}_{\tau_{1j}}\{a_j(v)\}|^2 \sum_l |\mathcal{F}_{\tau_{2l}}\{a_l(v)\}|^2 \\ &\quad + \left| \sum_j \mathcal{F}_{\tau_{1j}}^*\{a_j(v)\} \mathcal{F}_{\tau_{2j}}\{a_j(v)\} \right|^2 \end{aligned} \quad (6.19)$$

To complete the summations in Equation 6.19, we assume a large number of overlapped and partially overlapped wavepackets contribute to the photodetection events. Similar to our earlier discussion, in this case the summation in Equation 6.19 becomes an integral over  $t_0$ . We thus have

$$\begin{aligned} \Gamma^{(2)}(z_1, t_1; z_2, t_2) &\cong \int dt_0 |\mathcal{F}_{\tau_1-t_0}\{a(v)\}|^2 \int dt'_0 |\mathcal{F}_{\tau_2-t'_0}\{a(v)\}|^2 \\ &\quad + \left| \int dt_0 \mathcal{F}_{\tau_1-t_0}^*\{a(v)\} \mathcal{F}_{\tau_2-t_0}\{a(v)\} \right|^2 \\ &\cong \Gamma_0 [1 + |\mathcal{F}_\tau\{a^2(v)\}|^2], \end{aligned} \quad (6.20)$$

---

\* Perhaps it would be much easier to view this superposition or interference from a quantum picture in terms of the concept of photon. In the quantum theory of measurement, the superposition corresponds to a two-photon interference phenomenon, which involves a superposition between two different, yet indistinguishable, two-photon amplitudes: (1) photon  $j$  and photon  $l$  are annihilated at  $D_1$  and  $D_2$ , respectively; and (2) photon  $j$  and photon  $l$  are annihilated at  $D_2$  and  $D_1$ , respectively.

Equations 6.18 to 6.20 lead to the same result as if we apply the first-order coherence function directly to Equation 6.15. The normalized degree of second-order coherence  $\gamma^{(2)}(z_1, t_1; z_2, t_2)$  is therefore

$$\gamma^{(2)}(z_1, t_1; z_2, t_2) \cong 1 + |\mathcal{F}_\tau \{a^2(\nu)\}|^2. \quad (6.21)$$

It is obvious that the second-order temporal correlation as well as the degree of second-order temporal coherence of thermal light depend only on the relative delay  $\tau = \tau_1 - \tau_2 = (z_2 - z_1) + (\tau_1^\ell - \tau_2^\ell)$ , and are symmetric with respect to  $\tau$

$$\gamma^{(2)}(\tau) = \gamma^{(2)}(-\tau). \quad (6.22)$$

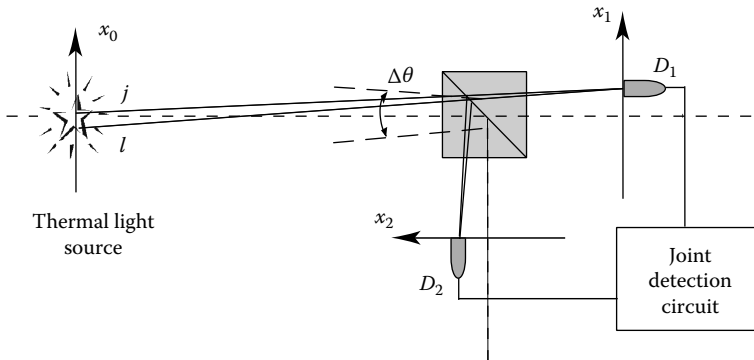
The above calculated expectations of  $\Gamma^{(2)}(\tau)$  and  $\gamma^{(2)}(\tau)$  agree with the experimental observations.

### 6.2.2 HBT Interferometer II: Second-Order Spatial Coherence

The spatial HBT interferometer, also named spatial intensity interferometer, has already been introduced in Figure 6.1. The HBT interferometer is similar to the Michelson stellar interferometer, except that the observation is the nontrivial spatial correlation measured by two photodetectors, instead of the first-order interference pattern. In a spatial HBT interferometer, the spatially randomly distributed thermal light is observed to have twice the chance of being captured by two independent photodetectors placed within a transverse area that equals the spatial coherence area of the thermal radiation. This kind of intensity interferometer has been widely used in astronomical observations for the measurement of the angular diameter of bright stars and objects in space.

A simplified spatial HBT interferometer, which can be easily realized in modern optics laboratories, is schematically shown in Figure 6.6. This interferometer measures the second-order spatial correlation  $\Gamma^{(2)}(x_1, t_1; x_2, t_2)$  of chaotic-thermal light, where  $x_1$  and  $x_2$  are the 1D transverse coordinates of the point photodetectors  $D_1$  and  $D_2$ , respectively. The second-order spatial correlation is measured under the condition of achieving its maximum temporal correlation by manipulating the electronic delays or the longitudinal optical delays of  $z_1$  and  $z_2$ . The time coordinates  $t_1$  and  $t_2$  are defined by the linear multiplier and the electronic delays, as described earlier. In the experiment we choose  $\tau = \tau_1 - \tau_2 \simeq 0$  to achieve maximum second-order temporal correlation. To simplify the mathematics and to focus our attention on the physics of spatial (transverse) correlation, we model the chaotic-thermal source in 1D and monochromatic as usual.

Now assume the radiation source contains a large number of independent point sub-sources, such as the  $j$ th and  $l$ th sub-source, that are randomly distributed transversely on the source. The angular size of the radiation

**FIGURE 6.6**

Schematic setup of a simplified spatial HBT interferometer, which measures the second-order spatial correlation function  $\Gamma^{(2)}(x_1, t_1; x_2, t_2)$  of thermal light. Imagine the measurement is in the far-field zone of a distant star.

source, defined as the angle subtended by the source at the detector, is  $\Delta\theta$  ( $\Delta\theta \sim D/z$ , with  $z_1 = z_2 = z$ , where  $D$  is the transverse size of the source), as illustrated in Figure 6.6. We start from Equation 6.14:

$$\Gamma^{(2)}(x_1, t_1; x_2, t_2) = \sum_j \sum_l \left| \frac{1}{\sqrt{2}} [E_j(x_1, t_1) E_l(x_2, t_2) + E_l(x_1, t_1) E_j(x_2, t_2)] \right|^2, \quad (6.23)$$

where the  $j$ th and the  $l$ th sub-sources are spatially distinguishable. The  $j$ th and the  $l$ th sub-sources are identified by their transverse coordinates on the  $x_0$  axis. The HBT measurement is in the far-field zone of the thermal source. Substituting the plane wave approximation into Equation 6.23, and simplifying the mathematics by assuming  $t_1 \simeq t_2$ , in a longitudinally symmetrical experimental arrangement,  $\Gamma^{(2)}(x_1, x_2)$  is approximately

$$\begin{aligned} \Gamma^{(2)}(x_1, x_2) &\simeq \int dx_0 \int dx'_0 \left| \frac{1}{\sqrt{2}} [a(x_0) e^{i\varphi(x_0)} e^{-ikr(x_0, x_1)} a(x'_0) e^{i\varphi(x'_0)} e^{-ikr(x'_0, x_2)} \right. \\ &\quad \left. + a(x'_0) e^{i\varphi(x'_0)} e^{-ikr(x'_0, x_1)} a(x_0) e^{i\varphi(x_0)} e^{-ikr(x_0, x_2)}] \right|^2 \\ &\simeq \int dx_0 a^2(x_0) \int dx'_0 a^2(x'_0) + \left| \int dx_0 a^2(x_0) e^{-ikx_0(x_1 - x_2)/z} \right|^2 \\ &\simeq I_0^2 \left[ 1 + \text{sinc}^2 \left( \frac{\pi \Delta\theta (x_1 - x_2)}{\lambda} \right) \right], \end{aligned} \quad (6.24)$$

where we have applied the far-field approximation and treated  $a(x_0) \simeq a$  as a constant with  $I_0 \simeq a^2 D$ . Comparing with the calculation of the first-order

spatial coherence function for thermal radiation of a distant star in Section 5.1, we see that  $x_1 - x_2$  is equivalent to the spatial separation  $b$  between the two pinholes. Notice, due to the chosen positive directions of  $x_1$  and  $x_2$ , we have  $x_1 - x_2 = b$ .

The degree of second-order spatial coherence  $\gamma^{(2)}$  is thus

$$\gamma^{(2)}(x_1, t_1; x_2, t_2) = 1 + \text{sinc}^2 \left[ \frac{\pi \Delta\theta(x_1 - x_2)}{\lambda} \right]. \quad (6.25)$$

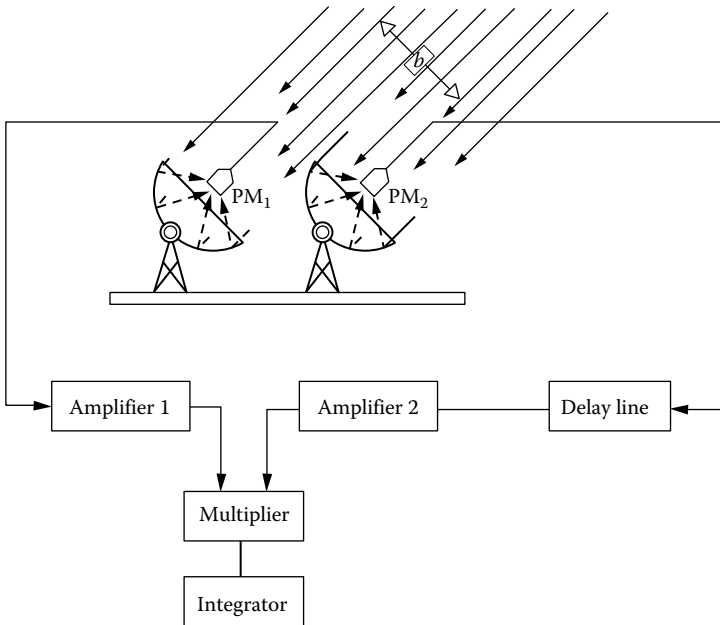
If the angular size  $\Delta\theta$  of the thermal source is not too small, for short-wavelength radiation such as visible light, the sinc-function in Equations 6.24 and 6.25 quickly drops from its maximum to minimum when  $x_1 - x_2$  goes from zero to a value such that  $\Delta\theta(x_1 - x_2)/\lambda = 1$ . In this case, we effectively have a “point”-to-“point” relationship between the  $x_1$  plane and the  $x_2$  plane. Notice, Equations 6.24 and 6.25 are functions of  $x_1 - x_2$ , which is independent of the absolute values of either  $x_1$  or  $x_2$ . This is a very important and useful property of thermal field. It signifies whatever transverse coordinate  $x_1$  we choose for  $D_1$ , there is a unique position  $x_2$  for  $D_2$  where the maximum joint-detection between  $D_1$  and  $D_2$  is expected, i.e., maximum constructive interference between  $E_j(x_1, t_1)E_l(x_2, t_2)$  and  $E_l(x_1, t_1)E_j(x_2, t_2)$  in Equation 6.23 is observable at that unique position.

We have mentioned earlier the measurement of second-order spatial correlation or the degree of second-order spatial coherence of thermal radiation is quite useful in astrophysics applications. By measuring the second-order coherence function, the angular diameter  $\Delta\theta$  of a distant star or object in space can be estimated. The HBT interferometer is especially useful for measuring celestial bodies of smaller angular size and their angular separation. For a small angular size  $\Delta\theta$ , a larger transverse spatial separation  $b$  between  $D_1$  and  $D_2$  in Figure 6.7 is necessary to reach the minimum correlation at  $\Delta\theta b/\lambda = 1$ . The greater the value of  $b$ , the smaller the  $\Delta\theta$  that is measurable. In modern applications,  $b$ , which is usually called the “base line,” can be as long as a few kilometers or more.

Hanbury Brown and Twiss successfully utilized the second-order spatial coherence of thermal light for astrophysics applications in the 1950s. A typical spatial HBT interferometer for such applications is schematically shown in Figure 6.7. The spatial HBT interferometer is similar to the Michelson stellar interferometer, except that the observation in the spatial HBT correlation is measured by two independent photodetectors instead of the first-order interference pattern. The long-base-line HBT intensity interferometer has been widely used in modern astronomical observations.

### 6.2.3 HBT Correlation and the Detection-Time Average

In an HBT interferometer, the directly measurable quantity is the output voltage of the linear multiplier  $V(t) \propto i_1(t)i_2(t)$ , as indicated in Equation 6.1.

**FIGURE 6.7**

Schematic of a typical HBT interferometer for astrophysics applications. The interferometer measures the angular size of a distant thermal radiation source by means of its second-order spatial coherence, or spatial correlation. In modern applications, the base line  $b$  can be as long as kilometers or more.

$V(t) \propto \Gamma^{(2)}$  is only true in the case of idealized detectors in which the time average on  $t_1 - t_2$  has negligible broadening on the nontrivial correlation function  $|\Gamma_{12}^{(1)}(\tau)|^2$ . In reality, we have to consider the finite response time  $t_c$  of the photodetectors. Time average over  $t_1 - t_2$  is unavoidable. The time average has no effect on the constant term of  $\Gamma_{11}^{(1)}\Gamma_{22}^{(1)}$ , but will broaden the width and reduce the amplitude of  $|\Gamma_{12}^{(1)}(\tau)|^2$  significantly if  $t_c \gg \tau_c$ , where  $\tau_c$  is the coherence time of the thermal field. Consequently, the visibility of the measured  $\Gamma^{(2)}$  and  $\gamma^{(2)}$  will be reduced significantly. This leads to an unfortunate condition for the realistic experimental demonstration of the HBT effect: a relatively narrow bandwidth of the thermal field or  $\tau_c > t_c$  is required. We have to be careful not to be confused by this experimental limitation. In principle, for *idealized photodetectors*, the bandwidth can be any value for the realization of Equations 6.20 and 6.21. In fact, the greater the bandwidth of the field, the narrower the correlation function  $|\Gamma_{12}^{(1)}(\tau)|^2$  will be.

In the following, we examine the unfortunate time-averaging effect of the photodetectors. We use a generic normalized function  $D_j(\bar{t}_j - t_j)$  to simulate the response distribution function of the  $j$ th photodetector, where

$\tilde{t}_j$  represents the mean time of a photodetection event. Function  $\mathcal{D}_j(\tilde{t}_j - t_j)$  is usually taken to be Gaussian. It is also common to use a square function to simplify the mathematics. The measured correlation is thus a convolution between the temporal degree of coherence of the radiation and the response function of the detectors,

$$|\gamma_{12}^{(1)}(\tau)|^2 = \int dt_1 \int dt_2 |\gamma(t_1 - t_2 - \tau)|^2 \mathcal{D}_1(\tilde{t}_1 - t_1) \mathcal{D}_2(\tilde{t}_2 - t_2), \quad (6.26)$$

where both integrals are taken from  $-\infty$  to  $+\infty$ .

In the ideal case of very fast detectors, i.e.,  $t_c \ll \tau_c$ , the response functions of the photodetectors can be considered  $\delta$ -functions. Equation 6.26 becomes

$$\begin{aligned} |\gamma_{12}^{(1)}(\tau)|^2 &= \int dt_1 \int dt_2 |\gamma(t_1 - t_2 - \tau)|^2 \delta(\tilde{t} - t_1) \delta(\tilde{t} - t_2) \\ &= |\gamma(\tau)|^2, \end{aligned} \quad (6.27)$$

where we have taken  $\tilde{t}_1 = \tilde{t}_2 = \tilde{t}$ .

In a general situation with nonidealized photodetectors,  $\mathcal{D}_j(\tilde{t} - t_j)$  cannot be treated as a  $\delta$ -function. The time average broadening has to be taken into consideration. To simplify the mathematics we use square functions to simulate the response function of the photodetectors

$$\mathcal{D}_j(\tilde{t} - t_j) = \begin{cases} 1/t_c & 0 \leq |\tilde{t}_j - t_j| \leq t_c \\ 0 & \text{otherwise.} \end{cases}$$

The double integral is approximated as

$$|\gamma_{12}^{(1)}(\tau)|^2 \simeq \frac{1}{t_c^2} \int_0^{t_c} dt'_1 \int_0^{t_c} dt'_2 |\gamma_{12}(t'_1 - t'_2 - \tau)|^2, \quad (6.28)$$

where  $t'_j = \tilde{t}_j - t_j$ ,  $j = 1, 2$ , and we have taken  $\tilde{t}_1 = \tilde{t}_2 = \tilde{t}$  to simplify the notation. The double integral can be easily done by changing the variables to  $t_+ = (t'_1 + t'_2)/2$  and  $t_- = t'_1 - t'_2$ , so that

$$\begin{aligned} |\gamma_{12}^{(1)}(\tau)|^2 &= \frac{2}{t_c^2} \int_0^{t_c} dt_- \left[ \int_{\frac{t_-}{2}}^{\frac{t_c - t_-}{2}} dt_+ \right] |\gamma_{12}(t_- - \tau)|^2 \\ &= \frac{2}{t_c^2} \int_0^{t_c} dt_- (t_c - t_-) |\gamma_{12}(t_- - \tau)|^2. \end{aligned} \quad (6.29)$$

Mapping the area of the integral from the  $t_1$  and  $t_2$  plane to the  $t_+$  and  $t_-$  plane follows a standard procedure. A simplified form of mapping can be

found in Appendix 6.A. Equation 6.29 is useful for evaluating the temporal performance of a given detection scheme. We note that the magnitude of  $|\gamma_{12}^{(1)}(\tau)|^2$  is closely connected to the coherence time of the field and the response time of the detectors. In the extreme case in which the coherence time is much smaller than the response time of the detector, the integral can be further simplified. If we assume the temporal degree of coherence to be a Gaussian of width  $\tau_c$ , Equation 6.29 reads

$$|\gamma_{12}^{(1)}(\tau)|^2 \sim \frac{1}{t_c^2} \int_{-\infty}^{\infty} dt_- t_c |\gamma_{12}(t_- - \tau)|^2 \sim \frac{\tau_c}{t_c}. \quad (6.30)$$

Therefore, in this case, the nontrivial contribution  $|\gamma_{12}^{(1)}(\tau)|^2$  is going to be relatively small compared to the normalized background constant of 1. This equation explains the low visibility of the measured correlation in the historical experiments of Hanbury Brown and Twiss. Their detectors were relatively slow comparing with the coherence time of the thermal field. This is also part of the reason why it is difficult to perceive high-contrast nontrivial correlation function from a thermal source with a relatively broadband spectrum. The physical situations analyzed above are extreme but give an important insight, we need to be careful in selecting the photodetectors and the coherence time of the thermal field in order to retrieve the HBT effects.

A general solution based on Equation 6.26 is obtainable numerically. Figure 6.8 illustrates four results of a numerical simulation in which four

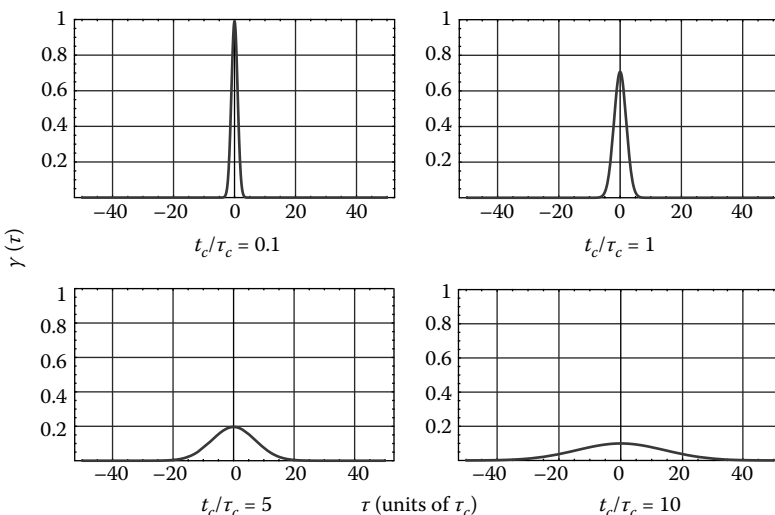


**FIGURE 6.8**

Numerical simulation of  $|\gamma_{12}^{(1)}(\tau)|^2$  for different response times of the photodetectors. The horizontal axis is  $\tau = \tau_1 - \tau_2$  in the unit of  $\tau_c$  and the vertical axis is  $|\gamma_{12}^{(1)}(\tau)|^2$ .

different values of  $t_c/\tau_c$  were selected. The numerical simulation is integrated from Equation 6.26 by assuming a Gaussian correlation of the radiation and Gaussian response functions of the photodetectors. In Figure 6.8, the horizontal axis is  $\tau = \tau_1 - \tau_2$  in the unit of  $\tau_c$  and the vertical axis is  $|\gamma_{12}^{(1)}(\tau)|^2$ . Note that, when the response time  $t_c$  of the detectors becomes equal to or greater than the coherence time  $\tau_c$  of the field, not only is the magnitude significantly attenuated but also the width of the function grows proportionally to the response time of the detectors, making very large delays necessary in order to study the temporal behavior of the second-order coherence.

It is also noticeable from Equation 6.29 that the time average on the variable  $t_+, t_+ = (\tilde{t}_1 + \tilde{t}_2) - (t_1 + t_2)$ , has a null effect on the coherence function. Taking advantage of this, a time-accumulative measurement may apply for achieving better experimental statistics.

---

### 6.3 The Physical Cause of the HBT Phenomenon

What is the physical cause of the HBT effect? What is the reason for the randomly distributed thermal radiations to have twice chance of being jointly observed within a time window that equals to its coherence time, and within a transverse area that equals its spatial coherence area? The HBT interferometer differs from the Young's double-slit interferometer and the Michelson stella interferometer in terms of their measurement mechanisms. In the view of classical theory, the Young's double-slit interferometer and the Michelson stella interferometer measure the first-order coherence property of the electromagnetic fields, whereas the HBT interferometer measure the statistical intensity-intensity correlation. In the view of quantum theory of light, the Young's double-slit interferometer and the Michelson stella interferometer measure the probability distribution function of a photon after passing the interferometer, whereas the HBT interferometer measures the probability distribution function for a randomly paired photons that are created from a thermal source to be jointly detected by two independent photodetectors at different space-time coordinates.

Historically, the most successful and widely accepted classical theory for HBT has been the statistical theory of intensity fluctuation correlation. Phenomenologically, this theory gives quite a reasonable interpretation to the far-field HBT experiment. In this theory, the nontrivial HBT correlation is caused by the statistical correlations of intensity fluctuations

$$\begin{aligned}\langle \Delta I(\mathbf{r}_1, t_1) \Delta I(\mathbf{r}_2, t_2) \rangle &= \langle [I(\mathbf{r}_1, t_1) - \bar{I}_1][I(\mathbf{r}_2, t_2) - \bar{I}_2] \rangle \\ &= \langle I(\mathbf{r}_1, t_1) I(\mathbf{r}_2, t_2) \rangle - \bar{I}_1 \bar{I}_2\end{aligned}\quad (6.31)$$

where  $\bar{I}_1$  and  $\bar{I}_2$  are the mean intensities of the field measured by photodetectors  $D_1$  and  $D_2$ , respectively. In classical theory, the joint-detection of  $D_1$  and  $D_2$  measures the statistical correlations between intensities  $I_1$  and  $I_2$ . If no correlation exists, the measurement gives a trivial product of two mean intensities. A nontrivial correlation function indicates the existence of a statistical correlation between the two measured intensities. Since the expectation function of  $\Gamma^{(2)}(\mathbf{r}_1, t_1; \mathbf{r}_2, t_2)$  is equivalent to the ensemble average  $\langle I(\mathbf{r}_1, t_1)I(\mathbf{r}_2, t_2) \rangle$ , the second-order correlation function is

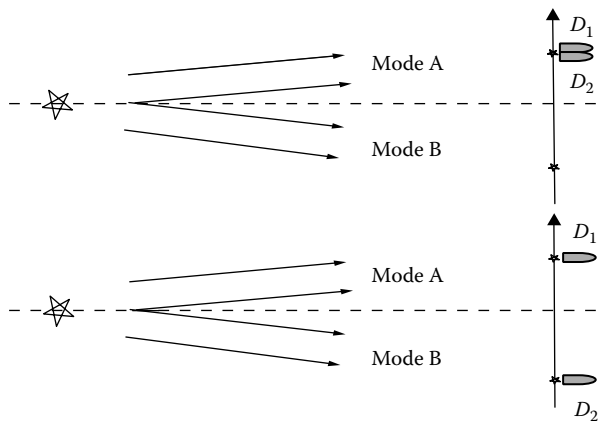
$$\begin{aligned}\Gamma^{(2)}(\mathbf{r}_1, t_1; \mathbf{r}_2, t_2) &= \Gamma_{11}^{(1)}\Gamma_{22}^{(1)} + |\Gamma^{(1)}(\mathbf{r}_1, t_1; \mathbf{r}_2, t_2)|^2 \\ &= \langle I_1 \rangle \langle I_2 \rangle + \langle \Delta I(\mathbf{r}_1, t_1) \Delta I(\mathbf{r}_2, t_2) \rangle\end{aligned}\quad (6.32)$$

In Equation 6.32, the nontrivial contribution of the second-order coherence function  $|\Gamma^{(1)}(\mathbf{r}_1, t_1; \mathbf{r}_2, t_2)|^2$  is in the same position as the statistical correlation of intensity fluctuations  $\langle \Delta I(\mathbf{r}_1, t_1) \Delta I(\mathbf{r}_2, t_2) \rangle$ . Therefore, the above theory concluded that the nontrivial contribution  $|\Gamma_{12}^{(1)}|^2$  is caused by the statistical correlation of intensity fluctuations  $\langle \Delta I_1 \Delta I_2 \rangle$ . Besides mathematics, the corresponding physical picture is reasonable for the HBT phenomenon: In the HBT interferometer, the measurement is in the far-field of the thermal radiation source, which is equivalent to the Fourier transform plane. When  $D_1$  and  $D_2$  are moved side by side, the two detectors measure the same mode of the radiation field. The measured intensities have the same fluctuations while the two photodetectors receive the same mode and thus yield a maximum value of  $\langle \Delta I_1 \Delta I_2 \rangle$  and give  $\gamma^{(2)} \sim 2$ . When the two photodetectors move apart to a certain distance,  $D_1$  and  $D_2$  start to measure different modes of the radiation field. In this case, the measured intensities have different fluctuations. The measurement yields  $\langle \Delta I_1 \Delta I_2 \rangle = 0$  and gives  $\gamma^{(2)} \sim 1$ . Figures 6.9 and 6.10 illustrate the above two different situations.

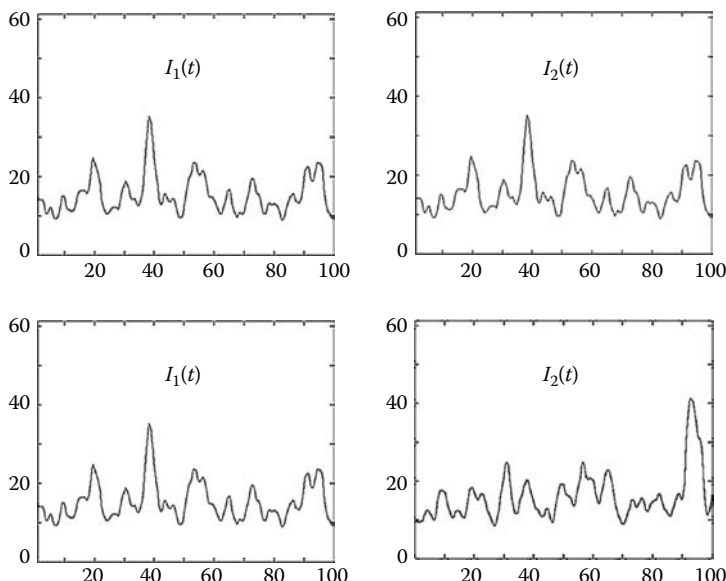
This theory has convinced us to believe that the observation of the nontrivial coherence function only occurs in the far-field of the thermal source. What will happen if we move the two HBT photodetectors to the “near field”\* as shown in the unfolded schematic of Figure 6.11? Is the nontrivial second-order coherence still observable in the near field according to this theory? It is easy to see that in the near field, (1) each photodetector,  $D_1$  and  $D_2$ , is able to receive radiations from a large number of sub-sources or spatial modes; and (2) in a joint-detection between  $D_1$  and  $D_2$ , the two photodetectors have more chances to be triggered by radiations coming from

---

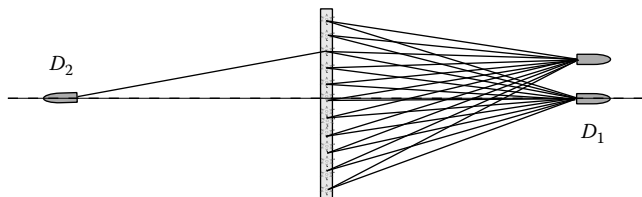
\* The concept of “near-field” was defined by Fresnel to be distinct from the Fraunhofer far-field. The Fresnel near-field is defined for a light source with angular size satisfying  $\Delta\theta > \lambda/D$ , where  $D$  is the diameter of the source. Sun is a typical Fresnel near-field radiation source to us, which has an opening angular diameter of  $\sim 0.53^\circ$ . The Fresnel near-field is different from the “near-surface-field.” The “near-surface-field” considers a distance of a few wavelengths from a surface.

**FIGURE 6.9**

A phenomenological interpretation of the historical HBT experiment. Upper: the two photodetectors receive identical modes of the far-field radiation and, thus, experience identical intensity fluctuations. The joint measurement of  $D_1$  and  $D_2$  gives a maximum value of  $\langle \Delta I_1 \Delta I_2 \rangle$ . Lower: the two photodetectors receive different modes of the far-field radiation. In this case, the joint measurement gives  $\langle \Delta I_1 \Delta I_2 \rangle = 0$ .

**FIGURE 6.10**

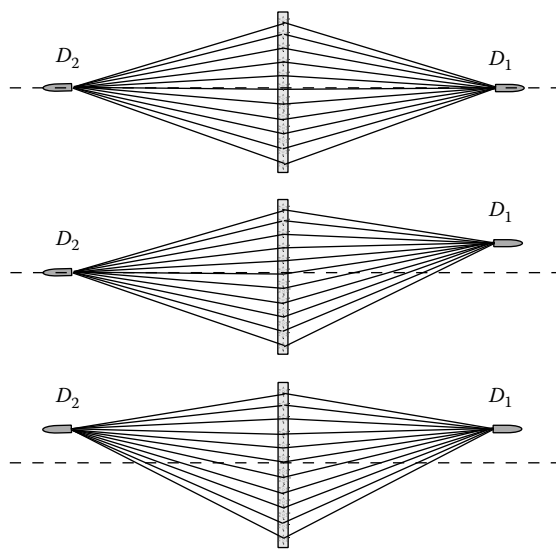
The two upper (lower) curves of  $I(t)$  correspond to the upper (lower) configuration in Figure 6.9.

**FIGURE 6.11**

(1) Each photodetector is able to receive radiations from a large number of sub-sources or spatial modes; (2) in a joint-detection between  $D_1$  and  $D_2$ , the two photodetectors have more chances to be triggered by radiations coming from different sub-sources or modes. The ratio between the joint-detections triggered by radiations coming from the same sub-source (mode) and those triggered by different sub-sources (modes) is roughly  $N/N^2 = 1/N$ ; and (3) despite the scanning position of  $D_1$  (or  $D_2$ ), the ratio of  $1/N$  does not change.

different sub-sources or modes. The ratio between the joint-detections triggered by radiations coming from the same sub-source (mode) and those triggered by different sub-sources (modes) is roughly  $N/N^2 = 1/N$ ; and (3) despite the scanning position of  $D_1$  (or  $D_2$ ) the ratio of  $1/N$  does not change. The above three points are clearly shown in Figure 6.11. Therefore, the statistical correlation theory of intensity fluctuations would conclude a constant second-order spatial coherence, which is false. An HBT-type nontrivial second-order coherence function of thermal light in near field was experimentally demonstrated by Scarelli et al. from 2005 to 2006. The experimental setup is similar to that of the historical HBT experiment, except that the far-field distant star is replaced by a near-field chaotic-thermal radiation source. The chaotic-thermal radiation source is a standard “pseudo-thermal” source, developed in the 1960s–1970s for HBT-type measurement, which contains a single-mode continuous wave laser beam and a fast-rotating, defusing ground glass. The transversely expanded laser beam is scattered by the rotating ground glass to simulate chaotic-thermal radiation. An adjustable pinhole is used immediately after the rotating ground glass to control the transverse size of the radiation. The pinhole size was chosen to be a few millimeters to centimeters. Similar to the HBT demonstrations, a 50/50 beamsplitter is used to split the chaotic-thermal light into two. The transmitted and reflected radiations, respectively, are coupled into  $D_1$  and  $D_2$ .  $D_1$  and  $D_2$  are placed at near-field *equal distances* of a few hundred millimeters from the light source for joint photodetection, either in photon counting coincidences or in HBT-type current-current correlations. An unfolded version of the schematic is shown in Figure 6.12, which might be easier for analyzing the physics.

Although the single detector counting rates or the output currents of  $D_1$  and  $D_2$  were monitored, respectively, to be constants during the measurement, nontrivial second-order correlations were observable with almost 50% contrast while the two point-like photodetectors,  $D_1$  and  $D_2$ , are aligned symmetrically on the transverse planes of  $x_1$  and  $x_2$ , as indicated in the

**FIGURE 6.12**

Near-field second-order spatial correlation measurement by Scarelli et al. Upper:  $D_1$  and  $D_2$  are placed at equal distances from the source and aligned symmetrically on the optical axis; a nontrivial  $g^{(2)}(x_1 - x_2)$  is observed with maximum value of  $\sim 2$ . Middle:  $D_1$  is moved up to a nonsymmetrical position;  $g^{(2)}(x_1 - x_2)$  becomes a constant of 1. Lower:  $D_2$  is moved up to the symmetrical position with  $D_1$ ; the nontrivial  $g^{(2)}(x_1 - x_2)$  is observable with a maximum value of  $\sim 2$  again.

upper and lower cases of Figure 6.12. In the upper measurement,  $D_1$  and  $D_2$  are aligned symmetrically on the optical axis. A sinc-like function of  $|\gamma_{12}^{(1)}|^2$  or  $\langle \Delta I_1 \Delta I_2 \rangle$  is observed by scanning either  $D_1$  or  $D_2$  transversely in the neighborhood of the optical axis. When  $D_1$  is moved a few millimeters up (or down) from its symmetrical position, as shown in the middle, the nontrivial correlation disappears with  $\langle \Delta I_1 \Delta I_2 \rangle \sim 0$ , when scanning either  $D_1$  or  $D_2$  in the neighborhood of that unsymmetrical position. In the lower measurement,  $D_2$  is moved up (or down) to a symmetrical position, again with respect to  $D_1$ . A similar sinc-like function of  $|\gamma_{12}^{(1)}|^2$  or  $\langle \Delta I_1 \Delta I_2 \rangle$  is observed by scanning either  $D_1$  or  $D_2$  in the neighborhood of their new symmetrical position. Note that *equal distance* between the photodetectors and the light source is required for the observation of the sinc-function-like correlation. For a large source of transverse dimension, a few millimeter difference may cause a complete disappearance of the nontrivial correlation.

The experimental result is quite surprising. First, it tells us that our 50 years' belief about the far-field condition has never been true. The nontrivial second-order spatial correlation of thermal light is observable in the near field. Second, based on the concept of intensity fluctuation correlation, there is no reason for the three measurements illustrated in Figure 6.12 to have such a significant difference.

1. As we have discussed in the beginning of this section, in near field,  $D_1$  and  $D_2$  can never achieve the condition in which they have more chance to be triggered by a single mode and less chance to be triggered by different modes, as is in the far-field HBT experiment. In the Fresnel near-axial applications, wherever we move  $D_1$  and  $D_2$  in their transverse planes, they receive the same large number of independent sub-fields or modes, and the chances of been triggered by a sub-source (mode) or by two different sub-sources (modes) does not change from one position to another. The ratio between these two chances is always  $\sim 1/N$ .
2. Although the transverse move of  $D_1$  and  $D_2$  may change the value of the temporal correlation of  $|\gamma^{(1)}(t_1 - t_2)|$ , however, the changes are indeed negligible by moving up or down a few millimeters. The observed second-order temporal correlation of the chaotic-thermal radiation used in the above measurement is illustrated in Figure 6.13 with a measured width in the order of  $\mu\text{s}$ , which implies that to change from the maximum (minimum) correlation to its minimum (maximum) value, a relative longitudinal delay of a few hundred meters is necessary.

It is true that statistical fluctuations are unavoidable in any optical measurements. It would be correct to say that the nontrivial second-order coherence is *observed* in the intensity fluctuations; however, it is not *caused* by the statistical correlation of the intensity fluctuations.

There has been a naive interpretation that is based on the use of an optical beamsplitter. Similar to the historical HBT experiments, the

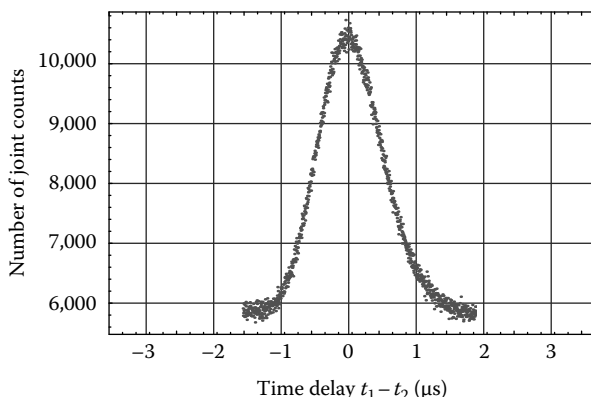


**FIGURE 6.13**

Second-order temporal coherence of the chaotic-thermal radiation used in the near-field HBT experiment. The coherent time of the simulated chaotic-thermal field is in the order of  $\mu\text{s}$ , corresponding to a longitudinal optical delay of  $\sim 300$  m.

laboratory demonstrations of the nontrivial near-field second-order correlation of chaotic-thermal light use 50/50 beamsplitter to split light into two. It was proposed that an optical beamsplitter produces two identical copies of light “speckles”:

$$\langle I(\vec{\rho}_1)I(\vec{\rho}_2) \rangle \sim \delta(\vec{\rho}_s - \vec{\rho}_1) \delta(\vec{\rho}_s - \vec{\rho}_2) \quad (6.33)$$

where  $\vec{\rho}_s$  is the transverse coordinate of the “speckle” in the light source. The two photodetectors measure the “same” speckle when taking  $\vec{\rho}_1 = \vec{\rho}_2$ . The two measured intensities would have the same fluctuations, leading to  $\langle \Delta I_1 \Delta I_2 \rangle \neq 0$ ; however, when taking  $\vec{\rho}_1 \neq \vec{\rho}_2$  the two photodetectors measure a “different” speckle, and the two measured intensities would have random fluctuations, leading to  $\langle \Delta I_1 \Delta I_2 \rangle = 0$ .

There are two major problems with this theory:

- (1) Neither quantum theory nor classical theory of optical beamsplitter is based on the splitting of intensities. In classical theory, a beam splitter transfers the electromagnetic fields from its input ports into the electromagnetic fields of its output ports with appropriate phase relations, leaving the energy conserved in the process of beamsplitting. In quantum theory, a unitary operator is defined for this job. This operator relates the field operators at the input ports of the beamsplitter with the field operators at its output ports as a unitary transformation. The electromagnetic fields, either quantized or classical, propagating from the source to the beamsplitter and then to the photodetectors, must follow certain physical rules. In classical theory, any electromagnetic field and its superposition at any space-time point must be a solution of the Maxwell wave equation. In fact, Equation 6.33 is neither a solution of classical theory nor a solution of quantum theory. In Chapter 3, we have discussed the propagation of light. A “speckle” of the thermal light source has a constant distribution on any distant plane. There is no way to make two identical copies of a source speckle onto the measurement planes of  $D_1$  and  $D_2$ , respectively, unless classical imaging systems are applied.
- (2) Even if a beamsplitter could make two identical copies of intensities right on its output ports, after a large distance propagation and separation there is no guarantee that the two intensities experience the same atmospheric fluctuations or turbulence; different local environmental conditions will change the temporal and spatial distributions if the two intensities fluctuate differently. In a modern HBT interferometer, the distance between  $D_1$  and  $D_2$  can be in kilometers. We have not found any modern HBT interferometer stopping its normal functioning due to different local environmental conditions at its two receivers. In addition, in Chapter 11 we will

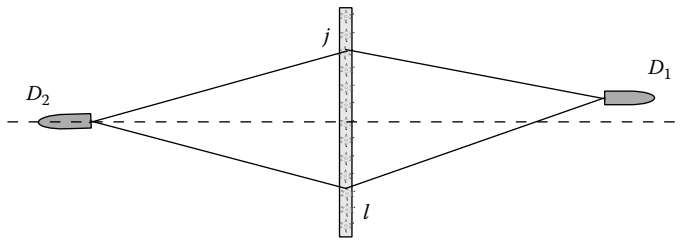
analyze a turbulence-free ghost imaging experiment. The result of that experiment further supports this point.

There is no doubt that the nontrivial second-order correlation of chaotic-thermal light is an interference phenomenon. However, this peculiar interference seems very different from the traditional classic concept of interference. Examining Equations 6.14, 6.17 and 6.23, it is easy to find that at least this interference is different from the following two types of classic interferences.

- (I) It is obviously different from the interference (diffraction) effect observable in the measurement of coherent radiation. In the measurement of coherent light, the local superposition of a large number of coherent fields  $|\sum_j E_j(\mathbf{r}_1, t_1)|^2$  and  $|\sum_j E_j(\mathbf{r}_2, t_2)|^2$  produces either two independent (factorizable) pulses in time or two independent (factorizable) diffraction patterns on the transverse observing planes. However, this has never happened in the measurement of chaotic-thermal light.
- (II) It is not the interference of  $|E(\mathbf{r}_1, t_1) + E(\mathbf{r}_2, t_2)|^2$ , where  $E(\mathbf{r}_1, t_1)$  and  $E(\mathbf{r}_2, t_2)$  are the fields measured at space-time coordinates  $(\mathbf{r}_1, t_1)$  and  $(\mathbf{r}_2, t_2)$  by  $D_1$  and  $D_2$ , respectively. In the Maxwell electromagnetic wave theory of light,  $E(\mathbf{r}_1, t_1)$  and  $E(\mathbf{r}_2, t_2)$  can never interfere with each other at a distance through the measurement of two independent photodetectors.

The interference involved in the second-order coherence measurement is  $|E_{j1}E_{l2} + E_{l1}E_{j2}|^2$ . Perhaps, quantum language is the best language to describe this superposition. In the view of quantum mechanics, this superposition implies two different, yet indistinguishable, alternative ways to trigger a joint-detection event between  $D_1$  and  $D_2$ : (1)  $D_1$  is triggered by photon  $j$ , that is created from the  $j$ th point sub-source, and  $D_2$  is triggered by photon  $l$ , that is created from the  $l$ th point sub-source; and (2)  $D_1$  is triggered by photon  $l$ , that is created from the  $l$ th point sub-source, and  $D_2$  is triggered by photon  $j$ , that is created from the  $j$ th point sub-source.  $E_{j1}E_{l2}$  and  $E_{l1}E_{j2}$ , respectively, correspond to the different, yet indistinguishable, two-photon amplitudes, representing the above two alternatives (1) and (2). Figure 6.14 schematically illustrates these two alternatives for an arbitrary pair of photons that are created at the  $j$ th and  $l$ th sub-sources, respectively.

Although  $|E_{j1}E_{l2} + E_{l1}E_{j2}|^2$  has a simple yet clear physical meaning in the quantum theory of light, it is difficult to accept from a classical point of view. First, the superposition of  $|E_{j1}E_{l2} + E_{l1}E_{j2}|^2$  is indeed outside the scope of the Maxwell electromagnetic wave theory. Different from nonlinear optics, here, no  $\chi^{(2)}$  material is present in the thermal source to produce nonlinear polarization that leads to the nonlinear wave equation. Neither  $E_{j1}E_{l2}$

**FIGURE 6.14**

Schematic of an “unfolded” version of the experimental setup of Figure 6.6. The optical arm of  $D_2$  is “unfolded” to the left side of the source. The thermal radiation source consists of a large number of independent point sub-sources. The superposition of  $|E_{j1}E_{l2} + E_{l1}E_{j2}|^2$  results in a joint-detection event between  $D_1$  and  $D_2$  at  $(\mathbf{r}_1, t_1)$  and  $(\mathbf{r}_2, t_2)$ .

nor  $E_{j1}E_{l2} + E_{l1}E_{j2}$  is a solution of the linear Maxwell wave equation. Second, perhaps this is the most troubling point in classical theory: the superposition of  $|E_{j1}E_{l2} + E_{l1}E_{j2}|^2$  is “nonlocal,” which occurs at separated space-time coordinates through the measurement of two independent photodetectors. Under certain experimental conditions, the two photodetection events are capable of being space-like separated events. Following EPR–Bell, we name this peculiar superposition “nonlocal.”

## 6.4 Near-Field Second-Order Spatial Coherence of Thermal Light

The observed near-field nontrivial second-order coherence of thermal light is indeed an interference phenomenon. In the following, we attempt a calculation starting from Equation 6.14 for the near-field second-order spatial coherence of thermal light  $\Gamma^{(2)}(\vec{\rho}_1, z_1; \vec{\rho}_2, z_2)$ ,

$$\begin{aligned} \Gamma^{(2)}(\vec{\rho}_1, z_1; \vec{\rho}_2, z_2) \\ = \sum_j \sum_l \left| \frac{1}{\sqrt{2}} [E_j(\vec{\rho}_1, z_1)E_l(\vec{\rho}_2, z_2) + E_l(\vec{\rho}_1, z_1)E_j(\vec{\rho}_2, z_2)] \right|^2, \end{aligned} \quad (6.34)$$

where we have used the transverse and longitudinal coordinates of  $\vec{\rho}$  and  $z$  to specify the spatial coordinates of the photodetectors. In Equation 6.34 we have ignored the temporal variables by a similar treatment as in our early calculations for second-order spatial correlation. In the near field we apply the Fresnel approximation as usual to propagate the field from each sub-source to the photodetectors. Substituting the Green’s functions derived in Section 3.2 into Equation 6.34, we have the following expression for  $\Gamma^{(2)}(\vec{\rho}_1, z_1; \vec{\rho}_2, z_2)$

in terms of the Green's functions:

$$\begin{aligned}
 \Gamma^{(2)}(\vec{\rho}_1, z_1; \vec{\rho}_2, z_2) &= \int d\vec{\kappa} d\vec{\kappa}' \left| \frac{1}{\sqrt{2}} [g(\vec{\rho}_1, z_1, \vec{\kappa}) g(\vec{\rho}_2, z_2, \vec{\kappa}') + g(\vec{\rho}_2, z_2, \vec{\kappa}) g(\vec{\rho}_1, z_1, \vec{\kappa}')] \right|^2 \\
 &= \int d\vec{\kappa} |g(\vec{\rho}_1, z_1, \vec{\kappa})|^2 \int d\vec{\kappa}' |g(\vec{\rho}_2, z_2, \vec{\kappa}')|^2 \\
 &\quad + \left| \int d\vec{\kappa} g^*(\vec{\rho}_1, z_1, \vec{\kappa}) g(\vec{\rho}_2, z_2, \vec{\kappa}) \right|^2. \tag{6.35}
 \end{aligned}$$

In Equation 6.35 we have changed the order between the summation of the sub-sources and the integral of the transverse wavevectors as usual. The summation of the sub-sources has been formally embedded into the Green's functions. Substituting the Green's function for free propagation

$$g(\vec{\rho}_j, z_j, \vec{\kappa}) = \frac{-i\omega}{2\pi c} \frac{e^{i\frac{\omega}{c}z_j}}{z_j} \int d\vec{\rho}_0 a(\vec{\rho}_0) e^{i\vec{\kappa} \cdot \vec{\rho}_0} e^{i\frac{\omega}{2cz_j}|\vec{\rho}_j - \vec{\rho}_0|^2}$$

into Equation 6.35, we obtain

$$\Gamma_{11}^{(1)} \Gamma_{22}^{(1)} \sim \text{constant},$$

and

$$\begin{aligned}
 \Gamma_{12}^{(1)}(\vec{\rho}_1, z_1; \vec{\rho}_2, z_2) &\propto \frac{1}{z_1 z_2} \int d\vec{\rho}_0 a^2(\vec{\rho}_0) e^{-i\frac{\omega}{c}z_1} e^{-i\frac{\omega}{2cz_1}|\vec{\rho}_1 - \vec{\rho}_0|^2} e^{i\frac{\omega}{c}z_2} e^{i\frac{\omega}{2cz_2}|\vec{\rho}_2 - \vec{\rho}_0|^2},
 \end{aligned}$$

where we have approximated the integral of  $d\vec{\kappa}$  to  $\delta(\vec{\rho}_0 - \vec{\rho}'_0)$  by assuming a large enough bandwidth of  $\Delta\vec{\kappa}$

$$\int d\vec{\kappa} e^{-i\vec{\kappa} \cdot (\vec{\rho}_0 - \vec{\rho}'_0)} \sim \delta(\vec{\rho}_0 - \vec{\rho}'_0).$$

Assuming  $a^2(\vec{\rho}_0) \sim \text{constant}$ , and taking  $z_1 = z_2 = d$ , we obtain

$$\begin{aligned}
 \Gamma_{12}^{(1)}(\vec{\rho}_1, \vec{\rho}_2) &\propto \int d\vec{\rho}_0 a^2(\vec{\rho}_0) e^{-i\frac{\omega}{2cd}|\vec{\rho}_1 - \vec{\rho}_0|^2} e^{i\frac{\omega}{2cd}|\vec{\rho}_2 - \vec{\rho}_0|^2} \\
 &\propto e^{-i\frac{\omega}{2cd}(|\vec{\rho}_1|^2 - |\vec{\rho}_2|^2)} \int d\vec{\rho}_0 a^2(\vec{\rho}_0) e^{i\frac{\omega}{cd}(\vec{\rho}_1 - \vec{\rho}_2) \cdot \vec{\rho}_0} \\
 &\propto e^{-i\frac{\omega}{2cd}(|\vec{\rho}_1|^2 - |\vec{\rho}_2|^2)} \text{somb} \left[ \frac{R}{d} \frac{\omega}{c} |\vec{\rho}_1 - \vec{\rho}_2| \right], \tag{6.36}
 \end{aligned}$$

where we have assumed a disk-like light source with a finite radius of  $R$ , and again,  $\text{somb}(x) = J_1(x)/x$ ,  $J_1(x)$  is the first-order Bessel Function. In Equation 6.36 we have absorbed all constants into the proportionality constant. The second-order spatial correlation function  $\Gamma^{(2)}(\vec{\rho}_1; \vec{\rho}_2)$  is thus

$$\Gamma^{(2)}(|\vec{\rho}_1 - \vec{\rho}_2|) = I_0^2 \left[ 1 + \text{somb}^2 \left( \frac{R}{d} \frac{\omega}{c} |\vec{\rho}_1 - \vec{\rho}_2| \right) \right]. \quad (6.37)$$

Consequently, the degree of second-order spatial coherence is

$$\gamma^{(2)}(|\vec{\rho}_1 - \vec{\rho}_2|) = 1 + \text{somb}^2 \left( \frac{R}{d} \frac{\omega}{c} |\vec{\rho}_1 - \vec{\rho}_2| \right). \quad (6.38)$$

For a large value of  $2R/d \sim \Delta\theta$ , where  $\Delta\theta$  is the angular size of the radiation source viewed at the photodetectors, the point-to-“spot” sombrero-like function can be approximated as a  $\delta$ -function of  $|\vec{\rho}_1 - \vec{\rho}_2|$ . We thus effectively have a “point”-to-“point” correlation between the transverse planes of  $z_1 = d$  and  $z_2 = d$ .

This calculation ended with a surprising and interesting result. Analogous to EPR’s language, the photodetectors  $D_1$  and  $D_2$  have equal chance to be triggered at any position on the transverse planes of  $z_1 = d$  and  $z_2 = d$ , however, if  $D_1$  is triggered at a certain position on the  $z_1 = d$  plane,  $D_2$  has twice chance to be triggered at a position  $\vec{\rho}_2 = \vec{\rho}_1$ . Although the non-trivial correlation is only partial with a constant background, this surprise has turned into a useful new technology: lensless ghost imaging. In fact, the above sombrero-like function is the observed ghost image of the point-like aperture of the point-like photodetector located on the object plane, when scanning the other point-like photodetector on the ghost image plane. The sombrero-like function is the same as that of the classical image-forming function, except replacing its numerical aperture  $D/s_0$ , where  $D$  is the diameter of the imaging lens and  $s_0$  the distance from the object to the lens, with  $D/d \sim \Delta\theta$ , where  $D$  is the diameter of the thermal source,  $d$  the distance between the object and the light source, and  $\Delta\theta$  the angular diameter of the thermal source. As we have discussed in classical imaging, the spot size of the sombrero-like point spread function determines the spatial resolution of the image. Similarly, the spot size of the sombrero-like point-to-spot function in Equation 6.38 will determine the spatial resolution of the lensless ghost image. Perhaps this is the most attractive property of lensless ghost imaging of thermal light in practical applications besides its nonlocal nature. For instance, using the sun as the light source we may achieve a spatial resolution equivalent to that of a classical camera with a lens of 92 meters when taking pictures at 10 kilometers.\* In certain applications, a piece of cloud or

---

\* The angular size of the sun is about  $0.53^\circ$ . To achieve a compatible numerical aperture, a camera must have a lens 92 m when taking a picture at 10 km.

a portion of bright sky can be used as the light source (either naturally scattering or artificially lighting) for thermal light ghost imaging, a much higher spatial resolution is expected.

The source-angular-size dependence of the point-to-spot correlation has been experimentally confirmed in 1D measurements. In 1D, Equations 6.37 and 6.38 become

$$\Gamma^{(2)}(x_1 - x_2) = I_0^2 \left[ 1 + \operatorname{sinc}^2 \left( \frac{D}{d} \frac{\pi(x_1 - x_2)}{\lambda} \right) \right] \quad (6.39)$$

and

$$\gamma^{(2)}(x_1 - x_2) = 1 + \operatorname{sinc}^2 \left( \frac{D}{d} \frac{\pi(x_1 - x_2)}{\lambda} \right). \quad (6.40)$$

In a recent experiment, Zhou et al. measured the 1D sinc-like function from a similar chaotic-thermal radiation source used by Scarcelli et al. in their near-field lensless ghost imaging experiment. Figure 6.15 shows the experimental results in which different angular-sized sources were chosen for the measurements. The fitting curves are calculated from Equation 6.40. The calculated  $\gamma^{(2)}(x_1 - x_2)$  functions agree with the experimental results within experimental error.

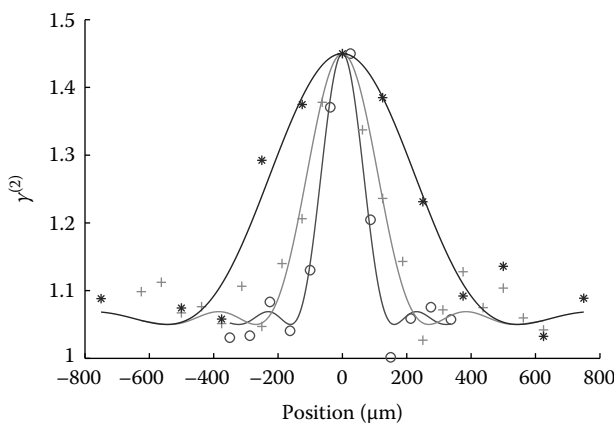


**FIGURE 6.15**

Measured point-to-'spot' spatial correlation of a chaotic-thermal radiation with 1 mm (star), 2 mm (cross) and 4 mm (circle) diameter sources, respectively. The fitting curves are calculated from Equation 6.40.

---

## 6.5 Nth-Order Coherence of Light

In this section, we introduce the concept of higher-order coherence of light. In general, the  $N$ th-order ( $N > 2$ ) coherence or correlation of light is defined as

$$\begin{aligned}\Gamma^{(N)}(\mathbf{r}_1, t_1; \mathbf{r}_2, t_2; \dots; \mathbf{r}_N, t_N) \\ = \langle E^*(\mathbf{r}_1, t_1)E(\mathbf{r}_1, t_1)E^*(\mathbf{r}_2, t_2)E(\mathbf{r}_2, t_2) \dots E^*(\mathbf{r}_N, t_N)E(\mathbf{r}_N, t_N) \rangle\end{aligned}\quad (6.41)$$

and the degree of  $N$ th-order coherence is defined as

$$\begin{aligned}\gamma^{(N)}(\mathbf{r}_1, t_1; \mathbf{r}_2, t_2; \dots; \mathbf{r}_N, t_N) \\ = \frac{\langle E^*(\mathbf{r}_1, t_1)E(\mathbf{r}_1, t_1)E^*(\mathbf{r}_2, t_2)E(\mathbf{r}_2, t_2) \dots E^*(\mathbf{r}_N, t_N)E(\mathbf{r}_N, t_N) \rangle}{\langle E^*(\mathbf{r}_1, t_1)E(\mathbf{r}_1, t_1) \rangle \langle E^*(\mathbf{r}_2, t_2)E(\mathbf{r}_2, t_2) \rangle \dots \langle E^*(\mathbf{r}_N, t_N)E(\mathbf{r}_N, t_N) \rangle}\end{aligned}\quad (6.42)$$

where the ensemble average,  $\langle \dots \rangle$  denotes, again, *taking into account all possible realizations of the field*.

It is easy to show that the  $N$ th-order correlation function of coherent light is factorizable into  $N$  independent first-order self-correlation functions (intensities), and consequently the degree of  $N$ th-order coherence of coherent radiation is

$$\gamma_{\text{coh}}^{(N)}(\mathbf{r}_1, t_1; \mathbf{r}_2, t_2; \dots; \mathbf{r}_N, t_N) = 1.$$

In the following, we will focus on the discussion of the nontrivial  $N$ th-order coherence function of thermal radiation. Assuming a thermal source with a large number of randomly distributed and randomly radiating independent point sub-sources, such as trillions of independent and randomly radiating atomic transitions, contribute to the measurement of each of the  $N$ -detectors. Each point sub-source contributes an independent spherical wave as a subfield of complex amplitude  $E_j = a_j e^{i\varphi_j}$ , where  $a_j$  is the real and positive amplitude of the  $j$ th subfield and  $\varphi_j$  is a *random* phase associated with the  $j$ th subfield. Basically, we have the following pictures for the source: (1) a large number of independent point sub-sources distributed randomly in space (counted spatially); (2) each point-source contains a large number of independently and randomly radiating atoms (counted temporally); and (3) a large number of sub-sources, either counted spatially or temporally, may

contribute to each of the independent radiation mode ( $\vec{\kappa}, \omega$ ) at each of the individual point photodetectors (counted by mode).

There is no surprise that the expectation value of the  $j$ th self-correlation function, or the  $j$ th intensity measured by the  $j$ th photodetector, is a constant:

$$\Gamma^{(1)}(\mathbf{r}_j, t_j; \mathbf{r}_j, t_j) = \langle E^*(\mathbf{r}_j, t_j)E(\mathbf{r}_j, t_j) \rangle = \text{constant},$$

where the expectation operation has taken into account all possible values of the phases of the subfields. Although each and all the  $N$ -intensities are constants, it does not prevent a nontrivial  $N$ th-order coherence or correlation in the joint measurement of  $N$  independent photodetectors. For instance, the third-order intensity coherence function,  $\Gamma^{(3)}(\mathbf{r}_1, t_1; \mathbf{r}_2, t_2; \mathbf{r}_3, t_3)$  is calculated as

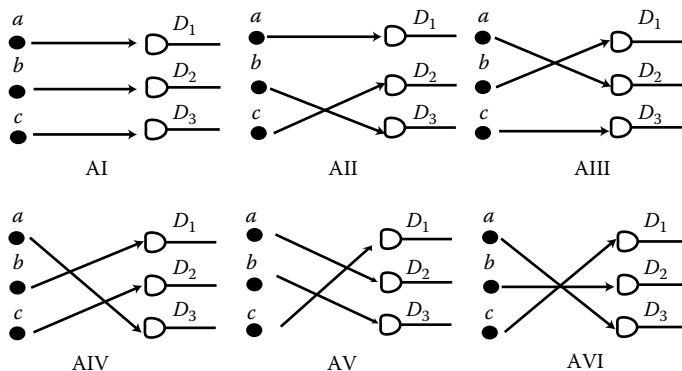
$$\begin{aligned} & \Gamma^{(3)}(\mathbf{r}_1, t_1; \mathbf{r}_2, t_2; \mathbf{r}_3, t_3) \\ & \equiv \langle E^*(\mathbf{r}_1, t_1)E(\mathbf{r}_1, t_1)E^*(\mathbf{r}_2, t_2)E(\mathbf{r}_2, t_2)E^*(\mathbf{r}_3, t_3)E(\mathbf{r}_3, t_3) \rangle \\ & = \left\langle \sum_j E_{j1}^* \sum_k E_{k1} \sum_l E_{l2}^* \sum_m E_{m2} \sum_n E_{n3}^* \sum_p E_{p3} \right\rangle \\ & = \sum_{j,k,l} \left| \frac{1}{\sqrt{6}} [E_{j1}E_{k2}E_{l3} + E_{j1}E_{k3}E_{l2} + E_{j2}E_{k1}E_{l3} \right. \\ & \quad \left. + E_{j2}E_{k3}E_{l1} + E_{j3}E_{k1}E_{l2} + E_{j3}E_{k2}E_{l1}] \right|^2, \end{aligned} \quad (6.43)$$

where  $E_{\alpha\beta}$  is short for  $E_\alpha(\mathbf{r}_\beta, t_\beta)$ , indicating the field at coordinate  $(\mathbf{r}_\beta, t_\beta)$  is originated from the  $\alpha$ th sub-source. Similar to Equation 6.14 of the second-order coherence of thermal light, a partial ensemble average has been taken in Equation 6.43 by means of *taking into account all possible phase values of the subfields*. We will show in the following that Equation 6.43 leads to a nontrivial function of  $\Gamma^{(3)}(\mathbf{r}_1, t_1; \mathbf{r}_2, t_2; \mathbf{r}_3, t_3)$ .

We now calculate the third-order temporal coherence. Assuming a similar experimental setup of the modified HBT, except the use of three photodetectors and threefold joint-detection coincidence counter or threefold current-current-current linear multiplier. To simplify the mathematics, we further assume equal distances from the thermal source to the three point photodetectors,  $z_1 = z_2 = z_3$ , the joint-detection counting rate or the joint current-current-current multiplication between  $D_1, D_2$ , and  $D_3$  is calculated from Equation 6.43

$$\begin{aligned}
 & \Gamma^{(3)}(t_1, t_2, t_3) \\
 &= \int d\omega \int d\omega' \int d\omega'' |f(\omega)|^2 |f(\omega')|^2 |f(\omega'')|^2 \\
 &\quad \times \left| \frac{1}{\sqrt{6}} [g(\omega, t_1)g(\omega', t_2)g(\omega'', t_3) + g(\omega, t_1)g(\omega'', t_2)g(\omega', t_3) \right. \\
 &\quad + g(\omega', t_1)g(\omega, t_2)g(\omega'', t_3) + g(\omega', t_1)g(\omega'', t_2)g(\omega, t_3) \\
 &\quad \left. + g(\omega'', t_1)g(\omega, t_2)g(\omega', t_3) + g(\omega'', t_1)g(\omega', t_2)g(\omega, t_3)] \right|^2, \quad (6.44)
 \end{aligned}$$

where  $g(\omega, t_j)$  is the Green's function that propagates the field from the source to the  $j$ th photodetector. Equation 6.44 is the key equation to see the three-photon interference nature of the nontrivial third-order correlation. The six terms of superposition in Equation 6.44 correspond to six different, yet indistinguishable, alternative ways for three independent photons to trigger a threefold joint-detection event. The six amplitudes are identified in Figure 6.16. At  $t_1 = t_2 = t_3$  (under the condition of  $z_1 = z_2 = z_3$ ), the six amplitudes are superposed constructively, and consequently  $\Gamma^{(3)}(t_1, t_2, t_3)$  achieves its maximum value when summed over these constructive interferences. On the other hand, at  $t_1 \neq t_2 \neq t_3$ , the six amplitudes are distinguishable or partially distinguishable, and consequently  $\Gamma^{(3)}(t_1, t_2, t_3)$  achieves less values. It is the three-photon interferences that caused the three randomly distributed photons to have six times greater chance of being captured at  $t_1 = t_2 = t_3$ . We usually write Equation 6.44 in the

**FIGURE 6.16**

Three independent photons  $a, b, c$  have six alternative ways of triggering a joint-detection event between  $D_1, D_2$ , and  $D_3$ . At equal distances from the source, the probability of observing a three-photon joint-detection event at  $(t_1, t_2, t_3)$  is determined by the superposition of the six three-photon amplitudes. At  $t_1 = t_2 = t_3$ , six amplitudes superpose constructively.  $\Gamma^{(3)}(t_1, t_2, t_3)$  achieves its maximum value by summing over these constructive interferences.

following form:

$$\begin{aligned}
 \Gamma^{(3)}(t_1, t_2, t_3) = & \Gamma^{(1)}(t_1, t_1)\Gamma^{(1)}(t_2, t_2)\Gamma^{(1)}(t_3, t_3) \\
 & + |\Gamma^{(1)}(t_1, t_2)|^2\Gamma^{(1)}(t_3, t_3) \\
 & + |\Gamma^{(1)}(t_2, t_3)|^2\Gamma^{(1)}(t_1, t_1) \\
 & + |\Gamma^{(1)}(t_3, t_1)|^2\Gamma^{(1)}(t_2, t_2) \\
 & + \Gamma^{(1)}(t_1, t_2)\Gamma^{(1)}(t_2, t_3)\Gamma^{(1)}(t_3, t_1) \\
 & + \Gamma^{(1)}(t_2, t_1)\Gamma^{(1)}(t_3, t_2)\Gamma^{(1)}(t_1, t_3)
 \end{aligned} \quad (6.45)$$

where  $\Gamma^{(1)}(t_j, t_k)$  for  $j = 1, 2, 3$  and  $k = 1, 2, 3$ , respectively, is defined as

$$\Gamma^{(1)}(t_j, t_k) \equiv \int d\omega |f(\omega)|^2 g^*(\omega, t_j)g(\omega, t_k). \quad (6.46)$$

Equation 6.45 can be normalized as

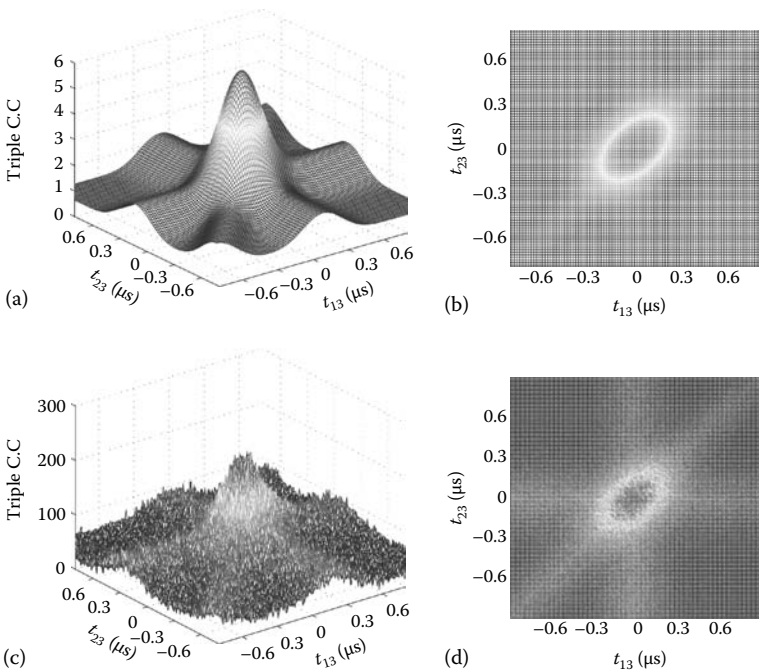
$$\begin{aligned}
 \gamma^{(3)}(t_1, t_2, t_3) \\
 = 1 + |\gamma_{12}^{(1)}|^2 + |\gamma_{13}^{(1)}|^2 + |\gamma_{23}^{(1)}|^2 + \gamma_{12}^{(1)}\gamma_{23}^{(1)}\gamma_{31}^{(1)} + \gamma_{21}^{(1)}\gamma_{32}^{(1)}\gamma_{13}^{(1)}
 \end{aligned} \quad (6.47)$$

where  $\gamma_{jk}^{(1)} = \Gamma_{jk}^{(1)} / \sqrt{\Gamma_{jj}^{(1)}\Gamma_{kk}^{(1)}}$ . To simplify the mathematics in calculating  $\gamma^{(3)}(t_1, t_2, t_3)$ , we assume a constant spectrum distribution  $f(\omega)$  within the bandwidth of the radiation field  $\Delta\omega$ . The integrals in Equation 6.46 yield sinc-functions for  $j \neq k$  and constants for  $j = k$ . The normalized third-order temporal correlation function  $\gamma^{(3)}(t_1, t_2, t_3)$  is thus

$$\begin{aligned}
 \gamma^{(3)}(t_1, t_2, t_3) = & 1 + \text{sinc}^2\left[\frac{\Delta\omega(t_1 - t_2)}{2}\right] \\
 & + \text{sinc}^2\left[\frac{\Delta\omega(t_2 - t_3)}{2}\right] + \text{sinc}^2\left[\frac{\Delta\omega(t_3 - t_1)}{2}\right] \\
 & + 2\text{sinc}\left[\frac{\Delta\omega(t_1 - t_2)}{2}\right]\text{sinc}\left[\frac{\Delta\omega(t_2 - t_3)}{2}\right]\text{sinc}\left[\frac{\Delta\omega(t_3 - t_1)}{2}\right].
 \end{aligned} \quad (6.48)$$

It is easy to see that when  $t_1 = t_2 = t_3$ ,  $\gamma^{(3)}(t_1, t_2, t_3) = 6$ . The third-order correlation function achieves a maximum contrast of 6 to 1 ( $\sim 71\%$  visibility).

The nontrivial third-order coherence function of thermal light has been measured by Zhou et al. recently. The measured  $\gamma^{(3)}(t_1, t_2, t_3)$  is shown in Figure 6.17. The experiment and the simulation are in agreement within allowed statistical error.

**FIGURE 6.17**

Calculated (upper, a and b) and measured (lower, c and d) third-order temporal correlation of thermal light. The 3-D three-photon joint-detection histogram is plotted as a function of  $t_{13} \equiv t_1 - t_3$  and  $t_{23} \equiv t_2 - t_3$ . The simulation function is calculated from Equation 6.48. In addition, the single-detector counting rates for  $D_1$ ,  $D_2$ , and  $D_3$  are all monitored to be constants.

The  $N$ th-order ( $N \geq 2$ ) coherence of thermal light can be easily extend from  $\Gamma^{(3)}(\mathbf{r}_1, t_1; \mathbf{r}_2, t_2; \mathbf{r}_3, t_3)$  to  $\Gamma^{(N)}(\mathbf{r}_1, t_1; \dots; \mathbf{r}_N, t_N)$ ,

$$\begin{aligned} \Gamma^{(N)}(\mathbf{r}_1, t_1; \dots; \mathbf{r}_N, t_N) \\ \equiv \langle E^*(\mathbf{r}_1, t_1)E(\mathbf{r}_1, t_1) \dots E^*(\mathbf{r}_N, t_N)E(\mathbf{r}_N, t_N) \rangle \\ \simeq \sum_{j,k,l,\dots} \left| \frac{1}{\sqrt{N!}} \left[ \sum_{N!} E_{j1}E_{k2}E_{l3}\dots \right] \right|^2, \end{aligned} \quad (6.49)$$

where  $\sum_{N!} E_{j1}E_{k2}E_{l3}\dots$  means the sum of  $N!$  terms of  $N$ -fold subfields, permuting in the orders of  $1, 2, 3, \dots, N, 1, 3, 2, \dots, N, 2, 1, 3, \dots, N$ , etc., corresponding to  $N!$  alternative ways for the  $N$  independent subfields (photons), created from a large number of independent sub-sources that are labeled by  $j, k, l, \dots$ , to produce a  $N$ -fold joint photodetection event between  $N$  independent photodetectors.

## 6.6 Nth-Order Near-Field Spatial Coherence of Thermal Light

In this section, we briefly discuss the Nth-order near-field spatial correlation of thermal light. As an example, we will give a third-order calculation. Now, considering a measurement similar to that of the third-order temporal coherence, except the scanning of three point photodetectors in the transverse planes of  $\vec{\rho}_1$ ,  $\vec{\rho}_2$ , and  $\vec{\rho}_3$ , respectively. Our calculation begins from Equation 6.43. To simplify the mathematics, we neglect the spectral frequency integrals by achieving a maximum temporal correlation at single wavelength operation as usual,

$$\begin{aligned} \Gamma^{(3)}(\vec{\rho}_1, \vec{\rho}_2, \vec{\rho}_3) \propto & \int d\vec{\kappa} |g_1(\vec{\kappa})|^2 \int d\vec{\kappa}' |g_2(\vec{\kappa}')|^2 \int d\vec{\kappa}'' |g_3(\vec{\kappa}'')|^2 \\ & + \int d\vec{\kappa} |g_1(\vec{\kappa})|^2 \int d\vec{\kappa}' g_2^*(\vec{\kappa}') g_3(\vec{\kappa}') \int d\vec{\kappa}'' g_3^*(\vec{\kappa}'') g_2(\vec{\kappa}'') \\ & + \int d\vec{\kappa}' |g_2(\vec{\kappa}')|^2 \int d\vec{\kappa} g_1^*(\vec{\kappa}) g_3(\vec{\kappa}) \int d\vec{\kappa}'' g_3^*(\vec{\kappa}'') g_1(\vec{\kappa}'') \\ & + \int d\vec{\kappa}'' |g_3(\vec{\kappa}'')|^2 \int d\vec{\kappa} g_1^*(\vec{\kappa}) g_2^*(\vec{\kappa}) \int d\vec{\kappa}' g_2^*(\vec{\kappa}', \omega) g_1(\vec{\kappa}') \\ & + \int d\vec{\kappa} g_1^*(\vec{\kappa}) g_2(\vec{\kappa}) \int d\vec{\kappa}' g_2^*(\vec{\kappa}') g_3(\vec{\kappa}') \int d\vec{\kappa}'' g_3^*(\vec{\kappa}'') g_1(\vec{\kappa}'') \\ & + \int d\vec{\kappa} g_2^*(\vec{\kappa}) g_1(\vec{\kappa}) \int d\vec{\kappa}' g_3^*(\vec{\kappa}') g_2(\vec{\kappa}') \int d\vec{\kappa}'' g_1^*(\vec{\kappa}'') g_3(\vec{\kappa}''). \end{aligned} \quad (6.50)$$

Substituting Green's function for near-field free propagation into Equation 6.50, each element of the integral  $\int d\vec{\kappa} g_j^*(\vec{\kappa}) g_k(\vec{\kappa})$  ( $j, k = 1, 2, 3$ ) is calculated as

$$\begin{aligned} & \int d\vec{\kappa} g_j^*(\vec{\kappa}) g_k(\vec{\kappa}) \\ &= \left(\frac{\omega}{2\pi c}\right)^2 \frac{e^{i\frac{\omega}{c}(z_j-z_k)}}{z_j z_k} \int d\vec{\kappa} e^{-i\vec{\kappa} \cdot (\vec{\rho}_0 - \vec{\rho}'_0)} \int d\vec{\rho}_0 a^*(\vec{\rho}_0) e^{-i\varphi(\vec{\rho}_0)} \\ & \quad \times e^{-i\frac{\omega}{2cz_j} |\vec{\rho}_0 - \vec{\rho}_j|^2} \int d\vec{\rho}'_0 a(\vec{\rho}'_0) e^{i\varphi(\vec{\rho}'_0)} e^{i\frac{\omega}{2cz_k} |\vec{\rho}'_0 - \vec{\rho}_k|^2}, \end{aligned} \quad (6.51)$$

where  $\vec{\rho}_0$  is the transverse coordinate in the source plane. For a large transverse-sized source with a large enough bandwidth of  $\Delta\vec{\kappa}$ ,

$$\int d\vec{\kappa} e^{-i\vec{\kappa} \cdot (\vec{\rho}_0 - \vec{\rho}'_0)} \sim \delta(\vec{\rho}_0 - \vec{\rho}'_0).$$

Substituting this  $\delta$ -function into Equation 6.51, assuming equal distances from the source to the  $N$  photodetectors,  $z_j = z_k = d$ , and  $a(\vec{\rho}_0) \sim \text{constant}$ ,

Equation 6.51 leads to a sombrero-like function approximation:

$$\int d\vec{\kappa} g_j^*(\vec{\kappa}) g_k(\vec{\kappa}) \simeq \text{somb} \left[ \frac{R}{d} \frac{\omega}{c} |\vec{\rho}_j - \vec{\rho}_k| \right].$$

In 1D, the integral results in a sinc-function

$$\int d\vec{\kappa} g_j^*(\vec{\kappa}) g_k(\vec{\kappa}) \simeq \text{sinc} \left[ \frac{R}{d} \frac{\omega}{c} (x_j - x_k) \right].$$

The normalized third-order coherence function  $\gamma^{(3)}(\vec{\rho}_1, \vec{\rho}_2, \vec{\rho}_3)$  is then approximated as

$$\begin{aligned} \gamma^{(3)}(\vec{\rho}_1, \vec{\rho}_2, \vec{\rho}_3) &= 1 + \text{somb}^2 \left[ \frac{D}{d} \frac{\pi}{\lambda} |\vec{\rho}_1 - \vec{\rho}_2| \right] \\ &\quad + \text{somb}^2 \left[ \frac{D}{d} \frac{\pi}{\lambda} |\vec{\rho}_2 - \vec{\rho}_3| \right] + \text{somb}^2 \left[ \frac{D}{d} \frac{\pi}{\lambda} |\vec{\rho}_3 - \vec{\rho}_1| \right] \\ &\quad + 2 \text{somb} \left[ \frac{D}{d} \frac{\pi}{\lambda} |\vec{\rho}_1 - \vec{\rho}_2| \right] \text{somb} \left[ \frac{D}{d} \frac{\pi}{\lambda} |\vec{\rho}_2 - \vec{\rho}_3| \right] \text{somb} \left[ \frac{D}{d} \frac{\pi}{\lambda} |\vec{\rho}_3 - \vec{\rho}_1| \right], \end{aligned} \quad (6.52)$$

where  $D/d = \Delta\theta$  is the angular size of the source from the view points of the photodetectors.

In 1D, the normalized third-order coherence function  $\gamma^{(3)}(x_1, x_2, x_3)$  is approximated to be

$$\begin{aligned} \gamma^{(3)}(x_1, x_2, x_3) &= 1 + \text{sinc}^2 \left[ \frac{D}{d} \frac{\pi}{\lambda} (x_1 - x_2) \right] \\ &\quad + \text{sinc}^2 \left[ \frac{D}{d} \frac{\pi}{\lambda} (x_2 - x_3) \right] + \text{sinc}^2 \left[ \frac{D}{d} \frac{\pi}{\lambda} (x_3 - x_1) \right] \\ &\quad + 2 \text{sinc} \left[ \frac{D}{d} \frac{\pi}{\lambda} (x_1 - x_2) \right] \text{sinc} \left[ \frac{D}{d} \frac{\pi}{\lambda} (x_2 - x_3) \right] \text{sinc} \left[ \frac{D}{d} \frac{\pi}{\lambda} (x_3 - x_1) \right]. \end{aligned} \quad (6.53)$$

For a large angular-sized thermal source, the sinc-like functions effectively turn into  $\delta$ -functions of  $(x_j - x_k)$ ,  $j, k = 1, 2, 3$ . The point-to-point-to-point non-trivial correlation between three transverse planes encourages three-photon lensless imaging of thermal light with enhanced spatial resolution. The

three-photon ghost imaging of thermal light exhibits a number of unusual interesting features that may be useful for certain applications.

The concept and calculation on thermal light third-order near-field spatial coherence are easily generalizable to higher orders. The physics and mathematics may all start from Equation 6.49, which is considered as the key equation to understand the  $N$ -photon interference nature of the nontrivial  $N$ th-order correlation of thermal light.

---

## Summary

In this chapter, we introduced the concept of second-order coherence of light together with the HBT interferometer. In general, the normalized degree of second-order coherence is defined and calculated as

$$\begin{aligned}\gamma^{(2)}(\mathbf{r}_1, t_1; \mathbf{r}_2, t_2) &= \frac{\langle I(\mathbf{r}_1, t_1) I(\mathbf{r}_2, t_2) \rangle}{\langle I(\mathbf{r}_1, t_1) \rangle \langle I(\mathbf{r}_2, t_2) \rangle} \\ &= \frac{\langle E^*(\mathbf{r}_1, t_1) E(\mathbf{r}_1, t_1) E^*(\mathbf{r}_2, t_2) E(\mathbf{r}_2, t_2) \rangle}{\langle E^*(\mathbf{r}_1, t_1) E(\mathbf{r}_1, t_1) \rangle \langle E^*(\mathbf{r}_2, t_2) E(\mathbf{r}_2, t_2) \rangle}\end{aligned}$$

Very different from the first-order coherence, the second-order coherence is measured by two photodetectors, directly and respectively, at space-time coordinates  $(\mathbf{r}_1, t_1)$  and  $(\mathbf{r}_2, t_2)$ .

This chapter put a considerable effort to distinguish the interference nature of the nontrivial second-order correlation from the statistical correlation of intensity fluctuations. The history has been interesting: although the discovery of HBT initiated a number of key concepts of modern quantum optics, the far-field HBT correlation itself was commonly accepted as the statistical intensity fluctuation correlation of identical mode. In fact, it is not too difficult to find out that the nontrivial intensity-intensity correlation is unnecessary to happen in the far field. We derived a similar second-order correlation in near field with multimode measurement and analyzed a few recent experiments to support the observation. We conclude that the observation is an interference phenomenon that involves a pair of subfields interfere with the pair itself:

$$\begin{aligned}\Gamma^{(2)}(\mathbf{r}_1, t_1; \mathbf{r}_2, t_2) &= \sum_j \sum_l \left| \frac{1}{\sqrt{2}} [E_j(\mathbf{r}_1, t_1) E_l(\mathbf{r}_2, t_2) + E_l(\mathbf{r}_1, t_1) E_j(\mathbf{r}_2, t_2)] \right|^2 \\ &= \Gamma_{11}^{(1)} \Gamma_{22}^{(1)} + \Gamma_{12}^{(1)} \Gamma_{21}^{(1)},\end{aligned}$$

where each subfield is associated with either a sub-source or sub-mode. Unfortunately, classical wave does not behave in such a manor. The Maxwell wave theory does not support this kind of superposition either. This lead to difficulties for the interpretation of the phenomenon in the framework of classical electromagnetic wave theory. Furthermore, this superposition happens at separate space-time coordinates through the measurement of two independent photodetectors, indicating its nonlocal nature. The concept of nonlocal interference, perhaps, can never be allowed in any classical theory.

In the last part of this chapter, we generalized the concept to  $N$ th-order

$$\Gamma^{(N)}(\mathbf{r}_1, t_1; \dots; \mathbf{r}_N, t_N) \equiv \langle E^*(\mathbf{r}_1, t_1)E(\mathbf{r}_1, t_1) \dots E^*(\mathbf{r}_N, t_N)E(\mathbf{r}_N, t_N) \rangle,$$

and extended the interference picture from a pair of subfields to  $N$ -fold subfields

$$\Gamma^{(N)}(\mathbf{r}_1, t_1; \dots; \mathbf{r}_N, t_N) \simeq \sum_{j,k,l,\dots} \left| \frac{1}{\sqrt{N!}} \left[ \sum_{N!} E_{j1}E_{k2}E_{l3} \dots \right] \right|^2,$$

where  $\sum_{N!} E_{j1}E_{k2}E_{l3} \dots$  means the sum of  $N!$  terms of  $N$ -fold subfields, permuted in the orders of  $1, 2, 3, \dots, N, 1, 3, 2, \dots, N, 2, 1, 3, \dots, N$ , etc., corresponding to  $N!$  alternative ways for  $N$  independent subfields (photons) to produce a  $N$ -fold joint photodetection event.

---

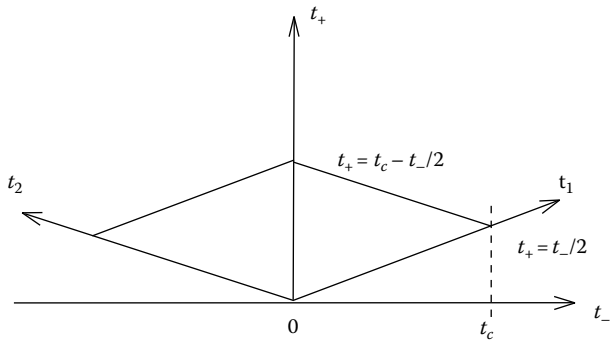
## Appendix 6.A

To integrate the double integral of Equation 6.28

$$|\gamma_{12}^{(1)}(\tau)|^2 = \frac{1}{t_c^2} \int_{t_c} dt_1 \int_{t_c} dt_2 |\gamma_{12}(t_1 - t_2 - \tau)|^2,$$

we follow the rules of the Jacobian to change the variables to  $t_+ = (t_1 + t_2)/2$  and  $t_- = t_1 - t_2$ ,

$$\begin{aligned} |\gamma_{12}^{(1)}(\tau)|^2 &= \frac{2}{t_c^2} \int_0^{t_c} dt_- \left[ \int_{\frac{t_-}{2}}^{t_c - \frac{t_-}{2}} dt_+ \right] |\gamma_{12}(t_- - \tau)|^2 \\ &= \frac{2}{t_c^2} \int_0^{t_c} dt_- (t_c - t_-) |\gamma_{12}(t_- - \tau)|^2. \end{aligned}$$

**FIGURE 6.A.1**

Mapping by the linear transformation of  $t_+ = (t_1 + t_2)/2$  and  $t_- = t_1 - t_2$ . The upper boundary of the integral  $dt_-$  is determined by the intersection between lines  $t_+ = (t_-)/2$  and  $t_+ = (t_c - t_-)/2$ . For each value of  $t_-$ ,  $t_+$  must be integrated from  $t_+ = t_-/2$  to  $t_+ = t_c - t_-/2$ .

Figure 6.A.1 illustrates the mapping of the area of the integral. This figure is helpful in finding the integral boundaries for  $t_-$  and  $t_+$ .

Note that the upper boundary of  $t_-$  is determined by the intersection between lines  $t_2 = 0$  and  $t_1 = t_c$  in the  $t_1$  and  $t_2$  plane. These two lines map onto the lines of  $t_+ = t_-/2$  and  $t_+ = t_c - t_-/2$ , respectively, in the  $t_-$  and  $t_+$ -plane. It is easy to see that the  $t_-$  value at the intersection of these two lines is  $t_c$ . Thus, the lower and the upper boundaries of  $t_-$  are determined to be 0 and  $t_c$ , respectively, where we have decided to integrate half of the mapping area then multiply by 2. For each chosen value of  $t_-$ ,  $t_+$  must be integrated from  $t_+ = t_-/2$  to  $t_+ = t_c - t_-/2$ . We thus obtain Equation 6.29.

## Suggested Reading

- Fano, U., *Am. J. Phys.* 29, 539 (1961).
- Glauber, R.J., *Quantum Optics*, S.M. Kay and A. Maitland (eds), Academic Press, New York, 1970.
- Hanbury-Brown, R., *Intensity Interferometer*, Taylor & Francis Ltd, London, U.K., 1974.
- Hanbury-Brown, R. and R.Q. Twiss, *Nature* 177, 27 (1956); 178, 1046 (1956); 178, 1447 (1956).
- Liu, J. and Y.H. Shih, *Phys. Rev. A* 79, 203819 (2009).
- Loudon, R., *The Quantum Theory of Light*, Oxford Science Publications, Oxford, U.K., 2000.
- Mandel, L. and E. Wolf (eds), *Selected Papers on Coherence and Fluctuations of Light*, Vols. 1 and 2, Dover, New York, 1970.
- Martienssen, W. and E. Spiller, *Am. J. Phys.* 32, 919 (1964).

- Scarelli, G., V. Berardi, and Y.H. Shih, *Phys. Rev. Lett.* 96, 063602 (2006).
- Scully, M.O. and M.S. Zubairy, *Quantum Optics*, Cambridge University Press, Cambridge, U.K., 1997.
- Valencia, A., G. Scarelli, M. D'Angelo, and Y.H. Shih, *Phys. Rev. Lett.* 94, 063601 (2005).
- Zhou, Y., J. Simon, J. Liu, and Y.H. Shih, *Phys. Rev. A* (2010).



# 7

---

## *Homodyne Detection and Heterodyne Detection of Light*

---

In this chapter, we introduce the concept of homodyne detection and heterodyne detection in the framework of the classical electromagnetic wave theory of light. Optical homodyne detection and heterodyne detection are both adapted from radio frequency modulation technology. Differing from the standard photodetection, homodyne detection and heterodyne detection measure the frequency modulated radiation by mixing with radiation of a reference frequency, which is generated by a local oscillator. In homodyne detection, the reference frequency equals that of the input signal radiation; in heterodyne detection, the reference light takes a different frequency.

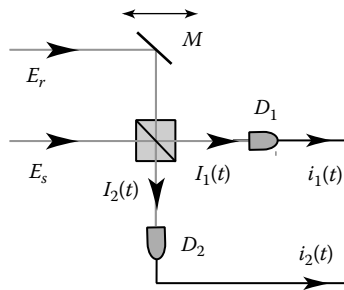
---

### **7.1 Optical Homodyne and Heterodyne Detection**

Figure 7.1 schematically shows an optical homodyne or heterodyne detection setup. The signal field and the reference field are mixed at a 50%–50% beamsplitter and superposed at photodetectors  $D_1$  and  $D_2$ . To simplify the notation, the following analysis will be in 1D by focusing on one of the polarizations of the signal and reference radiation. The intensities of  $I_1(t)$  and  $I_2(t)$  are the results of the superposition between the input signal field  $E_s$  and the reference field  $E_r$ ,

$$\begin{aligned} I_1(t) &= \left| \frac{1}{\sqrt{2}} [E_s(t) + E_r(t)] \right|^2 = \frac{1}{2} [|E_s(t)|^2 + |E_r(t)|^2] + \text{Re}[E_s(t)E_r^*(t)] \\ I_2(t) &= \left| \frac{1}{\sqrt{2}} [E_s(t) - E_r(t)] \right|^2 = \frac{1}{2} [|E_s(t)|^2 + |E_r(t)|^2] - \text{Re}[E_s(t)E_r^*(t)]. \end{aligned} \quad (7.1)$$

The common cross term  $E_s(t)E_r^*(t)$  is formally written as

**FIGURE 7.1**

Schematic setup of a homodyne or heterodyne detection experiment.

$$\begin{aligned}
 E_s(t)E_r^*(t) &= \left\{ \left[ \int d\nu \sum_j a_j(\nu) e^{i\varphi_j(\nu)} e^{-i\nu\tau_s} \right] e^{-i\omega_{s0}\tau_s} \right\} \left\{ a_r e^{-i\varphi_r} e^{i\omega_r\tau_r} \right\} \\
 &= \left\{ \int d\nu \left[ \sum_j a_j(\nu) a_r e^{i[\varphi_j(\nu) - \varphi_r + \omega_{s0}z_s/c - \omega_r z_r/c]} \right] e^{-i\nu\tau_s} \right\} e^{-i(\omega_{s0} - \omega_r)t},
 \end{aligned} \tag{7.2}$$

where

$\nu = \omega_s - \omega_{s0}$  is the detuning frequency

$\omega_{s0}$  the central frequency of the input signal radiation,  $\tau_s = t - z_s/c$ ,  $\tau_r = t - z_r/c$

In Equation 7.2, we have assumed a single-mode reference radiation field

$$E_r(t) = a_r e^{i\varphi_r} e^{-i\omega_r(t-z_r/c)}$$

and a general multi-sub-source and multi-Fourier-mode input signal field

$$E_s(t) = \left[ \int d\nu \sum_j a_j(\nu) e^{i\varphi_j(\nu)} e^{-i\nu\tau_s} \right] e^{-i\omega_{s0}\tau_s},$$

which is formally written as a wavepacket with carrier frequency  $\omega_{s0}$ .

For homodyne detection,  $\omega_r = \omega_{s0} = \omega_0$ , Equation 7.2 can be formally written as the Fourier transform of the spectrum

$$\begin{aligned}
 E_s(t)E_r^*(t) &= \int d\nu \left\{ \sum_j a_j(\nu) a_r e^{i[\varphi_j(\nu) - \varphi_r + \omega_0(z_s/c - z_r)/c]} \right\} e^{-i\nu\tau_s} \\
 &= \mathcal{F}_{\tau_s} \left\{ \sum_j A_j(\nu) e^{i[\varphi_j(\nu) - \varphi_r + \omega_0(z_s - z_r)/c]} \right\},
 \end{aligned} \tag{7.3}$$

where  $A_j(v) \equiv a_j(v) a_r$ , indicating an amplified amplitude of  $a_j(v)$  in the case of a strong local oscillator. The cross term  $E_s(t)E_r^*(t)$  represents the interference between the input signal radiation  $E_s(t)$  and the reference field  $E_r(t)$ . As we have studied earlier, the relative phases  $\varphi_j(v) - \varphi_r$  will play an important role in determining the measured values of  $I_1$  and  $I_2$ . The interference term will contribute to the measured values of  $I_1$  and  $I_2$  significantly when  $\varphi_j(v) - \varphi_r = \text{constant}$ , and will have null contribution if the relative phase  $\varphi_j(v) - \varphi_r$  takes all possible random values from 0 to  $2\pi$ . The optical path difference  $z_s - z_r$  is another factor in determining the contribution of the interference term in the case of  $\varphi_j(v) - \varphi_r = \text{constant}$ . The value of  $\omega_0(z_s - z_r)/c$  determines the constructive-destructive property of the interference and consequently determines the magnitude for each and for all of the Fourier amplitudes. It is interesting to see the relative phase  $\varphi_j(v) - \varphi_r$  and the relative phase delay  $\omega_0(z_s - z_r)/c$  between the input field and the local oscillator are both included in the Fourier transform. A spectrum analyzer can retrieve this important information for certain observations. This property has been widely adapted in the studies of squeezed state and other coherent and statistical properties of light.

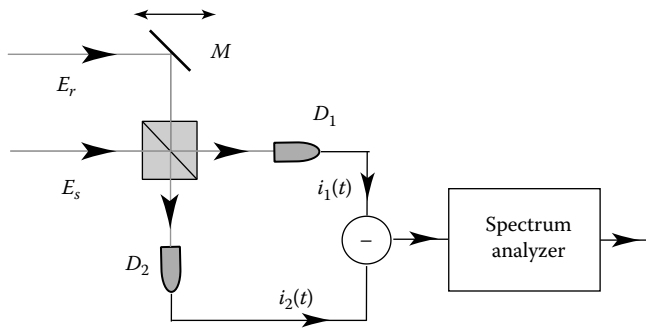
For heterodyne detection, taking  $\omega_r \neq \omega_{s0}$ , Equation 7.2 can be formally written as

$$\begin{aligned} E_s(t)E_r^*(t) &= \left\{ \int d\nu \left[ \sum_j a_j(v) a_r e^{i[\varphi_j(v) - \varphi_r + \omega_{s0}z_s/c - \omega_r z_r]/c} \right] e^{-iv\tau_s} \right\} e^{-i(\omega_{s0} - \omega_r)t} \\ &= \mathcal{F}_{\tau_s} \left\{ \sum_j A_j(v) e^{i[\varphi_j(v) - \varphi_r + (\omega_{s0}z_s - \omega_r z_r)/c]} \right\} e^{-i\omega_d t}, \end{aligned} \quad (7.4)$$

where  $\omega_d = \omega_r - \omega_{s0}$  is the beating frequency. Equation 7.4 is recognized as a modulated harmonic oscillation of frequency  $\omega_d = \omega_{s0} - \omega_r$ . The Fourier transform of the spectrum is the modulation function that modulates the harmonic oscillation.

## 7.2 Balanced Homodyne and Heterodyne Detection

Figure 7.2 schematically shows a balanced homodyne or heterodyne detection setup. The input signal field  $E_s(t)$  and the reference field  $E_r(t)$  are mixed at a 50/50 beamsplitter. The output fields are directed and superposed at photodetectors  $D_1$  and  $D_2$ . The photocurrent  $i_1(t)$  and  $i_2(t)$  are subtracted from each other in an electronic circuit. A standard spectrum analyzer follows to select, amplify, and rectify a certain bandwidth of the Fourier spectral

**FIGURE 7.2**

Schematic setup of a balanced homodyne and heterodyne detection experiment. In homodyne detection, the reference frequency equals the central frequency of the input signal radiation,  $\omega_r = \omega_{s0} = \omega_0$ .

composition in the waveform of  $i_1(t) - i_2(t)$ , electronically. The observed output of the spectrum analyzer is a measure of the amplitude of the chosen Fourier spectral composition.

Based on the experimental setup of Figure 7.2 we now calculate the expected output from the spectrum analyzer. We start from calculating  $i_1(t_-) - i_2(t_-) \propto I_1(t_1) - I_2(t_2)$ , where  $t_\alpha = t_- - \tau_\alpha^{(e)}$ ,  $\alpha = 1, 2$ , with  $\tau_\alpha^{(e)}$  the electronic delay in the cables and the electronic circuits associate with the  $\alpha$ th photodetector, and  $t_-$  is the time for photocurrent “subtraction.” To simplify the mathematics, we choose  $\tau_1^{(e)} = \tau_2^{(e)}$  to achieve  $t_1 = t_2 = t$ . It is easy to see from Equations 7.1, 7.3, and 7.4

$$\begin{aligned} I_1(t) - I_2(t) &= 2\text{Re} [E_s(t)E_r^*(t)] \\ &= 2\text{Re} \mathcal{F}_{\tau_s} \left\{ \sum_j A_j(\nu) e^{i[\varphi_j(\nu) - \varphi_r + \omega_0(z_s - z_r)/c]} \right\}, \end{aligned} \quad (7.5)$$

for balanced homodyne detection, and

$$\begin{aligned} I_1(t) - I_2(t) &= 2\text{Re} [E_s(t)E_r^*(t)] \\ &= 2\text{Re} \mathcal{F}_{\tau_s} \left\{ \sum_j A_j(\nu) e^{i[\varphi_j(\nu) - \varphi_r + (\omega_{s0}z_s - \omega_r z_r)/c]} \right\} e^{-i\omega_d t}, \end{aligned} \quad (7.6)$$

for balanced heterodyne detection. We may consider homodyne detection a special case of heterodyne detection when taking  $\omega_d = 0$ . There is no significant difference in the modulation function, except a trivial phase factor of  $\omega_0(z_s - z_r)/c$ . It is the spectrum of the modulation function that will be

analyzed by the spectrum analyzer. To simplify the discussion, we will focus our attention on the balanced homodyne detection in the following analysis. We will show how a spectrum analyzer works in determining the spectrum of the modulation function with the coherence and path information of the measured light. Before exploring the working mechanism of the spectrum analyzer, we estimate the expected value of its input current  $i_1(t) - i_2(t) \propto I_1(t) - I_2(t)$ .

The expectation value of  $\langle I_1(t) - I_2(t) \rangle$  is easy to calculate by taking into account all possible values of  $\varphi_j(v) - \varphi_r$  within the superposition. For single-mode reference field  $E_r(t)$ , the coherent behavior of the input signal, which is mainly determined by the phases of the subfields  $\varphi_j(v)$ , will determine the expectation. We discuss two extreme cases:

#### Case (I): Random $\varphi_j(v)$ -chaotic-thermal light

It is easy to see that the only surviving terms in the superposition are the terms with  $\varphi_j(v) = \varphi_r$  when taking into account all possible values of  $\varphi_j(v)$ . Obviously, the chances of having  $\varphi_j(v) = \varphi_r$  are quite small. The expectation value of  $\langle I_1(t) - I_2(t) \rangle$  is thus effectively zero in this case. In a real measurement, however, the superposition may not take all possible values of the random phases and the interference cancellation may not be complete. These noncanceled terms of  $I_1(t) - I_2(t)$  will be analyzed and displayed by the spectrum analyzer in terms of the Fourier composition of  $v$ , which is effectively the beating frequency  $\omega_s - \omega_r$  in the homodyne detection measurement,

$$\text{Re} \left\{ \int dv \left[ \sum_{\text{surv}} A_j(v) e^{i[\varphi_j(v) - \varphi_r + \omega_0(z_s - z_r)/c]} \right] e^{-iv\tau_s} \right\} \quad (7.7)$$

where  $\sum_{\text{surv}}$  represents the sum of the noncanceled surviving terms in the superposition. These surviving terms are traditionally treated as the noise or fluctuations of the radiation. The spectrum analyzer is thus considered to measure the spectrum of the noise or the fluctuations of the chaotic-thermal light.

#### Case (II): $\varphi_j(v) - \varphi_r = \text{constant}$

In the case of  $\varphi_j(v) - \varphi_r = \varphi_0$ , where  $\varphi_0 = \text{constant}$ , the intensity difference  $I_1(t) - I_2(t) \propto \text{Re}[E_s(t)E_r^*(t)]$ , i.e.,

$$\text{Re} \left\{ \int dv \left[ \sum_j A_j(v) e^{i[\varphi_0 + \omega_0(z_s - z_r)/c]} \right] e^{-iv\tau_s} \right\} \quad (7.8)$$

without interference cancellation will be received by the spectrum analyzer. The spectrum analyzer no longer measures the noise or the fluctuation

of the surviving input signal, instead, it receives and analyzes the entire interference term of  $E_s(t)E_r^*(t)$ .

The design and working mechanism of specific spectrum analyzers can be quite different from each other. Nevertheless, the output reading of modern spectrum analyzers can be roughly divided into two categories: linear normal spectrum and nonlinear power spectrum. Linear normal spectrum simply presents the spectral amplitude of the input signal as a function of frequency. The nonlinear power spectrum provides much more detail than the normal spectrum. A power spectrum includes not only the Fourier composition of the input current  $i_1(t) - i_2(t)$ , but also their beats and sum-frequencies that fall within the passband of the chosen spectral filter in the heterodyne circuit of the spectrum analyzer, such as the IF filter shown in Figure 7.3.

A simplified block diagram of a classic spectrum analyzer is illustrated in Figure 7.3. The input signal of  $i_1(t) - i_2(t)$ , which is either proportional to Equation 7.7 or Equation 7.8, is mixed with a sinusoidal reference current of tunable RF frequency  $\omega_{lo}$  in an electronic mixer. The RF current of  $\omega_{lo}$  is generated from a local oscillator. The mixer has a nonlinear response to the inputs. Taking account of the first-order and the second-order response of the mixer to a good approximation, the output of the mixer contains the input signal  $i_1(t) - i_2(t)$ , the reference oscillation of  $\omega_{lo}$ , their second-harmonics, and a cross term

$$\begin{aligned} i_{NL} &\propto \int d\nu \sum_{\text{Surv}} A_j(\nu) \cos\{\nu\tau_s - [\varphi_j(\nu) - \varphi_r] - \varphi(z_s, z_r)\} A_{lo} \cos\omega_{lo} t \\ &\propto \int d\nu \sum_{\text{Surv}} A_j(\nu) A_{lo} \left\{ \cos\{(\nu + \omega_{lo})t - [\varphi_j(\nu) - \varphi_r] - \varphi(z_s, z_r)\} \right. \\ &\quad \left. + \cos\{(\nu - \omega_{lo})t - [\varphi_j(\nu) - \varphi_r] - \varphi(z_s, z_r)\} \right\}, \end{aligned} \quad (7.9)$$

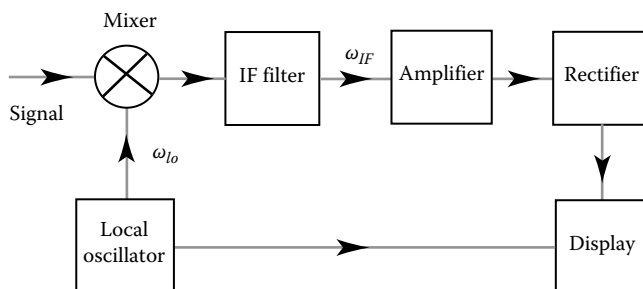


**FIGURE 7.3**

Simplified block diagram of a classic spectrum analyzer.

for the measurement of chaotic-thermal light, and

$$\begin{aligned} i_{NL} &\propto \int d\nu \sum_j A_j(\nu) \cos\{\nu\tau_s - \varphi - \varphi(z_s, z_r)\} A_{lo} \cos \omega_{lo} t \\ &\propto \int d\nu \sum_j A_j(\nu) A_{lo} \left\{ \cos\{(\nu + \omega_{lo})t - \varphi_0 - \varphi(z_s, z_r)\} \right. \\ &\quad \left. + \cos\{(\nu - \omega_{lo})t - \varphi_0 - \varphi(z_s, z_r)\} \right\}, \end{aligned} \quad (7.10)$$

for the measurement of coherent light, where  $\varphi(z_s, z_r) = \omega_{s0}(z_s - z_r)/c + v z_s/c$ , and we have assumed a simple harmonic local oscillator of frequency  $\omega_{lo}$ ,  $i_{lo}(t) = A_{lo} \cos \omega_{lo} t$ . Equations 7.9 and 7.10 indicate that the nonlinear response of the mixer produces a down-converted Fourier composition  $\omega_{IF} = \omega_{lo} - \nu$  and an up-converted Fourier composition  $\omega_{IF} = \omega_{lo} + \nu$  in terms of each Fourier composition of the input signal. An electronic spectral filter follows after the mixer to select a narrowband RF current of frequency  $\omega_{IF}$  from either the down-converted set or the up-converted set of the Fourier-modes.  $\omega_{IF}$  is technically called the intermediate frequency. To simplify the mathematics, we assume the bandwidth of  $\omega_{IF}$  to be much narrower than that of the input signal so that the selected Fourier composition of  $\omega_{IF}$  can be treated as single mode. The selected single-mode Fourier composition of  $\omega_{IF}$  is then amplified by a linear amplifier and rectified by a nonlinear envelope detector, resulting in an output that is proportional to the power spectrum

$$P(\nu) \propto \left\{ \sum_{\text{Surv}} A_j(\nu) \cos[\varphi_j(\nu) - \varphi_r + \varphi(z_s, z_r)] \right\}^2, \quad (7.11)$$

for the measurement of chaotic-thermal light, and

$$P(\nu) \propto \left\{ \sum_j A_j(\nu) \cos[\varphi_0 + \varphi(z_s, z_r)] \right\}^2, \quad (7.12)$$

for the measurement of coherent light.

#### Case (I): Chaotic-thermal light

Chaotic-thermal light is statistically stationary and ergodic, by choosing an appropriate time parameter (integration time) of the spectrum analyzer, we may treat the measurement as an ensemble average

$$\begin{aligned}
 \langle P(v) \rangle &\propto \left\langle \sum_{\text{Surv}} A_j(v) \cos[\varphi_j(v) - \varphi_r + \varphi(z_s, z_r)] \right. \\
 &\quad \times A_k(v) \cos[\varphi_k(v) - \varphi_r + \varphi(z_s, z_r)] \Bigg\rangle \\
 &\propto \left\langle \sum_{\text{Surv}} A_j(v) A_k(v) \left\{ \cos[\varphi_j(v) - \varphi_k(v)] \right. \right. \\
 &\quad \left. \left. + \cos[\varphi_j(v) + \varphi_k(v) - 2\varphi_r + 2\varphi(z_s, z_r)] \right\} \right\rangle, \quad (7.13)
 \end{aligned}$$

where  $\langle \dots \rangle$  denotes, again, an ensemble average by means of *taking into account all possible realizations of the field*. As we have discussed earlier, when taking into account all possible values of  $\varphi_j(v)$ , the incoherent superposition results in a nonzero value from the first cosine term, which includes all the surviving diagonal terms of  $j = k$ , and a zero value from the second cosine term of Equation 7.13. The expected power spectrum of chaotic-thermal light is thus a simple sum of the squared amplitudes

$$\langle P(v) \rangle \propto \sum_{\text{Surv}} A_j^2(v). \quad (7.14)$$

In reality, the radiation field may not take all possible realization within the time integral of the spectrum analyzer, the incomplete interference cancellation may still cause a random fluctuation in the neighborhood of  $\langle P(v) \rangle$  from time to time.

### Case (II): Coherent light

Taking  $\varphi_j(v) - \varphi_r = \varphi_0$  constant, Equation 7.13 becomes

$$\begin{aligned}
 P(v) &\propto \sum_{j,k} A_j(v) A_k(v) \left\{ 1 + \cos 2[\varphi_0 + \varphi(z_s, z_r)] \right\} \\
 &\propto \left\{ \sum_{j,k} A_j(v) A_k(v) \right\} \cos^2 \left[ \varphi_0 + \frac{(\omega_s z_s - \omega_r z_r)}{c} \right]. \quad (7.15)
 \end{aligned}$$

It is interesting to find from Equation 7.15 that the power spectrum of coherent light is a sinusoidal function of  $\varphi(z_s, z_r) = (\omega_s z_s - \omega_r z_r)/c \simeq \omega_{s0}(z_s - z_r)/c$ . The change of the relative optical path between the signal field and the reference field, which can be realized by adjusting the position of the mirror  $M$  in Figure 7.2, will produce an interference pattern as a function of  $z_s - z_r$ , similar to that of the interference between two individual but synchronized laser beams.

### 7.3 Balanced Homodyne Detection of Independent and Coupled Thermal Fields

We consider the experimental setup of Figure 7.4, in which two input thermal fields  $E_s$  and  $E_i$ , either independent or coupled, are measured by two individual balanced homodyne detection setups. The balanced homodyne detection setups are similar to that of Figure 7.2, except that the two outputs of the homodyne detection are subtracted again from each other by a third subtraction circuit. The power spectrum of the final output current  $[i_{1s}(t) - i_{2s}(t)] - [i_{1i}(t) - i_{2i}(t)]$  is measured by a spectrum analyzer and read out in terms of its Fourier composition.

To calculate the expected power spectrum, we start from Equation 7.5, which gives the estimated values of  $i_{1s}(t) - i_{2s}(t)$  and  $i_{1i}(t) - i_{2i}(t)$ . The output of the third subtraction circuit is therefore

$$\begin{aligned} & [i_{1s}(t) - i_{2s}(t)] - [i_{1i}(t) - i_{2i}(t)] \\ & \propto \operatorname{Re} \mathcal{F}_{\tau_s} \left\{ \sum_{\text{Surv}} A_j(\nu_s) e^{i[\varphi_j(\nu_s) - \varphi_r + \omega_{s0}(z_s - z_r)/c]} \right\} \\ & - \operatorname{Re} \mathcal{F}_{\tau_i} \left\{ \sum_{\text{Surv}} A_k(\nu_i) e^{i[\varphi_k(\nu_i) - \varphi_r + \omega_{i0}(z_i - z_r)/c]} \right\}. \end{aligned} \quad (7.16)$$

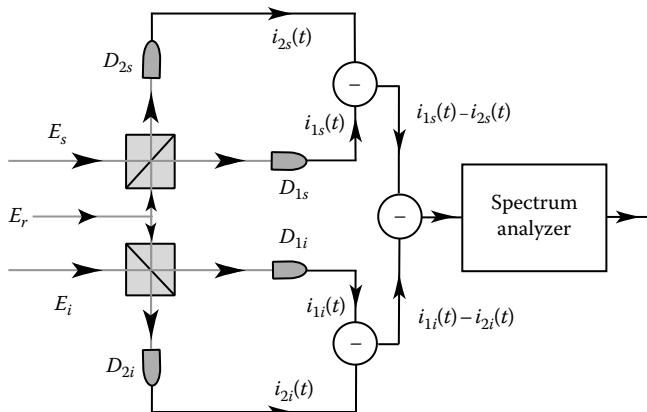


**FIGURE 7.4**

Schematic experimental setup for balanced homodyne detection of two independent or coupled thermal fields. Three subtraction circuits are used for manipulating the photocurrents  $i_{1s}(t)$ ,  $i_{2s}(t)$ ,  $i_{1i}(t)$ , and  $i_{2i}(t)$ . The spectrum analyzer displays the power spectrum of the final output current  $[i_{1s}(t) - i_{2s}(t)] - [i_{1i}(t) - i_{2i}(t)]$ .

The output current of the third subtraction circuit is mixed with a sinusoidal reference current of tunable RF frequency  $\omega_{lo}$  in the electronic mixer of the spectrum analyzer. The nonlinear response of the mixer produces the up-converted and down-converted frequencies

$$\begin{aligned} i_{NL} \propto & \int d\nu_s \sum_{\text{Surv}} A_j(\nu_s) A_{lo} \left\{ \cos\{(\nu_s + \omega_{lo})t - [\varphi_j(\nu_s) - \varphi_r] - \varphi(z_s, z_r)\} \right. \\ & + \cos\{(\nu_s - \omega_{lo})t - [\varphi_j(\nu_s) - \varphi_r] - \varphi(z_s, z_r)\} \Big\} \\ & - \int d\nu_i \sum_{\text{Surv}} A_k(\nu_i) A_{lo} \left\{ \cos\{(\nu_i + \omega_{lo})t - [\varphi_k(\nu_i) - \varphi_r] - \varphi(z_s, z_r)\} \right. \\ & + \cos\{(\nu_i - \omega_{lo})t - [\varphi_k(\nu_i) - \varphi_r] - \varphi(z_s, z_r)\} \Big\}. \end{aligned} \quad (7.17)$$

After the IF filter, the linear amplifier, and the nonlinear rectifier, the expected power spectrum is proportional to

$$\langle P(\nu) \rangle \propto \left\langle \left\{ \sum_{\text{Surv}} A_j(\nu_s) \cos\{\varphi_j(\nu_s) - \varphi_r + \varphi(z_s, z_r)\} \right. \right. \\ \left. \left. - \sum_{\text{Surv}} A_k(\nu_i) \cos\{\varphi_k(\nu_i) - \varphi_r + \varphi(z_s, z_r)\} \right\}^2 \right\rangle. \quad (7.18)$$

In the following, we discuss two measurements for different types of input radiations: independent thermal light and coupled thermal fields with  $\varphi_j(\nu_s) + \varphi_k(\nu_i) = \text{constant}$ .

Case (I): Independent chaotic-thermal light

Assuming the two inputs  $E_s$  and  $E_i$  are independent chaotic-thermal fields, the phases  $\varphi_j(\nu_s)$  and  $\varphi_k(\nu_i)$  may take any value randomly and independently. Equation 7.18 gives the following three contributions

$$(1) \left\langle \left\{ \sum_{\text{Surv}} A_j(\nu_s) \cos[\varphi_j(\nu_s) - \varphi_r + \varphi(z_s, z_r)] \right\}^2 \right\rangle = \frac{1}{2} \sum_{\text{Surv}} A_j^2(\nu_s)$$

$$(2) \left\langle \left\{ \sum_{\text{Surv}} A_k(\nu_i) \cos[\varphi_k(\nu_i) - \varphi_r + \varphi(z_s, z_r)] \right\}^2 \right\rangle = \frac{1}{2} \sum_{\text{Surv}} A_k^2(\nu_i)$$

$$(3) \left\langle \sum_{\text{Surv}} A_j(\nu_s) A_k(\nu_i) \cos[\varphi_j(\nu_s) - \varphi_r + \varphi(z_s, z_r)] \cos[\varphi_k(\nu_i) - \varphi_r + \varphi(z_s, z_r)] \right\rangle$$

$$\begin{aligned}
& \simeq \sum_{\text{Surv}} A_j(v_s) A_k(v_i) \left\{ \cos[\varphi_j(v_s) - \varphi_k(v_i)] \right. \\
& \quad \left. + \cos[\varphi_j(v_s) + \varphi_k(v_i) + -2\varphi_r + \varphi(z_s, z_r) + \varphi(z_i, z_r)] \right\} \\
& = 0,
\end{aligned} \tag{7.19}$$

where we have assumed  $z_s = z_i$  to simplify the notation. In Equation 7.19 the expectation evaluation has taken into account all possible random values of  $\varphi_j(v_s) - \varphi_k(v_i)$  and  $\varphi_j(v_s) + \varphi_k(v_i)$  in the superposition. The expected power spectrum sums the above three contributions

$$\langle P(v) \rangle \propto \sum_{\text{Surv}} A_j^2(v_s) + \sum_{\text{Surv}} A_k^2(v_i). \tag{7.20}$$

This result is reasonable for the measurement of two independent chaotic-thermal fields.

Case (II): Coupled thermal light with  $\varphi_j(v_s) + \varphi_k(v_i) = \text{constant}$

In case (II), we model each individual input fields  $E_s$  and  $E_i$  with random phases, however, the sum of the two phases are constant by means of  $\varphi_j(v_s) + \varphi_k(v_i) = \varphi_p = \text{constant}$ . A nonlinear optical parametric amplifier is able to generate such a state. This kind of radiation is known as “squeezed” light. To simplify the discussion, we assume the subfields,  $j$ th and  $k$ th, associated with a large number of subsources, all achieve this condition. In reality, this condition may not be achievable for all subfields. Due to the random stochastic nature of each individual field  $E_s$  and  $E_i$ , the self-square of the two terms in Equation 7.19 has the same contribution to the expected power spectrum  $\langle P(v) \rangle$  as that of case (I). The cross term of Equation 7.19, however, yields an interesting nontrivial contribution:

$$\begin{aligned}
& \left\langle \sum_{\text{Surv}} A_j(v_s) \cos \left[ \varphi_j(v_s) - \varphi_r + \omega_{s0} \frac{z_s - z_r}{c} + v_s \frac{z_s}{c} \right] \right. \\
& \quad \times \sum_{\text{Surv}} A_k(v_i) \cos \left[ \varphi_k(v_i) - \varphi_r + \omega_{i0} \frac{z_i - z_r}{c} + v_i \frac{z_i}{c} \right] \left. \right\rangle \\
& \simeq \sum_{\text{Surv}} A_j(v_s) A_k(v_i) \left\{ \cos[\varphi_j(v_s) - \varphi_k(v_i)] \right. \\
& \quad \left. + \cos \left[ \varphi_p + \omega_p \frac{z_{s,i} - z_r}{c} - 2\varphi_r + (v_s + v_i) \frac{z_{s,i}}{c} \right] \right\}.
\end{aligned} \tag{7.21}$$

In Equation 7.21, we have applied  $\varphi_j(v_s) + \varphi_k(v_i) = \varphi_p$  and  $\omega_{s0} + \omega_{i0} = \omega_p$ , where  $\varphi_p$  and  $\omega_p$  are constants corresponding to the pump phase and pump

frequency of a nonlinear optical parametric amplifier. To simplify the notation, in Equation 7.21 we have assumed  $z_s \simeq z_i = z_{s,i}$ . It is easy to find that the first cosine term yields a zero value when taking into account all possible values of  $\varphi_j(v_s) - \varphi_k(v_i)$ . The second cosine term has a nontrivial contribution to the power spectrum

$$\langle P(v) \rangle \propto \left\{ \sum_j A_j^2(v_s) + \sum_k A_k^2(v_i) \right\} \\ + 2 \sum_{jk} A_j(v_s) A_k(v_i) \cos \left[ \omega_p \frac{z_{s,i} - z_r}{c} + \varphi_{s,i,r} \right], \quad (7.22)$$

where  $\varphi_{s,i,r} = \varphi_p - 2\varphi_r + (v_s + v_i)z_{s,i}/c$ .

Equation 7.22 indicates that the expected power spectrum  $\langle P(v) \rangle$  is a cosine function of  $\omega_p(z_{s,i} - z_r)/c$ . The change of the relative optical path between the input fields  $E_s$  ( $E_i$ ) and the reference field  $E_r$  will produce a cosine interference modulation. This interference modulation, however, is different from a standard interference pattern, due to the relatively great contribution from the cross term. The cross term in Equation 7.22 can be much greater than the sum of the two diagonal terms when taking into account a large number of subfields. For a large number of  $N$  subfields, the ratio between the number of diagonal terms and the number of cross terms is roughly  $\sim 1/N$ . This effect causes unavoidable difficulties for a theory in which  $\langle P(v) \rangle$  is treated as the measure of statistical fluctuations of the radiation. Equation 7.22 indicates that, under certain experimental conditions,  $\langle P(v) \rangle$  is not only able to achieve a value below "shot noise," but also able to achieve a value of negative.

## Summary

In this chapter, we introduce the concept of homodyne detection and heterodyne detection in the framework of the classical electromagnetic wave theory of light. We analyzed the balanced homodyne and heterodyne detection in detail, including the working function of spectrum analyzer. In the last part of this chapter, we demonstrated an interesting phenomenon: for coupled thermal light with  $\varphi_j(v_s) + \varphi_k(v_i) = \text{constant}$ , the power spectrum turns out to be

$$\begin{aligned}\langle P(v) \rangle &\propto \left\{ \sum_j A_j^2(v_s) + \sum_k A_k^2(v_i) \right\} \\ &+ 2 \sum_{jk} A_j(v_s) A_k(v_i) \cos \left[ \omega_p \frac{z_{s,i} - z_r}{c} + \varphi_{s,i,r} \right].\end{aligned}$$

The sinusoidal modulation is observable when introducing optical path difference between  $z_{s,i}$  and  $z_r$ . Furthermore, the amplitude of the sinusoidal modulation can be much greater than that of the other two constant terms, when taking into account a large number of subfields. This means that under certain experimental conditions,  $\langle P(v) \rangle$  is not only able to achieve a value below "shot noise," but also able to achieve a value of negative.

### Suggested Reading

- Bachor, H.-A. and T.C. Ralph, *A Guide to Experiments in Quantum Optics*, Wiley-VCH, Weinheim, Germany, 2004.
- Gerry, C.C. and P.L. Knight, *Introductory Quantum Optics*, Cambridge University Press, Cambridge, U.K., 2006.
- Skolnik, M.I., *Introduction to Radar System*, McGraw-Hill, New York, 1962.



# 8

---

## *Quantum Theory of Light: Field Quantization and Measurement*

---

The quantum theory of light started at the beginning of the last century. The successful introduction of the concept of a photon, or a quantum of light, stimulated a new foundation of physics, namely, the quantum theory. Today, quantum theory has turned out to be the overarching principle of modern physics. It would be difficult to find a single subject among the physical science that is not affected in its foundations or in its applications by quantum theory.

After 100 years of studies, what do we know about the photon? The photon is a wave: it has no mass, it travels at the highest speed in the universe, and it interferes with itself. The photon is a particle: it has well-defined values of momentum and energy, and it even “spins” like a particle. The photon is neither a wave nor a particle, because whichever we think it is, we would be tripped into difficulties in explaining the other part of its behavior. The photon is a wave-like particle and/or a particle-like wave: a photon can never be divided into parts, but interference of a single photon can be easily observed by modern technologies. It seems that a photon passes both paths of an interferometer when interference patterns are observed; however, if the interferometer is set in such a way that its two paths are “distinguishable,” the photon “knows” which path to follow and never passes through both paths. Apparently, a photon has to make a choice in its behavior when facing an interferometer: a choice of “both-path” like a wave or “which-path” like a particle. Surprisingly, the choice is not necessary before passing through the interferometer. It has been experimentally demonstrated that the choice of “which-path” and/or “both-path” can be delayed until after the photon has passed through the interferometer. More surprisingly, the which-path information can even be “erased” after the annihilation of the photon itself. The behavior of a photon apparently does not follow any of the basic criterion: reality, causality, and locality, of our everyday life. Of course, the peculiarity of wave–particle duality is not the property of photons only, it belongs to all quanta in the quantum world. Perhaps, it is easy to accept the particle picture of an electron with mass,  $m_e$ , and charge,  $e$ ; it is definitely not easy to accept the particle nature of a photon. On the other hand, perhaps, it is easy to accept the wave picture of a photon with frequency,  $\omega$ , and wavevector,  $\mathbf{k}$ ; it is definitely not easy to accept the wave nature of an electron.

Although questions regarding the fundamental issues about the concept of a photon still exist, the quantum theory of light has contributed perhaps the most influential and successful, yet controversial part to quantum mechanics.

In this chapter, we will constrain ourselves to the following basic questions about the quantum theory of light: (1) Why quantization of the radiation field is necessary? (2) How to quantize the radiation field? (3) How to describe the state of the quantized field? and (4) How to physically model and mathematically formulate a photodetection event or a joint photodetection event?

---

## 8.1 The Experimental Foundation—Part I: Blackbody Radiation

Around the year of 1900, an unexpected observation happened in experimental physics. It was found that the experimentally observed spectrum distribution of blackbody radiation disagreed with the theoretical predication of classical physics.

A “blackbody” is a perfect absorber that absorbs all radiation incidents on it. The best approximation to a blackbody is a tiny pinhole in the wall of a hollow enclosure, or cavity. The intensity,  $I(\nu)$ , of radiation per unit solid angle, coming from the hole, in the frequency range between  $\nu$  and  $\nu + d\nu$  can be accurately measured. It was found experimentally that, under the condition of thermodynamic equilibrium, any blackbody has the same characteristic emission function  $I(\nu)$ . Typical curves of  $I(\nu)$  are shown in Figure 8.1.  $I(\nu)$  depends only on the temperature of the walls of the enclosure, and not on the material of which the enclosure is made nor on the shape of the cavity. At a particular temperature,  $I(\nu) \propto \nu^2$  for low frequencies, while at high frequencies  $I(\nu)$  drops off exponentially. Another interesting feature of the spectrum distribution is that the maximum  $I(\nu)$  is shifted toward higher frequencies while the temperature of the blackbody is raised. The four curves in Figure 8.1 clearly indicate these characteristics of the blackbody radiation.

It was indeed a surprise at that time that the theory of classical mechanics, electrodynamics, and thermodynamics all together failed to explain this simple observation.

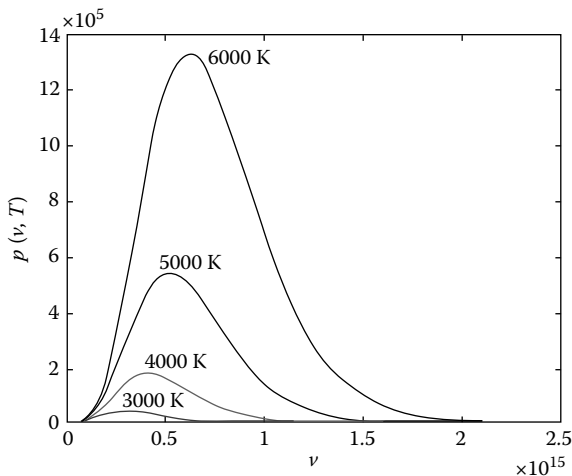
In the framework of classical electrodynamics, the intensity of the blackbody radiation per unit solid angle is related to the energy density of the radiation in the cavity, or the enclosure:

$$I(\nu) = \frac{c}{4\pi} u(\nu) \quad (8.1)$$

where

$c$  is the speed of light

$u(\nu)$  is the energy density of frequency  $\nu$

**FIGURE 8.1**

Blackbody radiation curves.  $I(v)$  depends only on the temperature of the walls of the enclosure. At a particular temperature,  $I(v) \propto v^2$  for low frequencies, while at high frequencies  $I(v)$  drops off exponentially. Another interesting feature of the spectrum is that the maximum  $I(v)$  is shifted toward higher frequencies while the temperature of the blackbody is raised.

Therefore, the measured intensity of blackbody radiation  $I(v)$  is determined by  $u(v)$  of the cavity. The source of the radiation energy in the cavity is obviously the walls of the enclosure, which continually emit waves of every possible frequency and wavevector, or say all possible modes. In thermodynamic equilibrium, the amount of energy  $u(v)dv$ , in the frequency range between  $v$  and  $v + dv$  is easily calculated. What we need is to (1) estimate the number of permissible modes under the boundary condition of the cavity and (2) calculate the mean energy of the permissible modes.

### (1) Number of modes

Suppose we have a rectangular cavity of dimension  $L_x$ ,  $L_y$ , and  $L_z$ . Applying the boundary condition required by electromagnetic theory, the allowed wavevector  $\mathbf{k}$  is thus

$$k_x = \frac{2\pi l}{L_x} \quad k_y = \frac{2\pi m}{L_y} \quad k_z = \frac{2\pi n}{L_z} \quad (8.2)$$

where  $l$ ,  $m$ , and  $n$  are integers taking values from  $-\infty$  to  $\infty$ . The number of allowed modes is therefore

$$\Delta N = \Delta l \Delta m \Delta n = \frac{V}{(2\pi)^3} dk_x dk_y dk_z, \quad (8.3)$$

where  $V = L_x L_y L_z$ . To estimate the number of permissible modes in the frequency range between  $\nu$  and  $\nu + d\nu$ , it is more convenient to adopt polar coordinates in  $\mathbf{k}$  space by considering the volume element  $dk_x dk_y dk_z = k^2 dk d\Omega$ , where  $d\Omega$  is the element of solid angle. The number of permissible modes in the frequency range between  $\nu$  and  $\nu + d\nu$  is thus

$$\Delta N = \frac{4\pi V}{(2\pi)^3} k^2 dk = \frac{4\pi V}{c^3} \nu^2 d\nu$$

where we have integrated over  $d\Omega$ , since we are not interested in the direction of the wavevector  $\mathbf{k}$ . Taking into consideration the polarization for each mode, the number of permissible modes in the frequency range between  $\nu$  and  $\nu + d\nu$  will be doubled:

$$\Delta N = \frac{8\pi V}{c^3} \nu^2 d\nu. \quad (8.4)$$

## (2) Mean energy of each mode

To calculate the mean energy of each mode, we will adopt the results of classical statistical mechanics. We consider each mode of radiation to be in thermodynamic equilibrium with the walls of the enclosure, which is treated as a heat reservoir. A heat reservoir is defined as a very large system with constant temperature. Physically, this means that the temperature of the enclosure remains unaffected by whatever small amount of energy it gives to the radiation mode. Under the condition of equilibrium, the probability of finding the radiation mode between  $E$  and  $E + dE$  follows the canonical distribution:

$$P(E) dE = \frac{e^{-E/kT} dE}{\int_0^\infty e^{-E/kT} dE}. \quad (8.5)$$

The mean value of the energy  $\bar{E}$  is calculated by weighting each possible energy according to its probability:

$$\bar{E} = \frac{\int_0^\infty E e^{-E/kT} dE}{\int_0^\infty e^{-E/kT} dE} = kT \frac{\int_0^\infty \epsilon e^{-\epsilon} d\epsilon}{\int_0^\infty e^{-\epsilon} d\epsilon} = kT \quad (8.6)$$

where  $\epsilon = E/kT$ . In Equation 8.6, we have used the solution of the  $\Gamma$ -function,  $\Gamma(n+1) = n!$  and  $\Gamma(1) = 1$ .

The mean energy of each radiation mode is  $kT$ . This is a good example of the theorem of equipartition of energy. The amount of radiation energy in the frequency range between  $\nu$  and  $\nu + d\nu$  is thus

$$u(\nu) d\nu = \bar{E} \Delta N = \frac{8\pi V}{c^3} kT \nu^2 d\nu \quad (8.7)$$

which is called the Rayleigh–Jean’s law. In fact, the above analysis directly follows the historical treatment of Rayleigh–Jean to formulate the distribution,  $I(v)$ , of the blackbody radiation.

Comparing with the blackbody radiation curves shown in Figure 8.1, Rayleigh–Jean’s law only agrees with the experimental observations at low frequencies; it gives too much power of radiation for high frequencies. In addition, if we integrate over all frequencies to calculate the total energy, the result diverges, meaning an infinite amount of energy contained in the cavity.

Wien attempted a different classical approach. Based on classical thermodynamic arguments, Wein showed that the blackbody radiation distribution must be of the form  $u(v) = v^3 f(v/T)$ . The function  $f(v/T)$ , however, cannot be determined from thermodynamics alone. Wien obtained a distribution function that was later named as Wein’s law:

$$u(v) dv \sim v^3 e^{-hv/kT} dv \quad (8.8)$$

where  $h$  is a constant determined experimentally by data fitting. This constant later turned out to be the symbolic constant of quantum theory and was named Planck’s constant. Wein’s distribution improved the high-frequency spectrum fitting, but got worse at low frequencies.

In history, all classical attempts, either the electrodynamic approaches or the thermodynamic treatments failed to give an accurate distribution function to fit the observation curves of blackbody radiation, within experimental error. We thus conclude the concepts we have used to derive these laws, or distributions, may not be adequate to describe the behavior of blackbody radiation.

In the year 1900, Planck decided to abandon the classical tradition and in doing so he succeed in fitting the experimentally measured blackbody radiation spectrum. Planck’s hypothesis was very simple. He assumed that a radiation mode can only take energy values of an integer multiple of a basic unit,  $E = nhv$ , where  $n$  is an integer running from 0 to  $\infty$ . This basic unit  $h\nu$  is not the same for all the modes, but rather is proportional to the frequency of the mode. With this assumption, phenomenologically, Planck explained the blackbody radiation by accurately fitting the experimentally measured distribution curves, within experimental error.

Planck’s assumption is truly inconsistent with classical concepts. According to classical mechanics and classical electrodynamics, there are no restrictions on the energy of a radiation mode. The only “restriction” regarding the energy of a radiation mode is the mean value,  $kT$ , which is independent of the frequency of the radiation. Planck’s assumption seems inconsistent with many of our everyday experiences also. For instance, the output power of an AM or FM radio oscillator may have any value. There is no experimental evidence that the energy of a radio oscillator must be quantized to  $E = nhv$ . Does it mean Planck’s theory is inadequate to describe the behavior of radio

waves? The answer is NO. The apparent inconsistency arises from the fact that  $h$  is a very small quantity,  $h \sim 6.6 \times 10^{-34}$  J-s. In the AM and FM radio frequencies, e.g.  $\nu \sim 10^6$  and  $10^8$  Hz, the basic unit of energy  $h\nu$  is on the order of  $6.6 \times 10^{-28}$  and  $6.6 \times 10^{-26}$  J which are not detectable by any available sensitive detection apparatus. With light waves, however, the values of  $h\nu$  increase significantly, for  $\nu \sim 10^{15}$  Hz,  $h\nu \sim 10^{-19}$  J. This value is measurable by modern measurement devices. Therefore, as we go to higher frequencies, Planck's quantization hypothesis is easier to verify.

We now derive the spectrum distribution function for blackbody radiation by following Planck's energy quantization. Similar to what we did in the early classical analysis, we recalculate the mean energy per mode by applying the canonical distribution. The probability for a mode to be in a given energy  $E_n = nh\nu$  is then

$$P(n) \propto e^{-E_n/kT} = e^{-nh\nu/kT} \quad (8.9)$$

Normalizing Equation 8.9, we obtain

$$P(n) = \frac{e^{-nh\nu/kT}}{\sum_{n=0}^{\infty} e^{-nh\nu/kT}} = \frac{e^{-nh\nu/kT}}{1 - e^{-h\nu/kT}}. \quad (8.10)$$

The mean energy per mode is then

$$\begin{aligned} \bar{E} &= \sum_{n=0}^{\infty} E_n P(n) = (1 - e^{-h\nu/kT})^{-1} \sum_{n=0}^{\infty} nh\nu e^{-nh\nu/kT} \\ &= h\nu (1 - e^{-h\nu/kT})^{-1} \sum_{n=0}^{\infty} n e^{-nh\nu/kT}. \end{aligned} \quad (8.11)$$

To evaluate Equation 8.11, we can write

$$\sum_{n=0}^{\infty} n e^{-nh\nu/kT} = -\frac{d}{d\alpha} \sum_{n=0}^{\infty} e^{-n\alpha} = -\frac{d}{d\alpha} \left( \frac{1}{1 - e^{-\alpha}} \right) = \frac{e^{-\alpha}}{(1 - e^{-\alpha})^2}$$

where  $\alpha = h\nu/kT$ . The mean energy per mode,  $\bar{E}$ , is then

$$\bar{E} = \frac{h\nu e^{-h\nu/kT}}{1 - e^{-h\nu/kT}}. \quad (8.12)$$

The amount of radiation energy in the frequency range between  $\nu$  and  $\nu + d\nu$  is found to be

$$u(\nu) d\nu = \bar{E} \Delta N = \frac{8\pi V}{c^3} h\nu^3 \frac{e^{-h\nu/kT}}{1 - e^{-h\nu/kT}} d\nu.$$

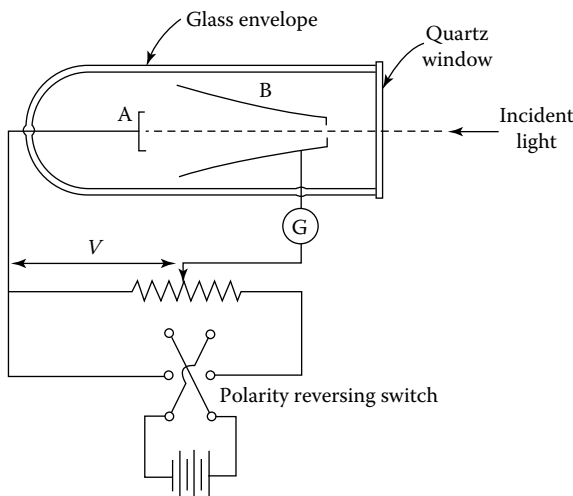
We thus obtain Planck's distribution

$$u(v) = \frac{8\pi V}{c^3} \frac{hv^3 e^{-hv/kT}}{1 - e^{-hv/kT}} \quad (8.13)$$

which is an exact fit, within experimental error, to the distribution of blackbody radiation.

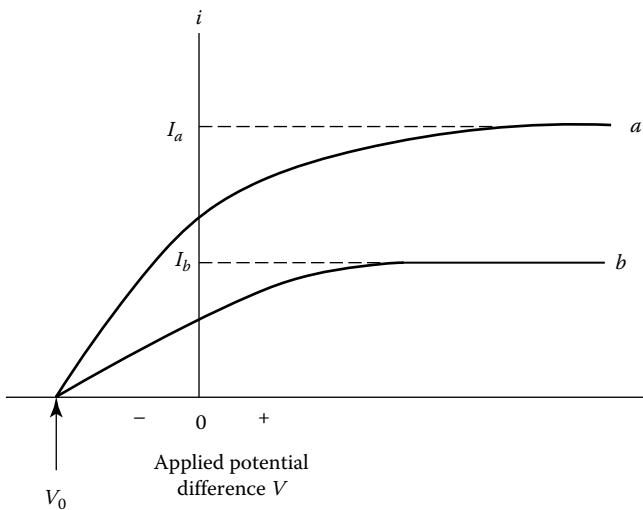
## 8.2 The Experimental Foundation—Part II: Photoelectric Effect

The study of blackbody radiation concluded indirectly that electromagnetic waves may increase or decrease energy only in the units of  $h\nu$ . The discovery of the photoelectric effect confirms this surprising conclusion in a more direct way. In fact, the photoelectric effect was first reported by Hertz in 1887, more than 10 years before Planck's work. The quantum explanation of the effect was given later by Einstein in 1905 as a result of 5 years of thinking about Planck's hypothesis. Figure 8.2 shows a typical experimental setup for observing the photoelectric effect. A simple vacuum tube, containing a metal plate, B, and an anode, A, is used for the experimental observation. Monochromatic light is incident through the quartz window of the vacuum tube on the metal B. The photoelectrons liberated from the surface of the metal B are collected by the anode A. An adjustable potential difference  $V$  is



**FIGURE 8.2**

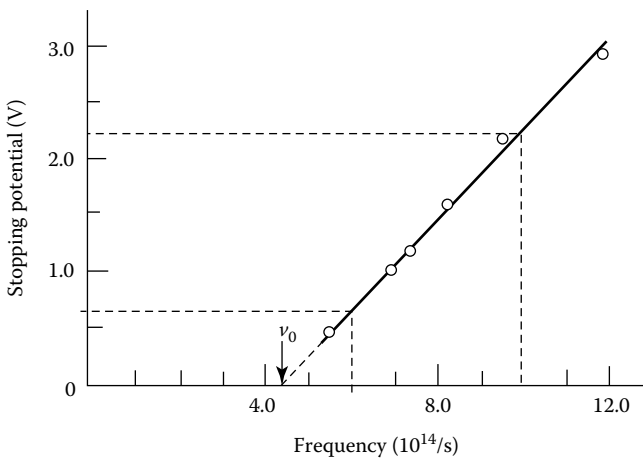
Typical schematic experimental setup for observing the photoelectric effect.

**FIGURE 8.3**

Typical measured photoelectric current,  $i$ , as a function of the applied voltage,  $V$ , between the metal plate, B, and the anode, A. Note, the voltage can be switched to negative or positive. The two curves,  $I_1$  and  $I_2$ , correspond to two different incident light intensities:  $I_1 = 2I_2$ . It is a surprise to find that  $V_0$  is independent of the incident light.

applied between the metal plate B and the anode A. The output photocurrent of the anode is monitored by a sensitive ammeter G.

Figure 8.3 is a typical observation of the photoelectric current,  $i$ , as a function of the applied potential difference,  $V$ . When  $V$  is positive and takes large enough values, the photocurrent  $i$  reaches a saturated value, which means all liberated photoelectrons are collected by the anode A. The saturated value of the photoelectric current  $i$  is proportional to the intensity of the incident light. This result is reasonable because a large intensity should indeed eject more photoelectrons. The surprise, however, comes when  $V$  is reversed, making it negative, and adjusted to reach the stopping potential  $V_0$  where the photoelectric current drops to zero,  $i \sim 0$ . It was found that  $V_0$  is independent of the intensity of the incident light, as shown in Figure 8.3. When a negative potential,  $V$ , is applied, the photoelectric current does not immediately drop to zero. This suggests the electron escapes from the surface of the metal with a certain kinetic energy. Some of the escaping electrons can still reach the anode, A, if their kinetic energies are large enough,  $K_{max} > eV_0$ , to overcome the applied electric potential against their motion. If the negative potential  $V$  is made large enough to be equal or greater than the maximum kinetic energy of the escaping electrons,  $eV_0 \geq K_{max}$ , no electrons can reach the anode, A, and consequently the photoelectric current  $i$  drops to zero. It is a surprise from the classical point of view that the stopping potential  $V_0$  and consequently the kinetic energy of a liberated electron do not depend on

**FIGURE 8.4**

Typical measurement of  $V_0$  as a linear function of the frequency of the incident light. The slope of the experimental curve is on the order of  $3.9 \times 10^{-15} \text{ V}\cdot\text{s}$ . There exists, for each different metal plate, a characteristic cutoff frequency  $v_0$ . For any frequency less than  $v_0$ , photoelectric effect stops occurring, no matter how intense the incident light.

the intensity of the incident light. In classical electromagnetic wave theory,  $I \propto |\mathbf{E}|^2$ . Since the force applied to an electron is  $e\mathbf{E}$ , the kinetic energy of the photoelectron should increase as the intensity of the incident light increases.

More surprises came later from Millikan's work. Millikan's experiment showed that the stopping potential,  $V_0$ , is linearly dependent on the frequency of the incident light and there exists, for each different metal plate, a characteristic cutoff frequency  $v_0$ . For any frequency lower than  $v_0$ , photoelectric effect stops occurring, no matter how intense the incident light. Figure 8.4 shows a typical measurement of  $V_0$  as a linear function of the incident light frequency. The slope of the experimental curve is on the order of  $3.9 \times 10^{-15} \text{ V}\cdot\text{s}$ . The existence of the cutoff frequency,  $v_0$ , is inconsistent with classical concepts of the electromagnetic wave theory. According to classical electrodynamics, the photoelectric effect should be observable for any frequency, provided the incident light is intense enough to give the necessary amount of kinetic energy to the photoelectron.

In 1905, Einstein proposed a theory which successfully explained the photoelectric effect. In his theory, Einstein quantized the radiation energy into localized "bundles,"  $E = h\nu$ , which were later named "photons" (1926). Einstein assumed that one photon, individually, is completely absorbed by one excited electron in the process of a photoelectron ejection. When the electron is ejected from the surface of the metal, its kinetic energy is given by

$$K = h\nu - W \quad (8.14)$$

where  $W$  is the work required to overcome the attractive forces of the atoms that bind the electron to the metal.  $W$  is called the work function.

How does Einstein's hypothesis explain the photoelectric effect? This question is assigned as an exercise at the end of the chapter. Here, we provide a very brief discussion regarding the cutoff frequency,  $\nu_0$ , which is the observation that conflicts the most with classical theory. Although Einstein's theory was published before Millikan's experiment, it provided a perfect explanation to Millikan's cutoff frequency  $\nu_0$ . When the kinetic energy of the escaped electron equals zero, we have  $h\nu_0 = W$ , which asserts that a photon of frequency  $\nu_0$  has just enough energy to overcome the work function. If the frequency of light is reduced below  $\nu_0$ , a photon will not have enough energy, individually, to eject a photoelectron, no matter how many photons are incident on the surface of the metal.

Einstein was the first physicist to relate the photoelectric effect with Planck's hypothesis. Einstein's equation (8.14) can be rewritten as

$$V_0 = \frac{h}{e} \nu - \frac{W}{e}, \quad (8.15)$$

where we have substituted  $eV_0$  for  $K_{max}$ , and  $V_0$  is the applied stopping potential at which the photoelectric current drops to zero. Equation 8.15 indicates a linear relationship between the stopping potential  $V_0$  and the frequency of the incident light, in agreement with Millikan's experimental results, see Figure 8.4. The measured slopes of the experimental curve in Millikan's experiment is

$$\frac{h}{e} \sim \frac{2.20V - 0.65V}{(10.0 - 6.0) \times 10^{14}/\text{s}} \simeq 3.9 \times 10^{-15} \text{ V-s.}$$

Multiplying the measured slope by the electronic charge,  $e$ , yields  $h \sim 6.2 \times 10^{-34} \text{ J-s}$  which is close to the value  $h \sim 6.6 \times 10^{-34} \text{ J-s}$ , appearing in Planck's distribution function of 1900. Later, more accurate photoelectric experiments measured  $h \sim 6.6262 \times 10^{-34} \text{ J-s}$ . The agreement between the two constants,  $h$ , appearing in the photoelectric experiments and the blackbody radiation observation is a strong confirmation that  $h$  is a universal constant and the radiation field can exchange energy only in units of  $h\nu$ .

At the heart of Einstein's theory is the particle picture of a photon. Einstein assumed that the radiation energy is quantized into localized bundles. A bundle of energy is initially localized in a small volume of space and remains localized as it moves away from the radiation source with velocity  $c$ . The energy of the bundle is related to its frequency by multiplication of a universal constant  $h$ . In the photoelectric process, one bundle of energy  $E = h\nu$ , or one photon, is completely absorbed by one electron originally bound with the metal. How can one bounded electron, which is a particle localized within a very small volume, completely absorb a photon to become

an photoelectron? The simplest physical picture is that the particle-like photon transferred all its energy to the electron during a collision. Is the photon a localized object? Yes and no. When facing its particle-like behavior, it must be localized. When facing its wave-like behavior, it cannot be localized. The biggest mistake happens when the photon is treated as a particle in the interpretation, but is treated as a wave in the calculation.

Although we still have questions regarding the wave–particle duality of a photon, nevertheless, we may draw a conclusion from the above experimental observations: The energy of the electromagnetic field is quantized in nature. The field quantization is necessary.

---

### 8.3 The Light Quantum and the Field Quantization

In blackbody radiation, the atoms on the walls of the cavity box continuously radiate electromagnetic waves into the cavity. In general, there are two fundamental principles governing the physical process of the radiation and determining the physical properties of the radiation field. The Schrödinger equation determines the quantized atomic energy level, and the Maxwell equations govern the behavior of the radiation field. The interaction of the field and the atom results in a quantized electromagnetic field. The energy and the frequency of the emitted photon are determined by the quantized energy levels of the atom,  $\hbar\omega = E_2 - E_1$ . On the other hand, any excited electromagnetic field must satisfy the Maxwell equations, which determine the harmonic mode structure and the superposition.

In the quantum theory of light, the radiation field is treated as a set of harmonic oscillators. The energy of each mode is quantized in a similar way as that of a harmonic oscillator. To quantize the field, we will follow the standard procedure. First, we proceed to link the Hamiltonian of the free electromagnetic field to a set of independent harmonic oscillators. The quantum mechanical results of harmonic oscillators are then adapted to the quantized radiation field. Notice, here, free field means no “sources” or “drains” of the radiation field in the chosen volume of  $V = L^3$  that covers the field of interest. The energy of the free field is given by

$$H = \frac{1}{2} \int_V d^3r \left[ \epsilon_0 \mathbf{E}^2(\mathbf{r}, t) + \frac{1}{\mu_0} \mathbf{B}^2(\mathbf{r}, t) \right], \quad (8.16)$$

where  $V$  is the total volume of the field of interest. The volume is usually, but not necessarily, treated as a large finite cubic cavity of  $L^3$  to simplify the mathematics. We will rewrite Equation 8.16 in the following form to link it with the Hamiltonian of a set of independent harmonic oscillators

$$H = \frac{1}{2} \sum_{\mathbf{k}} \left[ p_{\mathbf{k}}^2(t) + \omega^2 q_{\mathbf{k}}^2(t) \right], \quad (8.17)$$

where  $q_{\mathbf{k}}(t)$  and  $p_{\mathbf{k}}(t)$  are a pair of real canonical variables.

To achieve our goal, we start to construct a classical solution of the vector potential  $\mathbf{A}(\mathbf{r}, t)$  of the field. The vector potential of the free electromagnetic field satisfies the Maxwell wave equation

$$\nabla^2 \mathbf{A} - \frac{1}{c^2} \frac{\partial^2 \mathbf{A}}{\partial t^2} = 0 \quad (8.18)$$

with the Coulomb gauge

$$\nabla \cdot \mathbf{A} = 0.$$

The electric and magnetic fields,  $\mathbf{E}(\mathbf{r}, t)$  and  $\mathbf{B}(\mathbf{r}, t)$ , are thus given in terms of  $\mathbf{A}(\mathbf{r}, t)$ :

$$\begin{aligned} \mathbf{E}(\mathbf{r}, t) &= - \frac{\partial}{\partial t} \mathbf{A}(\mathbf{r}, t) \\ \mathbf{B}(\mathbf{r}, t) &= \nabla \times \mathbf{A}(\mathbf{r}, t). \end{aligned} \quad (8.19)$$

The most convenient way for analyzing the field structure is to begin with a very large but finite cubic cavity. Applying the periodic boundary condition, we write  $\mathbf{A}(\mathbf{r}, t)$  in terms of the Fourier expansion of plane-wave modes

$$\mathbf{A}(\mathbf{r}, t) = \sum_{\mathbf{k}} \mathbf{A}_{\mathbf{k}}(t) e^{i\mathbf{k} \cdot \mathbf{r}} \quad (8.20)$$

with

$$\mathbf{A}_{\mathbf{k}}(t) = \mathbf{A}_{-\mathbf{k}}^*(t).$$

Where we have introduced a wavevector

$$\mathbf{k} = \left\{ \frac{2\pi l}{L_x}, \frac{2\pi m}{L_y}, \frac{2\pi n}{L_z} \right\}, \quad (8.21)$$

with

$$l = 0, \pm 1, \pm 2, \dots$$

$$m = 0, \pm 1, \pm 2, \dots$$

$$n = 0, \pm 1, \pm 2, \dots$$

forming a discrete sum of  $\mathbf{k}$  in the Fourier expansion of Equation 8.20.

Considering the Coulomb gauge, we have

$$\sum_{\mathbf{k}} \mathbf{k} \cdot \mathbf{A}_{\mathbf{k}}(t) e^{i\mathbf{k} \cdot \mathbf{r}} = 0 \quad (8.22)$$

for all values of  $\mathbf{r}$ , which requires that

$$\mathbf{k} \cdot \mathbf{A}_{\mathbf{k}}(t) = 0. \quad (8.23)$$

Substituting Equation 8.20 into Equation 8.18, we have

$$\sum_{\mathbf{k}} \left( -k^2 - \frac{1}{c^2} \frac{\partial^2}{\partial t^2} \right) \mathbf{A}_{\mathbf{k}}(t) e^{i\mathbf{k} \cdot \mathbf{r}} = 0 \quad (8.24)$$

for all values of  $\mathbf{r}$ . Thus, we have an equation to determine each of the amplitudes,  $\mathbf{A}_{\mathbf{k}}(t)$ , of the Fourier expansion

$$\left( \frac{\partial^2}{\partial t^2} + \omega^2 \right) \mathbf{A}_{\mathbf{k}}(t) = 0, \quad (8.25)$$

where  $\omega = ck$  is the angular frequency of the mode. A solution of Equation 8.25 is given by

$$\mathbf{A}_{\mathbf{k}}(t) = \hat{\mathbf{e}}_1 \mathcal{A}_{\mathbf{k},1} \left( a_{-\mathbf{k},1}^* e^{i\omega t} + a_{\mathbf{k},1} e^{-i\omega t} \right) + \hat{\mathbf{e}}_2 \mathcal{A}_{\mathbf{k},2} \left( a_{-\mathbf{k},2}^* e^{i\omega t} + a_{\mathbf{k},2} e^{-i\omega t} \right), \quad (8.26)$$

where  $a_{\mathbf{k},s}$  ( $a_{\mathbf{k},s}^*$ ),  $s = 1, 2$  is the amplitude for the mode  $\mathbf{k}$  and the polarization  $s$ .  $\mathcal{A}_{\mathbf{k},s}$  is determined by the initial conditions of the electromagnetic field. In Equation 8.26 we have assigned two orthogonal polarization,  $\hat{\mathbf{e}}_1$  and  $\hat{\mathbf{e}}_2$ , by considering the transverse condition of Equation 8.23. The unit vectors  $\hat{\mathbf{e}}_1$ ,  $\hat{\mathbf{e}}_2$  and the unit vector  $\hat{\mathbf{k}}$  in the direction of the wavevector  $\mathbf{k}$ , together, form a right-hand, orthogonal, Cartesian basis.

To simplify the mathematical expression, we focus on one of the polarizations:

$$\mathbf{A}(\mathbf{r}, t) = \sum_{\mathbf{k}} \hat{\mathbf{e}} \mathcal{A}_{\mathbf{k}} [ a_{\mathbf{k}}(t) e^{i\mathbf{k} \cdot \mathbf{r}} + a_{\mathbf{k}}^*(t) e^{-i\mathbf{k} \cdot \mathbf{r}} ] \quad (8.27)$$

where  $a_{\mathbf{k}}(t) = a_{\mathbf{k}} e^{-i\omega t}$ ,  $a_{\mathbf{k}}^*(t) = a_{\mathbf{k}}^* e^{i\omega t}$ . The vector potential  $\mathbf{A}(\mathbf{r}, t)$  is written as a superposition of the orthogonal harmonic modes

$$q_{\mathbf{k}}(\mathbf{r}, t) = a_{\mathbf{k}}(t) e^{i\mathbf{k} \cdot \mathbf{r}} + a_{\mathbf{k}}^*(t) e^{-i\mathbf{k} \cdot \mathbf{r}} \quad (8.28)$$

These orthogonal (independent) harmonic modes are equivalent to the normal mode of a harmonic oscillator system. In the following, we will treat these orthogonal harmonic modes of the electromagnetic field as independent harmonic oscillators, and treat  $a_{\mathbf{k}}(t)$  ( $a_{\mathbf{k}}^*(t)$ ) as normal mode amplitudes. In terms of the vector potential  $\mathbf{A}(\mathbf{r}, t)$  of Equation 8.27, the electric field  $\mathbf{E}(\mathbf{r}, t)$  and the magnetic field  $\mathbf{B}(\mathbf{r}, t)$  are calculated from Equation 8.19

$$\begin{aligned}\mathbf{E}(\mathbf{r}, t) &= \sum_{\mathbf{k}} \omega \hat{\mathbf{e}} \mathcal{A}_{\mathbf{k}} [ i a_{\mathbf{k}}(t) e^{i\mathbf{k}\cdot\mathbf{r}} - i a_{\mathbf{k}}^*(t) e^{-i\mathbf{k}\cdot\mathbf{r}} ] \\ \mathbf{B}(\mathbf{r}, t) &= \sum_{\mathbf{k}} (\mathbf{k} \times \hat{\mathbf{e}}) \mathcal{A}_{\mathbf{k}} [ i a_{\mathbf{k}}(t) e^{i\mathbf{k}\cdot\mathbf{r}} - i a_{\mathbf{k}}^*(t) e^{-i\mathbf{k}\cdot\mathbf{r}} ].\end{aligned}\quad (8.29)$$

Now we examine the energy of the electromagnetic field. We can either treat the electromagnetic field as a system of independent harmonic oscillators or calculate the Hamiltonian of the field from Equation 8.16. Viewing the field as a set of independent harmonic oscillators, the Hamiltonian of the system is readily given in classical mechanics

$$H = 2 \int_V d^3r \sum_{\mathbf{k}} \omega^2 |q_{\mathbf{k}}(\mathbf{r}, t)|^2 = 2 \sum_{\mathbf{k}} \omega^2 |a_{\mathbf{k}}(t)|^2,\quad (8.30)$$

where  $a_{\mathbf{k}}(t)$  is treated as the normal mode amplitude. To calculate the Hamiltonian from Equation 8.16, substitute Equation 8.29 into Equation 8.16, the integral gives

$$H = 2 \sum_{\mathbf{k}} |\mathcal{A}_{\mathbf{k}}|^2 \omega^2 |a_{\mathbf{k}}(t)|^2.\quad (8.31)$$

To be consistent with the result of Equation 8.30, we may take a constant mode distribution of  $\mathcal{A}_{\mathbf{k}} = \mathcal{A}_0 = 1/\epsilon_0^{1/2} L^{3/2}$  to “normalize” the energy of the field to  $H = 2 \sum_{\mathbf{k}} \omega^2 |a_{\mathbf{k}}(t)|^2$ . It is quite reasonable to treat all the independent and “free” harmonic oscillators equally. Although, in reality, nonconstant mode distribution may have to be taken into consideration, it would not affect the quantization of each independent mode of the electromagnetic field.

Next, we introduce a pair of canonical variables  $q_{\mathbf{k}}(t)$  and  $p_{\mathbf{k}}(t)$

$$\begin{aligned}q_{\mathbf{k}}(t) &= a_{\mathbf{k}}(t) + a_{\mathbf{k}}^*(t) \\ p_{\mathbf{k}}(t) &= -i\omega [a_{\mathbf{k}}(t) - a_{\mathbf{k}}^*(t)].\end{aligned}\quad (8.32)$$

The Hamiltonian of the field in Equation 8.30 is then rewritten in terms of  $q_{\mathbf{k}}(t)$  and  $p_{\mathbf{k}}(t)$  as

$$H = \sum_{\mathbf{k}} \frac{1}{2} [ p_{\mathbf{k}}^2(t) + \omega^2 q_{\mathbf{k}}^2(t) ] = \sum_{\mathbf{k}} H_{\mathbf{k}},\quad (8.33)$$

which is recognized as the Hamiltonian of a harmonic oscillator system. Each harmonic oscillator of the system corresponds to a mode of the field specified by wavevector  $\mathbf{k}$ . In Equation 8.33  $H_{\mathbf{k}}$  indicates the Hamiltonian of the  $\mathbf{k}$ th harmonic oscillator. The Hamiltonian of a classical harmonic oscillator is allowed to take any nonnegative values, because  $p_{\mathbf{k}}$  and  $q_{\mathbf{k}}$  can take any values in classical theory. It is easy to derive from Equations 8.32 and 8.33 that  $q_{\mathbf{k}}(t)$  and  $p_{\mathbf{k}}(t)$  satisfy the classical canonic equations of motion:

$$\begin{aligned}\frac{\partial q_{\mathbf{k}}}{\partial t} &= \frac{\partial H}{\partial p_{\mathbf{k}}} \\ \frac{\partial p_{\mathbf{k}}}{\partial t} &= -\frac{\partial H}{\partial q_{\mathbf{k}}}.\end{aligned}\quad (8.34)$$

It is also easy to find the results of the following Poisson bracket:

$$\begin{aligned}[q_{\mathbf{k}}(t), p_{\mathbf{k}'}(t)] &= \delta_{\mathbf{kk}'} \\ [q_{\mathbf{k}}(t), q_{\mathbf{k}'}(t)] &= 0 \\ [p_{\mathbf{k}}(t), p_{\mathbf{k}'}(t)] &= 0.\end{aligned}\quad (8.35)$$

Now, we follow the quantum theory of the harmonic oscillator to formulate and quantize the electromagnetic field. As a standard procedure, we first replace the canonical variables of  $q_{\mathbf{k}}(t)$  and  $p_{\mathbf{k}}(t)$  with quantum-mechanical canonical conjugate operators  $\hat{q}_{\mathbf{k}}(t)$  and  $\hat{p}_{\mathbf{k}}(t)$  with the following commutation relations:

$$\begin{aligned}[\hat{q}_{\mathbf{k}}(t), \hat{p}_{\mathbf{k}'}(t)] &= i\hbar \delta_{\mathbf{kk}'} \\ [\hat{q}_{\mathbf{k}}(t), \hat{q}_{\mathbf{k}'}(t)] &= 0 \\ [\hat{p}_{\mathbf{k}}(t), \hat{p}_{\mathbf{k}'}(t)] &= 0.\end{aligned}\quad (8.36)$$

The quantum mechanical Hamiltonian of the harmonic oscillator system is thus written in terms of the operators  $\hat{q}_{\mathbf{k}}(t)$  and  $\hat{p}_{\mathbf{k}}(t)$

$$\hat{H} = \sum_{\mathbf{k}} \frac{1}{2} [\hat{p}_{\mathbf{k}}^2(t) + \omega^2 \hat{q}_{\mathbf{k}}^2(t)] = \sum_{\mathbf{k}} \hat{H}_{\mathbf{k}} \quad (8.37)$$

where  $\hat{H}_{\mathbf{k}}$  is the Hamiltonian operator of the  $\mathbf{k}$ th harmonic oscillator. Differing from the Hamiltonian,  $H_{\mathbf{k}}$ , of a classical oscillator in Equation 8.33, which may take any values,  $\hat{H}_{\mathbf{k}}$  in Equation 8.37 can only admit quantized energy.

To show the energy quantization of a quantum harmonic oscillator, we introduce a pair of non-Hermitian operators to replace the  $\hat{p}_{\mathbf{k}}$  and  $\hat{q}_{\mathbf{k}}$  in Equation 8.37:

$$\begin{aligned}\hat{a}_{\mathbf{k}}(t) &= \frac{1}{\sqrt{2\hbar\omega}} [\omega \hat{q}_{\mathbf{k}}(t) + i\hat{p}_{\mathbf{k}}(t)] \\ \hat{a}_{\mathbf{k}}^\dagger(t) &= \frac{1}{\sqrt{2\hbar\omega}} [\omega \hat{q}_{\mathbf{k}}(t) - i\hat{p}_{\mathbf{k}}(t)],\end{aligned}\quad (8.38)$$

and a set of commutation relations derived from Equation 8.36:

$$\begin{aligned}[\hat{a}_{\mathbf{k}}(t), \hat{a}_{\mathbf{k}'}^\dagger(t)] &= \delta_{\mathbf{k}\mathbf{k}'} \\ [\hat{a}_{\mathbf{k}}(t), \hat{a}_{\mathbf{k}'}(t)] &= 0, \\ [\hat{a}_{\mathbf{k}}^\dagger(t), \hat{a}_{\mathbf{k}'}^\dagger(t)] &= 0.\end{aligned}\quad (8.39)$$

The Hamiltonian of Equation 8.37 is thus written in terms of  $\hat{a}_{\mathbf{k}}(t)$  and  $\hat{a}_{\mathbf{k}}^\dagger(t)$

$$\begin{aligned}\hat{H} &= \frac{1}{2} \sum_{\mathbf{k}} \hbar\omega \left[ \hat{a}_{\mathbf{k}}(t) \hat{a}_{\mathbf{k}}^\dagger(t) + \hat{a}_{\mathbf{k}}^\dagger(t) \hat{a}_{\mathbf{k}}(t) \right] \\ &= \sum_{\mathbf{k}} \hbar\omega \left[ \hat{a}_{\mathbf{k}}^\dagger(t) \hat{a}_{\mathbf{k}}(t) + \frac{1}{2} \right] \\ &= \sum_{\mathbf{k}} \hbar\omega \left[ \hat{n}_{\mathbf{k}} + \frac{1}{2} \right] \\ &= \sum_{\mathbf{k}} \hat{H}_{\mathbf{k}},\end{aligned}\quad (8.40)$$

where we have used the commutation relations of Equation 8.39 and introduced the number operator  $\hat{n}_{\mathbf{k}} = \hat{a}_{\mathbf{k}}^\dagger(t) \hat{a}_{\mathbf{k}}(t)$  for the mode  $\mathbf{k}$ . It is clear that  $\hat{n}_{\mathbf{k}}$  is Hermitian and is independent of time.

We now show that the Hamiltonian,  $\hat{H}_{\mathbf{k}}$ , of the  $\mathbf{k}$ th harmonic oscillator, or mode, in Equation 8.40 only admits quantized energies. To simplify the notation, we will drop the subscript  $\mathbf{k}$  in the following discussion by considering a single harmonic oscillator, or mode.

Assume  $|n\rangle$  is an eigenstate of  $\hat{n}$  with eigenvalue of  $n$ ,

$$\hat{n}|n\rangle = n|n\rangle \quad (8.41)$$

where  $n$  must be real, since  $\hat{n}$  is Hermitian. It is easy to show that  $|n\rangle$  is also an eigenstate of  $\hat{H}$  with eigenvalue of  $E_n = \hbar\omega(n + 1/2)$ ,

$$\hat{H}|n\rangle = \hbar\omega \left[ \hat{n} + \frac{1}{2} \right] |n\rangle = \hbar\omega \left( n + \frac{1}{2} \right) |n\rangle. \quad (8.42)$$

We will show that the Hamiltonian in Equation 8.42 is quantized because the commutations of Equation 8.39 limit  $n$  to integer values. To prove this, we show that  $\hat{a}|n\rangle$  is an eigenstate of  $\hat{n}$  with eigenvalue of  $n - 1$ , since

$$\hat{n}\hat{a}|n\rangle = \hat{a}(n-1)|n\rangle = (n-1)\hat{a}|n\rangle \quad (8.43)$$

where we have used the commutation relations of Equation 8.39. If  $\langle n|n\rangle = 1$ , then  $\hat{a}|n\rangle$  has normalization

$$\langle n|\hat{a}^\dagger\hat{a}|n\rangle = \langle n|\hat{n}|n\rangle = n. \quad (8.44)$$

Therefore,

$$\hat{a}|n\rangle = \sqrt{n}|n-1\rangle \quad (8.45)$$

where state  $|n-1\rangle$  is normalized  $\langle n-1|n-1\rangle = 1$ .

Similarly,  $(\hat{a})^2|n\rangle$  is an eigenstate of  $\hat{n}$  with eigenvalue of  $n - 2$ , and

$$(\hat{a})^2|n\rangle = \sqrt{n(n-1)}|n-2\rangle.$$

Repeatedly applying the operator  $\hat{a}$ , we have all the normalized eigenstates in terms of  $|n\rangle$

$$(\hat{a})^m|n\rangle = \sqrt{n(n-1)\dots(n-m+1)}|n-m\rangle \quad (8.46)$$

Thus, if  $n$  is an eigenvalue of the number operator  $\hat{n}$ , then  $n-1, n-2, \dots$  are all eigenvalues of  $\hat{n}$ . Since

$$n = \langle n|\hat{n}|n\rangle = \langle n|\hat{a}^\dagger\hat{a}|n\rangle = \langle \Phi|\Phi\rangle \geq 0,$$

where  $|\Phi\rangle = \hat{a}|n\rangle$ , all the eigenvalues of  $\hat{n}$  must be positive. Therefore  $n$  must be an integer and bounded by the lowest eigenvalue of zero. The null eigenstate  $|0\rangle$ , or the vacuum state, is defined as

$$\hat{a}|1\rangle = |0\rangle \quad \text{and} \quad \hat{a}|0\rangle = 0. \quad (8.47)$$

The Hermitian operator  $\hat{n}$ , therefore takes eigenvalues from a set of integer  $0, 1, 2, \dots$ , and is called the number operator for mode  $\mathbf{k}$ . Regarding Equation 8.46, it is interesting that we can only apply the operator  $\hat{a}$   $n$  times to reach the lowest permissible vacuum state  $|0\rangle$  with a nonzero lowest energy  $E_0 = \hbar\omega/2$ :

$$(\hat{a})^n|n\rangle = \sqrt{n!}|0\rangle. \quad (8.48)$$

So far, we have explored two important differences between quantum theory and classical theory regarding the energy of a radiation mode: (1) the energy of a radiation mode is quantized and (2) the lowest energy of a radiation mode, the vacuum state  $|0\rangle$ , takes a nonzero value  $E_0 = \hbar\omega/2$  which is called the zero-point energy. It should be emphasized that both properties (1) and (2) follow from the commutation relation  $[\hat{a}, \hat{a}^\dagger] = 1$ . We will come back to discuss the physics associated with these two special features later.

Similar to  $\hat{a}|n\rangle$ ,  $\hat{a}^\dagger|n\rangle$  is also an eigenstate of  $\hat{n}$  with eigenvalue  $n+1$ , since

$$\hat{n}\hat{a}^\dagger|n\rangle = \hat{a}^\dagger(n+1)|n\rangle = (n+1)\hat{a}^\dagger|n\rangle, \quad (8.49)$$

where we have again used the commutation relations of Equation 8.39. It is easy to show that

$$\hat{a}^\dagger|n\rangle = \sqrt{n+1}|n+1\rangle, \quad (8.50)$$

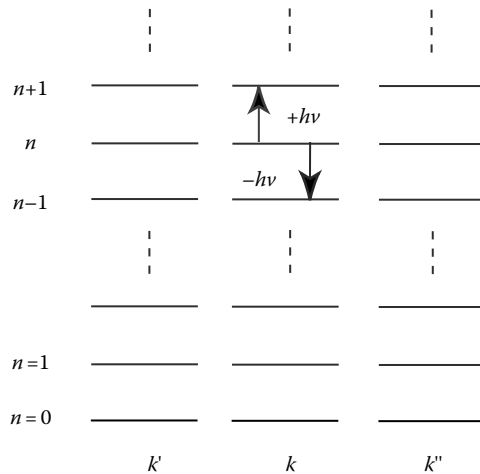
where the state  $|n+1\rangle$  is normalized,  $\langle n+1|n+1\rangle = 1$ . Unlike  $\hat{a}$  the eigenvalues of  $\hat{a}^\dagger$  are not bounded. by repeatedly applying  $\hat{a}^\dagger$  the eigenvalues of  $\hat{n}$  go to infinity and therefore are integers from zero to infinity. Using Equation 8.49, we have all the normalized eigenstates in terms of  $|0\rangle$ .

$$\begin{aligned} |1\rangle &= \hat{a}^\dagger|0\rangle \\ |2\rangle &= \frac{1}{\sqrt{2}}\hat{a}^\dagger|1\rangle = \frac{1}{\sqrt{2}}(\hat{a}^\dagger)^2|0\rangle \\ |3\rangle &= \frac{1}{\sqrt{3}}\hat{a}^\dagger|2\rangle = \frac{1}{\sqrt{6}}(\hat{a}^\dagger)^3|0\rangle \\ &\vdots \\ |n\rangle &= \frac{1}{\sqrt{n!}}(\hat{a}^\dagger)^n|0\rangle, \end{aligned} \quad (8.51)$$

where the state  $|n\rangle$  is normalized  $\langle n|n\rangle = 1$ .

By applying  $\hat{a}^\dagger$ , we have generated a set of normalized number states  $|n_k\rangle$ , which are eigenstates of the Hamiltonian  $\hat{H}_k$  for mode  $k$  and for polarization  $\hat{\mathbf{e}}_k$ . These energy eigenstates form a complete, orthonormal vector space for characterizing the radiation field. The eigenvalues of the Hamiltonian,  $\hat{H}_k$ , are quantized with discrete values of  $n\hbar\omega$ , or  $n\hbar v$ , in contrast to classical electromagnetic theory where the energy of a radiation mode can have any value. Figure 8.5 illustrates the quantized energy levels for a radiation mode of the electromagnetic field.

Connecting  $\hat{a}^\dagger$  and  $\hat{a}$  with Einstein's concept of an energy bundle, or a photon,  $\hat{a}^\dagger$  adds a quantum of energy,  $\hbar\omega$ , or a photon, to the  $k$ th mode of

**FIGURE 8.5**

Quantized energy levels for a radiation mode of an electromagnetic field. The creation operator  $\hat{a}_k^\dagger$  adds a quantum of energy  $\hbar\omega$ , or a photon, to the mode  $k$  to excite the mode to a higher energy level. The annihilation operator  $\hat{a}_k$  subtract the same amount of energy, or annihilate a photon, from the radiation mode. In connection with the concept of photon, the illustrated energy eigenstates of  $\hat{H}_k$  are also named as photon number states, or Fock states.

the radiation field. Consequently, it is called the *photon creation operator*. Similarly,  $\hat{a}$  subtracts a quantum of energy,  $\hbar\omega$ , from the  $k$ th mode of the radiation field. Therefore, it is called the *photon annihilation operator*. The excited state  $|n\rangle$  of a radiation mode contains  $n$  quanta of energy along with the zero-point energy, and  $n$  is called the *occupation number* or the number of photons. Accordingly, the set of energy eigenstates in Equation 8.51 are called *photon number states*. The physical process of photon creation and annihilation in an atomic transition will be addressed later, in the discussions of the quantum state and the field operator.

We are now ready to characterize the quantized radiation field in terms of the energy eigenstates of its Hamiltonian. In general, any state of a radiation field can be described as the superposition of the energy eigenstates,

$$|\Psi\rangle = \sum_n c_n |n\rangle, \quad (8.52)$$

where  $c_n$  is the complex amplitude associated with the photon number state  $|n\rangle$ . In principle, we are not restricted to using the energy eigenstates to characterize the state vector of a radiation mode. However, it is advantageous when calculating the time evolution of the radiation field. It is readily shown that an eigenstate of the Hamiltonian  $\hat{H}$  simply develops a phase factor  $e^{-iE_n(t-t_0)/\hbar}$ , from time  $t_0$  to  $t$ .

$$|\Psi_n(t)\rangle = e^{-iE_n(t-t_0)/\hbar} |\Psi_n(t_0)\rangle, \quad (8.53)$$

since

$$i\hbar \frac{\partial}{\partial t} |\Psi_n\rangle = \hat{H} |\Psi_n\rangle = E_n |\Psi_n\rangle.$$

With the radiation field quantized, we have simultaneously turned the electromagnetic field into operators in terms of the creation operator and the annihilation operator:

$$\begin{aligned}\hat{\mathbf{A}}(\mathbf{r}, t) &= \sum_{\mathbf{k}} \hat{\mathbf{e}}_{\mathbf{k}} \mathcal{A}_{\mathbf{k}} [\hat{a}_{\mathbf{k}}(t) e^{i\mathbf{k}\cdot\mathbf{r}} + \hat{a}_{\mathbf{k}}^\dagger(t) e^{-i\mathbf{k}\cdot\mathbf{r}}], \\ \hat{\mathbf{E}}(\mathbf{r}, t) &= \sum_{\mathbf{k}} \hat{\mathbf{e}}_{\mathbf{k}} \mathcal{E}_{\mathbf{k}} [i \hat{a}_{\mathbf{k}}(t) e^{i\mathbf{k}\cdot\mathbf{r}} - i \hat{a}_{\mathbf{k}}^\dagger(t) e^{-i\mathbf{k}\cdot\mathbf{r}}], \\ \hat{\mathbf{B}}(\mathbf{r}, t) &= \sum_{\mathbf{k}} (\mathbf{k} \times \hat{\mathbf{e}}_{\mathbf{k}}) \mathcal{B}_{\mathbf{k}} [i \hat{a}_{\mathbf{k}}(t) e^{i\mathbf{k}\cdot\mathbf{r}} - i \hat{a}_{\mathbf{k}}^\dagger(t) e^{-i\mathbf{k}\cdot\mathbf{r}}].\end{aligned}\quad (8.54)$$

We usually write the field operator into two parts:

$$\begin{aligned}\hat{\mathbf{E}}(\mathbf{r}, t) &= \sum_{\mathbf{k}} \hat{\mathbf{e}}_{\mathbf{k}} i \mathcal{E}_{\mathbf{k}} \hat{a}_{\mathbf{k}}(t) e^{i\mathbf{k}\cdot\mathbf{r}} + \sum_{\mathbf{k}} \hat{\mathbf{e}}_{\mathbf{k}} (-i) \mathcal{E}_{\mathbf{k}} \hat{a}_{\mathbf{k}}^\dagger(t) e^{-i\mathbf{k}\cdot\mathbf{r}} \\ &= \hat{\mathbf{E}}^{(+)}(\mathbf{r}, t) + \hat{\mathbf{E}}^{(-)}(\mathbf{r}, t)\end{aligned}\quad (8.55)$$

where  $\hat{\mathbf{E}}^{(+)}(\mathbf{r}, t)$  and  $\hat{\mathbf{E}}^{(-)}(\mathbf{r}, t)$  contain the annihilation and creation operators, respectively.

Notice in the above analysis we have simplified the mathematics by assuming a large but finite cubic cavity and by applying the plane-wave solutions. In certain experimental situations, the plane-wave solutions may need to be generalized for different size, shape, and nature of boundaries. We then replace the plane-wave solutions with the generalized spatial mode functions  $\mathbf{u}_k(\mathbf{r})$  in Equation 8.20:

$$\mathbf{A}(\mathbf{r}, t) = A_0 \sum_{\mathbf{k}} \mathbf{A}_{\mathbf{k}}(t) \mathbf{u}_k(\mathbf{r}), \quad (8.56)$$

corresponding to the excited frequency  $\omega_k$ .  $\mathbf{u}_k(\mathbf{r})$  must be a solution to the Helmholtz equation

$$\nabla^2 \mathbf{u}_k + \frac{\omega_k^2}{c^2} \mathbf{u}_k = 0 \quad (8.57)$$

subject to the corresponding boundary conditions. We further require that the mode functions form a complete orthonormal set

$$\int d\mathbf{r}^3 \mathbf{u}_l^*(\mathbf{r}) \mathbf{u}_m(\mathbf{r}) = \delta_{lm}, \quad (8.58)$$

with the condition

$$\nabla \cdot \mathbf{u}_k(\mathbf{r}) = 0.$$

Using the above three equations and the boundary conditions, we find a suitable set of mode functions for the field quantization. The non-plane-wave solutions will be used in later chapters.

In summary, we have quantized the electromagnetic field. We started from classical Maxwell equations and ended with a quantized electromagnetic field. The Maxwell equations require wave solutions of the electromagnetic field with a discrete or continual mode structure according to Equation 8.21, subject to certain boundary conditions. Quantum mechanics, in addition, quantized the energy of each mode of the radiation field according to Equation 8.40. Thus, there are two important physical concepts characterized by the state of the field: the mode distribution and the quantized energy of each mode. The electromagnetic field,  $\hat{\mathbf{E}}(\mathbf{r}, t)$  and  $\hat{\mathbf{B}}(\mathbf{r}, t)$ , are treated as operators in terms of the annihilation and creation operators.

## 8.4 Photon Number State of Radiation Field

By applying the creation operators, we have generated a set of normalized photon number states, which are eigenstates of the Hamiltonian in Equation 8.51 for mode  $\mathbf{k}$  and polarization  $\hat{\mathbf{e}}_k$ . These energy eigenstates form a complete, orthonormal vector space for characterizing the radiation field, or for characterizing the state of light quanta. We now proceed to generalize our discussion to multimode radiation. We will show that the generalized Fock state of Equation 8.59 is an eigenstate of the multimode Hamiltonian in Equation 8.40. In addition, we introduce a useful operator, namely, the total photon number operator,  $\hat{n}$ , in Equation 8.61.

The generalized multimode photon number state, or Fock state of the radiation field is written as

$$|\Psi\rangle = \prod_{\mathbf{k},s} |n_{\mathbf{k},s}\rangle = \prod_{\mathbf{k},s} \frac{1}{\sqrt{n_{\mathbf{k},s}!}} (\hat{a}_{\mathbf{k},s}^\dagger)^n |0\rangle \quad (8.59)$$

where  $\mathbf{k}$  and  $s$  indicate the mode and the polarization. Equation 8.59 defines the state for all and for each radiation mode and polarization.

It follows immediately that the multimode Fock state of Equation 8.59 is an eigenstate of the single-mode photon number operator  $\hat{n}_{\mathbf{k},s}$

$$\hat{n}_{\mathbf{k},s} \left( \prod_{\mathbf{k},s} |n_{\mathbf{k},s}\rangle \right) = n_{\mathbf{k},s} \prod_{\mathbf{k},s} |n_{\mathbf{k},s}\rangle, \quad (8.60)$$

where  $n_{\mathbf{k},s}$  is the occupation number of the radiation mode,  $\mathbf{k}$ , and polarization,  $s$ . We now define a total photon number operator,  $\hat{n}$ , by summing  $\hat{n}_{\mathbf{k},s}$  over all the radiation modes,  $\mathbf{k}$ , and all the polarizations,  $s$ ,

$$\hat{n} = \sum_{\mathbf{k},s} \hat{n}_{\mathbf{k},s}. \quad (8.61)$$

It is easy to find that the multimode Fock state of Equation 8.59 is an eigenstate of the total photon number operator,

$$\hat{n} \left( \prod_{\mathbf{k},s} |n_{\mathbf{k},s}\rangle \right) = \left( \sum_{\mathbf{k},s} n_{\mathbf{k},s} \right) \prod_{\mathbf{k},s} |n_{\mathbf{k},s}\rangle = n \prod_{\mathbf{k},s} |n_{\mathbf{k},s}\rangle, \quad (8.62)$$

where  $n = \sum n_{\mathbf{k},s}$  is the total number of photons in the radiation field.

It is easy to show that the multimode Fock state of Equation 8.59 is an eigenstate of the total Hamiltonian (multimode) in Equation 8.40,

$$\begin{aligned} \hat{H} |\Psi\rangle &= \left[ \sum_{\mathbf{k},s} \hbar\omega_{\mathbf{k},s} \left( \hat{n}_{\mathbf{k},s} + \frac{1}{2} \right) \right] \left( \prod_{\mathbf{k},s} |n_{\mathbf{k},s}\rangle \right) \\ &= \left[ \sum_{\mathbf{k},s} \hbar\omega_{\mathbf{k},s} \left( n_{\mathbf{k},s} + \frac{1}{2} \right) \right] \left( \prod_{\mathbf{k},s} |n_{\mathbf{k},s}\rangle \right) \\ &= E |\Psi\rangle, \end{aligned} \quad (8.63)$$

where  $E = \sum \hbar\omega_{\mathbf{k},s} (n_{\mathbf{k},s} + \frac{1}{2})$  is the total energy of the radiation.

For convenience, we define a short-hand notation  $\{n\}$  and rewrite the multimode Fock state of Equation 8.59 as

$$|\{n\}\rangle \equiv \prod_{\mathbf{k},s} |n_{\mathbf{k},s}\rangle. \quad (8.64)$$

Equation 8.62 is then rewritten, in short-hand form, as

$$\hat{n} |\{n\}\rangle = n |\{n\}\rangle, \quad (8.65)$$

which simply indicates that the multimode Fock state  $|\{n\}\rangle$  is an eigenstate of the total number operator,  $\hat{n}$ , defined in Equation 8.61 with an eigenvalue of  $n$ , which is the total number of photons in the radiation field.

The eigenvalue,  $n$ , of the total number operator, is commonly used to name the Fock state, either single-mode or multimode, as an  $n$ -photon state.

For instance, the state

$$|\Psi\rangle = \hat{a}_{\mathbf{k},s}^\dagger |0\rangle = |\dots 0, 1_{\mathbf{k},s}, 0, \dots\rangle \quad (8.66)$$

is a *single-photon* state ( $n = 1$ ) with an excited mode  $\mathbf{k}$  and polarization  $s$ . The states

$$|\Psi\rangle = \hat{a}_{\mathbf{k},s}^\dagger \hat{a}_{\mathbf{k}',s'}^\dagger |0\rangle = |\dots 0, 1_{\mathbf{k},s}, 0, \dots 1_{\mathbf{k}',s'}, 0, \dots\rangle \quad (8.67)$$

and

$$|\Psi\rangle = \frac{1}{\sqrt{2}} (\hat{a}_{\mathbf{k},s}^\dagger)^2 |0\rangle = |\dots 0, 2_{\mathbf{k},s}, 0, \dots\rangle \quad (8.68)$$

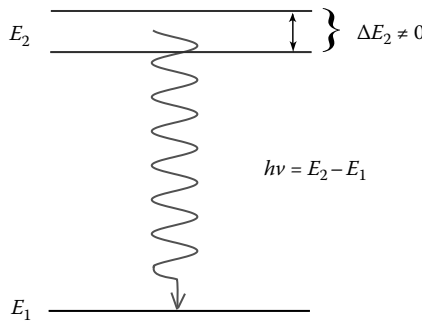
are both *two-photon states* ( $n = 2$ ) but characterize different physics. The state in Equation 8.67 indicates the excitation of two different radiation modes with occupation numbers  $n_{\mathbf{k},s} = 1$  and  $n_{\mathbf{k}',s'} = 1$ . The state in Equation 8.68 indicates the excitation of a radiation mode with occupation number  $n_{\mathbf{k},s} = 2$ . Such states in Equations 8.66 through 8.68 are all known as Fock states, or photon number states.

In connection with the concept of photons, Equation 8.66 indicates the excitation of one quantum of energy  $\hbar\omega_{\mathbf{k},s}$ , or a photon, to the radiation mode  $\mathbf{k}$  and polarization  $s$ . Equation 8.67 means the excitation of two photons with energies  $\hbar\omega_{\mathbf{k},s}$  and  $\hbar\omega_{\mathbf{k}',s'}$ , respectively, to the radiation mode  $\mathbf{k}$ -polarization  $s$  and the radiation mode  $\mathbf{k}'$ -polarization  $s'$ . Equation 8.68 corresponds to the excitation of two photons both with energy of  $\hbar\omega_{\mathbf{k},s}$  to the same radiation mode  $\mathbf{k}$  and polarization  $s$ . For convenience, sometimes we label the single-photon state of Equation 8.66 as  $|1_{\mathbf{k},s}\rangle$ , the two-photon state of Equation 8.67 as  $|1_{\mathbf{k},s} 1_{\mathbf{k}',s'}\rangle$ , and the two-photon state of Equation 8.68 as  $|2_{\mathbf{k},s}\rangle$ . Thus, the state of Equation 8.66 is described as a state of one-photon with wavevector  $\mathbf{k}$  and polarization  $s$ . The state in Equation 8.67 is described as a state of two photons, one with wavevector  $\mathbf{k}$  and polarization  $s$  and the other one with wavevector  $\mathbf{k}'$  and polarization  $s'$ . The state in Equation 8.68 is also described as a state of two photons, however, both with wavevector  $\mathbf{k}$  and polarization  $s$ . The two photons are "indistinguishable" or "degenerate."

Since Fock states form a complete, orthonormal vector space, following the rules of quantum mechanics, we are able to express any state vector of a radiation field in terms of a superposition of Fock states, or photon number states,

$$|\Psi\rangle = \sum_j c_j |\Psi_j\rangle = \sum_{\{n\}} f(\{n\}) |\{n\}\rangle, \quad (8.69)$$

where  $f(\{n\})$  is the normalized probability amplitude to find the radiation field in the state  $|\{n\}\rangle$ .

**FIGURE 8.6**

Schematic model of a possible atomic transition that generates the single-photon state, or wavepacket, characterized by Equation 8.70. A two level atom is placed inside a large but finite-sized cubic cavity. The upper energy level  $E_2$  has a finite width of  $\Delta E_2 \neq 0$ . The emitted photon may be in any, or in all permissible states, of  $|\Psi_j\rangle = \hat{a}_{\mathbf{k},s}^\dagger |0\rangle$  with probability amplitude  $f(\mathbf{k},s)$ .

As an example, Equation 8.70 represents a single-photon state:

$$|\Psi\rangle = \sum_j c_j |\Psi_j\rangle = \sum_{\mathbf{k},s} f(\mathbf{k},s) \hat{a}_{\mathbf{k},s}^\dagger |0\rangle \quad (8.70)$$

where  $c_j = f(\mathbf{k},s) = \langle \Psi_j | \Psi \rangle$  is the normalized probability amplitude for the radiation field to be in the Fock state  $|\Psi_j\rangle = |1_{\mathbf{k},s}\rangle = \hat{a}_{\mathbf{k},s}^\dagger |0\rangle$ . The state of Equation 8.70 is a pure state. It is a vector in the form of linear superposition of a special set of Fock states,  $|\Psi_j\rangle = |\dots 0, 1_{\mathbf{k},s}, 0, \dots\rangle$ , of total occupation number  $n = 1$ . The single-photon state of Equation 8.70 can be generated from a two-level atomic transition. Figure 8.6 illustrates a simple model of the process. A two level atom is placed inside a large but finite size cubic cavity. The upper energy level  $E_2$  has a finite width of  $\Delta E_2 \neq 0$ . A single-photon, or wavepacket, is emitted from the atomic transition from  $E_2$  to  $E_1$ . The created photon may excite any or excite all permissible states  $|\Psi_j\rangle = \hat{a}_{\mathbf{k},s}^\dagger |0\rangle$  with probability amplitude  $f(\mathbf{k},s)$ . The space-time behavior of each permissible radiation mode is determined by the boundary condition in solving the Maxwell equations. The probability amplitude distribution is determined by the property of the atomic transition and the property of the cavity, mainly the energy uncertainty  $\Delta E_2$ .

What can we learn from Equation 8.70 about the radiation field?

1. The field is characterized by a pure state, which means the field is prepared identically, in the same state, for each and for all measurements of an ensemble.

2. The radiation contains a set of possible excited modes  $(\mathbf{k}, s)$  with occupation number  $n_{\mathbf{k},s} = 1$  and with probability amplitude  $f(\mathbf{k}, s)$ . The radiation field is expressed as the superposition of a special set of Fock states of total photon number,  $n = 1$ .
3. The state of the field is not an eigenstate of the number operator  $\hat{n}_{\mathbf{k},s}$ . The mean occupation number of the mode  $(\mathbf{k}, s)$  is calculated as

$$\langle \Psi | \hat{n}_{\mathbf{k},s} | \Psi \rangle = |f(\mathbf{k}, s)|^2,$$

which equals the probability of exciting the mode  $(\mathbf{k}, s)$ .

4. The state of the field is an eigenstate of the total number operator  $\hat{n} = \sum_{\mathbf{k},s} \hat{n}_{\mathbf{k},s}$  with eigenvalue  $n = 1$ :

$$\hat{n} | \Psi \rangle = \sum_{\mathbf{k}',s'} \hat{n}_{\mathbf{k}',s'} \sum_{\mathbf{k},s} f(\mathbf{k}, s) \hat{a}_{\mathbf{k},s}^\dagger | 0 \rangle = 1 \sum_{\mathbf{k},s} f(\mathbf{k}, s) \hat{a}_{\mathbf{k},s}^\dagger | 0 \rangle.$$

5. The state of the field is not an eigenstate of the Hamiltonian  $\hat{H}_{\mathbf{k},s}$ . The mean energy of the mode  $(\mathbf{k}, s)$  is calculated as

$$\langle \Psi | \hat{H}_{\mathbf{k},s} | \Psi \rangle = |f(\mathbf{k}, s)|^2 \hbar \omega_{\mathbf{k},s}.$$

6. The state of the field is not an eigenstate of the total Hamiltonian  $\hat{H} = \sum_{\mathbf{k},s} \hat{H}_{\mathbf{k},s}$ . The expectation value of the total Hamiltonian, or the mean energy of the radiation, is calculated as

$$\langle \Psi | \hat{H} | \Psi \rangle = \sum_{\mathbf{k},s} |f(\mathbf{k}, s)|^2 \hbar \omega_{\mathbf{k},s},$$

which is the mean value of all possible quantized energy  $\hbar \omega_{\mathbf{k},s}$ , averaged statistically with a weighting function  $|f(\mathbf{k}, s)|^2$ .

What can we say about the state of Equation 8.70 in terms of the concept of photon?

1. Equation 8.70 is a pure single-photon state that characterizes the state of a photon and the state of an homogenous ensemble of identical photons.
2. The photon is not in any defined single-mode Fock state but has a certain probability to be in any or in all single-mode Fock state of  $n = 1$  within the superposition.
3. The photon does not have any defined energy of  $\hbar \omega$ , but may take any or all possible values of  $\hbar \omega_{\mathbf{k},s}$  within the superposition.

4. The photon is localized within a wavepacket, which is a vector in the Hilbert space.\*
  5. The wavepacket carries an amount of energy  $\sum_{\mathbf{k},s} |f(\mathbf{k},s)|^2 \hbar \omega_{\mathbf{k},s}$ , however, the energy of the localized photon is allowed only to take values of  $\hbar \omega_{\mathbf{k},s}$ .†
- 

## 8.5 Coherent State of Radiation Field

Coherent state is defined as the eigenstate of the annihilation operator

$$\hat{a}|\alpha\rangle = \alpha|\alpha\rangle. \quad (8.71)$$

It is convenient to write the eigenvalue  $\alpha$  in terms of an amplitude and a phase

$$\alpha = a e^{i\varphi} \text{ with } a = |\alpha|.$$

Coherent states form a complete set of vector space. Similar to number states, coherent states can be used as a vector basis for characterizing radiation field, except coherent states are nonorthogonal vectors in general. It is straightforward to obtain an expression of  $|\alpha\rangle$  in terms of the number state  $|n\rangle$  from Equation 8.71

$$|\alpha\rangle = e^{-|\alpha|^2/2} \sum_{n=0}^{\infty} \frac{\alpha^n}{\sqrt{n!}} |n\rangle, \quad (8.72)$$

by applying

$$\hat{a}|n\rangle = \sqrt{n}|n-1\rangle.$$

Since

$$|n\rangle = \frac{1}{\sqrt{n!}} (\hat{a}^\dagger)^n |0\rangle,$$

---

\* This statement is different from the statement of “photon is a wavepacket.” Perhaps, a more careful statement should be as follows: the created photon excites radiation field in the form of a localized wavepacket. Moreover, in certain measurements, the state of a photon may be described by a set of wavepackets, which means that a photon can be localized within a set of wavepackets.

† Perhaps, a more careful statement should be as follows: the photon has a certain probability of carrying energy  $\hbar \omega_{\mathbf{k},s}$ .

Equation 8.72 can be written as

$$|\alpha\rangle = e^{-|\alpha|^2/2} e^{\alpha\hat{a}^\dagger} |0\rangle. \quad (8.73)$$

Equation 8.73 is thus formally rewritten as

$$|\alpha\rangle = e^{-|\alpha|^2/2} e^{\alpha\hat{a}^\dagger} e^{-\alpha^*\hat{a}} |0\rangle = e^{\alpha\hat{a}^\dagger - \alpha^*\hat{a}} |0\rangle, \quad (8.74)$$

since

$$e^{-\alpha^*\hat{a}} |0\rangle = 0,$$

and

$$e^{\hat{A}+\hat{B}} = e^{[\hat{A}, \hat{B}]/2} e^{\hat{A}} e^{\hat{B}},$$

where  $\hat{A}$  and  $\hat{B}$  are any operators that satisfy

$$[[\hat{A}, \hat{B}], \hat{A}] = [[\hat{A}, \hat{B}], \hat{B}] = 0.$$

Here, we have taken  $\hat{A} = \alpha\hat{a}^\dagger$ ,  $\hat{B} = -\alpha^*\hat{a}$ . By writing  $|\alpha\rangle$  in the form of Equation 8.74, we introduced a unitary operator, namely, the displacement operator

$$\hat{D}(\alpha) = e^{\alpha\hat{a}^\dagger - \alpha^*\hat{a}} = e^{-|\alpha|^2/2} e^{\alpha\hat{a}^\dagger} e^{-\alpha^*\hat{a}} = e^{|\alpha|^2/2} e^{-\alpha^*\hat{a}} e^{\alpha\hat{a}^\dagger},$$

for the purpose of expressing  $|\alpha\rangle$  as a unitary transformation of  $|0\rangle$ :

$$|\alpha\rangle = \hat{D}(\alpha) |0\rangle. \quad (8.75)$$

Equation 8.75 is useful for certain theoretical concerns and discussions about coherent state.

Some important properties of the coherent state are as follows:

1. The mean number of photons in the coherent state  $|\alpha\rangle$  is  $|\alpha|^2$ :

$$\bar{n} = \langle \hat{n} \rangle = \langle \alpha | \hat{n} | \alpha \rangle = |\alpha|^2, \quad (8.76)$$

and the probability of finding  $n$  photons in  $|\alpha\rangle$  is given by a Poisson distribution

$$P(n) = \langle n | \alpha \rangle \langle \alpha | n \rangle = \frac{\bar{n}^n}{n!} e^{-\bar{n}}. \quad (8.77)$$

The photon number distribution of laser light is close to the Poisson distribution. The Poisson distribution is useful for simulating single-photon state. For instance, reducing the intensity of a laser field to mean number  $\bar{n} = 0.01$ ,

we find that the field has  $\sim 99\%$  probability to be in its ground state  $|0\rangle$ , the probability of being in  $|1\rangle$  and in  $|2\rangle$  are  $\sim 1\%$  and  $\sim 0.01\%$ , respectively. For a photon-counting-type experiment with  $1\%$  error, the contributions from  $|2\rangle$  and higher numbers are ignorable. Taking first-order approximation, the state of the measured field can be approximated as

$$|\Psi\rangle \simeq |0\rangle + \epsilon |1\rangle + \epsilon^2 \dots$$

where  $\epsilon \ll 1$ . The Poisson distribution is also useful for simulating number state of  $n \gg 1$ . For instance, achieving mean number of  $\bar{n} = 10^6$ , its photon number distribution has a peak at  $n = 10^6$  with  $\Delta n \sim 10^3$  which is three-orders smaller than  $\bar{n}$ .

2. The vector set of coherent states  $|\alpha\rangle$  is a complete set in Hilbert space:

$$\frac{1}{\pi} \int d^2\alpha |\alpha\rangle\langle\alpha| = 1. \quad (8.78)$$

The completeness relation of Equation 8.78 indicates that the coherent states can be used as a vector basis for expanding any quantum state of radiation. To prove this, we substitute the number state expansion of the coherent state into the integral, obtaining

$$\int d^2\alpha |\alpha\rangle\langle\alpha| = \int d^2\alpha e^{-|\alpha|^2} \frac{\alpha^n (\alpha^*)^n}{n!} \sum_n |n\rangle\langle n| = \pi \sum_n |n\rangle\langle n|, \quad (8.79)$$

where we have applied the result of the following integral\*

$$\int d^2\alpha e^{-|\alpha|^2} \frac{\alpha^n (\alpha^*)^n}{n!} = \pi.$$

Since the Fock states  $|n\rangle$  form a complete orthonormal set of vector basis, the sum in Equation 8.79 gives the unit operator.

3. Two coherent states  $|\alpha\rangle$  and  $|\alpha'\rangle$  are not orthogonal unless  $|\alpha - \alpha'| \gg 1$ ,

$$\langle\alpha|\alpha'\rangle = e^{-\frac{1}{2}(|\alpha|^2 - 2\alpha^*\alpha' + |\alpha'|^2)}, \quad (8.80)$$

and

$$|\langle\alpha|\alpha'\rangle|^2 = e^{-|\alpha-\alpha'|^2}. \quad (8.81)$$

---

\*  $\int d^2\alpha e^{-|\alpha|^2} \alpha^m (\alpha^*)^n = \int_0^\infty d|\alpha| e^{-|\alpha|^2} |\alpha|^{m+n+1} \int_0^{2\pi} d\varphi e^{i(m-n)\varphi} = \pi n! \delta_{mn}$ .

This means that the vector basis of coherent states is in principle overcomplete. However, if the experimental condition achieves  $|\alpha - \alpha'| \gg 1$  the set of coherent states can be approximated as orthonormal.

4. Similar to photon number state, we can define a multimode coherent state, which is written as a product of single-mode coherent state  $|\alpha_{\mathbf{k},s}\rangle$

$$|\{\alpha\}\rangle = \prod_{\mathbf{k},s} |\alpha_{\mathbf{k},s}\rangle, \quad (8.82)$$

where  $\mathbf{k}$  and  $s$  indicate the wavenumber vector and the polarization of the mode, respectively.  $|\{\alpha\}\rangle$  is an eigenstate of the annihilation operator with an eigenvalue  $\alpha_{\mathbf{k},s}$ ,

$$\hat{a}_{\mathbf{k},s} |\{\alpha\}\rangle = \alpha_{\mathbf{k},s} |\{\alpha\}\rangle. \quad (8.83)$$

Similar to the discussion for number state, we may also define a multimode annihilation operator

$$\hat{a} = \sum_{\mathbf{k},s} \hat{a}_{\mathbf{k},s}. \quad (8.84)$$

It is easy to find that the multimode coherent state defined in Equation 8.82 is an eigenstate of the multimode annihilation operator with eigenvalue  $\sum_{\mathbf{k},s} \alpha_{\mathbf{k},s}$

$$\hat{a} |\{\alpha\}\rangle = \left( \sum_{\mathbf{k},s} \hat{a}_{\mathbf{k},s} \right) \prod_{\mathbf{k},s} |\alpha_{\mathbf{k},s}\rangle = \left( \sum_{\mathbf{k},s} \alpha_{\mathbf{k},s} \right) |\{\alpha\}\rangle. \quad (8.85)$$

Similar to the number state, we may construct a two-mode coherent state

$$|\Psi\rangle = |0, \dots, 0, \alpha_{\mathbf{k},s}, 0, \dots, \alpha_{\mathbf{k}',s'}, 0, \dots\rangle, \quad (8.86)$$

which is an eigenstate of  $(\sum_{\mathbf{k},s} \hat{a}_{\mathbf{k},s})$  with eigenvalue  $(\alpha_{\mathbf{k},s} + \alpha_{\mathbf{k}',s'})$ ,

$$\begin{aligned} & \left( \sum_{\mathbf{k},s} \hat{a}_{\mathbf{k},s} \right) |0, \dots, 0, \alpha_{\mathbf{k},s}, 0, \dots, \alpha_{\mathbf{k}',s'}, 0, \dots\rangle \\ &= (\alpha_{\mathbf{k},s} + \alpha_{\mathbf{k}',s'}) |0, \dots, 0, \alpha_{\mathbf{k},s}, 0, \dots, \alpha_{\mathbf{k}',s'}, 0, \dots\rangle. \end{aligned}$$

## 8.6 Density Operator and Density Matrix

For a pure state, the expectation value of an observable (operator) is easily calculated as

$$\langle \hat{A} \rangle_{QM} = \langle \Psi | \hat{A} | \Psi \rangle. \quad (8.87)$$

Unfortunately, we are not always dealing with pure states. In certain experiments, the state of the radiation field can only be described statistically. We have to deal with mixed states. In this case, a density operator will be defined to characterize the probability distribution of the field. In addition to the quantum average, an ensemble average will be necessary in the expectation value calculations of an observable. The density operator is defined as follows: suppose the field has a probability  $P_j$  of being in the state  $|\Psi_j\rangle$ , the expectation value of an observable  $\hat{A}$  is calculated as an ensemble average

$$\langle\langle \hat{A} \rangle \rangle_{\text{Ensemble}} = \sum_j P_j \langle \Psi_j | \hat{A} | \Psi_j \rangle. \quad (8.88)$$

Applying completeness  $\sum_n |n\rangle \langle n| = 1$

$$\begin{aligned} \langle\langle \hat{A} \rangle \rangle_{\text{Ensemble}} &= \sum_n \sum_j P_j \langle \Psi_j | \hat{A} | n \rangle \langle n | \Psi_j \rangle \\ &= \sum_n \sum_j P_j \langle n | \Psi_j \rangle \langle \Psi_j | \hat{A} | n \rangle \\ &= \sum_n \langle n | \hat{\rho} \hat{A} | n \rangle. \end{aligned} \quad (8.89)$$

We thus introduce the density operator to specify radiation field statistically

$$\hat{\rho} = \sum_j P_j |\Psi_j\rangle \langle \Psi_j|. \quad (8.90)$$

Following Equation 8.89, the expectation value of an observable is then calculated as

$$\langle \hat{A} \rangle = \text{tr } \hat{\rho} \hat{A}, \quad (8.91)$$

where *tr* means trace of a matrix. Since any state  $|\Psi_j\rangle$  can be expanded in terms of a chosen vector basis, the density operator  $\hat{\rho}$  is also able to be expanded in terms of a chosen vector basis such as photon number states, coherent states, etc.,

$$\hat{\rho} = \sum_m \sum_n \sum_j P_j |m\rangle \langle m| |\Psi_j\rangle \langle \Psi_j| |n\rangle \langle n| \equiv \sum_m \sum_n \rho_{mn} |m\rangle \langle n|. \quad (8.92)$$

Equation 8.92 defines the density matrix.

Some useful properties of the density matrix are as follows:

1.  $\rho_{mm} \geq 0$ .

The diagonal elements of the density matrix are real, and non-negative. This follows immediately from  $\rho_{mm} = \langle m|\Psi_j\rangle \langle \Psi_j|m \rangle = |\langle m|\Psi_j\rangle|^2 \geq 0$ .

2.  $\sum_m \rho_{mm} = 1$  or  $\text{tr } \hat{\rho} = 1$ .

The density matrix is defined in terms of the normalized states,  $|\Psi_j\rangle$ , and the probability distribution of the field,  $P_j$ . This makes the interpretation of the diagonal elements as probabilities valid. It is obvious  $\rho_{mm} < 1$  for a mixed state. Pure state can be treated as a special case of mixed state in which the field is in the state  $|\Psi\rangle$  with certainty ( $P = 1$ ).

3.  $\rho_{mn}^* = \rho_{nm}$  or  $\hat{\rho}^\dagger = \hat{\rho}$ .

This means that the density matrix is Hermitian. Since the density matrix is Hermitian, it can be diagonalized by a unitary transformation. In this book, we will choose photon number state as the basis. Photon number states are the eigenstates of the Hamiltonian. The time evolution of photon number states involves phase propagation only in optical measurements. This property is useful for the propagation of the state or the operator. We will show in the next few sections that the density matrix of chaotic-thermal light only has diagonal elements in the basis of photon number states.

4.  $\hat{\rho}^2 = \hat{\rho}$  for pure state.

This property is easy to prove and is useful for distinguishing pure states from mixed states.

The following is an example of a density matrix that describes a single-photon mixed state:

$$\hat{\rho} = \sum_j P_j |\Psi_j\rangle \langle \Psi_j| = \sum_{\mathbf{k}, s} |f(\mathbf{k}, s)|^2 \hat{a}_{\mathbf{k}, s}^\dagger |0\rangle \langle 0| \hat{a}_{\mathbf{k}, s}, \quad (8.93)$$

where

$$\sum_j P_j = 1$$

$P_j = |f(\mathbf{k}, s)|^2$  is the probability of being in the Fock state  $|\Psi_j\rangle = \hat{a}_{\mathbf{k}, s}^\dagger |0\rangle$

It should be emphasized that the mixed state of Equation 8.93 is very different from the pure state of Equation 8.70, although a similar mode

distribution function may apply to both cases. One may find out the differences in mathematics and in physics from the following expectation value evaluations. To simplify the notation, we make the calculation in continuous 1D spectrum and for one polarization.

1. Coherent superposition (pure state) vs. incoherent mixture (mixed state):

$$\begin{aligned}\langle \hat{A} \rangle_{|\Psi\rangle} &= \langle \Psi | \hat{A} | \Psi \rangle \\ &= \iint d\omega d\omega' f^*(\omega) f(\omega') \langle 0 | \hat{a}(\omega) \hat{A} \hat{a}^\dagger(\omega') | 0 \rangle\end{aligned}\quad (8.94)$$

$$\begin{aligned}\langle \hat{A} \rangle_{\hat{\rho}} &= \text{tr } \hat{\rho} \hat{A} \\ &= \int d\omega |f(\omega)|^2 \langle 0 | \hat{a}(\omega) \hat{A} \hat{a}^\dagger(\omega) | 0 \rangle.\end{aligned}\quad (8.95)$$

In Equation 8.94 all off-diagonal elements may have their contribution; however, in Equation 8.95 only the diagonal elements contribute to the evaluation. Mathematically, the difference is clear. Physically, the two expectation value evaluations deal with different states and consequently deal with different type of averages, i.e.,  $\langle \hat{A} \rangle_{QM}$  vs.  $\langle \langle \hat{A} \rangle_{QM} \rangle_{\text{Ensemble}}$ .

2. Coherently superposed wavepackets vs. incoherently superposed (mixed) wavepackets. Suppose the state of the field can be formally written as a superposition of a large number of identical wavepackets, each labeled by its initial phase  $\varphi_j(\omega)$ :

$$|\Psi\rangle = \sum_j \int d\omega |f(\omega)| e^{i\varphi_j(\omega)} \hat{a}_j^\dagger(\omega) |0\rangle. \quad (8.96)$$

To simplify the notation, we have assumed identical amplitude distribution  $|f(\omega)|$  for all wavepackets. The expectation value of an observable is calculated formally as follows:

$$\begin{aligned}\langle \hat{A} \rangle_{QM} &= \left[ \sum_j \int d\omega |f(\omega)| e^{-i\varphi_j(\omega)} \langle 0 | \hat{a}_j(\omega) \right] \hat{A} \left[ \sum_k \int d\omega' |f(\omega')| e^{i\varphi_k(\omega')} \hat{a}_k^\dagger(\omega') |0\rangle \right] \\ &= \sum_j \sum_k \iint d\omega d\omega' |f(\omega)| |f(\omega')| e^{-i[\varphi_j(\omega) - \varphi_k(\omega')]} \langle 0 | \hat{a}_j(\omega) \hat{A} \hat{a}_k^\dagger(\omega') | 0 \rangle.\end{aligned}\quad (8.97)$$

The evaluation is now depending on the result of the sum and the integral. For coherent superposition,  $\varphi_j(\omega) - \varphi_k(\omega') = \text{constant}$ , all terms survive and

contribute to the expectation value; however, if  $\varphi_j(\omega) - \varphi_k(\omega')$  takes random values in terms of  $j, k$  and  $\omega, \omega'$ , due to destructive cancelation, the only surviving terms are these “diagonal” terms with  $j = k$  and  $\omega = \omega'$

$$\begin{aligned} \langle \langle \hat{A} \rangle_{\text{QM}} \rangle_{\text{Ensemble}} &= \left\langle \sum_j \sum_k \iint d\omega d\omega' |f(\omega)| |f(\omega')| \right. \\ &\quad \times e^{-i[\varphi_j(\omega) - \varphi_k(\omega')]} \langle 0 | \hat{a}_j(\omega) \hat{A} \hat{a}_k^\dagger(\omega') | 0 \rangle \Big\rangle \\ &= \sum_j \int d\omega |f(\omega)|^2 \langle 0 | \hat{a}_j(\omega) \hat{A} \hat{a}_j^\dagger(\omega) | 0 \rangle, \end{aligned} \quad (8.98)$$

where we have treated the sum as an ensemble average by taking into account all possible values of  $\varphi_j(\omega) - \varphi_k(\omega')$ . This treatment is reasonable for a large number of randomly distributed wavepackets. In a realistic experiment, the measurement always deals with large number of wavepackets, and  $\varphi_j(\omega) - \varphi_k(\omega')$  may take any or all possible values if the measured wavepackets are excited in a random manner.

A pure state represents a vector in Hilbert space. If the state of a photon can be described by a vector, the state of the quantum is said to be *pure*. On the contrary, if the state of a quantum cannot be described as a vector, but rather, a mixture of vectors by means of a density matrix, the quantum is said to be in a *mixed state*. In terms of the ensemble measurement, if the state of all the measured photons of the ensemble can be described by the same vector, the state of the ensemble, or the measured photon system, is said to be *homogeneous* or in a statistically *pure state*. In this case, the ensemble average is trivial. If the measured ensemble cannot be described by a vector, we only have the knowledge of finding a certain portion (percentage) of the ensemble to be in a certain state, the ensemble is referred to as *inhomogeneous* or in a statistically *mixed state*. The ensemble average will have nontrivial contribution to the expectation value calculation of an observable. We will have a detailed discussion about pure states and mixed states in Section 8.9.

Now it is possible for us to generalize the concept of density operator for characterizing the state of any radiation field:

$$\hat{\rho} = |\Psi\rangle\langle\Psi|$$

for pure state, and

$$\hat{\rho} = \sum_j P_j |\Psi_j\rangle\langle\Psi_j|$$

for mixed state. The expectation value of an observable is then formally given by

$$\langle \hat{A} \rangle = \text{tr } \hat{\rho} \hat{A}.$$

The density operator can be expanded in terms of any chosen vector basis, such as photon number states:

$$\hat{\rho} = \sum_m \sum_n |m\rangle \langle m| \hat{\rho} |n\rangle \langle n| = \sum_m \sum_n \rho_{mn} |m\rangle \langle n|, \quad (8.99)$$

or coherent states

$$\hat{\rho} = \iint \frac{d^2\alpha}{\pi} \frac{d^2\beta}{\pi} |\alpha\rangle \langle \alpha| \hat{\rho} |\beta\rangle \langle \beta| = \iint \frac{d^2\alpha}{\pi} \frac{d^2\beta}{\pi} \rho_{\alpha\beta} |\alpha\rangle \langle \beta|. \quad (8.100)$$

where  $\rho_{mn}$  and  $\rho_{\alpha\beta}$  describe the distribution of a radiation field in the vector space of photon number state and coherent state, respectively. We thus introduced the concept of density matrix in terms of a chosen vector basis. These concepts are introduced historically for characterizing statistical properties of different radiation fields, such as fluctuations and correlations. Based on the concept of  $\rho_{\alpha\beta}$ , a so-called coherent state representation or P-representation can be further defined to formulate the behavior of a quantized radiation field into the format of classical statistics.\*

It is not the philosophy of this book to treat quantum coherence, especially higher-order coherence, as classical statistical correlation. However, the concept of density operator and density matrix are useful in general and in particular when dealing with chaotic-thermal field which is impossible to be characterized by a state vector in the Hilbert space. In the following a few sections, we will give a simple model of radiation process at the single-photon level and characterize the state of the radiation in general by a density operator. The expectation value of an observable is then evaluated from principle

---

\* It is interesting to see in the literature that the quantized radiation fields are classified as classical and quantum in terms of their P-functions. Thermal field is historically defined as classical because of its positive Gaussian-like P-function. One should not be confused by these definitions when facing multiphoton interference phenomenon of thermal light. According to quantum mechanics, a photon of thermal field does interfere with itself, and a pair of measured photons of thermal field does interfere with the pair itself, despite the possibility of being formulated into the format of classical statistics.

$$\langle \langle \hat{A} \rangle_{\text{QM}} \rangle_{\text{Ensemble}} = \sum_j P_j \langle \Psi_j | \hat{A} | \Psi_j \rangle = \text{tr } \hat{\rho} \hat{A}. \quad (8.101)$$


---

## 8.7 Composite System and Two-Photon State of Radiation Field

In certain experimental measurements, we need to deal with two-photon states, which describe the state of a composite system of two photons. The subsystems may be spatially separated in large distance. Despite the distance between the subsystems, in quantum theory, a composite system composed of two subsystems is described by a Hilbert space constructed as the direct or tensor product of the Hilbert spaces of the two subsystems:

$$H = H_1 \otimes H_2. \quad (8.102)$$

If state  $|\Psi_1\rangle \in H_1$  and state  $|\Psi_2\rangle \in H_2$ , then we denote the direct product of these states by  $|\Psi\rangle = |\Psi_1\rangle \otimes |\Psi_2\rangle$ , or simply  $|\Psi\rangle = |\Psi_1\rangle |\Psi_2\rangle$ . The inner product on  $H$  is defined in terms of the inner product on  $H_1$  and  $H_2$  by

$$\langle \Psi | \Psi' \rangle = \langle \Psi_1 | \Psi'_1 \rangle \langle \Psi_2 | \Psi'_2 \rangle. \quad (8.103)$$

If  $\{|m\rangle\}$  is an orthonormal basis of  $H_1$  and  $\{|n\rangle\}$  is an orthonormal basis of  $H_2$ , then  $\{|m\rangle \otimes |n\rangle\}$  or simply  $\{|m\rangle |n\rangle\}$  is an orthonormal basis of  $H$ . This basis is usually called Schmidt basis.

In a composite system, the subsystems may be independent, correlated, or entangled. For independent subsystems the state of the composite system can be written as a product state

$$|\Psi\rangle = \sum_{m,n} c_m c_n |m\rangle |n\rangle = \sum_m c_m |m\rangle \sum_n c_n |n\rangle = |\Psi_1\rangle \otimes |\Psi_2\rangle, \quad (8.104)$$

where  $c_{mn} = c_m c_n$  is factorizable. When the two subsystems are correlated or entangled, in general,  $|\Psi\rangle$  cannot be written in the form of Equation 8.104, i.e.,  $c_{mn}$  is nonfactorizable and consequently the state is nonfactorizable

$$|\Psi\rangle = \sum_{m,n} c_{mn} |m\rangle |n\rangle. \quad (8.105)$$

We say the two subsystems are in a correlated state or in an entangled state, depending on the form of  $c_{mn}$ .

The simplest two-photon states are the Fock states of Equation 8.67. To simplify the mathematics, we rewrite Equation 8.67 in 1D and ignore the polarization

$$|\Psi\rangle = \hat{a}_1^\dagger(\omega) \hat{a}_2^\dagger(\omega') |0\rangle = |\dots 0, 1_1(\omega), 0, \dots\rangle |\dots 0, 1_2(\omega'), 0, \dots\rangle, \quad (8.106)$$

where we have also rewritten the state explicitly as that of a composite two subsystems. In general, we may deal with a set of two-photon Fock states either in a coherent superposition

$$|\Psi\rangle = \sum_{\omega} \sum_{\omega'} f(\omega, \omega') \hat{a}_1^\dagger(\omega) \hat{a}_2^\dagger(\omega') |0\rangle, \quad (8.107)$$

or in a incoherent mixture

$$\hat{\rho} = \sum_{\omega} \sum_{\omega'} |f(\omega, \omega')|^2 \hat{a}_1^\dagger(\omega) \hat{a}_2^\dagger(\omega') |0\rangle \langle 0| \hat{a}(\omega) \hat{a}(\omega'), \quad (8.108)$$

where  $f(\omega, \omega')$  is the probability amplitude for the quantized field to be in the two-photon Fock state  $|\dots 0, 1_\omega, 0, \dots\rangle |\dots 0, 1_{\omega'}, 0, \dots\rangle$ . The two-photon probability amplitude  $f(\omega, \omega')$  may be factorizable into a product of  $f_1(\omega) \times f_2(\omega')$ , or nonfactorizable at all. The physical properties of the states are very different between these two cases. If  $f(\omega, \omega')$  can be factorized into a product of  $f_1(\omega) \times f_2(\omega')$ , the state itself is also factorizable into a product state of two independent single-photons. If  $f(\omega, \omega')$  is nonfactorizable and consequently the state itself cannot be factorized into a product state, we name the state a correlated or an entangled two-photon state. In terms of the concept of a photon, the product states describe the behavior of two independent photons, the correlated states describe the behavior of two correlated photons, and the entangled states characterize the behavior of an entangled pair of photons. Below are three examples showing factorizable or nonfactorizable probability amplitudes. We will have a detailed study of entangled states in later chapters.

**Example (I): Product state**

Equation 8.109 is a two-photon state, which can be factorized into a product of two single-photon states:

$$|\Psi\rangle = \sum_{\omega} \sum_{\omega'} f(\omega) f'(\omega') \hat{a}_1^\dagger(\omega) \hat{a}_2^\dagger(\omega') |0\rangle \quad (8.109)$$

$$= \sum_{\omega} f(\omega) \hat{a}_1^\dagger(\omega) |0\rangle \times \sum_{\omega'} f'(\omega') \hat{a}_2^\dagger(\omega') |0\rangle \\ = |\Psi_1\rangle |\Psi_2\rangle, \quad (8.110)$$

where we have assumed a factorizable amplitude:  $f(\omega, \omega') = f(\omega) \times f'(\omega')$ .

### Example (II): EPR state

Equation 8.111 is a nonfactorizable two-photon state with total photon number  $n = 2$

$$|\Psi\rangle = \Psi_0 \sum_{\omega, \omega'} \delta[\omega + \omega' - \omega_0] \hat{a}_1^\dagger(\omega) \hat{a}_2^\dagger(\omega') |0\rangle, \quad (8.111)$$

where  $\Psi_0$  is a normalization constant, the delta function and the constant  $\omega_0$  together indicate the conservation of energy. In the state of Equation 8.111, a pair of modes are always excited together and the frequencies (energies) of the pair remains constant, although each mode may take any value within the superposition. The two-photon superposition state of Equation 8.111 has certain properties that may never be understood classically. For example, in terms of the concept of a photon, the energy of neither photon is determined; however, if one of the photons is measured with a certain value the energy of the other photon is determined with certainty, despite the distance between the two photons. These kind of states are called entangled states by Schrödinger following the 1935 paper of Einstein, Podolsky, and Rosen. Quantum entanglement will be intensively discussed in later chapters.

### Example (III): Number states

Equations 8.112 and 8.113 define another type of two-photon state with total photon number  $n = 2$ .

$$|\Psi\rangle = \sum_{\omega} f(\omega) [\hat{a}^\dagger(\omega)]^2 |0\rangle, \quad (8.112)$$

and

$$|\Psi\rangle = \sum_{\omega} f(\omega, \omega) \hat{a}_1^\dagger(\omega) \hat{a}_2^\dagger(\omega) |0\rangle. \quad (8.113)$$

It is very clear that the state Equation 8.113 is different from that of Equation 8.112. Although both states are called two-photon states with total photon number  $n = 2$ , Equation 8.113 indicates the excitation of two identical modes in two subsystems simultaneously, each with an occupation number  $n_{\omega} = 1$ . In each of the subsystems, the excited photon can be in any frequency mode  $\omega$ , however, if one of them is found in a mode of  $\omega$  the other must be in the same mode  $\omega$ , despite the distance between the two subsystems. On the other hand, Equation 8.112 indicates the excitation of one mode with occupation number  $n_{\omega} = 2$ . The physical mechanism for the generation of the states in Equations 8.113 and 8.112 are very different too.

It should be emphasized that the states in Equations 8.109, and 8.111 through 8.113 are all pure states. They are very different from the following corresponding mixed states:

$$\begin{aligned}\hat{\rho} &= \sum_{\omega, \omega'} P(\omega) P'(\omega') \hat{a}^\dagger(\omega) \hat{a}^\dagger(\omega') |0\rangle\langle 0| \hat{a}(\omega) \hat{a}(\omega') \\ \hat{\rho} &= \sum_{\omega, \omega'} \delta[\omega + \omega' - \omega_0] \hat{a}^\dagger(\omega) \hat{a}^\dagger(\omega') |0\rangle\langle 0| \hat{a}(\omega) \hat{a}(\omega') \\ \hat{\rho} &= \sum_{\omega, \omega'} P(\omega) [\hat{a}^\dagger(\omega)]^2 |0\rangle\langle 0| [\hat{a}(\omega)]^2 \\ \hat{\rho} &= \sum_{\omega, \omega'} P(\omega, \omega') \hat{a}_1^\dagger(\omega) \hat{a}_2^\dagger(\omega) |0\rangle\langle 0| \hat{a}_1(\omega) \hat{a}_2(\omega).\end{aligned}$$


---

## 8.8 A Simple Model of Incoherent and Coherent Radiation Source

To simplify the discussion and mathematics, we assume that a point light source contains a large number of atoms that are ready for two-level atomic transitions at any time  $t$ . For a point source, each atomic transition excites a subfield in the form of a symmetrical spherical wave propagating to all  $4\pi$  directions. The excited radiations are monitored by a point-like photodetector or a set of independent  $N$  point-like photodetectors that are placed at a distance, such as a light year, for single-photon-counting measurement or for joint  $N$ -photon-counting measurement. We assume that the measured light is weak enough to be at the single-photon level at such a distance.

Although the chance to have a spontaneous emission is very small, there is indeed a small probability for an atom to create a photon whenever the atom decays from its higher energy level  $E_2$  ( $\Delta E_2 \neq 0$ ) down to its ground energy state  $E_1$ . It is reasonable to approximate that the  $j$ th atomic transition excites a subfield in the following state:

$$\begin{aligned}|\Psi_j\rangle &= c_0|0\rangle + c_1 \sum_s \int d\mathbf{k} f_j(\mathbf{k}, s) \hat{a}_j^\dagger(\mathbf{k}, s) |0\rangle \\ &\simeq |0\rangle + \epsilon \sum_s \int d\mathbf{k} f_j(\mathbf{k}, s) \hat{a}_j^\dagger(\mathbf{k}, s) |0\rangle\end{aligned}\tag{8.114}$$

where

$|c_0| \sim 1$  is the probability amplitude for no-field-excitation and  $|c_1| = |\epsilon| \ll 1$  is the probability amplitude for the creation of a photon  
 $f(\mathbf{k}, s) = \langle \Psi_{\mathbf{k}, s} | \Psi \rangle$  is the probability amplitude for the radiation field to be in the Fock state of  $|\Psi_{\mathbf{k}, s}\rangle = |1_{\mathbf{k}, s}\rangle = \hat{a}^\dagger(\mathbf{k}, s)|0\rangle$   
 $|\mathbf{k}| = \omega/c = (E_2 - E_1)/\hbar c$

The function  $f_j(\mathbf{k}, s)$  is mainly determined by the distribution of  $E_2$  of the  $j$ th atom within  $\Delta E_2$ . The region of the integral on  $|\mathbf{k}|$  is also determined by

$\Delta E_2$  with  $\Delta|\mathbf{k}| = (\Delta E_2 - E_1)/\hbar c$ . The generalized state of the radiation field that is excited by the light source, which contains such a large number of atomic transitions, is formally written as

$$|\Psi\rangle = \prod_j \left\{ |0\rangle + \epsilon \sum_s \int d\mathbf{k} f_j(\mathbf{k}, s) \hat{a}_j^\dagger(\mathbf{k}, s) |0\rangle \right\}. \quad (8.115)$$

To simplify the mathematics, the following calculation will be in one dimension, which is reasonable for the far-field measurement of the point-like photodetector. The point-like photodetector selects a wavevector  $\mathbf{k}$ , and the measured field can be approximated as a plane wave at far-field. For the same purpose, the calculation will be for one polarization. The state is simplified as

$$\begin{aligned} |\Psi\rangle &= \prod_j \left\{ |0\rangle + \epsilon c_j \int d\omega f_j(\omega) e^{-i\varphi_j} \hat{a}_j^\dagger(\omega) |0\rangle \right\} \\ &\simeq |0\rangle + \epsilon \left[ \sum_j e^{-i\varphi_j} c_j \int d\omega f_j(\omega) \hat{a}_j^\dagger(\omega) |0\rangle \right] \\ &\quad + \epsilon^2 \left[ \sum_{j < k} e^{-i(\varphi_j + \varphi_k)} c_j c_k \int d\omega f_j(\omega) \hat{a}_j^\dagger(\omega) |0\rangle \int d\omega' f_k(\omega') \hat{a}_k^\dagger(\omega') |0\rangle \right] \\ &\quad + \dots \end{aligned} \quad (8.116)$$

where we have defined a phase factor  $e^{-i\varphi_j}$  associated with the  $j$ th atomic transition. In principle, this phase factor belongs to the amplitude of each excited mode associated with the creation operator. We assume a common phase for each wavepacket. This common phase is determined by a common physical parameter in the creation process, such as the creation time of the  $j$ th wavepacket. Since  $|\epsilon| \ll 1$ , in Equation 8.116 we listed the first-order and second-order approximations on  $\epsilon$ . For a particular measurement, only a certain lower-order approximation is necessary. In the following, we give four types of approximations corresponding to different types of measurements or different mechanisms of light generation.

### (I): Mixed single-photon state

We assume that all atomic transitions in the source are radiated randomly and independently with  $\varphi_j - \varphi_k =$  random number for  $j \neq k$ , and a point-like photon-counting detector is placed at a distance for far-field measurement. The first-order expansion on  $\epsilon$  in Equation 8.116 is a necessary approximation for this type of measurement. The higher-order approximations may contribute to the measurement; however, these contributions are usually

small enough under the weak light condition. A radiation is said to be at the single-photon level when the higher-order approximations are ignorable, and the field is characterized by the following single-photon state:

$$|\Psi\rangle \simeq \sum_j e^{-i\varphi_j} c_j |\Psi_j\rangle \quad (8.117)$$

with

$$|\Psi_j\rangle = \int d\omega f_j(\omega) \hat{a}_j^\dagger(\omega) |0\rangle$$

The first-order approximation is written in the form of an incoherent superposition of a set of state vectors or single-photon wavepackets. The incoherently superposed state can be considered as (1) the state of a measured photon that produced a photodetection event—the annihilated photon may be created from any or from all possible randomly radiated independent atomic transitions with probability  $|c_j|^2$ ; (2) the state of a large number of measured photons—each is created from a randomly radiated atomic transition, as an inhomogeneous ensemble.

The expectation value of an operator  $\hat{A}$  corresponding to the measurement is calculated from

$$\begin{aligned} \langle \langle \Psi | \hat{A} | \Psi \rangle \rangle_{\text{Ensemble}} &= \left\langle \sum_j c_j^* e^{i\varphi_j} \langle \Psi_j | \hat{A} \sum_k c_k e^{-i\varphi_k} |\Psi_k\rangle \right\rangle_{\text{Ensemble}} \\ &= \left\langle \sum_{j,k} c_j^* c_k e^{i(\varphi_j - \varphi_k)} \langle \Psi_j | \hat{A} | \Psi_k \rangle \right\rangle_{\text{Ensemble}} \\ &= \sum_j |c_j|^2 \langle \Psi_j | \hat{A} | \Psi_j \rangle \\ &= \text{tr } \hat{\rho}^{(1)} \hat{A} \end{aligned} \quad (8.118)$$

where we have defined a density operator to characterize the first-order-approximated mixed single-photon state

$$\hat{\rho}^{(1)} \equiv \sum_j |c_j|^2 |\Psi_j\rangle \langle \Psi_j| \quad (8.119)$$

The ensemble average in Equation 8.118 has taken into account all possible values of the relative phases  $\varphi_j - \varphi_k$ . Since only the diagonal elements in Equation 8.118 contribute to the expectation evaluation of an operator, the density operator  $\hat{\rho}$  is commonly used to specify the incoherently superposed mixed state of a radiation.

Under the above approximation, traditionally, we say the measured field is in a mixed single-photon state:

$$\begin{aligned}\hat{\rho} &= \sum_j P_j |\Psi_j\rangle\langle\Psi_j| \\ &= \sum_j P_j \int d\omega d\omega' f_j(\omega) f_j^*(\omega') \hat{a}_j^\dagger(\omega) |0\rangle\langle 0| \hat{a}_j(\omega')\end{aligned}\quad (8.120)$$

where  $P_j = |c_j|^2$ , satisfying  $\sum_j P_j = 1$ , is the normalized probability. If we further assume that the atoms have the same mode distribution  $f_j(\omega) = f(\omega)$  and each mode in the  $j$ th wavepacket has a phase  $\varphi_j(\omega)$  that is determined by the transition time  $t_{0j}$  of the  $j$ th atomic transition,  $\varphi_j(\omega) = \omega t_{0j}$ , and consider a random and continuous distribution on  $t_{0j}$ , the sum on  $j$  turns into an integral of  $t_0$ :

$$\begin{aligned}\hat{\rho} &= \int dt_0 e^{-i(\omega-\omega')t_0} \int d\omega d\omega' f(\omega) f^*(\omega') \hat{a}^\dagger(\omega) |0\rangle\langle 0| \hat{a}(\omega') \\ &\cong \int d\omega |f(\omega)|^2 \hat{a}^\dagger(\omega) |0\rangle\langle 0| \hat{a}(\omega)\end{aligned}\quad (8.121)$$

where the integral on  $t_0$  is approximated to be  $\delta(\omega - \omega')$  when taking  $t_0$  to  $\infty$ , and  $|f(\omega)|^2$  is normalized.

It is interesting to see that although we have assumed that each atomic transition produces a coherent wavepacket of the single-photon state as a state vector, by taking into account the randomly distributed phases  $e^{-i\varphi_j}$  of a large number of wavepackets, the incoherent superposition of these state vectors turns the field into a mixed single-photon state, and the system must be described statistically. Of course, it happens only in a stochastic process in which the atomic transitions are completely random and independent. Historically, we name this kind of radiation chaotic-thermal light. Thermal light is a typical example.

## (II): Mixed two-photon state

Now we consider two independent point-like photodetectors at a distance for joint photon-counting measurement, i.e., to count the number of events in which each of the two photodetectors observes a photoelectron, respectively. For this type of measurement, where there is no contribution from the first-order-approximated single-photon state, the second-order approximation is necessary. The third-order and higher-order approximations may also contribute to the measurement; however, these contributions are usually ignorable under the weak light condition. In the above given simple model, the second-order approximation, or the two-photon state, can be

approximated as

$$|\Psi\rangle \simeq \sum_{j < k} c_j c_k e^{-i(\varphi_j + \varphi_k)} |\Psi_j\rangle |\Psi_k\rangle \quad (8.122)$$

where, again,

$$|\Psi_j\rangle = \int d\omega f_j(\omega) \hat{a}_j^\dagger(\omega) |0\rangle$$

The state is a mixed state unless  $\varphi_j + \varphi_k = \text{constant}$  for all  $j$  and  $k$ . In the case of  $\varphi_j + \varphi_k = \text{random number}$  for all  $j$  and  $k$  and  $\varphi_j - \varphi_k = \text{random number}$  for all  $j \neq k$ , the incoherent superposition turns the first-order-approximated state and the second-order-approximated state both into mixed states. Chaotic-thermal radiation is a typical example. The state of Equation 8.122 is a mixed two-photon state. The incoherently superposed two-photon state can be considered as (1) the state of a jointly measured pair of photons that produced a joint photodetection event—the annihilated photon pair may be created from any two or from all possible randomly paired independent atomic transitions with probability  $P_{jk} = |c_j|^2 |c_k|^2$ ; (2) the state of a large number of jointly measured photon pairs—each is created from a randomly paired atomic transition, as an inhomogeneous ensemble.

It should be emphasized that the second-order approximation, namely, the incoherently superposed two-photon state, cannot be written as the product of two first-order approximations. For instance, the state of a radiation field created from a light source consisting of three independent and randomly radiated atomic transitions is approximated as

$$\begin{aligned} |\Psi\rangle &\simeq [|0\rangle + \epsilon c_a |\Psi_a\rangle] [|0\rangle + \epsilon c_b |\Psi_b\rangle] [|0\rangle + \epsilon c_c |\Psi_c\rangle] \\ &= |0\rangle + \epsilon [c_a |\Psi_a\rangle + c_b |\Psi_b\rangle + c_c |\Psi_c\rangle] \\ &\quad + \epsilon^2 [c_a c_b |\Psi_a\rangle |\Psi_b\rangle + c_a c_c |\Psi_a\rangle |\Psi_c\rangle + c_b c_c |\Psi_b\rangle |\Psi_c\rangle] \\ &\quad + \epsilon^3 [c_a c_b c_c |\Psi_a\rangle |\Psi_b\rangle |\Psi_c\rangle] \end{aligned} \quad (8.123)$$

The second-order expansion on  $\epsilon$  is thus

$$\begin{aligned} |\Psi\rangle &= c_a c_b |\Psi_a\rangle |\Psi_b\rangle + c_a c_c |\Psi_a\rangle |\Psi_c\rangle + c_b c_c |\Psi_b\rangle |\Psi_c\rangle \\ &\neq [c_a |\Psi_a\rangle + c_b |\Psi_b\rangle + c_c |\Psi_c\rangle]^2 \end{aligned} \quad (8.124)$$

where the first-order approximation is in the incoherent superposition of three wavepackets:

$$|\Psi\rangle = c_a |\Psi_a\rangle + c_b |\Psi_b\rangle + c_c |\Psi_c\rangle$$

For the mixed two-photon approximation, the expectation value of an operator is calculated from

$$\begin{aligned}
 & \langle\langle\Psi|\hat{A}|\Psi\rangle\rangle_{\text{Ensemble}} \\
 &= \left\langle \sum_{j<k} c_j^* c_k^* e^{i(\varphi_j + \varphi_k)} \langle\Psi_j| \langle\Psi_k| \hat{A} \sum_{n<m} c_m c_n e^{-i(\varphi_m + \varphi_n)} |\Psi_m\rangle |\Psi_n\rangle \right\rangle_{\text{Ensemble}} \\
 &= \left\langle \sum_{j<k, n<m} c_j^* c_k^* c_m c_n e^{i[(\varphi_j + \varphi_k) - (\varphi_m + \varphi_n)]} \langle\Psi_j| \langle\Psi_k| \hat{A} |\Psi_m\rangle |\Psi_n\rangle \right\rangle_{\text{Ensemble}} \\
 &\simeq \sum_{j<k} |c_j|^2 |c_k|^2 \langle\Psi_j| \langle\Psi_k| \hat{A} |\Psi_k\rangle |\Psi_j\rangle \\
 &= \text{tr } \hat{\rho}^{(2)} \hat{A}
 \end{aligned} \tag{8.125}$$

where we have defined a density operator to characterize the second-order-approximated mixed two-photon state:

$$\hat{\rho}^{(2)} \equiv \sum_{j<k} |c_j|^2 |c_k|^2 |\Psi_k\rangle |\Psi_j\rangle \langle\Psi_j| \langle\Psi_k|
 \tag{8.126}$$

The ensemble average in Equation 8.125 has taken into account all possible values of the relative phases  $(\varphi_j + \varphi_k) - (\varphi_m - \varphi_n)$ . Since only the diagonal elements in Equation 8.125 contribute to the expectation evaluation of an operator, the density operator  $\hat{\rho}^{(2)}$  is commonly used to characterize the incoherently superposed two-photon state of a radiation. If we further assume that the atoms have the same mode distribution  $f(\omega)$  and each mode in the  $j$ th wavepacket has a phase  $\varphi_j(\omega)$  that is determined by the transition time  $t_{0j}$  of the  $j$ th atomic transition,  $\varphi_j(\omega) = \omega t_{0j}$ , and consider a random and continuous distribution on  $t_{0j}$  and  $t_{0k}$ , similar to the single-photon state, the integrals on  $t_{0j}$  and  $t_{0k}$  turn the density operator into the following form:

$$\hat{\rho}^{(2)} \cong \int d\omega d\omega' |f(\omega)|^4 \hat{a}^\dagger(\omega) \hat{a}^\dagger(\omega') |0\rangle \langle 0| \hat{a}(\omega') \hat{a}(\omega)
 \tag{8.127}$$

where  $|f(\omega)|^4$  is normalized.

We will give a detailed discussion on the second-order coherence of thermal light in Chapter 9 by applying the mixed two-photon state of Equation 8.122 or 8.126.

### (III): Entangled two-photon state

In the second-order approximation, if a “peculiar” photon creation mechanism achieves  $\varphi_j + \varphi_k = \text{constant}$  for all  $j$  and  $k$ , but keeps  $\varphi_j - \varphi_k = \text{random number}$  for all  $j \neq k$ , the two-photon state turns to be a coherently

superposed pure state; however, the first-order approximation will still keep its nature of mixed single-photon state with incoherent superposition. In this case, the second-order approximation is written as

$$\begin{aligned} |\Psi\rangle &\simeq \sum_{j<k} c_j c_k e^{-i(\varphi_j + \varphi_k)} |\Psi_j\rangle |\Psi_k\rangle_{\varphi_j + \varphi_k = \varphi_0} \\ &= \sum_{j<k} c_j c_k \delta(\varphi_j + \varphi_k - \varphi_0) e^{-i(\varphi_j + \varphi_k)} |\Psi_j\rangle |\Psi_k\rangle \end{aligned} \quad (8.128)$$

where, again,

$$|\Psi_j\rangle = \int d\omega f_j(\omega) \hat{a}_j^\dagger(\omega) |0\rangle$$

Equation 8.128 defines a two-photon state that cannot be factorized into the product of two single-photon states. We name this type of state “entangled two-photon state.” The coherently superposed two-photon state of Equation 8.128 is a pure state that characterizes (1) the state of an entangled photon pair, created from any or from all possible paired atomic transitions in which  $\varphi_j + \varphi_k = \text{constant}$ ; and (2) the state of a large number of entangled photon pairs, all in the same two-photon state, as a homogeneous ensemble.

Achieving  $\varphi_j + \varphi_k = \text{constant}$  for all  $j$  and  $k$ , but keeping  $\varphi_j - \varphi_k = \text{random}$  number for all  $j \neq k$  is not easy, but possible. One of the experimentally available entangled two-photon states has a slightly different form:

$$|\Psi\rangle = \Psi_0 \int d\omega_s d\omega_i \delta(\omega_s + \omega_i - \omega_p) \hat{a}^\dagger(\omega_s) \hat{a}^\dagger(\omega_i) |0\rangle \quad (8.129)$$

where

$\Psi_0$  is the normalization constant representing a constant spectrum

$\omega_p$  is the frequency of the pump laser, which is approximated as constant

This state can be generated from a nonlinear optical process, namely, the process of spontaneous parametric down-conversion (SPDC). For historical reasons, the created pair of photons are named signal and idler. The signal photon and the idler photon are labeled by frequency  $\omega_s$  and  $\omega_i$ , respectively. The entangled two-photon state of the signal-idler photon pair is a pure state; however, the state of the signal photon and the idler photon, respectively, is a mixed single-photon state.

#### (IV): Coherent radiation

We assume that a certain photon creation mechanism to force the atomic transitions in phase. In this case, the radiations created from these atomic transitions are indistinguishable. The state of Equation 8.116 can be rewritten

in the following form:

$$|\Psi\rangle = \left\{ |0\rangle + \epsilon \int d\omega f(\omega) \hat{a}^\dagger(\omega) |0\rangle \right\}^n \quad (8.130)$$

where  $n$  is the number of atomic transitions participating in the coherent excitation of the radiation field. The expansion of Equation 8.130 is thus

$$\begin{aligned} |\Psi\rangle \simeq & |0\rangle + \epsilon \frac{n}{1!} |\Psi\rangle + \epsilon^2 \frac{n(n-1)}{2!} (|\Psi\rangle)^2 + \epsilon^3 \frac{n(n-1)(n-2)}{3!} (|\Psi\rangle)^3 + \dots \\ & + \epsilon^m \frac{n(n-1)(n-2)\cdots(n-m+1)}{m!} (|\Psi\rangle)^m + \dots , \end{aligned} \quad (8.131)$$

with

$$|\Psi\rangle = \int d\omega f(\omega) \hat{a}^\dagger(\omega) |0\rangle$$

In a single-mode approximation, the state  $|\Psi\rangle$  turns to be

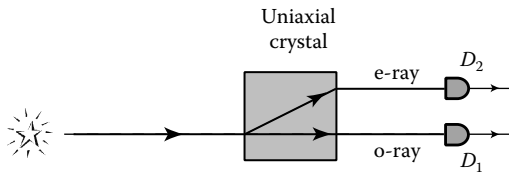
$$\begin{aligned} |\Psi\rangle \simeq & |0\rangle + \epsilon \frac{n}{1!} \hat{a}^\dagger(\omega) |0\rangle \\ & + \epsilon^2 \frac{n(n-1)}{2!} [\hat{a}^\dagger(\omega)]^2 |0\rangle + \epsilon^3 \frac{n(n-1)(n-2)}{3!} [\hat{a}^\dagger(\omega)]^3 |0\rangle \\ & + \epsilon^m \frac{n(n-1)(n-2)\cdots(n-m+1)}{m!} [\hat{a}^\dagger(\omega)]^m |0\rangle + \dots . \end{aligned} \quad (8.132)$$

It is not too difficult to generalize the above results to three dimensions. In three dimension, we may have a more complicated sum/integral with the ensemble averaging in terms of the spatial coordinate of the  $j$ th atomic transition. We will give a few discussions on spatial coherence later.

## 8.9 Pure State and Mixed State

The concepts of pure states and mixed states include two important aspects of physics: the state of the individual quantum and the state of the measured ensemble.

1. In terms of the individual quantum system: a pure state represents a vector in Hilbert space. If the state of a quantum can be described by a vector, the state of the quantum is said to be *pure*. On the contrary, if the state of a quantum cannot be described as a vector but rather a mixture of vectors, the quantum is said to be in a *mixed state*.

**FIGURE 8.7**

Polarization measurement of a photon.

2. In terms of the measured ensemble: if the state of all the measured quanta of the ensemble can be described by the same vector, the state of the ensemble, or the measured systems of quanta, is said to be *homogeneous* or in a statistically *pure state*. If the measured ensemble cannot be described by the same vector, or the measured ensemble has to be described by several, or by many different vectors, the ensemble is referred to as an inhomogenous *mixture*.

To explore the important physics behind the concepts, we give two simple examples: (I) polarization measurement of a single-photon state; (II) Schrödinger cat.

#### Example (I): Polarization measurement of a single-photon state

Consider the experimental setup of Figure 8.7 for polarization measurement experiment of Figure 8.7, which consists of a far-field single-photon radiation source of frequency  $\omega$ , a uniaxial crystal, and two photon-counting detectors. The point-like photodetectors  $D_1$  and  $D_2$  are used for measuring the ordinary-ray and the extraordinary-ray of the uniaxial crystal, respectively.

After a large number of measurements, we find (1) no joint photodetection event happens, i.e.,  $D_1$  and  $D_2$  are never triggered simultaneously; and (2) the ratio between the single-photon counting rates of  $D_1$  and  $D_2$  is 1, i.e., 50% of the photodetection events are registered by  $D_1$  and another 50% of the photodetection events are recorded by  $D_2$ . What is the state of the radiation field? From observation (1), the state can be considered a single-photon state. Observation (2) suggests at least three possible states:

Possibility one: The state can be a linearly polarized single-photon state with polarization either  $45^\circ$  or  $-45^\circ$  relative to the polarization of the ordinary-ray,

$$\begin{aligned} |\Psi_{45^\circ}\rangle &= \frac{1}{\sqrt{2}} [\hat{a}^\dagger(\omega, \hat{o})|0\rangle + \hat{a}^\dagger(\omega, \hat{e})|0\rangle] \\ |\Psi_{-45^\circ}\rangle &= \frac{1}{\sqrt{2}} [\hat{a}^\dagger(\omega, \hat{o})|0\rangle - \hat{a}^\dagger(\omega, \hat{e})|0\rangle], \end{aligned} \quad (8.133)$$

where

the unit vectors  $\hat{o}$  and  $\hat{e}$  indicate the polarization of the o-ray and the e-ray, respectively

the  $\pm$  sign indicates that the field is either polarized at  $45^\circ$  or  $-45^\circ$  relative to the unit vector  $\hat{o}$

If the measurements only focus on polarization, we may rewrite Equation 8.133 in the following simplified form

$$\begin{aligned} |\Psi_{45^\circ}\rangle &= |\hat{o}\rangle\langle\hat{o}|\Psi_{45^\circ}\rangle + |\hat{e}\rangle\langle\hat{e}|\Psi_{45^\circ}\rangle = \frac{1}{\sqrt{2}} [ |\hat{o}\rangle + |\hat{e}\rangle ] \\ |\Psi_{-45^\circ}\rangle &= |\hat{o}\rangle\langle\hat{o}|\Psi_{-45^\circ}\rangle + |\hat{e}\rangle\langle\hat{e}|\Psi_{-45^\circ}\rangle = \frac{1}{\sqrt{2}} [ |\hat{o}\rangle - |\hat{e}\rangle ], \end{aligned} \quad (8.134)$$

where  $|\hat{o}\rangle$  and  $|\hat{e}\rangle$  form a complete, orthonormal vector basis. We regard the linear polarization states of  $|\Psi_{45^\circ}\rangle$  and  $|\Psi_{-45^\circ}\rangle$  as coherent *superposition* of  $|\hat{o}\rangle$  and  $|\hat{e}\rangle$ . The state is a pure state. In the chosen 2D vector space, the matrix form of the density operator  $\hat{\rho} = |\Psi\rangle\langle\Psi|$  is written as

$$\hat{\rho}_{45^\circ} = \begin{pmatrix} 1/2 & 1/2 \\ 1/2 & 1/2 \end{pmatrix}, \quad \hat{\rho}_{-45^\circ} = \begin{pmatrix} 1/2 & -1/2 \\ -1/2 & 1/2 \end{pmatrix}. \quad (8.135)$$

Possibility two: The state can be a circularly polarized single-photon state with right-hand polarization or left-hand polarization:

$$\begin{aligned} |\Psi_R\rangle &= \frac{1}{\sqrt{2}} [ \hat{a}^\dagger(\omega, \hat{o})|0\rangle + i\hat{a}^\dagger(\omega, \hat{e})|0\rangle ] \\ |\Psi_L\rangle &= \frac{1}{\sqrt{2}} [ -\hat{a}^\dagger(\omega, \hat{o})|0\rangle + i\hat{a}^\dagger(\omega, \hat{e})|0\rangle ], \end{aligned} \quad (8.136)$$

where, again, the unit vectors  $\hat{o}$  and  $\hat{e}$  indicate the polarization of the o-ray and the e-ray, respectively. If the measurements only focus on polarization, we may rewrite Equation 8.136 in the following simplified form

$$\begin{aligned} |\Psi_R\rangle &= |\hat{o}\rangle\langle\hat{o}|\Psi_R\rangle + |\hat{e}\rangle\langle\hat{e}|\Psi_R\rangle = \frac{1}{\sqrt{2}} [ |\hat{o}\rangle + i|\hat{e}\rangle ] \\ |\Psi_L\rangle &= |\hat{o}\rangle\langle\hat{o}|\Psi_L\rangle + |\hat{e}\rangle\langle\hat{e}|\Psi_L\rangle = \frac{1}{\sqrt{2}} [ -|\hat{o}\rangle + i|\hat{e}\rangle ]. \end{aligned} \quad (8.137)$$

We regard the circular polarization states of  $|\Psi_R\rangle$  and  $|\Psi_L\rangle$  as coherent *superposition* of  $|\hat{o}\rangle$  and  $|\hat{e}\rangle$ . The state is a pure state. In the chosen 2D vector space of  $|\hat{o}\rangle$  and  $|\hat{e}\rangle$ , the matrix form of the density operator is written as

$$\hat{\rho}_R = \begin{pmatrix} 1/2 & -i/2 \\ i/2 & 1/2 \end{pmatrix}, \quad \hat{\rho}_L = \begin{pmatrix} 1/2 & i/2 \\ -i/2 & 1/2 \end{pmatrix}. \quad (8.138)$$

Possibility three: The radiation field could be unpolarized. We regard a mixed polarization state in terms of the ordinary-ray (o-ray) and the extraordinary-ray (e-ray) of the uniaxial crystal

$$\hat{\rho} = \frac{1}{2} [\hat{a}^\dagger(\omega, \hat{o}) |0\rangle\langle 0| \hat{a}(\omega, \hat{o}) + \hat{a}^\dagger(\omega, \hat{e}) |0\rangle\langle 0| \hat{a}(\omega, \hat{e})], \quad (8.139)$$

or in the simplified form

$$\hat{\rho} = P_o |\hat{o}\rangle\langle\hat{o}| + P_e |\hat{e}\rangle\langle\hat{e}| = \frac{1}{2} [|\hat{o}\rangle\langle\hat{o}| + |\hat{e}\rangle\langle\hat{e}|], \quad (8.140)$$

where  $P_o$  and  $P_e$  are the probabilities for the system to be in the polarization states  $|\hat{o}\rangle$  and  $|\hat{e}\rangle$ , respectively. In the chosen vector space in which  $|\hat{o}\rangle$  and  $|\hat{e}\rangle$  form a complete, orthonormal vector basis, the matrix form of the density operator is written as

$$\hat{\rho} = \begin{pmatrix} 1/2 & 0 \\ 0 & 1/2 \end{pmatrix}. \quad (8.141)$$

It is not difficult to see the above three states (possibilities) yield the same results for the experimental setup of Figure 8.7, i.e., 50%–50% chance to register an o-ray or an e-ray photon.

For a more general calculation of this kind of measurements, we introduce projection operators  $\hat{\theta} = |\hat{\theta}\rangle\langle\hat{\theta}|$  and  $\hat{\theta}_\perp = |\hat{\theta}_\perp\rangle\langle\hat{\theta}_\perp|$ , corresponding to a polarization analyzer oriented at angle  $\theta$ , see Figure 8.8, in the natural right-hand coordinate system. In the chosen vector space of  $|\hat{o}\rangle$  and  $|\hat{e}\rangle$ , the matrix form of the projection operators  $\hat{\theta}$  and  $\hat{\theta}_\perp$  are

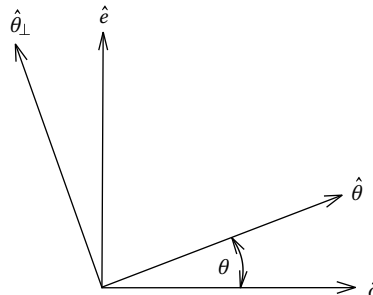


**FIGURE 8.8**

A polarization projection operator  $\hat{\theta} = |\hat{\theta}\rangle\langle\hat{\theta}|$  corresponds to a polarization analyzer oriented at angle  $\theta$  relative to vector  $\hat{o}$ .

$$\hat{\theta} = \begin{pmatrix} \cos^2 \theta & \cos \theta \sin \theta \\ \sin \theta \cos \theta & \sin^2 \theta \end{pmatrix}, \quad (8.142)$$

and

$$\hat{\theta}_\perp = \begin{pmatrix} \sin^2 \theta & -\sin \theta \cos \theta \\ -\cos \theta \sin \theta & \cos^2 \theta \end{pmatrix} \quad (8.143)$$

respectively, where the matrix elements  $\langle \hat{i} | \hat{\theta} \rangle \langle \hat{\theta} | \hat{j} \rangle = \cos(\hat{i}, \hat{\theta}) \cos(\hat{\theta}, \hat{j})$ , and  $\langle \hat{i} | \hat{\theta}_\perp \rangle \langle \hat{\theta}_\perp | \hat{j} \rangle = \cos(\hat{i}, \hat{\theta}_\perp) \cos(\hat{\theta}_\perp, \hat{j})$ , with  $\hat{i}, \hat{j} = \hat{o}, \hat{e}$ , and  $\theta$  is the angle between the unit vectors  $\hat{\theta}$  and  $\hat{o}$ .

In general, the expectation value of the polarization measurement is calculated by taking the trace of the matrix  $\hat{\rho} \hat{\theta}$  and  $\hat{\rho} \hat{\theta}_\perp$

$$\langle \hat{\theta} \rangle = \text{tr } \hat{\rho} \hat{\theta}, \quad \langle \hat{\theta}_\perp \rangle = \text{tr } \hat{\rho} \hat{\theta}_\perp. \quad (8.144)$$

We thus have

$$\begin{aligned} \langle \hat{\theta} \rangle &= \langle \Psi | \hat{\theta} \rangle \langle \hat{\theta} | \Psi \rangle = |\langle \hat{\theta} | \Psi \rangle|^2 \\ \langle \hat{\theta}_\perp \rangle &= \langle \Psi | \hat{\theta}_\perp \rangle \langle \hat{\theta}_\perp | \Psi \rangle = |\langle \hat{\theta}_\perp | \Psi \rangle|^2 \end{aligned} \quad (8.145)$$

for pure states, and

$$\begin{aligned} \langle \hat{\theta} \rangle &= \sum_j P_j \langle \Psi_j | \hat{\theta} \rangle \langle \hat{\theta} | \Psi_j \rangle = \sum_j P_j |\langle \hat{\theta} | \Psi_j \rangle|^2 \\ \langle \hat{\theta}_\perp \rangle &= \sum_j P_j \langle \Psi_j | \hat{\theta}_\perp \rangle \langle \hat{\theta}_\perp | \Psi_j \rangle = \sum_j P_j |\langle \hat{\theta}_\perp | \Psi_j \rangle|^2 \end{aligned} \quad (8.146)$$

for mixed states. In the measurement of Figure 8.7, the projection angle  $\theta$  of the polarization analyzer (the uniaxial crystal) is chosen to be either  $\theta = 0$  (o-ray) ( $\theta_\perp = 90^\circ$ ) or  $\theta = 90^\circ$  (e-ray) ( $\theta_\perp = 180^\circ$ ). Definitely, these measurements cannot distinguish the above three different states.

One may immediately ask the following question: Can we distinguish the pure states Equations 8.133 and 8.136 from the mixed state of Equation 8.139, in principle and in practice? For this kind of simple polarization measurement, the answer is positive. One may consider to rotate the crystal-detector system to either the  $|45^\circ\rangle$  ( $|-45^\circ\rangle$ ) direction, or the  $|R\rangle$  ( $|L\rangle$ ) direction in the polarization space. For the mixed state of Equation 8.139, the counting rate of the photodetectors would not show any difference in the  $|45^\circ\rangle$  ( $|-45^\circ\rangle$ ) or  $|R\rangle$  ( $|L\rangle$ ) measurements. In fact, the counting rate of the photodetectors will be constant in any chosen polarization vector basis. The pure state, however, gives different results. If  $D_1$  ( $D_2$ ) shows a maximum (minimum) counting rate at  $45^\circ$  and a minimum (maximum) counting rate at  $-45^\circ$ , the field is polarized at  $45^\circ$ . If  $D_1$  ( $D_2$ ) has a minimum (maximum) counting rate at  $45^\circ$  and a maximum (minimum) counting rate at  $-45^\circ$ , the field is polarized

at  $-45^\circ$ , i.e., the field, or the photon, is neither polarized as an o-ray nor an e-ray, rather it is polarized at  $45^\circ$  ("+" sign)

$$|\Psi\rangle = \hat{a}^\dagger(\omega, 45^\circ) |0\rangle$$

or  $-45^\circ$  ("—" sign)

$$|\Psi_\perp\rangle = \hat{a}^\dagger(\omega, -45^\circ) |0\rangle.$$

In general, the state of

$$|\Psi\rangle = \hat{a}^\dagger(\omega, \theta) |0\rangle$$

and

$$|\Psi_\perp\rangle = \hat{a}^\dagger(\omega, \theta_\perp) |0\rangle$$

form a complete vector basis for characterizing any polarization state, where  $\theta$  and  $\theta_\perp$  indicate two orthogonal orientations of the field polarization. For example, the states of the o-ray and the e-ray can be written as the superposition of  $45^\circ$  and  $-45^\circ$

$$\begin{aligned} |\Psi_o\rangle &= \frac{1}{\sqrt{2}} [\hat{a}^\dagger(\omega, 45^\circ) |0\rangle + \hat{a}^\dagger(\omega, -45^\circ) |0\rangle] \\ |\Psi_e\rangle &= \frac{1}{\sqrt{2}} [\hat{a}^\dagger(\omega, 45^\circ) |0\rangle - \hat{a}^\dagger(\omega, -45^\circ) |0\rangle]. \end{aligned} \quad (8.147)$$

Of course,  $\theta$  and  $\theta_\perp$  can be used to characterize a mixed polarization too:

$$\hat{\rho} = P(\theta) |\theta\rangle \langle \theta| + P(\theta_\perp) |\theta_\perp\rangle \langle \theta_\perp|. \quad (8.148)$$

Similarly, while  $D_1$  ( $D_2$ ) has a maximum (minimum) counting rate at the orientation  $|R\rangle$  and a minimum (maximum) counting rate at  $|L\rangle$ , the field is right-hand polarized, i.e., the field, or the photon, is neither polarized as an o-ray nor an e-ray, rather it is right-hand polarized:

$$|\Psi\rangle = \hat{a}^\dagger(\omega, +1) |0\rangle.$$

where  $+1$  (spin  $+1$ ) and  $-1$  (spin  $-1$ ) indicate right-hand and left-hand polarization. Otherwise, if  $D_1$  ( $D_2$ ) has a maximum (minimum) counting rate at orientation of  $|L\rangle$  and minimum (maximum) counting rate at  $|R\rangle$ , the field is left-hand polarized

$$|\Psi_\perp\rangle = \hat{a}^\dagger(\omega, -1) |0\rangle.$$

In general, the state of

$$|\Psi\rangle = \hat{a}^\dagger(\omega, +1) |0\rangle$$

and

$$|\Psi_\perp\rangle = \hat{a}^\dagger(\omega, -1) |0\rangle$$

form a complete orthogonal vector basis for characterizing any polarization state. For example, the states of the o-ray and the e-ray can be written as the superposition of  $|R\rangle$  and  $|L\rangle$

$$\begin{aligned} |\Psi_o\rangle &= \frac{1}{\sqrt{2}} [\hat{a}^\dagger(\omega, +1)|0\rangle - \hat{a}^\dagger(\omega, -1)|0\rangle] \\ |\Psi_e\rangle &= \frac{-i}{\sqrt{2}} [\hat{a}^\dagger(\omega, +1)|0\rangle + \hat{a}^\dagger(\omega, -1)|0\rangle]. \end{aligned} \quad (8.149)$$

Of course, the right-hand and left-hand polarization states can be used to characterize a mixed polarization too:

$$\hat{\rho} = P(+1)|R\rangle\langle R| + P(-1)|L\rangle\langle L|. \quad (8.150)$$

A pure state represents a vector in Hilbert space. If we could “rotate” our measurement device to identify the vector and its orthogonal conjugates, it is not surprising to have maximum and minimum counting rates at different “directions” in the chosen Hilbert space. Thus, in principle, it is possible, and “easy,” to distinguish a pure state from a mixed state as well as from its orthogonal states, such as the state with the “+” sign and the state with the “−” sign in Equation 8.133, by a simple rotation. If we consider the measurement operation a projection, to distinguish a pure state from mixed states as well as from its orthogonal states, we can project the pure state onto itself, or project it onto its orthogonal states. Mathematically, we may define a projection operator  $\hat{P} = |\Psi\rangle\langle\Psi|$ , which is nothing but the density operator, to write these projections as

$$\begin{aligned} \hat{P}|\Psi\rangle &= |\Psi\rangle\langle\Psi|\Psi\rangle = |\Psi\rangle \\ \hat{P}|\Psi_\perp\rangle &= |\Psi\rangle\langle\Psi|\Psi_\perp\rangle = 0. \end{aligned} \quad (8.151)$$

Equation 8.151 can be expressed in a general form in terms of the density operator

$$\hat{\rho}^2 = |\Psi\rangle\langle\Psi|\Psi\rangle\langle\Psi| = \hat{\rho}, \quad (8.152)$$

where the state  $|\Psi\rangle$  (and  $|\Psi\rangle_\perp$ ) is normalized as is in Equation 8.133. Any pure state must satisfy Equation 8.152.

It is easy to find that the states  $|45^\circ\rangle$  and  $| -45^\circ\rangle$  (as well as  $|R\rangle$  and  $|L\rangle$ ) form a complete orthonormal vector basis and satisfy the completeness relation

$$|\Psi\rangle\langle\Psi| + |\Psi_\perp\rangle\langle\Psi_\perp| = 1. \quad (8.153)$$

In measurements other than polarization, however, the situation is not that simple. In many cases, we cannot “rotate” our measurement-projection device in the chosen vector space, such as the vector space defined by the

eigenfunction of the Hamiltonian. We may have to keep the state vector as a superposition of the chosen set of eigenvectors of a known operator such as the Hamiltonian. The measurement can only project the state onto the eigenvectors of the operator. In this case, we may face difficulties again in understanding the physics of a quantum superposition. For example, if one insists that a photon has to be polarized as either an o-ray or an e-ray when propagated in the uniaxial crystal, it is very reasonable to ask: how could a  $45^\circ$  or  $-45^\circ$  polarized photon be an o-ray and an e-ray simultaneously? Since we know that an energy bundle of  $\hbar\omega$ , or a photon, can never be divided into parts. A similar question naturally follows: Has the photon been “which ray or both ray”? This is equivalent to the question, when considering a double-slit experiment at a single-photon level: Has the photon passed “which slit or both slit”? Regarding this historically long-standing problem, the Schrödinger cat may be considered the most vivid cartoon model.

Before turning to the physics of the Schrödinger cat, we need a brief discussion about the measurement of a single-photon. Talking about the measurement of a single-photon, it does not mean we only deal with a photon. In fact, one measurement of one photon cannot provide us any meaningful information. In quantum theory, any meaningful physics has to be learned from a large number of measurements, or from the measurement of an ensemble. There are two types of ensembles in quantum theory. The first type is said to be homogeneous or in a statistically *pure* state. In this case, each of the measured N systems in the ensemble is in the same pure state, and thus the ensemble itself is in a pure state. The second type is referred to as a *mixture*. In this case, the measured ensemble of N systems are not necessarily in the same pure state. The measured N systems can be in several, or in many, different states with certain probabilities, and thus the ensemble itself is in a mixed state.

We have two pictures of pure states. The pure state can represent (1) an individual photon or (2) an ensemble of photons. For example, in the polarization measurement, the pure states of Equation 8.133 can mean (1) each measured photon (individual) is polarized at  $45^\circ$  (with “+” sign) or  $-45^\circ$  (with “−” sign), (2) all measured photons (ensemble) are polarized at  $45^\circ$  or  $-45^\circ$ , or simply, the measured radiation field is polarized at  $45^\circ$  or  $-45^\circ$ . The mixed state of Equation 8.134 may have the following meaning: (1) each measured photon is neither polarized at  $45^\circ$  nor at  $-45^\circ$ , or (2) half of the measured photons in the ensemble are polarized at  $45^\circ$  and the other half of the measured photons in the ensemble are polarized at  $-45^\circ$ , or simply, the radiation field is unpolarized.

### Example (II): Schrödinger cat

There has been a famous *cat* in the history of physics, namely, the Schrödinger cat. Schrödinger's cat is in the superposition state of  $|\text{alive}\rangle$

and  $|\text{dead}\rangle$ :

$$|+\text{cat}\rangle = \frac{1}{\sqrt{2}} [ |\text{alive}\rangle + |\text{dead}\rangle ], \quad (8.154)$$

where  $|\text{alive}\rangle$  and  $|\text{dead}\rangle$  are the eigenvectors of the “life status” operator of a cat. Similar to the linear polarization of a radiation field, the vector space defined by the “life status” operator has a dimension of two. The eigenvectors  $|\text{alive}\rangle$  and  $|\text{dead}\rangle$  form a complete, orthonormal vector space. The Schrödinger cat is not in any of the eigenstates, but rather a superposition of the eigenstates. Of course, there is no such cat in our everyday life. In the quantum world, however, a Schrödinger cat is allowed to be alive and dead simultaneously. Besides the pure state of Equation 8.154, quantum theory permits another pure state, which is orthogonal to the state of Equation 8.154

$$|-\text{cat}\rangle = \frac{1}{\sqrt{2}} [ |\text{alive}\rangle - |\text{dead}\rangle ]. \quad (8.155)$$

First, both states  $|+\text{cat}\rangle$  and  $|-\text{cat}\rangle$  in Equations 8.154 and 8.155 are pure states. It is easy to show that

$$\hat{\rho}_{+\text{cat}}^2 = \hat{\rho}_{+\text{cat}}, \quad \hat{\rho}_{-\text{cat}}^2 = \hat{\rho}_{-\text{cat}}.$$

Second, the states of  $|\text{cat}\rangle$  and  $|-\text{cat}\rangle$  form a complete orthonormal set,

$$|+\text{cat}\rangle\langle+\text{cat}| + |-\text{cat}\rangle\langle-\text{cat}| = 1. \quad (8.156)$$

Therefore, any cat-states can be written as the superposition of  $|+\text{cat}\rangle$  and  $|-\text{cat}\rangle$ , such as

$$\begin{aligned} |\text{alive}\rangle &= \frac{1}{\sqrt{2}} [ |+\text{cat}\rangle + |-\text{cat}\rangle ] \\ |\text{dead}\rangle &= \frac{1}{\sqrt{2}} [ |+\text{cat}\rangle - |-\text{cat}\rangle ]. \end{aligned} \quad (8.157)$$

If we have a measurement-projection device capable of identifying  $|+\text{cat}\rangle$  and  $|-\text{cat}\rangle$ , we are going to find that an alive-cat (dead-cat as well) would be a  $|+\text{cat}\rangle$ -cat (Schrödinger cat) and  $|-\text{cat}\rangle$ -cat (conjugate Schrödinger cat) simultaneously. Should we ask: How could an alive-cat be a Schrödinger cat and its conjugate-cat simultaneously?

Third, the pure states of Equations 8.154 and 8.155 are very different from the mixed state

$$\hat{\rho} = \frac{1}{2} [ |\text{alive}\rangle\langle\text{alive}| + |\text{dead}\rangle\langle\text{dead}| ]. \quad (8.158)$$

Comparing with the linear polarization measurement in example one, the states of Equations 8.154 and 8.155 are equivalent to the linear polarization states of  $45^\circ$  and  $-45^\circ$ . We have made a similar rotation to achieve Equations 8.154 and 8.155. Theoretically, this is a simple rotation in the 2D “cat-space.” Unfortunately, no one knows how to achieve that rotation in practice. The only measurement we can do is to identify if a cat is alive or dead. If our measurement-projection device can only project a cat state onto the eigenstate  $|\text{alive}\rangle$  or  $|\text{dead}\rangle$ , we may never be able to distinguish the pure states of Equations 8.154 and 8.155 from the mixed state of Equation 8.158. Although we do not know how to achieve a rotation from  $|\text{alive}\rangle$  or  $|\text{dead}\rangle$  to  $|\text{alive}\rangle \pm |\text{dead}\rangle$  in the cat space, it does not mean the nonexistence of this kind of superposition states, especially if we know how to generate such a state.

Similar to the polarization measurement of a single-photon, one measurement of a Schrödinger cat does not give us any meaningful information. In the theory of Schrödinger’s cat, any meaningful physics has to be learned from the measurement of an ensemble of cats. If all measured cats are in the same state, such as that of Equation 8.154 or Equation 8.155, we say that each measured cat is in a pure state and the measured cat-system is in a pure state. If the measurement found some of the cats in the state of Equation 8.154 and the other cats in the state of Equation 8.155, the cat-system is referred to as a mixture.

We now discuss the state of the radiation field. We are going to ask the following questions: (1) What is the different physics behind the pure state of Equation 8.70 and the mixed state of Equation 8.93? (2) For the simplified model of the atomic radiation source of Section 8.8, is it possible to excite a pure state in the second-order approximation but keep the first-order approximation mixed state, or vice versa? If possible, what is the condition?

1. What is the different physics behind the pure state of Equation 8.70

$$|\Psi\rangle = \sum_{\mathbf{k}, s} f(\mathbf{k}, s) \hat{a}_{\mathbf{k}, s}^\dagger |0\rangle$$

and the mixed state of Equation 8.93

$$\hat{\rho} = \sum_{\mathbf{k}, s} |f(\mathbf{k}, s)|^2 \hat{a}_{\mathbf{k}, s}^\dagger |0\rangle \langle 0| \hat{a}_{\mathbf{k}, s}$$

In terms of the state of a photon, Equation 8.70 represents a vector in Hilbert space. If the state of a photon can be described by Equation 8.70, in principle, one should be able to “rotate” the measurement operation to project the state onto itself, or onto its orthogonal “direction.” The probability of receiving a “click” from a photon-counting detector is 100% against 0% in these two “directions.” On the contrary, Equation 8.93 represents a mixture of

vectors by means of a density matrix; the photon is in a mixed state. One can never find such a “rotation,” and thus the mixed state of Equation 8.93 can only describe the state of the single-photon statistically.

In terms of the ensemble, similar to the physics of the cat system, a pure state requires all photons of the ensemble in the same state, such as that of Equation 8.70. A mixed state means the photons in the ensemble are not in the same state, but rather in different states. Therefore, an ensemble average is necessary for calculating the expectation value of an observable.

2. For the simplified model of the atomic radiation source of Section 8.8, is it possible to excite a pure state in the second-order approximation but keep the first-order approximation mixed state, or vice versa? If possible, what is the condition?

In fact, the first part of the question has been addressed in Section 8.8. We have derived the condition  $\varphi_j + \varphi_k = \text{constant}$  for having an entangled two-photon state in the second-order approximation:

$$|\Psi\rangle = \sum_{j,k} c_j c_k \delta(\varphi_j + \varphi_k - \varphi_0) e^{-i(\varphi_j + \varphi_k)} |\Psi_j\rangle |\Psi_k\rangle$$

but keep the first-order approximation mixed state

$$\hat{\rho}^{(1)} = \sum_j P_j |\Psi_j\rangle \langle \Psi_j|$$

with the condition  $\varphi_j - \varphi_k = \text{random number}$  for  $j \neq k$ . Where in both states

$$|\Psi_j\rangle = \int d\omega f_j(\omega) e^{-i\varphi_j} \hat{a}_j^\dagger(\omega) |0\rangle$$

Now we discuss the second part of the question: Is it possible to excite a pure state in the first-order approximation but keep the second-order approximation mixed state? Let us examine the first-order and the second-order approximation:

$$\begin{aligned} |\Psi\rangle &= \prod_j \left\{ |0\rangle + \epsilon c_j e^{-i\varphi_j} \int d\omega f_j(\omega) \hat{a}_j^\dagger(\omega) |0\rangle \right\} \\ &\simeq |0\rangle + \epsilon \left[ \sum_j e^{-i\varphi_j} c_j \int d\omega f_j(\omega) \hat{a}_j^\dagger(\omega) |0\rangle \right] \\ &\quad + \epsilon^2 \left[ \sum_{j,k} e^{-i(\varphi_j + \varphi_k)} c_j c_k \int d\omega d\omega' f_j(\omega) f_k(\omega') \hat{a}_j^\dagger(\omega) \hat{a}_k^\dagger(\omega') |0\rangle \right] \end{aligned} \quad (8.159)$$

Similar to our earlier discussion in Section 8.8, the condition to have a pure state in the first-order approximation is  $\varphi_j - \varphi_k = \text{constant}$  for all  $j \neq k$ . However, the condition to have a pure state in the second-order approximation requires  $\varphi_j + \varphi_k = \text{random number}$  for all  $j$  and  $k$ .

## 8.10 Product State, Entangled State, and Mixed State of Photon Pairs

The concepts of product photon states and entangled photon states involve multiphoton systems. In this section, we restrict ourselves to two-photon states. We will give two simple discussions before introducing the entangled multimode two-photon states: (I) product, entangled and mixed states of Schrödinger's cats; (II) product, entangled and mixed polarization states of a two-photon system.

Example (I): Product, entangled and mixed states of Schrödinger's cats

### 1. Product state of two Schrödinger's cats

Suppose two Schrödinger's cats, cat-one and cat-two, are created from a cat source independently, cat-one is prepared in the state  $|+\text{cat}\rangle$  and cat-two is prepared in the state  $|-\text{cat}\rangle$ . Due to the independent creation process, there is no interaction between the two cats, the two created Schrödinger's cats can be treated as a cat system in product states

$$\begin{aligned} |\Psi\rangle &= |+\text{cat}_1\rangle \times |-\text{cat}_2\rangle \\ &= \frac{1}{2} [| \text{alive}_1 \rangle | \text{alive}_2 \rangle + | \text{dead}_1 \rangle | \text{dead}_2 \rangle \\ &\quad - | \text{alive}_1 \rangle | \text{dead}_2 \rangle - | \text{dead}_1 \rangle | \text{alive}_2 \rangle]. \end{aligned} \quad (8.160)$$

We further assume the two cats "propagate" freely in opposite directions with no interaction between them. If the propagation, or the time evolution, of the system simply develops an overall phase but keeps the relative phases between the four terms in the superposition, the state of the two Schrödinger's cats will remain the same as that of Equation 8.160, except the trivial overall phase. At a large distance, such as a light year, two observers decide to measure the live status of the two cats simultaneously, or the joint-live-status of the two cats. It is not surprising that the measurements show four equal possibilities: (1) cat-one and cat-two both alive, (2) cat-one and cat-two both dead, (3) cat-one alive and cat-two dead, and (4) cat-one dead and cat-two alive.

Here, “not surprising” means that there is no difference between the quantum predication and the classical convention.

## 2. Entangled state of two Schrödinger’s cats

Suppose a pair of Schrödinger’s cats is created at the cat-source with one of the following two-cat states

$$\begin{aligned} |\Psi^{(+)}\rangle &= \frac{1}{\sqrt{2}} [|\text{alive}_1\rangle|\text{alive}_2\rangle + |\text{dead}_1\rangle|\text{dead}_2\rangle], \\ |\Psi^{(-)}\rangle &= \frac{1}{\sqrt{2}} [|\text{alive}_1\rangle|\text{alive}_2\rangle - |\text{dead}_1\rangle|\text{dead}_2\rangle], \\ |\Phi^{(+)}\rangle &= \frac{1}{\sqrt{2}} [|\text{alive}_1\rangle|\text{dead}_2\rangle + |\text{dead}_1\rangle|\text{alive}_2\rangle], \\ |\Phi^{(-)}\rangle &= \frac{1}{\sqrt{2}} [|\text{alive}_1\rangle|\text{dead}_2\rangle - |\text{dead}_1\rangle|\text{alive}_2\rangle], \end{aligned} \quad (8.161)$$

and neither can be written in the form of a product state,  $|\Psi\rangle = |\Psi_1\rangle|\Psi_2\rangle$ . The pair of cats is in an entangled two-cat state. All four states in Equation 8.161 are defined as entangled two-cat states. We may name them Bell’s cat-states. Bell’s cat-states form a complete orthogonal vector basis in two-cat space.

If the same criterion for free propagation and time evolution of the system is applicable, i.e., the time evolution simply develops an overall phase but keeps the relative phase between the two terms in the superposition, the state of the two Schrödinger’s cats will remain the same as that shown in Equation 8.161, except for a trivial phase factor. Therefore, the outcome of any “correlation” measurement of the two cats will remain the same despite the distance between them.

Now, we consider a joint measurement of the cat system. Suppose two observers, at equal distances from the cat-source, measure the live-status of the cat pair simultaneously, equivalent to having a set of joint projection operators:

$$\begin{aligned} \langle\Psi|\text{alive}_1\rangle|\text{alive}_2\rangle\langle\text{alive}_2|\langle\text{alive}_1|\Psi\rangle &= |\langle\text{alive}_2|\langle\text{alive}_1|\Psi\rangle|^2, \\ \langle\Psi|\text{alive}_1\rangle|\text{dead}_2\rangle\langle\text{dead}_2|\langle\text{alive}_1|\Psi\rangle &= |\langle\text{dead}_2|\langle\text{alive}_1|\Psi\rangle|^2, \\ \langle\Psi|\text{dead}_1\rangle|\text{alive}_2\rangle\langle\text{alive}_2|\langle\text{dead}_1|\Psi\rangle &= |\langle\text{alive}_2|\langle\text{dead}_1|\Psi\rangle|^2, \\ \langle\Psi|\text{dead}_1\rangle|\text{dead}_2\rangle\langle\text{dead}_2|\langle\text{dead}_1|\Psi\rangle &= |\langle\text{dead}_2|\langle\text{dead}_1|\Psi\rangle|^2, \end{aligned} \quad (8.162)$$

for the four Bell’s cat-states in Equation 8.161. The following table lists the expectation values of the joint projection operators:

|   | $ \Psi^{(+)}\rangle$ | $ \Psi^{(-)}\rangle$ | $ \Phi^{(+)}\rangle$ | $ \Phi^{(-)}\rangle$ |
|---|----------------------|----------------------|----------------------|----------------------|
| $\langle \text{alive}_2   \langle \text{alive}_1  $ | 1/2                  | 1/2                  | 0                    | 0                    |
| $\langle \text{dead}_2   \langle \text{alive}_1  $  | 0                    | 0                    | 1/2                  | 1/2                  |
| $\langle \text{alive}_2   \langle \text{dead}_1  $  | 0                    | 0                    | 1/2                  | 1/2                  |
| $\langle \text{dead}_2   \langle \text{dead}_1  $   | 1/2                  | 1/2                  | 0                    | 0                    |

Again these results are not surprising. The quantum expectations are consistent with the classical convention. If the ensemble is prepared with 50%–50% “alive-alive” and “dead-dead” cat-pairs ( $|\Psi^{(+)}\rangle$  and  $|\Psi^{(-)}\rangle$ ), the two observers should have a 50%–50% chance of observing an “alive-alive” or “dead-dead” cat-pair. If the ensemble is prepared with 50%–50% “alive-dead” and “dead-alive” cat-pairs ( $|\Phi^{(+)}\rangle$  and  $|\Phi^{(-)}\rangle$ ), the two observers should have a 50%–50% chance of observing an “alive-dead” or “dead-alive” cat-pair.

Although this measurement distinguishes  $|\Psi^{(+)}\rangle$  and  $|\Psi^{(-)}\rangle$  from  $|\Phi^{(+)}\rangle$  and  $|\Phi^{(-)}\rangle$ , choosing the set of projection measurements in Equation 8.162 may not be the best choice. More importantly, this measurement cannot distinguish the entangled two-cat pure states from the mixed states of cat-pairs defined in Equation 8.164.

We now consider a different set of joint projection measurements defined by the vectors  $|+\text{cat}\rangle$  and  $|-\text{cat}\rangle$ ,

$$\begin{aligned} \langle \Psi | +\text{cat}_1\rangle |+\text{cat}_2\rangle \langle +\text{cat}_2| \langle +\text{cat}_1 | \Psi \rangle &= |\langle +\text{cat}_2 | \langle +\text{cat}_1 | \Psi \rangle|^2, \\ \langle \Psi | +\text{cat}_1\rangle |-\text{cat}_2\rangle \langle -\text{cat}_2| \langle +\text{cat}_1 | \Psi \rangle &= |\langle -\text{cat}_2 | \langle +\text{cat}_1 | \Psi \rangle|^2, \\ \langle \Psi | -\text{cat}_1\rangle |+\text{cat}_2\rangle \langle +\text{cat}_2| \langle -\text{cat}_1 | \Psi \rangle &= |\langle +\text{cat}_2 | \langle -\text{cat}_1 | \Psi \rangle|^2, \\ \langle \Psi | -\text{cat}_1\rangle |-\text{cat}_2\rangle \langle -\text{cat}_2| \langle -\text{cat}_1 | \Psi \rangle &= |\langle -\text{cat}_2 | \langle -\text{cat}_1 | \Psi \rangle|^2, \end{aligned} \quad (8.163)$$

for the four Bell’s cat-states in Equation 8.161. The following table lists the expectation values of the joint projection operators:

|   | $ \Psi^{(+)}\rangle$ | $ \Psi^{(-)}\rangle$ | $ \Phi^{(+)}\rangle$ | $ \Phi^{(-)}\rangle$ |
|---|----------------------|----------------------|----------------------|----------------------|
| $\langle +\text{cat}_2   \langle +\text{cat}_1  $ | 1/2                  | 0                    | 1/2                  | 0                    |
| $\langle -\text{cat}_2   \langle +\text{cat}_1  $ | 0                    | 1/2                  | 0                    | 1/2                  |
| $\langle +\text{cat}_2   \langle -\text{cat}_1  $ | 0                    | 1/2                  | 0                    | 1/2                  |
| $\langle -\text{cat}_2   \langle -\text{cat}_1  $ | 1/2                  | 0                    | 1/2                  | 0                    |

For states  $|\Psi^{(+)}\rangle$  and  $|\Phi^{(+)}\rangle$ , quantum mechanics predicts that both observers have a 50%–50% chance of registering a  $|+\text{cat}\rangle$  or a  $|-\text{cat}\rangle$  state. However, if one of them has found his cat in the state  $|+\text{cat}\rangle$  or the state  $|-\text{cat}\rangle$ ,

the other observer must find his cat in the same state. For states  $|\Psi^{(-)}\rangle$  and  $|\Phi^{(-)}\rangle$ , quantum mechanics predicts that the two observers both have a 50%–50% chance of registering a  $|+ \text{cat}\rangle$  or a  $|-\text{cat}\rangle$  state. However, if one of them has found his cat in the state  $|+ \text{cat}\rangle$  or the state  $|-\text{cat}\rangle$ , the other observer must find his cat in the orthogonal state. How can this be? This is indeed surprising. Remember, the ensemble is neither prepared with the “ $|+ \text{cat}\rangle \& |+ \text{cat}\rangle$ ” and “ $|-\text{cat}\rangle \& |-\text{cat}\rangle$ ” pairs for the  $|\Psi^{(+)}\rangle$  and  $|\Phi^{(+)}\rangle$  states nor with the “ $|+ \text{cat}\rangle \& |-\text{cat}\rangle$ ” and “ $|-\text{cat}\rangle \& |+ \text{cat}\rangle$ ” pairs for the  $|\Psi^{(-)}\rangle$  and  $|\Phi^{(-)}\rangle$  states. In classical point of view, the ensemble is prepared with the “ $|\text{alive}\rangle \& |\text{alive}\rangle$ ” and “ $|\text{dead}\rangle \& |\text{dead}\rangle$ ” pairs for the states of  $|\Psi^{(+)}\rangle$  and  $|\Psi^{(-)}\rangle$  and with the “ $|\text{alive}\rangle \& |\text{dead}\rangle$ ” and “ $|\text{dead}\rangle \& |\text{alive}\rangle$ ” pairs for the states  $|\Phi^{(+)}\rangle$  and  $|\Phi^{(-)}\rangle$ . According to Equation 8.157, the states  $|\text{alive}\rangle$  and  $|\text{dead}\rangle$  both have equal chances of being in the state  $|+ \text{cat}\rangle$  and in the state  $|-\text{cat}\rangle$ . Classically, the ensemble should have an equal number of four possible pair combinations: “ $|+ \text{cat}\rangle \& |+ \text{cat}\rangle$ ,” “ $|+ \text{cat}\rangle \& |-\text{cat}\rangle$ ,” “ $|-\text{cat}\rangle \& |+ \text{cat}\rangle$ ,” and “ $|-\text{cat}\rangle \& |-\text{cat}\rangle$ .”

We will learn in later chapters that this surprise is the result of an interference called “two-cat” interference, a unique phenomenon in the quantum world.

### 3. Mixed state

To simulate the entangled states of Equation 8.161, historically, the following mixed states were proposed:

$$\begin{aligned}\hat{\rho}^{(S)} &= \frac{1}{2} [| \text{alive}_1 \rangle \langle \text{alive}_2 | + | \text{dead}_1 \rangle \langle \text{dead}_2 |] \\ \hat{\rho}^{(A)} &= \frac{1}{2} [| \text{alive}_1 \rangle \langle \text{dead}_2 | + | \text{dead}_1 \rangle \langle \text{alive}_2 |],\end{aligned}\quad (8.164)$$

where the density operator is used to specify the mixed state of the ensemble of a cat system. The density operator  $\hat{\rho}^{(S)}$  indicates that the ensemble is prepared with one-half “alive & alive” cats and one-half “dead & dead” cats. The density operator  $\hat{\rho}^{(A)}$  indicates that the ensemble is prepared with one-half “alive & dead” cats and one-half “dead & alive” cats. There is no surprise that the two distant observers will have a 50%–50% chance of observing two alive cats or two dead cats simultaneously, if the ensemble is prepared in  $\hat{\rho}^{(S)}$ , or a 50%–50% chance of observing “cat one alive & cat two dead” or “cat one dead & cat two alive” simultaneously, if the ensemble is prepared in  $\hat{\rho}^{(A)}$ . However, neither  $\hat{\rho}^{(S)}$  nor  $\hat{\rho}^{(A)}$  can achieve the correlation or expectations of Bell’s cat-states for the measurements defined in Equation 8.163. In fact, these measurements on either  $\hat{\rho}^{(S)}$  or  $\hat{\rho}^{(A)}$  will have equal probabilities of observing the pairs “ $+ \text{cat}_1 \& + \text{cat}_2$ ,” “ $+ \text{cat}_1 \& - \text{cat}_2$ ,” “ $- \text{cat}_1 \& + \text{cat}_2$ ,” and “ $- \text{cat}_1 \& - \text{cat}_2$ ,” in the joint detection of the distant observers.

Example (II): Product, entangled, and mixed polarization state of photons

### 1. Product polarization state of two photons

Suppose two independent photons are created from a radiation source at time  $t = 0$  with photon-one polarized at  $45^\circ$  and photon-two polarized at  $-45^\circ$ . Due to the independent creation process, or noninteraction between the subsystems, the two created photons can be treated as a photon system of a product state

$$\begin{aligned} |\Psi\rangle &= |45^\circ_1\rangle \times |-45^\circ_2\rangle \\ &= \frac{1}{2} [|\hat{o}_1\rangle|\hat{o}_2\rangle + |\hat{e}_1\rangle|\hat{e}_2\rangle - |\hat{o}_1\rangle|\hat{e}_2\rangle - |\hat{e}_1\rangle|\hat{o}_2\rangle], \end{aligned} \quad (8.165)$$

where  $\hat{o}$  and  $\hat{e}$  indicate the ordinary-ray and the extraordinary-ray of the uniaxial crystal that we defined in Section 8.9 for polarization measurements.

We apply the same criterion for the free propagation and time evolution for the two-photon system as that for the cat system. It is not surprising that the two observers at large distances will observe four equal possibilities for the polarization correlation: (1) photon-one and photon-two are both polarized in the  $\hat{o}$  direction, (2) photon-one and photon-two are both polarized in the  $\hat{e}$  direction, (3) photon-one is polarized in the  $\hat{o}$  direction and photon-two is polarized in the  $\hat{e}$  direction, and (4) photon-one is polarized in the  $\hat{e}$  direction and photon-two is polarized in the  $\hat{o}$  direction.

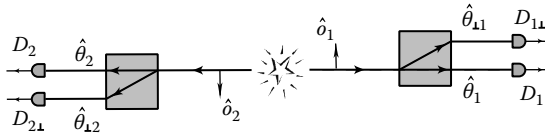
Again, “not surprising” means that there is no difference between the quantum prediction and the classical convention.

### 2. Entangled polarization state of two photons

Suppose a pair of photons is created at the radiation source in one of the following states

$$\begin{aligned} |\Psi^{(+)}\rangle &= \frac{1}{\sqrt{2}} [|\hat{o}_1\rangle|\hat{o}_2\rangle + |\hat{e}_1\rangle|\hat{e}_2\rangle] \\ |\Psi^{(-)}\rangle &= \frac{1}{\sqrt{2}} [|\hat{o}_1\rangle|\hat{o}_2\rangle - |\hat{e}_1\rangle|\hat{e}_2\rangle] \\ |\Phi^{(+)}\rangle &= \frac{1}{\sqrt{2}} [|\hat{o}_1\rangle|\hat{e}_2\rangle + |\hat{e}_1\rangle|\hat{o}_2\rangle] \\ |\Phi^{(-)}\rangle &= \frac{1}{\sqrt{2}} [|\hat{o}_1\rangle|\hat{e}_2\rangle - |\hat{e}_1\rangle|\hat{o}_2\rangle] \end{aligned} \quad (8.166)$$

where the state cannot be written in the form of a product  $|\Psi\rangle = |\Psi_1\rangle|\Psi_2\rangle$ , the state of the photon pair is defined as an entangled state. The above four states are called Bell’s states. Bell’s states form a complete, orthogonal two-photon polarization vector basis. It is worth emphasizing that although Bell’s states of the pair are pure states, the state of photon one and photon two are both

**FIGURE 8.9**

Polarization correlation measurement of a photon pair. Two independent polarization analyzers are oriented at angle  $\theta_1$  and  $\theta_2$  relative to the unit vector  $\hat{o}_1$  and  $\hat{o}_2$ , respectively. Each polarization analyzer has two output ports:  $\hat{\theta}_j$  and  $\hat{\theta}_{\perp j}$ . The four possible joint-detection events correspond to four projection operations defined in Equation 8.168. Remark: all unit vectors are defined in the natural right-hand coordinate system.

mixed states. The state of a subsystem can easily be found by taking a partial trace of its twin

$$\hat{\rho}_j = \frac{1}{2} [ |\hat{\theta}_j\rangle\langle\hat{\theta}_j| + |\hat{e}_j\rangle\langle\hat{e}_j| ] \quad (8.167)$$

where  $j = 1, 2$ . Equation 8.167 indicates that the subsystems are unpolarized.

Again, we apply the same criterion for free propagation and time evolution of the system. The state of the photon pair will remain the same as that of Equation 8.166, except for a trivial overall phase factor. Two distant observers decide to measure the polarization of the photon pair with two independent polarization analyzers oriented at angles  $\theta_1$  and  $\theta_2$  relative to the unit vectors  $\hat{o}_1$  and  $\hat{o}_2$ , respectively, as shown in Figure 8.9. Each polarization analyzer has two output ports:  $\theta_j$  and  $\theta_{\perp j}$ ,  $j = 1, 2$ . The four possible joint-detection events correspond to four joint-projections of the two-photon state defined as follows:

$$\begin{aligned} \langle \Psi | \hat{\theta}_1 \hat{\theta}_2 \rangle \langle \hat{\theta}_2 \hat{\theta}_1 | \Psi \rangle &= |\langle \hat{\theta}_2 \hat{\theta}_1 | \Psi \rangle|^2, \\ \langle \Psi | \hat{\theta}_{\perp 1} \hat{\theta}_{\perp 2} \rangle \langle \hat{\theta}_{\perp 2} \hat{\theta}_{\perp 1} | \Psi \rangle &= |\langle \hat{\theta}_{\perp 2} \hat{\theta}_{\perp 1} | \Psi \rangle|^2, \\ \langle \Psi | \hat{\theta}_1 \hat{\theta}_{\perp 2} \rangle \langle \hat{\theta}_{\perp 2} \hat{\theta}_1 | \Psi \rangle &= |\langle \hat{\theta}_{\perp 2} \hat{\theta}_1 | \Psi \rangle|^2, \\ \langle \Psi | \hat{\theta}_{\perp 1} \hat{\theta}_2 \rangle \langle \hat{\theta}_2 \hat{\theta}_{\perp 1} | \Psi \rangle &= |\langle \hat{\theta}_2 \hat{\theta}_{\perp 1} | \Psi \rangle|^2, \end{aligned} \quad (8.168)$$

where we have written  $|\hat{\theta}_1\rangle|\hat{\theta}_2\rangle$  as  $|\hat{\theta}_1\hat{\theta}_2\rangle$ . Bell's states have the following polarization correlation:

$$\begin{aligned} \langle \Psi^{(+)} | \hat{\theta}_1 \hat{\theta}_2 \rangle \langle \hat{\theta}_2 \hat{\theta}_1 | \Psi^{(+)} \rangle &= \frac{1}{2} \cos^2(\theta_1 - \theta_2) \\ \langle \Psi^{(+)} | \hat{\theta}_{\perp 1} \hat{\theta}_{\perp 2} \rangle \langle \hat{\theta}_{\perp 2} \hat{\theta}_{\perp 1} | \Psi^{(+)} \rangle &= \frac{1}{2} \cos^2(\theta_1 - \theta_2) \\ \langle \Psi^{(+)} | \hat{\theta}_1 \hat{\theta}_{\perp 2} \rangle \langle \hat{\theta}_{\perp 2} \hat{\theta}_1 | \Psi^{(+)} \rangle &= \frac{1}{2} \sin^2(\theta_1 - \theta_2) \\ \langle \Psi^{(+)} | \hat{\theta}_{\perp 1} \hat{\theta}_2 \rangle \langle \hat{\theta}_2 \hat{\theta}_{\perp 1} | \Psi^{(+)} \rangle &= \frac{1}{2} \sin^2(\theta_1 - \theta_2) \end{aligned} \quad (8.169)$$

$$\begin{aligned}
\langle \Psi^{(-)} | \hat{\theta}_1 \hat{\theta}_2 \rangle \langle \hat{\theta}_2 \hat{\theta}_1 | \Psi^{(-)} \rangle &= \frac{1}{2} \cos^2(\theta_1 + \theta_2) \\
\langle \Psi^{(-)} | \hat{\theta}_{\perp 1} \hat{\theta}_{\perp 2} \rangle \langle \hat{\theta}_{\perp 2} \hat{\theta}_{\perp 1} | \Psi^{(-)} \rangle &= \frac{1}{2} \cos^2(\theta_1 + \theta_2) \\
\langle \Psi^{(-)} | \hat{\theta}_1 \hat{\theta}_{\perp 2} \rangle \langle \hat{\theta}_{\perp 2} \hat{\theta}_1 | \Psi^{(-)} \rangle &= \frac{1}{2} \sin^2(\theta_1 + \theta_2) \\
\langle \Psi^{(-)} | \hat{\theta}_{\perp 1} \hat{\theta}_2 \rangle \langle \hat{\theta}_2 \hat{\theta}_{\perp 1} | \Psi^{(-)} \rangle &= \frac{1}{2} \sin^2(\theta_1 + \theta_2)
\end{aligned} \tag{8.170}$$

$$\begin{aligned}
\langle \Phi^{(+)} | \hat{\theta}_1 \hat{\theta}_2 \rangle \langle \hat{\theta}_2 \hat{\theta}_1 | \Phi^{(+)} \rangle &= \frac{1}{2} \sin^2(\theta_1 + \theta_2) \\
\langle \Phi^{(+)} | \hat{\theta}_{\perp 1} \hat{\theta}_{\perp 2} \rangle \langle \hat{\theta}_{\perp 2} \hat{\theta}_{\perp 1} | \Phi^{(+)} \rangle &= \frac{1}{2} \sin^2(\theta_1 + \theta_2) \\
\langle \Phi^{(+)} | \hat{\theta}_1 \hat{\theta}_{\perp 2} \rangle \langle \hat{\theta}_{\perp 2} \hat{\theta}_1 | \Phi^{(+)} \rangle &= \frac{1}{2} \cos^2(\theta_1 + \theta_2) \\
\langle \Phi^{(+)} | \hat{\theta}_{\perp 1} \hat{\theta}_2 \rangle \langle \hat{\theta}_2 \hat{\theta}_{\perp 1} | \Phi^{(+)} \rangle &= \frac{1}{2} \cos^2(\theta_1 + \theta_2)
\end{aligned} \tag{8.171}$$

$$\begin{aligned}
\langle \Phi^{(-)} | \hat{\theta}_1 \hat{\theta}_2 \rangle \langle \hat{\theta}_2 \hat{\theta}_1 | \Phi^{(-)} \rangle &= \frac{1}{2} \sin^2(\theta_1 - \theta_2) \\
\langle \Phi^{(-)} | \hat{\theta}_{\perp 1} \hat{\theta}_{\perp 2} \rangle \langle \hat{\theta}_{\perp 2} \hat{\theta}_{\perp 1} | \Phi^{(-)} \rangle &= \frac{1}{2} \sin^2(\theta_1 - \theta_2) \\
\langle \Phi^{(-)} | \hat{\theta}_1 \hat{\theta}_{\perp 2} \rangle \langle \hat{\theta}_{\perp 2} \hat{\theta}_1 | \Phi^{(-)} \rangle &= \frac{1}{2} \cos^2(\theta_1 - \theta_2) \\
\langle \Phi^{(-)} | \hat{\theta}_{\perp 1} \hat{\theta}_2 \rangle \langle \hat{\theta}_2 \hat{\theta}_{\perp 1} | \Phi^{(-)} \rangle &= \frac{1}{2} \cos^2(\theta_1 - \theta_2)
\end{aligned} \tag{8.172}$$

The correlation functions in Equations 8.169 through 8.172 specify the probabilities for the photodetector at output port  $\theta_1$  ( $\theta_2$ ) to register a photon while its twin is registered at output port  $\theta_2$  ( $\theta_1$ ), for each of the Bell's states. It is easy to see that for any value of  $\theta_1$  ( $\theta_2$ ) there is a unique orientation,  $\theta_2$  ( $\theta_1$ ), for which we expect a maximum probability of 1/2 to register the pair simultaneously, while the pair is prepared in any one of the Bell's states. This is truly a surprise. For each photon pair, coming from the two-photon source, each polarization analyzer has a 50%–50% chance to register its photon at  $\theta_j$  or  $\theta_{\perp j}$ , as if the photon is unpolarized. However, whenever observer one (two) finds a photon polarized along  $\theta_1$  ( $\theta_2$ ) or  $\theta_{\perp 1}$  ( $\theta_{\perp 2}$ ), the photon measured by observer two (one) must be polarized at a unique orientation  $\theta_2$  ( $\theta_1$ ) or  $\theta_{\perp 2}$  ( $\theta_{\perp 1}$ ). Surprisingly, after a large number of measurements, the two distant observers conclude that although the polarization of neither photon one nor photon two is defined, if one of the photons is measured with a polarization along a certain orientation, the polarization of its twin is uniquely determined, despite the distance between the two observers. Remember (1) there is no interaction between the two photons during their propagation and there is no

communication between the two observers either and (2) the ensemble is neither prepared with the photon pairs of  $|\hat{\theta}_1\rangle \& |\hat{\theta}_2\rangle$  and  $|\hat{\theta}_{\perp 1}\rangle \& |\hat{\theta}_{\perp 2}\rangle$  nor with those of  $|\hat{\theta}_1\rangle \& |\hat{\theta}_{\perp 2}\rangle$  and  $|\hat{\theta}_{\perp 1}\rangle \& |\hat{\theta}_2\rangle$ , except when  $\hat{\theta} = \hat{o}$ , or  $\hat{\theta} = \hat{e}$ .

Here, again, a “surprise” means that the quantum predication is different from the classical convention and it seems impossible to understand it under the framework of classical physics.

### 3. Mixed state

It is very clear that the Bell’s states in Equation 8.166 are very different from the following mixed states

$$\begin{aligned}\hat{\rho}^{(S)} &= \frac{1}{2} [ |\hat{o}_1\rangle\langle\hat{o}_2| + |\hat{e}_1\rangle\langle\hat{e}_2| ] \\ \hat{\rho}^{(A)} &= \frac{1}{2} [ |\hat{o}_1\rangle\langle\hat{e}_2| + |\hat{e}_1\rangle\langle\hat{o}_2| ],\end{aligned}\quad (8.173)$$

where the ensemble is prepared with one-half of the photon pairs with polarization  $\hat{o}_1 \& \hat{o}_2$  ( $\hat{o}_1 \& \hat{e}_2$ ) and the other one-half photon pairs with polarization  $\hat{e}_1 \& \hat{e}_2$  ( $\hat{e}_1 \& \hat{o}_2$ ) for  $\hat{\rho}^{(S)}$  ( $\hat{\rho}^{(A)}$ ). Although in  $\hat{\rho}^{(S)}$  ( $\hat{\rho}^{(A)}$ ) the two distant observers will receive half of the pairs in  $\hat{o}_1 \& \hat{o}_2$  ( $\hat{o}_1 \& \hat{e}_2$ ) and another half of the pairs in  $\hat{e}_1 \& \hat{e}_2$  ( $\hat{e}_1 \& \hat{o}_2$ ), neither  $\hat{\rho}^{(S)}$  nor  $\hat{\rho}^{(A)}$  can achieve any correlation similar to that in Equations 8.169 through 8.172, if  $\theta_1$  and  $\theta_2$  are chosen at orientations other than  $\hat{o}$  and  $\hat{e}$ .

---

## 8.11 Time-Dependent Perturbation Theory

In certain problems of practice, Schrödinger equation may not be solvable with exact solutions, but only with a good approximation. In quantum optics, we usually face a problem in finding the eigenstates and the eigenvalues of a Hamiltonian in the form of  $H_0 + V(t)$ , where  $V(t)$  is time dependent and  $H_0$  has exact solutions. This problem is formulated in general as time-dependent perturbation theory in quantum mechanics. We will have a very brief review of the subject. A model and calculation of the photon-counting process will follow as an excise of the time-dependent perturbation theory.

Suppose we shine light on an atomic system at time  $t_0$  and ask what are the chances that the light ionizes the atoms, or releases one photoelectron, two photoelectrons, three photoelectrons, ..., or  $N$  photo-electrons from the atomic system. Alternatively, the problem may be stated in a more general way: we begin with a system of Hamiltonian  $H_0$  and then add a time-dependent perturbation  $V(t)$  at time  $t_0$ . What changes in the eigenstates and eigenvalues of the system occurred due to the perturbation?

It is assumed that, before time  $t_0$ , the system is in state  $|\Psi^{(0)}\rangle$ , which is an exact solution of the Schrödinger equation

$$i\hbar \frac{\partial}{\partial t} |\Psi^{(0)}\rangle = H_0 |\Psi^{(0)}\rangle, \quad t < t_0 \quad (8.174)$$

and the time-dependent perturbation  $V(t)$  is applied at  $t_0$ . To find the new state  $|\Psi^{(t)}\rangle$  of the system, we need to solve the Schrödinger equation

$$i\hbar \frac{\partial}{\partial t} |\Psi^{(t)}\rangle = [H_0 + V(t)] |\Psi^{(t)}\rangle, \quad t > t_0 \quad (8.175)$$

subject to the boundary condition  $|\Psi^{(0)}\rangle = |\Psi^{(t)}\rangle$  at  $t = t_0$ .

Although we may not be able to find exact solutions for Equation 8.175, a good approximation of  $|\Psi^{(t)}\rangle$  is permissible in terms of the superposition

$$|\Psi^{(t)}\rangle = \sum_j c_j |j\rangle \quad (8.176)$$

where  $c_j$  is the probability amplitude of being in the  $j$ th eigenstate,  $|j\rangle$ , of  $H_0$ , and  $|j\rangle$  forms a complete orthonormal vector basis. Furthermore, if  $V(t)$  is much smaller than  $H_0$ , only a few lower-order terms of the expansion are necessary for a good approximation. In this case,  $V(t)$  is treated as a perturbation. In the following discussion, we will assume  $V(t) \ll H_0$ . Thus,  $|\Psi^{(t)}\rangle$  can be written as

$$|\Psi^{(t)}\rangle = e^{-iH_0 t/\hbar} |\Psi(t)\rangle, \quad (8.177)$$

where  $e^{-iH_0 t/\hbar}$  dominates the time dependence of  $|\Psi^{(t)}\rangle$ . It is easy to see that this term contributes to the  $j$ th eigenstate of  $H_0$  a phase factor  $e^{-iE_j t/\hbar} = e^{-i\omega_j t}$ .

Substituting Equation 8.177 into Equation 8.175, we obtain the Schrödinger equation that  $|\Psi(t)\rangle$  must obey

$$i\hbar \frac{\partial}{\partial t} |\Psi(t)\rangle = H_I(t) |\Psi(t)\rangle, \quad (8.178)$$

where

$$H_I(t) = e^{iH_0 t/\hbar} V(t) e^{-iH_0 t/\hbar}. \quad (8.179)$$

The state  $|\Psi(t)\rangle$  and the operator  $H_I(t)$  in Equation 8.178 are said to be in the interaction representation. In quantum mechanics, Equation 8.179 defines the interaction representation for any operator.

Equation 8.178 can be formally integrated:

$$|\Psi(t)\rangle = \left[ e^{\frac{1}{i\hbar} \int_{t_0}^t dt' H_I(t')} \right]_T |\Psi(t_0)\rangle, \quad (8.180)$$

where  $T$  stands for time order. The first three leading terms of the state, i.e., the zero-order, the first-order, and the second-order changes of the state are thus

$$\begin{aligned} |\Psi(t)\rangle &\cong |\Psi(t)\rangle^{(0)} + |\Psi(t)\rangle^{(1)} + |\Psi(t)\rangle^{(2)} \\ &= |\Psi(t_0)\rangle - \frac{i}{\hbar} \int_{t_0}^t dt' H_I(t') |\Psi(t_0)\rangle \\ &\quad + \frac{1}{(i\hbar)^2} \int_{t_0}^t dt' \int_{t_0}^{t'} dt'' H_I(t') H_I(t'') |\Psi(t_0)\rangle. \end{aligned} \quad (8.181)$$

The notation  $|\Psi(t)\rangle^{(j)}$ ,  $j = 0, 1, 2, \dots$ , indicates the  $j$ th order changes of the state. It should be emphasized that the operators in  $|\Psi(t)\rangle^{(2)}$  are in time order. Care has to be taken when the operators do not commute and, in general, this is the more likely case.

It is interesting to find, term by term, the physical correspondence of Equation 8.181, in connection with the photodetection process. The zero-order term  $|\Psi(t)\rangle^{(0)}$ , of course, is the no-action term. The state of the atomic system and the state of the field have no changes. The second term,  $|\Psi(t)\rangle^{(1)}$ , and the third term,  $|\Psi(t)\rangle^{(2)}$ , in Equation 8.181 are the first-order and the second-order changes of the state corresponding to the annihilation of one photon and two photons from the field, respectively.

## 8.12 Measurement of Light: Photon Counting

In classical theory, a photodetector measures the intensity of a light wave and thus relates to the electromagnetic fields in a phenomenological way. It is quantum theory that provides a successful solution to the physical process of atomic transition-photon annihilation. Although a detailed study of the theory is not the goal of the following discussion, a brief review of the concepts are necessary for understanding the physics of photon-counting detection and the measurement of quantum correlations.

We start by defining an idealized photon-counting detector as a point detector. One may imagine it as an atom with all concerned transition probabilities in terms of the frequencies of the light field.  $H_0$  has two parts,

$$H_0 = H_0^A + H_0^F, \quad (8.182)$$

where  $H_0^A$  and  $H_0^F$  are the Hamiltonian for the free atom and the free field, with complete sets of orthonormal eigenstates  $|j\rangle$  and  $|n\rangle$ , respectively. To simplify the analysis, we assume the atom is in its ground state  $|0\rangle$  before the

interaction. The initial state of the field,  $|\Psi_F^{(0)}\rangle$ , will be treated more generally as a superposition, in terms of the eigenstates,  $|n\rangle$ , of  $H_0^F = \hbar\omega\hat{N}$ , where  $\hat{N}$  is the number operator. To simplify the discussion, we will restrict ourselves to single mode. The result can be easily generalized to the multimode case. Assume the atom is ionized from its ground state due to the dipole–field interaction,  $V(t) = -\hat{\mu} \cdot \hat{E}^{(+)}$ , where  $\hat{\mu}$  is the dipole moment of the atom. The interaction Hamiltonian is thus

$$\begin{aligned} H_I(t) &= e^{iH_0t/\hbar} V(t) e^{-iH_0t/\hbar} \\ &= -e^{iH_0^At/\hbar} \hat{\mu} e^{-iH_0^At/\hbar} e^{iH_0^Ft/\hbar} \hat{E}^{(+)} e^{-iH_0^Ft/\hbar}, \end{aligned} \quad (8.183)$$

where we have simplified the problem to one dimension. Following Equation 8.181, the state  $|\Psi(t)\rangle$  in first-order approximation is thus

$$|\Psi(t)\rangle \cong |0\rangle \left| \Psi_F^{(0)} \right\rangle - \frac{i}{\hbar} \int_{t_0}^t dt' e^{iH_0t'/\hbar} (-\hat{\mu} \hat{E}^{(+)}) e^{-iH_0t'/\hbar} |0\rangle \left| \Psi_F^{(0)} \right\rangle \quad (8.184)$$

The total probability of ionizing the atom from its ground state to a set of possible final states by absorbing a photon from the field is thus

$$\begin{aligned} P &= \sum_f |\langle f | \Psi(t) \rangle|^2 \\ &\cong \frac{1}{\hbar^2} \int_{t_0}^t dt' \int_{t_0}^{t'} dt'' \sum_{j,n} \langle 0 | e^{-iH_0^At''/\hbar} \hat{\mu}^* e^{iH_0^At''/\hbar} | j \rangle \langle j | e^{iH_0^At'/\hbar} \hat{\mu} e^{-iH_0^At'/\hbar} | 0 \rangle \\ &\quad \left\langle \Psi_F^{(0)} \left| e^{-iH_0^Ft''/\hbar} \hat{E}^{(-)}(t'') e^{iH_0^Ft''/\hbar} | n \rangle \langle n | e^{iH_0^Ft'/\hbar} \hat{E}^{(+)}(t') e^{-iH_0^Ft'/\hbar} \right| \Psi_F^{(0)} \right\rangle \\ &\cong \frac{1}{\hbar^2} \int_{t_0}^t dt' \int_{t_0}^{t'} dt'' \sum_{j,n} e^{-i\left(\frac{E_j-E_0}{\hbar}-\omega\right)(t''-t')} \langle 0 | \hat{\mu}^* | j \rangle \langle j | \hat{\mu} | 0 \rangle \\ &\quad \left\langle \Psi_F^{(0)} \left| \hat{E}^{(-)}(t'') | n \rangle \langle n |, \hat{E}^{(+)}(t') \right| \Psi_F^{(0)} \right\rangle. \end{aligned} \quad (8.185)$$

To complete the calculation, we first consider summing Equation 8.185 over all final states. Suppose  $\langle j | \hat{\mu} | 0 \rangle$  and  $\langle n | \hat{E}^{(+)} | \Psi_F^{(0)} \rangle$  do not change violently within the group of final states. The sum turns into an integral over the energy  $E_j$  with a certain density distribution function. We further assume a smooth density distribution function. The total transition probability is thus proportional to

$$P \propto \int_{t_0}^t dt' \left\langle \Psi_F^{(0)} \left| \hat{E}^{(-)}(t') \hat{E}^{(+)}(t') \right| \Psi_F^{(0)} \right\rangle, \quad (8.186)$$

where we have used the completeness relation

$$\sum_m |m\rangle\langle m| = 1 \quad (8.187)$$

and the mathematical approximation for broadband integral

$$\int dE_j e^{-i\left(\frac{E_j-E_0}{\hbar}-\omega\right)(t''-t')} \sim \delta(t'' - t'). \quad (8.188)$$

The transition rate of ionizing the atom by absorbing a photon from the field at coordinate  $\mathbf{r}$  between time  $t$  and  $t + dt$  is thus

$$G(\mathbf{r}, t) \propto \left\langle \Psi_F^{(0)} \left| \hat{E}^{(-)}(\mathbf{r}, t) \hat{E}^{(+)}(\mathbf{r}, t) \right| \Psi_F^{(0)} \right\rangle. \quad (8.189)$$

In summary, we have concluded that the probability of annihilating a photon as a photodetection event at space-time point  $(\mathbf{r}, t)$ , is proportional to

$$\langle \Psi | \hat{E}^{(-)}(\mathbf{r}, t) \hat{E}^{(+)}(\mathbf{r}, t) | \Psi \rangle = |\hat{E}^{(+)}(\mathbf{r}, t)| \Psi \rangle|^2.$$

Notice that a pure state has been used in the above discussion. Equation 8.189 can be easily generalized to a mixed state

$$\begin{aligned} G(\mathbf{r}, t) &\propto \sum_j P_j \langle \Psi_j | \hat{E}^{(-)}(\mathbf{r}, t) \hat{E}^{(+)}(\mathbf{r}, t) | \Psi_j \rangle \\ &= Tr [\hat{\rho} \hat{E}^{(-)}(\mathbf{r}, t) \hat{E}^{(+)}(\mathbf{r}, t)] \end{aligned} \quad (8.190)$$

where  $P_j$  is the probability of being in the  $j$ th pure state  $|\Psi_j\rangle$ , and

$$\hat{\rho} = \sum_j P_j |\Psi_j\rangle\langle\Psi_j| \quad (8.191)$$

is the density operator of the field or the system of photons. Notice that we have dropped the superscript from the state  $|\Psi_j^{(0)}\rangle$ . The time-averaged photon-counting rate is thus

$$R \propto \frac{1}{T} \int_0^T dt G(\mathbf{r}, t) = \int_T dt \langle \hat{E}^{(-)}(\mathbf{r}, t) \hat{E}^{(+)}(\mathbf{r}, t) \rangle, \quad (8.192)$$

where  $T$  is the total time of averaging. The time averaging here is no different than that given in Chapter 1.

### 8.13 Measurement of Light: Joint Detection of Photons

In the following, we calculate the probability of the joint detection of photon pairs by two independent photon-counting detectors. Again, we assume

idealized point detectors. To simplify the analysis, we assume the two independent atoms are both in their ground state,  $|0_1\rangle$  and  $|0_2\rangle$ , before the interaction, where the subscripts label the individual atoms, or the point photon-counting detectors. The Hamiltonian  $H_0$  has three parts:

$$H_0 = H_{01}^A + H_{02}^A + H_0^F, \quad (8.193)$$

where  $H_{0j}^A$ ,  $j = 1, 2$ , is the Hamiltonian of the  $j$ th free atom. Assume the two atoms are both ionized from their ground state due to the dipole–field interaction  $V_1(t) = -\hat{\mu}_1 \cdot \hat{E}_1^{(+)}$  and  $V_2(t) = -\hat{\mu}_2 \cdot \hat{E}_2^{(+)}$ , where  $\hat{\mu}_j$ ,  $j = 1, 2$ , is the dipole moment of the  $j$ th atom. The interaction Hamiltonian is thus

$$\begin{aligned} H_I(t) &= e^{iH_0t/\hbar} [V_1(t) + V_2(t)] e^{-iH_0t/\hbar} \\ &= -e^{iH_{01}^At/\hbar} \hat{\mu}_1 e^{-iH_{01}^At/\hbar} e^{iH_0^Ft/\hbar} \hat{E}_1^{(+)} e^{-iH_0^Ft/\hbar} \\ &\quad - e^{iH_{02}^At/\hbar} \hat{\mu}_2 e^{-iH_{02}^At/\hbar} e^{iH_0^Ft/\hbar} \hat{E}_2^{(+)} e^{-iH_0^Ft/\hbar} \\ &= H_{I1}(t) + H_{I2}(t). \end{aligned} \quad (8.194)$$

Following Equation 8.181, the first-order change of the state,  $|\Psi(t)\rangle^{(1)}$  is thus

$$|\Psi(t)\rangle^{(1)} = -\frac{i}{\hbar} \int_{t_0}^t dt' H_{I1}(t') |\Psi(t_0)\rangle - \frac{i}{\hbar} \int_{t_0}^t dt' H_{I2}(t') |\Psi(t_0)\rangle.$$

The two terms correspond to the single-photon transition of atoms one and two, respectively. The second order change of the state,  $|\Psi(t)\rangle^{(2)}$ , has four terms

$$\begin{aligned} |\Psi(t)\rangle^{(2)} &= \frac{1}{(i\hbar)^2} \int_{t_0}^t dt' \int_{t_0}^{t'} dt'' H_{I1}(t') H_{I1}(t'') |\Psi(t_0)\rangle \\ &\quad + \frac{1}{(i\hbar)^2} \int_{t_0}^t dt' \int_{t_0}^{t'} dt'' H_{I2}(t') H_{I2}(t'') |\Psi(t_0)\rangle \\ &\quad + \frac{1}{(i\hbar)^2} \int_{t_0}^t dt' \int_{t_0}^{t'} dt'' H_{I1}(t') H_{I2}(t'') |\Psi(t_0)\rangle \\ &\quad + \frac{1}{(i\hbar)^2} \int_{t_0}^t dt' \int_{t_0}^{t'} dt'' H_{I2}(t') H_{I1}(t'') |\Psi(t_0)\rangle. \end{aligned}$$

All four terms correspond to the joint annihilation of two photons from the field. The first two terms correspond to the two-photon transition associated

with an atom that contributes to the single detector counting rate. For the joint detection events of two photodetectors, we are interested in the last two terms of this group. Assume the coincidence detection circuit only selects one of these joint detection events by time ordering. The total probability of jointly ionizing atom one and atom two from their ground states to a set of possible final states is thus

$$\sum_f |\langle f | \Psi(t) \rangle|^2 \cong \frac{1}{\hbar^4} \int_{t_0}^{t_1} dt'_1 \int_{t_0}^{t'_1} dt''_1 \int_{t_0}^{t_2} dt'_2 \int_{t_0}^{t'_2} dt''_2$$

$$\sum_{j_1, j_2, n,} \langle 0_1 | e^{-iH_{01}^A t''_1/\hbar} \hat{\mu}_1^* e^{iH_{01}^A t''_1/\hbar} | j_1 \rangle \langle j_1 | e^{iH_{01}^A t'_1/\hbar} \hat{\mu}_1 e^{-iH_{01}^A t'_1/\hbar} | 0_1 \rangle$$

$$\langle 0_2 | e^{-iH_{02}^A t''_2/\hbar} \hat{\mu}_2^* e^{iH_{02}^A t''_2/\hbar} | j_2 \rangle \langle j_2 | e^{iH_{02}^A t'_2/\hbar} \hat{\mu}_2 e^{-iH_{02}^A t'_2/\hbar} | 0_2 \rangle$$

$$\langle \Psi_F^{(0)} | e^{-iH_{01}^F t''_1/\hbar} e^{-iH_{02}^F t''_2/\hbar} \hat{E}_1^{(-)}(t''_1) \hat{E}_2^{(-)}(t''_2) e^{iH_{02}^F t''_2/\hbar} e^{iH_{01}^F t''_1/\hbar} | n \rangle$$

$$\langle n | e^{iH_{01}^F t'_1/\hbar} e^{iH_{02}^F t'_2/\hbar} \hat{E}_2^{(+)}(t'_2) \hat{E}_1^{(+)}(t'_1) e^{-iH_{02}^F t'_2/\hbar} e^{-iH_{01}^F t'_1/\hbar} | \Psi_F^{(0)} \rangle. \quad (8.195)$$

Similar to the single-detection case, to complete the calculation, we first consider summing Equation 8.195 over all final states and then apply the completeness relation and the delta function approximation. The total joint transition probability is thus proportional to

$$P \propto \int_{t_0}^{t_1} dt'_1 \int_{t_0}^{t_2} dt'_2 \langle \Psi_F^{(0)} | \hat{E}_1^{(-)}(t'_1) \hat{E}_2^{(-)}(t'_2) \hat{E}_2^{(+)}(t'_2) \hat{E}_1^{(+)}(t'_1) | \Psi_F^{(0)} \rangle.$$

The joint transition rate of ionizing the two atoms by absorbing a photon from the field at coordinate  $\mathbf{r}_1$  between time  $t_1$  and  $t_1 + dt_1$  and another photon from the field at coordinate  $\mathbf{r}_2$  between time  $t_2$  and  $t_2 + dt_2$  is thus

$$G(\mathbf{r}_1, t_1; \mathbf{r}_2, t_2)$$

$$\propto \langle \Psi_F^{(0)} | \hat{E}_1^{(-)}(\mathbf{r}_1, t_1) \hat{E}_2^{(-)}(\mathbf{r}_2, t_2) \hat{E}_2^{(+)}(\mathbf{r}_2, t_2) \hat{E}_1^{(+)}(\mathbf{r}_1, t_1) | \Psi_F^{(0)} \rangle. \quad (8.196)$$

In summary, we have concluded that the joint atomic transition rate, or the probability of jointly annihilating a photon as a photodetection event occurs at space-time point  $(\mathbf{r}_1, t_1)$ , and a second photodetection event occurs at space-time point  $(\mathbf{r}_2, t_2)$ , is proportional to the expectation value of the Hermitian operator  $\hat{E}_1^{(-)} \hat{E}_2^{(-)} \hat{E}_2^{(+)} \hat{E}_1^{(+)}$  on the initial state of the light field  $|\Psi_F^{(0)}\rangle$ . This Hermitian operator is a fourth order operator of the field, and thus, is also called the fourth order moment. It should be emphasized that the operator  $\hat{E}_1^{(-)} \hat{E}_2^{(-)} \hat{E}_2^{(+)} \hat{E}_1^{(+)}$ , in general, cannot be defined as the product of two

intensity operators due to the commutation property of the field operators. Although  $G(\mathbf{r}_1, t_1; \mathbf{r}_2, t_2)$  is sometimes written in the following form:

$$G(\mathbf{r}_1, t_1; \mathbf{r}_2, t_2) = \langle : \hat{I}(\mathbf{r}_1, t_1) \hat{I}(\mathbf{r}_2, t_2) : \rangle, \quad (8.197)$$

where  $\langle : \dots : \rangle$  denotes normal order. We should not be confused with the notation. The notation means nothing except writing Equation 8.196 in a different form. The commutation rule of the field operators distinguishes Equation 8.196 from its classical analogy.

Notice again that we have been using a pure state in the above calculation. The result of Equation 8.196 can easily be generalized to a mixed state

$$\begin{aligned} G(\mathbf{r}_1, t_1; \mathbf{r}_2, t_2) &\propto \sum_j P_j \langle \Psi_j | \hat{E}^{(-)}(\mathbf{r}_1, t_1) \hat{E}^{(-)}(\mathbf{r}_2, t_2) \hat{E}^{(+)}(\mathbf{r}_2, t_2) \hat{E}^{(+)}(\mathbf{r}_1, t_1) | \Psi_j \rangle \\ &= \text{tr} [ \hat{\rho} \hat{E}^{(-)}(\mathbf{r}_1, t_1) \hat{E}^{(-)}(\mathbf{r}_2, t_2) \hat{E}^{(+)}(\mathbf{r}_2, t_2) \hat{E}^{(+)}(\mathbf{r}_1, t_1) ], \end{aligned} \quad (8.198)$$

where

$P_j$  is the probability of being in the  $j$ th initial pure state  $|\Psi_j\rangle$

$\hat{\rho}$  is the density operator of the field or the system of photons, as defined earlier

The averaged joint detection counting rate is thus

$$\begin{aligned} R &\propto \int_T dt_1 \int_T dt_2 G(\mathbf{r}_1, t_1; \mathbf{r}_2, t_2) \\ &= \int_T dt_1 \int_T dt_2 \langle \hat{E}^{(-)}(\mathbf{r}_1, t_1) \hat{E}^{(-)}(\mathbf{r}_2, t_2) \hat{E}^{(+)}(\mathbf{r}_2, t_2) \hat{E}^{(+)}(\mathbf{r}_1, t_1) \rangle \end{aligned} \quad (8.199)$$

where  $T$  is the total time of averaging.

## 8.14 Field Propagation in Space-Time

The quantum theory of photodetection is a straightforward application of the quantum theory of time-dependent perturbation. The first-order approximation calculates the probability that a photon is annihilated at space-time point  $(\mathbf{r}, t)$  of the photodetection event, or the photon-counting rate of a photodetector at position  $\mathbf{r}$  and time  $t$ ,

$$G(\mathbf{r}, t) \propto \left\langle \Psi_F^{(0)} \left| \hat{E}^{(-)}(\mathbf{r}, t) \hat{E}^{(+)}(\mathbf{r}, t) \right| \Psi_F^{(0)} \right\rangle.$$

The second-order approximation gives the probability that a pair of photons is annihilated jointly at the space-time points  $(\mathbf{r}_1, t_1)$  and  $(\mathbf{r}_2, t_2)$ : or the joint-detection counting rate of a pair of photodetectors at positions  $(\mathbf{r}_1, \mathbf{r}_2)$ , and times  $(t_1, t_2)$ :

$$G(\mathbf{r}_1, t_1; \mathbf{r}_2, t_2) \propto \left\langle \Psi_F^{(0)} \left| \hat{E}^{(-)}(\mathbf{r}_1, t_1) \hat{E}^{(-)}(\mathbf{r}_2, t_2) \hat{E}^{(+)}(\mathbf{r}_2, t_2) \hat{E}^{(+)}(\mathbf{r}_1, t_1) \right| \Psi_F^{(0)} \right\rangle.$$

The joint-detection counting rate is also called "coincidence"-counting rate, although  $t_1$  is not necessarily equal to  $t_2$ . In these formulas,  $\left| \Psi_F^{(0)} \right\rangle$  is the state of the field at  $t_0$ , which is the time when the perturbation  $V(t)$  is applied, i.e., at the very beginning of the photodetection event. In typical optical measurements,  $\left| \Psi_F^{(0)} \right\rangle$  is often evaluated from state  $|\Psi(0)\rangle$  that is prepared at the radiation source. The state  $|\Psi(0)\rangle$  of the field that is excited at the radiation source is usually known from early measurements or predictable through the study of the radiation mechanism of the light source.

This is a typical quantum-mechanical dynamical problem: we are interested in knowing the expectation value of an operator  $\hat{A}$  at time  $t$

$$\langle \hat{A} \rangle_t = \langle \Psi(t) | \hat{A} | \Psi(t) \rangle, \quad (8.200)$$

with the knowledge of the quantum state of the system at an early time, such as  $|\Psi(0)\rangle$  at time  $t = 0$ .

Since we have shown that any state of a radiation field can be described by the superposition of the eigenstates of the Hamiltonian, such as Equation 8.52, and proved that an energy eigenstate simply develops a phase factor,  $e^{-iE_n t/\hbar}$ , from time  $t = 0$  to  $t$ . The quantum state of the field at time  $t$  is thus written as

$$\begin{aligned} |\Psi(t)\rangle &= \sum_E e^{-iE_n t/\hbar} |E\rangle \langle E| \Psi(0) \rangle \\ &= e^{-i\hat{H}t/\hbar} |\Psi(0)\rangle, \end{aligned} \quad (8.201)$$

where  $|E\rangle$  represents the eigenstate of the Hamiltonian. To obtain the result of Equation 8.201, we have assumed a complete orthogonal set of energy eigenstates

$$\sum_E |E\rangle \langle E| = 1.$$

Equation 8.200 is thus rewritten as

$$\langle \hat{A} \rangle_t = \langle \Psi(0) | e^{i\hat{H}t/\hbar} \hat{A} e^{-i\hat{H}t/\hbar} | \Psi(0) \rangle. \quad (8.202)$$

We are ready to work in the Heisenberg representation to propagate the field operator from  $t = 0$  at the radiation source to  $t_0$  of the photodetection

event, rather than working in the Schrödinger representation to develop the state of  $|\Psi(0)\rangle$ . If we define a time-dependent operator  $\hat{A}(t)$  by

$$\hat{A}(t) = e^{i\hat{H}t/\hbar} \hat{A} e^{-i\hat{H}t/\hbar}, \quad (8.203)$$

then we can rewrite Equation 8.202 as

$$\langle \hat{A} \rangle_t = \langle \Psi(0) | \hat{A}(t) | \Psi(0) \rangle. \quad (8.204)$$

Differentiating Equation 8.203 with respect to time  $t$ , we find

$$i\hbar \frac{d\hat{A}(t)}{dt} = [\hat{A}(t), \hat{H}], \quad (8.205)$$

if  $\hat{A}(t)$  does not depend explicitly on time  $t$ . In Equation 8.205, we have assumed that  $\hat{H}$  commutes with  $e^{-i\hat{H}t/\hbar}$ . Equation 8.205 is called Heisenberg equation of motion for operators.

It is easy to show that for any product of two or more operators, such as  $\hat{A} = \hat{B}\hat{C}$ , we can define a product of two or more time-dependent operators, such as  $\hat{A}(t) = \hat{B}(t)\hat{C}(t)$ ,

$$\begin{aligned} \langle \Psi(t) | \hat{B} \hat{C} | \Psi(t) \rangle &= \langle \Psi(0) | e^{i\hat{H}t/\hbar} \hat{B} \hat{C} e^{-i\hat{H}t/\hbar} | \Psi(0) \rangle \\ &= \langle \Psi(0) | e^{i\hat{H}t/\hbar} \hat{B} e^{-i\hat{H}t/\hbar} e^{i\hat{H}t/\hbar} \hat{C} e^{-i\hat{H}t/\hbar} | \Psi(0) \rangle \\ &= \langle \Psi(0) | \hat{B}(t) \hat{C}(t) | \Psi(0) \rangle, \end{aligned} \quad (8.206)$$

where  $e^{-i\hat{H}t/\hbar} e^{i\hat{H}t/\hbar} = \mathbf{1}$  has been used. It is also easy to show that  $\hat{B}(t)$  and  $\hat{C}(t)$  obey the Heisenberg equation of motion, respectively, and thus can be propagated, individually,

$$i\hbar \frac{d\hat{B}(t)}{dt} = [\hat{B}(t), \hat{H}], \quad i\hbar \frac{d\hat{C}(t)}{dt} = [\hat{C}(t), \hat{H}]. \quad (8.207)$$

Based on the above results, in the Heisenberg representation, we have the counting rate of a photodetector, or the probability for a photon to be annihilated at space-time point  $(\mathbf{r}, t)$ ,

$$\begin{aligned} G(\mathbf{r}, t) &\propto \langle \Psi(0) | \hat{E}^{(-)}(\mathbf{r}, t) \hat{E}^{(+)}(\mathbf{r}, t) | \Psi(0) \rangle \\ &= |\hat{E}^{(+)}(\mathbf{r}, t) | \Psi(0) \rangle|^2, \end{aligned} \quad (8.208)$$

and the joint-detection counting rate of a pair of photodetectors, or the probability for a pair of photons to be annihilated jointly at space-time points

$(\mathbf{r}_1, t_1)$  and  $(\mathbf{r}_2, t_2)$ :

$$\begin{aligned} G(\mathbf{r}_1, t_1; \mathbf{r}_2, t_2) &\propto \langle \Psi(0) | \hat{E}^{(-)}(\mathbf{r}_1, t_1) \hat{E}^{(-)}(\mathbf{r}_2, t_2) \hat{E}_2^{(+)}(\mathbf{r}_2, t_2) \hat{E}_1^{(+)}(\mathbf{r}_1, t_1) | \Psi(0) \rangle \\ &= |\hat{E}_2^{(+)}(\mathbf{r}_2, t_2) \hat{E}_1^{(+)}(\mathbf{r}_1, t_1) | \Psi(0) \rangle|^2 \end{aligned} \quad (8.209)$$

with the understanding that the field operators  $\hat{E}^{(\pm)}(\mathbf{r}_j, t_j)$  are propagated from  $(\mathbf{r}^0, t^0)$  of the radiation source. Notice, we have used a different notation,  $t^0$ , to distinguish the perturbation time,  $t_0$ , of the photodetection event. To simplify the notation, we usually choose  $t^0 = 0$  and write the state  $|\Psi(0)\rangle$  as  $|\Psi\rangle$ . If the radiation source can be treated as a point source, we may also choose  $\mathbf{r}^0 = 0$ . Care has to be taken in the cases when the finite size of the source has to be taken into account, especially in “near-field” measurements. Equations 8.208 and 8.209 are the basic formalisms for photon-counting measurements.

Regarding the propagation of the field operator in space-time, in general, we need to obtain the time evolution of the annihilation and creation operator and to find the solution of the Helmholtz equation subject to the corresponding boundary condition of the field. The mathematical tools for defining the spatial mode function of the field are well developed in classical optics and there is no difference in quantum optics. The time evolution of the annihilation operator,  $\hat{a}_{\mathbf{k}}(t)$ , and the creation operator,  $\hat{a}_{\mathbf{k}}^\dagger(t)$ , can be easily obtained for certain types of Hamiltonians, such as the free-field Hamiltonian of Equation 8.40, by solving the Heisenberg equation of motion

$$\begin{aligned} \frac{d}{dt} \hat{a}_{\mathbf{k}}(t) &= \frac{1}{i\hbar} [\hat{a}_{\mathbf{k}}(t), \hat{H}] = -i\omega \hat{a}_{\mathbf{k}}(t) \\ \frac{d}{dt} \hat{a}_{\mathbf{k}}^\dagger(t) &= \frac{1}{i\hbar} [\hat{a}_{\mathbf{k}}^\dagger(t), \hat{H}] = i\omega \hat{a}_{\mathbf{k}}^\dagger(t) \end{aligned} \quad (8.210)$$

with the solution

$$\begin{aligned} \hat{a}_{\mathbf{k}}(t) &= \hat{a}_{\mathbf{k}}(0) e^{-i\omega t} \\ \hat{a}_{\mathbf{k}}^\dagger(t) &= \hat{a}_{\mathbf{k}}^\dagger(0) e^{i\omega t}, \end{aligned} \quad (8.211)$$

where we have assigned  $t^0 = 0$ . We thus write the free field operator in the Heisenberg representation

$$\begin{aligned} \hat{\mathbf{E}}(\mathbf{r}, t) &= \sum_{\mathbf{k}} \hat{\mathbf{e}}_k i \mathcal{E}_{\mathbf{k}} \hat{a}_{\mathbf{k}}(0) e^{-i\omega t} u_k(\mathbf{r}) + \sum_{\mathbf{k}} \hat{\mathbf{e}}_k (-i) \mathcal{E}_{\mathbf{k}} \hat{a}_{\mathbf{k}}^\dagger(0) e^{i\omega t} u_k^*(\mathbf{r}) \\ &= \hat{\mathbf{E}}^{(+)}(\mathbf{r}, t) + \hat{\mathbf{E}}^{(-)}(\mathbf{r}, t), \end{aligned} \quad (8.212)$$

where  $\mathbf{u}_k(\mathbf{r})$  is the solution of the Helmholtz equation of Equation 8.57 subject to the required boundary conditions. In Equation 8.212,  $\hat{\mathbf{E}}^{(+)}(\mathbf{r}, t)$  and

$\hat{\mathbf{E}}^{(-)}(\mathbf{r}, t)$  correspond to the physical processes of photon annihilation and creation at the space-time point  $(\mathbf{r}, t)$ , respectively.

Under certain experimental conditions, such as far-field measurements, the plane wave is a good approximation. The positive and the negative field operators in Equation 8.212 can then be written as

$$\begin{aligned}\hat{\mathbf{E}}^{(+)}(\mathbf{r}, t) &= \sum_{\mathbf{k}} \hat{\mathbf{e}}_k i \mathcal{E}_{\mathbf{k}} \hat{a}_{\mathbf{k}}(0) e^{-i(\omega t - \mathbf{k} \cdot \mathbf{r})} \\ \hat{\mathbf{E}}^{(-)}(\mathbf{r}, t) &= \sum_{\mathbf{k}} \hat{\mathbf{e}}_k (-i) \mathcal{E}_{\mathbf{k}} \hat{a}_{\mathbf{k}}^\dagger(0) e^{i(\omega t - \mathbf{k} \cdot \mathbf{r})}\end{aligned}\quad (8.213)$$


---

## Summary

In this chapter, we quantized the radiation field and introduced a number of key concepts of quantum optics. Why do we need to quantize the radiation field? This chapter reviewed two important discoveries in the history of physics to answer this question. The analysis on field quantization and light quantum are standard, similar to most of the text books. In this chapter, we introduced the number state and coherent state as two sets of convenient vector bases to specify the state of radiation field. Based on these concepts, a simple model of light source containing of a large number of two-level atomic transitions is introduced to simulate incoherent and coherent radiation sources. We especially analyzed the simulation for the generation of multimode single-photon state and two-photon state. Under the concept of single-photon state, we distinguished the pure states from mixed states. Under the concept of two-photon state, we analyzed the differences between product states, entangled states, and mixed states of photon pairs. After the review of time-dependent perturbation theory, finally, this chapter introduced the Glauber photodetection theory in first-order photon counting and in second-order coincidence photon-counting. The last part of this chapter gives example for the calculation of first-order photon-counting measurement and second-order coincidence photon-counting measurement in terms of Schrödinger representation and Heisenberg representation.

---

## Suggested Reading

Baym, G., *Lectures on Quantum Mechanics*, Benjamin/Cummings, Metro Park, CA 1981.

Dirac, P.A.M., *Proc. Roy. Soc., A* 114, 243 (1927).

- Einstein, A., *Ann. Phys.* 17, 132 (1905).
- Glauber, R.J., *Phys. Rev.* 130, 2529 (1963); *Phys. Rev.* 131, 2766 (1963).
- Hertz, H.R., *Ann. Phys.* 267, 421, 983 (1987).
- Jeans, J.H., *Phil. Mag.* 10, 91 (1905).
- Loudon, R., *The Quantum Theory of Light*, Oxford Science Publications, Oxford, U.K., 2000.
- Mandel, L. and E. Wolf, *Optical Coherence and Quantum Optics*, Cambridge University Press, London, U.K., 1995.
- Planck, M., *Verh. dt. Phys. Ges.* 2, 202, 237 (1900).
- Rayleigh, J.W.S., *Phil. Mag.* 49, 539 (1900); *Nature* 72, 54, 243 (1905).
- Scully, M.O. and M.S. Zubairy, *Quantum Optics*, Cambridge University Press, Cambridge, U.K., 1997.
- Wien, W., *Ann. Phys.* 58, 662 (1896).



# 9

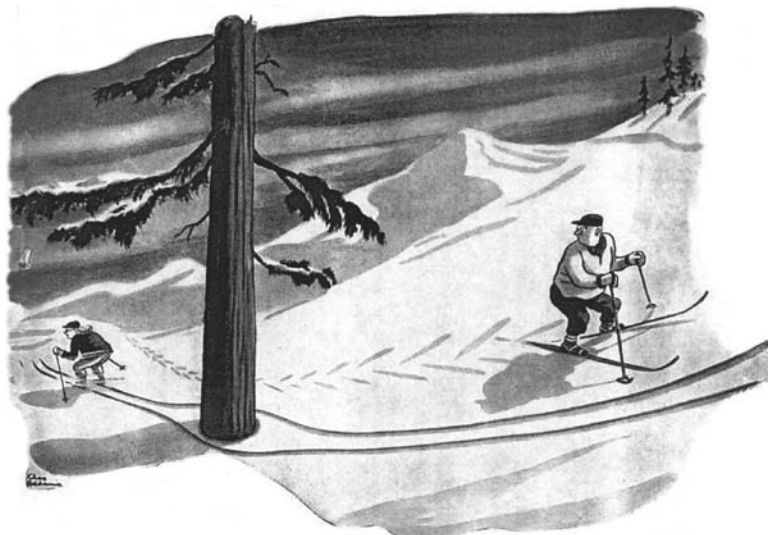
---

## *Quantum Theory of Optical Coherence*

---

In this chapter, we study the quantum theory of optical coherence, which has been especially successful in dealing with the coherent phenomena of light at the quantum level. In fact, we have inexplicitly introduced the quantum concepts into the simple model of radiation from the very beginning of Chapter 1, although no quantization is involved. The large number of sub-sources, either radiate independently or coherently, are connected with a large number of atomic transitions. The very basic contribution to the radiation field from each sub-source is therefore the creation of a photon. In the classical bright light condition, a measurement may involve the creation and annihilation of a large number of photons. The individual behavior of a photon may not be that significant in the final observation. However, it does not prevent us to ask very simple questions: What would happen if a photon and only one photon presents in the observation? Can a photon interfere with itself? In a “single-photon interferometer,” does a photon pass “both-paths” or “which-path”? Or: What would happen if a pair of photons and only a pair of photons presents in the observation? If one photon is observed at a certain space-time coordinate, can we find the other one at another unique space-time coordinate with certainty? Quantum theory of coherence deals with this kind of physics and gives its quantitative predictions and qualitative interpretations according to the principles of quantum mechanics. In the light of new technology, we are now able to study these problems experimentally. In certain aspects, we may say that quantum theory of coherence studies the interference of a photon with itself, or a group of photons interference with the group itself, see Figure 9.1. In this regard, the quantum degree of first-order coherence is introduced in terms of the superposition of single-photon amplitudes, or single-photon interference; and the quantum degree of higher-order coherence is introduced in terms of the superposition of multiphoton amplitudes, or multiphoton interference.

We have emphasized in Chapter 1 that the concept of optical coherence involves two aspects of physics: (1) the coherence property that classifies light into coherent and incoherent radiation, such as laser beam and chaotic-thermal light; (2) the degree of first-order coherence and the degree of higher-order coherence that measure the interference ability in the first-order correlation measurement and in the higher-order correlation measurement in terms of temporal delay and spatial separation. In classical theory of optical coherence, the coherence or incoherence property of light classified in (1)

**FIGURE 9.1**

On one hand, in quantum theory of light a photon can never be divided into parts; on the other hand, we have never lost interference at single-photon level. In fact, according to quantum theory, interference is a single-photon phenomenon. In Dirac's language: "...photon ...only interferes with itself." (© Charles Addams. With permission from Tee and Charles Addams Foundation.)

is the result of the coherent or incoherent superposition among a large number of sub-radiations. Mathematically, it is the result of an ensemble average when taking into account all possible realizations of the field. Corresponding to the classical classification (1), in the quantum theory of coherence, the coherence or incoherence property of radiation is determined by the state of the quantized field, which is predetermined in the light source by the mechanism of the state preparation. The radiation may be in a pure state or in a mixed state. In the case of mixed state, a density operator is defined to characterize the state of the radiation field, which includes a statistical ensemble averaging among all possible states of the field, similar to that of the classical theory. Regarding the classical classification (2), the quantum theory of photodetection provides solutions to the degree of first-order coherence and the degree of higher-order coherence based on the concept of quantized radiation field, or the concept of photon. In the language of Dirac, the degree of first-order coherence reflects the ability of a photon to interfere with itself; the degree of higher-order coherence reflects the ability for a group of photons to interfere with the group itself.

Quantum theory of optical coherence also deals with the generation of different quantum states of light.\* However, it is not the main goal

---

\* The theory of coherent light generation is covered in laser physics and nonlinear optics.

of this chapter to discuss the preparation of quantum states. This chapter emphasizes the first-order and higher-order interference phenomena in the first-order correlation measurement and in the higher-order correlation measurement of the fields based on the quantum states that is given by different types of sources. We especially emphasize measurements at quantum level by means of single photon counting and coincidence photon counting.

It is interesting to see that some literatures classify light into “classical” and “quantum” in terms of the state of the quantized field, and classify the coherence property of light into “classical” and “quantum” too. Although it is not the philosophy of this book to define or classify light and its coherence property in such a manner, it does not prevent us to ask a reasonable question: Is there any coherent effect in the first-order measurement or in the second-order measurement occurring (or observable) only at quantum level or at a certain class of quantum states? We have not been able to find yet any coherent effect from the first-order measurements that gives different results at quantum level and at classical bright condition, as well as for different states. In fact, there is no clear cut between quantum coherence and classical coherence in the first-order measurement. The linear superposition between single-photon amplitudes and the linear superposition between electromagnetic fields in bright light condition are equivalently applicable to all known first-order optical interference phenomena, except at single-photon regime we may have to interpret the observation in terms of the language of quantum mechanics, although the quantum mechanical language and concepts may bring difficulties to our everyday life experiences. The situation is different in the second-order and higher-order optical coherence. Regarding the question: Is there any second-order or higher-order coherence effect occurs only at quantum level? Yes, there exists such phenomena. In these observations, a certain nontrivial second-order or higher-order coherence or correlation is observable only at quantum level. In the classical limit of bright light condition, the nontrivial correlation may turn to be a trivial constant or become unrecognizable with low visibility. Regarding the question: Is there any second-order or higher-order coherence effect only with certain class of states? The answer is positive too. In this chapter, we will discuss two kinds of second-order coherence phenomena that occur only with entangled biphoton state and with chaotic-thermal light.

Quantum theory and classical theory view the higher-order coherence phenomena differently. Quantum theory of optical coherence treats second-order and higher-order correlation of light as interference effects that involve the superposition of two-photon or multiphoton amplitudes, a nonclassical entity corresponding to different yet indistinguishable alternative ways of producing a joint-detection event between two or more individual photodetectors. The superposition of quantum amplitudes is a common phenomenon in quantum mechanics. It is quite common to have two or more than two different alternative “paths,” namely the two-particle or multiparticle Feynman paths, to produce a joint-detection event by two

or more particles. Quantum theory calculates the probability of observing a joint-detection event at space-time point  $(\mathbf{r}_1, t_1; \mathbf{r}_2, t_2)$  or  $(\mathbf{r}_1, t_1; \mathbf{r}_2, t_2; \dots; \mathbf{r}_N, t_N)$  as the result of the linear superposition of these two-photon or multiphoton amplitudes. Classical theory of optical coherence treats the second-order and higher-order coherence of light as statistical correlation of intensity fluctuations. As an example, the joint-detection of two individual photodetectors  $D_1$  and  $D_2$  measures the statistical correlation of the two measured intensities  $I(\mathbf{r}_1, t_1)$  and  $I(\mathbf{r}_2, t_2)$  at space-time coordinates  $(\mathbf{r}_1, t_1)$  and  $(\mathbf{r}_2, t_2)$ , respectively,

$$\langle I_1 I_2 \rangle = \langle I_1 \rangle \langle I_2 \rangle + \langle \Delta I_1 \Delta I_2 \rangle,$$

which has been discussed in previous chapters. Classical theory calculates and interprets the second-order and higher-order coherence of light as statistical correlation of intensities. Classical theory does not support the superposition of any classical entity similar to the two-photon and multiphoton amplitudes, which involves joint-detection of distant photodetection events. In the Maxwell electromagnetic wave theory of light, the electromagnetic waves are superposed linearly and locally at a space-time point.

One of the goals of this chapter is to find an answer to the question: Can second-order and higher-order coherence of light be considered as the statistical intensity fluctuation correlation? We have concluded earlier that the first-order sinusoidal interference modulation, either spatial or temporal, in the neighborhood of the mean intensity cannot be treated as statistical intensity fluctuations. This conclusion is extendable to second-order and higher-order coherence phenomena. In fact, all observable second-order and higher-order correlations are the results of interferences. It is fundamentally important and may be practically useful to distinguish its interference nature from the interpretation of statistical correction of intensity fluctuations.

## **9.1 Quantum Degree of First-Order Coherence**

To be consistent with the classical analysis, we start from Young's double-pinhole interference experiment. The concept of quantum degree of first-order coherence or first-order correlation will be introduced during the analysis of the experiment. To emphasize the quantum nature of the concept, in this section, we will focus on the following photon-counting type measurements: (1) the measurement of a photon and (2) the accumulative measurement of a large number of photons.

The schematic setup of Young's double-pinhole interference experiment is the same as that shown in Figure 5.1, except that the measurement device is now a single-photon detector operated in photon-counting mode. Following the photodetection theory introduced in Chapter 8, the probability

of observing a photoelectron event by annihilating a photon in a point-like photodetector at space-time point  $(\mathbf{r}, t)$  is

$$\begin{aligned} P(\mathbf{r}, t) &\propto \langle \hat{E}^{(-)}(\mathbf{r}, t) \hat{E}^{(+)}(\mathbf{r}, t) \rangle \\ &= \left\langle \langle \hat{E}^{(-)}(\mathbf{r}, t) \hat{E}^{(+)}(\mathbf{r}, t) \rangle_{QM} \right\rangle_{\text{Ensemble}}, \end{aligned} \quad (9.1)$$

where

$\hat{E}^{(-)}$  and  $\hat{E}^{(+)}$  are the negative frequency and the positive frequency field operators, respectively

the expectation value is calculated by averaging the field operators over the quantum state, which may be a pure state or a mixed state, depending on the light source

The field  $E(\mathbf{r}, t)$  at space-time point  $(\mathbf{r}, t)$  is the result of the superposition of the fields  $E(\mathbf{r}_1, t_1)$  and  $E(\mathbf{r}_2, t_2)$ , which passed the upper pinhole of  $\mathbf{r}_1$  and the lower pinhole of  $\mathbf{r}_2$ , respectively, at earlier times  $t_1$  and  $t_2$ ,

$$\begin{aligned} &\langle \hat{E}^{(-)}(\mathbf{r}, t) \hat{E}^{(+)}(\mathbf{r}, t) \rangle \\ &= \langle [\hat{E}^{(-)}(\mathbf{r}_1, t_1) + \hat{E}^{(-)}(\mathbf{r}_2, t_2)][\hat{E}^{(+)}(\mathbf{r}_1, t_1) + \hat{E}^{(+)}(\mathbf{r}_2, t_2)] \rangle \\ &= \langle \hat{E}^{(-)}(\mathbf{r}_1, t_1) \hat{E}^{(+)}(\mathbf{r}_1, t_1) \rangle + \langle \hat{E}^{(-)}(\mathbf{r}_2, t_2) \hat{E}^{(+)}(\mathbf{r}_2, t_2) \rangle \\ &\quad + \langle \hat{E}^{(-)}(\mathbf{r}_1, t_1) \hat{E}^{(+)}(\mathbf{r}_2, t_2) \rangle + \langle \hat{E}^{(-)}(\mathbf{r}_2, t_2) \hat{E}^{(+)}(\mathbf{r}_1, t_1) \rangle, \end{aligned} \quad (9.2)$$

where  $t_1 \equiv t - s_1/c$  and  $t_2 \equiv t - s_2/c$  (in vacuum); again,  $s_1$  ( $s_2$ ) denotes the optical path from the upper-slit (lower-slit) to the photodetector.

We define the first-order self-coherence function or self-correlation function between field  $E(\mathbf{r}_j, t_j)$ ,  $j = 1, 2$ , and the field itself as

$$\begin{aligned} G^{(1)}(\mathbf{r}_1, t_1; \mathbf{r}_1, t_1) &\equiv \langle \hat{E}^{(-)}(\mathbf{r}_1, t_1) \hat{E}^{(+)}(\mathbf{r}_1, t_1) \rangle = G_{11}^{(1)}, \\ G^{(1)}(\mathbf{r}_2, t_2; \mathbf{r}_2, t_2) &\equiv \langle \hat{E}^{(-)}(\mathbf{r}_2, t_2) \hat{E}^{(+)}(\mathbf{r}_2, t_2) \rangle = G_{22}^{(1)}, \end{aligned} \quad (9.3)$$

and the first-order mutual-coherence function or cross-correlation function between fields  $E(\mathbf{r}_1, t_1)$  and  $E(\mathbf{r}_2, t_2)$  as

$$\begin{aligned} G^{(1)}(\mathbf{r}_1, t_1; \mathbf{r}_2, t_2) &\equiv \langle \hat{E}^{(-)}(\mathbf{r}_1, t_1) \hat{E}^{(+)}(\mathbf{r}_2, t_2) \rangle = G_{12}^{(1)}, \\ G^{(1)}(\mathbf{r}_2, t_2; \mathbf{r}_1, t_1) &\equiv \langle \hat{E}^{(-)}(\mathbf{r}_2, t_2) \hat{E}^{(+)}(\mathbf{r}_1, t_1) \rangle = G_{21}^{(1)}. \end{aligned} \quad (9.4)$$

The probability of producing a photoelectron by annihilating a photon at space-time point  $(\mathbf{r}, t)$  is thus written in terms of the first-order coherence functions of the fields  $E(\mathbf{r}_1, t_1)$  and  $E(\mathbf{r}_2, t_2)$ :

$$\begin{aligned}
 P(\mathbf{r}, t) &\propto G^{(1)}(\mathbf{r}_1, t_1; \mathbf{r}_1, t_1) + G^{(1)}(\mathbf{r}_2, t_2; \mathbf{r}_2, t_2) \\
 &\quad + G^{(1)}(\mathbf{r}_1, t_1; \mathbf{r}_2, t_2) + G^{(1)}(\mathbf{r}_2, t_2; \mathbf{r}_1, t_1) \\
 &= G_{11}^{(1)} + G_{22}^{(1)} + G_{12}^{(1)} + G_{21}^{(1)}. \tag{9.5}
 \end{aligned}$$

The first two terms are the self-coherence or self-correlation functions and the last two terms are the mutual-coherence or cross-correlation functions.

In the above discussion we have used “coherence function” and “correlation function” to define the same mathematical expression. The name of “coherence” emphasizes the interference nature of the phenomenon. The terminology of “correlation” emphasizes the statistical process of the measurement. In quantum mechanics, the superposition of quantum amplitudes quantitatively specifies the interference behavior of a single photon. However, the measurement of one photon cannot provide us any meaningful information about the physics except the registration of a photoelectron event. To learn meaningful physics from an experimental observation, a large number of single-photon-based measurements are always necessary. Quantum theory of light predicts the probability for a photodetection event to occur at space-time coordinate  $(\mathbf{r}, t)$  and specifies the cause of the nontrivial statistical distribution function as the result of interference. We will use either “coherence function” or “correlation function” in the following discussion. Keep in mind that both names represent the same physics from the same measurement.

In the view of quantum theory of light, the observation of a photoelectron is the result of a photodetection event of a photodetector that is triggered by a photon created in an early atomic transition at the light source. Young’s double-pinhole interferometer provides two different yet indistinguishable alternative ways for this photon to produce a photodetection event at  $(\mathbf{r}, t)$ . The superposition of the quantum amplitudes determines a nontrivial probability distribution function for observing a photon at  $(\mathbf{r}, t)$ . If we have to give each term in Equation 9.5 a physical meaning, the self-correlation function corresponds to the probability of having the photon passing through either the upper or the lower pinholes (which-path); the cross-correlation functions (third and the fourth terms), which determine the interference, correspond to the probabilities of having the photon passing through both the upper and lower pinholes (both-path) simultaneously. We then have to deal with “negative probability” problem.\* In the last line of Equation 9.5, we have used an abbreviation notation, which is useful in later discussions.

---

\* The cross-correlation function in the double-pinhole experiment is a sinusoidal function with both positive (constructive interference) and negative (destructive interference) values. If one insists to interpret the cross-correlation as the probability of having a photon passing through both upper and lower pinholes (both-path) simultaneously, one cannot avoid facing “negative probability” problems in this simple classic interference measurement.

The degree of first-order coherence, namely the normalized first-order correlation function between radiation fields  $E(\mathbf{r}_1, t_1)$  at space-time  $(\mathbf{r}_1, t_1)$  and  $E(\mathbf{r}_2, t_2)$  at space-time  $(\mathbf{r}_2, t_2)$  is defined as

$$\begin{aligned} g^{(1)}(\mathbf{r}_1, t_1; \mathbf{r}_2, t_2) &= \frac{\langle \hat{E}^{(-)}(\mathbf{r}_1, t_1) \hat{E}^{(+)}(\mathbf{r}_2, t_2) \rangle}{\sqrt{\langle \hat{E}^{(-)}(\mathbf{r}_1, t_1) \hat{E}^{(+)}(\mathbf{r}_1, t_1) \rangle \langle \hat{E}^{(-)}(\mathbf{r}_2, t_2) \hat{E}^{(+)}(\mathbf{r}_2, t_2) \rangle}} \\ &= \frac{G^{(1)}(\mathbf{r}_1, t_1; \mathbf{r}_2, t_2)}{\sqrt{G^{(1)}(\mathbf{r}_1, t_1; \mathbf{r}_1, t_1) G^{(1)}(\mathbf{r}_2, t_2; \mathbf{r}_2, t_2)}}. \end{aligned} \quad (9.6)$$

$|g^{(1)}(\mathbf{r}_1, t_1; \mathbf{r}_2, t_2)|$  takes a value between 1 and 0. Similar to that of the classical theory, we name the quantized fields as coherent fields, partial coherent fields, and incoherent fields accordingly:

|                         |    |   |
|-------------------------|----|---|
| Coherent fields         | if | $ g^{(1)}(\mathbf{r}_1, t_1; \mathbf{r}_2, t_2)  = 1$     |
| Partial coherent fields | if | $0 <  g^{(1)}(\mathbf{r}_1, t_1; \mathbf{r}_2, t_2)  < 1$ |
| Incoherent fields       | if | $ g^{(1)}(\mathbf{r}_1, t_1; \mathbf{r}_2, t_2)  = 0$ .   |

In Young's double-pinhole interferometer, the probability of having a "click" event at space-time point  $(\mathbf{r}, t)$  is then written in terms of the degree of first-order coherence function  $g^{(1)}(\mathbf{r}_1, t_1; \mathbf{r}_2, t_2)$ :

$$P(\mathbf{r}, t) \propto 1 + R e g^{(1)}(\mathbf{r}_1, t_1; \mathbf{r}_2, t_2), \quad (9.7)$$

where, to simplify the physical picture, we have assumed  $G^{(1)}(\mathbf{r}_1, t_1; \mathbf{r}_1, t_1) = G^{(1)}(\mathbf{r}_2, t_2; \mathbf{r}_2, t_2)$ . The value of  $g^{(1)}(\mathbf{r}_1, t_1; \mathbf{r}_2, t_2)$  is a measure of the interference visibility. The relationship between  $g^{(1)}(\mathbf{r}_1, t_1; \mathbf{r}_2, t_2)$  and the interference visibility is similar to the classical situation of Chapter 5.

From Equations 9.3 and 9.6, the first-order correlation function and the normalized first-order coherence function between  $E(\mathbf{r}_1, t_1)$  and  $E(\mathbf{r}_2, t_2)$  obviously have the following property:

$$\begin{aligned} G^{(1)}(\mathbf{r}_1, t_1; \mathbf{r}_2, t_2) &= G^{*(1)}(\mathbf{r}_2, t_2; \mathbf{r}_1, t_1) \\ g^{(1)}(\mathbf{r}_1, t_1; \mathbf{r}_2, t_2) &= g^{*(1)}(\mathbf{r}_2, t_2; \mathbf{r}_1, t_1). \end{aligned} \quad (9.8)$$

Quantum theory has provided us with a set of tools, formulated in Heisenberg representation, for the evaluation of first-order optical correlation or coherence. Light fields at two space-time points are said to be coherent if interference is observable in principle. The higher the visibility of the interference fringes, the higher the degree of coherence. Different

quantum states may produce different coherence functions for a certain measurement.

The calculation of the first-order coherence functions  $G^{(1)}(\mathbf{r}_j, t_j; \mathbf{r}_k, t_k)$ ,  $j=1, 2, k=1, 2$ , for a pure state is straightforward

$$G^{(1)}(\mathbf{r}_j, t_j; \mathbf{r}_k, t_k) = \langle \Psi | \hat{E}^{(-)}(\mathbf{r}_j, t_j) \hat{E}^{(+)}(\mathbf{r}_k, t_k) | \Psi \rangle, \quad (9.9)$$

where  $|\Psi\rangle$  is the state of the field. Mixed state is usually characterized by a density operator or matrix,

$$\hat{\rho} = \sum_j P_n |\Psi_n\rangle\langle\Psi_n|,$$

where  $P_n$  is the probability of finding the field in a given set of state vectors  $|\Psi_n\rangle$ . The first-order coherence functions are formally calculated from

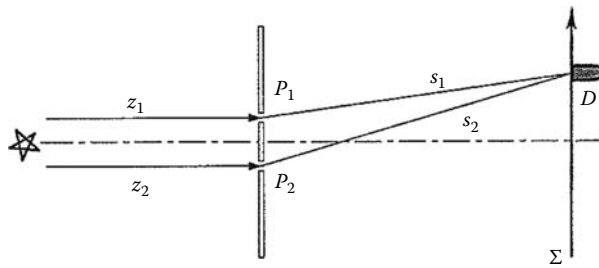
$$\begin{aligned} G^{(1)}(\mathbf{r}_j, t_j; \mathbf{r}_k, t_k) &= \left\langle \langle \hat{E}^{(-)}(\mathbf{r}_j, t_j) \hat{E}^{(+)}(\mathbf{r}_k, t_k) \rangle_{QM} \right\rangle_{\text{Ensemble}} \\ &= \text{tr} [ \hat{\rho} \hat{E}^{(-)}(\mathbf{r}_j, t_j) \hat{E}^{(+)}(\mathbf{r}_k, t_k) ] \\ &= \sum_n P_n \langle \Psi_n | \hat{E}^{(-)}(\mathbf{r}_j, t_j) \hat{E}^{(+)}(\mathbf{r}_k, t_k) | \Psi_n \rangle \\ &= \sum_n P_n G_n^{(1)}(\mathbf{r}_j, t_j; \mathbf{r}_k, t_k). \end{aligned} \quad (9.10)$$

Equation 9.10 is a statistical weighted sum over all individual contributions of the  $G_n^{(1)}$ 's.

In the following, we give a few examples on the calculation of first-order temporal coherence for different quantum states. At the same time, we introduce a useful concept of effective wavefunction for a photon and for a photon system. Similar to the classical treatment of first-order temporal coherence in Section 5.1, the following analysis is based on the same Young's double-pinhole interferometer of Figure 9.2 with a distant point light source at  $\mathbf{r}=0$ , which contains a large number of incoherent or coherent sub-sources.

## 1. Single-photon wavepacket

The following is simply an exercise on the evaluation of the self-coherence function and mutual-coherence function of a single-photon wavepacket as pure state. This exercise serves two main purposes: (1) it teaches us a few

**FIGURE 9.2**

Schematic of the same Young's double-pinhole interference experiment of Section 5.1, which measures the temporal coherence of light produced from a far-field point source containing a large number of atoms that are ready for two-level atomic transitions.

basic techniques for this type calculation and (2) it introduces the concept of effective wavefunction.

The concept of single-photon wavepacket has been introduced earlier. Following our earlier discussion, we take the following approximation to characterize the state of the measured field:

$$|\Psi\rangle = \int d\omega f(\omega) \hat{a}^\dagger(\omega) |0\rangle, \quad (9.11)$$

indicating a single-photon state in the form of coherent superposition of Fock states  $\hat{a}^\dagger(\omega)|0\rangle = |\dots, 0, 1_\omega, \dots, 0, \dots\rangle$ , and  $f(\omega)$  is the normalized complex probability amplitude of the Fock state, which may contain a phase factor  $e^{i\omega t_0}$  for the mode  $\omega$ , as we have discussed in Section 8.8. We will write this phase factor explicitly into the form of  $f(\omega)e^{-i\omega t_0}$  in some of the following calculations to emphasize certain necessary physical concepts and mechanisms. In the notation of  $f(\omega)e^{i\omega t_0}$ ,  $f(\omega)$  is assumed to be real and positive. Not to make the notation too complicated, both the notations will appear in the calculation. It is not too difficult to distinguish the two notations from their Fourier transforms. The state of Equation 9.11 is a pure single-photon state by means of (1) each photodetection event is produced by a photon that is characterized by a coherently superposed wavepacket and (2) all observed photodetection events are produced from the same single-photon state as a homogeneous ensemble.

In far-field, we simplify the field operators into the following form:

$$\begin{aligned} \hat{E}^{(+)}(z, t) &\simeq \mathcal{E}_0 \int d\omega e^{-i(\omega t - kz)} \hat{a}(\omega) \\ \hat{E}^{(-)}(z, t) &\simeq \mathcal{E}_0 \int d\omega e^{i(\omega t - kz)} \hat{a}^\dagger(\omega), \end{aligned} \quad (9.12)$$

where we have approximated  $\mathcal{E}_\omega = \mathcal{E}_0$  by ignoring the slow function of frequency, and propagated the field operator from time  $t = 0$  at the source  $z = 0$ .

to the space-time coordinate of the photodetection event  $(z, t)$ . To simplify the notation, we will further renormalize  $\mathcal{E}_0 = 1$  in the following calculations.

The first-order coherence function  $G^{(1)}(z_1, t_1; z_2, t_2)$  is calculated as

$$\begin{aligned}
 G^{(1)}(z_1, t_1; z_2, t_2) &= \langle \Psi | \hat{E}^{(-)}(z_1, t_1) \hat{E}^{(+)}(z_2, t_2) | \Psi \rangle \\
 &= \sum_n \langle \Psi | \hat{E}^{(-)}(z_1, t_1) | n \rangle \langle n | \hat{E}^{(+)}(z_2, t_2) | \Psi \rangle \\
 &= \left[ \int d\omega f^*(\omega) \langle 0 | \hat{a}(\omega) \right] \left[ \int d\omega'' \hat{a}^\dagger(\omega'') e^{i(\omega''t_1 - k''z_1)} \right] | 0 \rangle \\
 &\quad \times \langle 0 | \left[ \int d\omega''' \hat{a}(\omega''') e^{-i(\omega'''t_2 - k'''z_2)} \right] \left[ \int d\omega' f(\omega') \hat{a}^\dagger(\omega') | 0 \rangle \right] \\
 &= \left\{ \int d\omega f^*(\omega) e^{i(\omega t_1 - kz_1)} \right\} \left\{ \int d\omega' f(\omega') e^{-i(\omega' t_2 - k' z_2)} \right\} \\
 &= \left[ e^{i\omega_0(\tau_1 - t_0)} \mathcal{F}_{\tau_1 - t_0}^* \{ f(v) \} \right] \left[ e^{-i\omega_0(\tau_2 - t_0)} \mathcal{F}_{\tau_2 - t_0} \{ f(v) \} \right] \tag{9.13}
 \end{aligned}$$

where we have used the notation  $f(\omega)e^{i\omega t_0}$  in the Fourier transform. In Equation 9.13, we have also defined  $v = \omega - \omega_0$ ,  $t_j = t - s_j/c$  (in vacuum),  $j = 1, 2$ , and  $\tau_j = t_j - z_j/c$  (in vacuum) as usual. To derive the above result again, we have applied the completeness relation

$$\sum_n |n\rangle \langle n| = 1.$$

For a pure state of single-photon wavepacket,  $G^{(1)}(z_1, t_1; z_2, t_2)$  cannot be written as a stationary function of  $t_1 - t_2$  in general; however, it can be easily written as a product of two time-dependent wavepackets  $\Psi^*(z_1, t_1)$  and  $\Psi(z_2, t_2)$  with

$$\Psi(z_j, t_j) = e^{-i\omega_0(\tau_j - t_0)} \mathcal{F}_{\tau_j - t_0} \{ f(v) \}. \tag{9.14}$$

Here we have introduced  $t_0$  to indicate the creation time of the wavepacket from the atomic transition. Sometimes, we write the wavepackets in the form

$$\Psi(z_j, t_j) = e^{-i\omega_0(\tau_j - t_0)} \mathcal{F}_{\tau_j} \{ f(v) \}.$$

In this form, the phase factor is embedded into the complex amplitude  $f(v)$ . The Fourier transform of the complex function  $f(v)$ , which contains a phase factor  $e^{i\omega t_0}$ , will shift the wavepacket from  $\tau_j$  to  $\tau_j - t_0$ . It is clear

that the first-order temporal coherence is determined by the overlapping and nonoverlapping of the effective wavefunction and its conjugate.

Similar to the mutual-coherence function  $G^{(1)}(z_1, t_1; z_2, t_2)$ , the self-correlation functions  $G^{(1)}(z_1, t_1; z_1, t_1)$  and  $G^{(1)}(z_2, t_2; z_2, t_2)$  can be expressed as the products of the time-dependent wavepackets  $\Psi(z_1, t_1)$  and  $\Psi(z_2, t_2)$  with their conjugates:

$$\begin{aligned} G^{(1)}(z_1, t_1; z_1, t_1) &= |\mathcal{F}_{\tau_1 - t_0} \{f(v)\}|^2 = |\Psi(z_1, t_1)|^2 \\ G^{(1)}(z_2, t_2; z_2, t_2) &= |\mathcal{F}_{\tau_2 - t_0} \{f(v)\}|^2 = |\Psi(z_2, t_2)|^2. \end{aligned} \quad (9.15)$$

The probability of having a photodetection event (a “click”) at space-time point  $(\mathbf{r}, t)$  is thus written in terms of the superposition of the wavepackets  $\Psi(z_1, t_1)$  and  $\Psi(z_2, t_2)$ :

$$\begin{aligned} P(\mathbf{r}, t) &\propto |\Psi(\mathbf{r}, t)|^2 \\ &= |\Psi(z_1, t_1) + \Psi(z_2, t_2)|^2 \\ &= \left[ |\Psi(z_1, t_1)|^2 + |\Psi(z_2, t_2)|^2 + \Psi^*(z_1, t_1)\Psi(z_2, t_2) + \Psi(z_1, t_1)\Psi^*(z_2, t_2) \right], \end{aligned} \quad (9.16)$$

Although there is no wavefunction defined for a photon in quantum mechanics, it is interesting to see that  $\Psi(\mathbf{r}, t)$  plays the role of wavefunction in Equation 9.16. We define  $\Psi(\mathbf{r}, t)$  the effective wavefunction. The effective wavefunction represents the probability amplitude of observing a photon at space-time point  $(\mathbf{r}, t)$ , or the probability amplitude of having a photodetection event at space-time point  $(\mathbf{r}, t)$ . In the above experiment, the effective wavefunction  $\Psi(\mathbf{r}, t)$  has two different yet indistinguishable\* amplitudes  $\Psi(z_1, t_1)$  and  $\Psi(z_2, t_2)$ , namely, the probability amplitude of observing a photon at  $(z_1, t_1)$  and the probability amplitude of observing a photon at  $(z_2, t_2)$ , respectively. Each amplitude is in the form of a wavepacket in space-time. The total effective wavefunction  $\Psi(\mathbf{r}, t)$  is the result of the superposition of two effective wavefunctions or two dynamical wavepackets in space-time. The effective wavefunction reflects the wave-particle nature of a photon. The normalized degree of first-order temporal coherence function is thus written in terms of the effective wavefunction of a photon:

$$g^{(1)}(z_1, t_1; z_2, t_2) = \frac{\Psi^*(z_1, t_1)\Psi(z_2, t_2)}{\sqrt{|\Psi(z_1, t_1)|^2|\Psi(z_2, t_2)|^2}}. \quad (9.17)$$

---

\* Note, here “indistinguishable” refers to a photodetection event at space-time point  $(\mathbf{r}, t)$ .

## 2. Thermal light

Similar to the model of chaotic-thermal radiation in Section 8.8, we assume a far-field point light source containing a large number of independent and randomly radiated atoms that are ready for two-level atomic transitions. Taking the lowest-order contribution to a photodetection event of  $D$ , see Section 8.8, the first-order temporal self-coherence function and mutual-coherence functions can be calculated from

$$G^{(1)}(z_j, t_j; z_k, t_k) = \left\langle \langle \Psi | \hat{E}^{(-)}(z_j, t_j) \hat{E}^{(+)}(z_k, t_k) | \Psi \rangle \right\rangle_{\text{Ensemble}}, \quad (9.18)$$

where  $j = 1, 2, k = 1, 2$ , and

$$|\Psi\rangle = \sum_n c_n \int d\omega f_n(\omega) \hat{a}_n^\dagger(\omega) |0\rangle = \sum_n c_n |\Psi_n\rangle,$$

is the first-order approximated state of thermal field, representing (1) the state of a photon, which produced the observed photodetection event, as an incoherent superposition of all possible single-photon states associated with all possible atomic transitions, and (2) the state of a large number of photons created from a large number of independent and randomly radiated atomic transitions as an inhomogeneous ensemble. Due to the stochastic nature of thermal radiation,  $G^{(1)}(z_j, t_j; z_k, t_k)$  can also be calculated from its density operator,

$$G^{(1)}(z_j, t_j; z_k, t_k) = \text{tr } \hat{\rho}^{(1)} \hat{E}^{(-)}(z_j, t_j) \hat{E}^{(+)}(z_k, t_k), \quad (9.19)$$

with either the density operator

$$\hat{\rho}^{(1)} = \sum_n P_n |\Psi_n\rangle \langle \Psi_n|$$

or the density operator

$$\hat{\rho}^{(1)} = \int d\omega |f(\omega)|^2 \hat{a}^\dagger(\omega) |0\rangle \langle 0| \hat{a}^\dagger(\omega).$$

The only difference between Equations 9.18 and 9.19 is that the ensemble average has been completed when deriving the density operator of Equation 9.19 from the very beginning. To have a complete view on the quantum mechanical treatment, the following exercises are based on Equation 9.18, which will repeat the exercise of ensemble averaging similar to the calculation of the density operator.

Substituting the far-field  $\hat{E}^{(-)}(z_j, t_j)$  and  $\hat{E}^{(+)}(z_k, t_k)$

$$\begin{aligned}\hat{E}^{(-)}(z_j, t_j) &= \sum_m \int d\omega e^{i\omega\tau_j} \hat{a}_m^\dagger(\omega) \equiv \sum_m \hat{E}_m^{(-)}(z_j, t_j), \\ \hat{E}^{(+)}(z_k, t_k) &= \sum_n \int d\omega' e^{-i\omega'\tau_k} \hat{a}_n(\omega') \equiv \sum_n \hat{E}_n^{(+)}(z_k, t_k),\end{aligned}\quad (9.20)$$

into Equation (9.18), the self-coherence function  $G(z_j, t_j; z_j, t_j)$ ,  $j = 1, 2$  is calculated from

$$\begin{aligned}G^{(1)}(z_j, t_j; z_j, t_j) &= \left\langle \sum_m c_m^* \left\langle \Psi_m \left| \hat{E}^{(-)}(z_j, t_j) \hat{E}^{(+)}(z_j, t_j) \sum_n c_n \right| \Psi_n \right\rangle \right\rangle_{\text{Ensemble}} \\ &= \left\langle \sum_l \sum_m c_m^* \left\langle \Psi_m \left| \hat{E}^{(-)}(z_j, t_j) \right| l \right\rangle \left\langle l \left| \hat{E}^{(+)}(z_j, t_j) \sum_n c_n \right| \Psi_n \right\rangle \right\rangle_{\text{Ensemble}} \\ &= \left\langle \left| \left\langle 0 \left| \hat{E}^{(+)}(z_j, t_j) \sum_n c_n \right| \Psi_n \right\rangle \right|^2 \right\rangle_{\text{Ensemble}} \\ &= \left\langle \left| \Psi(z_j, t_j) \right|^2 \right\rangle_{\text{Ensemble}}\end{aligned}\quad (9.21)$$

where we have introduced an effective wavefunction for the photon system:

$$\Psi(z_j, t_j) \equiv \left\langle 0 \left| \hat{E}^{(+)}(z_j, t_j) \sum_n c_n \right| \Psi_n \right\rangle = \langle 0 | \hat{E}^{(+)}(z_j, t_j) | \Psi \rangle \quad (9.22)$$

and an effective wavefunction for the  $n$ th photon:

$$\Psi_n(z_j, t_j) \equiv \langle 0 | \hat{E}^{(+)}(z_j, t_j) | \Psi_n \rangle, \quad (9.23)$$

with

$$\Psi(z_j, t_j) = \sum_n c_n \Psi_n(z_j, t_j). \quad (9.24)$$

Substituting the effective wavefunction of Equation 9.14 into Equation 9.21,  $G^{(1)}(z_j, t_j; z_j, t_j)$  is evaluated from the following ensemble average:

$$\begin{aligned}
 G^{(1)}(z_j, t_j; z_j, t_j) &= \left\langle \sum_{m,n} c_m^* c_n e^{-i\omega_0(t_{0m}-t_{0n})} \mathcal{F}_{\tau_j-t_{0m}}^* \{f(v)\} \mathcal{F}_{\tau_j-t_{0n}} \{f(v)\} \right\rangle_{\text{Ensemble}} \\
 &\simeq \sum_n |c_n|^2 \left| \mathcal{F}_{\tau_j-t_{0n}} \{f(v)\} \right|^2 \\
 &= \sum_n |c_n|^2 |\Psi_n(z_j, t_j)|^2
 \end{aligned} \tag{9.25}$$

where we have assumed a large number of atomic transitions with the same spectrum distribution and the same central frequency  $\omega_0$ . The physics behind Equation 9.25, especially the cancelation of the cross terms between the  $m$ th and the  $n$ th effective wavefunction, is similar to that of the classical model of thermal light with a large number of wavepackets produced from a large number of independent and randomly radiated sub-sources, except that the concept of classical wavepacket is replaced with the concept of the effective wavefunction of a photon.

The mutual-coherence function  $G^{(1)}(z_1, t_1; z_2, t_2) = G^{*(1)}(z_2, t_2; z_1, t_1)$  is calculated in a similar way:

$$\begin{aligned}
 G^{(1)}(z_1, t_1; z_2, t_2) &= \left\langle \sum_m c_m^* \left\langle \Psi_m \left| \hat{E}^{(-)}(z_1, t_1) \hat{E}^{(+)}(z_2, t_2) \sum_n c_n \right| \Psi_n \right\rangle \right\rangle_{\text{Ensemble}} \\
 &= \left\langle \sum_l \sum_m c_m^* \left\langle \Psi_m \left| \hat{E}^{(-)}(z_1, t_1) \right| l \right\rangle \left\langle l \left| \hat{E}^{(+)}(z_2, t_2) \sum_n c_n \right| \Psi_n \right\rangle \right\rangle_{\text{Ensemble}} \\
 &= \left\langle \sum_m c_m^* \left\langle \Psi_m \left| \hat{E}^{(-)}(z_1, t_1) \right| 0 \right\rangle \left\langle 0 \left| \hat{E}^{(+)}(z_2, t_2) \sum_n c_n \right| \Psi_n \right\rangle \right\rangle_{\text{Ensemble}} \\
 &= \langle \Psi^*(z_1, t_1) \Psi(z_2, t_2) \rangle_{\text{Ensemble}}
 \end{aligned} \tag{9.26}$$

where, again, we have defined the effective wavefunction for the photon system and for the  $n$ th photon, which are the same as shown in Equations 9.22 and 9.23.

Substituting the effective wavefunctions of Equation 9.14 into Equation 9.26,  $G^{(1)}(z_1, t_1; z_2, t_2)$  can be written as

$$\begin{aligned}
 G^{(1)}(z_1, t_1; z_2, t_2) &\propto \left\langle \sum_{m,n} c_m^* c_n e^{-i\omega_0(t_{0m}-t_{0n})} e^{i\omega_0\tau} \mathcal{F}_{\tau_1-t_{0m}}^* \{f(v)\} \mathcal{F}_{\tau_2-t_{0n}} \{f(v)\} \right\rangle_{\text{Ensemble}} \\
 &\simeq \sum_n |c_n|^2 e^{i\omega_0\tau} \mathcal{F}_{\tau_1-t_{0n}}^* \{f(v)\} \mathcal{F}_{\tau_2-t_{0n}} \{f(v)\} \\
 &= \sum_n |c_n|^2 \Psi_n^*(z_1, t_1) \Psi_n(z_2, t_2). \tag{9.27}
 \end{aligned}$$

Equation 9.27 indicates that the first-order temporal coherence is determined by the overlapping and nonoverlapping of the effective wavefunction and its conjugate, similar to that of the classical model of thermal light with a large number of wavepackets produced from a large number of independent and randomly radiated sub-sources.

The probability of observing a photoelectron event from the photon-counting detector  $D$  at space-time coordinate  $(\mathbf{r}, t)$  is therefore

$$\begin{aligned}
 P(\mathbf{r}, t) &\propto G_{11}^{(1)} + G_{22}^{(1)} + G_{12}^{(1)} + G_{21}^{(1)} \\
 &\propto \sum_n |c_n|^2 \left[ |\Psi_n(z_1, t_1)|^2 + |\Psi_n(z_2, t_2)|^2 \right. \\
 &\quad \left. + \Psi_n^*(z_1, t_1) \Psi_n(z_2, t_2) + \Psi_n(z_1, t_1) \Psi_n^*(z_2, t_2) \right] \\
 &= \sum_n |c_n|^2 |\Psi_n(z_1, t_1) + \Psi_n(z_2, t_2)|^2. \tag{9.28}
 \end{aligned}$$

Equation 9.28 indicates that for thermal light, or a radiation system that consists of a large number of possible independently and randomly created photons, "...photon... only interferes with itself. Interference between two different photons never occurs." The physical picture is very clear: each independently and randomly created photon may produce an interference pattern by means of a probability distribution function of that photon in space-time. The sum of these individual single-photon interferences yields the final observed interference. Replacing the effective wavefunctions  $\Psi_n(z_j, t_j)$  in Equation 9.28 with their Fourier transform representation as wavepackets, we obtain

$$\begin{aligned}
P(\mathbf{r}, t) &\propto \sum_n |c_n| \left[ |\mathcal{F}_{\tau_1-t_{0n}}\{f(v)\}|^2 + |\mathcal{F}_{\tau_2-t_{0n}}\{f(v)\}|^2 \right. \\
&\quad \left. + 2Re e^{i\omega_0\tau} \mathcal{F}_{\tau_1-t_{0n}}^*\{f(v)\} \mathcal{F}_{\tau_2-t_{0n}}\{f_n(v)\} \right] \\
&\simeq \int dt_{0n} \left[ |\mathcal{F}_{\tau_1-t_{0n}}\{f(v)\}|^2 + |\mathcal{F}_{\tau_2-t_{0n}}\{f(v)\}|^2 \right. \\
&\quad \left. + 2Re e^{i\omega_0\tau} \mathcal{F}_{\tau_1-t_{0n}}^*\{f(v)\} \mathcal{F}_{\tau_2-t_{0n}}\{f_n(v)\} \right] \\
&\propto 1 + \mathcal{F}_\tau\{|f(v)|^2\} \cos \omega_0\tau,
\end{aligned} \tag{9.29}$$

where we have assumed a random and continuous distribution of  $t_{0n}$  with  $|c_n|^2 = \text{constant}$ . Again,  $\tau = \tau_1 - \tau_2 = (s_2 - s_1)/c$  for the experimental setup of Figure 9.2. The integral over  $t_0$  is mathematically equivalent to a time integral. The results of the integrals are easily obtained by applying the Parseval theorem:

$$G^{(1)}(z_j, t_j; z_j, t_j) \simeq \int dt_0 \left| \mathcal{F}_{\tau_j-t_0}\{f(v)\} \right|^2 \simeq 1,$$

and the Wiener–Khintchine theorem:

$$\begin{aligned}
G^{(1)}(z_1, t_1; z_2, t_2) &\simeq e^{i\omega_0\tau} \int dt_0 \mathcal{F}_{\tau_1-t_0}^*\{f(v)\} \mathcal{F}_{\tau_2-t_0}\{f(v)\} \\
&\simeq e^{i\omega_0\tau} \mathcal{F}_\tau\{|f(v)|^2\}.
\end{aligned}$$

The calculation is similar to what we have done in Chapter 5 for the classical field, except that the spectrum distribution function  $f(v)$  is normalized for the quantum effective wavefunction:

$$\int dv |f(v)|^2 = 1.$$

The contribution from higher-order approximations to the first-order self-coherence function and mutual-coherence function are not too difficult to calculate. For instance, it is straightforward to show that the mixed two-photon state produces the same first-order temporal mutual-coherence function:

$$\begin{aligned}
G^{(1)}(z_1, t_1; z_2, t_2) &= \sum_{m < n} |c_n|^2 |c_m|^2 \langle \Psi_n | \langle \Psi_m | \hat{E}^{(-)}(z_1, t_1) \hat{E}^{(+)}(z_2, t_2) \sum_{m < n} |c_n|^2 |c_m|^2 |\Psi_m\rangle | \Psi_n \rangle \\
&\simeq e^{i\omega_0\tau} \mathcal{F}_\tau\{|f(v)|^2\}.
\end{aligned} \tag{9.30}$$

### 3. Coherent state

Consider the same Young's double-pinhole interferometer, which provides two different optical paths for propagating its input radiation to a

photodetector for photodetection. In this exercise, we model the input radiation as a multimode coherent state with one polarization, which is written as a product state of a set of single-mode coherent states:

$$|\{\alpha\}\rangle = \prod_{\mathbf{k}} |\alpha_{\mathbf{k}}\rangle.$$

The following exercise is for the calculation of one-dimensional temporal mutual-coherence function:

$$\begin{aligned} G^{(1)}(z_1, t_1; z_2, t_2) &= \langle \{\alpha\} | \hat{E}^{(-)}(z_1, t_1) \hat{E}^{(+)}(z_2, t_2) | \{\alpha\} \rangle \\ &= \langle \{\alpha\} | \int d\omega \hat{a}^\dagger(\omega) e^{i\omega\tau_1} \int d\omega' e^{-i\omega'\tau_2} \hat{a}(\omega') | \{\alpha\} \rangle \\ &= \int d\omega a(\omega) e^{-i\varphi(\omega)} e^{i\omega\tau_1} \int d\omega' a(\omega) e^{-i\varphi(\omega')} e^{-i\omega'\tau_2} \\ &= E^*(z_1, t_1) E(z_2, t_2). \end{aligned} \quad (9.31)$$

where  $\alpha(\omega) = a(\omega)e^{i\varphi(\omega)}$  is the eigenvalue of the annihilation operator  $\hat{a}(\omega)$ . In the final integrals of Equation 9.31,  $a(\omega)e^{i\varphi(\omega)}$  is the complex amplitude of the Fourier mode  $\omega$  of the wavepacket. Notice that the field operator in Equation 9.31 has taken the form of Equation 9.12 instead of Equation 9.20. It is interesting to see that the first-order temporal mutual-coherence function  $G^{(1)}(z_1, t_1; z_2, t_2)$  of coherent state is formally connected with the classical fields  $E(z_1, t_1)$  and  $E(z_2, t_2)$ . The remaining calculations are similar to that of the classical treatment.

## 9.2 Photon and Effective Wavefunction

If the field is characterized by a pure state with total photon number of  $n = 1$ , it is found that

$$\begin{aligned} G^{(1)}(\mathbf{r}_i, t_i; \mathbf{r}_j, t_j) &= \langle \Psi | \hat{E}^{(-)}(\mathbf{r}_i, t_i) \hat{E}^{(+)}(\mathbf{r}_j, t_j) | \Psi \rangle \\ &= \sum_n \langle \Psi | \hat{E}^{(-)}(\mathbf{r}_i, t_i) | n \rangle \langle n | \hat{E}^{(+)}(\mathbf{r}_j, t_j) | \Psi \rangle \\ &= \langle \Psi | \hat{E}^{(-)}(\mathbf{r}_i, t_i) | 0 \rangle \langle 0 | \hat{E}^{(+)}(\mathbf{r}_j, t_j) | \Psi \rangle \\ &= \Psi^*(\mathbf{r}_i, t_i) \Psi(\mathbf{r}_j, t_j) \end{aligned} \quad (9.32)$$

where, in the third line, we have used the completeness relation

$$\sum_n |n\rangle\langle n| = 1. \quad (9.33)$$

The effective wavefunction is formulated in Equation 9.32 as

$$\Psi(\mathbf{r}_j, t_j) = \langle 0 | \hat{E}^{(+)}(\mathbf{r}_j, t_j) | \Psi \rangle \quad (9.34)$$

where  $j = 1, 2$ .

It is easy to find the following linear superposition relationship between the effective wavefunctions:

$$\begin{aligned} \Psi(\mathbf{r}, t) &= \langle 0 | \hat{E}^{(+)}(\mathbf{r}, t) | \Psi \rangle \\ &= \langle 0 | \hat{E}^{(+)}(\mathbf{r}_1, t_1) | \Psi \rangle + \langle 0 | \hat{E}^{(+)}(\mathbf{r}_2, t_2) | \Psi \rangle \\ &= \Psi(\mathbf{r}_1, t_1) + \Psi(\mathbf{r}_2, t_2) \end{aligned} \quad (9.35)$$

with the assumption

$$\hat{E}^{(+)}(\mathbf{r}, t) = \hat{E}^{(+)}(\mathbf{r}_1, t_1) + \hat{E}^{(+)}(\mathbf{r}_2, t_2).$$

## 1. Heisenberg picture and Schrödinger picture

$G^{(1)}(\mathbf{r}_1, t_1; \mathbf{r}_2, t_2)$  is referred to as the correlation function between fields at space-time points  $(\mathbf{r}_1, t_1)$  and  $(\mathbf{r}_2, t_2)$ . We use  $(\mathbf{r}_1, t_1)$  and  $(\mathbf{r}_2, t_2)$  to mark the space-time dependence of the field operators. As we have emphasized earlier, however,  $G^{(1)}(\mathbf{r}_1, t_1; \mathbf{r}_2, t_2)$  is not directly measured at these two points. The photodetection event happens at space-time point  $(\mathbf{r}, t)$  (see Figure 9.2).  $t_1 = t - s_1/c$ ,  $t_2 = t - s_2/c$ , referring to the earlier times of the fields at the upper and the lower pinholes  $\mathbf{r}_1$  and  $\mathbf{r}_2$ , respectively. In the Heisenberg picture, the states (or wavefunctions) are independent of time. The time dependence is carried by the operator.

On the other hand, the concept of wavefunction belongs to the Schrödinger picture. In the Schrödinger representation, the time dependence is carried with the wavefunction. The counting rate of a photodetector is proportional to the probability of producing a photoelectron by annihilating a photon at space-time point  $(\mathbf{r}, t)$ , which equals the normal square of the probability amplitude or the effective wavefunction of a photon,  $\Psi(\mathbf{r}, t)$ . The total effective wavefunction (probability amplitude)  $\Psi(\mathbf{r}, t)$  is the result of the superposition of two earlier effective wavefunctions (probability amplitudes):  $\Psi(\mathbf{r}_1, t_1)$  and  $\Psi(\mathbf{r}_2, t_2)$ . Although having different optical

paths,  $\Psi(\mathbf{r}_1, t_1)$  and  $\Psi(\mathbf{r}_2, t_2)$  contribute to the same photoelectron event at space-time  $(\mathbf{r}, t)$  by means of quantum mechanical superposition. The physical picture associated with the concept of the effective wavefunction of a photon is the same as the wavefunction of the Schrödinger picture for a mass particle.

The effective wavefunction is a very useful concept. It is calculated from the Heisenberg representation but interpreted in the Schrödinger picture. The mathematics is basically Fourier transform.

Although the effective wavefunction is formally defined in the Heisenberg representation, it should be consistent with that of the Schrödinger representation:

$$\begin{aligned}
 \Psi(r, t) &= \langle 0 | \hat{E}^{(+)}(r, t) | \Psi(0) \rangle \\
 &= \langle 0 | \int d\omega g(r, t; \omega) \hat{a}(\omega) \int d\omega' f(\omega') \hat{a}^\dagger(\omega') | 0 \rangle \\
 &= \langle 0 | \int d\omega \hat{a}(\omega) \int d\omega' f(\omega') g(r, t; \omega') \hat{a}^\dagger(\omega') | 0 \rangle \\
 &= \langle 0 | \int d\omega \hat{a}(\omega) | \Psi(t) \rangle \\
 &= \langle 0 | \hat{E}^{(+)}(0) | \Psi(t) \rangle,
 \end{aligned} \tag{9.36}$$

where we have simplified the discussion in one-dimension and assumed  $\mathbf{r}_0 = 0$  and  $t_0 = 0$  as usual. In Equation 9.36, we have successfully evolved the initial state  $|\Psi(0)\rangle$  to the finally measured state of  $|\Psi(t)\rangle$  with the help of Green's function  $g(r, t; \omega)$ .

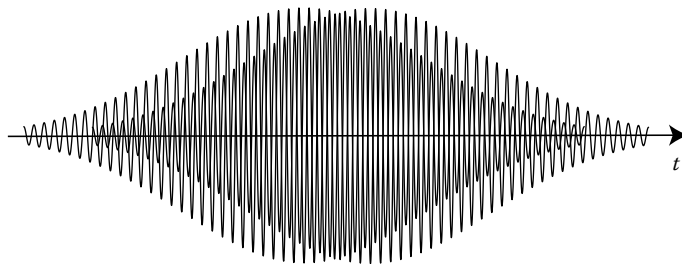
## 2. The physics

Substituting the single-photon state into Equation 9.34, the temporal effective wavefunction of the photon is calculated to be

$$\Psi(z_j, t_j) = \mathcal{F}_{\tau_j} \{f(v)\} e^{-i\omega_0 \tau_j} \tag{9.37}$$

where  $\tau_j = t_j - z_j/c$  (in vacuum). We will assume all the effective wavefunction calculations in the rest of this chapter in vacuum unless otherwise specified. Equation 9.37 indicates a typical wavepacket in space-time.

The schematic picture of a Gaussian wavepacket is the same as shown in Figure 1.2. There should be no surprise that Equation 9.37 is no different from the classical wavepacket of Equation 1.24. Equations 1.24 and 9.37 describe the same dynamic properties of light, except that the effective wavefunction is associated with the quantized field and the concept of a photon, or the dynamic picture of a photon in space-time.

**FIGURE 9.3**

Schematic of two partially overlapped Gaussian wavepackets at the photon-counting detector. Interference is expected with fringe visibility of less than 100%.

### 3. Photon interferes with itself

In terms of the effective wavefunction and the concept of photon, we may now view Young's double-pinhole experiment from a new perspective: a photon is emitted from the light source at space-time ( $\mathbf{r}=0, t=0$ ) (event 1) and later excites an atom at space-time coordinate  $(\mathbf{r}, t)$  to produce a photoelectron (event 2). The photon has two possible paths between the source and the photon-counting detector. The two possible paths quantum mechanically correspond to two probability amplitudes that contribute to the superposition of the effective wavefunction. The probability to produce a photoelectron at space-time point  $(\mathbf{r}, t)$  is determined by the relative "phase" delay and "group" delay between the two amplitudes, i.e., the delay between the two wavepackets  $\Psi(\mathbf{r}_1, t_1)$  and  $\Psi(\mathbf{r}_2, t_2)$ . If  $\Psi(\mathbf{r}_1, t_1)$  and  $\Psi(\mathbf{r}_2, t_2)$  are well separated at space-time point  $(\mathbf{r}, t)$ , there would be no interference. If  $\Psi(\mathbf{r}_1, t_2)$  and  $\Psi(\mathbf{r}_2, t_2)$  are indistinguishable or partially indistinguishable at space-time point  $(\mathbf{r}, t)$ , interference is observable. The greater the overlapping is, the greater the interference visibility and the higher the degree of coherence will be. Figure 9.3 schematically shows partially overlapped Gaussian wavepackets. Interference is expected with fringe visibility of less than 100%.

Based on Figure 9.3, it seems that we have enough reason to conclude that "a photon only interferes with itself." We may never know through which slit (or both slits) a single photon has been passing in Young's double-pinhole experiment. We can, however, accurately predict the counting rate of the photodetector as a function of the relative delay between the two effective wavefunctions of the photon.

## 9.3 Measurement of the First-Order Coherence or Correlation

We have emphasized earlier that in the quantum theory of light, a measurement of a photon or a wavepacket cannot provide us any meaningful

knowledge of physics, except the registration of a photoelectron event. A time-accumulative measurement, which involves a large number of photons, is always necessary. This type of measurement is named photon counting. A photon counter with an idealized point photodetector counts how many photoelectron events occur within a chosen time interval at a chosen spatial coordinate of the photodetector. Basically, it provides a time-averaged photon-counting rate

$$R_d = \int_T dt \langle \hat{E}^{(-)}(\mathbf{r}, t) \hat{E}^{(+)}(\mathbf{r}, t) \rangle, \quad (9.38)$$

where  $T$  is the accumulative time interval of the photon counting. In Young's double-pinhole interferometer, a photon counter measures the time-averaged first-order coherence function by means of an interference pattern

$$R_d = \int_T dt \left[ G^{(1)}(\mathbf{r}_1, t_1; \mathbf{r}_1, t_1) + G^{(1)}(\mathbf{r}_2, t_2; \mathbf{r}_2, t_2) \right. \\ \left. + G^{(1)}(\mathbf{r}_1, t_1; \mathbf{r}_2, t_2) + G^{(1)}(\mathbf{r}_2, t_2; \mathbf{r}_1, t_1) \right]. \quad (9.39)$$

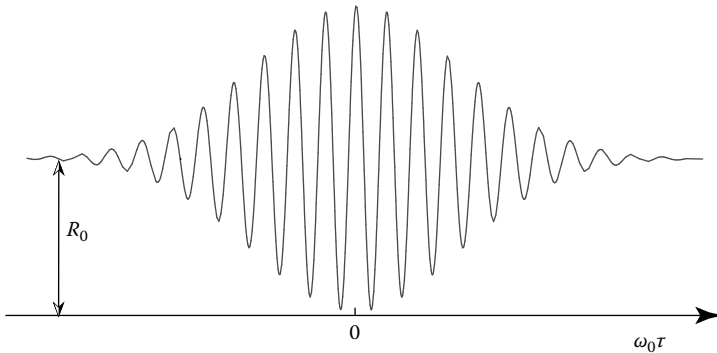
As we have learned, time average and ensemble average are equivalent for stationary fields. Time averaging may not have any effect on the first-order coherence function of a stationary field; however, a time average may not be trivial for a time-dependent effective wavefunction or a first-order coherence function. What do we learn about the first-order coherence of a single-photon state after the time average?

### Example (I): Pure Single-Photon State

The following discussion will focus on the first-order mutual-coherence function or cross-correlation function  $G^{(1)}(\mathbf{r}_1, t_1; \mathbf{r}_2, t_2)$ . In the case of pure single-photon state, the first-order mutual-coherence function is a product of two wavepackets in space-time:  $G^{(1)}(\mathbf{r}_1, t_1; \mathbf{r}_2, t_2) = \Psi^*(\mathbf{r}_1, t_1) \Psi(\mathbf{r}_2, t_2)$ . In general, it cannot be written as a time-independent function of  $t_1 - t_2$ .

The time-averaged  $G^{(1)}(\mathbf{r}_1, t_1; \mathbf{r}_2, t_2)$  of a pure single-photon state, which is measurable in Young's double-pinhole interferometer, can be formally calculated from

$$\int_T dt \Psi^*(z_1, t_1) \Psi(z_2, t_2) \\ \simeq \int_{T \sim \infty} dt e^{i(\omega_0 t_1 - k_0 z_1)} \mathcal{F}_{\tau_1}^* \{ f(v) \} e^{-i(\omega_0 t_2 - k_0 z_2)} \mathcal{F}_{\tau_2} \{ f(v) \} \\ = \mathcal{F}_{\tau} \left\{ |f(v)|^2 \right\} e^{-i\omega_0 \tau} \quad (9.40)$$

**FIGURE 9.4**

Counting rate of the photon-counting detector as a function of  $\omega_0\tau$  in Young's double-pinhole experiment. The observed interference measures the time-averaged first-order coherence. In this observation, a Gaussian spectrum is assumed.

where, again,  $v = \omega - \omega_0$ ,  $\omega_0$  is the center frequency of the spectrum, and  $\tau = [(z_2 + s_2) - (z_1 + s_1)]/c$  for arbitrary  $z_1$  and  $z_2$ .

Substituting Equation 9.40 into Equation 9.39 and assuming equal chance for a photon to pass the upper and the lower pinholes, the time-averaged counting rate of the photon-counting detector at a chosen coordinate is thus a function of  $\tau$ :

$$R_d(\tau) = R_0 [1 + \mathcal{F}_\tau \left\{ |f(v)|^2 \right\} \cos \omega_0 \tau] \quad (9.41)$$

where  $R_0$  is a constant that is calculated from the time integral of the self-correlation function. Figure 9.4 shows a measured result of a photon-counting detector. Its time-averaged counting rate is a function of  $\tau$ . This is the only information we can directly observe from the measurement.

### **Example (II): Mixed Single-Photon State**

For a mixed single-photon state, the calculation of the time-averaged first-order mutual-coherence function is also straightforward:

$$\begin{aligned} \int_T dt G^{(1)}(z_1, t_1; z_2, t_2) &= \int_T dt \text{tr} \left[ \hat{\rho} \hat{E}^{(-)}(z_1, t_1) \hat{\rho} \hat{E}^{(+)}(z_2, t_2) \right] \\ &= \int_T dt \sum_n P_n G_n^{(1)}(z_1, t_1; z_2, t_2) \\ &\propto \mathcal{F}_\tau \left\{ |f(v)|^2 \right\} \cos \omega_0 \tau. \end{aligned} \quad (9.42)$$

It is clearly shown that the time averaging is equivalent to the statistical ensemble averaging in this case. Although after ensemble averaging time averaging becomes a trivial calculation in this example, a time accumulative integral is always necessary for a photon-counting measurement. The observed interference pattern is thus the same as that of Example (I):

$$R_d(\tau) = R_0 \left[ 1 + \mathcal{F}_\tau \left\{ |f(v)|^2 \right\} \cos \omega_0 \tau \right].$$

A time-averaged measurement of first-order coherence cannot distinguish a pure state from a mixed state. This point has been emphasized in previous chapters from the classical point of view.

## 9.4 Interference between Independent Radiations

In this section, we discuss the interference of two independent radiations. To be consistent with the early discussions, the following treatment is also based on the experimental setup of Young's double-pinhole interferometer (Figure 9.5). Two independent input radiations are placed behind the upper pinhole, which is labeled by the letter A, and the lower pinhole, which is labeled by the letter B, respectively. In the following, we calculate the mutual-coherence function for different input states. The input state behind A-pinhole (B-pinhole) will be labeled as state A (state B).

Case (I): Independent coherent states

Assuming the input states are multimode coherent states,

$$|\Psi\rangle = |\Psi_A\rangle|\Psi_B\rangle = |\{\alpha\}\rangle|\{\beta\}\rangle. \quad (9.43)$$

In this setup, the field operators at  $(z_1, t_1)$  and  $(z_2, t_2)$  are

$$\begin{aligned} \hat{E}^{(-)}(z_1, t_1) &= \int d\omega \hat{a}^\dagger(\omega) e^{i\omega t_1}, \\ \hat{E}^{(+)}(z_2, t_2) &= \int d\omega' \hat{b}(\omega') e^{-i\omega' t_2}. \end{aligned} \quad (9.44)$$

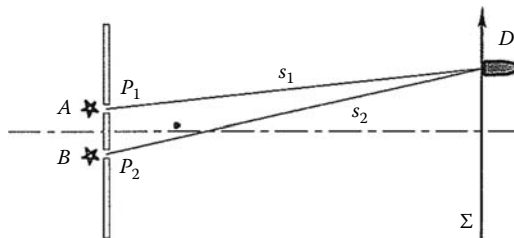


**FIGURE 9.5**

Schematic of an Young's double-pinhole interference experiment. The interferometer is the same as that shown in our early discussions, except the light source. Two independent input radiations are placed behind the upper pinhole, which is labeled by the letter A, and the lower pinhole, which is labeled by the letter B, respectively.

Since the coherent state is the eigenstate of the field operator, a very simple calculation turns the mutual-coherence function a product of two conjugate wavepackets:

$$\begin{aligned} G^{(1)}(z_1, t_1; z_2, t_2) &= \int d\omega \alpha^*(\omega) e^{i\omega t_1} \int d\omega' \beta(\omega') e^{-i\omega' t_2} \\ &= \mathcal{F}_{\tau_1-t_{0\alpha}}^* \{a(v)\} \mathcal{F}_{\tau_2-t_{0\beta}} \{b(v)\} e^{-i\omega_0(t_{0\alpha}-t_{0\beta})} e^{i\omega_0\tau}. \end{aligned} \quad (9.45)$$

It is easy to see that if the experimental measurement achieves (1) overlapping of the two wavepackets and (2)  $e^{-i\omega_0(t_{0\alpha}-t_{0\beta})} = \text{constant}$  within the observation time, then  $G^{(1)}(z_1, t_1; z_2, t_2)$  and  $G^{(1)}(z_2, t_2; z_1, t_1)$  will contribute an observable interference. The experimental condition (1) is achievable by choosing  $s_1 \simeq s_2$ . The other condition (2) is achievable either by “phase locking” the two input states or by taking a short time observation that is much shorter than the coherent time of the input radiation, such as a fast film exposure. The above result has been confirmed experimentally. In fact, soon after the invention of laser, Mandel and coworkers demonstrated the first-order interference between two independent laser beams.

### Case (II): Independent single-photon wavepackets

Although first-order interference between independent laser beams can be easily demonstrated in modern optics laboratories, it is interesting to know what will happen when the two independent input radiations are at the single-photon level. In the following measurement, we replace the radiation source with two independent atomic transitions. Atom *A* is placed behind the upper pinhole; atom *B* is placed behind the lower pinhole. Similar to our early model of thermal light in Section 8.8, the state of the radiation can be written as

$$\begin{aligned} |\Psi\rangle &= [|0\rangle + \epsilon|\Psi_A\rangle][|0\rangle + \epsilon|\Psi_B\rangle] \\ &= |0\rangle + \epsilon[|\Psi_A\rangle + |\Psi_B\rangle] + \epsilon^2[|\Psi_A\rangle|\Psi_B\rangle], \end{aligned} \quad (9.46)$$

with

$$|\Psi_A\rangle = \int d\omega f_A(\omega) \hat{a}^\dagger(\omega) |0\rangle, \quad |\Psi_B\rangle = \int d\omega f_B(\omega) \hat{b}^\dagger(\omega) |0\rangle,$$

where the complex amplitudes  $f_A(\omega)$  and  $f_B(\omega)$  will be treated with identical spectrum distribution but different phases that are determined by the initial times of the transitions.

Now we calculate the first-order temporal mutual-coherence function with the same field operators shown in Equation 9.44. Since the state is written in the sum of first-order expansion and the second-order expansion on  $\epsilon$ , we break the calculation into two: (1) taking the input state in the first-order

expansion of  $\epsilon$  and (2) taking the input state in the second-order expansion of  $\epsilon^2$ .

$$1. \ |\Psi\rangle = |\Psi_A\rangle + |\Psi_B\rangle$$

The first-order temporal mutual-coherence function  $G^{(1)}(z_1, t_1; z_2, t_2)$  is calculated as

$$\begin{aligned} G^{(1)}(z_1, t_1; z_2, t_2) &= [\langle \Psi_A | + \langle \Psi_B |] \hat{E}^{(-)}(z_1, t_1) \hat{E}^{(+)}(z_2, t_2) [|\Psi_A\rangle + |\Psi_B\rangle] \\ &= \Psi_A^*(z_1, t_1) \Psi_B(z_2, t_2) \\ &\simeq \mathcal{F}_{\tau_1 - t_{0A}}^* \{f(v)\} \mathcal{F}_{\tau_2 - t_{0B}} \{f(v)\} e^{-i\omega_0(t_{0A} - t_{0B})} e^{i\omega_0\tau}. \end{aligned} \quad (9.47)$$

The experimental condition for observing an interference from the first-order expansion is the same as that of the coherent state, except that one photodetection event may not be able to give us any meaningful information. A large number of photons are always necessary for this type of experiment. In a time-accumulative measurement, however,  $t_{0A} - t_{0B}$  may take random values from time to time. The situation is exactly the same as that of thermal light. After averaging on  $t_{0A} - t_{0B}$ , the interference is unobservable. Is it possible to observe interference from two independent atomic transitions? In principle, if we can keep  $e^{-i\omega_0(t_{0A} - t_{0B})} = \text{constant}$  from time to time, from one “independent” pair to another “independent” pair, the interference will be observable. How to “phase-lock” two individual atomic transitions is still a subject of research.

$$2. \ |\Psi\rangle = |\Psi_A\rangle |\Psi_B\rangle$$

The first-order temporal mutual-coherence function  $G^{(1)}(z_1, t_1; z_2, t_2)$  is calculated as

$$\begin{aligned} G^{(1)}(z_1, t_1; z_2, t_2) &= \langle \Psi_A | \langle \Psi_B | \hat{E}^{(-)}(z_1, t_1) \hat{E}^{(+)}(z_2, t_2) |\Psi_A\rangle |\Psi_B\rangle \\ &= 0 \end{aligned} \quad (9.48)$$

The second-order expansion has no contribution to the first-order coherence in this case. We will learn in the next section that the second-order expansion on  $\epsilon$ ,  $|\Psi\rangle = |\Psi_A\rangle |\Psi_B\rangle$ , may contribute to the second-order coherence measurement by means of a nontrivial correlation or interference observable from a

coincidence counter, namely, a joint photon-counting measurement between two independent photon-counting detectors.

## 9.5 Quantum Degree of Second-Order Coherence

The second-order coherence of radiation is defined as follows:

$$\begin{aligned}
 G^{(2)}(\mathbf{r}_1, t_1; \mathbf{r}_2, t_2) \\
 \equiv \langle E^{(-)}(\mathbf{r}_1, t_1)E^{(-)}(\mathbf{r}_2, t_2)E^{(+)}(\mathbf{r}_2, t_2)E^{(+)}(\mathbf{r}_1, t_1) \rangle \\
 = \left\langle \langle E^{(-)}(\mathbf{r}_1, t_1)E^{(-)}(\mathbf{r}_2, t_2)E^{(+)}(\mathbf{r}_2, t_2)E^{(+)}(\mathbf{r}_1, t_1) \rangle_{QM} \right\rangle_{\text{Ensemble}}, \quad (9.49)
 \end{aligned}$$

which is recognized as the expectation value of the normal-ordered field operators at space-time coordinates  $(\mathbf{r}_1, t_1)$  and  $(\mathbf{r}_2, t_2)$ . In the view of quantum theory of light,  $G^{(2)}(\mathbf{r}_1, t_1; \mathbf{r}_2, t_2)$  is thus a measure of the probability for jointly observing a pair of photons at  $(\mathbf{r}_1, t_1)$  and  $(\mathbf{r}_2, t_2)$  from a radiation field. Differing from the first-order coherence or correlation function, the second-order coherence or correlation function is directly measurable by two photodetectors at space-time coordinates  $(\mathbf{r}_1, t_1)$  and  $(\mathbf{r}_2, t_2)$ . It is very important to keep in mind that  $t_1$  and  $t_2$  are the physical times of the two photodetection events, or the registration times of a pair of photons, instead of the “referred early times” of a photodetection event at  $(\mathbf{r}, t)$ . Figure 9.6 illustrates an experiment setup for measuring  $G^{(2)}(\mathbf{r}_1, t_1; \mathbf{r}_2, t_2)$ . Having a better comparison with the first-order coherence, the measurement employs

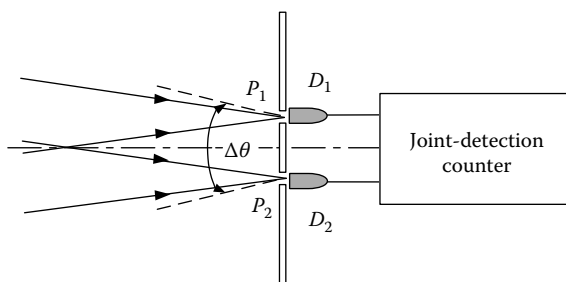


**FIGURE 9.6**

Schematic setup of a second-order coherence measurement. A pair of photons from a light source produces a joint photodetection event at space-time coordinates  $(\mathbf{r}_1, t_1)$  and  $(\mathbf{r}_2, t_2)$ . A coincidence counter, consisting of two photon-counting detectors  $D_1$ ,  $D_2$  and a coincidence circuit, is used to count the number of joint photodetection events.

the same Young's double-pinhole interferometer, except that it replaces two photon-counting detectors  $D_1$  and  $D_2$  behind the upper pinhole and the lower pinhole, respectively, for coincidence photon counting. In the view of quantum theory of photodetection, the counting rate of a coincidence counter measures the probability of observing a joint photodetection event of two photons at  $(\mathbf{r}_1, t_1)$  and  $(\mathbf{r}_2, t_2)$ , which is proportional to the expectation value of the normal-ordered field operators.

To be consistent with the theory of first-order coherence, a normalized correlation function, namely, the degree of second-order coherence, is defined accordingly:

$$\begin{aligned} g^{(2)}(\mathbf{r}_1, t_1; \mathbf{r}_2, t_2) \\ \equiv \frac{\langle E^{(-)}(\mathbf{r}_1, t_1)E^{(-)}(\mathbf{r}_2, t_2)E^{(+)}(\mathbf{r}_2, t_2)E^{(+)}(\mathbf{r}_1, t_1) \rangle}{\langle E^{(-)}(\mathbf{r}_1, t_1)E^{(+)}(\mathbf{r}_1, t_1) \rangle \langle E^{(-)}(\mathbf{r}_2, t_2)E^{(+)}(\mathbf{r}_2, t_2) \rangle}. \end{aligned} \quad (9.50)$$

In the case of a pure two-photon state, similar to the effective wavefunction of a photon, a two-photon effective wavefunction that represents the probability amplitude of jointly observing two photons at  $(\mathbf{r}_1, t_1)$  and  $(\mathbf{r}_2, t_2)$ , respectively, is formulated from the calculation of the second-order coherence function  $G^{(2)}(\mathbf{r}_1, t_1; \mathbf{r}_2, t_2)$ :

$$\begin{aligned} G^{(2)}(\mathbf{r}_1, t_1; \mathbf{r}_2, t_2) \\ = \langle \Psi | E^{(-)}(\mathbf{r}_1, t_1)E^{(-)}(\mathbf{r}_2, t_2)E^{(+)}(\mathbf{r}_2, t_2)E^{(+)}(\mathbf{r}_1, t_1) | \Psi \rangle \\ = \sum_n \langle \Psi | E^{(-)}(\mathbf{r}_1, t_1)E^{(-)}(\mathbf{r}_2, t_2) | n \rangle \langle n | E^{(+)}(\mathbf{r}_2, t_2)E^{(+)}(\mathbf{r}_1, t_1) | \Psi \rangle \\ = \langle \Psi | E^{(-)}(\mathbf{r}_1, t_1)E^{(-)}(\mathbf{r}_2, t_2) | 0 \rangle \langle 0 | E^{(+)}(\mathbf{r}_2, t_2)E^{(+)}(\mathbf{r}_1, t_1) | \Psi \rangle \\ = |\Psi(\mathbf{r}_1, t_1; \mathbf{r}_2, t_2)|^2, \end{aligned} \quad (9.51)$$

where, in the third line, we have used the completeness relation

$$\sum_n |n\rangle \langle n| = 1.$$

The effective wavefunction of a pair of photons that is characterized by a pure two-photon state  $|\Psi\rangle$ , is defined in Equation 9.51 as

$$\Psi(\mathbf{r}_1, t_1; \mathbf{r}_2, t_2) = \langle 0 | E^{(+)}(\mathbf{r}_2, t_2)E^{(+)}(\mathbf{r}_1, t_1) | \Psi \rangle. \quad (9.52)$$

In the case of a mixed two-photon state,  $G^{(2)}(\mathbf{r}_1, t_1; \mathbf{r}_2, t_2)$  is calculated from

$$\begin{aligned}
G^{(2)}(\mathbf{r}_1, t_1; \mathbf{r}_2, t_2) &= \left\langle \left\langle E^{(-)}(\mathbf{r}_1, t_1) E^{(-)}(\mathbf{r}_2, t_2) E^{(+)}(\mathbf{r}_2, t_2) E^{(+)}(\mathbf{r}_1, t_1) \right\rangle_{\text{QM}} \right\rangle_{\text{Ensemble}} \\
&= \text{tr} \left[ \hat{\rho} E^{(-)}(\mathbf{r}_1, t_1) E^{(-)}(\mathbf{r}_2, t_2) E^{(+)}(\mathbf{r}_2, t_2) E^{(+)}(\mathbf{r}_1, t_1) \right] \\
&= \sum_j P_j \langle \Psi_j | E^{(-)}(\mathbf{r}_1, t_1) E^{(-)}(\mathbf{r}_2, t_2) E^{(+)}(\mathbf{r}_2, t_2) E^{(+)}(\mathbf{r}_1, t_1) | \Psi_j \rangle \\
&= \sum_j P_j G_j^{(2)}(\mathbf{r}_1, t_1; \mathbf{r}_2, t_2) = \sum_j P_j |\Psi_j(\mathbf{r}_1, t_1; \mathbf{r}_2, t_2)|^2,
\end{aligned} \tag{9.53}$$

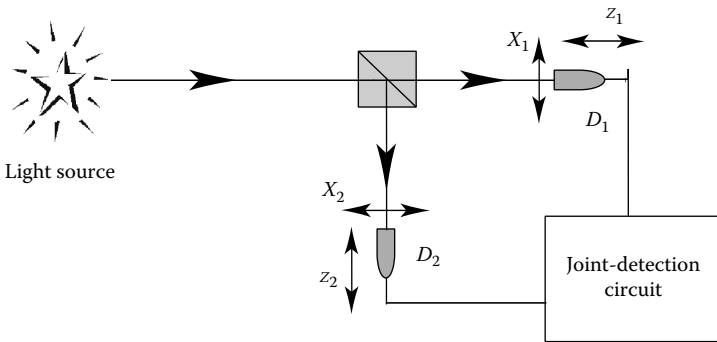
where  $P_j$  is the probability to find the radiation in the two-photon state  $|\Psi_j\rangle$ , and

$$\Psi_j(\mathbf{r}_1, t_1; \mathbf{r}_2, t_2) = \langle 0 | E^{(+)}(\mathbf{r}_2, t_2) E^{(+)}(\mathbf{r}_1, t_1) | \Psi_j \rangle \tag{9.54}$$

is the probability amplitude to observe the  $j$ th pair of photons to be jointly observed at space-time coordinates  $(\mathbf{r}_1, t_1)$  and  $(\mathbf{r}_2, t_2)$ .

The second-order correlation  $G^{(2)}(\mathbf{r}_1, t_1; \mathbf{r}_2, t_2)$  of a radiation is obviously determined by the state of the jointly measured photon pair. There is no surprise that different two-photon states result in different second-order correlations. In the following exercises, we evaluate  $G^{(2)}(\mathbf{r}_1, t_1; \mathbf{r}_2, t_2)$  for five categories of states: (I) product state of two single-photon wavepackets, (II) mixed two-photon state of thermal light, (III) entangled two-photon state, (IV) number state of  $n_\omega = 2$ , and (V) coherent state.

Before the exercises, we introduce a modified HBT type two-photon interferometer, which might be helpful for some of the following analyses. The two-photon interferometer is schematically shown in Figure 9.7. In principle, this setup is the same as that of Figure 9.6, except the uses of a 50/50 beamsplitter to separate the measurements of  $D_1$  and  $D_2$  in the transmitted and reflected radiations, respectively. This setup allows an easier choice on either the temporal part or the spatial part correlation. For instance, the measurement gives second-order temporal correlation by scanning the longitudinal coordinate  $z_1$  of  $D_1$  and/or  $z_2$  of  $D_2$  when choosing a set of fixed transverse coordinates of  $x_1 = x_2$ , and *vise versa*.

**FIGURE 9.7**

A schematic measurement of second-order correlation function  $G^{(2)}(\mathbf{r}_1, t_1; \mathbf{r}_2, t_2)$  with different radiation sources.  $D_1$  and  $D_2$  are idealized point-like photodetectors, and are both scannable along their longitudinal axes and on their transverse planes. For most of the following discussions, we assume  $D_1$  and  $D_2$  are operated at photon-counting mode.  $D_1$  and  $D_2$  together with a joint-detection circuit play the role of a coincidence counter.

#### Category (I): Product state of two single-photon wavepackets

The following exercise evaluates the second-order temporal correlation or coherence of a product state of two single-photon wavepackets that are produced from a point light source. Based on the simple model of incoherent or coherent radiation in Section 8.8, we assume the observation of a joint photodetection event in which  $D_1$  annihilates a photon that is created from atomic transition  $A$ , and  $D_2$  annihilates another photon that is created from atomic transition  $B$ . We further assume that a large number of joint photodetection events of  $D_1$  and  $D_2$  are produced from the same two-photon state as a homogeneous ensemble. Therefore, the measured radiation can be characterized by a pure state in the form of a product of two single-photon wavepackets:

$$|\Psi\rangle = |\Psi_B\rangle|\Psi_A\rangle, \quad (9.55)$$

with

$$|\Psi_A\rangle = \int d\omega f_A(\omega) \hat{a}^\dagger(\omega) |0\rangle, \quad |\Psi_B\rangle = \int d\omega f_B(\omega) \hat{b}^\dagger(\omega) |0\rangle,$$

where the complex amplitudes  $f_A(\omega)$  and  $f_B(\omega)$  will be treated with identical spectrum distribution but different phases that are determined by the initial times of the atomic transitions.

For the experimental setup of Figure 9.7, the two single-photon wavepackets both have 50%–50% chances to be transmitted or reflected from the beamsplitter. The two wavepackets have a certain probability to be jointly measured by  $D_1$  and  $D_2$ ; however, quantum mechanics does not

allow a single-photon wavepacket to be jointly measured by  $D_1$  and  $D_2$ . For far-field temporal coherence measurements, the field operators are simplified as

$$\begin{aligned}\hat{E}^{(+)}(z_j, t_j) &= \frac{E_0}{\sqrt{2}} \left[ \int d\omega e^{i\omega\tau_j} \hat{a}(\omega) + \int d\omega' e^{i\omega'\tau_j} \hat{b}(\omega') \right] \\ &\equiv \hat{E}_A^{(+)}(z_j, t_j) + \hat{E}_B^{(+)}(z_j, t_j), \quad j = 1, 2.\end{aligned}$$

The effective two-photon wavefunction is calculated from

$$\begin{aligned}\Psi(z_1, t_1; z_2, t_2) &= \langle 0 | \hat{E}_B^{(+)}(z_2, t_2) \hat{E}_A^{(+)}(z_1, t_1) | \Psi \rangle \\ &= \Psi_{AB}(z_1, t_1; z_2, t_2) + \Psi_{BA}(z_1, t_1; z_2, t_2)\end{aligned}\tag{9.56}$$

where

$$\begin{aligned}\Psi_{AB}(z_1, t_1; z_2, t_2) &\equiv \left\langle 0 \left| \hat{E}_B^{(+)}(z_2, t_2) \hat{E}_A^{(+)}(z_1, t_1) \right| \Psi \right\rangle \\ &= \left\langle 0 \left| \hat{E}_A^{(+)}(z_1, t_1) \right| \Psi_A \right\rangle \left\langle 0 \left| \hat{E}_B^{(+)}(z_2, t_2) \right| \Psi_B \right\rangle \\ &= \Psi_A(z_1, t_1) \Psi_B(z_2, t_2) \\ \Psi_{BA}(z_1, t_1; z_2, t_2) &\equiv \left\langle 0 \left| \hat{E}_A^{(+)}(z_2, t_2) \hat{E}_B^{(+)}(z_1, t_1) \right| \Psi \right\rangle \\ &= \left\langle 0 \left| \hat{E}_B^{(+)}(z_1, t_1) \right| \Psi_B \right\rangle \left\langle 0 \left| \hat{E}_A^{(+)}(z_2, t_2) \right| \Psi_A \right\rangle \\ &= \Psi_B(z_1, t_1) \Psi_A(z_2, t_2).\end{aligned}\tag{9.57}$$

The two effective wavefunctions in Equation 9.57 represent two different yet indistinguishable two-photon amplitudes: (1) the wavepackets  $A$  and  $B$  are measured at  $D_1$  and  $D_2$ , respectively and (2) the wavepackets  $A$  and  $B$  are measured at  $D_2$  and  $D_1$ , respectively. The superposition of these two-photon amplitudes yields a nontrivial second-order correlation

$$\begin{aligned}G^{(2)}(z_1, t_1; z_2, t_2) &= |\Psi_{AB}(\mathbf{r}_1, t_1; \mathbf{r}_2, t_2) + \Psi_{BA}(\mathbf{r}_1, t_1; \mathbf{r}_2, t_2)|^2 \\ &= G_{11}^{(1)} G_{22}^{(1)} + G_{12}^{(1)} G_{21}^{(1)},\end{aligned}\tag{9.58}$$

where

$$\begin{aligned}
 G_{11}^{(1)} G_{22}^{(1)} &= |\Psi_A(z_1, t_1)|^2 |\Psi_B(z_2, t_2)|^2 \\
 &= |\mathcal{F}_{\tau_1-t_{0A}} \{f(v)\}|^2 |\mathcal{F}_{\tau_2-t_{0B}} \{f(v)\}|^2 \\
 G_{12}^{(1)} G_{21}^{(1)} &= \Psi_A^*(z_1, t_1) \Psi_A(z_2, t_2) \Psi_B^*(z_2, t_2) \Psi_B(z_1, t_1) \\
 &= \left[ \mathcal{F}_{\tau_1-t_{0A}}^* \{f(v)\} \mathcal{F}_{\tau_2-t_{0A}} \{f(v)\} \right] \\
 &\quad \times \left[ \mathcal{F}_{\tau_2-t_{0B}}^* \{f(v)\} \mathcal{F}_{\tau_1-t_{0B}} \{f(v)\} \right].
 \end{aligned}$$

where we have taken the wavepackets in the form of their Fourier transforms. The second-order coherence function is thus connected with the first-order self-coherence and mutual-coherence functions. It is clearly shown in the above exercise that this peculiar behavior is determined by the product nature of the two-photon state.

#### Category (II): Mixed two-photon state of thermal light

Now we are ready to calculate the second-order temporal correlation or coherence of thermal light. We assume an experimental setup shown either in Figure 9.6 or in Figure 9.7 with a point light source. Applying the same model of chaotic-thermal light of Section 8.8, taking the early results of  $\hat{\rho} \simeq \hat{\rho}^{(1)} + \hat{\rho}^{(2)} + \dots$ , the necessary lowest-order approximation that contributes to the second-order correlation measurement is

$$\hat{\rho}^{(2)} = \sum_j P_j |\Psi_j\rangle\langle\Psi_j| \simeq \sum_{m < n} |c_m|^2 |c_n|^2 |\Psi_m\rangle|\Psi_n\rangle\langle\Psi_n|\langle\Psi_m| \quad (9.59)$$

with

$$|\Psi_m\rangle = \int d\omega f_m(\omega) e^{i\omega t_{0m}} \hat{a}_m^\dagger(\omega) |0\rangle.$$

The state of Equation 9.59 is a mixed two-photon state, which characterizes (1) the state of a photon pair, which produced a joint photodetection event, as an incoherent superposition of a set of orthogonal paired single-photon states created from all possible independent and randomly radiated atomic transitions; and (2) the state of a large number of jointly measured photon pairs, each created from a randomly paired atomic transitions, as an inhomogeneous ensemble.

The field operators are the same as that of the first-order coherence measurement:

$$\hat{E}^{(+)}(\mathbf{r}_j, t_j) = \sum_m \hat{E}_m^{(+)}(\mathbf{r}_j, t_j), \quad j = 1, 2,$$

$$\hat{E}^{(-)}(\mathbf{r}_k, t_k) = \sum_n \hat{E}_n^{(-)}(z_k, t_k), \quad k = 1, 2.$$

We now calculate  $G_j^{(2)}(\mathbf{r}_1, t_1; \mathbf{r}_2, t_2)$  based on Equation 9.59:

$$\begin{aligned} G_j^{(2)}(\mathbf{r}_1, t_1; \mathbf{r}_2, t_2) &= \langle \Psi_j | E^{(-)}(\mathbf{r}_1, t_1) E^{(-)}(\mathbf{r}_2, t_2) E^{(+)}(\mathbf{r}_2, t_2) E^{(+)}(\mathbf{r}_1, t_1) | \Psi_j \rangle \\ &= |[\langle 0 | E_m^{(+)}(\mathbf{r}_2, t_2) | \Psi_m \rangle \langle 0 | E_n^{(+)}(\mathbf{r}_1, t_1) | \Psi_n \rangle \\ &\quad + \langle 0 | E_n^{(+)}(\mathbf{r}_2, t_2) | \Psi_n \rangle \langle 0 | E_m^{(+)}(\mathbf{r}_1, t_1) | \Psi_m \rangle]|^2 \\ &= |[\Psi_{mn}(\mathbf{r}_1, t_1; \mathbf{r}_2, t_2) + \Psi_{nm}(\mathbf{r}_1, t_1; \mathbf{r}_2, t_2)]|^2 \\ &= |\Psi_j(\mathbf{r}_1, t_1; \mathbf{r}_2, t_2)|^2 \end{aligned} \quad (9.60)$$

where

$$\Psi_j(\mathbf{r}_1, t_1; \mathbf{r}_2, t_2) = \Psi_{mn}(\mathbf{r}_1, t_1; \mathbf{r}_2, t_2) + \Psi_{nm}(\mathbf{r}_1, t_1; \mathbf{r}_2, t_2) \quad (9.61)$$

is defined as the effective wavefunction of the annihilated  $j$ th photon pair, and

$$\begin{aligned} \Psi_{mn}(\mathbf{r}_1, t_1; \mathbf{r}_2, t_2) &= \langle 0 | E_m^{(+)}(\mathbf{r}_1, t_1) | \Psi_m \rangle \langle 0 | E_n^{(+)}(\mathbf{r}_2, t_2) | \Psi_n \rangle \\ &= \Psi_m(\mathbf{r}_1, t_1) \Psi_n(\mathbf{r}_2, t_2) \\ \Psi_{nm}(\mathbf{r}_1, t_1; \mathbf{r}_2, t_2) &= \langle 0 | E_n^{(+)}(\mathbf{r}_1, t_1) | \Psi_n \rangle \langle 0 | E_m^{(+)}(\mathbf{r}_2, t_2) | \Psi_m \rangle \\ &= \Psi_n(\mathbf{r}_1, t_1) \Psi_m(\mathbf{r}_2, t_2) \end{aligned}$$

represent two different yet indistinguishable two-photon amplitudes that contribute to a joint-detection event of  $D_1$  and  $D_2$ . We also use a different but equivalent notations to emphasize the peculiar physics behind the

superposition of Equation 9.61, namely, the physics of a photon pair interfere with the pair itself:

$$\Psi_j(\mathbf{r}_1, t_1; \mathbf{r}_2, t_2) = \mathcal{A}_{mn}(\mathbf{r}_1, t_1; \mathbf{r}_2, t_2) + \mathcal{A}_{nm}(\mathbf{r}_1, t_1; \mathbf{r}_2, t_2).$$

In this notation, it is easy to see that the  $j$ th photon pair, which is created from a randomly paired atomic transitions  $m$  and  $n$ , has two alternative ways to produce the  $j$ th joint photodetection event. The linearly superposed two-photon amplitudes belong to the same photon pair.

It is interesting to see the effective wavefunction  $\Psi_j(\mathbf{r}_1, t_1; \mathbf{r}_2, t_2)$  is the result of a linear superposition of  $\Psi_{mn}(\mathbf{r}_1, t_1; \mathbf{r}_2, t_2)$  and  $\Psi_{nm}(\mathbf{r}_1, t_1; \mathbf{r}_2, t_2)$ , similar to a symmetrized wavefunction of identical particles in quantum mechanics. This peculiar optical interference phenomenon, namely, a photon pair interfere with the pair itself, is conceptually different from the classical interference. The interference is not due to the superposition of electromagnetic fields at a local point of space-time; it takes place between two two-photon amplitudes that correspond to two alternatives, different yet indistinguishable, resulting in a joint photodetection event at two space-time points  $(\mathbf{r}_1, t_1)$  and  $(\mathbf{r}_2, t_2)$ : (1) photon  $m$  and photon  $n$  are annihilated at  $(\mathbf{r}_1, t_1)$  and  $(\mathbf{r}_2, t_2)$ , respectively, or (2) photon  $n$  and photon  $m$  are annihilated at  $(\mathbf{r}_1, t_1)$  and  $(\mathbf{r}_2, t_2)$ , respectively.  $\Psi_j(\mathbf{r}_1, t_1; \mathbf{r}_2, t_2)$  is not only similar to the symmetrized wavefunction of identical particles but also plays the same role as that of the symmetrized wavefunction of identical particles. The probability to jointly annihilate a pair of photons at space-time coordinates  $(\mathbf{r}_1, t_1; \mathbf{r}_2, t_2)$  is thus proportional to

$$\begin{aligned} G^{(2)}(\mathbf{r}_1, t_1; \mathbf{r}_2, t_2) &= \sum_j P_j |\Psi_j(\mathbf{r}_1, t_1; \mathbf{r}_2, t_2)|^2 \\ &\simeq \int dt_{0m} dt_{0n} |\Psi_{mn}(\mathbf{r}_1, t_1; \mathbf{r}_2, t_2) + \Psi_{nm}(\mathbf{r}_1, t_1; \mathbf{r}_2, t_2)|^2, \end{aligned} \quad (9.62)$$

where we have assumed, again,  $P_j \sim \text{constant}$ , corresponding to randomly distributed chaotic-thermal radiation. The physics behind Equation 9.62 is very clear: each measured photon pair has two different yet indistinguishable alternative ways to produce a joint-detection event of  $D_1$  and  $D_2$  at  $(\mathbf{r}_1, t_1)$  and  $(\mathbf{r}_2, t_2)$ . The superposition of these probability amplitudes yields a two-photon interference pattern as a function of  $(\mathbf{r}_1, t_1; \mathbf{r}_2, t_2)$ . A large number of these interference patterns add statistically, resulting in a nontrivial second-order coherent function  $G^{(2)}(\mathbf{r}_1, t_1; \mathbf{r}_2, t_2)$ .

Next, we formally connect  $G^{(2)}(\mathbf{r}_1, t_1; \mathbf{r}_2, t_2)$  with the first-order coherence functions,

$$\begin{aligned} G^{(2)}(\mathbf{r}_1, t_1; \mathbf{r}_2, t_2) &\propto \int dt_{0m} |\Psi_m(\mathbf{r}_1, t_1)|^2 \int dt_{0n} |\Psi_n(\mathbf{r}_2, t_2)|^2 \\ &\quad + \int dt_{0m} \Psi_m(\mathbf{r}_1, t_1) \Psi_m^*(\mathbf{r}_2, t_2) \int dt_{0n} \Psi_n(\mathbf{r}_2, t_2) \Psi_n^*(\mathbf{r}_1, t_1) \\ &= G_{11}^{(1)} G_{22}^{(1)} + |G_{12}^{(1)}|^2, \end{aligned} \quad (9.63)$$

where we have used the short notations  $G_{11}^{(1)}$ ,  $G_{22}^{(1)}$ ,  $G_{12}^{(1)}$ , and  $G_{21}^{(1)}$  for the first-order self-coherence and mutual-coherence functions. Although  $G^{(2)}$  is written in terms of the first-order coherence functions, it is important to keep in mind that  $G^{(2)}$  as well as  $|G_{12}^{(1)}|^2$  in Equation 9.63 are measured by two independent photodetectors involving the joint annihilation of two photons at space-time points  $(\mathbf{r}_1, t_1)$  and  $(\mathbf{r}_2, t_2)$ . The quantum theory of second-order interference of radiation represents a troubling concept to classical physics. The superposition involves two individual photodetectors at separate space-time coordinates. Do we have this kind superposition in the classical Maxwell electromagnetic wave theory?

Using the early results of the first-order self-coherence and mutual-coherence functions for thermal light to complete the calculation of the second-order coherence as a function of the temporal (longitudinal) coordinates, we obtain

$$G^{(2)}(z_1, t_1; z_2, t_2) \propto \left[ \int d\nu |f(\nu)|^2 \right]^2 + \left| \mathcal{F}_\tau \left\{ |f(\nu)|^2 \right\} \right|^2, \quad (9.64)$$

where we have assumed  $G_{11}^{(1)} = G_{22}^{(1)}$ . The degree of second-order coherence is thus

$$g^{(2)}(z_1, t_1; z_2, t_2) = 1 + \frac{\left| \mathcal{F}_\tau \left\{ |f(\nu)|^2 \right\} \right|^2}{\left[ \int d\nu |f(\nu)|^2 \right]^2}. \quad (9.65)$$

The degree of second-order coherence achieves its maximum value at  $\tau = \tau_1 - \tau_2 = 0$ , i.e.,  $(t_1 - t_2) = (z_1 - z_2)/c$ . Under this condition, the two alternatives, namely, the two-photon amplitudes  $\Psi_{mn}(z_1, t_1; z_2, t_2)$  and  $\Psi_{nm}(z_1, t_1; z_2, t_2)$ , overlap completely in space-time. It is easy to see that if we take fixed values of the coordinates  $z_1$  and  $z_2$ , the second-order correlation and the normalized second-order coherence are functions of the relative time delay  $t_1 - t_2$ , which can be observed directly by measuring the registration

times of the photodetectors. On the other hand, if we take a fixed value of  $t_1 - t_2$ , the second-order correlation and the degree of second-order coherence are functions of  $z_1 - z_2$ . However, in photon-counting regime, a time accumulative joint measurement is always necessary. The coincidence-counting rate involves a time average on  $t_1$  and  $t_2$  within the coincidence time window  $S(t_1 - t_2)$ :

$$R_c(z_1, z_2) = \int_T dt_1 dt_2 S(t_1 - t_2) G^{(2)}(z_1, t_1; z_2, t_2). \quad (9.66)$$

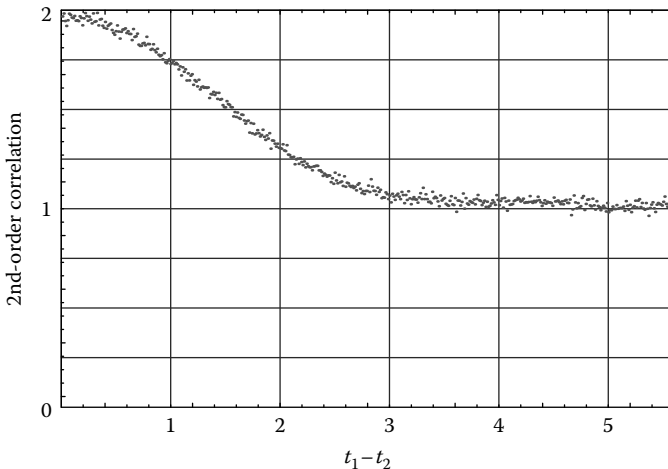
where  $S(t_1 - t_2)$  is a step-function to simulate the time window of the joint-detection.

In summary, we may divide the above calculation into two parts: (1) the superposition of two-photon amplitudes in a joint-detection event produced by an arbitrarily paired photons and (2) the integration of a large number of joint-detection events produced from an inhomogeneous ensemble of randomly radiated photons. On one hand, two-photon interference involves a measured photon pair only; it is reasonable to say that a measured photon pair only interferes with itself. On the other hand, the second-order coherence or correlation statistically involves a large number of measured photon pairs. The property of  $G^{(2)}(\mathbf{r}_1, t_1; \mathbf{r}_2, t_2)$ , either trivial or nontrivial, is determined by the interference of each measured pair of photons, and by the collective behavior of the measured ensemble of pairs. In certain space-time coordinates, each and every two-photon interference may occur constructively or destructively. Statistically, the averaged sum of these interferences will result in a nontrivial correlation function of  $G^{(2)}(\mathbf{r}_1, t_1; \mathbf{r}_2, t_2)$ .

Now, we show a different but equivalent calculation of  $G^{(2)}(\mathbf{r}_1, t_1; \mathbf{r}_2, t_2)$  of thermal light by using the density matrix of Equation 8.127. Substituting Equation 8.127 into Equation 9.53, the second-order temporal correlation function  $G^{(2)}(\tau_1, \tau_2)$  is thus

$$\begin{aligned} & G^{(2)}(\tau_1, \tau_2) \\ & \propto \int d\omega d\omega' |f(\omega)|^2 |f(\omega')|^2 |\Psi_{\omega, \omega'}(\tau_1, \tau_2) + \Psi_{\omega', \omega}(\tau_1, \tau_2)|^2 \\ & = \left[ \int d\nu |f(\nu)|^2 \right]^2 + |\mathcal{F}_\tau \{ |f(\nu)|^2 \}|^2 \end{aligned} \quad (9.67)$$

where, again,  $\nu = \omega - \omega_0$ ; and  $\tau_j = t_j - z_j/c$ ,  $j = 1, 2$ ,  $\tau = \tau_1 - \tau_2$ . There should be no surprise to have the same result as Equation 9.64. Differing from the model of two independent wavepackets with finite size in space-time, we now have a slightly different physical picture of interference. Here, the interference takes place between the following amplitudes: (1) mode  $\omega$  and mode  $\omega'$  are annihilated at  $(\mathbf{r}_1, t_1)$  and  $(\mathbf{r}_2, t_2)$ , respectively, or (2) mode  $\omega'$  and mode  $\omega$  are annihilated at  $(\mathbf{r}_1, t_1)$  and  $(\mathbf{r}_2, t_2)$ , respectively. Of course, one

**FIGURE 9.8**

Experimental data for the measurement of second-order temporal coherence function of chaotic-thermal light. The horizontal axis  $t_1 - t_2$ , in the unit of  $10^{-8}$  s, labels the registration time differences of the photon pair measured by photodetectors  $D_1$  and  $D_2$  at  $z_1 = z_2$ .

may model a single-mode transition of  $\hbar\omega = E_2 - E_1$  with  $\Delta E_2 = \Delta E_1 = 0$  and define an infinite long “wavepacket” in space-time. Each randomly paired infinite long wavepackets  $\omega$  and  $\omega'$  interferes with the pair itself resulting in an independent interference “pattern.” The final result is a statistical sum of all independent interference patterns with different  $\hbar\omega$  and  $\hbar\omega'$ .

Figure 9.8 is a typical measured degree of second-order temporal coherence of chaotic-thermal light,  $g^{(2)}(t_1 - t_2)$ , which approves Equation 9.65. The experimental results clearly show that the photons have a twice greater chance of being jointly detected at  $t_1 = t_2$  by photodetectors  $D_1$  and  $D_2$  located at  $z_1 = z_2$ . This experimental effect was named “photon bunching” in the history. The observation of “photon bunching” is quite a surprise, which apparently contradicts the random nature of chaotic-thermal light. Remember that we have modeled chaotic-thermal radiation with equal probability of having two photons radiated at any  $t_{0m}$  and  $t_{0n}$ . Statistically, there seems no reason to have photons to be radiated in “bunching” at a chaotic-thermal source. In the view of two-photon interference, the interpretation is straightforward and reasonable: the “photon bunching” is nothing but a *two-photon interference* phenomenon. In the quantum theory of second-order coherence, the photons are all radiated independently and randomly from the source. It is the two-photon interference that produces a twice greater chance for the randomly radiated photons to be jointly detected at  $t_1 - t_2 = 0$ . It should be emphasized that two-photon interference is not the interference between two photons. The interference takes place between two different yet indistinguishable alternatives, namely, the

two-photon amplitudes or effective two-photon wavefunctions that contributed to a joint photodetection event. Although the quantum interference picture for the phenomenon is quite straightforward, one may feel uncomfortable, perhaps due to the “nonlocal” superposition, which involves the measurements of two independent photodetectors at different space time coordinates. This superposition has no counterpart in the Maxwell electromagnetic wave theory of light, especially in the case of thermal light. Thermal light is traditionally considered “classical” radiation.

### Category (III): Entangled two-photon state

We will have a detailed discussion on quantum entanglement in Chapter 10. Here, we simply introduce an entangled two-photon system to replace the thermal radiation in the measurement of Figure 9.7. In the following, a simplified EPR state will be applied for the calculation of the second-order coherence or correlation function  $G^{(2)}(\mathbf{r}_1, t_1; \mathbf{r}_2, t_2)$ .

Roughly speaking, an entangled two-photon state is a non-factorizable state of two photons: the state cannot be written as a product of that of two photons. In other words, the two photons cannot be considered as independent. The EPR state is a very special entangled two-particle state. The two subsystems are “perfectly correlated,” i.e., by measuring the state of one, the state of the other is determined with certainty although none of the subsystems is in a defined state before the measurement. The entangled photon pair was named biphoton by Klyshko. In Chapter 8, we have introduced a simple example of a non-factorizable biphoton state with total photon number  $n = 2$ :

$$\begin{aligned} |\Psi\rangle &= \int d\omega_s d\omega_i \delta(\omega_s + \omega_i - \omega_p) f(\omega_s, \omega_i) \hat{a}^\dagger(\omega_s) \hat{a}^\dagger(\omega_i) |0\rangle \\ &\simeq \int_{-\infty}^{\infty} dv f(v) a^\dagger(\omega_s^0 + v) a^\dagger(\omega_i^0 - v) |0\rangle \end{aligned} \quad (9.68)$$

with

$$\omega_s = \omega_s^0 + v, \quad \omega_i = \omega_i^0 - v, \quad \omega_s + \omega_i = \omega_p = \text{constant}$$

where  $\delta(\omega_p - \omega_s - \omega_i)$  has been applied,  $\omega_s^0$  and  $\omega_i^0$  are the center frequencies for the  $\omega_s$  and  $\omega_i$  modes, respectively. We have generalized the integral to infinity with the help of the spectral density function  $f(v)$ . The biphoton state of Equation 9.68 is a pure state by means: (1) the state of a signal-idler pair, which produced a joint photodetection event, is a state vector in the form of a coherent superposition of all possible Fock states  $|\dots, 0, 1_{\omega_s}, \dots, 1_{\omega_i}, 0, \dots\rangle$ ; (2) a large number of jointly measured signal-idler photon pairs are in the same state, which can be treated as a homogenous ensemble.

The second-order temporal coherence or correlation function is thus calculated as

$$\begin{aligned}
& G^{(2)}(z_1, t_1; z_2, t_2) \\
&= \langle \Psi | \hat{E}^{(-)}(z_1, t_1) \hat{E}^{(-)}(z_2, t_2) \hat{E}^{(+)}(z_2, t_2) \hat{E}^{(+)}(z_1, t_1) | \Psi \rangle \\
&= | \langle 0 | \hat{E}^{(+)}(z_2, t_2) \hat{E}^{(+)}(z_1, t_1) | \Psi \rangle |^2 \\
&= | \Psi(z_1, t_1; z_2, t_2) |^2
\end{aligned} \tag{9.69}$$

where, again, we have defined the two-photon effective wavefunction

$$\Psi(z_1, t_1; z_2, t_2) = \langle 0 | \hat{E}^{(+)}(z_2, t_2) \hat{E}^{(+)}(z_1, t_1) | \Psi \rangle. \tag{9.70}$$

The two-photon effective wavefunction is calculated as

$$\begin{aligned}
& \Psi(z_1, t_1; z_2, t_2) \\
&= \left\langle 0 \left| \left[ \int d\omega a(\omega) e^{-i(\omega t_2 - kz_2)} \right] \left[ \int d\omega' a(\omega') e^{-i(\omega' t_1 - k' z_1)} \right] \right. \right. \\
&\quad \times \left. \left. \left[ \int_{-\infty}^{\infty} dv f(v) a^\dagger(\omega_s^0 + v) a^\dagger(\omega_i^0 - v) \right] \middle| 0 \right\rangle \right] \\
&\cong \int d\omega \int d\omega' \int_{-\infty}^{\infty} dv f(v) e^{-i\omega' \tau_2} e^{-i\omega \tau_1} \\
&\quad \times \left\langle 0 \left| a(\omega) a(\omega') a^\dagger(\omega_s^0 + v) a^\dagger(\omega_i^0 - v) \right| 0 \right\rangle.
\end{aligned} \tag{9.71}$$

- (1): Nondegenerate,  $\omega_s^0 \neq \omega_i^0$ , and the photodetector  $D_1$  that is located at  $z_1$  only receives the  $\omega_s$  modes and the photodetector  $D_2$  that is located at  $z_2$  only receives the  $\omega_i$  modes. The nondegenerate modes can be distinguished experimentally either by spectral filters or by polarization analyzers if the two modes are orthogonally polarized. In this case, only one term in Equation 9.71 survives:

$$\begin{aligned}
\Psi(z_1, t_1; z_2, t_2) &\cong \int_{-\infty}^{\infty} dv f(v) e^{-i(\omega_i^0 - v)\tau_2} e^{-i(\omega_s^0 + v)\tau_1} \\
&= e^{-i(\omega_s^0 \tau_1 + \omega_i^0 \tau_2)} \mathcal{F}_{\tau_2 - \tau_1} \{f(v)\}.
\end{aligned} \tag{9.72}$$

It is clear that the two-photon effective wavefunction of this biphoton state cannot be written as a product of two effective wavefunctions of a single-photon state. The entangled two photons are characterized by a nonlocal wavepacket instead of two wavepackets. We will discuss this in detail in Chapter 10.

- (2): Degenerate,  $\omega_s^0 = \omega_i^0$ , the photodetector  $D_1$  that is located at  $z_1$  and the photodetector  $D_2$  that is located at  $z_2$  cannot distinguish the  $\omega_s$  and the  $\omega_i$  modes. In this case, the surviving terms are these when  $\omega = \omega_s^0 + v$  with  $\omega' = \omega_i^0 - v$ , and  $\omega = \omega_i^0 - v$  with  $\omega' = \omega_s^0 + v$ ; thus

$$\begin{aligned}
& \Psi(z_1, t_1; z_2, t_2) \\
& \cong \int_{-\infty}^{\infty} d\nu f(\nu) \left[ e^{-i(\omega_s^0 + \nu)\tau_2} e^{-i(\omega_i^0 - \nu)\tau_1} + e^{-i(\omega_i^0 - \nu)\tau_2} e^{-i(\omega_s^0 + \nu)\tau_1} \right] \\
& = e^{-i\omega_p(\tau_2 + \tau_1)} \left[ \int_{-\infty}^{\infty} d\nu f(\nu) e^{-i\nu(\tau_2 - \tau_1)} + \int_{-\infty}^{\infty} d\nu f(\nu) e^{-i\nu(\tau_1 - \tau_2)} \right] \\
& = \Psi_1(z_1, t_1; z_2, t_2) + \Psi_2(z_1, t_1; z_2, t_2), \tag{9.73}
\end{aligned}$$

where  $\Psi_1(z_1, t_1; z_2, t_2) = \Psi_2^*(z_1, t_1; z_2, t_2)$ . In the degenerate case, the two-photon effective wavefunction is the result of a superposition of two wavepackets  $\Psi_1(z_1, t_1; z_2, t_2)$  and  $\Psi_2(z_1, t_1; z_2, t_2)$  corresponding to two different yet indistinguishable alternative ways for the entangled two photons to produce a joint-detection event. Again,  $\Psi(z_1, t_1; z_2, t_2)$  cannot be written as the product of  $\Psi(z_1, t_1)$  and  $\Psi(z_2, t_2)$ . The entangled two photons are characterized by a non-factorizable 2-D function, which is a nonlocal wavepacket in space-time.

In either case, the second-order coherence or correlation function is written as the normal square of the non-factorizable effective two-photon wavefunction:

$$G^{(2)}(z_1, t_1; z_2, t_2) = |\Psi(z_1, t_1; z_2, t_2)|^2. \tag{9.74}$$

Equation 9.74 is very different from Equation 9.64 of the chaotic-thermal radiation. For entangled states, it is impossible to write  $G^{(2)}(z_1, t_1; z_2, t_2)$  in terms of the product of  $G^{(1)}$ s.

It is interesting to see that  $G^{(2)}(z_1, t_1; z_2, t_2)$  will be a delta-like function of  $\tau_2 - \tau_1$  if  $\Delta\nu \sim \infty$ . This means that if  $D_1$  registers a photon at  $t_1$ , then there is a unique precise time  $t_2$  for  $D_2$  to register its twin, even though none of the photons are localized in time and the two photodetectors are separated by a very large distance. This kind of correlation is known as EPR correlation.

It is also interesting to see that an anti-correlation is observable if the biphoton superposition achieves its destructive interference condition:

$$\begin{aligned}
& \Psi(z_1, t_1; z_2, t_2) \\
& \cong \int_{-\infty}^{\infty} d\nu f(\nu) \left[ e^{-i(\omega_s^0 + \nu)\tau_2} e^{-i(\omega_i^0 - \nu)\tau_1} - e^{-i(\omega_i^0 - \nu)\tau_2} e^{-i(\omega_s^0 + \nu)\tau_1} \right] \\
& = \Psi_1(z_1, t_1; z_2, t_2) - \Psi_2(z_1, t_1; z_2, t_2). \tag{9.75}
\end{aligned}$$

The degree of second-order coherence achieves its minimum value when  $\Psi_1(z_1, t_1; z_2, t_2)$  and  $\Psi_2(z_1, t_1; z_2, t_2)$  overlap completely in space-time. The joint-detection counting rate will be zero when  $\tau_1 = \tau_2$ . This means that if  $D_1$  registers a photon at  $t_1$ , then  $D_2$  is forbidden to register its twin at  $t_1 = t_2$ , if  $z_1 = z_2$  is chosen.

A schematic picture of a biphoton wavepacket described by Equation 9.72, is illustrated in Figure 9.9. It shows clearly that  $\Psi(z_1, t_1; z_2, t_2)$  of the entangled two-photon system is represented by a non-factorizable 2-D wavepacket instead of a product of two wavepackets. The non-factorizable wavepacket, again, from a different point of view, illustrates the entangled nature of the two-photon state. One should not be surprised by the fact that the system does not have two individual wavepackets associated with the signal photon and the idler photon. The biphoton state is formed from a coherent superposition of Fock states of  $n=2$  instead of a product of two individual single-photon wavepackets. The coherent superposition of these Fock states results in the non-factorizable effective wavefunction or the biphoton wavepacket. This is very different from the “classical” case. It may be easier to see the connection between the picture of a single-photon wavepacket and the concept of a photon. It is definitely uneasy to accept the fact that the connection between the biphoton wavepacket and the concept of biphoton is the same as that of the single-photon. The biphoton wavepacket describes the dynamic property of the entangled photon pair as one system in space-time. We will return to the discussion of these important concepts later.

Phenomenologically, unlike the single-photon wavepacket, (1) the biphoton wavepacket is dynamically propagating along the axis  $z_1$  and  $z_2$  in different directions; however, (2) the propagation is never independent. The joint photoelectron events happen in such a way that whenever a photoelectron event occurs at space-time  $(\mathbf{r}_1, t_1)$ , the other one can happen only in the neighborhood of space-time point  $(\mathbf{r}_2, t_2)$ , which is related to  $(\mathbf{r}_1, t_1)$  by  $(t_1 - t_2) - (z_1 - z_2)/c = 0$ . The statement of point (1) is formulated by

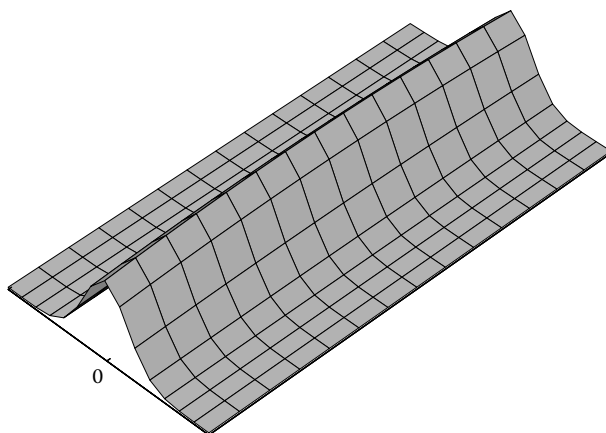


**FIGURE 9.9**

A schematic envelope of a biphoton wavepacket with a Gaussian shape along  $\tau_1 - \tau_2$ . The wavepacket is uniformly distributed along  $\tau_1 + \tau_2$  due to the assumption of  $\omega_p = \text{constant}$ .

$e^{-i(\omega_0 t_2 - k_0 z_2)} e^{-i(\omega_0 t_1 - k_0 z_1)}$  or  $e^{-i\omega_0(\tau_1 + \tau_2)}$  along the  $\tau_1 + \tau_2$  axis. The statement of point (2) is formulated by  $\mathcal{F}_{\tau_1 - \tau_2}\{f(v)\}$  along the  $\tau_1 - \tau_2$  axis. This phenomenon is interesting. On one hand, the signal photon and the idler photon are both in mixed single-photon state with randomly distributed probability of producing a photoelectron event along both  $z_1$  and  $z_2$  axes in space and along  $t_1$  and  $t_2$  in time. It means that neither the signal photon nor the idler photon is localized in space-time. On the other hand, the space-time correlation between the joint photoelectron events,  $(t_1 - t_2) - (z_1 - z_2)/c = 0$ , determines the location and time of finding the idler (signal) photon after the annihilation of the signal (idler) photon. How could the detection of the signal (idler) photon localize the idler (signal) photon? The problem gets more interesting when the two photo-detection events become space-like separated events: the two detectors could be separated in light-years but the determination, however, is made instantaneously. It seems that we may have to give up the concept of two photons when thinking about an EPR two-photon state. The signal-idler system might be better treated as a whole, as described by the non-factorizable biphoton wavepacket. If one insists that the signal photon and the idler photon are two individual systems, the EPR paradox may be unavoidable. This point will be emphasized again in Chapter 10.

Category (IV): Number state of  $n_\omega = 2$

In Chapter 8 we have given an example of number state of  $n_\omega = 2$

$$\begin{aligned} |\Psi\rangle &= \sum_{\omega} f(\omega) [\hat{a}^\dagger(\omega)]^2 |0\rangle \\ &\simeq \int_{-\infty}^{\infty} dv f(v) [a^\dagger(\omega_0 + v)]^2 |0\rangle \end{aligned} \quad (9.76)$$

The two-photon effective wavefunction is calculated as

$$\begin{aligned} \Psi(z_1, t_1; z_2, t_2) &= \langle 0 | \left[ \int d\omega a(\omega) e^{-i(\omega t_2 - k z_2)} \right] \left[ \int d\omega' a(\omega') e^{-i(\omega' t_1 - k' z_1)} \right] \\ &\times \left[ \int_{-\infty}^{\infty} dv f(v) a^\dagger(\omega_0 + v) a^\dagger(\omega_0 + v) |0\rangle \right] \\ &\cong \int d\omega \int d\omega' \int_{-\infty}^{\infty} dv f(v) e^{-i\omega'\tau_2} e^{-i\omega\tau_1} \\ &\times \langle 0 | a(\omega) a(\omega') a^\dagger(\omega_0 + v) a^\dagger(\omega_0 + v) |0\rangle. \end{aligned} \quad (9.77)$$

The photodetector  $D_1$  that is located at  $z_1$  and the photodetector  $D_2$  that is located at  $z_2$  cannot distinguish the two modes of  $\omega = \omega_0 + \nu$ . In this case, the surviving terms are these when  $\omega = \omega' = \omega_0 + \nu$ ; thus

$$\begin{aligned}\Psi(z_1, t_1; z_2, t_2) &\cong \int_{-\infty}^{\infty} d\nu f(\nu) \left[ e^{-i(\omega_0+\nu)(\tau_2+\tau_1)} \right] \\ &= e^{-i\omega_0(\tau_2+\tau_1)} \mathcal{F}_{\tau_2+\tau_1} \{f(\nu)\}. \quad (9.78)\end{aligned}$$

Again,  $\Psi(z_1, t_1; z_2, t_2)$  cannot be written as the product of  $\Psi(z_1, t_1)$  and  $\Psi(z_2, t_2)$ . The number state of  $n_\omega = 2$  is also characterized by a non-factorizable 2-D function. However, this 2-D function is very different from either Equation 9.72 or Equation 9.73. It is interesting to see that  $G^{(2)}(z_1, t_1; z_2, t_2)$  will be a delta-like function of  $\tau_2 + \tau_1$  if  $\Delta\nu \sim \infty$ . In this case,  $(t_1 + t_2) \simeq (z_1 + z_2)/c$ . The physics behind is very different from that of the entangled states too.

#### Category (V): Coherent state

Similar to the first-order coherence, in the following calculation we consider a multimode coherent state, which is written as a product of single-mode coherent state  $|\alpha_k\rangle$

$$|\{\alpha\}\rangle = \prod_k |\alpha_k\rangle,$$

which is an eigenstate of the annihilation operator with an eigenvalue  $\alpha_k$ ,

$$\hat{a}_k |\{\alpha\}\rangle = \alpha_k |\{\alpha\}\rangle.$$

It is easy to show

$$\begin{aligned}G^{(2)}(\mathbf{r}_1, t_1; \mathbf{r}_2, t_2) \\ &= \langle \{\alpha\} | \hat{E}^{(-)}(\mathbf{r}_1, t_1) \hat{E}^{(-)}(\mathbf{r}_2, t_2) \hat{E}^{(+)}(\mathbf{r}_2, t_2) \hat{E}^{(+)}(\mathbf{r}_1, t_1) | \{\alpha\} \rangle \\ &= G^{(1)}(\mathbf{r}_1, t_1; \mathbf{r}_1, t_1) G^{(1)}(\mathbf{r}_2, t_2; \mathbf{r}_2, t_2), \quad (9.79)\end{aligned}$$

which is a product of  $G^{(1)}(\mathbf{r}_1, t_1; \mathbf{r}_1, t_1)$  and  $G^{(1)}(\mathbf{r}_2, t_2; \mathbf{r}_2, t_2)$ . Consequently, the quantum degree of second-order coherence for coherent state is

$$g^{(2)}(\mathbf{r}_1, t_1; \mathbf{r}_2, t_2) = 1. \quad (9.80)$$

## 9.6 Two-Photon Interference vs. Statistical Correlation of Intensity Fluctuations

Based on the same experimental setup, we have obtained three types of second-order coherence function for different radiation sources:

Type I: Coherent state

$$G^{(2)}(\mathbf{r}_1, t_1; \mathbf{r}_2, t_2) = G_{11}^{(1)} G_{22}^{(1)}, \quad (9.81)$$

which is a factorizable function of  $G_{11}^{(1)} = \langle I_1 \rangle$  and  $G_{22}^{(1)} = \langle I_2 \rangle$ .  $G_{11}^{(1)}$  and  $G_{22}^{(1)}$  are measurable by photodetectors  $D_1$  and  $D_2$ , respectively.

Type II: Chaotic-thermal state

$$G^{(2)}(\mathbf{r}_1, t_1; \mathbf{r}_2, t_2) = G_{11}^{(1)} G_{22}^{(1)} + \left| G_{12}^{(1)} \right|^2, \quad (9.82)$$

which is non-factorizable, but can be written as a function of the  $G^{(1)}$ s; however,  $\left| G_{12}^{(1)} \right|^2$  is measurable only in the joint detection of two individual photodetectors.

Type III: Entangled two-photon state (including number state of  $n_\omega = 2$ )

$$G^{(2)}(\mathbf{r}_1, t_1; \mathbf{r}_2, t_2) = |\Psi(\mathbf{r}_1, t_1; \mathbf{r}_2, t_2)|^2, \quad (9.83)$$

which is non-factorizable, yet can never be written as a function of the  $G^{(1)}$ s. The measurement of  $\Psi(\mathbf{r}_1, t_1; \mathbf{r}_2, t_2)$  always involves the joint detection of two individual photodetectors.

In quantum mechanics, a factorizable  $G^{(2)}(\mathbf{r}_1, t_1; \mathbf{r}_2, t_2)$  means the probability of observing a photon at  $(\mathbf{r}_1, t_1)$  has no relationship with the observation of another photon at  $(\mathbf{r}_2, t_2)$ , although the two photons are detected in coincidence. From a classical point of view, a factorizable  $G^{(2)}(\mathbf{r}_1, t_1; \mathbf{r}_2, t_2)$  means that the two measured intensities are independent of each other. A non-factorizable  $G^{(2)}(\mathbf{r}_1, t_1; \mathbf{r}_2, t_2)$  indicates opposite physics quantum mechanically and classically. For instance, in the measurement of an entangled two-photon system, the probability of observing one photon at  $(\mathbf{r}_1, t_1)$  is completely determined by the observation of its twin at  $(\mathbf{r}_2, t_2)$ . In the measurement of chaotic-thermal light, the probability of observing one photon at  $(\mathbf{r}_1, t_1)$  is partially determined by the observation of another photon at  $(\mathbf{r}_2, t_2)$  that contributes to the joint-detection event. After releasing from a radiation source, a photon propagates independently either behaving as a particle and/or as a wave. What is the physical cause for the detection of one photon to determine the probability of observing another photon at a

distance? Especially in a chaotic-thermal source in which all the atomic transitions, as well as the created photons, are stochastic with a full degree of randomness.

In the view of quantum mechanics, this nonlocal effect is the result of two-photon interference, involving the superposition of two-photon amplitudes, representing different yet indistinguishable alternative ways of producing a joint-detection event at  $(\mathbf{r}_1, t_1)$  and  $(\mathbf{r}_2, t_2)$ . Different from quantum mechanics, the traditional classical theory has treated this effect as the statistical correlation of intensity fluctuations. Examining the classical statistical correlation between the two measured intensities  $I(\mathbf{r}_1, t_1)$  and  $I(\mathbf{r}_2, t_2)$ ,

$$\langle I(\mathbf{r}_1, t_1) I(\mathbf{r}_2, t_2) \rangle = \langle I_1 \rangle \langle I_2 \rangle + \langle \Delta I_1 \Delta I_2 \rangle, \quad (9.84)$$

we may conclude (1) in the case of coherent radiation, the two measured intensities have no statistical correlation in space-time, i.e.,  $\langle I_1 \rangle \langle I_2 \rangle \neq 0$   $\langle \Delta I_1 \Delta I_2 \rangle = 0$ ; (2) in the case of chaotic-thermal light, the two measured intensities are partially correlated in space-time, i.e.,  $\langle I_1 \rangle \langle I_2 \rangle \neq 0$  and  $\langle \Delta I_1 \Delta I_2 \rangle \neq 0$ ; (3) in the case of entangled two-photon state, the two measured intensity are fully correlated, i.e.,  $\langle I_1 \rangle \langle I_2 \rangle = 0$  and  $\langle \Delta I_1 \Delta I_2 \rangle \neq 0$ .

In the last a few decades, extensive study on quantum entanglement has brought new challenges to the classical statistical correlation interpretation. Based on the concept of classical statistical correlation of intensity fluctuation, the mean intensities  $\langle I_1 \rangle$  and  $\langle I_2 \rangle$  must be zero, otherwise Equation 9.83 leads to nonphysical conclusions. The measurements, however, never yield zero mean values of  $\langle I_1 \rangle$  and  $\langle I_2 \rangle$  in any circumstances. Thus, the concept of classical statistical correlation of intensity fluctuation may not be applicable to entangled two-photon states. Two-photon correlation experiments with entangled photons have been treated quantum mechanically and explained in terms of the superposition of indistinguishable alternatives or two-photon probability amplitudes that lead to a joint-detection event.

Does the statistical theory of intensity fluctuation correlation work for classical thermal light? We will address this question in detail later. In the following, we provide a simple discussion to show that the classical statistical theory gives certain different expectations than that of the quantum theory. To simplify the discussion, we will concentrate to the temporal part of the second-order coherence and write  $g^{(2)}(z_1, t_1; z_2, t_2)$  into the following form by taking advantage of the stationary nature of the chaotic-thermal light:

$$g^{(2)}(\tau) = \frac{\langle I(t) I(t + \tau) \rangle}{\langle I(t) \rangle^2}, \quad (9.85)$$

where we have assumed  $z_1 = z_2$  as usual. Now, we follow the classical theory of statistics to derive an inequality for  $\tau = 0$ . Since

$$\langle [\Delta I(t)]^2 \rangle \geq 0, \quad (9.86)$$

we have

$$\langle [I(t) - \langle I(t) \rangle]^2 \rangle = \langle I(t)I(t) \rangle - \langle I(t) \rangle^2 \geq 0. \quad (9.87)$$

Therefore,

$$g^{(2)}(0) = \frac{\langle I(t)I(t) \rangle}{\langle I(t) \rangle^2} \geq 1. \quad (9.88)$$

In the view of quantum mechanics, however, Equation 9.88 is not necessarily true. For instance, if the two-photon superposition achieves a destructive interference condition,

$$\begin{aligned} G^{(2)}(z_1, t_1; z_2, t_2) \\ \propto \int dt_{0m} dt_{0n} |\Psi_{mn}(z_1, t_1; z_2, t_2) - \Psi_{nm}(z_1, t_1; z_2, t_2)|^2, \end{aligned} \quad (9.89)$$

it is easy to find

$$g^{(2)}(\tau) = 1 - \frac{|\mathcal{F}_\tau \{ |f(v)|^2 \}|^2}{\left[ \int dv |f(v)|^2 \right]^2}. \quad (9.90)$$

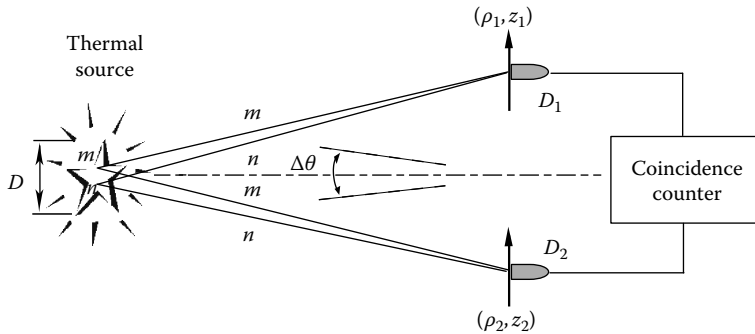
Obviously, Equation 9.90 leads to

$$g^{(2)}(0) < 1. \quad (9.91)$$

Equation 9.91 has been observed experimentally in the measurement of chaotic-thermal light and in the measurement of entangled photon pairs.

## 9.7 Second-Order Spatial Correlation of Thermal Light

In Chapter 6, we have analyzed second-order spatial correlation of thermal light in classical formula. When the intensity of thermal light is weak enough to achieve the single-photon level, do we still expect the same nontrivial spatial correlation in far-field ( $\Delta\theta < \lambda/D$ ) and in near-field ( $\Delta\theta > \lambda/D$ )? In this section, we give a quantum mechanical treatment based on a simplified second-order spatial correlation measurement that is schematically shown in Figure 9.10. In this setup, two point-like photon counting detectors  $D_1$  and  $D_2$  are placed at spatial coordinates  $(\vec{r}_1, z_1)$  and  $(\vec{r}_2, z_2)$ , respectively. What is the probability for the two point-like detectors to jointly observe a photoelectron event at  $(\vec{r}_1, z_1, t_1)$  and another photoelectron event at  $(\vec{r}_2, z_2, t_2)$ ? As we

**FIGURE 9.10**

Schematic setup of a simplified second-order spatial correlation measurement. Two point-like photon-counting detectors  $D_1$  and  $D_2$  are scannable on their chosen transverse planes  $z_1 = \text{constant}$  and  $z_2 = \text{constant}$ , respectively. A coincidence counter-records the joint-detection events between the annihilation of two independent randomly radiated photons from a thermal source of diameter  $D$  (or angular size of  $\Delta\theta$ ), which can be in the far-field ( $\Delta\theta < \lambda/D$ ) or in the Fresnel near-field ( $\Delta\theta > \lambda/D$ ). What is the probability for the two point-like detectors to jointly observe a photoelectron event at  $(\vec{\rho}_1, z_1, t_1)$  and another photoelectron event at  $(\vec{\rho}_2, z_2, t_2)$ ?

have emphasized earlier, in the view of quantum theory, an idealized point photodetector measures the probability of observing a photodetection event at space-time point  $(\mathbf{r}, t)$

$$G^{(1)}(\vec{\rho}, z, t) = \text{tr} \left\{ \hat{\rho} \hat{E}^{(-)}(\vec{\rho}, z, t) \hat{E}^{(+)}(\vec{\rho}, z, t) \right\}, \quad (9.92)$$

where

$\hat{\rho}$  is the density operator that characterizes the state of the quantized chaotic-thermal field

$E^{(-)}(\vec{\rho}, z, t)$  and  $E^{(+)}(\vec{\rho}, z, t)$  the negative and positive field operators at space-time coordinate  $(\vec{\rho}, z, t)$

The counting rate of a point photon-counting detector, or the output current of a point analog photodetector, is proportional to  $G^{(1)}(\vec{\rho}, z, t)$ . A joint detection of two independent point photodetectors measures the probability of observing a joint-detection event of two photons at space-time points  $(\vec{\rho}_1, z_1, t_1)$  and  $(\vec{\rho}_2, z_2, t_2)$

$$G^{(2)}(\vec{\rho}_1, z_1, t_1; \vec{\rho}_2, z_2, t_2)$$

$$= \text{tr} \left\{ \hat{\rho} \hat{E}^{(-)}(\vec{\rho}_1, z_1, t_1) \hat{E}^{(-)}(\vec{\rho}_2, z_2, t_2) \hat{E}^{(+)}(\vec{\rho}_2, z_2, t_2) \hat{E}^{(+)}(\vec{\rho}_1, z_1, t_1) \right\}, \quad (9.93)$$

where  $(\vec{\rho}_j, z_j, t_j)$ ,  $j=1, 2$ , is the space-time coordinate of a photodetection event at the  $j$ th photodetector. The coincidence-counting rate of two photon-counting detectors is proportional to  $G^{(2)}(\vec{\rho}_1, z_1, t_1; \vec{\rho}_2, z_2, t_2)$ . To calculate the second-order spatial correlation, we need (1) to estimate the state, or the density matrix, of the thermal radiation; and (2) to propagate the field operators from the radiation source to the detection planes.

Assume a large transverse-sized chaotic-thermal source consisting of a large number of independent and randomly radiating point sub-sources, such as the  $m$ th and  $n$ th sub-sources illustrated in Figure 9.10. Each point sub-source may also consist of a large number of independent atoms that are ready for two-level atomic transitions in a random manner. To simplify the calculation, we will focus on the transverse spatial correlation only by assuming single-frequency transitions with monochromatic light as usual, i.e.,  $\hbar\omega = E_2 - E_1$  with  $\Delta E_2 = 0$  and  $\Delta E_1 = 0$ . Repeating the mathematical procedure in our early discussion on the second-order temporal coherence, the density operator for evaluating the second-order spatial coherence can be approximated as

$$\begin{aligned} \hat{\rho} \simeq & |0\rangle\langle 0| + |\epsilon|^2 \int d\vec{\kappa} \hat{a}^\dagger(\vec{\kappa}) |0\rangle\langle 0| \hat{a}(\vec{\kappa}) \\ & + |\epsilon|^4 \int d\vec{\kappa} d\vec{\kappa}' \hat{a}^\dagger(\vec{\kappa}) \hat{a}^\dagger(\vec{\kappa}') |0\rangle\langle 0| \hat{a}(\vec{\kappa}') \hat{a}(\vec{\kappa}), \end{aligned} \quad (9.94)$$

where  $\vec{\kappa}$  is the transverse wavevector, and each  $\vec{\kappa}$  is associated with a point sub-source or an atomic transition located at a certain transverse coordinate on the source plane (see Figure 9.10). Comparing with the density matrix for temporal coherence calculation, it is easy to see that  $\vec{\kappa}$  plays the same role as  $\omega$ . In Equation 9.94, all constants have been absorbed into  $|\epsilon|^2$  and  $|\epsilon|^4$ . Deriving Equation 9.94, we have assumed a random distribution of the sub-sources on the transverse source plane and considered the stochastic nature of the sub-radiations. Basically we are modeling the light source as an incoherent mixed state of single-photon states and two-photon states with equal probability of having any transverse momentum. The spatial part of the second-order coherence function is thus calculated as

$$\begin{aligned} G^{(2)}(\vec{\rho}_1, z_1; \vec{\rho}_2, z_2) &= \text{tr}[\hat{\rho} \hat{E}^{(-)}(\vec{\rho}_1, z_1) \hat{E}^{(-)}(\vec{\rho}_2, z_2) \hat{E}^{(+)}(\vec{\rho}_2, z_2) \hat{E}^{(+)}(\vec{\rho}_1, z_1)] \\ &= \int d\vec{\kappa} d\vec{\kappa}' \langle 1_{\vec{\kappa}} 1_{\vec{\kappa}'} | \hat{E}^{(-)}(\vec{\rho}_1, z_1) \hat{E}^{(-)}(\vec{\rho}_2, z_2) \hat{E}^{(+)}(\vec{\rho}_2, z_2) \hat{E}^{(+)}(\vec{\rho}_1, z_1) | 1_{\vec{\kappa}} 1_{\vec{\kappa}'} \rangle \\ &\equiv \int d\vec{\kappa} d\vec{\kappa}' |\Psi_{\vec{\kappa}, \vec{\kappa}'}(\vec{\rho}_1, z_1; \vec{\rho}_2, z_2)|^2, \end{aligned} \quad (9.95)$$

where we have defined an effective two-photon wavefunction in transverse spatial coordinates

$$\Psi_{\vec{\kappa}, \vec{\kappa}'}(\vec{\rho}_1, z_1; \vec{\rho}_2, z_2) = \langle 0 | \hat{E}^{(+)}(\vec{\rho}_2, z_2) \hat{E}^{(+)}(\vec{\rho}_1, z_1) | 1_{\vec{\kappa}} 1_{\vec{\kappa}'} \rangle. \quad (9.96)$$

The transverse part of the field operator can be written as

$$\hat{E}^{(+)}(\vec{\rho}_j, z_j) \propto \sum_{\vec{\kappa}} g_j(\vec{\rho}_j, z_j; \vec{\kappa}) \hat{a}(\vec{\kappa}), \quad (9.97)$$

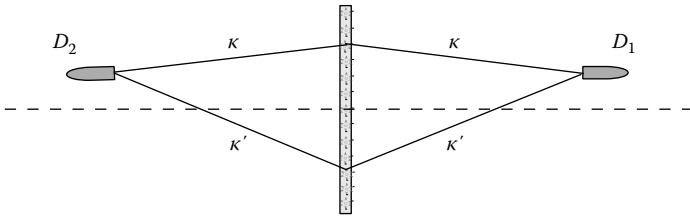
again,  $g_j(\vec{\rho}_j, z_j; \vec{\kappa})$  is Green's function. Substituting the field operators into Equation 9.96 we have

$$\begin{aligned} \Psi_{\vec{\kappa}, \vec{\kappa}'}(\vec{\rho}_1, z_1; \vec{\rho}_2, z_2) \\ = g_2(\vec{\rho}_2, z_2; \vec{\kappa}) g_1(\vec{\rho}_1, z_1; \vec{\kappa}') + g_2(\vec{\rho}_2, z_2; \vec{\kappa}') g_1(\vec{\rho}_1, z_1; \vec{\kappa}) \end{aligned} \quad (9.98)$$

and

$$\begin{aligned} G^{(2)}(\vec{\rho}_1, z_1; \vec{\rho}_2, z_2) \\ = \int d\vec{\kappa} d\vec{\kappa}' |g_2(\vec{\rho}_2, z_2; \vec{\kappa}) g_1(\vec{\rho}_1, z_1; \vec{\kappa}') + g_2(\vec{\rho}_2, z_2; \vec{\kappa}') g_1(\vec{\rho}_1, z_1; \vec{\kappa})|^2. \end{aligned} \quad (9.99)$$

Equations 9.98 and 9.99 indicate an interference between two quantum amplitudes, corresponding to two different yet indistinguishable alternatives that lead to a joint photodetection event. This interference phenomenon is not, as in classical optics, due to the superposition of electromagnetic fields at a local point of space-time. This interference is the result of the superposition between  $g_2(\vec{\rho}_2, z_2; \vec{\kappa}) g_1(\vec{\rho}_1, z_1; \vec{\kappa}')$  and  $g_2(\vec{\rho}_2, z_2; \vec{\kappa}') g_1(\vec{\rho}_1, z_1; \vec{\kappa})$ , the so-called two-photon amplitudes involving both arms of the optical setup as well as two distant photodetection events at  $(\vec{\rho}_1, z_1)$  and  $(\vec{\rho}_2, z_2)$ . Examining the effective wavefunction of Equation 9.98, we find this symmetrized effective wavefunction plays the same role as that of the symmetrized wavefunction of identical particles. This peculiar nonlocal superposition makes the spatial correlation "turbulence-free," i.e., any index fluctuation type disturbance in the optical path has no influence on the correlation. Figure 9.11 schematically illustrates the two alternatives for a pair of mode  $\vec{\kappa}$  and  $\vec{\kappa}'$  to produce a joint photodetection event:  $(\vec{\kappa} \text{ to } D_1) \times (\vec{\kappa}' \text{ to } D_2)$  and  $(\vec{\kappa} \text{ to } D_2) \times (\vec{\kappa}' \text{ to } D_1)$ . The superposition of each pair of these amplitudes interferes individually in the joint-detection space of  $(\vec{\rho}_1, z_1, t_1; \vec{\rho}_2, z_2, t_2)$ . A large number of these interferences simply add together resulting in a non-trivial  $G^{(2)}(\vec{\rho}_1, z_1; \vec{\rho}_2, z_2)$  function. It is easy to see that each pair of the two-photon amplitudes, illustrated in Figure 9.11, either in the conditions of far-field or near-field, will superpose constructively whenever  $D_1$  and  $D_2$

**FIGURE 9.11**

Schematic illustration of two-photon interference: a superposition between two-photon amplitudes  $g_2(\vec{\rho}_2, z_2; \vec{\kappa})g_1(\vec{\rho}_1, z_1; \vec{\kappa}')$  and  $g_2(\vec{\rho}_2, z_2; \vec{\kappa}')g_1(\vec{\rho}_1, z_1; \vec{\kappa})$ . It is clear that the amplitudes  $g_2(\vec{\rho}_2, z_2; \vec{\kappa})g_1(\vec{\rho}_1, z_1; \vec{\kappa}')$  and  $g_2(\vec{\rho}_2, z_2; \vec{\kappa}')g_1(\vec{\rho}_1, z_1; \vec{\kappa})$  will experience equal optical path propagation and superpose constructively when  $D_1$  and  $D_2$  are located at  $\vec{\rho}_1 \simeq \vec{\rho}_2$  and  $z_1 \simeq z_2$ . This nonlocal superposition has no classical correspondence.

are placed in the positions satisfying  $\vec{\rho}_1 \simeq \vec{\rho}_2$  and  $z_1 \simeq z_2$ , and, consequently,  $G^{(2)}(\vec{\rho}_1, z_1; \vec{\rho}_2, z_2)$  achieves its maximum value as the result of the sum of these individual constructive interferences. In other coordinates, however, the superposition of each individual pair of the two-photon amplitudes may yield different values between constructive maximum and destructive minimum due to unequal optical path propagation, resulting in an averaged sum.

#### Case (I): Fraunhofer far-field ( $\Delta\theta < \lambda/D$ )

The far-field Green's function is simply a function of plane wave. The calculations of the far-field  $G^{(1)}$  and  $G^{(2)}$  of chaotic-thermal light are similar to that of the classical  $\Gamma^{(1)}$  and  $\Gamma^{(2)}$ . We will not repeat this simple calculation again.

#### Case (II): Fresnel near-field ( $\Delta\theta > \lambda/D$ )

The calculations of the near-field  $G^{(1)}$  and  $G^{(2)}$  are also similar to that of the classical  $\Gamma^{(1)}$  and  $\Gamma^{(2)}$ . We will give a brief discussion in the following. Before calculating  $G^{(2)}(\vec{\rho}_1, z_1; \vec{\rho}_2, z_2)$ , we examine the single counting rate of the point photodetectors  $D_1$  and  $D_2$ , which are placed at  $(\vec{\rho}_1, z_1)$  and  $(\vec{\rho}_2, z_2)$ , respectively. With reference to the experimental setup of Figure 9.10,

$$g_1(\vec{\rho}_1, z_1; \vec{\kappa}) = \int d\vec{\rho}_0 \left\{ \frac{-i\omega}{2\pi c} \frac{e^{i\frac{\omega}{c}z_1}}{z_1} e^{i\frac{\omega}{2cz_1}|\vec{\rho}_1 - \vec{\rho}_0|^2} \right\} e^{-i\vec{\kappa} \cdot \vec{\rho}_0},$$

$$g_2(\vec{\rho}_2, z_2; \vec{\kappa}) = \int d\vec{\rho}'_0 \left\{ \frac{-i\omega}{2\pi c} \frac{e^{i\frac{\omega}{c}z_2}}{z_2} e^{i\frac{\omega}{2cz_2}|\vec{\rho}_2 - \vec{\rho}'_0|^2} \right\} e^{-i\vec{\kappa} \cdot \vec{\rho}'_0},$$

where  $\vec{\rho}_0$  is the transverse vector in the source plane, and the field has propagated from the source to the  $\vec{\rho}_1$  plane and  $\vec{\rho}_2$  plane in arms 1 and 2,

respectively. The single-detector-counting rate or the output photocurrent is proportional to  $G^{(1)}(\vec{r}, t)$ ,

$$G^{(1)}(\vec{\rho}_j, z_j) = \text{tr} \left\{ \hat{\rho} \hat{E}^{(-)}(\vec{\rho}_j, z_j) \hat{E}^{(+)}(\vec{\rho}_j, z_j) \right\} \sim \text{constant}, \quad (9.100)$$

where  $j = 1, 2$  indicating the  $j$ th photodetector.

Although  $G^{(1)}(\vec{\rho}_1, z_1)$  and  $G^{(1)}(\vec{\rho}_2, z_2)$  are both constants, the second-order spatial coherence function  $G^{(2)}(\vec{\rho}_1, z_1; \vec{\rho}_2, z_2)$  turns to be a nontrivial function of  $(\vec{\rho}_1, z_1)$  and  $(\vec{\rho}_2, z_2)$  due to the interference cross term of Equation 9.99

$$\begin{aligned} & \left| G^{(1)}(\vec{\rho}_1, z_1; \vec{\rho}_2, z_2) \right|^2 \\ &= \left| \int d\vec{k} g_1^*(\vec{\rho}_1, z_1; \vec{k}) g_2(\vec{\rho}_2, z_2; \vec{k}) \right|^2 \\ &\propto \left| \int d\vec{\rho}_0 e^{-i\frac{\omega}{c}z_1} e^{-i\frac{\omega}{2cz_1}|\vec{\rho}_1 - \vec{\rho}_0|^2} e^{i\frac{\omega}{c}z_2} e^{i\frac{\omega}{2cz_2}|\vec{\rho}_2 - \vec{\rho}_0|^2} \right|^2. \end{aligned} \quad (9.101)$$

If we choose the distances from the source to the two detectors to be equal ( $z_1 = z_2 = d$ ), the above integral of  $d\vec{\rho}_0$  yields a point-to-point correlation between the transverse planes  $z_1 = d$  and  $z_2 = d$ ,

$$\begin{aligned} & \left| G_{12}^{(1)}(\vec{\rho}_1; \vec{\rho}_2) \right|^2 \propto \left| \int d\vec{\rho}_0 e^{i\frac{\omega}{cd}(\vec{\rho}_1 - \vec{\rho}_2) \cdot \vec{\rho}_0} \right|^2 \\ &= \text{somb}^2 \left[ \frac{R}{d} \frac{\omega}{c} |\vec{\rho}_1 - \vec{\rho}_2| \right] \\ &\sim \delta(\vec{\rho}_1 - \vec{\rho}_2), \end{aligned} \quad (9.102)$$

where the  $\delta$ -function is an approximation by assuming a large-enough thermal source of angular size  $\Delta\theta \sim R/d$  and a high-enough frequency  $\omega$ , such as a visible light source. The normalized  $g^{(2)}$  function, i.e., the degree of second-order coherence, is therefore

$$g^{(2)}(\vec{\rho}_1; \vec{\rho}_2) = 1 + \text{somb}^2 \left[ \frac{R}{d} \frac{\omega}{c} |\vec{\rho}_1 - \vec{\rho}_2| \right] \simeq 1 + \delta(\vec{\rho}_1 - \vec{\rho}_2). \quad (9.103)$$

Following Equations 9.103,  $g^{(2)} = 2$  when  $\vec{\rho}_1 = \vec{\rho}_2$ , or  $|\vec{\rho}_1 - \vec{\rho}_2| < \lambda/\Delta\theta$ , where  $\Delta\theta \simeq 2R/d$  is the angular diameter of the thermal source. The second-order coherence function of thermal light indicates a peculiar phenomena: the photons created from a large number of randomly distributed atomic transitions on the output plane of a thermal source have twice the chance of being observed in pairs at  $\vec{\rho}_1 = \vec{\rho}_2$ , or within an area  $|\vec{\rho}_1 - \vec{\rho}_2| \simeq \lambda/\Delta\theta$ . In the measurement of first-order coherence, the quantity  $\lambda/\Delta\theta$ , where  $\Delta\theta$  is the angular separation between the double-pinholes of Young's interferometer,

has been defined as “coherence area,” indicating an observable interference pattern within that area on a far-field observation plane. It is important to keep in mind the very different physics and measurement behind the quantity  $\lambda/\Delta\theta$ .

Recently, this partial point-to-point or point-to-spot correlation of thermal light has been utilized for reproducing nonlocal ghost images. We will be discussing this interesting phenomenon in Chapter 11.

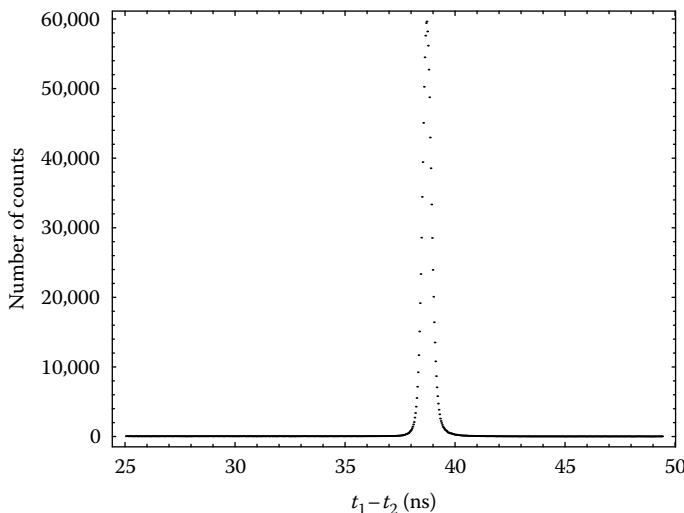
So far, we have successfully derived an analytical solution for second-order spatial correlation of thermal radiation at the necessary lowest-order approximation. We have shown that the partial point-to-point correlation of thermal radiation is the result of a constructive-destructive interference caused by the superposition of two-photon amplitudes, corresponding to different alternative ways for a randomly paired photon to produce a joint-detection event. In fact, the above analysis is not restricted to the necessary lowest-order approximation. The partial point-to-point correlation of  $G^{(2)}(\vec{r}_1; \vec{r}_2)$  is generally true for any higher-order approximations of quantized thermal radiation. The calculation is lengthy but straightforward. The mathematical procedure is similar to that in our early discussion of temporal coherence.

## 9.8 Photon Counting and Measurement of $G^{(2)}$

In photon counting regime, similar to the first-order coherence measurement, the second-order coherence is also based on the measurement of a large number of joint-detection events. Unlike the first-order correlation function, the second-order coherence function  $G^{(2)}(\mathbf{r}_1, t_1; \mathbf{r}_2, t_2)$  is a directly measurable function of space-time variables. Therefore,  $G^{(2)}(\mathbf{r}_1, t_1; \mathbf{r}_2, t_2)$  can be measured by means of time-averaged joint-detection counting rate as a function of chosen spatial variables or by examining the statistical histogram of a large number of joint-detection events as a function of  $t_1 - t_2$ . The photon registration events of the photodetectors  $D_1$  and  $D_2$  can be recorded with an accuracy of  $10^{-12}$  s in modern technologies.  $G^{(2)}$  can thus be measured as a function of  $t_1 - t_2$  in picosecond resolution by recording the registration time for each individual photon pairs. In the following, we show two examples of  $G^{(2)}$  measurements in photon-counting regime.

### 1. Measurement of $G^{(2)}(t_1 - t_2)$ and $g^{(2)}(t_1 - t_2)$

In these types of measurements, the spatial coordinates of the photodetectors,  $\mathbf{r}_1$  and  $\mathbf{r}_2$ , are chosen to be constants during the measurement. The measurement electronics is able to read and record the registration times  $t_1$  and  $t_2$  or the registration time difference  $t_1 - t_2$  for each of the

**FIGURE 9.12**

Second-order correlation function for entangled photon pairs. The horizontal axis  $t_1 - t_2$ , which labels the measured registration time difference of the photon pair, corresponds to  $\tau_1 - \tau_2$  with fixed values of  $z_1$  and  $z_2$ .

measured photon pairs. A statistical histogram, showing the number of joint-detection events against  $t_1 - t_2$ , is made after counting a large number of joint-detection events. This distribution corresponds to the second-order correlation function  $G^{(2)}(t_1 - t_2)$ . We have shown a typical measured degree of second-order coherence function  $g^{(2)}(t_1 - t_2)$ , i.e., the normalized second-order coherence function, for chaotic-thermal light, in Figure 9.8, which confirms Equation 9.65.

Figure 9.12 is a measured  $G^{(2)}(t_1 - t_2)$  function for entangled photon pairs of SPDC. The horizontal axis  $t_1 - t_2$  labels the registration time differences of the photon pairs corresponding to  $\tau_1 - \tau_2$  with constant spatial coordinates  $\mathbf{r}_1$  and  $\mathbf{r}_2$ . The vertical axis indicates the number of photon pairs that are observed with the value of  $t_1 - t_2$ . We may draw two conclusions from Figure 9.12 directly: (1) the entangled photon pair is likely to be generated simultaneously and (2) the measured  $t_1 - t_2$  are independent of the creation time of the pair.

The two examples above are typical measurements of  $G^{(2)}(t_1 - t_2)$  and  $g^{(2)}(t_1 - t_2)$  in photon counting. The measurement electronics records the photodetection time difference  $t_1 - t_2$  for each photon pair. The observed function is based on the statistics of a large number of photon pairs. The distribution function or the histogram that illustrates the number of counts against  $t_1 - t_2$ , statistically corresponds to the second-order correlation function  $G^{(2)}(t_1 - t_2)$  that is calculated based on the knowledge of the state of the radiation.

Due to the limited ability of photodetectors in determining the registration time of a photoelectron, the response time of the photodetectors and the associated electronics will affect the measurement of  $G^{(2)}(t_1 - t_2)$ . For instance, the calculated width of  $G^{(2)}(t_1 - t_2)$  for entangled signal-idler pairs of SPDC is typically on the order of a few femtoseconds to a few hundred femtoseconds. The observed width in Figure 9.12, however, is about 700 ps. The broadening is due to the slow response of the photodetectors. In the observation of a photoelectron event accompanied with the annihilation of a photon at time  $t$ , the photodetector exports a pulse of electric current to an electronic circuit that is able to analyze the pulse and to determine the electronic registration time  $\tilde{t}$  within a certain uncertainty. The jitter of the leading edge of the pulse, as well as the fluctuations of the pulse height, all contribute to the uncertainty of the electronic registration times, or the measured times, of  $\tilde{t}_1$  and  $\tilde{t}_2$ . We may characterize this uncertainty as a response function of the photodetector,  $D(\tilde{t} - t)$ , where  $t$  is the photon annihilation time and  $\tilde{t}$  is the electronic registration time. Thus, the joint-detection measurement of  $D_1$  and  $D_2$  can be treated as a convolution between the response functions and the second-order correlation function  $G^{(2)}(t_1 - t_2)$ :

$$G^{(2)}(\tilde{t}_1 - \tilde{t}_2) = \frac{1}{t_c^2} \int dt_1 \int dt_2 G^{(2)}(t_1 - t_2) D(\tilde{t}_1 - t_1) D(\tilde{t}_2 - t_2) \quad (9.104)$$

where we have chosen

$$\int dt D(\tilde{t} - t) = t_c, \quad D(0) = 1 \quad (9.105)$$

where  $t_c$  is defined as the response time of the photodetector. When the width of the response functions is much narrower than that of  $G^{(2)}(t_1 - t_2)$ , the response function can be treated as delta functions,  $D(\tilde{t} - t) \sim t_c \delta(\tilde{t} - t)$ . In this extreme case, the measured second-order correlation function will reveal the theoretical expectation of  $G^{(2)}(t_1 - t_2)$ :

$$\begin{aligned} G^{(2)}(\tilde{t}_1 - \tilde{t}_2) &= \int dt_1 \int dt_2 G^{(2)}(t_1 - t_2) \delta(\tilde{t}_1 - t_1) \delta(\tilde{t}_2 - t_2) \\ &= G^{(2)}(t_1 - t_2). \end{aligned} \quad (9.106)$$

However, when the response time is in the same order or even greater than the width of the correlation function, the situation is completely different. Especially when the width of the response functions are much wider than that of  $G^{(2)}(t_1 - t_2)$ , the second-order correlation function itself can then be treated as a delta function. Thus, Equation 9.104 turns into the following convolution between the response functions of the two photon-counting detectors:

$$G^{(2)}(\tilde{t}_1 - \tilde{t}_2) = G^{(2)}(0) \left( \frac{\tau_0}{t_c^2} \right) \int d\tau D(\tilde{t}_1 - \tilde{t}_2 - \tau) D(\tau). \quad (9.107)$$

where we have chosen

$$\int dt G^{(2)}(t) = G^{(2)}(0)\tau_0 \simeq \int dt G^{(2)}(0)\tau_0 \delta(t), \quad (9.108)$$

where  $\tau_0$  is a constant and is named as the second-order correlation time. Equation 9.107 indicates the following: (1) The width of the observed  $G^{(2)}(\tilde{t}_1 - \tilde{t}_2)$  is now determined by the response function of the photodetectors, which could be significantly broadened. This is what has happened in the measurement of Figure 9.12. (2) The relative slow response time of the photodetectors may reduce the magnitude of the measured second-order correlation. This reduction may not be a problem in the measurement of entangled states; however, it may affect the observation of  $G^{(2)}$  function of chaotic-thermal light significantly. This is due to the nonzero constant background of the second-order coherence function of chaotic-thermal light. The time integral does not change the constant background; however, it reduces the magnitude of the maximum value of measured  $G^{(2)}$  significantly when  $\tau_0 \ll t_c$ .

## 2. About “coincidence” measurement

A coincidence measurement does not measure  $G^{(2)}(t_1 - t_2)$  but rather cumulatively counts the joint-detection events that fall into a certain coincidence time window  $\Delta t_c$  around a chosen value of  $t_1 - t_2 = \tau$ , where  $\tau$  is a time constant that is determined by a particular experimental arrangement. Mathematically, this is equivalent to having a time integral on the second-order coherence function  $G^{(2)}(t_1 - t_2)$ :

$$R_c = \int_{\Delta T} dt_1 dt_2 G^{(2)}(t_1 - t_2) S(t_1 - t_2), \quad (9.109)$$

where

$R_c$  is the coincidence counting rate

$S(t_1 - t_2)$  represents the time window of the coincidence circuit

$$S(t_1 - t_2) = \begin{cases} 1 & \tau - \Delta t_c/2 \leq t_1 - t_2 \leq \tau + \Delta t_c/2 \\ 0 & \text{otherwise.} \end{cases}$$

## 3. Measurement of $G^{(2)}(z_1 - z_2)$ or $G^{(2)}(\vec{\rho}_1 - \vec{\rho}_2)$

The longitudinal and transverse spatial correlation measurements have been discussed earlier. A coincidence counter or a linear multiplier and associated electronics can be used to measure the correlation by scanning the point-like photodetector longitudinally or transversely. In the photon-counting measurements, the coincidence counter counts and records all the joint-detection

events that fall into the coincidence time window of  $\tau - \Delta t_c/2 \leq t_1 - t_2 \leq \tau + \Delta t_c/2$  as a function of  $z_1 - z_2$  or  $\vec{p}_1 - \vec{p}_2$ . In the current-current correlation measurements, the linear multiplier and associated electronics integrates and records the output reading of the linear multiplier that is proportional to  $i_1(t)i_2(t) \propto I(t_1)I(t_2)$ . The delays of the electronic cables between the linear multiplier and the photodetectors  $D_1$  and  $D_2$  define the early times  $t_1 = t - \tau_1^e$ ,  $t_2 = t - \tau_2^e$  of the measured photodetection events,\* as well as  $t_1 - t_2 = \tau_1^e - \tau_2^e$ .  $G^{(2)}(z_1 - z_2)$  is measured by means of reading and recording the coincidence-counting rate or the integrated output of the linear multiplier as a function of  $z_1 - z_2$  or  $\vec{p}_1 - \vec{p}_2$ . The variation of  $z_1 - z_2$  or  $\vec{p}_1 - \vec{p}_2$  can be achieved by scanning one of the photodetectors along its longitudinal axis or its transverse plane.<sup>†</sup>

It should be emphasized that the temporal and the transverse correlation may not be treated as independent. For instance, in the measurement of the second-order transverse spatial coherence function  $G^{(2)}(\vec{p}_1 - \vec{p}_2)$ , the value of  $\tau_1 - \tau_2$  must be carefully chosen to achieve a nonzero constant value (usually the maximum value) of  $G^{(2)}(z_1, t_1; z_2, t_2)$  during the scanning of the transverse coordinates of the point-like photodetectors.

## 9.9 Quantum Degree of Nth-Order Coherence

We now generalize the concept of quantum coherence to  $N$ th-order ( $N > 2$ ), namely, the  $N$ th-order coherence of light:

$$G^{(N)}(\mathbf{r}_1, t_1; \mathbf{r}_2, t_2; \dots; \mathbf{r}_N, t_N) = \left\langle \langle \hat{E}^{(-)}(\mathbf{r}_1, t_1) \hat{E}^{(-)}(\mathbf{r}_2, t_2) \dots \hat{E}^{(-)}(\mathbf{r}_N, t_N) \hat{E}^{(+)}(\mathbf{r}_N, t_N) \dots \hat{E}^{(+)}(\mathbf{r}_2, t_2) \hat{E}^{(+)}(\mathbf{r}_1, t_1) \rangle_{QM} \right\rangle_{\text{Ensemble}}, \quad (9.110)$$

and the normalized quantum degree of  $N$ th-order coherence

$$g^{(N)}(\mathbf{r}_1, t_1; \mathbf{r}_2, t_2; \dots; \mathbf{r}_N, t_N) = \frac{G^N(\mathbf{r}_1, t_1; \mathbf{r}_2, t_2; \dots; \mathbf{r}_N, t_N)}{G^{(1)}(\mathbf{r}_1, t_1; \mathbf{r}_1, t_1) G^{(1)}(\mathbf{r}_2, t_2; \mathbf{r}_2, t_2) \dots G^{(1)}(\mathbf{r}_N, t_N; \mathbf{r}_N, t_N)}. \quad (9.111)$$

\* The linear multiplier measures the current-current correlation of the photodetectors  $D_1$  and  $D_2$  at time  $t$ :  $V_{12}(t) \propto i_1(t)i_2(t) \propto I(t_1)I(t_2)$ , where  $V_{12}(t)$  is the output reading of the linear multiplier at time  $t$ , and  $i_1(t)$  and  $i_2(t)$  are the output currents of the photodetectors at time  $t$ . The delays of the electronic cables between the linear multiplier and the photodetectors  $D_1$  and  $D_2$  define the early times  $t_1 = t - \tau_1^e$ ,  $t_2 = t - \tau_2^e$  of the measured photodetection events, as well as  $t_1 - t_2 = \tau_1^e - \tau_2^e$ .

<sup>†</sup> The linear multiplier can also be used for the measurement of  $G^{(2)}(t_1 - t_2)$  of stationary light by varying the cable length of the delay-line or by other means of the electronic delays with fixed values of  $\mathbf{r}_1$  and  $\mathbf{r}_2$ .

An  $N$ -fold joint-detection counter, which involves the joint photodetection of  $N$ -independent photon-counting detectors, measures the  $N$ th-order coherence or correlation function as well as the degree of  $N$ th-order coherence. Similar to the two-photon effective wavefunction, we define the effective wavefunction of  $N$ -photon as follows:

$$\Psi(\mathbf{r}_1, t_1; \mathbf{r}_2, t_2; \dots; \mathbf{r}_N, t_N) \equiv \langle 0 | \hat{E}^{(+)}(\mathbf{r}_N, t_N) \dots \hat{E}^{(+)}(\mathbf{r}_2, t_2) \hat{E}^{(+)}(\mathbf{r}_1, t_1) | \Psi \rangle \quad (9.112)$$

where  $|\Psi\rangle$  is the  $N$ -photon state. The  $N$ -photon effective wavefunction may have two or more amplitudes, corresponding to different yet indistinguishable alternative ways for the group of  $N$  photons to produce an  $N$ -fold joint photodetection event. The constructive or destructive superposition of these  $N$ -photon amplitudes may produce a nontrivial correlation or anti-correlation function observable in the  $N$ -fold joint-detection counting rate:

$$\begin{aligned} G^{(N)}(\mathbf{r}_1, t_1; \mathbf{r}_2, t_2; \dots; \mathbf{r}_N, t_N) \\ = tr \rho \hat{E}^{(-)}(\mathbf{r}_1, t_1) \hat{E}^{(-)}(\mathbf{r}_2, t_2) \dots \hat{E}^{(-)}(\mathbf{r}_N, t_N) \hat{E}^{(+)}(\mathbf{r}_N, t_N) \dots \hat{E}^{+}(\mathbf{r}_2, t_2) \hat{E}^{(+)}(\mathbf{r}_1, t_1) \\ = \sum_l P_l |\Psi_l(\mathbf{r}_1, t_1; \mathbf{r}_2, t_2; \dots; \mathbf{r}_N, t_N)|^2 = \sum_l P_l \left| \sum_m A_{l,m}(\mathbf{r}_1, t_1; \mathbf{r}_2, t_2; \dots; \mathbf{r}_N, t_N) \right|^2 \end{aligned} \quad (9.113)$$

where we have assumed a generic  $N$ -photon mixed state of inhomogeneous ensemble,  $\Psi_l(\mathbf{r}_1, t_1; \mathbf{r}_2, t_2; \dots; \mathbf{r}_N, t_N)$  is the effective wavefunction associated with the  $l$ th  $N$ -photon state,  $P_l$  is the probability for a group of  $N$  photons to be in the  $l$ th  $N$ -photon state.

## Summary

In this chapter, we introduced the quantum theory of optical coherence. In quantum theory, a photodetection event measures the probability for a photon to be annihilated at space-time  $(\mathbf{r}, t)$ . A twofold photodetection event measures the probability of jointly annihilating a pair of photons at  $(\mathbf{r}_1, t_1)$  and  $(\mathbf{r}_2, t_2)$ , respectively. An  $N$ -fold photodetection event measures the probability of jointly annihilating  $N$  photons at  $(\mathbf{r}_1, t_1)$ ,  $(\mathbf{r}_2, t_2)$  ..., and  $(\mathbf{r}_N, t_N)$ , respectively. If there exist two or more alternative ways for a photon, for a pair of photons, or for a group of  $N$  photons to produce a photodetection event, a twofold photodetection event, or an  $N$ -fold photodetection event, quantum interferences may occur. The interferences are the results of the superposition among the one-photon amplitudes, two-photon amplitudes, or  $N$ -photon amplitudes, respectively. In the language of Dirac, the quantum

theory of first-order coherence is about a photon interferer with the photon itself; the quantum theory of second-order coherence is about a pair of photon interferers with the pair itself; and the quantum theory of  $N$ th-order coherence is about a group of  $N$ -photon interferers with the group itself. Differing from classical theory, which treats the  $N$ th-order ( $N \geq 2$ ) coherence or correlation as statistical intensity fluctuation correlation of  $N$  jointly measured intensities, quantum theory considers the  $N$ th-order coherence or correlation as  $N$ -photon interference phenomena.

In this regard, we introduced the concepts of the effective wavefunction of a photon, the effective wavefunction of two photons, and the effective wavefunction of  $N$  photons:

$$\begin{aligned}\Psi(\mathbf{r}, t) &= \langle 0 | \hat{E}^{(+)}(\mathbf{r}, t) | \Psi \rangle \\ \Psi(\mathbf{r}_1, t_1; \mathbf{r}_2, t_2) &= \langle 0 | \hat{E}^{(+)}(\mathbf{r}_2, t_2) \hat{E}^{(+)}(\mathbf{r}_1, t_1) | \Psi \rangle \\ \Psi(\mathbf{r}_1, t_1; \dots; \mathbf{r}_N, t_N) &= \langle 0 | \hat{E}^{(+)}(\mathbf{r}_N, t_N) \cdots \hat{E}^{(+)}(\mathbf{r}_1, t_1) | \Psi \rangle.\end{aligned}$$

The  $N$ -photon effective wavefunction or wavepacket ( $N \geq 2$ ) may be factorizable or non-factorizable, depending on the state of the radiation field. EPR state is a non-factorizable entangled biphoton state, which is characterized by a non-factorizable 2-D nonlocal wavepacket. The effective wavefunctions may have two or more than two amplitudes, corresponding to different yet indistinguishable alternative ways of producing a photodetection event or a multiphoton joint-detection event. Interference is thus the result of superposition between single-photon amplitudes, two-photon amplitudes, or  $N$ -photon amplitudes:

Case (I): Pure states

$$\begin{aligned}G^{(1)}(\mathbf{r}_j, t_j; \mathbf{r}_k, t_k) &= \Psi(\mathbf{r}_j, t_j) \Psi^*(\mathbf{r}_k, t_k) \\ &= \sum_m \Psi_m(\mathbf{r}_j, t_j) \sum_n \Psi_n^*(\mathbf{r}_k, t_k), \quad j, k = 1, 2, \\ G^{(2)}(\mathbf{r}_1, t_1; \mathbf{r}_2, t_2) &= |\Psi(\mathbf{r}_1, t_1; \mathbf{r}_2, t_2)|^2 = \left| \sum_m A_m(\mathbf{r}_1, t_1; \mathbf{r}_2, t_2) \right|^2, \\ G^{(N)}(\mathbf{r}_1, t_1; \mathbf{r}_2, t_2; \dots; \mathbf{r}_N, t_N) &= |\Psi(\mathbf{r}_1, t_1; \mathbf{r}_2, t_2; \dots; \mathbf{r}_N, t_N)|^2 \\ &= \left| \sum_m A_m(\mathbf{r}_1, t_1; \mathbf{r}_2, t_2; \dots; \mathbf{r}_N, t_N) \right|^2\end{aligned}$$

Case (II): Mixed states

$$\begin{aligned}
 G^{(1)}(\mathbf{r}_j, t_j; \mathbf{r}_k, t_k) &= \sum_l P_l \Psi_l(\mathbf{r}_j, t_j) \Psi_l^*(\mathbf{r}_k, t_k) \\
 &= \sum_l P_l \sum_m \Psi_{l,m}(\mathbf{r}_j, t_j) \sum_n \Psi_{l,n}^*(\mathbf{r}_k, t_k), \quad j, k = 1, 2, \\
 G^{(2)}(\mathbf{r}_1, t_1; \mathbf{r}_2, t_2) &= \sum_l P_l |\Psi_l(\mathbf{r}_1, t_1; \mathbf{r}_2, t_2)|^2 \\
 &= \sum_l P_l \left| \sum_m A_{l,m}(\mathbf{r}_1, t_1; \mathbf{r}_2, t_2) \right|^2, \\
 G^{(N)}(\mathbf{r}_1, t_1; \mathbf{r}_2, t_2; \dots; \mathbf{r}_N, t_N) &= \sum_l p_l |\Psi_l(\mathbf{r}_1, t_1; \mathbf{r}_2, t_2; \dots; \mathbf{r}_N, t_N)|^2 \\
 &= \sum_l P_l \left| \sum_m A_{l,m}(\mathbf{r}_1, t_1; \mathbf{r}_2, t_2; \dots; \mathbf{r}_N, t_N) \right|^2.
 \end{aligned}$$

After introducing these concepts, this chapter provided a few detailed discussions on typical temporal and spatial second-order coherence or correlation for different quantum states, including coherent state, entangled state, and chaotic-thermal state.

## Suggested Reading

1. Fano, U., *Am. J. Phys.* 29, 539 (1961).
2. Glauber, R.J., *Phys. Rev.* 130, 2529 (1963); 131, 2766 (1963).
3. Hanbury-Brown, R., *Intensity Interferometer*, Taylor & Francis Ltd., London, U.K., 1974.
4. Hanbury-Brown, R. and R.Q. Twiss, *Nature* 177, 27 (1956); 178, 1046, (1956); 178, 1447 (1956).
5. Loudon, R., *The Quantum Theory of Light*, Oxford Science Publications, Oxford, U.K., 2000.
6. Mandel, L. and E. Wolf, *Optical Coherence and Quantum Optics*, Cambridge University Press, London, U.K., 1995.
7. Rubin, M.H., D.N. Klyshko, Y.H. Shih, and A.V. Sergienko, *Phys. Rev. A* 50, 5122 (1994).
8. Scully, M.O. and M.S. Zubairy, *Quantum Optics*, Cambridge University Press, Cambridge, U.K., 1997.
9. Shih, Y.H., *IEEE J. Select. Top. Quantum Electron.* 9(6) (2003).

# 10

---

## *Quantum Entanglement*

---

In quantum theory, *a particle* is allowed to be in a state of coherent superposition between a set of orthogonal states. A vivid picture of this concept is the Schrödinger cat: *a cat* is alive and dead simultaneously. This would be no surprise if one means a large number of an ensemble of cats with 50% alive and 50% dead. But, Schrödinger cat is *a cat*. We are talking about *a cat* being alive and dead simultaneously. In mathematics, the best word to characterize the states of “alive” and “dead” is perhaps “orthogonal.” In quantum mechanics, the superposition of orthogonal states is used to describe the state of a quantum object, or a particle. The superposition principle is indeed a mystery compared to our everyday classical life experience.

In this chapter, we turn to another surprising consequence of quantum mechanics, namely, the quantum entanglement. Quantum entanglement involves a multiparticle system and coherent superposition of orthogonal multiparticle states. The Schrödinger cat is perhaps still the best example to picturize quantum entanglement. Now, we are talking about a pair of Schrödinger cats “propagating” to distant locations. The two cats are non-classical by means of the following two features: (1) each of the cats is in the state of alive and dead simultaneously; (2) the two have to be observed both alive or both dead whenever we look at them, despite the distance between the two. There would be probably no surprise if our observation is based on a large number of twin cats that are prepared to be half alive-alive and another half dead-dead. In this case, obviously, we have 50% chance to observe an alive-alive pair and 50% chance to observe a dead-dead pair for each joint-observation. However, we are talking about *a pair* of cats, i.e., each pair of cats, to be in the state of alive-alive and dead-dead simultaneously, and, in addition, each of the cats in the pair must be alive and dead simultaneously. It seems impossible to have such cats in classical reality.

Beyond the superposition of orthogonal single-particle states, the superposition of orthogonal multiparticle states represents an even more troubling concept in classical theory. It is not only because the superposition of multiparticle states has no counterpart in classical wave theory, but also because it represents nonlocal behavior of particles, which may never be explained classically.

## 10.1 EPR Experiment and EPR State

The concept of quantum entanglement started in 1935. Einstein, Podolsky, and Rosen (EPR), suggested a *gedankenexperiment* and introduced an entangled two-particle system based on the superposition of two-particle wavefunction. The EPR system composes two distant interaction-free particles, which are characterized by the following wavefunction:

$$\begin{aligned}\Psi(x_1, x_2) &= \frac{1}{2\pi\hbar} \int dp_1 dp_2 \delta(p_1 + p_2) e^{ip_1(x_1 - x_0)/\hbar} e^{ip_2 x_2/\hbar} \\ &= \delta(x_1 - x_2 - x_0)\end{aligned}\quad (10.1)$$

where  $e^{ip_1(x_1 - x_0)/\hbar}$  and  $e^{ip_2 x_2/\hbar}$  are the eigenfunctions, with eigenvalues  $p_1 = p$  and  $p_2 = -p$ , respectively, of the momentum operators  $\hat{p}_1$  and  $\hat{p}_2$  associated with particles 1 and 2;  $x_1$  and  $x_2$  are the coordinate variables to describe the positions of particles 1 and 2, respectively; and  $x_0$  is a constant. The EPR state is very peculiar. Although there is no interaction between the two distant particles, the two-particle superposition cannot be factorized into a product of two individual superposition of two particles. Quantum theory does not prevent such states.

What can we learn from the EPR state of Equation 10.1?

1. In coordinate representation, the wavefunction is a delta function:  $\delta(x_1 - x_2 - x_0)$ . The two particles are always separated in space with a constant value of  $x_1 - x_2 = x_0$ , although the coordinates  $x_1$  and  $x_2$  of the two particles are both unspecified.
2. The delta wavefunction  $\delta(x_1 - x_2 - x_0)$  is the result of the superposition of the plane wavefunctions of free particle one,  $e^{ip_1(x_1 - x_0)/\hbar}$ , and free particle two,  $e^{ip_2 x_2/\hbar}$ , with a particular distribution  $\delta(p_1 + p_2)$ . It is  $\delta(p_1 + p_2)$  that made the superposition special: although the momentum of particle one and particle two may take on any values, the delta function restricts the superposition with only these terms in which the total momentum of the system takes a constant value of zero.

Now, we transfer the wavefunction from coordinate representation to momentum representation:

$$\begin{aligned}\Psi(p_1, p_2) &= \frac{1}{2\pi\hbar} \int dx_1 dx_2 \delta(x_1 - x_2 - x_0) e^{-ip_1(x_1 - x_0)/\hbar} e^{-ip_2 x_2/\hbar} \\ &= \delta(p_1 + p_2).\end{aligned}\quad (10.2)$$

What can we learn from the EPR state of Equation 10.2?

1. In momentum representation, the wavefunction is a delta function:  $\delta(p_1 + p_2)$ . The total momentum of the two-particle system takes a

constant value of  $p_1 + p_2 = 0$ , although momenta  $p_1$  and  $p_2$  are both unspecified.

2. The delta wavefunction  $\delta(p_1 + p_2)$  is the result of the superposition of the plane wavefunctions of free particle one,  $e^{-ip_1(x_1 - x_0)/\hbar}$ , and free particle two,  $e^{-ip_2x_2/\hbar}$ , with a particular distribution  $\delta(x_1 - x_2 - x_0)$ . It is  $\delta(x_1 - x_2 - x_0)$  that made the superposition special: although the coordinates of particle one and particle two may take on any values, the delta function restricts the superposition with only these terms in which  $x_1 - x_2$  is a constant value of  $x_0$ .

In an EPR system, the value of the momentum (position) for neither single subsystem is determined. However, if one of the subsystems is measured to be at a certain momentum (position), the other one is determined with a unique corresponding value, despite the distance between them. An idealized EPR state of a two-particle system is therefore characterized by  $\Delta(p_1 + p_2) = 0$  and  $\Delta(x_1 - x_2) = 0$  simultaneously, even if the momentum and position of each individual free particle are completely undefined, i.e.,  $\Delta p_j \sim \infty$  and  $\Delta x_j \sim \infty$ ,  $j = 1, 2$ . In other words, each of the subsystems may have completely random values or all possible values of momentum and position in the course of their motion, but the correlations of the two subsystems are determined with certainty whenever a joint measurement is performed.

The EPR states of Equations 10.1 and 10.2 are simply the results of the quantum mechanical *superposition of two-particle states*. The physics behind EPR states is far beyond the acceptable limit of Einstein.

Does a free particle have a defined momentum and position in the state of Equations 10.1 and 10.2, regardless of whether we measure it or not? On one hand, the momentum and position of neither independent particle are specified and the superposition is taken over all possible values of the momentum and position. We may have to believe that the particles do not have any defined momentum and position, or have all possible values of momentum and position within the superposition, during the course of their motion. On the other hand, if the measured momentum or position of one particle uniquely determines the momentum or position of the other distant particle, it would be hard for anyone who believes no action-at-a-distance to imagine that the momentum and position of the two particles are not predetermined with defined values before the measurement. EPR thus puts us into a paradoxical situation. It seems reasonable for us to ask the same question that EPR had asked in 1935: “Can quantum-mechanical description of physical reality be considered complete?”

In their 1935 article, Einstein, Podolsky, and Rosen argued that the existence of the entangled two-particle state of Equations 10.1 and 10.2, a straightforward quantum mechanical superposition of two-particle state, led to the violation of the uncertainty principle of quantum theory. To draw their conclusion, EPR started from the following criteria:

*Locality:* there is no action-at-a-distance;

*Reality:* “if, without in any way disturbing a system, we can predict with certainty the value of a physical quantity, then there exist an element of physical reality corresponding to this quantity.” According to the delta wavefunctions, we can predict with certainty the outcome result of measuring the momentum (position) of particle 1 by measuring the momentum (position) of particle 2, and the measurement of particle 2 cannot cause any disturbance to particle 1, if the measurements are space-like separated events. Thus, the momentum and position of particle 1 must both be elements of physical reality regardless of whether we measure it or not. This, however, is not allowed by quantum theory. Now consider:

*Completeness:* “every element of the physical reality must have a counterpart in the complete theory.” This led to the question as the title of their 1935 article: “Can Quantum-Mechanical Description of Physical Reality Be Considered Complete?”

EPR’s arguments were never appreciated by Copenhagen. One objection was regarding EPR’s criterion of physical reality: “it is too narrow,” was a criticism from Bohr. It is perhaps not easy to find a wider criterion. A memorable quote from Wheeler, “No elementary quantum phenomenon is a phenomenon until it is a recorded phenomenon,” summarizes what Copenhagen has been trying to tell us. By 1927, most physicists accepted the Copenhagen interpretation as the standard view of quantum formalism. Einstein, however, refused to compromise. As Pais recalled in his book, during a walk around 1950, Einstein suddenly stopped and “asked me if I really believed that the moon (pion) exists only if I look at it.”

There has been arguments considering  $\Delta(p_1 + p_2)\Delta(x_1 - x_2) = 0$  a violation of the uncertainty principle. This argument is false. It is easy to find that  $p_1 + p_2$  and  $x_1 - x_2$  are not conjugate variables. As we know, nonconjugate variables correspond to commuting operators in quantum mechanics, if the corresponding operators exist.\* To have  $\Delta(p_1 + p_2) = 0$  and  $\Delta(x_1 - x_2) = 0$  simultaneously, or to have  $\Delta(p_1 + p_2)\Delta(x_1 - x_2) = 0$ , is not a violation of the uncertainty principle. This point can be easily seen from the following two-dimensional Fourier transforms:

$$\begin{aligned}\Psi(x_1, x_2) &= \frac{1}{2\pi\hbar} \int dp_1 dp_2 \delta(p_1 + p_2) e^{ip_1(x_1-x_0)/\hbar} e^{ip_2x_2/\hbar} \\ &= \frac{1}{2\pi\hbar} \int d(p_1 + p_2) \delta(p_1 + p_2) e^{i(p_1+p_2)(x'_1+x_2)/2\hbar} \\ &\quad \times \int d(p_1 - p_2)/2 e^{i(p_1-p_2)(x'_1-x_2)/2\hbar} \\ &= 1 \times \delta(x_1 - x_2 - x_0)\end{aligned}$$

---

\* It is possible that a measurable physical variable has no quantum mechanical operator associated with it, such as time  $t$ . From this perspective, an uncertainty relation based on variables rather than operators is more general.

where  $x' = x_1 - x_0$ ;

$$\begin{aligned}\Psi(p_1, p_2) &= \frac{1}{2\pi\hbar} \int dx_1 dx_2 \delta(x_1 - x_2 - x_0) e^{-ip_1(x_1-x_0)/\hbar} e^{-ip_2x_2/\hbar} \\ &= \frac{1}{2\pi\hbar} \int d(x'_1 + x_2) e^{-i(p_1+p_2)(x'_1+x_2)/2\hbar} \\ &\quad \times \int d(x'_1 - x_2)/2 \delta(x'_1 - x_2) e^{-i(p_1-p_2)(x'_1-x_2)/2\hbar} \\ &= \delta(p_1 + p_2) \times 1.\end{aligned}$$

The Fourier conjugate variables are  $(x_1 + x_2) \Leftrightarrow (p_1 + p_2)$  and  $(x_1 - x_2) \Leftrightarrow (p_1 - p_2)$ . Although it is possible to have  $\Delta(x_1 - x_2) \sim 0$  and  $\Delta(p_1 + p_2) \sim 0$  simultaneously, the uncertainty relations must hold for the Fourier conjugates  $\Delta(x_1 + x_2)\Delta(p_1 + p_2) \geq \hbar$ , and  $\Delta(x_1 - x_2)\Delta(p_1 - p_2) \geq \hbar$ ; with  $\Delta(p_1 - p_2) \sim \infty$  and  $\Delta(x_1 + x_2) \sim \infty$ .

In fact, in their 1935 paper, EPR never questioned  $\Delta(x_1 - x_2)\Delta(p_1 + p_2) = 0$  as a violation of the uncertainty principle. The violation of the uncertainty principle was probably not Einstein's concern at all, although their 1935 paradox was based on the argument of the uncertainty principle. What really bothered Einstein so much? In all his life, Einstein, a true believer of realism, never accepted that a particle does not have a defined momentum and position during its motion, but rather is specified by probability amplitude of certain momentum and position. "God does not play dice" was the most vivid criticism from Einstein to refuse the Schrödinger cat. The entangled two-particle system was used as an example to clarify and to reinforce Einstein's realistic opinion. To Einstein, the acceptance of Schrödinger cat probably means action-at-a-distance or an inconsistency between quantum mechanics and the theory of relativity, when dealing with the entangled EPR two-particle system. Let us follow Copenhagen to consider that *each particle* in an EPR pair has no defined momentum and position, or has all possible momentum and position within the superposition, i.e., assuming  $\Delta p_j \neq 0$ ,  $\Delta x_j \neq 0$ ,  $j = 1, 2$ , for *each single-particle* until the measurement. Assume the measurement devices are particle-counting devices for the measurement of position. For each registration of a particle, the measurement device records a value of its position. No one can predict what value is registered for each measurement; the best knowledge we may have is the probability to register that value. If we further assume no physical interaction between the two distant particles and believe no action-at-a-distance in nature, we would also believe that no matter how the two particles are created, the two registered values must be independent of each other. Thus, the value of  $x_1 - x_2$  is unpredictable within the uncertainties of  $\Delta x_1$  and  $\Delta x_2$ . The above statement is also valid for the momentum measurement. Therefore, after a set of measurements on a large number of particle pairs, the statistical uncertainty of the measurement on  $p_1 + p_2$  and  $x_1 - x_2$  must obey the following inequalities:

$$\begin{aligned}\Delta(p_1 + p_2) &= \sqrt{(\Delta p_1)^2 + (\Delta p_2)^2} > \text{Max}(\Delta p_1, \Delta p_2) \\ \Delta(x_1 - x_2) &= \sqrt{(\Delta x_1)^2 + (\Delta x_2)^2} > \text{Max}(\Delta x_1, \Delta x_2).\end{aligned}\tag{10.3}$$

Equation 10.3 is obviously true in statistics, especially when we are sure that no disturbance is possible between the two independent local measurements. The condition of “no disturbance is possible between the two independent local measurements” can be easily realized by making the two measurement events space-like separated events. The classical inequality of Equation 10.3 would not allow  $\Delta(p_1 + p_2) = 0$  and  $\Delta(x_1 - x_2) = 0$  as required in the EPR state, unless  $\Delta p_1 = 0$ ,  $\Delta p_2 = 0$ ,  $\Delta x_1 = 0$  and  $\Delta x_2 = 0$ , simultaneously. Unfortunately, the assumption of  $\Delta p_1 = 0$ ,  $\Delta p_2 = 0$ ,  $\Delta x_1 = 0$ ,  $\Delta x_2 = 0$  cannot be true because it violates the uncertainty relations  $\Delta p_1 \Delta x_1 \geq \hbar$  and  $\Delta p_2 \Delta x_2 \geq \hbar$ .

In a non-perfect entangled system, the uncertainties of  $p_1 + p_2$  and  $x_1 - x_2$  may differ from zero. Nevertheless, the measurements may still satisfy the EPR inequalities:

$$\begin{aligned}\Delta(p_1 + p_2) &< \text{min}(\Delta p_1, \Delta p_2) \\ \Delta(x_1 - x_2) &< \text{min}(\Delta x_1, \Delta x_2).\end{aligned}\tag{10.4}$$

The apparent contradiction between the classical inequality Equation 10.3 and the EPR inequality Equation 10.4 deeply troubled Einstein. While one sees the measurements of  $p_1 + p_2$  and  $x_1 - x_2$  of the two distant individual free particles satisfying Equation 10.4, but believing Equation 10.3, one might easily be trapped into concluding either there is a violation of the uncertainty principle or there exists action-at-a-distance.

Is it possible to have a “better” theory, which provides correct predictions of the behavior of a particle similar to quantum theory and, at the same time, respects its description of physical reality by EPR as “complete”? The followers of Einstein’s realism have tried in many different ways to formulate a realistic theory of quantum mechanics. It was Bohm who first attempted a version of a so-called hidden variable theory, which seemed to satisfy these requirements. The hidden variable theory was successfully applied to many different quantum phenomena until 1964, when Bell proved a theorem to show that an inequality, which is violated by certain quantum mechanical statistical predictions, can be used to distinguish local hidden variable theory from quantum mechanics. Since then, the testing of Bell’s inequalities became a standard instrument for the study of fundamental problems of quantum theory. The experimental testing of Bell’s inequality started from the early 1970s. Most of the historical experiments concluded the violation of Bell’s inequality and thus disapproved the local hidden variable theory. A detailed discussion of Bell’s theorem and experimental testing of Bell’s inequality will be given later.

In the following discussion, we examine a set of simple yet popular classical models that attempted to simulate the behavior of the entangled EPR system. These models are based on the statistical behavior of an ensemble of particles instead of the superposition state of a particle. In other words, it is not based on the concept of Schrödinger cat (a cat is alive and dead simultaneously, or a pair of cats that is in the state of alive-alive and dead-dead simultaneously), but rather, a large number of twin cats in which 50% are alive twins and 50% are dead twins.

We may have three models:

1. In model one, each single pair of particles holds defined momenta  $p_1 = \text{constant}$  and  $p_2 = \text{constant}$  with  $p_1 + p_2 = 0$ . From pair to pair, the values of  $p_1$  and  $p_2$  may vary significantly. The sum of  $p_1$  and  $p_2$ , however, keeps constant of zero. Thus, each joint detection of the two distant particles measures precisely the constant values of  $p_1$  and  $p_2$  and measures  $p_1 + p_2 = 0$ . The uncertainties of  $\Delta p_1$  and  $\Delta p_2$  only have statistical meaning in terms of the measurements of an ensemble. This model successfully simulated  $\Delta p_1 \sim \infty$ ,  $\Delta p_2 \sim \infty$  and  $\Delta(p_1 + p_2) = 0$  based on the measurement of a large number of classically correlated particle pairs. This is, however, only half of the EPR story. Can we have  $\Delta x_1 \sim \infty$ ,  $\Delta x_2 \sim \infty$  and  $\Delta(x_1 - x_2) = 0$  in this model? We do have  $\Delta x_1 \sim \infty$  and  $\Delta x_2 \sim \infty$ , otherwise the uncertainty principle will be violated; the position correlation, however, can never achieve  $\Delta(x_1 - x_2) = 0$  by any means.
2. In model two, each single pair of particles holds defined position  $x_1 = \text{constant}$  and  $x_2 = \text{constant}$  with  $x_1 - x_2 = x_0$ . From pair to pair, the values of  $x_1$  and  $x_2$  may vary significantly. The difference of  $x_1$  and  $x_2$ , however, keeps constant of  $x_0$ . Thus, each joint detection of the two distant particles measures precisely the constant values of  $x_1$  and  $x_2$  and measures  $x_1 - x_2 = x_0$ . The uncertainties of  $\Delta x_1$  and  $\Delta x_2$  only have statistical meaning in terms of the measurements of an ensemble. This model successfully simulated  $\Delta x_1 \sim \infty$ ,  $\Delta x_2 \sim \infty$  and  $\Delta(x_1 - x_2) = 0$  based on the measurement of a large number of classically correlated particle pairs. This is, however, only half of the EPR story. Can we have  $\Delta p_1 \sim \infty$ ,  $\Delta p_2 \sim \infty$  and  $\Delta(p_1 + p_2) = 0$  in this model? We do have  $\Delta p_1 \sim \infty$  and  $\Delta p_2 \sim \infty$ , otherwise the uncertainty principle will be violated; the momentum correlation, however, can never achieve  $\Delta(p_1 + p_2) = 0$  by any means.

The above two models of classically correlated particle pairs can never achieve both  $\Delta(p_1 + p_2) = 0$  and  $\Delta(x_1 - x_2) = 0$ . What would happen if we combine the two parts together? This leads to the third model of classical simulation.

3. In model three, among a large number of classically correlated particle pairs, we assume 50% in model one and the other 50% in model two. The  $p_1 + p_2$  measurements would have 50% chance with  $p_1 + p_2 = 0$  and 50% chance with  $p_1 + p_2 = \text{random value}$ . On the other hand, the  $x_1 - x_2$  measurements would have 50% chance with  $x_1 - x_2 = x_0$  and 50% chance with

$x_1 - x_2 = \text{random value}$ . What are the statistical uncertainties on the measurements of  $(p_1 + p_2)$  and  $(x_1 - x_2)$  in this case? If we focus on only these events of model one, the statistical uncertainty on the measurement of  $(p_1 + p_2)$  is  $\Delta(p_1 + p_2) = 0$ , and if we focus on these events of model two, the statistical uncertainty on the measurement of  $(x_1 - x_2)$  is  $\Delta(x_1 - x_2) = 0$ ; however, if we consider all the measurements together, the statistical uncertainties on the measurements of  $(p_1 + p_2)$  and  $(x_1 - x_2)$ , are both infinity:  $\Delta(p_1 + p_2) = \infty$  and  $\Delta(x_1 - x_2) = \infty$ .

In conclusion, classically correlated particle pairs may partially simulate EPR correlation with three types of optimized observations:

$$(1) \quad \Delta(p_1 + p_2) = 0 \text{ (100\%)} \quad \text{and} \quad \Delta(x_1 - x_2) = \infty \text{ (100\%);}$$

$$\Delta p_1 = 0, \quad \Delta p_2 = 0; \quad \Delta x_1 = \infty, \quad \Delta x_2 = \infty.$$

$$(2) \quad \Delta(x_1 - x_2) = 0 \text{ (100\%)} \quad \text{and} \quad \Delta(p_1 + p_2) = \infty \text{ (100\%);}$$

$$\Delta x_1 = 0, \quad \Delta x_2 = 0; \quad \Delta p_1 = \infty, \quad \Delta p_2 = \infty.$$

$$(3) \quad \Delta(p_1 + p_2) = 0 \text{ (50\%)} \quad \text{and} \quad \Delta(x_1 - x_2) = 0 \text{ (50\%);}$$

$$\Delta p_1 = \infty, \quad \Delta p_2 = \infty; \quad \Delta x_1 = \infty, \quad \Delta x_2 = \infty.$$

Within one setup of experimental measurements, only the entangled EPR states result in the simultaneous observation of

$$\Delta(p_1 + p_2) = 0 \text{ (100\%)} \quad \text{and} \quad \Delta(x_1 - x_2) = 0 \text{ (100\%)}$$

$$\Delta p_1 \sim \infty, \quad \Delta p_2 \sim \infty, \quad \Delta x_1 \sim \infty, \quad \Delta x_2 \sim \infty.$$

We thus have another tool, besides the testing of Bell's inequality, to distinguish quantum entangled states from classically correlated particle pairs.

## 10.2 Product State, Entangled State, and Classically Correlated State

### 10.2.1 Product State

In general, a product state describes the behavior of a system composed of two or more independent subsystems. Usually, the measurement involves the joint detection of two or more independent particles. For example, an experiment measures the coincidence counts of two or more

particle-counting detectors within a certain time window. The experimental setup is similar to that of the EPR correlation measurement, however, the measurement only deals with independent particles. The independent particle system can be characterized as a product state, i.e., the state of the system is factorizable into a product of states of two or more subsystems. For example,

$$\hat{\rho} = \hat{\rho}_1 \otimes \hat{\rho}_2. \quad (10.5)$$

The density matrix  $\hat{\rho}$  in Equation 10.5 characterizes a quantum system composed of two independent subsystems of  $\hat{\rho}_1$  and  $\hat{\rho}_2$ . In Equation 10.5, each independent subsystem can be in any state. The simplest case is a product of two pure states:

$$|\Psi\rangle = \sum_{a,b} f(a)g(b) |a\rangle |b\rangle = \sum_a f(a) |a\rangle \cdot \sum_b g(b) |b\rangle, \quad (10.6)$$

where  $\{|a\rangle\}$  and  $\{|b\rangle\}$  are two sets of orthogonal vectors for subsystems 1 and 2, respectively.

### 10.2.2 Entangled State

Differing from product states, entangled states describe the behavior of entangled quantum systems. The two-particle entangled state was mathematically formulated by Schrödinger. Consider a pure state for a system composed of two spatially separated subsystems,

$$\hat{\rho} = |\Psi\rangle \langle \Psi| \quad |\Psi\rangle = \sum_{a,b} c(a,b) |a\rangle |b\rangle \quad (10.7)$$

where

$\{|a\rangle\}$  and  $\{|b\rangle\}$  are two sets of orthogonal vectors for subsystems 1 and 2, respectively

$\hat{\rho}$  is the density matrix

If  $c(a,b)$  does not factor into a product of the form  $f(a) \times g(b)$ , then it follows that the state does not factor into a product state for subsystems 1 and 2:

$$\hat{\rho} \neq \hat{\rho}_1 \otimes \hat{\rho}_2 \quad (10.8)$$

the state was defined by Schrödinger as the entangled state.

Following this notation, the first classic example of a two-particle entangled state, the EPR state of Equations 10.1 and 10.2, is thus written as:

$$\begin{aligned} |\Psi\rangle_{\text{EPR}} &= \sum_{x_1, x_2} \delta(x_1 - x_2 + x_0) |x_1\rangle|x_2\rangle \\ &= \sum_{p_1, p_2} \delta(p_1 + p_2) |p_1\rangle|p_2\rangle, \end{aligned} \quad (10.9)$$

where we have described the EPR entangled system as the coherent superposition of the momentum eigenstates as well as the coherent superposition of the position eigenstates of each particle. One clear property of the EPR state is its independence of vector bases. The two  $\delta$ -functions in Equation 10.9 represent, respectively and simultaneously, the perfect position–position correlation and momentum–momentum correlation. Although the two distant particles are interaction free, the superposition selects only the eigenstates which are specified by the  $\delta$ -function. We may use the following statement to summarize the surprising feature of the EPR state: *the values of the momentum and the position for neither interaction-free single subsystem is determinate. However, if one of the subsystems is measured to be at a certain value of momentum and/or position, the momentum and/or position of the other one is 100% determined, despite the distance between them.*

It is necessary to emphasize that Equation 10.9 is true, simultaneously, in the conjugate momentum and position space.

### 10.2.3 Classically Correlated State

There exist many different types of classically correlated states. The following are two typical classically correlated states that have been used to simulate the EPR state of Equation 10.9:

$$\hat{\rho} = \sum_{p_1, p_2} \delta(p_1 + p_2) |p_1\rangle|p_2\rangle\langle p_2|\langle p_1|, \quad (10.10)$$

or

$$\hat{\rho} = \sum_{x_1, x_2} \delta(x_1 - x_2 + x_0) |x_1\rangle|x_2\rangle\langle x_2|\langle x_1|. \quad (10.11)$$

Differing from entangled states, Equations 10.10 and 10.11 cannot be simultaneously true for one system as we have discussed earlier.

## 10.3 Entangled States in Spin Variables

A different classic example of entangled two-particle system was suggested by Bohm. Instead of using continuous space-time variables, Bohm simplified

the entangled two-particle state to discrete spin variables. EPR–Bohm state is a singlet state of two spin 1/2 particles:

$$|\Psi\rangle = \frac{1}{\sqrt{2}} \left[ |\uparrow\rangle_1 |\downarrow\rangle_2 - |\downarrow\rangle_1 |\uparrow\rangle_2 \right] \quad (10.12)$$

where the kets  $|\uparrow\rangle$  and  $|\downarrow\rangle$  represent states of spin “up” and spin “down,” respectively, along an *arbitrary* direction. Again, for this state, *the spin of neither particle is determined; however, if one particle is measured to be spin up along a certain direction, the other one must be spin down along that direction, despite the distance between the two spin 1/2 particles.* Similar to the original EPR state, Equation 10.12 is independent of the choice of the spin directions and the eigenstates of the associated spin operators. It is easy to show that Equation 10.12 is true, simultaneously, in the three orthogonal spin representations. Equation 10.12 is very different from the classically correlated state. It is easy to show that classically correlated states are coordinate dependent. The state does not hold the same form if choosing the other orthogonal spin directions.

The most widely used entangled two-particle states might have been the “Bell states” (or EPR–Bohm–Bell states). Bell states are a set of polarization states for a pair of entangled photons. The four Bell states that form a complete orthonormal basis of two-photon state are usually represented as

$$\begin{aligned} |\Phi_{12}^{(\pm)}\rangle &= \frac{1}{\sqrt{2}} [ |0_1 0_2\rangle \pm |1_1 1_2\rangle ], \\ |\Psi_{12}^{(\pm)}\rangle &= \frac{1}{\sqrt{2}} [ |0_1 1_2\rangle \pm |1_1 0_2\rangle ] \end{aligned} \quad (10.13)$$

where  $|0\rangle$  and  $|1\rangle$  represent two arbitrary orthogonal polarization bases, e.g.,  $|0\rangle = |H\rangle$  (horizontal) and  $|1\rangle = |V\rangle$  (vertical) linear polarization, respectively. We will have a detailed discussion on Bell states later.

## 10.4 Entangled Biphoton State

The state of a signal-idler photon pair created in spontaneous parametric down-conversion (SPDC) is a typical EPR state. Roughly speaking, the process of SPDC involves sending a pump laser beam into a nonlinear material,

such as a non-centrasymmetric crystal. Occasionally, the nonlinear interaction leads to the annihilation of a high-frequency pump photon and the simultaneous creation of a pair of lower-frequency signal–idler photons into an entangled two-photon state:

$$|\Psi\rangle = \Psi_0 \sum_{s,i} \delta(\omega_s + \omega_i - \omega_p) \delta(\mathbf{k}_s + \mathbf{k}_i - \mathbf{k}_p) \hat{a}_s^\dagger(\mathbf{k}_s) \hat{a}_i^\dagger(\mathbf{k}_i) |0\rangle \quad (10.14)$$

where

$\omega_j, \mathbf{k}_j$  ( $j = s, i, p$ ) are the frequency and wavevector of the signal (s), idler (i), and pump (p)

$\hat{a}_s^\dagger$  and  $\hat{a}_i^\dagger$  are creation operators for the signal and the idler photon, respectively

$\Psi_0$  is the normalization constant

We have assumed a CW monochromatic laser pump, i.e.,  $\omega_p$  and  $\mathbf{k}_p$  are considered as constants. The two delta functions in Equation 10.14 are technically named as phase-matching condition:

$$\omega_p = \omega_s + \omega_i, \quad \mathbf{k}_p = \mathbf{k}_s + \mathbf{k}_i. \quad (10.15)$$

The names *signal* and *idler* are historical leftovers. The names probably came about due to the fact that in the early days of SPDC, most of the experiments were done with nondegenerate processes. One radiation was in the visible range (and thus easily detected, the signal), and the other was in IR range (usually not detected, the idler). We will see in the following discussions that the role of the idler is not any less than that of the signal. The SPDC process is referred to as type-I if the signal and idler photons have identical polarizations, and type-II if they have orthogonal polarizations. The process is said to be *degenerate* if the SPDC photon pair have the same free-space wavelength (e.g.,  $\lambda_i = \lambda_s = 2\lambda_p$ ), and *nondegenerate* otherwise. In general, the pair exit the crystal *noncollinearly*, i.e., propagate to different directions defined by the second equation in Equation 10.15 and Snell's law. Of course, the pair may also exit *collinearly*, in the same direction, together with the pump.

The state of the signal–idler pair can be derived, quantum mechanically, by the first order perturbation theory with the help of the nonlinear interaction Hamiltonian. The SPDC interaction arises in a nonlinear crystal driven by a pump laser beam. The polarization, i.e., the dipole moment per unit volume, is given by

$$P_i = \chi_{i,j}^{(1)} E_j + \chi_{i,j,k}^{(2)} E_j E_k + \chi_{i,j,k,l}^{(3)} E_j E_k E_l + \dots \quad (10.16)$$

where  $\chi^{(m)}$  is the  $m$ th order electrical susceptibility tensor. In SPDC, it is the second order nonlinear susceptibility  $\chi^{(2)}$  that plays the role. The second-order nonlinear interaction Hamiltonian can be written as

$$H = \epsilon_0 \int_V d\mathbf{r} \chi_{ijk}^{(2)} E_i E_j E_k \quad (10.17)$$

where the integral is taken over the interaction volume  $V$ .

It is convenient to use the Fourier representation for the electrical fields in Equation 10.17:

$$\mathbf{E}(\mathbf{r}, t) = \int d\mathbf{k} \left[ \hat{\mathbf{E}}^{(-)}(\mathbf{k}) e^{-i(\omega(\mathbf{k})t - \mathbf{k} \cdot \mathbf{r})} + \hat{\mathbf{E}}^{(+)}(\mathbf{k}) e^{i(\omega(\mathbf{k})t - \mathbf{k} \cdot \mathbf{r})} \right]. \quad (10.18)$$

Substituting Equation 10.18 into Equation 10.17 and keeping only the terms of interest, we obtain the SPDC Hamiltonian in the interaction representation:

$$\begin{aligned} H_{\text{int}}(t) = & \epsilon_0 \int_V d\mathbf{r} \int d\mathbf{k}_s d\mathbf{k}_i \chi_{lmn}^{(2)} \hat{E}_{pl}^{(+)} e^{i(\omega_p t - \mathbf{k}_p \cdot \mathbf{r})} \\ & \hat{E}_{sm}^{(-)} e^{-i(\omega_s(\mathbf{k}_s)t - \mathbf{k}_s \cdot \mathbf{r})} \hat{E}_{in}^{(-)} e^{-i(\omega_i(\mathbf{k}_i)t - \mathbf{k}_i \cdot \mathbf{r})} + h.c., \end{aligned} \quad (10.19)$$

where *h.c.* stands for Hermitian conjugate. To simplify the calculation, we have also assumed the pump field to be plane and monochromatic with wavevector  $\mathbf{k}_p$  and frequency  $\omega_p$ .

It is easily noticeable that in Equation 10.19, the volume integration can be done for some simplified cases. At this point, we assume that  $V$  is infinitely large. Later, we will see that the finite size of  $V$  in longitudinal and/or transversal directions may have to be taken into account. For an infinite volume  $V$ , the interaction Hamiltonian Equation 10.19 is written as

$$\begin{aligned} H_{\text{int}}(t) = & \epsilon_0 \int d\mathbf{k}_s d\mathbf{k}_i \chi_{lmn}^{(2)} \hat{E}_{pl}^{(+)} \hat{E}_{sm}^{(-)} \hat{E}_{in}^{(-)} \\ & \times \delta(\mathbf{k}_p - \mathbf{k}_s - \mathbf{k}_i) e^{i(\omega_p - \omega_s(\mathbf{k}_s) - \omega_i(\mathbf{k}_i))t} + h.c. \end{aligned} \quad (10.20)$$

It is reasonable to consider the pump field classical, which is usually a laser beam, and quantize the signal and idler fields, which are both in the single-photon level:

$$\begin{aligned} \hat{E}^{(-)}(\mathbf{k}) &= i\sqrt{\frac{2\pi\hbar\omega}{V}} \hat{a}^\dagger(\mathbf{k}), \\ \hat{E}^{(+)}(\mathbf{k}) &= i\sqrt{\frac{2\pi\hbar\omega}{V}} a(\mathbf{k}), \end{aligned} \quad (10.21)$$

where  $\hat{a}^\dagger(\mathbf{k})$  and  $a(\mathbf{k})$  are photon creation and annihilation operators, respectively. The state of the emitted photon pair can be calculated by applying the first-order perturbation

$$|\Psi\rangle = -\frac{i}{\hbar} \int dt H_{int}(t) |0\rangle. \quad (10.22)$$

By using vacuum  $|0\rangle$  for the initial state in Equation 10.22, we assume that there is no input radiation in any signal and idler modes, i.e., we have an SPDC process.

Further assuming an infinite interaction time, evaluating the time integral in Equation 10.22 and omitting altogether the constants and slow (square root) functions of  $\omega$ , we obtain the *entangled* two-photon state of Equation 10.14 in the form of integral:

$$|\Psi\rangle = \Psi_0 \int d\mathbf{k}_s d\mathbf{k}_i \delta[\omega_p - \omega_s(\mathbf{k}_s) - \omega_i(\mathbf{k}_i)] \delta(\mathbf{k}_p - \mathbf{k}_s - \mathbf{k}_i) \hat{a}_s^\dagger(\mathbf{k}_s) \hat{a}_i^\dagger(\mathbf{k}_i) |0\rangle \quad (10.23)$$

where  $\Psi_0$  is a normalization constant, which has absorbed all omitted constants. Equation 10.23 has been used in Chapter 3 for the calculation of second-order correlation function.

The way of achieving phase matching, i.e., the way of achieving the delta functions in Equation 10.23 basically determines how the signal-idler pair “looks.” For example, in a negative uniaxial crystal, one can use a linearly polarized pump laser beam as an extraordinary ray of the crystal to generate a signal-idler pair both polarized as the ordinary rays of the crystal, which is defined as type-I phase matching. One can alternatively generate a signal-idler pair with one ordinary polarized and another extraordinary polarized, which is defined as type II phase matching. Figure 10.1 shows three examples of SPDC two-photon source. All three

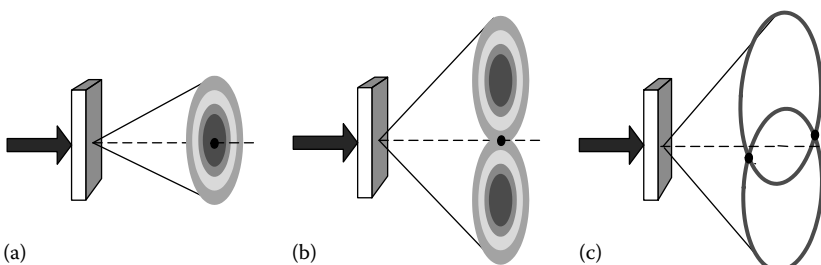


**FIGURE 10.1**

Three widely used SPDC setups. (a) Type-I SPDC. (b) Collinear degenerate type-II SPDC. Two rings overlap at one region. (c) Noncollinear degenerate type-II SPDC. For clarity, only two degenerate rings, one for e-polarization and the other for o-polarization, are shown.

schemes have been widely used for different experimental purposes. Technical details can be found from text books and research references in nonlinear optics.

The two-photon state in the forms of Equation 10.14 or Equation 10.23 is a pure state, which describes the behavior of a signal–idler photon pair mathematically. Does the signal or the idler photon in the EPR state of Equation 10.14 or Equation 10.23 have a defined energy and momentum regardless of whether we measure it or not? Quantum mechanics answers: No! However, if one of the subsystems is measured with a certain energy and momentum, the other one is determined with certainty, despite the distance between them.

In the above calculation of the two-photon state, we have approximated an infinitely large volume of nonlinear interaction. For a finite volume of nonlinear interaction, we may write the state of the signal–idler photon pair in a more general form:

$$|\Psi\rangle = \int d\mathbf{k}_s d\mathbf{k}_i F(\mathbf{k}_s, \mathbf{k}_i) \hat{a}_i^\dagger(\mathbf{k}_s) \hat{a}_s^\dagger(\mathbf{k}_i) |0\rangle \quad (10.24)$$

where

$$\begin{aligned} F(\mathbf{k}_s, \mathbf{k}_i) &= \epsilon \delta(\omega_p - \omega_s - \omega_i) f(\Delta_z L) h_{tr}(\vec{\kappa}_1 + \vec{\kappa}_2) \\ f(\Delta_z L) &= \int_L dz e^{-i(k_p - k_{sz} - k_{iz})z} \\ h_{tr}(\vec{\kappa}_1 + \vec{\kappa}_2) &= \int_A d\vec{\rho} \tilde{h}_{tr}(\vec{\rho}) e^{-i(\vec{\kappa}_s + \vec{\kappa}_i) \cdot \vec{\rho}} \\ \Delta_z &= k_p - k_{sz} - k_{iz} \end{aligned} \quad (10.25)$$

where

$\epsilon$  is named as parametric gain

$\epsilon$  is proportional to the second-order electric susceptibility  $\chi^{(2)}$  and is usually treated as a constant

$L$  is the length of the nonlinear interaction

the integral in  $\vec{\kappa}$  is evaluated over the cross section  $A$  of the nonlinear material illuminated by the pump

$\vec{\rho}$  is the transverse coordinate vector

$\vec{\kappa}_j$  (with  $j = s, i$ ) is the transverse wavevector of the signal and idler

$f(|\vec{\rho}|)$  is the transverse profile of the pump, which can be treated as a Gaussian in most of the experimental conditions

The functions  $f(\Delta_z L)$  and  $h_{tr}(\vec{\kappa}_1 + \vec{\kappa}_2)$  can be approximated as  $\delta$ -functions for an infinitely long ( $L \sim \infty$ ) and wide ( $A \sim \infty$ ) nonlinear interaction region.

The reason we have chosen the form of Equation 10.25 is to separate the “longitudinal” and the “transverse” correlations. We will show that  $\delta(\omega_p - \omega_s - \omega_i)$  and  $f(\Delta_z L)$  together can be rewritten as a function of  $\omega_s - \omega_i$ . To simplify the mathematics, we assume near co-linearly SPDC. In this situation,  $|\vec{\kappa}_{s,i}| \ll |\mathbf{k}_{s,i}|$ .

Basically, function  $f(\Delta_z L)$  determines the “longitudinal” space-time correlation. Finding the solution of the integral is straightforward:

$$\begin{aligned} f(\Delta_z L) &= \int_0^L dz e^{-i(k_p - k_{sz} - k_{iz})z} \\ &= e^{-i\Delta_z L/2} \operatorname{sinc}\left(\frac{\Delta_z L}{2}\right). \end{aligned} \quad (10.26)$$

Now, we consider  $f(\Delta_z L)$  with  $\delta(\omega_p - \omega_s - \omega_i)$  together, and taking advantage of the  $\delta$ -function in frequencies by introducing a detuning frequency  $\nu$  to evaluate function  $f(\Delta_z L)$ :

$$\begin{aligned} \omega_s &= \omega_s^0 + \nu \\ \omega_i &= \omega_i^0 - \nu \\ \omega_p &= \omega_s + \omega_i = \omega_s^0 + \omega_i^0. \end{aligned} \quad (10.27)$$

The dispersion relation  $k(\omega)$  allows us to express the wave numbers through the detuning frequency  $\nu$ :

$$\begin{aligned} k_s &\approx k(\omega_s^0) + \nu \frac{dk}{d\omega} \Big|_{\omega_s^0} = k(\omega_s^0) + \frac{\nu}{u_s}, \\ k_i &\approx k(\omega_i^0) - \nu \frac{dk}{d\omega} \Big|_{\omega_i^0} = k(\omega_i^0) - \frac{\nu}{u_i} \end{aligned} \quad (10.28)$$

where  $u_s$  and  $u_i$  are group velocities for the signal and the idler, respectively. Now, we connect  $\Delta_z$  with the detuning frequency  $\nu$ :

$$\begin{aligned} \Delta_z &= k_p - k_{sz} - k_{iz} \\ &= k_p - \sqrt{(k_s)^2 - (\vec{\kappa}_s)^2} - \sqrt{(k_i)^2 - (\vec{\kappa}_i)^2} \\ &\cong k_p - k_s - k_i + \frac{(\vec{\kappa}_s)^2}{2k_s} + \frac{(\vec{\kappa}_i)^2}{2k_i} \\ &\cong k_p - k(\omega_s^0) - k(\omega_i^0) + \frac{\nu}{u_s} - \frac{\nu}{u_i} + \frac{(\vec{\kappa}_s)^2}{2k_s} + \frac{(\vec{\kappa}_i)^2}{2k_i} \\ &\cong D\nu \end{aligned} \quad (10.29)$$

where  $D \equiv 1/u_s - 1/u_i$ . We have also applied  $k_p - k(\omega_s^0) - k(\omega_i^0) = 0$  and  $|\vec{\kappa}_{s,i}| \ll |\mathbf{k}_{s,i}|$ . The “longitudinal” wavevector correlation function is rewritten as a function of the detuning frequency  $\nu$ :  $f(\Delta_z L) \cong f(\nu DL)$ . In addition to the above approximations, we have inexplicitly assumed the angular independence of the wavevector  $k = n(\theta)\omega/c$ . For type II SPDC, the refraction index of the extraordinary-ray depends on the angle between the wavevector and the optical axis and an additional term appears in the expansion. Making the approximation valid, we have restricted our calculation to near-collinear process. Thus, for a good approximation, in the near-collinear experimental setup

$$\Delta_z L \cong \nu DL = \frac{(\omega_s - \omega_i)DL}{2}. \quad (10.30)$$

Type-I degenerate SPDC is a special case. Due to the fact that  $u_s = u_i$ , and hence,  $D = 0$ , the expansion of  $k(\omega)$  should be carried out up to the second order. Instead of (10.30), we have

$$\Delta_z L \cong -\nu^2 D'L = -\frac{(\omega_s - \omega_i)^2 D'L}{4} \quad (10.31)$$

where

$$D' \equiv \frac{d}{d\omega} \left( \frac{1}{u} \right) \Big|_{\omega^0}.$$

The two-photon state of the signal–idler pair is then approximated as

$$|\Psi\rangle = \int d\nu d\vec{\kappa}_s d\vec{\kappa}_i f(\nu) h_{tr}(\vec{\kappa}_s + \vec{\kappa}_i) \hat{a}_s^\dagger(\omega_s^0 + \nu, \vec{\kappa}_s) \hat{a}_i^\dagger(\omega_i^0 - \nu, \vec{\kappa}_i) |0\rangle \quad (10.32)$$

where the normalization constant has been absorbed into  $f(\nu)$ .

## 10.5 EPR Correlation of Entangled Biphoton System

EPR state is a pure state that characterizes the behavior of an entangled biphoton system. The state is in the form of coherent superposition among a set of specially selected two-photon states. The EPR correlation, or the non-trivial second-order coherence  $G^{(2)}(\mathbf{r}_1, t_1; \mathbf{r}_2, t_2)$ , is the result of a nonlocal interference among this peculiar set of biphoton amplitudes, which specifies the probability for jointly detecting a photon pair at coordinates  $(\mathbf{r}_1, t_1)$  and  $(\mathbf{r}_2, t_2)$ . In principle, one joint-detection event of an EPR pair involves the superposition of all biphoton amplitudes that are specified by the EPR state. One measurement of an EPR pair is able to provide all information

about the interference. A question naturally comes in this regard: Can we then observe the EPR correlation from the measurement of one EPR pair? Generally speaking, in quantum mechanics, we may never learn any meaningful physics from the measurement of one pair of particles. On one hand, in photon counting, the outcome of a measurement is just a *yes* (a count or a “click”) or *no* (no count). In a joint measurement of two photon-counting detectors, the outcome of *yes* means a *yes-yes* or a “click-click” joint-detection event. A joint-detection event of *yes* may occur at any pair of space-time coordinates  $(\mathbf{r}_1, t_1; \mathbf{r}_2, t_2)$  for a measurement, but definitely cannot occur at all points of an interference pattern. On the other hand, quantum mechanics does not predict precise coordinates  $(\mathbf{r}_1, t_1)$  and  $(\mathbf{r}_2, t_2)$  for a photon pair to appear. Rather, quantum mechanics predicts the probability for a joint-detection event to occur at a space-time point  $(\mathbf{r}_1, t_1)$  and  $(\mathbf{r}_2, t_2)$ . To learn the EPR correlation, an ensemble measurement on a large number of *identical* pairs are necessary, where *identical* means that all pairs that are involved in the measurement must be prepared in the same EPR state. The measurement of quantum coherence or correlation is typically statistical. Statistically, if the outcome of a joint measurement has its maximum probability for *yes* to occur at a certain set of values of physical observable or under a certain relationship between physical variables and 100% *no* otherwise, the measured quantum system is considered to have an EPR correlation on that observable. As a good example, EPR’s *gedankenexperiment* suggested to us a system of particle pairs with perfect correlation  $\delta(x_1 - x_2 + x_0)$  in position. To confirm the EPR correlation, we need to observe *yes* only when the positions of the two distant detectors satisfy  $x_1 - x_2 = x_0$ , and 100% *no* otherwise when  $x_1 - x_2 \neq x_0$ . To observe this peculiar EPR correlation, a realistic approach is to measure the joint-detection counting rate at each pair of chosen coordinates  $x_1$  and  $x_2$  by scanning all possible values of  $x_1 - x_2$ . In quantum optics, this means the measurement of the second-order correlation function of  $G^{(2)}(\tau_1 - \tau_2)$  (longitudinal), and/or  $G^{(2)}(\vec{\rho}_1 - \vec{\rho}_2)$  (transverse), where  $\tau_j = t_j - z_j/c$ ,  $j = 1, 2$ , and  $\vec{\rho}_j$  is the transverse coordinate of the  $j$ th point-like photon-counting detector.

Now, we exam the second-order coherence or correlation of the entangled signal–idler photon pair of SPDC

$$G^{(2)}(\mathbf{r}_1, t_1; \mathbf{r}_2, t_2) = \langle \hat{E}^{(-)}(\mathbf{r}_1, t_1) \hat{E}^{(-)}(\mathbf{r}_2, t_2) \hat{E}^{(+)}(\mathbf{r}_2, t_2) \hat{E}^{(+)}(\mathbf{r}_1, t_1) \rangle$$

where  $\hat{E}^{(-)}$  and  $\hat{E}^{(+)}$  are the negative-frequency and the positive-frequency field operators of the detection events at space-time points  $(\mathbf{r}_1, t_1)$  and  $(\mathbf{r}_2, t_2)$ . For the entangled biphoton state of SPDC,

$$\begin{aligned} G^{(2)}(\mathbf{r}_1, t_1; \mathbf{r}_2, t_2) &= |\langle 0 | \hat{E}^{(+)}(\mathbf{r}_2, t_2) \hat{E}^{(+)}(\mathbf{r}_1, t_1) | \Psi \rangle|^2 \\ &= |\psi(\mathbf{r}_1, t_1; \mathbf{r}_2, t_2)|^2 \end{aligned}$$

where

$|\Psi\rangle$  is the biphoton state

$\Psi(\mathbf{r}_1, t_1; \mathbf{r}_2, t_2)$  is the biphoton effective wavefunction that we have discussed earlier

To evaluate  $G^{(2)}(\mathbf{r}_1, t_1; \mathbf{r}_2, t_2)$  and  $\psi(\mathbf{r}_1, t_1; \mathbf{r}_2, t_2)$ , we need to propagate the field operators from the source to the space-time coordinates  $(\mathbf{r}_1, t_1)$  and  $(\mathbf{r}_2, t_2)$ .

In general, the field operator  $\hat{E}^{(+)}(\mathbf{r}, t)$  at space-time point  $(\mathbf{r}, t)$  can be written in terms of Green's function, which propagates each Fourier mode from space-time point  $(\mathbf{r}_0, t_0)$  to  $(\mathbf{r}, t)$ :

$$\hat{E}^{(+)}(\mathbf{r}, t) = \sum_{\mathbf{k}} g(\mathbf{k}, \mathbf{r} - \mathbf{r}_0, t - t_0) \hat{E}^{(+)}(\mathbf{k}, \mathbf{r}_0, t_0). \quad (10.33)$$

To simplify the notation, we have assumed one polarization in Equation 10.33. Green's function  $g(\mathbf{k}, \mathbf{r} - \mathbf{r}_0, t - t_0)$  is also called optical transfer function. For different experimental setup,  $g(\mathbf{k}, \mathbf{r} - \mathbf{r}_0, t - t_0)$  can be quite different.

Considering an idealized simple experimental setup shown in Figure 10.2, in which degenerate signal and idler pairs are received by two point photon-counting detectors  $D_1$  and  $D_2$ , respectively, for longitudinal  $G^{(2)}(\tau_1 - \tau_2)$  and transverse  $G^{(2)}(\vec{\rho}_1 - \vec{\rho}_2)$  correlation measurements. To simplify the mathematics, we further assume paraxial experimental condition. In the discussion of longitudinal and transverse correlation measurements, it is convenient to write the field  $\hat{E}^{(+)}(\mathbf{r}_j, t_j)$  in terms of its longitudinal and transverse space-time variables under the Fresnel paraxial approximation:

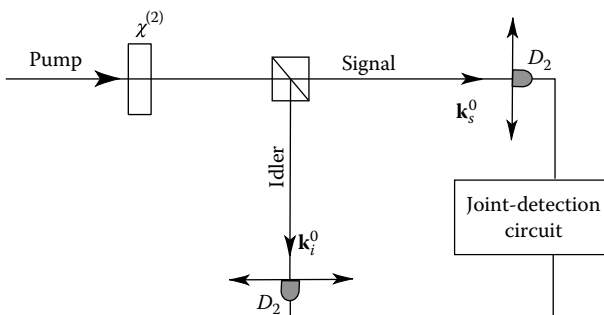


FIGURE 10.2

Degenerate signal-idler photon pair ( $\mathbf{k}_s^0 = \mathbf{k}_i^0$  at the output of SPDC) are received by two distant point photodetectors  $D_1$  and  $D_2$ , respectively, for longitudinal  $G^{(2)}(\tau_1 - \tau_2)$  and transverse  $G^{(2)}(\vec{\rho}_1 - \vec{\rho}_2)$  correlation measurements. To simplify the mathematics, we assume paraxial propagation of the signal-idler photon pair. The  $z_1$  and  $z_2$  are chosen along the central wavevector  $\mathbf{k}_s^0$  and  $\mathbf{k}_i^0$ .

$$\begin{aligned}\hat{E}^{(+)}(\vec{\rho}_j, z_j, t_j) &\cong \int d\omega d\vec{\kappa} g(\vec{\kappa}, \omega; \vec{\rho}_j, z_j) e^{-i\omega t_j} a(\omega, \vec{\kappa}) \\ &\cong \int d\omega d\vec{\kappa} \gamma(\vec{\kappa}, \omega; \vec{\rho}_j, z_j) e^{-i\omega t_j} a(\omega, \vec{\kappa})\end{aligned}\quad (10.34)$$

where

$g(\vec{\kappa}, \omega; \vec{\rho}_j, z_j) = \gamma(\vec{\kappa}, \omega; \vec{\rho}_j, z_j) e^{i\omega z_j/c}$  is the spatial part of the Green's function  
 $\vec{\rho}_j$  and  $z_j$  are the transverse and longitudinal coordinates of the  $j$ th photodetector

$\vec{\kappa}$  is the transverse wavevector

We have chosen  $z_0 = 0$  and  $t_0 = 0$  at the output plane of the SPDC. For convenience, all constants associated with the field are absorbed into  $g(\vec{\kappa}, \omega; \vec{\rho}_j, z_j)$ .

The two-photon effective wavefunction  $\Psi(\vec{\rho}_1, z_1, t_1; \vec{\rho}_2, z_2, t_2)$  is thus calculated as a superposition of biphoton amplitudes

$$\begin{aligned}\Psi(\vec{\rho}_1, z_1, t_1; \vec{\rho}_2, z_2, t_2) &= \langle 0 | \int d\omega' d\vec{\kappa}' g(\vec{\kappa}', \omega'; \vec{\rho}_2, z_2) e^{-i\omega' t_2} a(\omega', \vec{\kappa}') \\ &\quad \times \int d\omega'' d\vec{\kappa}'' g(\vec{\kappa}'', \omega''; \vec{\rho}_1, z_1) e^{-i\omega'' t_1} a(\omega'', \vec{\kappa}'') \\ &\quad \times \int dv d\vec{k}_s d\vec{k}_i f(v) h_{tr}(\vec{k}_s + \vec{k}_i) \hat{a}_s^\dagger(\omega_s^0 + v, \vec{k}_s) \hat{a}_i^\dagger(\omega_i^0 - v, \vec{k}_i) | 0 \rangle \\ &= e^{-i(\omega_s^0 \tau_1 + \omega_i^0 \tau_2)} \int dv d\vec{k}_s d\vec{k}_i f(v) h_{tr}(\vec{k}_s + \vec{k}_i) \\ &\quad \times e^{-iv(\tau_1 - \tau_2)} \gamma(\vec{k}_s, v; \vec{\rho}_1, z_1) \gamma(\vec{k}_i, -v; \vec{\rho}_2, z_2).\end{aligned}\quad (10.35)$$

Although Equation 10.35 cannot be factorized into a product of longitudinal and transverse integrals, it is not difficult to calculate the temporal correlation and the transverse spatial correlation separately by choosing suitable experimental conditions.

Typical experiment may be designed for measuring either temporal (longitudinal) or spatial (transverse) correlation only. Thus, based on different experimental setups, we may simplify the calculation to either temporal (longitudinal) correlation

$$\Psi(\tau_1; \tau_2) = \Psi_0 e^{-i(\omega_s^0 \tau_1 + \omega_i^0 \tau_2)} \int dv f(v) e^{-iv(\tau_1 - \tau_2)} \quad (10.36)$$

or spatial (transverse) correlation

$$\Psi(\vec{\rho}_1, z_1; \vec{\rho}_2, z_2) = \Psi_0 \int d\vec{k}_s d\vec{k}_i h_{tr}(\vec{k}_s + \vec{k}_i) g(\vec{k}_s, \omega_s; \vec{\rho}_1, z_1) g(\vec{k}_i, \omega_i; \vec{\rho}_2, z_2). \quad (10.37)$$

In certain experimental conditions, we may approximate  $h_{tr}(\vec{\kappa}_s + \vec{\kappa}_i) \sim \delta(\vec{\kappa}_s + \vec{\kappa}_i)$ .

### (I) Biphoton temporal correlation

To measure the biphoton temporal correlation of SPDC, we select a pair of transverse wavevector  $\vec{\kappa}_s = -\vec{\kappa}_i$  in Equation 10.35 by using appropriate optical apertures. The effective two-photon wavefunction is thus simplified to that of Equation 10.36

$$\begin{aligned}\Psi(\tau_1; \tau_2) &\cong \Psi_0 e^{-i(\omega_s^0 \tau_1 + \omega_i^0 \tau_2)} \int d\nu f(\nu) e^{-i\nu(\tau_1 - \tau_2)} \\ &= [\Psi_0 e^{-\frac{i}{2}(\omega_s^0 + \omega_i^0)(\tau_1 + \tau_2)}] [\mathcal{F}_{\tau_1 - \tau_2} \{f(\nu)\} e^{-\frac{i}{2}(\omega_s^0 - \omega_i^0)(\tau_1 - \tau_2)}]\end{aligned}\quad (10.38)$$

where, again,  $\mathcal{F}_{\tau_1 - \tau_2} \{f(\nu)\}$  is the Fourier transform of the spectrum amplitude function  $f(\nu)$ . Equation 10.38 indicates a 2D wavepacket: a  $\delta$ -function like narrow envelope along axis  $\tau_1 - \tau_2$  with constant amplitude in axis  $\tau_1 + \tau_2$ . For fixed positions of the photodetectors  $D_1$  and  $D_2$ , the 2D wavepacket means the following: the signal-idler pair may be jointly detected at any time; however, if the signal is registered at a certain time  $t_1$ , the idler must be registered at a unique time of  $t_2 \sim t_1 - (z_1 - z_2)/c$ . In other words, although the joint-detection of the pair may happen at any times of  $t_1$  and  $t_2$  with equal probability ( $\Delta(t_1 + t_2) \sim \infty$ ), the registration time difference of the pair must be a constant  $\Delta(t_1 - t_2) \sim 0$ . A schematic of the wavepacket has been shown in Chapter 9.

As we have discussed in Chapter 9, the longitudinal correlation function  $G^{(2)}(\tau_1 - \tau_2)$  is thus

$$G^{(2)}(\tau_1 - \tau_2) \propto |\mathcal{F}_{\tau_1 - \tau_2} \{f(\nu)\}|^2,$$

which is a  $\delta$ -function-like function in the case of SPDC. Thus, we have shown the entangled signal-idler photon pair of SPDC hold a typical EPR correlation in energy and time:

$$\Delta(\omega_s + \omega_i) \sim 0 \quad \text{and} \quad \Delta(t_1 - t_2) \sim 0$$

with

$$\Delta\omega_s \sim \infty, \quad \Delta\omega_i \sim \infty, \quad \Delta t_1 \sim \infty, \quad \Delta t_2 \sim \infty.$$

### (II) Biphoton spatial correlation

In the following, we study the spatial correlation  $G^{(2)}(\vec{p}_1, z_1; \vec{p}_2, z_2)$  of entangled biphoton state in three different measurements: (1) in the output plane of the source, (2) in the Fraunhofer far field, and (3) in the Fresnel near field. Similar to that of the biphoton temporal correlation, we will calculate the

effective biphoton wavefunction of the signal–idler pair under the above three conditions. To simplify the mathematics, we will concentrate our calculation on the spatial function only by choosing a pair of monochromatic conjugate frequencies  $\omega_s$  and  $\omega_i$ . In this case, the effective two-photon wavefunction of Equation 10.35 is simplified to that of Equation 10.37:

$$\Psi(\vec{\rho}_1, z_1; \vec{\rho}_2, z_2) = \Psi_0 \int d\vec{k}_s d\vec{k}_i \delta(\vec{k}_s + \vec{k}_i) g(\vec{k}_s, \omega_s, \vec{\rho}_1, z_1) g(\vec{k}_i, \omega_i, \vec{\rho}_2, z_2)$$

where we have assumed  $h_{tr}(\vec{k}_s + \vec{k}_i) \sim \delta(\vec{k}_s + \vec{k}_i)$ , which is reasonable for a large transverse sized SPDC.

### 1. $\Psi(\vec{\rho}_1, z_1; \vec{\rho}_2, z_2)$ in the output plane of SPDC

The integral of  $d\vec{k}_s$  and  $d\vec{k}_i$  can be evaluated easily with the help of the EPR-type transverse wavevector correlation  $\delta(\vec{k}_s + \vec{k}_i)$ :

$$\begin{aligned} & \int d\vec{k}_s d\vec{k}_i \delta(\vec{k}_s + \vec{k}_i) e^{-i\vec{k}_s \cdot \vec{\rho}_s} e^{-i\vec{k}_i \cdot \vec{\rho}_i} \\ &= \int d(\vec{k}_s + \vec{k}_i) \delta(\vec{k}_s + \vec{k}_i) e^{-i(\vec{k}_s + \vec{k}_i) \cdot (\vec{\rho}_s + \vec{\rho}_i)/2} \int d(\vec{k}_s - \vec{k}_i) e^{-i(\vec{k}_s - \vec{k}_i) \cdot (\vec{\rho}_s - \vec{\rho}_i)/2} \\ &\simeq 1 \times \delta(\vec{\rho}_s - \vec{\rho}_i), \end{aligned} \quad (10.39)$$

where we have assumed uniformly distributed signal–idler fields with incident (or output) angle  $\theta_s \sim |\vec{k}_s|/|\mathbf{k}_s|$  and  $\theta_i \sim |\vec{k}_i|/|\mathbf{k}_i|$  relative to the output plane:  $A(\vec{\rho}_s) \sim e^{-i\vec{k}_s \cdot \vec{\rho}_s}$  and  $A(\vec{\rho}_i) \sim e^{-i\vec{k}_i \cdot \vec{\rho}_i}$ . Equation 10.39 indicates an idealized 2D wavepacket in terms of its transverse spatial coordinates: a normalized constant distribution along the axis of  $(\vec{\rho}_s + \vec{\rho}_i)$ , which is the Fourier transform of  $\delta(\vec{k}_s + \vec{k}_i)$ ; and a  $\delta$ -function along the axis of  $(\vec{\rho}_s - \vec{\rho}_i)$ , which is the Fourier transform of a normalized constant.

Thus, we have shown that the entangled signal–idler photon pair of SPDC holds a typical EPR correlation in transverse momentum and position, which is very close to the original proposal of EPR:

$$\Delta(\vec{k}_s + \vec{k}_i) \sim 0 \quad \text{and} \quad \Delta(\vec{\rho}_s - \vec{\rho}_i) \sim 0$$

with

$$\Delta\vec{k}_s \sim \infty, \quad \Delta\vec{k}_i \sim \infty, \quad \Delta\vec{\rho}_s \sim \infty, \quad \Delta\vec{\rho}_i \sim \infty.$$

In EPR's language, we may never know where to locate the signal photon and the idler photon on the output plane of the source, however, if the signal (idler) is found at a certain position, the idler (signal) must be observed at a corresponding unique position. Simultaneously, the signal photon and the idler may have any transverse momentum, however, if the signal (idler) is measured with a transverse momentum, the transverse momentum of the idler (signal) is uniquely determined with certainty. In the *collinear* SPDC: the signal–idler pair is always emitted from the same point in the output plane of the two-photon source,  $\vec{\rho}_s = \vec{\rho}_i$ , and if one of them

propagates slightly off from the collinear axes, the other one must propagate to the opposite direction with  $\vec{\kappa}_s = -\vec{\kappa}_i$ . This interesting behavior has been experimentally utilized in quantum imaging.

One may not have too much problem to face the above statement. The interaction of spontaneous parametric down-conversion is nevertheless a local phenomenon that occurs inside the nonlinear material. The nonlinear interaction coherently creates mode in pairs that satisfy the phase match conditions of Equation 10.15 which is also named as the energy conservation and momentum conservation. The signal–idler photon pair can be excited to any of these coupled modes or in all of these coupled modes simultaneously, resulting in a particular two-photon superposition. It is this “peculiar” two-photon superposition made the signal–idler pair comes out from the same point of the source and propagates to opposite directions with  $\vec{\kappa}_s = -\vec{\kappa}_i$ .\*

## 2. $\Psi(\vec{\rho}_1, z_1; \vec{\rho}_2, z_2)$ in the Fraunhofer far field

The two-photon superposition is getting more interesting when the signal–idler is propagated to a large distance, either by free propagation or guided by optical components such as lenses. In classical opinion, the signal photon and the idler photon are considered independent whenever they are released from the source because there is no interaction more between the pair in free space. Therefore, the signal photon and the idler photon should have independent and random distributions in terms of their transverse position  $\vec{\rho}_1$  and  $\vec{\rho}_2$ . This classical picture, however, is incorrect. It is found that the signal–idler biphoton system would not lose its entangled nature in transverse position. This interesting behavior has been experimentally observed in quantum imaging, indicating an EPR-type correlation of  $\delta(\vec{\rho}_1 - \vec{\rho}_2)$ . The sub-diffraction limit spatial resolution observed in the “quantum lithography” experiment and the nonlocal correlation observed in the “ghost imaging” experiment are both the results of two-photon superposition. Two-photon superposition does happen to a distant joint detection event of a signal–idler photon pair. There is no surprise one would have difficulties to face this effect. The two-photon superposition is a nonlocal concept in this case. The biphoton amplitudes in the two-photon superposition correspond to different yet indistinguishable alternative ways of triggering a joint photodetection event at distance. There is no counterpart for this concept in classical theory and may never be understood classically.

---

\* Mathematically, we have approved  $\vec{\kappa}_s \simeq -\vec{\kappa}_i$  and  $\vec{\rho}_s \simeq \vec{\rho}_i$  in SPDC. Physically, this peculiar behavior distinguishes the entangled biphoton radiation from classical light. Applying  $\vec{\kappa}_s = -\vec{\kappa}_i$  directly to the calculation, the integral of Equation 10.39 can be simplified as

$$\int d\vec{\kappa}_s d\vec{\kappa}_i \delta(\vec{\kappa}_s + \vec{\kappa}_i) e^{-i\vec{\kappa}_s \cdot \vec{\rho}_s} e^{-i\vec{\kappa}_i \cdot \vec{\rho}_i} \simeq \int d\vec{\kappa}_s e^{-i\vec{\kappa}_s \cdot (\vec{\rho}_s - \vec{\rho}_i)} \simeq \delta(\vec{\rho}_s - \vec{\rho}_i),$$

and effectively gives  $\vec{\rho}_s \simeq \vec{\rho}_i$ . Physically and mathematically, based on  $\vec{\kappa}_s \simeq -\vec{\kappa}_i$  and  $\vec{\rho}_s \simeq \vec{\rho}_i$  we may find a better way to view the physics behind the observation and to simplify the calculation significantly.

Now we consider propagating the signal–idler pair away from the source to the far-field observation points  $(\vec{\rho}_1, z_1)$  and  $(\vec{\rho}_2, z_2)$ , respectively. To simplify the discussion, we place  $D_1$  and  $D_2$  on the plane of  $z_1 = z_2$ . In the far field, either achieved by moving  $D_1$  and  $D_2$  to distances or by the use of a Fourier transform lens, we take a first-order approximation in the phase delay, i.e.,  $r \simeq r_0 - \vec{k} \cdot \vec{\rho}_0$ , where  $r$  is the distance from point  $\vec{\rho}_0$  to  $D_1$  or  $D_2$ ,  $r_0$  is the distance from the origin point of the coordinate system, which is defined as the center point in the output plane of the SPDC, to  $D_1$  or  $D_2$ . In this case, the effective biphoton wavefunction is approximated as

$$\begin{aligned}\Psi(\vec{\rho}_1, z_1; \vec{\rho}_2, z_2) &\simeq \langle 0 | \frac{e^{-i(\omega t_1 - k_1 r_{01})}}{r_{01}} \int d\vec{\rho}_0 A(\vec{\rho}_0) e^{-i\vec{k}_1 \cdot \vec{\rho}_0} \hat{a}(\vec{k}_1) \\ &\quad \times \frac{e^{-i(\omega t_2 - k_2 r_{02})}}{r_{02}} \int d\vec{\rho}'_0 A(\vec{\rho}'_0) e^{-i\vec{k}_2 \cdot \vec{\rho}'_0} \hat{a}(\vec{k}_2) \\ &\quad \times \int d\vec{k}_s d\vec{k}_i \delta(\vec{k}_s + \vec{k}_i) \hat{a}^\dagger(\vec{k}_s) \hat{a}^\dagger(\vec{k}_i) | 0 \rangle \\ &\propto \int d\vec{\rho}_0 d\vec{\rho}'_0 \delta(\vec{\rho}_0 - \vec{\rho}'_0) e^{-i\vec{k}_1 \cdot \vec{\rho}_0} e^{-i\vec{k}_2 \cdot \vec{\rho}'_0} \\ &\propto 1 \times \delta(\vec{\rho}_1 + \vec{\rho}_2).\end{aligned}\tag{10.40}$$

The  $\delta$ -function of  $\delta(\vec{\rho}_0 - \vec{\rho}'_0)$  in Equation 10.40 is obtained from the double integral of  $d\vec{k}_s$  and  $d\vec{k}_i$  with  $A(\vec{\rho}_0) \sim A_0 e^{-i\vec{k}_s \cdot \vec{\rho}_0}$  and  $A(\vec{\rho}'_0) \sim A_0 e^{-i\vec{k}_i \cdot \vec{\rho}'_0}$  where  $A_0$  is a constant. The physics is very clear in the above calculation. (1) The far-filed plane is the Fourier transform plane of the SPDC. Each point on the Fourier transform plane corresponds to a  $\vec{k}_s$  or  $\vec{k}_i$ . The  $\delta$ -function  $\delta(\vec{\rho}_1 + \vec{\rho}_2)$  on the Fourier transform plane confirms  $\delta(\vec{k}_s + \vec{k}_i)$ . (2) The 2D wavepacket in transverse spatial coordinates is the result of a superposition among a large number of biphoton amplitudes. Each biphoton amplitude starts from a point on the output plane of SPDC (at  $\vec{\rho}_0 = \vec{\rho}'_0$ ) and ends at point photodetectors  $D_1$  and  $D_2$ . The 2D wavepacket indicates a typical EPR correlation: we may observe the signal photon and the idler photon at any point on a far-field plane of the entangled biphoton source, however, if one of them is observed at a certain point, the other one can only be observed at a unique point.

In the the above calculation, we have treated all integrals to infinity. This approximation yields  $\delta$ -function for constant distributions. In reality, the finite size of the biphoton source or the applied lenses in the experimental setup may have to be taken into account. Let us assume a finite integral on a circular area from  $|\vec{\rho}_0| = 0$  to  $|\vec{\rho}_0| = R$  for degenerate SPDC ( $\omega_s = \omega_i$ ), the integral of Equation 10.40 turns

$$\begin{aligned}\Psi(\vec{\rho}_1, z_1; \vec{\rho}_2, z_2) &\propto \int_A d\vec{\rho}_0 e^{-i(\vec{k}_1 + \vec{k}_2) \cdot \vec{\rho}_0} \simeq \frac{2J_1[R|\vec{k}_1 + \vec{k}_2|]}{R|\vec{k}_1 + \vec{k}_2|} \\ &= \text{somb} \left[ \frac{R\omega}{zc}(\vec{\rho}_1 + \vec{\rho}_2) \right],\end{aligned}\tag{10.41}$$

indicating a Fraunhofer diffraction pattern in the joint-detection of  $D_1$  and  $D_2$ , which is a sombrero-function of  $\vec{\rho}_1 + \vec{\rho}_2$ . For large-sized SPDC, nevertheless,  $\delta$ -functions are good approximations.

### 3. $\Psi(\vec{\rho}_1, z_1; \vec{\rho}_2, z_2)$ in the Fresnel near-field

We now consider the Fresnel near-field measurement by moving  $D_1$  and  $D_2$  to the near field of the biphoton source. We further assume the two-photon source has a finite but large transverse dimension. Under this simple experimental setup, the Green's function, or the optical transfer function describing arm- $j$ ,  $j = 1, 2$ , in which the signal and the idler freely propagate to photodetectors  $D_1$  and  $D_2$ , respectively. Substituting the  $g_j(\omega, \vec{\kappa}; z_j, \vec{\rho}_j)$  of free propagation,  $j = 1, 2$ , into Equation 10.37, the effective wavefunction is thus

$$\begin{aligned} & \Psi(\vec{\rho}_1, z_1; \vec{\rho}_2, z_2) \\ &= \Psi_0 \int d\vec{\kappa}_s d\vec{\kappa}_i \delta(\vec{\kappa}_s + \vec{\kappa}_i) e^{-i\vec{\kappa}_s \cdot \vec{\rho}_0} e^{-i\vec{\kappa}_i \cdot \vec{\rho}'_0} \\ & \quad \times \int_A d\vec{\rho}_0 \frac{-i\omega_s}{2\pi c z_1} e^{i\frac{\omega_s}{c} z_1} G\left(|\vec{\rho}_1 - \vec{\rho}_s|, \frac{\omega_s}{cz_1}\right) \\ & \quad \times \int_A d\vec{\rho}'_0 \frac{-i\omega_i}{2\pi c z_2} e^{i\frac{\omega_i}{c} z_2} G\left(|\vec{\rho}_2 - \vec{\rho}'_0|, \frac{\omega_i}{cz_2}\right) \\ & \simeq \frac{-\omega_s \omega_i}{2\pi^2 c^2 z_1 z_2} e^{i\left(\frac{\omega_s}{c} z_1 + \frac{\omega_i}{c} z_2\right)} \int_A d\vec{\rho}_0 e^{i\left[\frac{\omega_s}{2cz_1} |\vec{\rho}_1 - \vec{\rho}_0|^2 + \frac{\omega_i}{2cz_2} |\vec{\rho}_2 - \vec{\rho}_0|^2\right]} \end{aligned} \quad (10.42)$$

where  $\vec{\rho}_0$  ( $\vec{\kappa}_s$ ) and  $\vec{\rho}'_0$  ( $\vec{\kappa}_i$ ) are the transverse coordinates (wavevectors) for the signal and the idler fields, respectively, defined on the output plane of the biphoton source. The superposition of the above large number of biphoton amplitudes will produce a biphoton Fresnel diffraction pattern as a function of  $\vec{\rho}_1$  and  $\vec{\rho}_2$ . Mathematically, it may not be easy to find an analytical solution for arbitrary  $\vec{\rho}_1$  and  $\vec{\rho}_2$ , numerical solutions are always helpful for comparing with the experimental observation.

## 10.6 Subsystem in an Entangled Two-Photon State

The entangled EPR two-particle state is a pure state. The precise correlation of the subsystems is completely described by the state. The measurement, however, is not necessarily always for the two-particle system. It is an experimental choice to study only one subsystem and to ignore the other. What can we learn about a subsystem from these kinds of measurements? Mathematically, it is easy to show that by taking a partial trace of a two-particle

pure state, the subsystems are both in mixed states with entropy greater than zero. One can only learn statistical properties of the subsystems in this kind of measurement.

In the following, again, we use the signal–idler pair of SPDC as an example to explore the physics. The biphoton state of SPDC is a pure state that satisfies

$$\hat{\rho}^2 = \hat{\rho}, \quad \hat{\rho} \equiv |\Psi\rangle\langle\Psi| \quad (10.43)$$

where  $\hat{\rho}$  is the density matrix operator corresponding to the biphoton state of SPDC. The state of the signal photon and the idler photon, respectively,

$$\hat{\rho}_s = \text{tr}_i |\Psi\rangle\langle\Psi|, \quad \hat{\rho}_i = \text{tr}_s |\Psi\rangle\langle\Psi|, \quad (10.44)$$

are not. To calculate the signal (idler) state from the biphoton state, we have to take a partial trace, as usual, summing over the idler (signal) modes.

We assume a type II SPDC. The orthogonally polarized signal and idler are degenerate in frequency around  $\omega^0 \cong \omega_p/2$ . To simplify the discussion, by assuming appropriate experimental conditions, we trivialize the transverse part of the state and write the biphoton state in the following simplified form:

$$|\Psi\rangle = \Psi_0 \int d\nu \Phi(DL\nu) \hat{a}_s^\dagger(\omega^0 + \nu) \hat{a}_i^\dagger(\omega^0 - \nu) |0\rangle$$

where  $\Phi(DL\nu)$  is a *sinc*-like function:

$$\Phi(DL\nu) = \frac{1 - e^{-iDL\nu}}{iDL\nu}$$

which is a function of the crystal length  $L$ , and the difference of inverse group velocities of the signal (ordinary) and the idler (extraordinary),  $D \equiv 1/u_o - 1/u_e$ . The constant  $\Psi_0$  is calculated from the normalization  $\text{tr } \hat{\rho} = \langle \Psi | \Psi \rangle = 1$ . It is easy to calculate and to find  $\hat{\rho}^2 = \hat{\rho}$  for the biphoton state of the signal–idler pair.

Summing over the idler modes, the density matrix of signal is given by

$$\hat{\rho}_s = \Psi_0^2 \int d\nu |\Phi(\nu)|^2 \hat{a}_s^\dagger(\omega^0 + \nu) |0\rangle\langle 0| \hat{a}_s(\omega^0 + \nu) \quad (10.45)$$

with

$$|\Phi(\nu)|^2 = \text{sinc}^2 \frac{DL\nu}{2} \quad (10.46)$$

where all constants coming from the integral have been absorbed into  $\Psi_0$ . First, we find immediately that  $\hat{\rho}_s^2 \neq \hat{\rho}_s$ . It means the state of the signal is a mixed state (as is the idler). Second, it is very interesting to find that

the spectrum of the signal dependents on the group velocity of the idler. This, however, should not come as a surprise, because the state of the signal photon is calculated from the biphoton state by summing over the idler modes.

The spectrum of the signal and idler has been experimentally verified by Strekalov et al. by using a Michelson interferometer in a standard Fourier spectroscopy-type measurement. The measured interference pattern is shown in Figure 10.3. The envelope of the sinusoidal modulations (in segments) is fitted very well by two “notch” functions (upper and lower part of the envelope). The experimental data agrees with the theoretical analysis of the experiment.

The following is a simple calculation to explain the observed notch function. We first define the field operators:

$$\hat{E}^{(+)}(t, z_d) = \hat{E}_1^{(+)}\left(t - \frac{z_1}{c}, z_0\right) + \hat{E}_2^{(+)}\left(t - \frac{z_2}{c}, z_0\right)$$

where

$z_d$  is the position of the photodetector

$z_0$  is the input point of the interferometer

$t_1 = t - \frac{z_1}{c}$  and  $t_2 = t - \frac{z_2}{c}$ , respectively, are the early times before prop-

agated to the photodetector at time  $t$  with time delays of  $z_1/c$  and  $z_2/c$ , where  $z_1$  and  $z_2$  are the optical paths in arm 1 and arm 2 of the interferometer

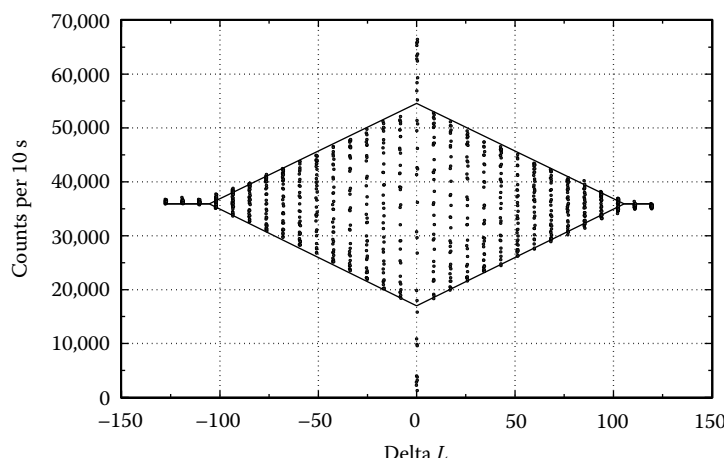


**FIGURE 10.3**

Experimental data indicated a “double notch” envelope. Each of the dotted single vertical lines contains many cycles of sinusoidal modulation.

We have defined a very general field operator, which is the superposition of two early fields propagated individually through arm 1 and arm 2 of any type of interferometer. The counting rate of the photon-counting detector is thus

$$\begin{aligned}
 R_d &= \text{tr} [\hat{\rho}_s \hat{E}^{(-)}(t, z_d) \hat{E}^{(+)}(t, z_d)] \\
 &= \Psi_0^2 \int d\nu |\Phi(\nu)|^2 |\langle 0 | \hat{E}^{(+)}(t, z_d) \hat{a}_s^\dagger(\omega^0 + \nu) | 0 \rangle|^2 \\
 &= \Psi_0^2 \int d\nu |\Phi(\nu)|^2 \left| \langle 0 | \left[ \hat{E}_1^{(+)} \left( t - \frac{z_1}{c}, z_0 \right) \right. \right. \\
 &\quad \left. \left. + \hat{E}_2^{(+)} \left( t - \frac{z_1}{c}, z_0 \right) \right] \hat{a}_s^\dagger(\omega^0 + \nu) | 0 \rangle \right|^2 \\
 &\propto 1 + \text{Re} \left\{ e^{-i\omega^0 \tau} \int d\nu \text{sinc}^2 \frac{DL\nu}{2} e^{-i\nu\tau} \right\}
 \end{aligned} \tag{10.47}$$

where  $\tau = (z_1 - z_2)/c$ . The Fourier transform of  $\text{sinc}^2(DL\nu/2)$  has a notch shape. It is noticed that the base of the notch function is determined by parameter  $DL$  of the SPDC, which is easily confirmed from the experiment.

Now we turn to another interesting aspect of physics, namely, the physics of entropy. Entropy is an important concept in the information theory. The concept, named as von Neumann entropy, is given by the state

$$S = -\text{tr}(\hat{\rho} \log \hat{\rho}). \tag{10.48}$$

It is easy to find that the entropy of the entangled two-photon pure state is zero. The entropy of both its subsystems, however, is greater than zero. The value of the von Neumann entropy can be numerically evaluated from the measured spectrum. Note that the density operator of the subsystem is diagonal. Taking its trace is simply performing an integral over the frequency spectrum with the measured spectrum function. It is straightforward to find the entropy of the subsystems  $S_s > 0$ . This is an expected result due to the nature of the mixed state of the subsystems. Considering that the entropy of the two-photon system is zero and the entropy of the subsystems are both greater than zero, does this mean that negative entropy is present somewhere in the entangled two-photon system? According to classical information theory, for the entangled two-photon system,  $S_s + S_{s|i} = 0$ , where  $S_{s|i}$  is the conditional entropy. It is this conditional entropy that must be negative, which means that *given the result of a measurement over one particle, the result of measurement over the other must yield negative information*. This paradoxical statement is similar and, in fact, closely related to the EPR “paradox.” It comes from the same philosophy as that of the EPR.

## 10.7 Biphoton in Dispersive Media

In this section, we study the propagation of entangled photons in optical dispersive medium. Dispersion contains rich physics in general. It is not our goal to discuss in detail about biphoton dispersion, here, we give a simple analysis on the propagation of the entangled signal–idler pair of a CW-pumped SPDC in group-dispersive optical fibers. As we have learned, although a biphoton wavepacket is defined with the two-photon state of SPDC, there is no wavepacket defined with the subsystems of the signal and the idler. After propagating the signal and the idler a certain distance in optical fibers, do we expect a “broadened” signal or idler photon? It is interesting to find that there is no wavepacket, either broadened or unbroadened, associated with the propagation of either signal or idler individually. It is the biphoton wavefunction  $\psi(t_1, r_1; t_2, r_2)$  or the second-order correlation function  $G^{(2)}(t_1, r_1; t_2, r_2)$  that is broadened in the dispersive medium. The biphoton wavepacket in dispersive medium propagates like a classical optical pulse.

Let us consider a simple experiment, as shown in Figure 10.4. We use a biphoton source of a CW laser-pumped SPDC and two point-like photon-counting detectors with a photon-counting coincidence circuit to setup a standard second-order temporal correlation measurement. The photodetectors  $D_1$  and  $D_2$  are placed in the far-field zone of  $z_1$  and  $z_2$ , respectively, for the detection of the signal and the idler photons. The photon-counting circuit records the registration time difference,  $t_1 - t_2$ , for each signal (registered at  $t_1$ )–idler (registered at  $t_2$ ) pair. After measuring a large number of pairs, the circuit reports a histogram that summarizes how many total number of

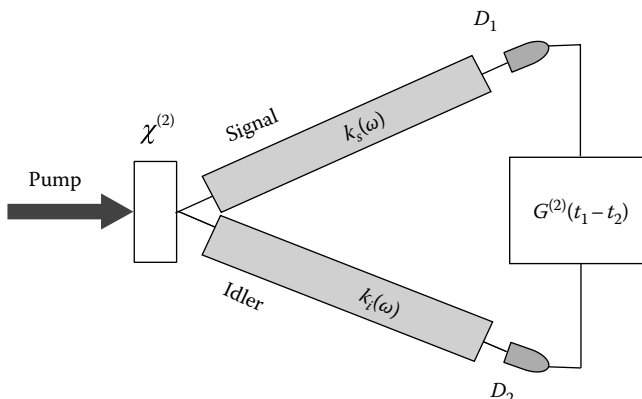


**FIGURE 10.4**

Broadening of  $G^{(2)}(t_1 - t_2)$  due to the propagation of the signal and idler photon pair in group-dispersive media.

pairs (vertical axis) are measured with each value of  $t_1 - t_2$  (horizontal axis). The measured histogram, number of joint-detection counting rate against  $t_1 - t_2$ , corresponds to the seconder-order temporal correlation function  $G^{(2)}(t_1 - t_2)$ .

In vacuum, or realistically in the air, the observed function  $G^{(2)}(t_1 - t_2)$  in the temporal correlation measurement. As we have learned earlier, the observed function  $G^{(2)}(t_1 - t_2)$  is mainly determined by the phase-matching condition of the SPDC. There is no contribution from the group broadening of either signal or idler propagation. Now, we put dispersive medium, such as optical fibers, between the two-photon source and the photodetectors,  $D_1$  and  $D_2$ . The dispersive medium has unignoreable first-order and second-order dispersions:

$$\frac{dk(\omega)}{d\omega} \Big|_{\omega_s^0} = k' \neq 0 \quad \text{and} \quad \frac{d^2k(\omega)}{d\omega^2} \Big|_{\omega_i^0} = k'' \neq 0$$

at the neighborhood of the wavelengths  $\omega_s^0$  and  $\omega_i^0$ , where  $\omega_s^0$  and  $\omega_i^0$  are the central frequencies of the signal–idler radiation. The following calculation will answer the questions about what will happen to the  $G^{(2)}(t_1 - t_2)$  function: Is the function  $G^{(2)}(t_1 - t_2)$  broadened by the dispersive propagation of the signal and the idler?

The state of the signal–idler biphoton pair of SPDC, generated by a CW laser beam at frequency  $\omega_p$ , can be written in the following simplified form as we have derived earlier:

$$|\Psi\rangle = \int_{-\infty}^{\infty} d\nu f(\nu) \hat{a}_s^\dagger(\omega_s^0 + \nu) \hat{a}_i^\dagger(\omega_i^0 - \nu) |0\rangle$$

where, again,  $\omega_s^0$  and  $\omega_i^0$  are the central frequencies of the signal–idler;  $\nu$  is the returning frequency. The spectral amplitude,  $f(\nu)$ , provides all the information about the correlation properties of the two-photon light.  $f(\nu)$  is basically determined by the longitudinal part of the phase matching in SPDC. Based on the simplified biphoton state and the field operators,

$$\begin{aligned}\hat{E}_1^{(+)} &= \int d\omega_s a(\omega_s) e^{-i[\omega_s t_1 - k(\omega_s) z_1]} \\ \hat{E}_2^{(+)} &= \int d\omega_i a(\omega_i) e^{-i[\omega_i t_2 - k(\omega_i) z_2]}\end{aligned}$$

the biphoton wavepacket is calculated to be:

$$\psi(t_1, r_1; t_2, r_2) = \int d\omega_s f(\omega_s) e^{-i[\omega_s t_1 - k(\omega_s) z_1]} e^{-i[\omega_i t_2 - k(\omega_i) z_2]}. \quad (10.49)$$

Considering the first-order and the second-order dispersion of the propagation along  $z_1$  and  $z_2$ , The biphoton wavepacket turns out to be

$$\begin{aligned}\psi(t_1, z_1; t_2, z_2) &= \left\{ e^{-i\{\omega_s^0 t_1 + \omega_i^0 t_2 - [k(\omega_s^0)z_1 + k(\omega_i^0)z_2]\}} \right\} \\ &\quad \times \int_{-\infty}^{\infty} dv f(v) e^{i(k_s'' z_1 + k_i'' z_2)(v^2/2)} e^{-iv[(t_1 - t_2) - (z_1/u_s - z_2/u_i)]} \\ &= \left\{ e^{-i\{\omega_s^0 t_1 + \omega_i^0 t_2 - [k(\omega_s^0)z_1 + k(\omega_i^0)z_2]\}} \right\} \\ &\quad \times \mathcal{F}_\tau \left\{ f(v) e^{i(k_s'' z_1 + k_i'' z_2)(v^2/2)} \right\},\end{aligned}\tag{10.50}$$

where we have defined

$$\begin{aligned}\tau &\equiv (t_1 - t_2) - [z_1/u_s - z_2/u_i] \\ &= [t_1 - z_1/u_s] - [t_2 - z_2/u_i] \\ &\equiv \tau_1 - \tau_2.\end{aligned}$$

The second-order temporal correlation function  $G^{(2)}(\tau)$  is thus

$$G^{(2)}(\tau) \propto |\mathcal{F}_\tau \{ f(v) e^{i(k_s'' z_1 + k_i'' z_2)(v^2/2)} \}|^2.\tag{10.51}$$

In Equations 10.50 and 10.51,  $\mathcal{F}_\tau \{ f(v) e^{i(k_s'' z_1 + k_i'' z_2)(v^2/2)} \}$  denotes as the Fourier transform of function  $f(v) e^{i(k_s'' z_1 + k_i'' z_2)(v^2/2)}$ . It is easy to find mathematically that the Gaussian function  $e^{i(k_s'' z_1 + k_i'' z_2)v^2/2}$ , corresponding to the second-order dispersion in both optical paths of the signal and the idler, contributes to the broadening of the biphoton wavepacket  $\psi(t_1, z_1; t_2, z_2)$  as well as the second-order correlation function  $G^{(2)}(\tau)$ .

In summary, we have the following conclusions regarding to the propagation of biphoton wavepacket in dispersion media:

1. The concept of broadening of a biphoton wavepacket is fundamentally different from the broadening of two classical wavepackets. The broadening of the second-order correlation function in classical case, which can be measured by an optical autocorrelator, is due to the broadening of each measured individual pulses. In the measurement of entangled biphoton system, however, there is no wavepacket, either broadened or unbroadened, associated with the propagation of either signal or idler individually. It is the  $G^{(2)}(\tau)$  function that is broadened by the group dispersion media in 2D space of  $\tau = \tau_1 - \tau_2$ . Comparing with a classical pulse propagating in group dispersion medium, we find that it is  $G^{(2)}(\tau)$  in Equation 10.51 that plays the role of a pulse, except propagating in the 2D space of  $\tau = \tau_1 - \tau_2$ . The second-order

correlation function  $G^{(2)}(t_1, 0; t_2, 0)$  observed at the output plane of SPDC has been calculated earlier

$$G^{(2)}(t_1 - t_2) \propto |\mathcal{F}_{t_1-t_2}\{f(v)\}|^2 \sim \delta(t_1 - t_2)$$

for a large-sized  $\chi^{(2)}$  material. The  $\delta$ -function like second-order correlation function will be broadened by the dispersive media after a certain distance propagation, which is given in Equation 10.51. The broadening process is similar to that of a laser pulse propagating in the same dispersive medium.\*

2. Nonlocal dispersion cancellation: one may have realized already an interesting aspect of physics from Equation 10.50. It is easy to see that any positive (negative) group dispersion of the signal can be cancelled nonlocally by applying a negative (positive) dispersive medium in the path of the idler by achieving

$$k_s''z_1 + k_i''z_2 = 0. \quad (10.52)$$

This interesting behavior has been named “nonlocal two-photon dispersion cancellation.” No classical interpretation seems to be possible to explain this effect. Suppose we have two weak light pulses propagating through the positive and negative group-dispersion media channels, respectively, to reach  $D_1$  and  $D_2$  for second-order correlation measurement. In the view of classical physics, each pulse will be broadened locally and independently by the dispersion medium, and thus causing a statistically broadened temporal width of the second-order correlation function

$$\sigma_{12} \geq \sqrt{\sigma_1^2 + \sigma_2^2}, \quad (10.53)$$

where  $\sigma_{12}$ ,  $\sigma_1$ , and  $\sigma_2$  are the broadened widths of the correlation function and the two propagating pulses. Two-photon dispersion cancellation

\* Behaving like classical pulse in optical fiber, when the length of a group-dispersive medium is greater than its “characteristic dispersion length,”  $z_{dis} = \Delta\tau_0^2/2\pi k''$ , where  $\Delta\tau_0$  is the unbroadened initial width of  $G^{(2)}$ , the second-order correlation function  $G^{(2)}(\tau)$  is found to be

$$G^{(2)}(\tau) \sim \left| f\left(\frac{\tau}{k_s''z_1 + k_i''z_2}\right) \right|^2$$

i.e., achieving the same function as the spectrum of the SPDC. Furthermore, the width of  $G^{(2)}(\tau)$ ,  $\Delta\tau$ , is proportional to the propagation distance along the dispersive medium

$$\Delta\tau = \Delta\tau_0 \frac{z}{z_{dis}}.$$

In the far-field-zone, i.e.,  $z > z_{dis}$ ,  $\psi(t_1, z_1; t_2, z_2)$  acquires a stable form, which takes the same “shape” as the spectrum function,  $f(v)$ , and the width of  $G^{(2)}(\tau)$  is linearly proportional to the length of the known dispersive medium. This effect has been observed experimentally by Valencia et al.

is useful in certain applications, such as nonlocal timing and positioning and distant clock synchronization, in which delta-function-like EPR correlation in  $t_1 - t_2$  or in  $z_1 - z_2$  is expected.

---

## Summary

In this chapter, we discussed the physics of quantum entanglement. Quantum entanglement has been considered as one of the most surprising consequences of quantum mechanics. We have addressed three important issues in this chapter: (1) the surprising EPR correlation is the result of multiparticle (photon) interference; (2) the multiparticle (photon) superposition is nonlocal, which occurs at distant space-time coordinates and involves multiparticle (photon) detection events through the measurement of distant particle (photon) detectors; and (3) the result of multiparticle interference of entangled EPR state is special and peculiar by means of its nonfactorizable effective wavefunction, which means that the entangled particles may not be considered as independent, even if the particles are separated in large distances and are interaction free.

In this chapter, we introduced the historical EPR *gedankenexperiment*, the EPR–Bohm spin 1/2 particle system and the EPR–Bohm–Bell states. We specified the concerns of EPR on *locality*, *reality*, and *completeness*. We analyzed a typical entangled biphoton state of SPDC in detail, from the generation of the state to the calculation of the second-order correlation and the effective wavefunction in far field and near field. We have also discussed the behavior of the signal photon and the idler photon as subsystems of the biphoton state. The biphoton state of SPDC is a simple, yet good, example of entangled multiparticle system. These analysis are helpful in understanding the basic physics of quantum entanglement.

---

## Suggested Reading

- Bohm, D., *Quantum Theory*, Prentice Hall Inc., New York, 1951.
- Boyd, R.W., *Nonlinear Optics*, Academic Press, San Diego, CA, 1992.
- Einstein, A., B. Podolsky, and N. Rosen, *Phys. Rev.* 47, 777 (1935).
- Franson, J.D., *Phys. Rev. A* 45, 3126 (1992); 80, 032119 (2009); 81, 023825 (2010).
- Klyshko, D.N., *Photon and Nonlinear Optics*, Gordon & Breach Science, New York, 1988.
- Rubin, M.H., D.N. Klyshko, Y.H. Shih, and A.V. Sergienko, *Phys. Rev. A* 50, 5122 (1994).
- Schrödinger, E., *Naturwissenschaften* 23, 807, 823, 844 (1935); Translations appear in *Quantum Theory and Measurement*, J.A. Wheeler and W.H. Zurek (eds.), Princeton University Press, New York, 1983.

- Sergienko, A.V., Y.H. Shih, and M.H. Rubin, *JOSAB* 12, 859 (1995).
- Shih, Y.H., Two-photon entanglement and quantum reality, in *Advances in Atomic, Molecular, and Optical Physics*, B. Bederson and H. Walther (eds.), Academic Press, Cambridge, 1997; Entangled photons, *IEEE J. Select. Top. Quantum Electron.* 9, 6 2003.
- Strekalov, D.V., T.B. Pittman, and Y.H. Shih, *Phys. Rev. A* 57, 567 (1998).
- Strekalov, D.V., Y.H. Kim, and Y.H. Shih, *Phys. Rev. A* 60, 2685 (1999).
- Valencia, A., M.V. Chekhova, A. Trifonov, and Y.H. Shih, *Phys. Rev. Lett.* 88, 183601 (2002).
- Yariv, A., *Quantum Electronics*, John Wiley & Sons, New York, 1989.

# 11

---

## *Quantum Imaging*

---

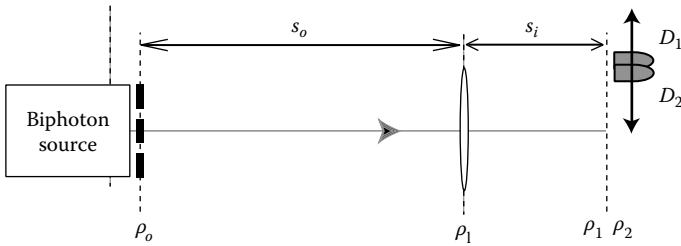
Although questions regarding fundamental issues of quantum theory still exist, quantum entanglement has started to play important roles in practical engineering applications. Quantum imaging is one of these exciting areas. Quantum imaging has so far demonstrated three peculiar features: (1) enhancing the spatial resolution of imaging beyond the diffraction limit, (2) reproducing ghost images in a “nonlocal” manner, and (3) dispersion-cancellation or turbulence-free imaging. The enhanced spatial resolution apparently violates the uncertainty principle. Ghost imaging is considered as a “nonlocal” phenomenon due to a point-to-point correlation of two interaction-free photons at distance. All the above peculiar features are the results of two-photon interference, which involves the superposition of two-photon amplitudes, a nonclassical entity corresponding to different, yet indistinguishable, alternative ways of creating a joint-detection event. The concept of two-photon interference was introduced from the study of entangled states. It is not, however, restricted to entangled states only. Multiphoton interference is a general phenomenon occurring in multiphoton joint-detection events.

In this chapter, we will focus our discussion on quantum imaging with entangled photons and with chaotic-thermal field. We will first discuss the physics of biphoton imaging including biphoton ghost imaging, and then discuss the ghost imaging of chaotic-thermal light.

---

### **11.1 Biphoton Imaging**

The concept of optical imaging has been discussed earlier. Now, we consider a standard imaging setup as shown in Figure 11.1 but replace the classical light source with entangled photon sources for joint-detection of  $N$ -fold point photodetectors. The entangled  $N$ -photon source will reproduce an image of the object with enhanced spatial resolution by a factor of  $N$ , despite the Rayleigh diffraction limit. Is the violation of classical diffraction limit equivalent to the violation of the uncertainty principle? The answer is no! The uncertainty relation for an entangled  $N$ -photon system in an  $N$ -fold joint-detection is radically different from that for  $N$  independent photons. In terms of the terminology of imaging, what we have found is that the image-forming point-spread function  $\text{somb}(x)$  has a different form in the

**FIGURE 11.1**

A typical setup of optical imaging. A lens of finite size is used to produce a magnified or demagnified image of an object with limited spatial resolution. Differing from classical imaging setup, the observation is in the joint-detection of two point-like photon-counting detectors  $D_1$  and  $D_2$ . Replacing classical light with an entangled biphoton system, the spatial resolution can be improved by a factor of 2, despite the Rayleigh diffraction limit.

case of entangled states. For example, an entangled biphoton system may produce an image in coincidences

$$R_c(\vec{\rho}_i) = \int_{\text{obj}} d\vec{\rho}_o |A(\vec{\rho}_o)|^2 \text{somb}^2 \left[ \frac{R}{s_o} \frac{2\omega}{c} \left| \vec{\rho}_o + \frac{\vec{\rho}_i}{m} \right| \right],$$

with a twice narrower point-spread function

$$\text{somb}^2 \left[ \frac{R}{s_o} \frac{2\omega}{c} \left| \vec{\rho}_o + \frac{\vec{\rho}_i}{m} \right| \right].$$

Comparing with the classical case, it is easy to see that the factor of  $2\omega$  yields a twice narrower image-forming function and results in a doubling spatial resolution for biphoton imaging.

Based on the setup of Figure 11.1, we now calculate biphoton imaging by replacing classical light source with entangled signal–idler photon pair of spontaneous parametric down-conversion (SPDC) and replacing the ordinary graphic film with a two-photon film, which is coated with two-photon material that is sensitive to two-photon transition only. We will show that in the same experimental setup, the entangled biphoton state gives rise to, on a two-photon film or equivalently a twofold joint-detection system as shown in Figure 11.1, a point-spread function twice narrower than the one obtained in classical imaging at the same wavelength. Then, without applying shorter wavelengths, entangled biphoton states improve the spatial resolution of a *two-photon image* by a factor of 2. We will also show that the entangled biphoton system yields a peculiar Fourier transform function as if it is produced by a light source with  $\lambda/2$ .

To simplify the calculation, we place the biphoton source of SPDC close enough to the object plane so that the output plane of the biphoton effectively coincides with the object plane. The above condition can be physically achieved by imaging the output plane of the SPDC onto the object plane. In this case, the signal–idler pair will be either transmitted (shown

in Figure 11.1) or reflected (in a more general setup in which the entangled photons are reflected from the surface of the object) from the same point of the object with  $\vec{\rho}_s = \vec{\rho}_i$ . We now propagate the field from the object plane to an arbitrary plane of  $z = s_0 + d$ , where  $d$  may take any values for different experimental purposes:

$$\begin{aligned} g(\vec{k}_j, \omega_j; \vec{\rho}_k, z = s_0 + d) \\ = \int_{obj} d\vec{\rho}_o \int_{lens} d\vec{\rho}_l A(\vec{\rho}_o) e^{i\vec{k}_j \cdot \vec{\rho}_o} \left\{ \frac{-i\omega_j}{2\pi c s_0} e^{i\frac{\omega_j}{c} s_0} G\left(|\vec{\rho}_o - \vec{\rho}_l|, \frac{\omega_j}{cs_0}\right) \right\} \\ \times G\left(|\vec{\rho}_l|, -\frac{\omega_j}{cd}\right) \left\{ \frac{-i\omega_j}{2\pi cd} e^{i\frac{\omega_j}{c} d} G\left(|\vec{\rho}_l - \vec{\rho}_k|, \frac{\omega_j}{cd}\right) \right\}, \end{aligned} \quad (11.1)$$

where

$\vec{\rho}_o$ ,  $\vec{\rho}_l$ , and  $\vec{\rho}_j$  are two-dimensional vectors defined, respectively, on the (transverse) output plane of the source (which coincide with the object plane), on the transverse plane of the imaging lens, and on the detection plane

$j = s, i$ , labels the signal and the idler

$k = 1, 2$ , labels the photodetectors  $D_1$  and  $D_2$

The function  $A(\vec{\rho}_o) e^{i\vec{k}_j \cdot \vec{\rho}_o}$  is the complex object-aperture function with a real and positive amplitude  $A(\vec{\rho}_o)$  and a phase  $e^{i\vec{k}_j \cdot \vec{\rho}_o}$ , while the terms in the first and second curly brackets of Equation 11.1 describe, respectively, free propagation from the output plane of the source/object to the imaging lens, and from the imaging lens to the detection plane. Applying the properties of the Gaussian function, Equation 11.1 can be simplified as

$$\begin{aligned} g(\vec{k}_j, \omega_j; \vec{\rho}_k, z = s_0 + d) \\ = \frac{-\omega_j^2}{(2\pi c)^2 s_0 d} e^{i\frac{\omega_j}{c} (s_0 + d)} G\left(|\vec{\rho}_k|, \frac{\omega_j}{cd}\right) \int_{obj} d\vec{\rho}_o A(\vec{\rho}_o) e^{i\vec{k}_j \cdot \vec{\rho}_o} G\left(|\vec{\rho}_o|, \frac{\omega_j}{cs_0}\right) \\ \times \int_{lens} d\vec{\rho}_l G\left(|\vec{\rho}_l|, \frac{\omega_j}{c} \left[\frac{1}{s_0} + \frac{1}{d} - \frac{1}{f}\right]\right) e^{-i\frac{\omega_j}{c} \left(\frac{\vec{\rho}_o}{s_0} + \frac{\vec{\rho}_k}{d}\right) \cdot \vec{\rho}_l}. \end{aligned} \quad (11.2)$$

Substituting Green's functions into Equation 10.37, the effective two-photon wavefunction  $\Psi(\vec{\rho}_1, z; \vec{\rho}_2, z)$  is thus

$$\begin{aligned} \Psi(\vec{\rho}_1, z; \vec{\rho}_2, z) = \Psi_0 \int_{obj} d\vec{\rho}_o A(\vec{\rho}_o) G\left(|\vec{\rho}_o|, \frac{\omega_s}{cs_0}\right) \int_{obj} d\vec{\rho}'_o A(\vec{\rho}'_o) G\left(|\vec{\rho}'_o|, \frac{\omega_i}{cs_0}\right) \\ \times \int_{lens} d\vec{\rho}_l G\left(|\vec{\rho}_l|, \frac{\omega_s}{c} \left[\frac{1}{s_0} + \frac{1}{d} - \frac{1}{f}\right]\right) e^{-i\frac{\omega_s}{c} \left(\frac{\vec{\rho}_o}{s_0} + \frac{\vec{\rho}_1}{d}\right) \cdot \vec{\rho}_l} \end{aligned}$$

$$\begin{aligned} & \times \int_{lens} d\vec{\rho}'_l G\left(|\vec{\rho}'_l|, \frac{\omega_i}{c} \left[ \frac{1}{s_o} + \frac{1}{d} - \frac{1}{f} \right] \right) e^{-i\frac{\omega_i}{c} \left( \frac{\vec{\rho}_o}{s_o} + \frac{\vec{\rho}_i}{d} \right) \cdot \vec{\rho}'_l} \\ & \times \int d\vec{\kappa}_s d\vec{\kappa}_i \delta(\vec{\kappa}_s + \vec{\kappa}_i) e^{i(\vec{\kappa}_s \cdot \vec{\rho}_o + \vec{\kappa}_i \cdot \vec{\rho}'_o)} \end{aligned} \quad (11.3)$$

where we have absorbed all constants into  $\Psi_0$ , including the phase factor

$$e^{i\frac{\omega_s}{c}(s_o+d)} e^{i\frac{\omega_i}{c}(s_o+d)} = e^{i\frac{\omega_p}{c}(s_o+d)}$$

and

$$G\left(|\vec{\rho}_1|, \frac{\omega_s}{cd}\right) G\left(|\vec{\rho}_2|, \frac{\omega_i}{cd}\right).$$

The above phase factors have no contribution to  $|\Psi(\vec{\rho}_1, z; \vec{\rho}_2, z)|^2$ . Let us first complete the double integral of  $d\vec{\kappa}_s$  and  $d\vec{\kappa}_i$  under the EPR correlation of  $\delta(\vec{\kappa}_s + \vec{\kappa}_i)$  on the transverse momentum of the photon pair. Similar to the early calculation, the double integral of  $d\vec{\kappa}_s$  and  $d\vec{\kappa}_i$  yields a  $\delta$ -function of  $\delta(\vec{\rho}_o - \vec{\rho}'_o)$ . Equation 11.3 is then simplified as

$$\begin{aligned} \Psi(\vec{\rho}_1, z; \vec{\rho}_2, z) = & \Psi_0 \int_{obj} d\vec{\rho}_o A^2(\vec{\rho}_o) G\left(|\vec{\rho}_o|, \frac{\omega_p}{cs_o}\right) \\ & \times \int_{lens} d\vec{\rho}_l G\left(|\vec{\rho}_l|, \frac{\omega_s}{c} \left[ \frac{1}{s_o} + \frac{1}{d} - \frac{1}{f} \right] \right) e^{-i\frac{\omega_s}{c} \left( \frac{\vec{\rho}_o}{s_o} + \frac{\vec{\rho}_l}{d} \right) \cdot \vec{\rho}_l} \\ & \times \int_{lens} d\vec{\rho}'_l G\left(|\vec{\rho}'_l|, \frac{\omega_i}{c} \left[ \frac{1}{s_o} + \frac{1}{d} - \frac{1}{f} \right] \right) e^{-i\frac{\omega_i}{c} \left( \frac{\vec{\rho}_o}{s_o} + \frac{\vec{\rho}_l}{d} \right) \cdot \vec{\rho}'_l}. \end{aligned} \quad (11.4)$$

To complete Equation 11.4, we divide the calculation into two parts corresponding to two different measurements:

Case (I): On the imaging plane for  $\vec{\rho}_1 = \vec{\rho}_2 = \vec{\rho}$

In this case, Equation 11.4 is simplified as

$$\begin{aligned} \Psi(\vec{\rho}, z; \vec{\rho}, z) = & \Psi_0 \int_{obj} d\vec{\rho}_o A^2(\vec{\rho}_o) G\left(|\vec{\rho}_o|, \frac{\omega_p}{cs_o}\right) \\ & \times \int_{lens} d\vec{\rho}_l e^{-i\frac{\omega_s}{c} \left( \frac{\vec{\rho}_o}{s_o} + \frac{\vec{\rho}_l}{s_l} \right) \cdot \vec{\rho}_l} \int_{lens} d\vec{\rho}'_l e^{-i\frac{\omega_i}{c} \left( \frac{\vec{\rho}_o}{s_o} + \frac{\vec{\rho}_l}{s_l} \right) \cdot \vec{\rho}'_l}. \end{aligned} \quad (11.5)$$

In the above double integral, we have taken advantage of the EPR correlation  $\vec{\rho}_0 = \vec{\rho}'_0$  of the entangled biphoton state. We now change the double integral of  $d\vec{\rho}_l$  and  $d\vec{\rho}'_l$  to  $d(\vec{\rho}_l - \vec{\rho}'_l)$  and  $d(\vec{\rho}_l + \vec{\rho}'_l)$

$$\begin{aligned}
& \int_{lens} d\vec{\rho}_l e^{-i\frac{\omega_s}{c}\left(\frac{\vec{\rho}_o}{s_o} + \frac{\vec{\rho}}{s_i}\right) \cdot \vec{\rho}_l} \int_{lens} d\vec{\rho}'_l e^{-i\frac{\omega_i}{c}\left(\frac{\vec{\rho}_o}{s_o} + \frac{\vec{\rho}}{s_i}\right) \cdot \vec{\rho}'_l} \\
&= \int_{lens} d(\vec{\rho}_l - \vec{\rho}'_l) e^{-i\left(\frac{\omega_s - \omega_i}{2c}\right)\left(\frac{\vec{\rho}_o}{s_o} + \frac{\vec{\rho}}{s_i}\right) \cdot (\vec{\rho}_l - \vec{\rho}'_l)} \\
&\quad \times \int_{lens} d(\vec{\rho}_l + \vec{\rho}'_l) e^{-i\left(\frac{\omega_p}{2c}\right)\left(\frac{\vec{\rho}_o}{s_o} + \frac{\vec{\rho}}{s_i}\right) \cdot (\vec{\rho}_l + \vec{\rho}'_l)}.
\end{aligned}$$

The integral of  $d(\vec{\rho}_l - \vec{\rho}'_l)$  can be easily evaluated for degenerate monochromatic SPDC  $\omega_s = \omega_i$ , which contributes a trivial constant. The integral of  $d(\vec{\rho}_l + \vec{\rho}'_l)$  yields a point-spread sombrero-function

$$\int_{lens} d(\vec{\rho}_l + \vec{\rho}'_l) e^{-i\left(\frac{\omega_p}{2c}\right)\left(\frac{\vec{\rho}_o}{s_o} + \frac{\vec{\rho}}{s_i}\right) \cdot (\vec{\rho}_l + \vec{\rho}'_l)} = \frac{2J_1\left(\frac{R}{s_o} \frac{\omega_p}{c} |\vec{\rho}_o + \frac{\vec{\rho}}{m}| \right)}{\left(\frac{R}{s_o} \frac{\omega_p}{c} |\vec{\rho}_o + \frac{\vec{\rho}}{m}| \right)}.$$

The joint-detection of a twofold photodetector or a two-photon graphic film gives

$$G^{(2)}(\vec{\rho}, \vec{\rho}) \propto \left| \int_{obj} d\vec{\rho}_o A^2(\vec{\rho}_o) e^{i\frac{\omega_p}{2cs_o} |\vec{\rho}_o|^2} \text{somb}\left(\frac{R}{s_o} \frac{\omega_p}{c} \left|\vec{\rho}_o + \frac{\vec{\rho}}{m}\right| \right) \right|^2, \quad (11.6)$$

indicating a coherent image of the object on the image plane with magnification of  $m = s_i/s_o$ . In Equation 11.6, the point-spread function is characterized by the pump wavelength  $\lambda_p = \lambda_{s,i}/2$ ; hence, the point-spread function is twice narrower than that of the classical case. An entangled two-photon state thus gives an image in joint-detection with double spatial resolution when compared to what one would obtain in classical imaging.

Case (II): On the Fourier transform plane for  $\vec{\rho}_1 = \vec{\rho}_2 = \vec{\rho}$

The detectors are now placed in the focal plane, i.e.,  $d = f$ . In this case, the spatial effective two-photon wavefunction  $\Psi(\vec{\rho}, z; \vec{\rho}, z)$  becomes

$$\begin{aligned}
\Psi(\vec{\rho}, z; \vec{\rho}, z) &\propto \int_{obj} d\vec{\rho}_o A^2(\vec{\rho}_o) G\left(|\vec{\rho}_o|, \frac{\omega_p}{cs_o}\right) \\
&\quad \times \int_{lens} d\vec{\rho}_l G\left(|\vec{\rho}_l|, \frac{\omega_s}{cs_o}\right) e^{-i\frac{\omega_s}{c}\left(\frac{\vec{\rho}_o}{s_o} + \frac{\vec{\rho}}{f}\right) \cdot \vec{\rho}_l} \\
&\quad \times \int_{lens} d\vec{\rho}'_l G\left(|\vec{\rho}'_l|, \frac{\omega_i}{cs_o}\right) e^{-i\frac{\omega_i}{c}\left(\frac{\vec{\rho}_o}{s_o} + \frac{\vec{\rho}}{f}\right) \cdot \vec{\rho}'_l}. \quad (11.7)
\end{aligned}$$

We will first evaluate the double integrals over the lens. To simplify the mathematics, we approximate the integral to infinity. Differing from the calculation for imaging resolution, the purpose of this evaluation is to find out the Fourier transform. Thus, the approximation of an infinite-sized lens is appropriate. By applying the properties of the Gaussian function, the double integrals over the lens contribute the following function of  $\vec{\rho}_o$  to the integral of  $d\vec{\rho}_o$  in Equation 11.7:

$$C G \left( |\vec{\rho}_o|, -\frac{\omega_p}{c s_o} \right) e^{-i \frac{\omega_p}{cf} \vec{\rho}_o \cdot \vec{\rho}}$$

where  $C$  absorbs all constants including a phase factor  $G \left( |\vec{\rho}|, -\frac{\omega_p}{cf^2/s_o} \right)$ . Replacing this result with the double integrals of  $d\vec{\rho}_l$  and  $d\vec{\rho}'_l$  in Equation 11.7, we obtain

$$\int_{obj} d\vec{\rho}_o A^2(\vec{\rho}_o) e^{-i \frac{\omega_p}{cf} \vec{\rho} \cdot \vec{\rho}_o} \propto \mathcal{F}_{\left[ \frac{\omega_p}{cf} \vec{\rho} \right]} \{ A^2(\vec{\rho}_o) \}, \quad (11.8)$$

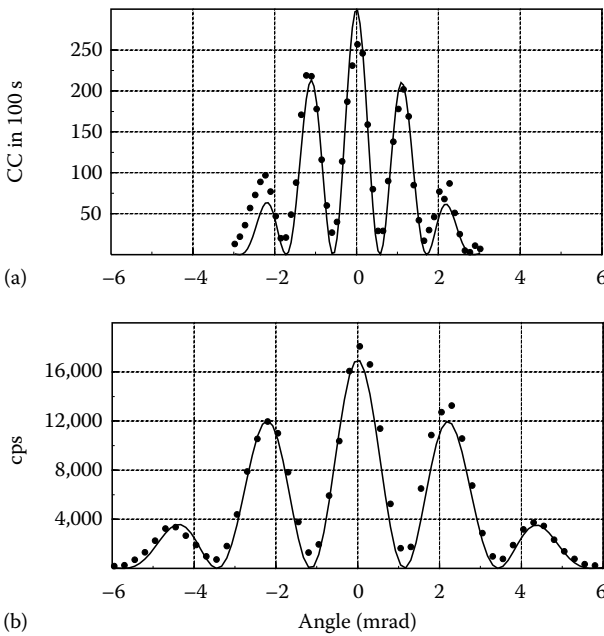
which is the Fourier transform of the object-aperture function. When the two photodetectors scan together (i.e.,  $\vec{\rho}_1 = \vec{\rho}_2 = \vec{\rho}$ ).

Thus, by replacing classical light with entangled biphoton source, in the double-slit setup of Figure 11.1, a Young's double-slit interference-diffraction pattern with twice the interference modulation and twice narrower pattern width, compared to that of classical light at wavelength  $\lambda_{s,i} = 2\lambda_p$ , is observable in the joint detection. This effect has been confirmed in the "quantum lithography" experiments.

Due to the lack of two-photon sensitive material, the first experimental demonstration of quantum lithography of D'Angelo et al. was measured on the Fourier transform plane, instead of the image plane. Two point-like photon-counting detectors were scanned jointly, similar to the setup illustrated in Figure 11.1, for the observation of the biphoton interference-diffraction pattern. Figure 11.2 is the published result. It is clear that the biphoton Young's double-slit interference-diffraction pattern is twice narrower with twice the interference modulation compared to that of the classical case although the wavelengths are both 916 nm.

Following linear Fourier optics, it is not difficult to see that, with the help of another lens (equivalently building a microscope), one can transform the Fourier transform function of the double-slit back onto its image plane to observe its image with twice the spatial resolution.

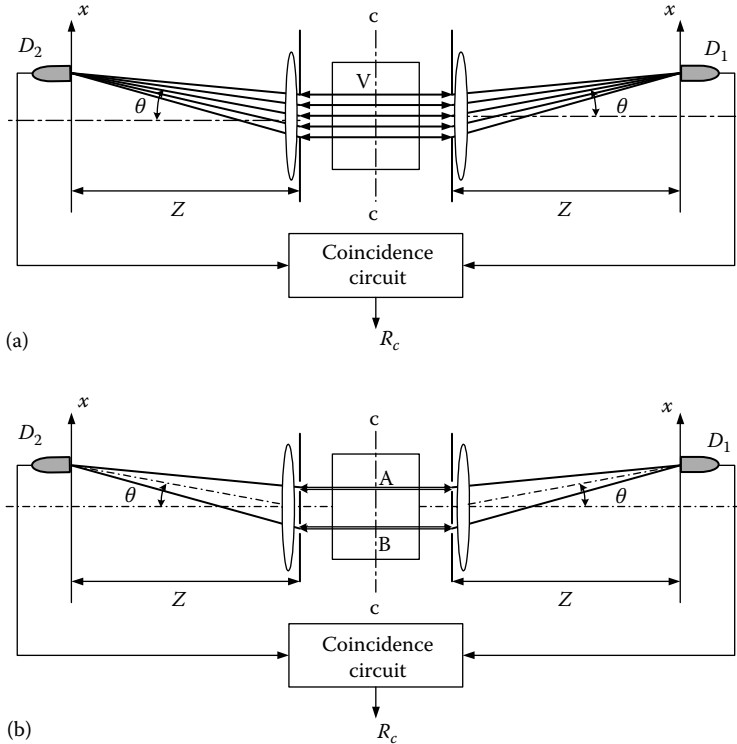
The key to understanding the physics of this experiment is again the entangled nature of the signal-idler biphoton system. As we have discussed earlier, the pair is always emitted from the same point on the output plane of the source, thus always passing the same slit together if the double-slit

**FIGURE 11.2**

(a) Two-photon Fourier transform of a double-slit. The light source was a collinear degenerate SPDC of  $\lambda_{s,i} = 916$  nm. (b) Classical Fourier transform of the same double-slit. A classical light source of  $\lambda = 916$  nm was used.

is placed close to the surface of the nonlinear crystal. There is no chance for the signal–idler pair to pass different slits in this setup. In other words, each point of the object is “illuminated” by the pair “together” and the pair “stops” on the image plane “together.” The point–“spot” correspondence between the object plane and the image plane are based on the physics of two-photon diffraction, resulting in a twice narrower Fourier transform function in the Fourier transform plane and twice the image resolution in the image plane. The unfolded schematic setup, which is shown in Figure 11.3, may be helpful for understanding the physics. It is not difficult to calculate the interference-diffraction function under the experimental condition indicated in Figure 11.3. The nonclassical observation is due to the superposition of the two-photon amplitudes resulting in a joint detection event, which are indicated by the straight lines connecting  $D_1$  and  $D_2$ . The two-photon diffraction, which restricts the spatial resolution of a two-photon image, is different from that of classical light. Thus, there should be no surprise in having an improved spatial resolution even beyond the classical limit.

It is worthwhile to emphasize the following important aspects of physics in this simplified illustration:

**FIGURE 11.3**

Unfolded experimental setup. The joint measurement is on the Fourier transform plane. Each point of the object is “illuminated” by the signal–idler pair “together,” resulting in twice narrower interference-diffraction pattern width in the Fourier transform plane through the joint detection of the signal–idler pair, equivalent to the use of classical light of  $\lambda/2$ .

1. The goal of lithography is the reproduction of demagnified images of complicated patterns. The sub-wavelength interference feature does not necessarily translate into an improvement of the lithographic performances. In fact, the Fourier transform argument works for *imaging setup* only; sub-wavelength interference in a Mach–Zehnder-type interferometer, for instance, does not necessarily lead to an image.
2. In the imaging setup, it is the peculiar nature of the entangled  $N$ -photon system to allow one to generate an image with  $N$ -times of spatial resolution: the entangled photons come out from one point of the object plane, undergo  $N$ -photon diffraction, and stop in the image plane within an  $N$ -times narrower spot than that of the classical imaging. The historical experiment by D’Angelo et al., in which the working principle of quantum lithography was first demonstrated, has taken advantage of the entangled biphoton state

of SPDC: the signal-idler photon pair comes out from either the upper slit or the lower slit that is in the object plane, undergoes two-photon diffraction, and stops in the image plane within a twice narrower image than that of the classical one. Although the measurement is on the Fourier transform plane, it is easy to show that a second Fourier transform, by means of a second lens to form a simple microscope, that reproduces an image on the image plane with double spatial resolution.

## 11.2 Ghost Imaging

The *nonlocal* position–position and momentum–momentum correlation of the entangled biphoton system of SPDC was successfully demonstrated in 1995. The experiment was immediately named as “ghost” imaging in the physics community. The important physics demonstrated in that experiment, however, may not be the so-called ghost. Indeed, the original purpose of the experiment was to study the EPR correlation in position and in momentum and to test the EPR inequality of Equation 10.4 for an entangled biphoton state.

The schematic setup of the ghost image experiment is shown in Figure 11.4. A CW laser is used to pump a nonlinear crystal, which is cut

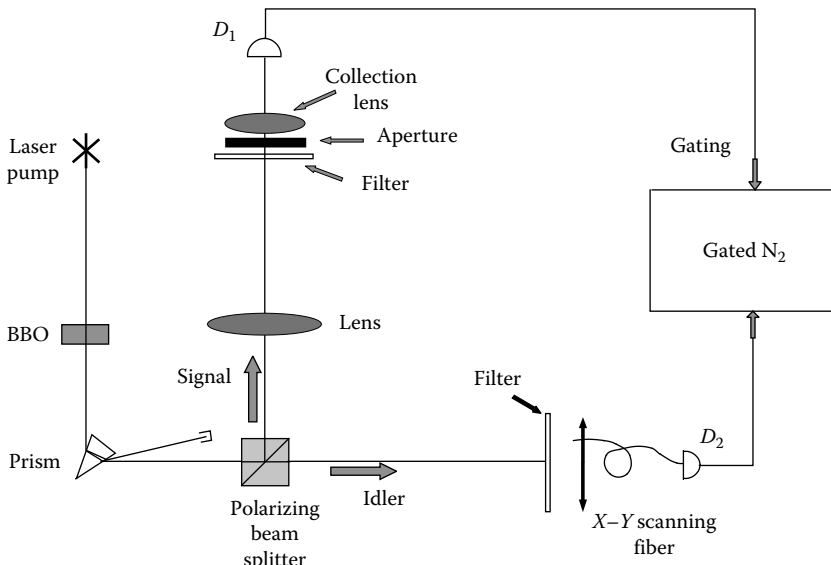


**FIGURE 11.4**

Schematic setup of the “ghost” image experiment.

for degenerate type-II phase matching to produce a pair of orthogonally polarized signal (e-ray of the crystal) and idler (o-ray of the crystal) photon. The pair emerges from the crystal as collinear, with  $\omega_s \cong \omega_i \cong \omega_p/2$ . The pump is then separated from the signal-idler pair by a dispersion prism, and the remaining signal and idler beams are sent in different directions by a polarization beamsplitting Thompson prism. The signal beam passes through a convex lens with a 400 mm focal length and illuminates a chosen aperture (mask). As an example, one of the demonstrations used letters "UMBC" for the object mask. Behind the aperture is the "bucket" detector package  $D_1$ , which consists of a short focal length collection lens in whose focal spot is an avalanche photodiode.  $D_1$  is mounted in a fixed position during the experiment. The idler beam is met by detector package  $D_2$ , which consists of an optical fiber whose output is mated with another avalanche photodiode. The input tip of the fiber is scannable in the transverse plane by two step motors. The output pulses of each detector, which are operated in photon-counting mode, are sent to a coincidence circuit for counting the joint-detection event of the signal-idler pair.

By recording the coincidence counts as a function of the fiber tip's transverse plane coordinates, the image of the chosen aperture (e.g. "UMBC") is observed, as reported in Figure 11.5. It is interesting to note that while

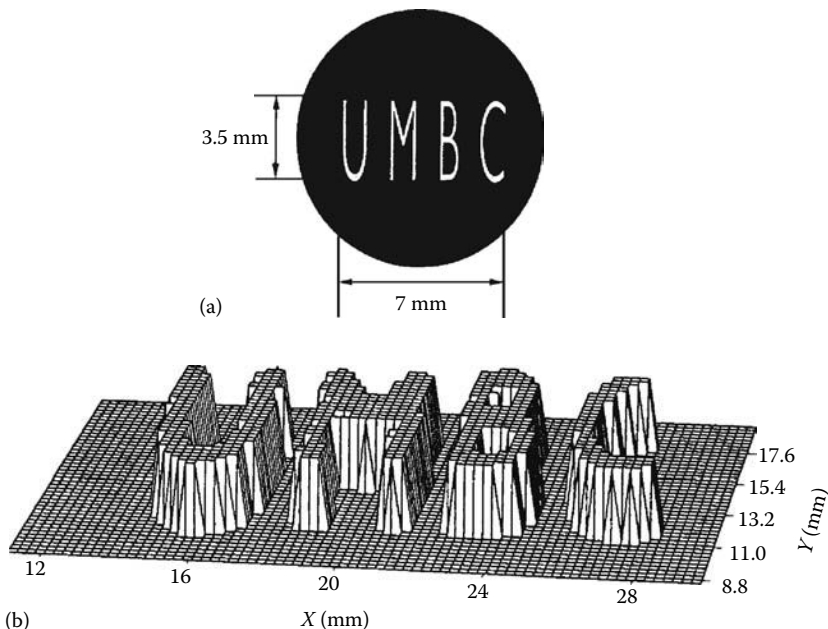


**FIGURE 11.5**

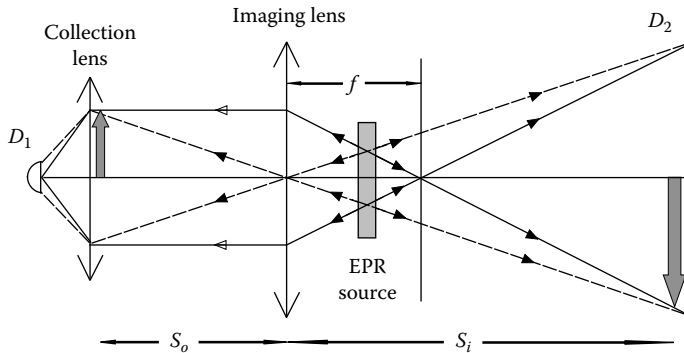
(a) A reproduction of the actual aperture "UMBC" placed in the signal beam. (b) The image of "UMBC": coincidence counts as a function of the fiber tip's transverse plane coordinates. The step size is 0.25 mm. The image shown is a "slice" at the half maximum value.

the size of the “UMBC” aperture inserted in the signal beam is only about  $3.5\text{ mm} \times 7\text{ mm}$ , the observed image measures  $7\text{ mm} \times 14\text{ mm}$ . The image is therefore magnified by a factor of 2. The observation also confirms that the focal length of the imaging lens  $f$ , the aperture’s optical distance from the lens  $s_o$ , and the image’s optical distance from the lens  $s_i$  (which is from the imaging lens going backward along the signal photon path to the two-photon source of SPDC crystal then going forward along the path of idler photon to the image), satisfy the Gaussian thin lens equation. In this experiment,  $s_o$  was chosen to be  $s_o = 600\text{ mm}$ , and the twice magnified clear image was found when the fiber tip was on the plane of  $s_i = 1200\text{ mm}$ . While  $D_2$  was scanned on transverse planes other than that of  $s_i = 1200\text{ mm}$ , the images blurred out.

The measurements of the signal and the idler subsystems themselves are very different. The single-photon-counting rate of  $D_2$  was recorded during the scanning of the image and was found fairly constant in the entire region of the image. This means that the transverse coordinate uncertainty of either signal or idler is considerably large compared to that of the transverse correlation of the entangled signal-idler photon pair:  $\Delta x_1$  ( $\Delta y_1$ ) and  $\Delta x_2$  ( $\Delta y_2$ ) are much greater than  $\Delta(x_1 - x_2)$  ( $\Delta(y_1 - y_2)$ ).

The EPR  $\delta$ -functions,  $\delta(\vec{\rho}_s - \vec{\rho}_i)$  and  $\delta(\vec{\kappa}_s + \vec{\kappa}_i)$  in transverse dimension, are the key to understand this interesting phenomenon. In degenerate SPDC, although the signal-idler photon pair has equal probability to be emitted from any points on the output surface of the nonlinear crystal, the transverse position  $\delta$ -function indicates that if one of them is observed at one position, the other one must be found at the same position. In other words, the pair is always emitted from the same point on the output plane of the two-photon source. The transverse momentum  $\delta$ -function defines the angular correlation of the signal-idler pair: the transverse momenta of a signal-idler amplitude are equal but pointed in opposite directions:  $\vec{\kappa}_s = -\vec{\kappa}_i$ . In other words, the two-photon amplitudes are always existing at roughly equal yet opposite angles relative to the pump. This then allows for a simple explanation of the experiment in terms of “usual” geometrical optics in the following manner: we envision the nonlinear crystal as a “hinge point” and “unfold” the schematic of Figure 11.4 into that shown in Figure 11.6. The signal-idler two-photon amplitudes can then be represented by straight lines (but keep in mind the different propagation directions) and, therefore, the image is produced well in coincidences when the aperture, lens, and fiber tip are located according to the Gaussian thin lens equation of Equation 11.2. The image is exactly the same as one would observe on a screen placed at the fiber tip if detector  $D_1$  were replaced by a point-like light source and the nonlinear crystal by a reflecting mirror.

Following a similar analysis in geometric optics, it is not difficult to find that any geometrical “light spot” on the subject plane, which is the intersection point of all possible two-photon amplitudes coming from the two-photon light source, corresponds to a unique geometrical “light spot”

**FIGURE 11.6**

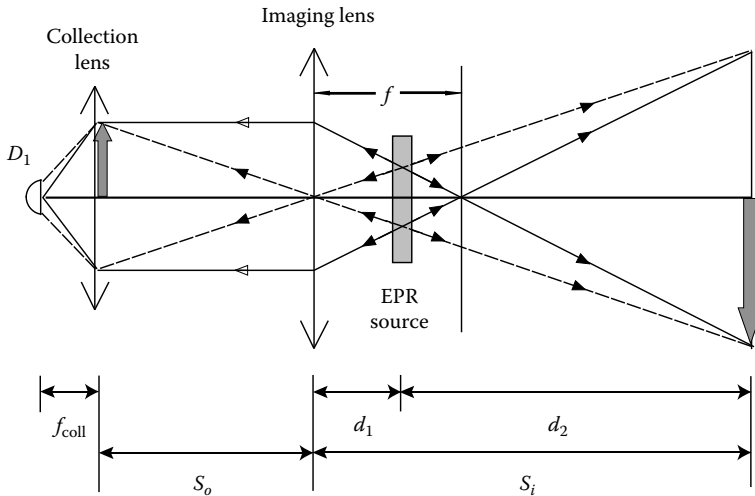
An unfolded setup of the “ghost” imaging experiment, which is helpful for understanding the physics. Since the two-photon “light” propagates along “straight-lines,” it is not difficult to find that any geometrical light point on the subject plane corresponds to a unique geometrical light point on the image plane. Thus, a “ghost” image of the subject is made nonlocally in the image plane. Although the placement of the lens, the object, and detector  $D_2$  obeys the Gaussian thin lens equation, it is important to remember that the geometric rays in the figure actually represent the two-photon amplitudes of an entangled photon pair. The point-to-point correspondence is the result of the superposition of these two-photon amplitudes.

on the image plane, which is another intersection point of all the possible two-photon amplitudes. This point-to-point correspondence made the “ghost” image of the subject aperture possible. Despite the completely different physics from classical geometrical optics, the remarkable feature is that the relationship between the focal length of the lens  $f$ , the aperture’s optical distance from the lens  $S_o$ , and the image’s optical distance from the lens  $S_i$ , satisfy the Gaussian thin lens equation:

$$\frac{1}{S_o} + \frac{1}{S_i} = \frac{1}{f}.$$

Although the placement of the lens, the object, and the detector  $D_2$  obeys the Gaussian thin lens equation, it is important to remember that the geometric rays in the figure actually represent the two-photon amplitudes of a signal-idler photon pair and the point-to-point correspondence is the result of the superposition of these two-photon amplitudes. The “ghost” image is a realization of the 1935 EPR *gedankenexperiment*.

Now we calculate  $G^{(2)}(\vec{\rho}_o, \vec{\rho}_i)$  for the “ghost” imaging experiment, where  $\vec{\rho}_o$  and  $\vec{\rho}_i$  are the transverse coordinates on the object plane and the image plane. We will show that there exists a  $\delta$ -function like point-to-point relationship between the object plane and the image plane, i.e., if one measures the signal photon at a position of  $\vec{\rho}_o$  on the object plane the idler photon can be found only at a certain unique position of  $\vec{\rho}_i$  on the image plane satisfying  $\delta(m\vec{\rho}_o - \vec{\rho}_i)$ , where  $m = -(s_i/s_o)$  is the image-object magnification factor.

**FIGURE 11.7**

In arm-1, the signal propagates freely over a distance  $d_1$  from the output plane of the source to the imaging lens, then passes an object aperture at distance  $s_o$ , and then is focused onto a photon-counting detector  $D_1$  by a collection lens. In arm-2, the idler propagates freely over a distance  $d_2$  from the output plane of the source to a point-like photon-counting detector  $D_2$ .

After demonstrating the  $\delta$ -function, we show how the object function of  $t(\vec{\rho}_o)$  is transferred to the image plane as a magnified image  $t(\vec{\rho}_i/m)$ . Before showing the calculation, it is worth emphasizing again that the “straight lines” in Figure 11.6 schematically represent the two-photon amplitudes all belonging to a pair of signal-idler photon. A “click-click” joint measurement at  $(\mathbf{r}_1, t_1)$ , which is on the object plane, and  $(\mathbf{r}_2, t_2)$ , which is on the image plane, in the form of EPR  $\delta$ -function, is the result of the coherent superposition of all these two-photon amplitudes.

We follow the unfolded experimental setup shown in Figure 11.7 to establish Green’s functions  $g(\vec{k}_s, \omega_s, \vec{\rho}_o, z_o)$  and  $g(\vec{k}_i, \omega_i, \vec{\rho}_2, z_2)$ . In arm-1, the signal propagates freely over a distance  $d_1$  from the output plane of the source to the imaging lens, then passes an object aperture at distance  $s_o$ , and then is focused onto a photon-counting detector  $D_1$  by a collection lens. We will evaluate  $g(\vec{k}_s, \omega_s, \vec{\rho}_o, z_o)$  by propagating the field from the output plane of the two-photon source to the object plane. In arm-2, the idler propagates freely over a distance  $d_2$  from the output plane of the two-photon source to a point-like detector  $D_2$ .  $g(\vec{k}_i, \omega_i, \vec{\rho}_2, z_2)$  is thus a free propagator.

#### (I) Arm-1 (source to object):

The optical transfer function or Green’s function in arm-1, which propagates the field from the source plane to the object plane, is given by

$$\begin{aligned}
& g(\vec{\kappa}_s, \omega_s; \vec{\rho}_o, z_o = d_1 + s_o) \\
&= e^{i\frac{\omega_s}{c}z_o} \int_{lens} d\vec{\rho}_l \int_{source} d\vec{\rho}_S \left\{ \frac{-i\omega_s}{2\pi cd_1} e^{i\vec{\kappa}_s \cdot \vec{\rho}_S} G\left(|\vec{\rho}_S - \vec{\rho}_l|, \frac{\omega_s}{cd_1}\right) \right\} \\
&\quad \times \left\{ G\left(|\vec{\rho}_l|, \frac{\omega_s}{cf}\right) \right\} \left\{ \frac{-i\omega_s}{2\pi cs_o} G\left(|\vec{\rho}_l - \vec{\rho}_o|, \frac{\omega_s}{cs_o}\right) \right\}, \tag{11.9}
\end{aligned}$$

where  $\vec{\rho}_S$  and  $\vec{\rho}_l$  are the transverse vectors defined, respectively, on the output plane of the source and on the plane of the imaging lens. The terms in the first and third curly brackets in Equation 11.9 describe free-space propagation from the output plane of the source to the imaging lens and from the imaging lens to the object plane, respectively. The function  $G\left(|\vec{\rho}_l|, \frac{\omega}{cf}\right)$  in the second curly brackets is the transformation function of the imaging lens. Here, we treat it as a thin-lens:  $G\left(|\vec{\rho}_l|, \frac{\omega}{cf}\right) \cong e^{-i\frac{\omega}{2f}|\vec{\rho}_l|^2}$ .

(II) Arm-2 (from source to image):

In arm-2, the idler propagates freely from the source to the plane of  $D_2$ , which is also the plane of the image. Green's function is thus

$$\begin{aligned}
& g(\vec{\kappa}_i, \omega_i; \vec{\rho}_2, z_2 = d_2) \\
&= \frac{-i\omega_i}{2\pi cd_2} e^{i\frac{\omega_i}{c}d_2} \int_{source} d\vec{\rho}_S' G\left(|\vec{\rho}_S' - \vec{\rho}_2|, \frac{\omega_i}{cd_2}\right) e^{i\vec{\kappa}_i \cdot \vec{\rho}_S'} \tag{11.10}
\end{aligned}$$

where  $\vec{\rho}_S'$  and  $\vec{\rho}_2$  are the transverse vectors defined, respectively, on the output plane of the source and on the plane of the photodetector  $D_2$ .

(III)  $\Psi(\vec{\rho}_o, \vec{\rho}_i)$  (object plane-image plane):

To simplify the calculation and to focus on the transverse correlation, in the following calculation we assume degenerate ( $\omega_s = \omega_i = \omega$ ) and collinear SPDC. The transverse two-photon effective wavefunction  $\Psi(\vec{\rho}_o, \vec{\rho}_2)$  is then evaluated by substituting Green's functions  $g(\vec{\kappa}_s, \omega; \vec{\rho}_o, z_o)$  and  $g(\vec{\kappa}_i, \omega; \vec{\rho}_2, z_2)$  into the expression given in Equation 10.37:

$$\begin{aligned}
\Psi(\vec{\rho}_o, \vec{\rho}_2) &\propto \int d\vec{\kappa}_s d\vec{\kappa}_i \delta(\vec{\kappa}_s + \vec{\kappa}_i) g(\vec{\kappa}_s, \omega; \vec{\rho}_o, z_o) g(\vec{\kappa}_i, \omega; \vec{\rho}_2, z_2) \\
&\propto e^{i\frac{\omega}{c}(s_0 + s_i)} \int d\vec{\kappa}_s d\vec{\kappa}_i \delta(\vec{\kappa}_s + \vec{\kappa}_i) \\
&\quad \times \int_{lens} d\vec{\rho}_l \int_{source} d\vec{\rho}_S e^{i\vec{\kappa}_s \cdot \vec{\rho}_S} G\left(|\vec{\rho}_S - \vec{\rho}_l|, \frac{\omega}{cd_1}\right)
\end{aligned}$$

$$\begin{aligned} & \times G\left(|\vec{\rho}_l|, \frac{\omega}{cf}\right) G\left(|\vec{\rho}_l - \vec{\rho}_o|, \frac{\omega}{cs_o}\right) \\ & \times \int_{source} d\vec{\rho}'_S e^{i\vec{k}_i \cdot \vec{\rho}'_S} G\left(|\vec{\rho}'_S - \vec{\rho}_2|, \frac{\omega}{cd_2}\right) \end{aligned} \quad (11.11)$$

where we have ignored all the proportional constants. Completing the double integral of  $d\vec{k}_S$  and  $d\vec{k}_i$

$$\int d\vec{k}_S d\vec{k}_i \delta(\vec{k}_S + \vec{k}_i) e^{i\vec{k}_S \cdot \vec{\rho}_S} e^{i\vec{k}_i \cdot \vec{\rho}'_S} \sim \delta(\vec{\rho}_S - \vec{\rho}'_S), \quad (11.12)$$

Equation 11.11 becomes:

$$\begin{aligned} \Psi(\vec{\rho}_o, \vec{\rho}_2) \propto & \int_{lens} d\vec{\rho}_l \int_{source} d\vec{\rho}'_S G\left(|\vec{\rho}_2 - \vec{\rho}_S|, \frac{\omega}{cd_2}\right) G\left(|\vec{\rho}_S - \vec{\rho}_l|, \frac{\omega}{cd_1}\right) \\ & \times G\left(|\vec{\rho}_l|, \frac{\omega}{cf}\right) G\left(|\vec{\rho}_l - \vec{\rho}_o|, \frac{\omega}{cs_o}\right). \end{aligned} \quad (11.13)$$

We then apply the properties of the Gaussian functions and complete the integral on  $d\vec{\rho}_S$  by assuming a large enough transverse size of source to be treated as infinity,

$$\Psi(\vec{\rho}_o, \vec{\rho}_2) \propto \int_{lens} d\vec{\rho}_l G\left(|\vec{\rho}_2 - \vec{\rho}_l|, \frac{\omega}{cs_i}\right) G\left(|\vec{\rho}_l|, \frac{\omega}{cf}\right) G\left(|\vec{\rho}_l - \vec{\rho}_o|, \frac{\omega}{cs_o}\right). \quad (11.14)$$

Although the signal and idler propagate to different directions along two optical arms, interestingly, the Green function in Equation 11.14 is equivalent to that of a classical imaging setup, if we imagine the fields start propagating from a point  $\vec{\rho}_o$  on the object plane to the lens and then stop at point  $\vec{\rho}_2$  on the imaging plane. The mathematics is consistent with our previous qualitative analysis of the experiment.

The integral on  $d\vec{\rho}_l$  yields a point-to-point relationship between the object plane and the image plane that are defined by the Gaussian thin-lens equation:

$$\int_{lens} d\vec{\rho}_l G\left(|\vec{\rho}_l|, \frac{\omega}{c} \left[ \frac{1}{s_o} + \frac{1}{s_i} - \frac{1}{f} \right] \right) e^{-i\frac{\omega}{c} \left( \frac{\vec{\rho}_o}{s_o} + \frac{\vec{\rho}_i}{s_i} \right) \cdot \vec{\rho}_l} \propto \delta\left(\vec{\rho}_o + \frac{\vec{\rho}_i}{m}\right) \quad (11.15)$$

where the integral is approximated to infinity and the Gaussian thin-lens equation of  $1/s_o + 1/s_i = 1/f$  is applied. We have also defined  $m = s_i/s_o$  as the magnification factor of the imaging system. The function  $\delta(\vec{\rho}_o + \vec{\rho}_i/m)$

indicates that a point of  $\vec{\rho}_o$  on the object plane corresponds to a unique point of  $\vec{\rho}_i$  on the image plane. The two vectors pointed to opposite directions and the magnitudes of the two vectors hold a ratio of  $m = |\vec{\rho}_i|/|\vec{\rho}_o|$ .

If the finite size of the imaging lens has to be taken into account (finite diameter  $D$ ), the integral yields a point-spread function of  $\text{somb}(x)$ :

$$\int_{\text{lens}} d\vec{\rho}_l e^{-i\frac{\omega}{c}(\frac{\vec{\rho}_o}{s_o} + \frac{\vec{\rho}_i}{s_i}) \cdot \vec{\rho}_l} \propto \text{somb}\left(\frac{R}{s_o} \frac{\omega}{c} \left[\vec{\rho}_o + \frac{\vec{\rho}_i}{m}\right]\right) \quad (11.16)$$

where

$\text{somb}(x) = 2J_1(x)/x$ ,  $J_1(x)$  is the first-order Bessel function

$R/s_o$  is named as the numerical aperture

The point-spread function turns the point-to-point correspondence between the object plane and the image plane into a point-to-“spot” relationship and thus limits the spatial resolution. This point has been discussed in detail in the last section.

Therefore, by imposing the condition of the Gaussian thin-lens equation, the transverse two-photon effective wavefunction is approximated as a  $\delta$  function

$$\Psi(\vec{\rho}_o, \vec{\rho}_i) \propto \delta\left(\vec{\rho}_o + \frac{\vec{\rho}_i}{m}\right) \quad (11.17)$$

where  $\vec{\rho}_o$  and  $\vec{\rho}_i$ , again, are the transverse coordinates on the object plane and the image plane, respectively, defined by the Gaussian thin-lens equation. Thus, the second-order spatial correlation function  $G^{(2)}(\vec{\rho}_o, \vec{\rho}_i)$  turns out to be

$$G^{(2)}(\vec{\rho}_o, \vec{\rho}_i) = |\Psi(\vec{\rho}_o, \vec{\rho}_i)|^2 \propto \left|\delta\left(\vec{\rho}_o + \frac{\vec{\rho}_i}{m}\right)\right|^2. \quad (11.18)$$

Equation 11.18 indicates a point-to-point EPR correlation between the object plane and the image plane, i.e., if one observes the signal photon at a position of  $\vec{\rho}_o$  on the object plane, the idler photon can only be found at a certain unique position of  $\vec{\rho}_i$  on the image plane satisfying  $\delta(\vec{\rho}_o + \vec{\rho}_i/m)$  with  $m = s_i/s_o$ .

We now include an object-aperture function, a collection lens and a photon-counting detector  $D_1$  into the optical transfer function of arm-1, as shown in Figure 11.4.

First, we treat the collection-lens- $D_1$  package as a “bucket” detector. The “bucket” detector integrates all  $\Psi(\vec{\rho}_o, \vec{\rho}_2)$  that pass the object aperture  $A(\vec{\rho}_o)$  as a joint photodetection event. This process is equivalent to the following convolution:

$$\begin{aligned} R_{1,2} &\propto \int_{\text{obj}} d\vec{\rho}_o |A(\vec{\rho}_o)|^2 g^{(2)}(\vec{\rho}_o, \vec{\rho}_i) \\ &= \int_{\text{obj}} d\vec{\rho}_o |A(\vec{\rho}_o)|^2 |\Psi(\vec{\rho}_o, \vec{\rho}_i)|^2 \simeq \left| A\left(\frac{-\vec{\rho}_i}{m}\right) \right|^2 \end{aligned} \quad (11.19)$$

where, again,  $D_2$  is scanning in the image plane,  $\vec{\rho}_2 = \vec{\rho}_i$ . Equation 11.19 indicates a magnified (or demagnified) image of the object-aperture function by means of the joint-detection events between distant photodetectors  $D_1$  and  $D_2$ . The “ $-$ ” sign in  $A(-\vec{\rho}_i/m)$  indicates opposite orientation of the image. The model of “bucket” detector is a good and realistic approximation.

Second, we calculate Green’s function from the source to  $D_1$  in detail by including the object-aperture function, the collection lens and the photon-counting detector  $D_1$  into arm 1. The Green’s function of Equation 11.9 becomes:

$$\begin{aligned} g(\vec{k}_s, \omega_s; \vec{\rho}_1, z_1 = d_1 + s_o + f_{\text{coll}}) &= e^{i\frac{\omega_s}{c}z_1} \int_{\text{obj}} d\vec{\rho}_o \int_{\text{lens}} d\vec{\rho}_l \int_{\text{source}} d\vec{\rho}_s \left\{ \frac{-i\omega_s}{2\pi c d_1} e^{i\vec{k}_s \cdot \vec{\rho}_s} G\left(|\vec{\rho}_s - \vec{\rho}_l|, \frac{\omega_s}{cd_1}\right) \right\} \\ &\times G\left(|\vec{\rho}_l|, \frac{\omega_s}{cf}\right) \left\{ \frac{-i\omega_s}{2\pi c s_o} G\left(|\vec{\rho}_l - \vec{\rho}_o|, \frac{\omega_s}{cs_o}\right) \right\} A(\vec{\rho}_o) \\ &\times G\left(|\vec{\rho}_o|, \frac{\omega_s}{cf_{\text{coll}}}\right) \left\{ \frac{-i\omega_s}{2\pi cf_{\text{coll}}} G\left(|\vec{\rho}_o - \vec{\rho}_1|, \frac{\omega_s}{cf_{\text{coll}}}\right) \right\} \end{aligned} \quad (11.20)$$

where

$f_{\text{coll}}$  is the focal length of the collection lens

$D_1$  is placed on the focal point of the collection lens

Repeating the previous calculation, we obtain the transverse two-photon effective wavefunction:

$$\Psi(\vec{\rho}_1, \vec{\rho}_2) \propto \int_{\text{obj}} d\vec{\rho}_o A(\vec{\rho}_o) \delta\left(\vec{\rho}_o + \frac{\vec{\rho}_2}{m}\right) = A(\vec{\rho}_o) \otimes \delta\left(\vec{\rho}_o + \frac{\vec{\rho}_2}{m}\right) \quad (11.21)$$

where  $\otimes$  means convolution. Note, in Equation 11.21 we have ignored the phase factors which have no contribution to the formation of the image. The joint-detection counting rate,  $R_{1,2}$ , between photon-counting detectors  $D_1$  and  $D_2$  is thus:

$$R_{1,2} \propto G^{(2)}(\vec{\rho}_1, \vec{\rho}_2) \propto \left| A(\vec{\rho}_o) \otimes \delta\left(\vec{\rho}_o + \frac{\vec{\rho}_2}{m}\right) \right|^2 = \left| A\left(\frac{-\vec{\rho}_2}{m}\right) \right|^2 \quad (11.22)$$

where, again,  $\vec{\rho}_2 = \vec{\rho}_i$ .

The physical process corresponding to the above convolution can be summarized as follows. Due to the unique point-to-point correlation between the object plane and the image plane, whenever the bucket detector receives a signal photon that is either transmitted, scattered, or reflected from a unique point of the object, the scanning point photodetector  $D_2$  or a CCD element that receives the idler photon identifies the coordinate of  $\vec{\rho}_o$  and the value of the aperture function  $A(\vec{\rho}_o)$  for that joint-photodetection event. For instance, at time  $t$ , the bucket detector receives a signal photon that is either transmitted, scattered, or reflected from a unique point  $\vec{\rho}_o$  of the object plane within a coincidence time window. The joint-detection of the idler photon by the scanning point detector  $D_2$  or a CCD element, with known coordinate  $\vec{\rho}_l$ , identifies  $\vec{\rho}_o$  immediately for that event. At time  $t'$ , the bucket detector receives another signal photon that is either transmitted, scattered, or reflected from another unique point  $\vec{\rho}'_o$  of the object plane within the coincidence window, and the joint-detection of the idler photon by the scanning point detector  $D_2$  or a CCD element, with known coordinate  $\vec{\rho}'_l$ , identifies  $\vec{\rho}'_o$  immediately for that event. The probability of receiving a joint-photodetection event at  $(\vec{\rho}_o, \vec{\rho}_l)$  and at  $(\vec{\rho}'_o, \vec{\rho}'_l)$  is proportional to the value of the aperture function  $A(\vec{\rho}_o)$  and  $A(\vec{\rho}'_o)$ , respectively. Accumulating a large number of joint-detection events at each transverse coordinate on the image plane reproduces the aperture function  $A(\vec{\rho}_o)$  in the joint-detection as a function of  $\vec{\rho}_l$ .

As we have discussed earlier, the point-to-point EPR correlation is the result of the coherent superposition of the biphoton probability amplitudes. In principle, one signal–idler pair contains all the necessary biphoton probability amplitudes that generate the ghost image. We name this kind of image as *two-photon coherent* image to distinguish the *two-photon incoherent* image of thermal light.

### **11.3 Ghost Imaging and Uncertainty Relation**

In quantum mechanics, a particle cannot have precise position and momentum simultaneously. It is prohibited. We say that the quantum observable *position* and *momentum* are *complementary* because the precise knowledge of the position (momentum) implies that all possible outcomes of measuring the momentum (position) are equally probable.

From a classical point of view, however, it is truly hard to imagine a particle does not have a defined momentum (position) when its position (momentum) is observed with a precise value. As a “metaphysical realist,” Karl Popper shared the same philosophical view on physical reality with Einstein, Podolsky, and Rosen: a particle must have precise position and momentum during its creation, propagation, and annihilation. In their

opinion, the quantum formalism *should* be, *could* be, and *must* be interpreted realistically. In this regard, Popper invented a thought experiment in the early 1930s aimed to support his realistic interpretation of quantum mechanics. What Popper intended to show in his thought experiment is that a particle can have both precise position and momentum simultaneously through the correlation measurement of an entangled two-particle system.

Similar to EPR's *gedankenexperiment*, Popper's thought experiment is also based on the feature of two-particle *entanglement*: if the position or momentum of particle 1 is known, the corresponding observable of its twin, particle 2, is then 100% determined. Popper's original thought experiment is schematically shown in Figure 11.8. A point source S, positronium as Popper suggested, is placed at the center of the experimental arrangement from which entangled pairs of particles 1 and 2 are emitted in opposite directions along the respective positive and negative  $x$ -axes toward two screens A and B. There are slits on both screens parallel to the  $y$ -axis and the slits may be adjusted by varying their widths  $\Delta y$ . Beyond the slits on each side stand an array of Geiger counters for the joint measurement of the particle pairs, as shown in the figure. The entangled pair could be emitted to any direction in  $4\pi$  solid angles from the point source. However, if particle 1 is detected in a

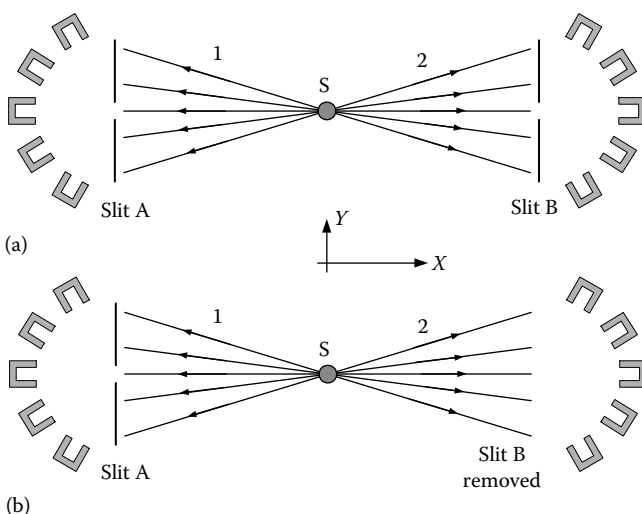


**FIGURE 11.8**

Popper's thought experiment. An entangled pair of particles are emitted from a point source with momentum conservation. A narrow slit on screen A is placed in the path of particle 1 to provide the precise knowledge of its position on the  $y$ -axis and this also determines the precise  $y$ -position of its twin, particle 2, on screen B. (a) Slits A and B are both adjusted very narrowly. (b) Slit A is kept very narrow and slit B is left wide open.

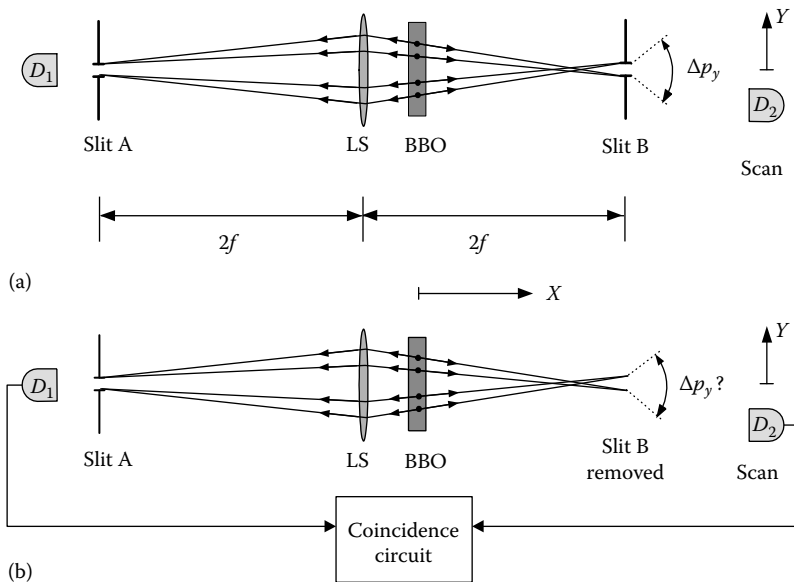
certain direction, particle 2 is then known to be in the opposite direction due to the momentum conservation of the quanta pair.

First, let us imagine the case in which slits A and B are both adjusted very narrowly. In this circumstance, particle 1 and particle 2 experience diffraction at slit A and slit B, respectively, and exhibit greater  $\Delta p_y$  for smaller  $\Delta y$  of the slits. There seems to be no disagreement in this situation between Copenhagen and Popper.

Next, suppose we keep slit A very narrow and leave slit B wide open. The main purpose of the narrow slit A is to provide the precise knowledge of the position  $y$  of particle 1 and this subsequently determines the precise position of its twin (particle 2) on side B through quantum entanglement. Now, Popper asks, in the absence of the physical interaction with an actual slit, does particle 2 experience a greater uncertainty in  $\Delta p_y$  due to the precise knowledge of its position? Based on his beliefs, Popper provides a straightforward prediction: *particle 2 must not experience a greater  $\Delta p_y$  unless a real physical narrow slit B is applied*. However, if Popper's conjecture is correct, this would imply the product of  $\Delta y$  and  $\Delta p_y$  of particle 2 could be smaller than  $h$  ( $\Delta y \Delta p_y < h$ ). This may pose a serious difficulty for Copenhagen and perhaps for many of us. On the other hand, if particle 2 going to the right does scatter like its twin, which has passed though slit A, while slit B is wide open, we are then confronted with an apparent *action-at-a-distance*!

The use of a *point source* in Popper's proposal has been criticized historically as the fundamental error Popper made. It is true that a point source can never produce a pair of entangled particles, which preserves EPR correlation in momentum as Popper expected. However, notice that a *point source* is *not* a necessary requirement for Popper's experiment. What is required is a precise position-position EPR correlation: if the position of particle 1 is precisely known, the position of particle 2 is 100% determined. As we have shown in the last section, ghost imaging is a perfect tool to achieve this.

In 1998, Popper's experiment was realized by Y.H. Kim et al. with the help of biphoton ghost imaging. Figure 11.9 is a schematic diagram that is useful for comparison with Popper's original thought experiment. It is easy to see that this is a typical ghost imaging experimental setup. An entangled photon pair is used to image slit A onto a distant image plane of "screen" B. In the setup,  $s_o$  is chosen to be twice the focal length of the imaging lens  $LS$ ,  $s_o = 2f$ . According to the Gaussian thin lens equation, an equal size "ghost" image of slit A appears on the two-photon image plane at  $s_i = 2f$ . The use of slit A provides a precise knowledge of the position of photon 1 on the  $y$ -axis and also determines the precise  $y$ -position of its twin, photon 2, on screen B by means of biphoton ghost imaging. The experimental condition specified in Popper's experiment is then achieved: when slit A is adjusted to a certain narrow width and slit B is wide open, slit A provides precise knowledge about the position of photon 1 on the  $y$ -axis up to an accuracy  $\Delta y$ , which equals the width of slit A, and the corresponding ghost image of pinhole A at screen B determines the precise position  $y$  of photon 2 to be

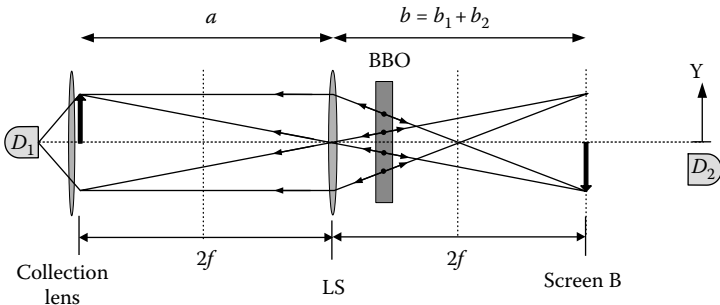
**FIGURE 11.9**

Modified version of Popper's experiment. An entangled photon pair is generated by SPDC. A lens and a narrow slit A are placed in the path of photon 1 to provide the precise knowledge of its position on the  $y$ -axis and also to determine the precise  $y$ -position of its twin, photon 2, on screen B by means of biphoton ghost imaging. Photon-counting detectors  $D_1$  and  $D_2$  are used to scan in  $y$ -directions for joint detections. (a) Slits A and B are both adjusted very narrowly. (b) Slit A is kept very narrow and slit B is left wide open.

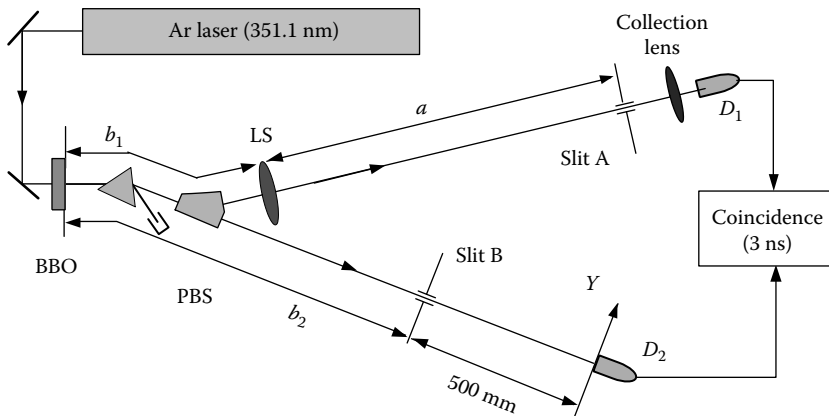
within the same accuracy  $\Delta y$ .  $\Delta p_y$  of photon 2 can be independently studied by measuring the width of its “diffraction pattern” at a certain distance from “screen” B. This is obtained by recording coincidences between detectors  $D_1$  and  $D_2$  while scanning detector  $D_2$  along its  $y$ -axis, which is behind screen B at a certain distance.

Figure 11.10 is a conceptual diagram to connect the modified Popper's experiment with biphoton ghost imaging. In this unfolded ghost imaging setup, we assume the entangled signal-idler photon pair holds a perfect EPR correlation in momentum with  $\delta(\mathbf{k}_s + \mathbf{k}_i)$ , by assuming  $k_p = 0$ . In fact, the perfect transverse momentum correlation of  $\vec{k}_s + \vec{k}_i = 0$  can be easily realized in a large transverse sized SPDC. In this experiment, we have chosen  $s_o = s_i = 2f$ . Thus, an equal size ghost image of slit A is expected to appear on the image plane of screen B.

The detailed experimental setup is shown in Figure 11.11 with indications of the various distances. A CW Argon ion laser line of  $\lambda_p = 351.1$  nm is used to pump a 3 mm long beta barium borate (BBO) crystal for type-II SPDC to generate an orthogonally polarized signal-idler photon pair. The laser beam is about 3 mm in diameter with a diffraction-limited divergence. It is

**FIGURE 11.10**

An unfolded schematic of ghost imaging. We assume the entangled signal-idler photon pair holds a perfect momentum correlation  $\delta(\mathbf{k}_s + \mathbf{k}_i) \sim 0$ . The locations of the slit A, the imaging lens LS, and the ghost image must be governed by the Gaussian thin lens equation. In this experiment, we have chosen  $s_o = s_i = 2f$ . Thus, the ghost image of slit A is expected to be the same size as that of slit A.

**FIGURE 11.11**

Schematic of the experimental setup. The laser beam is about 3 mm in diameter. The “phase-matching condition” is well reinforced. Slit A (0.16 mm) is placed 1000 mm =  $2f$  behind the converging lens, LS ( $f = 500$  mm). The one-to-one ghost image (0.16 mm) of slit A is located at B. The optical distance from LS in the signal beam taken as back through PBS to the SPDC crystal ( $b_1 = 255$  mm) and then along the idler beam to “screen B” ( $b_2 = 745$  mm) is 1000 mm =  $2f$  ( $b = b_1 + b_2$ ).

important not to focus the pump beam so that the phase-matching condition,  $\mathbf{k}_s + \mathbf{k}_i = \mathbf{k}_p$ , is well reinforced in the SPDC process, where  $\mathbf{k}_j$  ( $j = s, i, p$ ) is the wavevectors of the signal (s), idler (i), and pump (p), respectively. The collinear signal-idler beams, with  $\lambda_s = \lambda_i = 702.2$  nm =  $2\lambda_p$  are separated from the pump beam by a fused quartz dispersion prism, and then split by a polarization beamsplitter PBS. The signal beam (photon 1) passes through the converging lens LS with a 500 mm focal length and a 25 mm diameter.

A 0.16 mm slit is placed at location A, which is 1000 mm ( $s_o = 2f$ ) behind the lens LS. A short focal length lens is used with  $D_1$  for collecting all the signal beam that passes through slit A. The point-like photon-counting detector  $D_2$  is located 500 mm behind "screen B." "Screen B" is the image plane defined by the Gaussian thin equation. Slit B, either adjusted as the same size as that of slit A or opened completely, is placed to coincide with the ghost image. The output pulses from the detectors are sent to a coincidence circuit. During the measurements, the bucket detector  $D_1$  is fixed behind slit A while the point detector  $D_2$  is scanned on the  $y$ -axis by a step motor.

*Measurement 1:* Measurement 1 studied the case in which both slits A and B were adjusted to be 0.16 mm. The  $y$ -coordinate of  $D_1$  was chosen to be 0 (center) while  $D_2$  was allowed to scan along its  $y$ -axis. The circled dot data points in Figure 11.12 show the *coincidence* counting rates against the  $y$ -coordinates of  $D_2$ . It is a typical single-slit diffraction pattern with  $\Delta y \Delta p_y = h$ . Nothing is special in this measurement except that we have learned the width of the diffraction pattern for the 0.16 mm slit and this represents the minimum uncertainty of  $\Delta p_y$ . We should emphasize at this point that the *single* detector counting rate of  $D_2$  as a function of its position  $y$  is basically the same as that of the coincidence counts except for a higher counting rate.

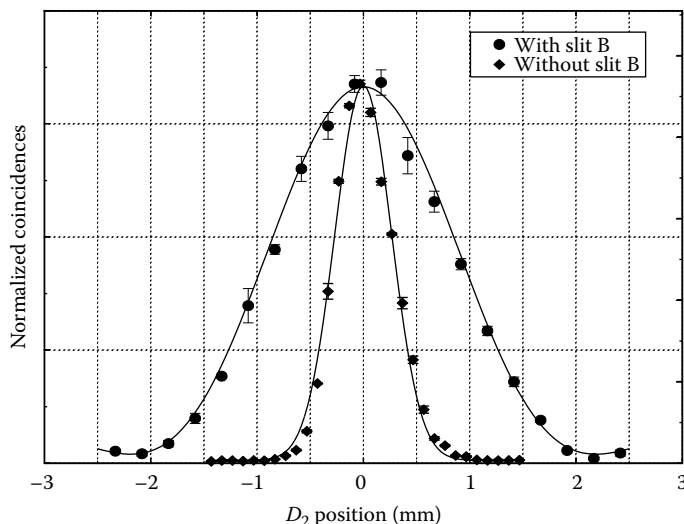


**FIGURE 11.12**

The observed coincidence patterns. The  $y$ -coordinate of  $D_1$  was chosen to be 0 (center) while  $D_2$  was allowed to scan along its  $y$ -axis. Circle dot points: slit A = slit B = 0.16 mm. Diamond dot points: slit A = 0.16 mm, slit B wide open. The width of the sinc-function curve fitted by the circle dot points is a measure of the minimum  $\Delta p_y$  determined by a 0.16 mm slit. The fitting curve for the diamond dots is numerical result of Equation 11.23, indicating a *blurred* ghost image of slit A.

*Measurement 2:* The same experimental conditions were maintained except that slit B was left wide open. This measurement is a test of Popper's prediction. The  $y$ -coordinate of  $D_1$  was chosen to be 0 (center) while  $D_2$  was allowed to scan along its  $y$ -axis. Due to the entangled nature of the signal-idler photon pair and the use of coincidence measurement circuit, only those twins that have passed through slit A and the "ghost image" of slit A at screen B with an uncertainty of  $\Delta y = 0.16$  mm (which is the same width as the real slit B we have used in measurement 1) would contribute to the coincidence counts through the joint detection of  $D_1$  and  $D_2$ . The diamond dot data points in Figure 11.12 report the measured coincidence-counting rates against the  $y$  coordinates of  $D_2$ . The measured width of the pattern is narrower than that of the diffraction pattern shown in measurement 1. It is also interesting to notice that the single detector-counting rate of  $D_2$  remains constant in the entire scanning range, which is very different from that in measurement 1. The experimental data has provided a clear indication of  $\Delta y \Delta p_y < h$  in the joint measurements of the entangled photon pairs.

Given that  $\Delta y \Delta p_y < h$ , is this a violation of the uncertainty principle? Does quantum mechanics agree with this peculiar experimental result? If quantum mechanics does provide a solution with  $\Delta y \Delta p_y < h$  for photon 2. We would indeed be forced to face a paradox as EPR had pointed out in 1935.

Quantum mechanics does provide a solution that agrees with the experimental result. However, it is not the solution for photon 2. Instead, it is for a joint measurement of the entangled photon pair.

We now examine the experimental results with the quantum mechanical calculation by adopting the formalisms from the ghost image experiment with two modifications:

Case (I): Slit A = 0.16 mm, slit B = 0.16 mm

This is the experimental condition for measurement one: slit B is adjusted to be the same as slit A. There is nothing surprising about this measurement. The measurement simply provides us the knowledge of  $\Delta p$  of photon 2 after the diffraction caused by slit B of  $\Delta y = 0.16$  mm. The experimental data shown in Figure 11.12 agrees with the calculation. Note that slit B is about 745 mm away from the 3 mm two-photon source, the angular size of the light source is roughly the same as  $\lambda/\Delta y$ ,  $\Delta\theta \sim \lambda/\Delta y$ , where  $\lambda = 702$  nm is the wavelength and  $\Delta y = 0.16$  mm is the width of the slit. The calculated diffraction pattern is very close to that of the "far-field" Fraunhofer diffraction of a 0.16 mm single slit.

Case (II): Slit A = 0.16 mm, slit B  $\sim \infty$  (wide open).

Now we remove slit B from the ghost image plane. The calculation of the transverse effective two-photon wavefunction and the second-order correlation is the same as that of the ghost image except the observation plane of  $D_2$  is moved behind from the image plane at a distance of 500 mm. The two-photon image of slit A is located at a distance  $s_i = 2f = 1000$  mm ( $b_1 + b_2$ )

from the imaging lens, in this measurement  $D_2$  is placed at  $d = 1500$  mm from the imaging lens. The measured pattern is simply a “blurred” two-photon image of slit A. The “blurred” two-photon image can be calculated from Equation 11.23, which is a slightly modified version of Equation 11.14

$$\begin{aligned}\Psi(\vec{\rho}_o, \vec{\rho}_2) &\propto \int_{\text{lens}} d\vec{\rho}_l G\left(|\vec{\rho}_2 - \vec{\rho}_l|, \frac{\omega}{cd}\right) G\left(|\vec{\rho}_l|, \frac{\omega}{cf}\right) G\left(|\vec{\rho}_l - \vec{\rho}_o|, \frac{\omega}{cs_o}\right) \\ &\propto \int_{\text{lens}} d\vec{\rho}_l G\left(|\vec{\rho}_l|, \frac{\omega}{c} \left[ \frac{1}{s_o} + \frac{1}{d} - \frac{1}{f} \right] \right) e^{-i\frac{\omega}{c} \left( \frac{\vec{\rho}_o}{s_o} + \frac{\vec{\rho}_l}{d} \right) \cdot \vec{\rho}_l} \quad (11.23)\end{aligned}$$

where  $d$  is the distance between the imaging lens and  $D_2$ . In this measurement,  $D_2$  was placed 500 mm behind the image plane, i.e.,  $d = s_i + 500$  mm. The numerical calculated “blurred” image, which is narrower than that of the diffraction pattern of the 0.16 mm slit B, agrees with the measured result of Figure 11.12 within experimental error.

The measurement does show a result of  $\Delta y \Delta p_y < h$ . The measurement, however, has nothing to do with the uncertainty relation that governs the behavior of photon 2 (the idler). Popper and EPR were correct in the prediction of the outcomes of their experiments. Popper and EPR, on the other hand, made the same error by applying the results of two-particle physics to the explanation of the behavior of an individual particle.

In both the Popper and EPR experiments, the measurements are *joint detection* between two detectors applied to entangled states. Quantum mechanically, an entangled two-particle state only provides *the precise knowledge of the correlations of the pair*. The behavior of photon 2 observed in the joint measurement is conditioned upon the measurement of its twin. A quantum must obey the uncertainty principle but the *conditional behavior* of a quantum in an entangled biparticle system is different in principle. We believe paradoxes are unavoidable if one insists the *conditional behavior* of a particle is the *behavior* of the particle. This is the central problem in the rationale behind both Popper and EPR.  $\Delta y \Delta p_y \geq h$  is not applicable to the conditional behavior of either *photon 1* or *photon 2* in the experiments of Popper and EPR.

The behavior of photon 2 being conditioned upon the measurement of photon 1 is well represented by the two-photon amplitudes. Each of the *straight lines* in Figure 11.10 corresponds to a two-photon amplitude. Quantum mechanically, the superposition of these two-photon amplitudes are responsible for a “click-click” measurement of the entangled pair. A “click-click” joint measurement of the two-particle entangled state projects out certain two-particle amplitudes, and only these two-particle amplitudes are featured in the quantum formalism. In the above analysis we never consider photon 1 or photon 2 *individually*. Popper’s question about the momentum uncertainty of photon 2 is then inappropriate. The correct question to ask in these measurements should be as follows: what is the uncertainty of  $\Delta p_y$  for the signal-idler *pair* that are localized within  $\Delta y = 0.16$  mm at “screen”

A with and without slit B? This is indeed the central point for Popper's experiment.

Once again, the demonstration of Popper's experiment calls our attention to the important message: the physics of the entangled two-particle system must inherently be very different from that of individual particles.

---

## 11.4 Thermal Light Ghost Imaging

Ten years after the experimental demonstration of ghost imaging with entangled photon pairs, Valencia et al. found that the near-field, natural, nonfactorizable, point-to-point image-forming correlation is not only the property of entangled photon pairs. It can be realized in the joint-detection of an arbitrary pair of randomly distributed photons from chaotic-thermal source in a lensless configuration for ghost imaging, except with a 50% constant background noise,

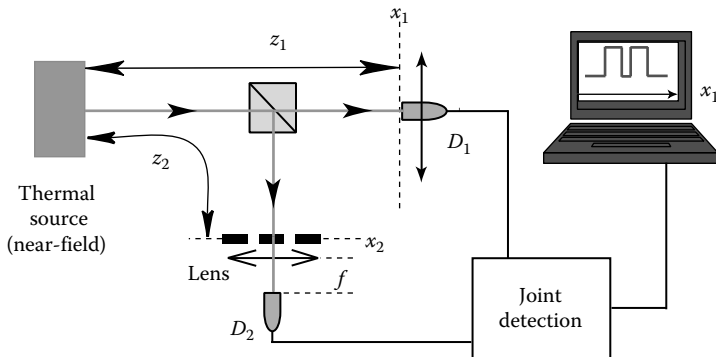
$$g^{(2)}(\vec{\rho}_o, \vec{\rho}_i) \sim 1 + \delta(\vec{\rho}_o + \vec{\rho}_i), \quad (11.24)$$

where  $\vec{\rho}_o$  and  $\vec{\rho}_i$  are the transverse coordinates on the object plane and the image plane, respectively. Image plane is the observation plane which has equal distance to the chaotic source as that of the object plane. The goal of this section is to analyze the two-photon interference nature of the above point-to-point image-forming correlation, as well as that of the thermal light ghost imaging.

The lensless near-field ghost imaging with chaotic radiation was demonstrated by D'Angelo et al. and Scarcelli et al. in the years 2005–2006. Figure 11.13 is the schematic experimental setup of their 2006 demonstration. A chaotic-thermal radiation with a narrow spectral bandwidth,  $\Delta\omega$ , and fairly large bandwidth of spatial frequency,  $\Delta k_x$ ,\* is divided into two by

---

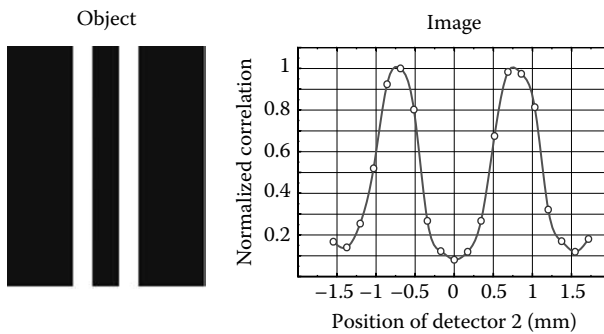
\* A Fresnel “near-field” lensless configuration was applied in the ghost imaging experiment of Scarcelli et al. to achieve this condition, in which the angular diameter,  $\Delta\theta$ , of the source is greater than  $\lambda/D$ . In the first a few experiments of Scarcelli et al., the transverse diameter of the source  $D$  was chosen to be a few millimeters, and  $z_1 = z_2$  was chosen to be a few hundred millimeters, with a pseudothermal light source of  $\lambda = 632$  nm,  $\Delta\theta \sim 10\lambda/D$  to  $40\lambda/D$ . Note, Fresnel near-field is not “near-surface-field.” One cannot assume to have a copy of identical “speckles” on the object plane and the image plane without the use of classical imaging systems, even if there exists such a point-like “speckle” distribution on the thermal light source. For thermal light, each point-like “speckle” will propagate to all directions in the form of spherical waves. After the propagation, each point-like “speckle” will occupy the entire object plane and the image plane. Imagine we are using sunlight for ghost imaging (sun is in Fresnel near-field to us), one cannot claim a copy of a “speckles” of the sun without the use of a lens system. Any “speckle” will become a big “spot,” perhaps much bigger than the object itself, after its propagation, in principle, the smaller the size of the “speckle” in the source plane, the greater the size of the “spot” in the near-field planes.

**FIGURE 11.13**

Lensless near-field ( $\Delta\theta > \lambda/D$ ) ghost imaging with chaotic light demonstrated in 2006 by Scarcelli et al. In the first a few demonstrations, the diameter of the source was chosen to be a few millimeters, and  $z_1 = z_2$  was chosen to be a few hundred millimeters, with a pseudothermal light source of  $\lambda = 632\text{ nm}$ ,  $\Delta\theta \sim 10\lambda/D$  to  $40\lambda/D$ .  $D_1$  is a point-like photodetector that is scannable along the  $x_1$ -axis. The joint-detection between  $D_1$  and the bucket detector  $D_2$  is realized either by a photon-counting coincidence counter or by a standard HBT linear multiplier (RF mixer). In this measurement  $D_2$  is fixed in the focal point of a convex lens, playing the role of a bucket detector. The counting rate or the photocurrent of  $D_1$  and  $D_2$ , respectively, are measured to be constants. Surprisingly, an image of the 1-D object is observed in the joint-detection between  $D_1$  and  $D_2$  by scanning  $D_1$  in the plane of  $z_1 = z_2$  along the  $x_1$ -axis. The image, is blurred out when  $z_1 \neq z_2$ . There is no doubt that thermal radiations propagate to any transverse plane in a random and chaotic manner. There is no lens applied to force the thermal radiation “collapsing” to a point or speckle either. What is the physical cause of the point-to-point image-forming correlation in coincidences?

an optical beamsplitter. The reflected light is propagated and focused onto a point-like photodetector  $D_2$  (bucket detector) after passing through an object mask, which is a simple double slit in Figure 11.13.  $D_2$  is fixed in the focal plane of the focusing convex lens. It is clear that  $D_2$ , known as a bucket detector, cannot retrieve any information about the spatial distribution, or the aperture function of the object mask. The transmitted light is freely propagated to the plane of  $x_1$  to be detected by the scanning point-like photodetector  $D_1$ . The joint-detection between  $D_1$  and  $D_2$  is realized either by a photon-counting-coincidence counter or by a standard HBT type current-current linear multiplier. Although the single-detector counting rates of  $D_1$  and  $D_2$  are both constants during the measurement, surprisingly, an equal-sized 1D image of the object mask is observed in the joint detection when  $D_1$  is scanned in the plane of  $z_1 = z_2$  along the  $x_1$ -axis. The image contrast measures almost 50%, which is the maximum contrast we can expect. Figure 11.14 reports the measured image of the double-slit. Note that the constant background has been removed from the correlation.

After a large number of repeated measurements for different experimental schemes and conditions, Scarcelli et al. reported the following observations.

**FIGURE 11.14**

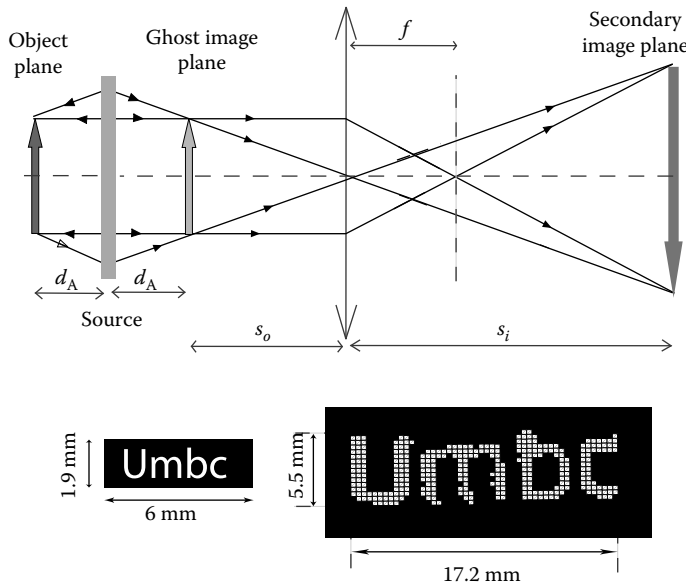
The measured ghost image of a double-slit. The lensless ghost image is observed to have equal size as that of the object. The same images can be observed from either photon-counting-coincidence or standard HBT type current-current correlator. Notice, the constant background has been removed from the correlation.

*Observation (1):* A typical measured ghost image of the double slit is shown in Figure 11.14. The measured curve reports the joint-detection counting rate between  $D_1$  and  $D_2$ , or the output current of an HBT linear multiplier, as a function of the transverse position of the point detector  $D_1$  along  $x_1$ -axis.

*Observation (2):* The measured contrasts vary significantly under different experimental schemes and conditions. It was found that the image contrast can achieve  $\sim 50\%$  in photon-counting measurement if no more than one joint-detection event occurs within the time window of the coincidence circuit. The maximum image contrast we expect for thermal light ghost imaging is 50%.

*Observation (3):* To achieve less than one joint-detection event per coincidence time window, weak light source is not a necessary condition. It can be easily achieved under bright light condition by using adjustable ND-filters with  $D_1$  and  $D_2$ .

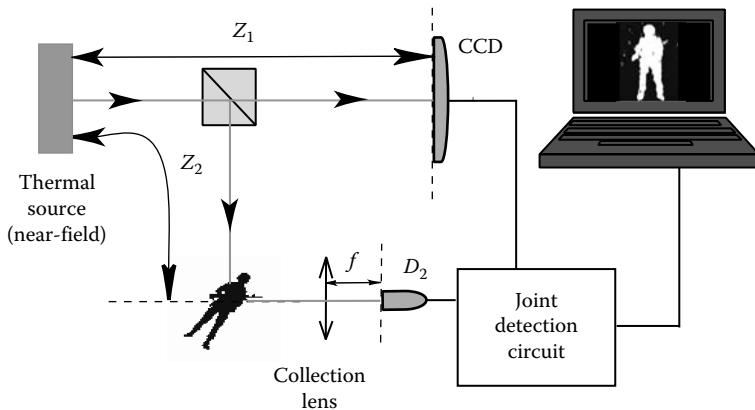
To confirm the observation is an image and not a “projection shadow,” Scarcelli et al. constructed a secondary imaging system, which is illustrated in the upper part of Figure 11.15. By using a convex imaging lens of focus length  $f$ , the ghost image is imaged onto a secondary image plane, where the scanning photodetector  $D_1$  is placed. The secondary image of the ghost image is recorded in the joint detection between  $D_1$  and  $D_2$  by means of either photon-counting coincidences or current-current correlation. The lower part of Figure 11.15 shows a secondary image of the ghost image of “UMBC” with a magnification factor of  $m = s_i/s_o \sim 2.9$ . The secondary imaging system is useful in certain experimental conditions, especially when the size of the 1:1 ghost image is either too big or too small to be captured by the CCD (scanning photodetector  $D_1$ ). A demagnified or enlarged secondary image would be helpful for certain applications. For instance, in a satellite-based ghost imaging system, the spatial resolution of the 1:1 primary ghost image,

**FIGURE 11.15**

Upper: unfolded schematic experimental setup of a secondary image measurement of the ghost image and the measured secondary images. By using a convex lens of focal length  $f$ , the ghost image is imaged onto a secondary image plane, which is defined by the Gaussian thin-lens equation,  $1/s_0 + 1/s_i = 1/f$ , with magnification  $m = -s_i/s_0$ . This setup is useful for distant large scale ghost imaging applications. Lower: a secondary image of the ghost image of "UMBC" with a magnification factor of  $m = s_i/s_0 \sim 2.9$ . Note that the secondary image is "blurred" out quickly when the scanning photodetector  $D_1$  is moved away from the image plane.

which could be as large as kilometers, is determined by the angular size of the thermal source such as the sun. When capturing the entire view of the 1:1 ghost image, the spatial resolution of the secondary image will be limited by the classical imaging system, however, the secondary ghost image may achieve the same spatial resolution of the primary ghost image by reducing its field of view and to reconstruct the entire ghost image piece by piece.

In 2008, Meyers et al. published a modified version of the original near-field lensless ghost imaging experiment. Figure 11.16 schematically illustrates their experimental setup. Figure 11.17 shows an observed ghost image of a toy soldier. This experiment improves the ghost imaging experiment of Scarcelli et al. in two aspects: (1) the bucket detector is not triggered by the transmitted light that passes through a mask but is instead triggered by the randomly scattered and reflected photons from the surface of a toy soldier; (2) no scanning point photodetector, but instead a CCD array of 2D operated at photon counting regime is used for the joint-detection with the bucket detector  $D_2$ . A ghost image of the toy soldier is captured by the gated CCD when taking  $z_1 = z_2$ . The spatial resolution of the ghost image is determined by the angular size of the thermal source: the greater

**FIGURE 11.16**

Improved near-field lensless ghost imaging of chaotic-thermal light demonstrated by Meyers et al. The bucket detector collects the randomly scattered and reflected photons from an object. The CCD cannot “see” the object, but is facing the light source. In their first a few laboratory demonstrations, the diameter of the pseudothermal source of  $\lambda = 632 \text{ nm}$  were chosen from millimeters to centimeters, and  $z_1 = z_2$  were chosen to be a few hundred millimeters to a few meters, all satisfy the Fresnel near-field condition  $\Delta\theta > \lambda/D$ .

**FIGURE 11.17**

Ghost image of a toy soldier model.

the angular size of the thermal source is the higher spatial resolution of the ghost image.

We now analyze the mathematical and physical processes of the lensless ghost imaging of thermal light. This discussion will show how the point-to-point second-order correlation of thermal light reproduces the ghost image of an aperture function  $A(\vec{r}_{obj})$  mathematically and physically.

Similar to the ghost imaging of entangled photon pairs, mathematically, the reproduction of the aperture function on the image plane is the result of a convolution between the aperture function and the second-order correlation function,

$$\begin{aligned} R_{12} &\propto \int_{\text{object}} d\vec{\rho}_2 |A(\vec{\rho}_2)|^2 g^{(2)}(\vec{\rho}_1, \vec{\rho}_2) \\ &= \int_{\text{object}} d\vec{\rho}_2 |A(\vec{\rho}_2)|^2 \left[ 1 + \text{somb}^2 \left( \frac{D}{d} \frac{\pi}{\lambda} |\vec{\rho}_1 - \vec{\rho}_2| \right) \right] \end{aligned} \quad (11.25)$$

in 2D, or

$$R_{12} \propto \int_{\text{object}} dx_2 |A(x_2)|^2 \left[ 1 + \text{sinc}^2 \left( \frac{D \pi (x_1 - x_2)}{d \lambda} \right) \right] \quad (11.26)$$

in 1D. Here,  $R_{12}$  is the joint counting rate of  $D_1$  and  $D_2$  or the output reading from the standard HBT current-current linear multiplier. The ghost image is expected to be

$$R_{12} \sim \text{constant} + |A(x_1)|^2, \quad (11.27)$$

if the sinc-function can be approximated as a  $\delta$ -function of  $x_1 - x_2$ . It is clear that the spatial resolution of the ghost image is determined by the angular diameter of the light source: the larger the size of the source in transverse dimensions, the higher the spatial resolution of the lensless ghost image achievable.

Similar to that of the ghost imaging of entangled photon pairs, the physical process corresponding to the above convolution is rather simple if the sombrero-like correlation function can be approximated as a  $\delta$ -function of  $|\vec{\rho}_1 - \vec{\rho}_2|$ , which is true for a large angular-sized thermal source radiating at visible and shorter wavelengths such as the sun. Suppose the scanning point detector  $D_1$  or a CCD element is triggered by a photon at a transverse position of  $\vec{\rho}_1$  in a joint-detection event with the bucket detector  $D_2$ , which is triggered by another photon that is scattered from the object. At  $z_1 = z_2$ , this photon would have twice the probability to be scattered from  $\vec{\rho}_{obj} = \vec{\rho}_1$ . After moving  $D_1$  to another transverse position  $\vec{\rho}'_1$ , and registering another joint-detection event between  $D_1$  and  $D_2$ , the photon that triggers  $D_2$  would have twice the probability of being scattered from  $\vec{\rho}'_{obj} = \vec{\rho}'_1$ . The probability of receiving a joint detection event at  $\vec{\rho}_1 = \vec{\rho}_{obj}$  and at  $\vec{\rho}'_1 = \vec{\rho}'_{obj}$  is proportional to the value of the aperture function  $A(\vec{\rho}_{obj})$  and  $A(\vec{\rho}'_{obj})$ , respectively. After accumulating a large number of joint-detection events at different transverse coordinates  $\vec{\rho}_1$ , a 50% contrast aperture function  $A(\vec{\rho}_1) = A(\vec{\rho}_{obj})$  is thus reproduced in the joint-detection as a function of  $\vec{\rho}_1$ .

A necessary condition for observing high contrast ghost image of thermal light requires single-photon detection of the bucket detector within

the coincidence time window. Otherwise, the information of  $A(\vec{\rho}_{obj})$  and  $A(\vec{\rho}'_{obj})$  will be mixed up by the scanning point photodetector  $D_1$  or by the CCD elements located at  $\vec{\rho}_1 = \vec{\rho}_{obj}$  and  $\vec{\rho}'_1 = \vec{\rho}'_{obj}$ . With mixed  $A(\vec{\rho}_{obj})$  and  $A(\vec{\rho}'_{obj})$  at  $\vec{\rho}_1$  and  $\vec{\rho}'_1$ , we will lose the ability to reproduce a joint-detection counting rate that is proportional to  $A(\vec{\rho}_{obj})$  at  $\vec{\rho}_1$  only, and a different joint-detection counting rate that is proportional to  $A(\vec{\rho}'_{obj})$  at  $\vec{\rho}'_1$  only, i.e., lose the ability of imaging. However, this requirement does not require single-photon sources. Due to the chaotic nature of the thermal light, the jointly detected photon pair is just two randomly distributed photons that fall into the coincidence time window by chance. The single-photon detection condition can be easily achieved by using adjustable ND-filters with  $D_1$  and  $D_2$ . High-contrast ghost image of thermal light can be reproduced with either bright or weak light sources, provided that no more than one joint-detection event within the coincidence time window is registered.\* Observing a ghost image, the natural, nonfactorizable, point-to-point image-forming correlation of thermal light must be obtainable at quantum level. Thus, the lensless near-field ghost imaging of thermal light essentially belongs to quantum imaging.

It is necessary to emphasize that the mathematics of the convolution between the aperture function and the point-to-point image-forming function has no difference in any optical imaging systems, including the traditional classical imaging, the ghost imaging with thermal light, and the ghost imaging with entangled states. Differences between different imaging systems come from different mechanisms that produce the point-to-point or point-to-“spot” image-forming function in that particular imaging system. In a classical imaging system, it is the first-order constructive–destructive interference that causes the point-to-point correspondence between the object and image planes, i.e., any radiation that is radiated (or reflected) from a point on the object plane will arrive at an unique point on the image plane. In the lensless ghost imaging system of thermal light, it is the two-photon interference that causes the nonlocal second-order correlation between the object and image planes. Analogous to the ghost image of entangled photon pairs, this natural, nonfactorizable, point-to-point correlation represents a nonlocal behavior of a measured pair of independent and randomly radiated photons: neither photon 1 nor photon 2 “knows” precisely where to go when they are created at each independent sub-source; however, if one is observed at a point on the object plane, the other one has twice the probability of arriving at a unique corresponding point on the image plane.†

---

\* In certain imaging applications, the goal is to recognize the “shape” of the object. For these kind of applications, this condition can be released.

† Similar to the far-field HBT correlation, the contrast of the near-field point-to-point image-forming function is 50%, i.e., a 2:1 ratio between the maximum value and the constant background.

## 11.5 Classical Simulation of Ghost Imaging

It is always possible to replace the natural, nonfactorizable, point-to-point correlation of thermal light or entangled photon pairs by an artificial correlation made from a radiation source in which the “light knows where to go” when it is prepared at the source. There have been quite a few attempts to simulate the point-to-point ghost image-forming correlation. Different from the randomly distributed and propagated chaotic-thermal radiation or entangled photon pairs in ghost imaging, the radiations in these classical simulations are prepared in such a way that each light beam or intensity “speckle” is propagated to a precise chosen “spot” of the object and a corresponding “spot” of the image plane. For each detection, the coordinate  $\vec{p}_{obj}$ , which is chosen by the light source, is recorded against the counting rate of the bucket detector at that coordinate, which is proportional to  $A(\vec{p}_{obj})$ , or recorded against the coordinate of the light “spot” on the image plane. The object function  $A(\vec{p}_{obj})$  is thus calculated and reproduced after a large number of such records. In fact, for this kind of light source, it is unnecessary to use two photodetectors for joint-detection. One bucket detector is sufficient to reproduce the image of the object.

We briefly discuss three classical simulations in the following:

### (I) Correlated laser beams

In 2002, Bennink et al. simulated ghost imaging by two correlated laser beams. The authors intended to show that two correlated co-rotating laser beams can simulate similar physical effects of entangled photon pairs. Figure 11.18 is a schematic picture of the experiment of Bennink

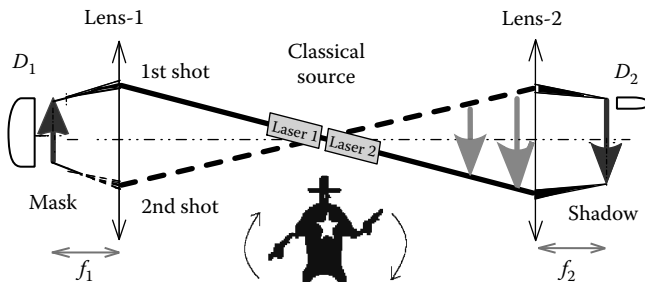


**FIGURE 11.18**

The point-to-point correlation is made shot by shot by two co-rotating laser beams. A ghost shadow can be made in coincidences by “blocking-unblocking” of the correlated laser beams, or simply by “blocking-unblocking” two correlated gun shots. In fact, the coincidence detection is unnecessary if the angular position of the laser beam-1 is known during the recording of the counting rate of  $D_1$ . What one needs to do is simply to record the counting rate of  $D_1$  against the angular coordinate of the laser beam. The shape of the mask will be recognized in the shot by shot operation of the rotating laser beam.

et al. Different from ghost imaging, here the point-to-point correspondence between the object plane and the “image plane” is made artificially by two co-rotating laser beams “shot by shot.” The laser beams propagated in opposite directions and focused on the object and image planes, respectively. If laser beam-1 is blocked by the object mask there would be no joint-detection between  $D_1$  and  $D_2$  for that “shot,” while if laser beam-1 is unblocked, a coincidence count will be recorded against that angular position of the co-rotating laser beams. A shadow of the object mask is then reconstructed in coincidences by the blocking-unblocking of laser beam-1.

The point-to-point correlation of Bennink et al. is made shot by shot between well-defined laser beams, which is not only different from that of ghost imaging, but also different from the standard statistical intensity fluctuation correlations. Nevertheless, the experiment of Bennink et al. obtained a ghost shadow, which may be useful for certain purposes. In fact, this experiment can be considered as a good example to distinguish a man-made factorizable classical intensity–intensity correlation from a natural, nonfactorizable second-order correlation that is caused by nonlocal two-photon interference.

## (II) Correlated speckles

Following a similar philosophy, Gatti et al. proposed a classical correlation between “speckles.” The experimental setup of Gatti et al. is depicted in Figure 11.19. Their experiments use either entangled photon pairs of SPDC or pseudothermal light for simulating ghost images in coincidences. The “ghost image” observed in coincidences comes from a man-made classical speckle-to-speckle correlation. The speckles observed on the object and image planes are the classical images of the speckles of the radiation source, reconstructed

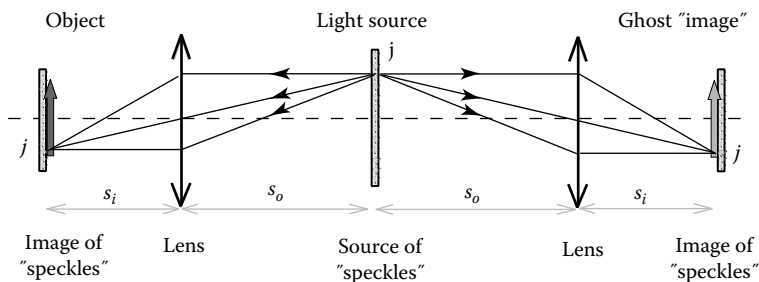


**FIGURE 11.19**

A ghost image is made by a man-made correlation of “speckles.” The two identical sets of speckles are the *classical images* of the speckles of the light source. The lens, which may be part of a CCD camera used for the joint measurement, reconstructs classical images of the speckles of the source onto the object plane and the image plane, respectively.  $s_o$  and  $s_i$  satisfy the Gaussian thin lens equation  $1/s_o + 1/s_i = 1/f$ .

by the lenses shown in the figure (the lens may be part of a CCD *camera* used for the joint measurement). Each speckle on the source, such as the  $j$ th speckle near the top of the source, has two identical images on the object plane and on the image plane. Mathematically, the speckle-to-speckle correlation is factorizable into a product of two classical images,

$$\gamma(\vec{\rho}_1, \vec{\rho}_2) \simeq \delta\left(\vec{\rho}_s - \frac{\vec{\rho}_1}{m}\right) \delta\left(\vec{\rho}_s - \frac{\vec{\rho}_2}{m}\right), \quad (11.28)$$

where

$\vec{\rho}_s$  is the transverse coordinate of the light source plane

$m = s_i/s_0$  is the classical imaging magnification factor\*

$z_1$  and  $z_2$  are defined as the optical distance between the plane of the light source and the planes of the object and the ghost image

The choices of  $z_1$  and  $z_2$  must satisfy the Gaussian thin lens equations for the two sets of classical imaging systems, respectively, see Figure 11.19. It is easy to see from Figure 11.19 that  $D_1$  and  $D_2$  will have more chance to be triggered jointly when they are in the position within the two identical speckles, such as the two  $j$ th speckles near the bottom of the object plane and the image plane. It is also easy to see that the size of the identical speckles determines the spatial resolution of the ghost shadow. This observation has been confirmed by quite a few experimental demonstrations. The classical simulation of Gatti et al. might be useful for certain applications. However, the man-made factorizable speckle-to-speckle correlation of Gatti et al. is fundamentally different from the natural, nonfactorizable point-to-point image-forming correlation observed in the ghost imaging experiment of Pittman et al. with entangled photon pairs and the lensless ghost imaging experiment of Scarcelli et al. with chaotic-thermal light.

### (III) “Computational” imaging

As we have concluded that it is unnecessary to use two photodetectors to reconstruct an image by a deterministic light source. The working principle is very simple: in each shot of the operation, the light beam illuminates a precise chosen “spot” of the object. The coordinate  $\vec{\rho}_o$ , which is chosen by the light source, is recorded against the counting rate of the bucket detector at that coordinate, which is proportional to  $|A(\vec{\rho}_o)|^2$ . The object function  $|A(\vec{\rho}_o)|^2$  is thus reproduced or calculated after a large number of such records. If the purpose of the imaging is for recognizing the “shape” of the object only, the light source may not necessarily illuminate a precise spot on the target object in each of its shot-to-shot operation. Instead, it may prepare a known “function” of intensity speckles on the target object plane, which is

---

\* The original publications of Gatti et al. chose  $m = 2f/2f = 1$  with  $1/2f + 1/2f = 1/f$  to image the speckles of the source onto the object plane and the ghost image plane.

randomly determined by the source from shot to shot. The measured counting rate of the bucket detector will be added to these coordinates in each shot of its operation. After a large number of accumulation, the shape of the object, or the shape of the mask, can be estimated statistically.

In the same sprite, Shapiro proposed a “computational” ghost imaging experiment, which consists of a controllable (deterministic) light source, an object for imaging, and a bucket photodetector.

Computational imaging technology has been intensively studied in the field of computer science in recent years. In these studies, spatial modulations of light, statistical modeling, and computation decoding are usually involved in the process of image computation and reconstruction for the purpose of optimizing the measurement efficiency and maximizing the information carried by each bit of the data.

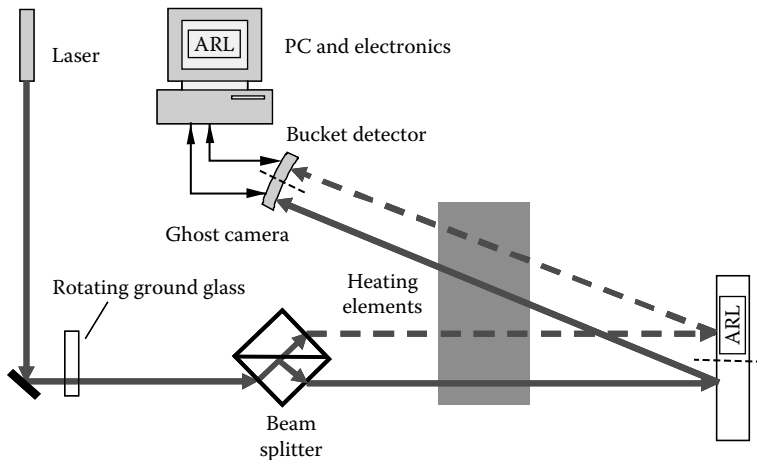
---

## 11.6 Turbulence-Free Ghost Imaging

The multiphoton interference nature of ghost imaging determines its peculiar features: (1) it is nonlocal and (2) its imaging resolution differs from that of classical. In this section, we analyze a recent ghost imaging experiment of Meyers et al., which demonstrated another interesting yet peculiar feature of ghost imaging of thermal light: “turbulence-free,” i.e., any index fluctuation-type turbulence occurring in the optical path would not affect the quality of the ghost image. As we know, atmospheric turbulence is a serious problem for classical satellite and aircraft-ground-based distant imaging. This feature is thus useful for these applications.

The schematic setup of the experiment is shown in Figure 11.20. It is a typical thermal light lensless ghost imaging setup, except for the addition of heating elements to produce laboratory atmospheric turbulence. In this experiment, turbulence is introduced to the optical paths by adding heating elements underneath the optical paths. Figure 11.20 illustrates the most serious situation in which turbulence occurs in all optical paths of the setup. The heating elements can be isolated to produce turbulence for any individual optical path too. Heating of the air causes temporal and spatial fluctuations on its index of refraction that makes the classical image of the object to jitter about randomly on the image plane of a classical camera.

Similar to their earlier demonstration of ghost imaging, the chaotic-thermal light is generated from a fairly large angular sized pseudo-thermal source and is split into two by a 50/50 beamsplitter. In the first a few laboratory experimental demonstrations, the diameter of the source were chosen to be a few millimeters to a few centimeters and the distances between the light source and the object,  $z_1$ , were chosen to be a few hundred millimeters to a few meters, guarantee the high resolution Fresnel near-field operation for

**FIGURE 11.20**

Schematic setup of a typical thermal light lensless ghost imaging experiment in which significant turbulence is introduced in its optical paths. Dashed line and arrows indicate the optical path of the “bucket” detector. The solid line and arrows indicate the optical path of the ghost image arm.

ghost imaging. The scattered and reflected photons from the object are collected and counted by a bucket detector, which is simulated by the right half of the CCDs in Figure 11.20. The other beam propagates to the ghost image plane of  $z_1 = z_2$ . We have learned from early analysis of thermal light ghost imaging experiments, placing a CCD array on the ghost image plane, the CCD array will capture the ghost image of the object if its exposure is gated by the bucket detector. In this experiment, the CCD array is replaced by a piece of glossy white paper. The scattered and reflect light from the glossy white paper, which contains the information of the ghost image, is then captured by the left half of the high-resolution CCD camera, which is operated at the photon-counting regime. The CCD camera is focused onto the ghost image plane and is gated by the bucket detector for the observation of the secondary ghost image. The secondary ghost image captured by the left half of the CCD camera is the image of the primary ghost image located at  $z_1 = z_2$ . In this special setup, the left half and the right half of the CCD camera may play the roles of two independent classical cameras in their “normal” ungated operation, and simultaneously capture the secondary ghost image in their gated joint-detection operation. The hardware circuit and the software program are designed to monitor the outputs of the left half and the right half of the CCD, individually, as two independent classical cameras, and simultaneously monitoring the gated output of the left half CCD as a ghost camera. In the measurement, the classical image and the secondary ghost image of the object were captured and monitored simultaneously when the turbulence is introduced to each or to all optical paths.

The effect of turbulence on a classical image can be easily seen from the blurring of the images. Technically the turbulence is characterized by the refractive index structure parameter  $C_n^2$ . The turbulence in this experiment achieved  $C_n^2 = 1.2^{-12}$  for the CCD arm and  $C_n^2 = 1.5^{-12}$  for the bucket detector arm. These values correspond extremely high levels of atmospheric turbulence, causing significant temporal and spatial fluctuations of the index of refraction, as well as the blurring of a classical image. Under the same turbulence, however, the ghost images behave differently, neither its spatial resolution nor its contrast were affected by the turbulence.

The turbulence-free ghost imaging is the result of the turbulence-free nonfactorizable, point-to-point image-forming correlation, which is caused by two-photon interference: superposition between paired two-photon amplitudes, corresponding to two different, yet indistinguishable, alternative ways of triggering a joint-detection event by two independent photons. We give a simple analysis in the following starting from Equation 9.99

$$G^{(2)}(\vec{\rho}_1, z_1; \vec{\rho}_2, z_2) \\ = \int d\vec{\kappa} d\vec{\kappa}' \left| \frac{1}{\sqrt{2}} [g_2(\vec{\rho}_2, z_2; \vec{\kappa}) g_1(\vec{\rho}_1, z_1; \vec{\kappa}') + g_2(\vec{\rho}_2, z_2; \vec{\kappa}') g_1(\vec{\rho}_1, z_1; \vec{\kappa})] \right|^2.$$

Equation 9.99 indicates an interference between two quantum amplitudes, corresponding to two alternatives, different yet indistinguishable, which leads to a joint photodetection event. This interference involves both arms of the optical setup as well as two distant photodetection events at  $(\vec{\rho}_1, z_1)$  and  $(\vec{\rho}_2, z_2)$ , respectively.

Now, we introduce an arbitrary phase disturbance  $e^{i\varphi_1(\vec{\rho}_1)}$  into the ghost image arm and another phase disturbance  $e^{i\varphi_2(\vec{\rho}_2)}$  into the object-bucket-detector arm to simulate the turbulence, where  $\varphi_1(\vec{\rho}_1)$  and  $\varphi_2(\vec{\rho}_2)$  add random phases onto the radiation of transverse coordinate  $\vec{\rho}_1$  and  $\vec{\rho}_2$ , respectively. The second-order correlation with turbulence turns out to be

$$G_{\text{Turb}}^{(2)}(\vec{\rho}_1, z_1; \vec{\rho}_2, z_2) \\ = \int d\vec{\kappa} d\vec{\kappa}' \left| \frac{1}{\sqrt{2}} \left[ g_2(\vec{\rho}_2, z_2; \vec{\kappa}) e^{i\varphi_2(\vec{\rho}_2)} g_1(\vec{\rho}_1, z_1; \vec{\kappa}') e^{i\varphi_1(\vec{\rho}_1)} \right. \right. \\ \left. \left. + g_2(\vec{\rho}_2, z_2; \vec{\kappa}') e^{i\varphi_2(\vec{\rho}_2)} g_1(\vec{\rho}_1, z_1; \vec{\kappa}) e^{i\varphi_1(\vec{\rho}_1)} \right] \right|^2 \\ = G^{(2)}(\vec{\rho}_1, z_1; \vec{\rho}_2, z_2). \quad (11.29)$$

It is easy to see that the phase turbulence has a null effect on the second-order correlation function  $G^{(2)}(\vec{\rho}_1, z_1; \vec{\rho}_2, z_2)$  of Equation 9.99. The normalized non-factorizable, point-to-point image-forming correlation  $g^{(2)}(\vec{\rho}_1; \vec{\rho}_2)$  of thermal light is thus turbulence free. The joint-detection counting rate between the

bucket detector and the CCD array will therefore reproduce the aperture function as a turbulence-free ghost image

$$R_{12} \propto \int d\vec{\rho}_2 |A(\vec{\rho}_2)|^2 g^{(2)}(\vec{\rho}_1; \vec{\rho}_2) \sim R_0 + |A(\vec{\rho}_1)|^2$$

where

$R_0$  is a constant

$A(\vec{\rho}_2)$  is the aperture function of the object

It should be emphasized that classical simulations of ghost imaging cannot obtain turbulence-free images. For instance, it is easy to see that the man-made factorizable speckle-to-speckle correlation

$$\gamma^{(2)}(\vec{\rho}_o, \vec{\rho}_i) \simeq \delta\left(\vec{\rho}_s - \frac{\vec{\rho}_o}{m}\right) \delta\left(\vec{\rho}_s - \frac{\vec{\rho}_i}{m}\right),$$

which is made by classically imaging the speckles of the common light source onto the object and image planes (with magnification factor  $m$ ) will be “blurred” under turbulence, because each classical image of the speckle will be “blurred” independently.

## Summary

In this chapter, we discussed the physics of quantum imaging. Quantum imaging was stimulated in recent years by the research development of quantum entanglement. Although questions regarding fundamental issues of quantum theory still exist, quantum entanglement has started to play important roles in practical applications. Quantum imaging is one of these exciting areas. Quantum imaging reproduces the image of an object through the measurement of nontrivial second-order or higher-order ( $N > 2$ ) coherence of entangled photon system or chaotic-thermal radiation. Quantum imaging is the result of a point-to-point imaging-forming correlation between the object plane and the imaging plane. In general, a two-photon imaging can be mathematically expressed as the convolution of the object aperture function and the second-order point-to-point, image-forming correlation of a measured pair of photons:

$$R_c(\vec{\rho}_i) = \int_{obj} d\vec{\rho}_o |A(\vec{\rho}_o)|^2 G^{(2)}(\vec{\rho}_o, \vec{\rho}_i).$$

Ghost imaging is perhaps the most surprising and interesting observation in the family of quantum imaging. We introduced two types of ghost

imaging in this chapter. Type-I ghost imaging takes advantage of a nonlocal point-to-point correlation of an entangled photon pair

$$G^{(2)}(\vec{\rho}_o, \vec{\rho}_i) \sim \delta\left(\vec{\rho}_o + \frac{\vec{\rho}_i}{m}\right).$$

Type-II ghost imaging utilized the nontrivial correlation of chaotic-thermal radiation at distance

$$G^{(2)}(\vec{\rho}_o, \vec{\rho}_i) \sim 1 + \delta(\vec{\rho}_o - \vec{\rho}_i).$$

Quantum imaging has so far demonstrated three peculiar features: (1) enhancing the spatial resolution of imaging beyond the diffraction limit, (2) reproducing ghost images in a “nonlocal” manner, and (3) dispersion-cancellation (type-I) and turbulence-free (type-II) imaging. All these features are the results of multiphoton interference.

In this chapter, we have also analyzed an experiment that realized the historical thought-experiment of Popper. In that experiment, ghost imaging played an important role. Popper was criticized to be mistaken because his proposed point source can never provide the perfect momentum correlation of a particle pair as he expected. In fact, a point source is unnecessary. With the help of ghost imaging, the required measurement condition can be easily achieved. Similar to EPR, Popper predicted the correct outcomes of his thought experiment, however, his interpretation of the experiment and especially his challenge on the uncertainty principle of quantum mechanics are incorrect as analyzed in the experimental realization.

## Suggested Reading

- Bennink, R.S., S.J. Bentley, and R.W. Boyd, *Phys. Rev. Lett.* 89, 113601 (2002).  
 Bennink, R.S. et al., *Phys. Rev. Lett.* 92, 033601 (2004).  
 Boto, A.N. et al., *Phys. Rev. Lett.* 85, 27333 (2000).  
 Cai, Y.J. and S.Y. Zhu, quant-ph/0407240, *Phys. Rev. E* 71, 056607 (2005).  
 D'Angelo, M., M.V. Chekhova, and Y.H. Shih, *Phys. Rev. Lett.* 87, 013602 (2001).  
 D'Angelo, M., A. Valencia, M.H. Rubin, and Y.H. Shih, *Phys. Rev. A* 72, 013810 (2005).  
 Gatti, A., E. Brambilla, M. Bache, and L.A. Lugiato, *Phys. Rev. A* 70, 013802, (2004a).  
 Gatti, A., E. Brambilla, M. Bache, and L.A. Lugiato, *Phys. Rev. Lett.* 93, 093602 (2004b).  
 Goodman, J.W., *Introduction to Fourier Optics*, McGraw-Hill Publishing Company, New York, 1968.  
 Kim, Y.H., and Y.H. Shih, *Found. Phys.* 29, 1849 (1999).  
 Klyshko, D.N., *Usp. Fiz. Nauk* 154, 133 (1988a).  
 Klyshko, D.N., *Sov. Phys. Usp* 31, 74 (1988b).  
 Klyshko, D.N., *Phys. Lett. A* 132, 299 (1988c).  
 Klyshko, D.N., *Photon and Nonlinear Optics*, Gordon & Breach Science, New York, 1988d.

- Martienssen, W., and E. Spiller, *Am. J. Phys.* 32, 919 (1964).
- Meyers, R., K.S. Deacon, and Y.H. Shih, *Phys. Rev. A* 77, 041801(2008).
- Meyers, R., K.S. Deacon, and Y.H. Shih, Turbulence-free ghost imaging, to be published.
- Pittman, T.B., Y.H. Shih, D.V. Strekalov, and A.V. Sergienko, *Phys. Rev. A* 52, R3429 (1995). [This experiment was named “ghost” imaging by the physics community.]
- Popper, K.R., *Naturwissenschaften* 22, 807 (1934).
- Popper, K.R., Realism in quantum mechanics and a new version of the EPR experiment, in *Open Questions in Quantum Physics*, G. Tarozzi and A. van der Merwe (eds), D. Reidel Publishing, Dordrecht, the Netherlands, 1985.
- Rubin, M.H., *Phys. Rev. A* 54, 5349 (1996).
- Scarcelli, G., A. Valencia, and Y.H. Shih, *Europhys. Lett.* 68, 618 (2004).
- Scarcelli, G., V. Berardi, and Y.H. Shih, *Phys. Rev. Lett.* 96, 063602 (2006).
- Shapiro, J.H., *Phys. Rev. A* 78, 061802(R) (2008).
- Shih, Y.H., *IEEE J. Select. Top. Quantum Electron.* 13, 1016 (2007).
- Strekalov, D.V., A.V. Sergienko, D.N. Klyshko, and Y.H. Shih, *Phys. Rev. Lett.* 74, 3600 (1995). [This experiment was named “ghost” interference by the physics community.]
- Valencia, A., G. Scarcelli, M. D’Angelo, and Y.H. Shih, *Phys. Rev. Lett.* 94, 063601 (2005).
- Wang, K., D. Cao, quant-ph/0404078; Cao, D., J. Xiong, and K. Wang, quant-ph/0407065 (2004).



# 12

---

## Two-Photon Interferometry—I: Biphoton Interference

---

Two-photon interferometry started to play an important role in quantum optics since the 1980s. In that time, Dirac was criticized to be mistaken because he stated in his book, *The Principles of Quantum Mechanics*, that “...photon... only interferes with itself. Interference between two different photons never occurs.” Two-photon interference was considered as the interference between two photons.

Is two-photon interference the interference of two photons? In the following discussion, we will provide a negative answer to this question: two-photon interference is not the interference between two photons. Two-photon interference is the result of the superposition of two-photon amplitudes, a nonclassical entity corresponding to different, yet indistinguishable, alternatives, which lead to a joint-photodetection event. In Dirac’s language, “... a pair of photon only interferes with itself ....”

In fact, neither classical theory nor quantum theory suggested the interference between different photons. Classical theory views optical interference as the result of coherent superposition between electromagnetic waves. In quantum theory, the superposition occurs between quantum amplitudes, which corresponds to alternative ways of annihilating a photon in a photoelectron event, or annihilating two photons in a joint-detection between two individual photodetectors, or annihilating  $N$  photons in an  $N$ -fold joint-detection between  $N$  individual photodetectors. Perhaps, the idea of interference between different photons came from the successful experimental observation of the first-order interference between radiations of independent light sources. The concept of interference between different photons was introduced simultaneously with Mandel’s experiments, which demonstrated the interferences between two individual CW laser beams and between two pulses produced from two synchronized lasers.\* Since then, interference between two photons became a hot and controversial topic in

---

\* (1) In the CW case, in order to obtain an observable interference pattern, the exposure time of the graphic film has to be less than the coherent time of the laser radiation. Although the observed interference patterns may differ from one exposure to another significantly, there is no doubt about interference in each individual exposure. (2) In the case of pulsed lasers, the two pulses have to be synchronized to overlap in time. The interference pattern may differ from pulse to pulse with random phases, the experiment of Mandel et al. observed clear interference pattern in each exposure of a pair of overlapped pulses.

the study of optical interferometry. Before the 1980s most experimental and theoretical studies focused on the first-order phenomena between coherent laser sources, which involve the measurement of a large number of photons. It is hard to distinguish the behavior of one photon, two photons, or a few photons from a bright laser beam or coherent electromagnet laser field, unless reducing the intensity to the single-photon level. However, at the single-photon level, on one hand, one “exposure” of two individual photons cannot provide us an observable interference pattern either spatially or temporally. On the other hand, a statistical measurement based on a large number of photons averages out any possible observable interference pattern due to the random phases between “patterns” from one “exposure” to another “exposure.” We may never be able to draw a definite conclusion to support or to reject the idea of interference of two photons.

The situation changed in the mid-1980s since the observation of two-photon interference of an entangled photon pair of SPDC. In a two-photon interferometer, Alley and Shih successfully demonstrated the interference of an orthogonally polarized signal–idler photon pair in 1986. In that experiment, the signal photon and the idler photon were prepared with a well-defined orthogonal polarization, either in the linear  $|X\rangle$  and  $|Y\rangle$  base or in the circular  $|R\rangle$  and  $|L\rangle$  base. With the help of a beamsplitter, the photon pair seemed to lose their original polarization and exhibited a typical EPR–Bohm–Bell correlation with the violation of Bell’s inequality. How could a pair of well-polarized photon turn into an entangled Bell state in which no polarization for either photon is specified? Alley and Shih provided an interpretation of the phenomenon as the result of a superposition between two different, yet indistinguishable, biphoton amplitudes\*: In addition to the Bell-type polarization correlation, a two-photon correlation ( $g^{(2)}(0) = 2$ ) and an anticorrelation ( $g^{(2)}(0) = 0$ ) were also observed with different chosen set of orientations of the polarization analyzers. The two-photon interference picture provided reasonable interpretation to that observation too: under the condition of complete overlapping, when the two biphoton amplitudes superpose in phase (with a “+” sign in between) the joint-detection of the two distant photodetectors reaches its maximum counting rate as the sign of “correlation,” i.e.,  $g^{(2)}(0) = 2$ ; when the two biphoton amplitudes superpose out of phase (with a “−” sign in between) the joint-detection counting rate achieves its minimum value as the signature of “anti-correlation,” i.e.,  $g^{(2)}(0) = 0$ ; when the two biphoton amplitudes superpose with other relative phases, a sinusoidal joint-detection counting rate comes out as the sign of two-photon interference. In 1987, Hong, Ou, Mandel, using a similar two-photon interferometer, reported an anticorrelation “dip” by selecting one polarization. Hong, Ou, and Mandel provided a different interpretation of the phenomenon as the interference between two different photons: the observation of anticorrelation requires the signal photon and the idler

---

\* The terminology *biphoton* was introduced by Klyshko.

photon to “meet” at the beamsplitter, indicating the interference between the signal photon and the idler photon. The debate took a decade to draw its conclusion. We will address this fundamentally important debate in the following section. The physics of two-photon interferometry will be discussed in the rest of this chapter in the process of analyzing a few historical two-photon interference experiments.

## 12.1 Is Two-Photon Interference the Interference of Two Photons?

Figure 12.1 illustrates a typical historical two-photon interference experiment for the observation of biphoton anticorrelation or “dip.” The entangled signal–idler photon pair generated in SPDC is mixed by a 50/50 near-normal incident beamsplitter,\* BS, and detected by two detectors,  $D_1$  and  $D_2$ , for coincidences. Balancing the signal and idler optical paths by positioning the beamsplitter, one can observe a “null” in coincidences, which indicates a complete destructive interference. When the optical path difference is increased from zero to unbalanced values, a coincidence curve of “dip” is observed. The width of the “dip” equals the coherence length of the signal

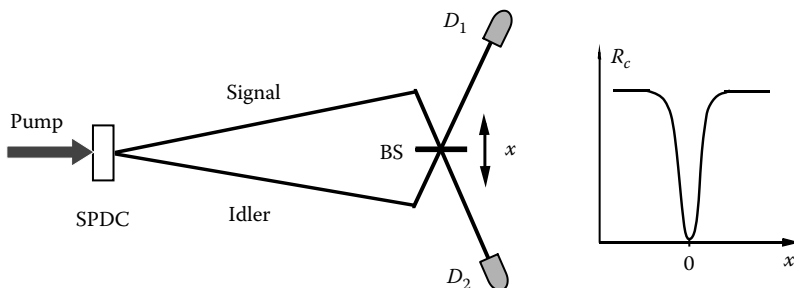


**FIGURE 12.1**

Schematic of a typical two-photon interferometer. Taking  $x = 0$ , in the balanced position, the signal photon “meets” the idler photon at BS. The joint-detection of the biphoton pair is taken between photon counting detectors  $D_1$  and  $D_2$ . A biphoton anticorrelation is observable in coincidences by scanning BS along the  $x$ -axis.

\* The first few historical “dip” experiments adopted this near-normal incidence configuration from Alley and Shih’s two-photon interferometer, which used orthogonal polarization for observing both anticorrelation and correlation. Near-normal incidence is the only configuration to achieve 50%–50% transmission–reflection for both S and P polarization. In fact, it is unnecessary to choose near-normal incident beamsplitter for an interferometer that uses one polarization for “dip” measurement only. For one polarization, 50%–50% can be achieved at any incident angle.

and idler, which is mainly determined by the spectral bandwidth of the filters placed in front of  $D_1$  and  $D_2$ .

It is quite tempting to rely on a picture, which somehow envisions the interference as arising from two individual photons of a given signal-idler pair meeting at the beamsplitter. Loosely speaking, indistinguishability leads to interference, for one sees that when the condition for total destructive interference is held, the two optical paths of the interferometer are of exactly the same length. It appears the signal and idler photons “meet” at the beamsplitter, and then it becomes impossible to distinguish which photon caused which single-detector detection event. Interference between the signal and idler photons occurs.

The picture of “interference between two photons” is further reinforced by the fact that changing the position of the beamsplitter from its balanced position, which begins to make these paths distinguishable, will bring about a degradation of interference. The coincidence-counting rate seems to depend on the amount of overlap of the signal “wavepacket” and the idler “wavepacket” that is achieved. The shape of the “dip” is determined by the temporal convolution of the signal “wavepacket” and the idler “wavepacket,” and therefore provides information about them. The “dip” was interpreted as the result of “photon bunching” or “anti-bunching” effects as well.

Is the above explanation correct? Does the observation of the “dip” mean the interference of the signal photon and the idler photon at the beamsplitter? Has the statement of Dirac failed in this experiment? We will provide an answer to these questions in the following way.

Let us examine a slightly modified experiment that is illustrated in Figure 12.2. The experimental set up is similar to Figure 12.1, except that the signal has two paths: one path length is  $L_l$  (longer path), the other is  $L_s$  (short

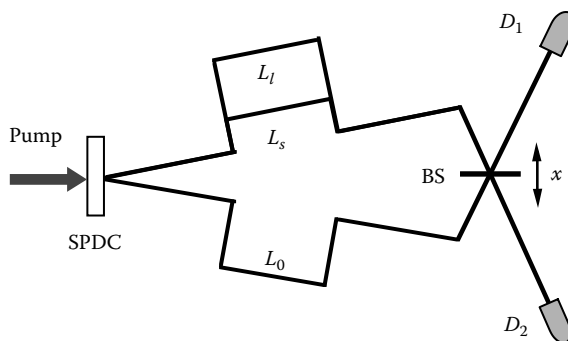


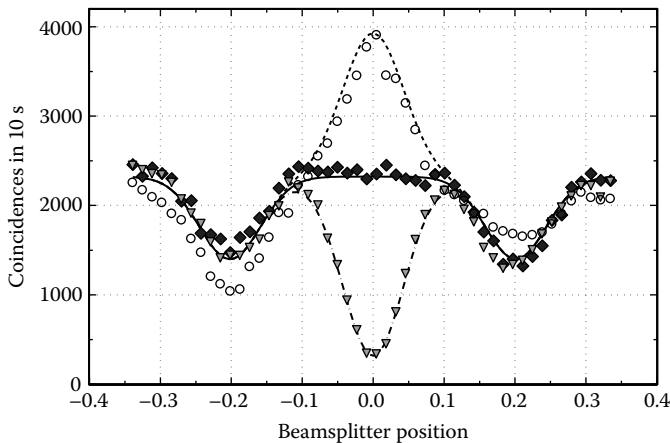
**FIGURE 12.2**

Schematic of a modified two-photon interferometer. In contrast with Figure 12.1, there exists two optical paths,  $L_l$  (long) and  $L_s$  (short), for the signal. The idler path is  $L_0 = (L_l + L_s)/2$  (middle). In this setup, the signal photon and the idler photon never “meet” at the beamsplitter when taking  $x = 0$ . Do we expect a “dip” at  $x = 0$ ?

path) with  $L_l - L_s \equiv 2\Delta L$ , such that  $l_{s,i}^{coh} < \Delta L \ll l_p^{coh}$ , where  $l_{s,i}^{coh}$  and  $l_p^{coh}$  are the coherence length of the signal–idler field and the pump field, respectively. Experimentally,  $l_{s,i}^{coh}$  is usually determined by the chosen spectral filters for the photodetectors,  $l_p^{coh}$  is determined by the spectral bandwidth of the pump laser. Due to the condition of  $\Delta L > l_{s,i}^{coh}$ , although the setup provides two paths for the signal, there is no observable first-order interference of the signal photon itself. The counting rates of the single detectors,  $D_1$  and  $D_2$ , respectively, remain constant. When the position of the beamsplitter BS is chosen to be  $x = 0$ , the path length of the idler arm takes its value of  $L_0$  such that  $L_l - L_0 = L_0 - L_s = \Delta L$ , i.e.,  $L_0$  is in the middle between  $L_l$  and  $L_s$ :  $L_0 = (L_l + L_s)/2$ .

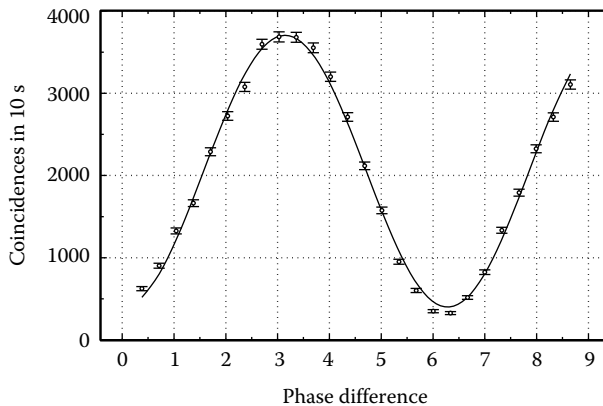
Based on the idea of “distinguishability of two photons,” the interference arising from the overlap of the signal and idler “wavepackets,” “dips” are expected to appear for two positions of the beamsplitter only, i.e.,  $x = \pm\Delta L/2$ . In these two cases, the idler photon has a 50% chance of overlapping with the signal photon. This partial distinguishability results in that the contrast of these two dips should be at most 50%. When  $x = 0$ , however, the photons do not meet. There is no overlap of the signal and idler photon “wavepackets” because of  $\Delta L > l_{s,i}^{coh}$ . Moreover, the detectors fire at random: in 50% of the joint-detections  $D_1$  fires ahead of  $D_2$  by  $\tau = \Delta L/c$ ; in the other 50% the opposite happens. So, no interference is expected.

Figure 12.3 shows the experimental result, which tells quite a different story. We observe a high contrast interference “dip” in the middle ( $x = 0$ ). In addition, the “dip” can turn into a “peak,” or any Gaussian-like function between the “peak” and “dip,” if the experimental conditions are slightly



**FIGURE 12.3**

A high contrast “dip” is observed. In addition, the destructive “dip” can turn to a constructive “peak” when  $L_l - L_s$  is slightly changed.

**FIGURE 12.4**

The dip-peak transition is shown as function of  $\phi$ .

changed. The transition from “dip” to “peak” depends on  $\phi = \omega_p \tau$ , where  $\tau = \Delta L/c$  is the time delay between the long path and the short path. Fixing  $x=0$  and varying  $\phi$ , by slightly increasing or decreasing the value of  $\Delta L$ , we observe a sinusoidal fringe in the joint-detection counting rate, which is shown in Figure 12.4, corresponding to a transition from “dip” to “peak” shown in Figure 12.3. The experimental data indicates that it is not a necessary condition to have the signal photon and the idler photon meeting each other at the beamsplitter for observing two-photon correlation, anticorrelation, or two-photon interference. The idea of “destructive interference between signal and idler photons” has failed to give a correct prediction. Thus, the “dip” or “peak” may not be considered as the interference between the signal and idler photons.

Two-photon interference is not the interference between two individual photons. We will see from the discussion that two-photon interference arises from the superposition of two-photon amplitudes, different yet indistinguishable alternatives that result in a click-click joint-detection event between two photodetectors. In this regard, the statement of Dirac is still valid if we modify it slightly: “...biphoton... only interferes with itself. Interference between two different biphotos never occurs.” Probably, Dirac’s statement “...photon... only interferes with itself” is confusing from the beginning, we may modify his statement as follows:

Interference is the result of the superposition of quantum amplitudes, a nonclassical entity corresponding to different yet indistinguishable alternatives which lead to a photodetection event or a joint-photodetection event. Interference between different photons or photon pairs never occurs.

#### I. Analysis of the historical “dip” experiment in Figure 12.1

Let us first analyze the historical experiments of Figure 12.1. As we have discussed earlier, the joint-detection counting rate,  $R_c$ , of detectors  $D_1$  and  $D_2$  on the time interval  $T$  is given by the Glauber theory in a general form:

$$\begin{aligned} R_c &\propto \int_T dt_1 dt_2 S(t_1 - t_2) G^{(2)}(\mathbf{r}_1, t_1; \mathbf{r}_2, t_2) \\ &= \int_T dt_1 dt_2 S(t_1 - t_2) \langle \Psi | \hat{E}_1^{(-)} \hat{E}_2^{(-)} \hat{E}_2^{(+)} \hat{E}_1^{(+)} | \Psi \rangle \\ &= \int_T dt_1 dt_2 S(t_1 - t_2) |\langle 0 | \hat{E}_2^{(+)} \hat{E}_1^{(+)} | \Psi \rangle|^2 \end{aligned} \quad (12.1)$$

where  $\hat{E}_j^{(\pm)}$ ,  $j = 1, 2$ , are positive- and negative-frequency components of the field at detectors  $D_1$  and  $D_2$ , respectively, and  $|\Psi\rangle$  is the state of the signal-idler photon pair:

$$|\Psi\rangle \simeq \int d\omega_p g(\omega_p) \int d\omega_s f(\omega_p, \omega_s) \hat{a}_s^\dagger(\omega_s) \hat{a}_i^\dagger(\omega_p - \omega_s) |0\rangle \quad (12.2)$$

where, again, we will concentrate to the temporal part of the state by selecting a pair of conjugate mode  $\mathbf{k}_s$  and  $\mathbf{k}_i$  for the measurement. Different from earlier discussions, here, the single mode requirement of  $\omega_p = \text{constant}$  has been released. We assume a well-collimated pump beam ( $\Delta\vec{\kappa} \sim 0$ ) with longitudinal mode distribution function  $g(\omega_p)$ . In the study of two-photon interference, we need to deal with finite bandwidth of pump, especially in the case of pulse-pumped SPDC. In Equation 12.1,  $S(t_1 - t_2)$  is a step function simulating the coincidence time window. The second-order temporal coherence  $G^{(2)}(t_1 - t_2)$  of SPDC, in general, is much narrower than the coincidence time window.  $S(t_1 - t_2)$  can be approximated as constant in this case. To simplify the notation we will ignore  $S(t_1 - t_2)$  from the time integral in the following discussions.

The fields  $\hat{E}_1^{(+)}$  and  $\hat{E}_2^{(+)}$  both have two contributions. Propagating the field operators from the source to the photodetector, and ignoring the transverse part of Green's function:

$$\begin{aligned} \hat{E}_1^{(+)} &= \frac{1}{\sqrt{2}} \left[ i \int d\omega E_0(\omega) e^{-i\omega\tau_1^R} \hat{a}_s(\omega) + \int d\omega E_0(\omega) e^{-i\omega\tau_1^T} \hat{a}_i(\omega) \right] \\ \hat{E}_2^{(+)} &= \frac{1}{\sqrt{2}} \left[ \int d\omega E_0(\omega) e^{-i\omega\tau_2^T} \hat{a}_s(\omega) + i \int d\omega E_0(\omega) e^{-i\omega\tau_2^R} \hat{a}_i(\omega) \right] \end{aligned}$$

where the superscripts  $R$  and  $T$  stand for reflection and transmission; again, only one polarization is considered.  $E_0(\omega) = \sqrt{\hbar\omega/2\epsilon_0 V}$ ,  $V$  is the quantization volume,  $\tau \equiv t - z/c$ ; again,  $z$  is the longitudinal coordinate along the optical path. Similar to earlier calculations, we will treat  $E_0(\omega)$  as a constant.

Applying the biphoton state of the signal-idler pair to Equation 12.1, it is easy to find that the effective two-photon wavefunction has two amplitudes:

$$\Psi_{21} = \langle 0 | \hat{E}_2^{(+)} \hat{E}_1^{(+)} | \Psi \rangle = \Psi(\tau_2^T, \tau_1^T) - \Psi(\tau_2^R, \tau_1^R). \quad (12.3)$$

where  $\Psi(\tau_2^T, \tau_1^T) = \langle 0 | E(\tau_2^T) E(\tau_1^T) | \Psi \rangle$  corresponds to the case when both signal and idler are transmitted at the beamsplitter, while  $\Psi(\tau_2^R, \tau_1^R) = \langle 0 | E(\tau_2^R) E(\tau_1^R) | \Psi \rangle$  corresponds to their reflection. The normalization constant has been absorbed into each of the amplitudes. The superposition of these two different, yet indistinguishable, two-photon amplitudes, or biphoton wavepackets, which contribute to a click-click joint-detection event between photodetectors  $D_1$  and  $D_2$ , determine the probability of having a joint-detection at space-time  $(\mathbf{r}_1, t_1; \mathbf{r}_2, t_2)$ :

$$\begin{aligned} G^{(2)}(\mathbf{r}_1, t_1; \mathbf{r}_2, t_2) &= |\Psi(\tau_2^T, \tau_1^T) - \Psi(\tau_2^R, \tau_1^R)|^2 \\ &= |\Psi(\tau_2^T, \tau_1^T)|^2 + |\Psi(\tau_2^R, \tau_1^R)|^2 \\ &\quad - \Psi^*(\tau_2^T, \tau_1^T)\Psi(\tau_2^R, \tau_1^R) - \Psi(\tau_2^T, \tau_1^T)\Psi^*(\tau_2^R, \tau_1^R). \end{aligned} \quad (12.4)$$

The biphoton interference is thus observable in the coincidence-counting rate

$$R_c \propto \int_T dt_1 dt_2 |\Psi(\tau_2^T, \tau_1^T) - \Psi(\tau_2^R, \tau_1^R)|^2. \quad (12.5)$$

Examining Equations 12.4 and 12.5, when  $\Psi(\tau_2^T, \tau_1^T)$  and  $\Psi(\tau_2^R, \tau_1^R)$  are completely “overlapped” in space-time, or are completely indistinguishable in the joint-detection events, the coincidence-counting rate is expected to be “null.” Shifting the position of the beamsplitter from its balanced position, which begins to make these wavepackets nonoverlapping, or distinguishable, will bring about a degradation of interference, i.e., observing a “dip” in coincidences. This is the result of the convolution of the biphoton wavepackets. In addition, if one could change the “–” to “+,” e.g., by playing with the polarization of the photon pair, one can make a “pick” instead of a “dip.” Both “dip” and “pick” can be easily observed in a polarization two-photon interferometer, which will be discussed later.

Further, for computing the interference as a function of the optical path difference of the two-photon interferometer, we need to calculate the biphoton wavepackets and their convolution. The biphoton wavepacket of SPDC has been calculated earlier in the case of monochromatic plane-wave pump. Similar to the earlier calculation, except taking into account of the pump distribution function  $g(\omega_p)$ , the biphoton wavepacket is thus:

$$\begin{aligned} \Psi(\tau_2, \tau_1) &= \Psi_0 \int d\omega_p g(\omega_p) e^{-i\frac{1}{2}\omega_p(\tau_2+\tau_1)} \\ &\times \int d\omega_s f(\omega_p, \omega_s) e^{-i\frac{1}{2}(\omega_s-\omega_i)(\tau_2-\tau_1)} \end{aligned} \quad (12.6)$$

where  $\Psi_0$  absorbs all constants from the field and the state. To simplify the mathematics, we start with a factorizable integral by imposing the following

approximations:

$$\begin{aligned}\omega_s &= \omega_s^0 + v, \quad \omega_i = \omega_i^0 - v, \\ \omega_s^0 + \omega_i^0 &\simeq \omega_p^0, \quad \omega_p = \omega_p^0 + v_p\end{aligned}\tag{12.7}$$

where  $\omega_s^0$ ,  $\omega_i^0$ , and  $\omega_p^0$  are the center frequencies for the signal, idler, and pump, respectively.  $\omega_s^0$ ,  $\omega_i^0$ , and  $\omega_p^0$  are considered as constants. Equation 12.6 is then simplified to a product of two functions:

$$\Psi(\tau_2, \tau_1) = \Psi_0 v(\tau_2 + \tau_1) u(\tau_2 - \tau_1),\tag{12.8}$$

with

$$v(\tau_2 + \tau_1) = e^{-i\omega_p^0(\tau_2 + \tau_1)/2} \int_{-\infty}^{\infty} d\nu_p g(\nu_p) e^{-i\nu_p(\tau_2 + \tau_1)/2}\tag{12.9}$$

and

$$u(\tau_2 - \tau_1) = e^{-i\frac{1}{2}(\omega_s^0 - \omega_i^0)(\tau_2 - \tau_1)} \int_{-\infty}^{\infty} d\nu f(\nu) e^{-i\nu(\tau_2 - \tau_1)}.\tag{12.10}$$

Basically, we have assumed the integral of  $u(\tau_2 - \tau_1)$  independent of  $\omega_p$ . This approximation is valid only for narrow bandwidth of  $g(\nu_p)$  such as that of a CW laser pump. This approximation cannot be used for short pulse pump, especially in the case of femtosecond laser-pumped SPDC. The discussion for ultrashort pulse-pumped SPDC will be given later.

The functions  $v(\tau_2 + \tau_1)$  and  $u(\tau_2 - \tau_1)$  can be written in terms of the Fourier transforms of  $g(\nu_p) \rightarrow \mathcal{F}_{\tau_+}\{g(\nu_p)\}$  and  $f(\nu) \rightarrow \mathcal{F}_{\tau_-}\{f(\nu)\}$ , where  $\tau_+ \equiv (\tau_2 + \tau_1)/2$  and  $\tau_- \equiv \tau_2 - \tau_1$ . The effective two-photon wavefunction, or biphoton wavepacket, is given by

$$\begin{aligned}\Psi(\tau_2, \tau_1) &= \Psi_0 \mathcal{F}_{\tau_+}\{g(\nu_p)\} e^{-i\omega_p^0\tau_+} \mathcal{F}_{\tau_-}\{f(\nu)\} e^{-i\omega_d^0\tau_-} \\ &= \Psi_0 \mathcal{F}_{\tau_+}\{g(\nu_p)\} \mathcal{F}_{\tau_-}\{f(\nu)\} e^{-i\omega_s^0\tau_2} e^{-i\omega_i^0\tau_1}\end{aligned}\tag{12.11}$$

where  $\omega_d^0 \equiv \frac{1}{2}(\omega_s^0 - \omega_i^0)$ .

The cross interference term in Equation 12.5 is calculated as follows:

$$\begin{aligned}&\int dt_1 dt_2 \Psi^*(\tau_2^T, \tau_1^T) \Psi(\tau_2^R, \tau_1^R) \\ &= |\Psi_0|^2 \int dt_+ \mathcal{F}_{\tau_+^T}^*\{g(\nu_p)\} \mathcal{F}_{\tau_+^R}\{g(\nu_p)\} e^{i\omega_p^0(\tau_+^T - \tau_+^R)} \\ &\quad \times \int dt_- \mathcal{F}_{\tau_-^T}^*\{f(\nu)\} \mathcal{F}_{\tau_-^R}\{f(\nu)\} e^{i\omega_d^0(\tau_-^T - \tau_-^R)}\end{aligned}$$

$$\begin{aligned} &\simeq |\Psi_0|^2 \int dt_- \mathcal{F}_{t_-}^* \{f(v)\} \mathcal{F}_{t_- - \delta} \{f(v)\} \\ &= |\Psi_0|^2 \mathcal{F}_{t_-}^* \{f(v)\} \otimes \mathcal{F}_{t_- - \delta} \{f(v)\} \end{aligned} \quad (12.12)$$

where  $t_+ \equiv t_2 + t_1$ ,  $t_- \equiv t_2 - t_1$ , and  $\delta = [(z_2^R - z_1^R) - (z_2^T - z_1^T)]/c$  is the optical path difference introduced by moving the beamsplitter upward from its balanced position in the two-photon interferometer of Figure 12.1. We have assumed degenerate ( $\omega_d^0 = 0$ ) type I SPDC in the above calculation. The coincidence-counting rate  $R_c$  is therefore

$$R_c(\delta) = R_0 [1 - \mathcal{F}_{t_-}^* \{f(v)\} \otimes \mathcal{F}_{t_- - \delta} \{f(v)\}], \quad (12.13)$$

where  $R_0$  is a constant. Assuming Gaussian wavepackets, the convolution yields a Gaussian function  $|\Psi_0|^2 e^{-\delta^2/\tau_c^2}$  with  $\tau_c = l_{s,i}^{coh}/c$  the coherence time of the signal and idler fields. The coincidence-counting rate  $R_c$  is approximately

$$R_c(\delta) = R_0 [1 - e^{-\delta^2/\tau_c^2}].$$

It is now clear that the observed “dip” is a biphoton “destructive interference” phenomenon. Mathematically, the “dip” is the result of a convolution, or cross correlation, of the biphoton wavepackets,  $\Psi(\tau_2^T, \tau_1^T)$  and  $\Psi(\tau_2^R, \tau_1^R)$ , along  $\tau_-$  axis. Figure 12.5 shows two conceptual Feynman diagrams for the two-photon interference experiment of Figure 12.1. While the beamsplitter is in its balanced position, the two Feynman alternatives (reflect-reflect vs transmit-transmit) are indistinguishable. Moving the beamsplitter away from its balanced position, the optical path difference of the two Feynman

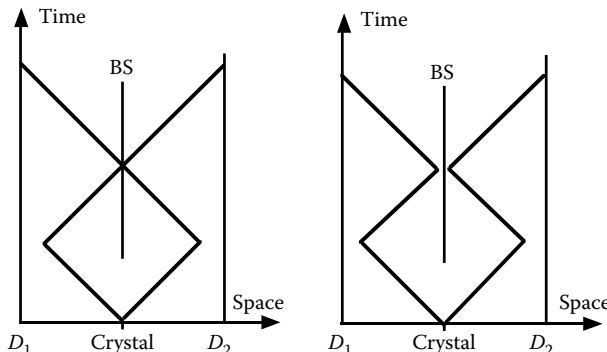


**FIGURE 12.5**

Conceptual Feynman diagrams. The beamsplitter is represented by the thin vertical lines. The biphoton amplitudes, or biphoton wavepackets, are represented by “straight lines.” Left:  $\Psi(\tau_2^T, \tau_1^T)$  (transmit-transmit); Right:  $\Psi(\tau_2^R, \tau_1^R)$  (reflect-reflect). The two Feynman alternatives both contribute to a “click-click” joint-detection event of  $D_1$  and  $D_2$ .

paths are no longer the same, corresponds to the moving away of the 2D wavepacket along the  $\tau_-$  axis. The superposition takes place between the transmit-transmit and the reflect-reflect biphoton amplitudes, instead of the signal photon and the idler photon. In Dirac's language: it is the interference of biphoton itself, but not the interference between the signal and the idler photons.

In general, the biphoton interference can occur in two different ways: (1) the convolution takes place along  $\tau_-$  direction or (2) the convolution takes place along  $\tau_+$  direction. In the experiment shown in Figure 12.1, the biphoton wavepackets,  $\Psi(\tau_2^T, \tau_1^T)$  and  $\Psi(\tau_2^R, \tau_1^R)$  completely "overlap" along  $\tau_+$ , since  $\tau_+^T = \tau_+^R$  in any position of the beamsplitter.  $\Psi(\tau_2^R, \tau_1^R)$ , however, moves away from  $\Psi(\tau_2^T, \tau_1^T)$  along  $\tau_-$ , when scanning the beamsplitter from its balanced position.

## II. Analysis of the modified "dip" experiment in Figure 12.2

In the view of biphoton interference, we now present an interpretation for the experiment of Figure 12.2. Differing from that of the experiment of Figure 12.1, the special experimental setup in Figure 12.2 achieves four alternatives of producing a joint-detection event between  $D_1$  and  $D_2$ . The effective biphoton wavefunction thus consists of four amplitudes:

$$\Psi_{21} = \Psi(\tau_2^{LT}, \tau_1^{0T}) - \Psi(\tau_2^{0R}, \tau_1^{LR}) + \Psi(\tau_2^{ST}, \tau_1^{0T}) - \Psi(\tau_2^{0R}, \tau_1^{SR})$$

where the superscripts  $L$ ,  $S$ , and  $0$  represent the long path, the short path, and the middle path of Figure 12.2, respectively. Consequently,  $G^{(2)}$  has 16 terms contributing to the coincidence photon counting:

$$G^{(2)} = |\Psi(\tau_2^{LT}, \tau_1^{0T}) - \Psi(\tau_2^{0R}, \tau_1^{LR}) + \Psi(\tau_2^{ST}, \tau_1^{0T}) - \Psi(\tau_2^{0R}, \tau_1^{SR})|^2.$$

However, due to the experimental condition that we have chosen,  $L_l - L_0 = L_0 - L_s \equiv \Delta L \gg l_{s,i}^{coh}$ , where, again,  $l_{s,i}^{coh}$  is the coherence length of the signal and idler, only four cross terms are nonzero. We have the following eight nonzero contributions to the coincidence-counting rate of  $D_1$  and  $D_2$ :

$$\begin{aligned} R_c \propto \int_T dt_1 dt_2 & \left\{ |\Psi(\tau_2^{LT}, \tau_1^{0T})|^2 + |\Psi(\tau_2^{0R}, \tau_1^{LR})|^2 \right. \\ & + |\Psi(\tau_2^{ST}, \tau_1^{0T})|^2 + |\Psi(\tau_2^{0R}, \tau_1^{SR})|^2 \\ & - \Psi^*(\tau_2^{LT}, \tau_1^{0T})\Psi(\tau_2^{0R}, \tau_1^{SR}) - \Psi(\tau_2^{LT}, \tau_1^{0T})\Psi^*(\tau_2^{0R}, \tau_1^{SR}) \\ & \left. - \Psi^*(\tau_2^{ST}, \tau_1^{0T})\Psi(\tau_2^{0R}, \tau_1^{LR}) - \Psi(\tau_2^{ST}, \tau_1^{0T})\Psi^*(\tau_2^{0R}, \tau_1^{LR}) \right\}. \end{aligned} \quad (12.14)$$

The interference cross terms are calculated as

$$\begin{aligned} & \Psi^*(\tau_2^{LT}, \tau_1^{0T}) \Psi(\tau_2^{0R}, \tau_1^{SR}) \\ &= |\Psi_0|^2 e^{-i\omega_p^0 \frac{\Delta L}{c}} \mathcal{F}_{t+}^* \{g(v_p)\} \mathcal{F}_{t_+ + \frac{\Delta L}{c}} \{g(v_p)\} \mathcal{F}_{t-}^* \{f(v)\} \mathcal{F}_{t_- - \delta} \{f(v)\}, \\ & \Psi^*(\tau_2^{ST}, \tau_1^{0T}) \Psi(\tau_2^{0R}, \tau_1^{LR}) \\ &= |\Psi_0|^2 e^{i\omega_p^0 \frac{\Delta L}{c}} \mathcal{F}_{t+}^* \{g(v_p)\} \mathcal{F}_{t_+ - \frac{\Delta L}{c}} \{g(v_p)\} \mathcal{F}_{t-}^* \{f(v)\} \mathcal{F}_{t_- - \delta} \{f(v)\}, \end{aligned}$$

where  $\delta = [(z_2^{0R} - z_1^{SR}) - (z_2^{LT} - z_1^{0T})]/c$  is the additional optical path difference introduced by moving the beamsplitter upward from its “balanced” position  $x = 0$ .

The Feynman paths for this experiment are illustrated in Figure 12.6. The upper two correspond to  $\Psi(\tau_2^{LT}, \tau_1^{0T})$  and  $\Psi(\tau_2^{0R}, \tau_1^{SR})$ ; the lower two correspond to  $\Psi(\tau_2^{ST}, \tau_1^{0T})$  and  $\Psi(\tau_2^{0R}, \tau_1^{LR})$ . Notice that if  $\Delta L \ll l_p^{coh}$ , the upper two and the lower two Feynman paths, respectively, are indistinguishable by means of the click-click joint-photodetection of  $D_1$  and  $D_2$ .

By increasing or decreasing  $\Delta L$  or  $\delta$ , we have two freedom to “shift” the 2-D biphoton wavepackets, independently, along  $\tau_+$  and  $\tau_-$  axes:

$$\left[ \mathcal{F}_{t+}^* \{g(v_p)\} \otimes \mathcal{F}_{t_+ \pm \frac{\Delta L}{c}} \{g(v_p)\} \right] \left[ \mathcal{F}_{t-}^* \{f(v)\} \otimes \mathcal{F}_{t_- - \delta} \{f(v)\} \right].$$

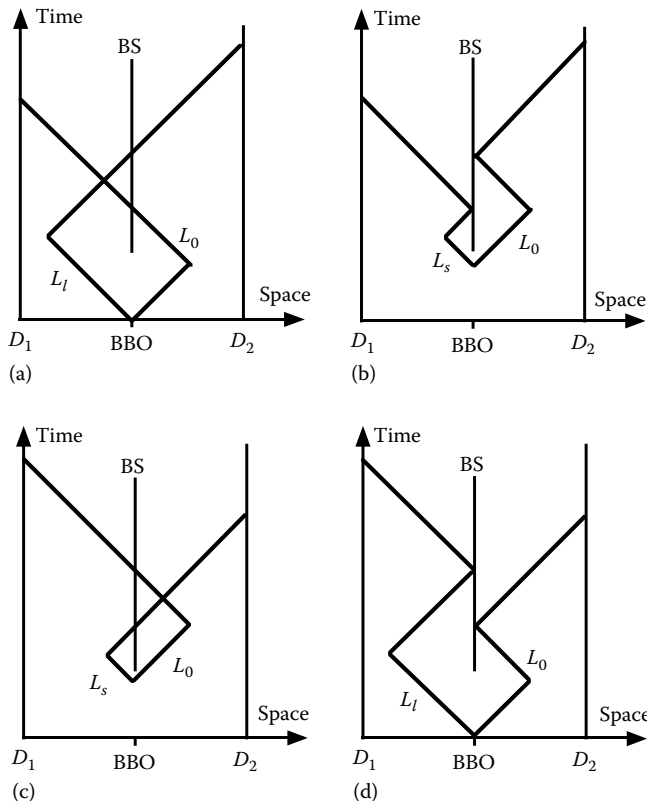
For a chosen value of  $\delta \ll l_p^{coh}$ , the upper pair and the lower pair of 2D wavepackets illustrated in Figure 12.6 are almost 100% overlapped along the  $\tau_+$  axis, respectively, yields  $\mathcal{F}_{t+}^* \{g(v_p)\} \otimes \mathcal{F}_{t_+ \pm \Delta L/c} \{g(v_p)\} \sim 1$ . The joint-detection counting rate in the neighborhood of  $x = 0$  is thus

$$R_c(\delta) = R_0 [1 - \cos \phi \mathcal{F}_{t-}^* \{f(v)\} \otimes \mathcal{F}_{t_- - \delta} \{f(v)\}]. \quad (12.15)$$

For Gaussian wavepackets along the  $t_-$  axis,  $R_c$  is approximately

$$R_c(\delta) = R_0 [1 - \cos \phi e^{-\delta^2/\tau_c^2}].$$

Equation 12.15 indicates a  $\sim 100\%$  interference modulation while scanning the beamsplitter in the neighborhood of  $x = 0$ . It is noticed that the phase factor  $\phi = \omega_p^0 (\Delta L/c)$  plays an important role in this measurement. Subsequently setting the phase  $\phi$  to be equal to  $\pi$ ,  $0$ , or  $\pi/2$  we observe, respectively, a peak, dip, or flat coincidence rate  $R_c$  distribution centered at the “balanced” position of the beamsplitter, agreeing with the experimental results shown in Figures 12.3 and 12.4. The mechanism of manipulating phase  $\phi$  along  $\tau_+$  axis is very useful for the preparation of Bell states. We will learn more about it in next section.

**FIGURE 12.6**

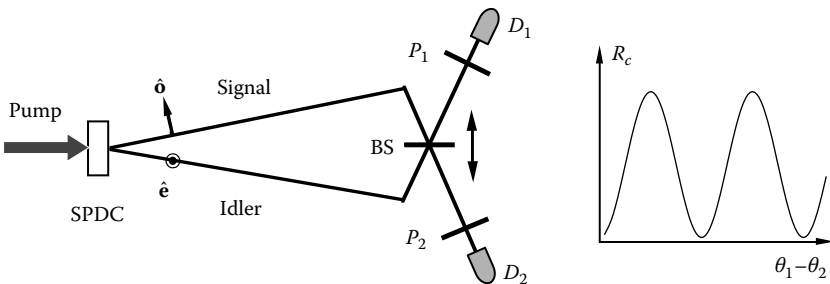
Conceptual Feynman diagrams. (a) and (b) are two amplitudes for a joint detection such that  $D_1$  fires ahead of  $D_2$ ; (c) and (d) are two amplitudes in the reversed order. If  $\Delta L \ll l_p^{coh}$ , the upper two and the lower two, respectively, are indistinguishable.

## 12.2 Two-Photon Interference with Orthogonal Polarization

In the history of two-photon interferometry, a great driving force was the experimental testing of Bell's inequality. In fact, the first historical two-photon interferometer was designed for that purpose. Before the discussions of Bell's states and Bell's inequality, we analyze a simple two-photon interferometer with a pair of orthogonal polarized photons and a pair of independent polarization analyzers that is schematically illustrated in Figure 12.7.

Assuming an idealized biphoton source generates an orthogonal polarized signal-idler pair in the following state:

$$|\Psi\rangle \simeq \int d\nu f(\nu) \hat{\mathbf{a}}_s^\dagger(\omega_s^0 + \nu) \hat{\mathbf{e}} \hat{a}_i^\dagger(\omega_i^0 - \nu) |0\rangle \quad (12.16)$$

**FIGURE 12.7**

Schematic of a typical two-photon polarization interferometer. The type-II SPDC produces an orthogonal polarized signal-idler pair. BS is a 50%–50% beamsplitter for both  $\hat{o}$  and  $\hat{e}$  polarized signal and idler photons. The polarization analyzers  $P_1$  and  $P_2$  are oriented at any chosen angles  $\theta_1$  and  $\theta_2$  for polarization correlation measurement. Fixing BS at  $x = 0$  by examining the correlation “peak” and the anticorrelation “dip,” a sinusoidal polarization correlation of  $\sin^2(\theta_1 - \theta_2)$  is observed in the coincidences of  $D_1$  and  $D_2$ .

where  $\hat{o}$  and  $\hat{e}$  are unit vectors along the o-ray and the e-ray polarization direction of the SPDC crystal. In Equation 12.16, we have assumed perfect phase matching  $\omega_s + \omega_i - \omega_p = 0$  and  $k_{s,o} + k_{i,e} - k_p = 0$ . Suppose the polarizers of the detectors  $D_1$  and  $D_2$  are set at angles  $\theta_1$  and  $\theta_2$ , relative to the polarization direction of the o-ray of the SPDC crystal, respectively, the field operators can be written as

$$\begin{aligned}\hat{E}_1^{(+)} &= \frac{1}{\sqrt{2}} \left[ i \int d\omega E_0(\omega) e^{-i\omega\tau_1^R} \hat{\theta}_1 \hat{a}_s(\omega) + \int d\omega E_0(\omega) e^{-i\omega\tau_1^T} \hat{\theta}_1 \hat{a}_i(\omega) \right] \\ \hat{E}_2^{(+)} &= \frac{1}{\sqrt{2}} \left[ \int d\omega E_0(\omega) e^{-i\omega\tau_2^T} \hat{\theta}_2 \hat{a}_s(\omega) + i \int d\omega E_0(\omega) e^{-i\omega\tau_2^R} \hat{\theta}_2 \hat{a}_i(\omega) \right]\end{aligned}$$

where  $\hat{\theta}_j$ ,  $j = 1, 2$ , is the unit vector along the  $j$ th analyzer direction. The effective wavefunction that contribute to the joint-detection events of  $D_1$  and  $D_2$  is calculated to be

$$\Psi_{21} = (\hat{\theta}_1 \cdot \hat{e})(\hat{\theta}_2 \cdot \hat{o}) \Psi(\tau_2^T, \tau_1^T) - (\hat{\theta}_1 \cdot \hat{o})(\hat{\theta}_2 \cdot \hat{e}) \Psi(\tau_2^R, \tau_1^R). \quad (12.17)$$

The joint-detection counting rate of  $D_1$  and  $D_2$  is thus

$$\begin{aligned}R_c &\propto \int_T dt_1 dt_2 |(\hat{\theta}_1 \cdot \hat{e})(\hat{\theta}_2 \cdot \hat{o}) \Psi(\tau_2^T, \tau_1^T) - (\hat{\theta}_1 \cdot \hat{o})(\hat{\theta}_2 \cdot \hat{e}) \Psi(\tau_1^R, \tau_2^R)|^2 \\ &= R_0 \left\{ \sin^2 \theta_1 \cos^2 \theta_2 + \cos^2 \theta_1 \sin^2 \theta_2 - \sin \theta_1 \cos \theta_2 \cos \theta_1 \sin \theta_2 \right. \\ &\quad \times \left. \frac{1}{R_0} \int_T dt_1 dt_2 [\Psi^*(\tau_2^T, \tau_1^T) \Psi(\tau_2^R, \tau_2^R) + \Psi(\tau_2^T, \tau_1^T) \Psi^*(\tau_2^R, \tau_2^R)] \right\} \quad (12.18)\end{aligned}$$

where  $\Psi(\tau_2^T, \tau_1^T)$  and  $\Psi(\tau_2^R, \tau_1^R)$  are the transmitted-transmitted and reflected-reflected biphoton wavepackets with the following time averaging:

$$\int_T dt_1 dt_2 |\Psi(\tau_1, \tau_2)|^2 = R_0.$$

The third term of Equation 12.18 determines the degree of two-photon coherence. Considering degenerate CW laser-pumped SPDC, the biphoton wavepacket of Equation 12.8 can be simplified as

$$\Psi(\tau_2, \tau_1) = \Psi_0 \mathcal{F}_{\tau_-} \{f(v)\}.$$

Where we have absorbed the phase factor  $e^{-i\omega_p(\tau_1+\tau_2)/2}$  into  $\Psi_0$ . The coefficient of  $(\sin \theta_1 \cos \theta_2 \cos \theta_1 \sin \theta_2)$  in the third term of Equation 12.18 is thus

$$\begin{aligned} & \int_T dt_1 dt_2 \mathcal{F}_{\tau_2^T - \tau_1^T} \{f(v)\} \mathcal{F}_{\tau_2^R - \tau_1^R} \{f(v)\} \\ &= \mathcal{F}_{t_-} \{f(v)\} \otimes \mathcal{F}_{t_- - \delta} \{f(v)\}, \end{aligned}$$

where, again,  $\delta$  is the optical path difference introduced by moving the beamsplitter from its balanced position of  $x = 0$ .

In a polarization two-photon interferometer, we will be able to observe two biphoton interference effects:

### I. Anticorrelation “dip” and correlation “peak”

In this measurement, we fix  $\theta_1$  and  $\theta_2$ , such that  $\theta_1 = 45^\circ$  with  $\theta_2 = 45^\circ$  or  $\theta_1 = 45^\circ$  with  $\theta_2 = -45^\circ$ , an anticorrelation—“dip” or a correlation—“peak” as function of  $\delta$  will be observed in the coincidence-counting rate  $R_c$  when scanning  $\delta$  in the neighborhood of  $x = 0$ ,

$$R_c(\delta) = R_0 [1 \mp \mathcal{F}_{t_-}^* \{f(v)\} \otimes \mathcal{F}_{t_- - \delta} \{f(v)\}]. \quad (12.19)$$

### II. Polarization correlation

In this measurement, we make  $\delta = 0$  to achieve complete overlapping between biphoton wavepackets  $\Psi(\tau_2^T, \tau_1^T)$  and  $\Psi(\tau_2^R, \tau_1^R)$ . The coefficient of  $(\sin \theta_1 \cos \theta_2 \cos \theta_1 \sin \theta_2)$  in the third term of Equation 12.18 achieves its maximum value of 2. The coincidence-counting rate will be a function of  $\theta_1 - \theta_2$  when manipulating the relative angle of the two polarization analyzers:

$$R_c(\theta_1, \theta_2) = R_0 \sin^2(\theta_1 - \theta_2). \quad (12.20)$$

This result is equivalent to the polarization correlation measurement for Bell's state

$$|\Psi\rangle = \frac{1}{\sqrt{2}} [ |X_1\rangle|Y_2\rangle - |Y_1\rangle|X_2\rangle ],$$

where  $|X_1\rangle$  and  $|Y_1\rangle$  are defined as the polarization states that, respectively, coincide with the *o*-ray and *e*-ray polarization direction of SPDC. Bell's states and polarization correlation will be discussed in detail in Chapter 14.

Since Einstein, Podolsky, and Rosen published their 1935 paper, the concept of “physical reality” became an important subject of study for physicists and philosophers. In the early 1950s, Bohm simplified the Einstein–Podolsky–Rosen state of 1935 to discrete spin variables by introducing the singlet state of two spin 1/2 particles:

$$|\Psi\rangle = \frac{1}{\sqrt{2}} [ |\uparrow\rangle_1 |\downarrow\rangle_2 - |\downarrow\rangle_1 |\uparrow\rangle_2 ]$$

where the kets  $|\uparrow\rangle$  and  $|\downarrow\rangle$  represent states of spin “up” and spin “down,” respectively, along an *arbitrary* direction. For the EPR–Bohm state, the spin of neither particle is determined; however, if one particle is measured to be spin up along a certain direction, the other one must be spin down along that direction, despite the distance between the two spin 1/2 particles and the orientation of the Stern–Gerlach analyzers (SGA). The nonlocal behavior of this two-particle system leads to the questions of EPR–Bohm: Are the two spin 1/2 particles prepared with defined spins at the source and in the course of their propagation? Is spin a physical reality of a particle independent of the observation?

In the Alley–Shih experiment, the same question was asked in a slightly different way: if two particles are prepared with well-defined spin, can we expect similar nonlocal behavior? This question leads to their 1986 experiment. With the help of a two-photon interferometer, Alley and Shih discovered that a pair of photons with well-defined polarization can give similar EPR–Bohm type correlation. Since then, the complete set of Bell states have been experimentally observed

$$\begin{aligned} |\Psi^{(\pm)}\rangle &= \frac{1}{\sqrt{2}} [ |H_1\rangle|V_2\rangle \pm |V_1\rangle|H_2\rangle ] \\ |\Phi^{(\pm)}\rangle &= \frac{1}{\sqrt{2}} [ |H_1\rangle|H_2\rangle \pm |V_1\rangle|V_2\rangle ]. \end{aligned}$$

where  $|H\rangle$  and  $|V\rangle$ , respectively, indicate well-defined horizontal and vertical polarization. In fact, any set of orthogonal polarization can be used to construct Bell states. In general, we use polarization state vector  $|X\rangle$  and  $|Y\rangle$ , which can be defined in any orthogonal orientation, to replace  $|H\rangle$  and  $|V\rangle$ .

This observation has been puzzling us for two decades. (1) There seems nothing “hidden” in this experiment. The signal photon and the idler photon both have well-defined polarization before entering into the interferometer. (2) The signal-field and the idler field are first-order incoherent, the incoherent superposition of the signal-idler fields cannot change the polarization of the signal and idler, either during the course of their propagation or in the process of their annihilation. What is the cause of the nonlocal EPR–Bohm–Bell correlation for a pair of photons with well-defined polarization? We have attempted to introduce the concept of two-photon (two-particle) interference since 1986. In fact, this concept has been applied in the above analysis of the Alley–Shih experiment. In this regard, the nonlocal behavior of the EPR–Bohm spin 1/2 particles is a two-particle interference phenomenon. The EPR–Bohm state specifies a coherent superposition of two-particle amplitudes, corresponding to two different, yet indistinguishable, alternative ways for the two spin 1/2 particles to trigger a joint-detection event through the two distant SGAs. We will continue our discussion on the concept of physical reality and the physics behind this interesting observation.

### 12.3 Franson Interferometer

In 1989, Franson proposed an interferometer to explore the surprising behavior of entangled photon pairs. Figure 12.8 is a schematic setup of a Franson interferometer, which consists of an entangled biphoton source, and a pair of classic unbalanced interferometers with photon-counting detectors coupled at their output ports. A pair of entangled photons, such as the signal photon and the idler photon of SPDC are sent into the unbalanced interferometers 1 and 2, respectively. The photon-counting detectors are used for monitoring the single-detector counting rates, independently, and for observing the joint-detection counting rate, coincidentally. The optical path differences of

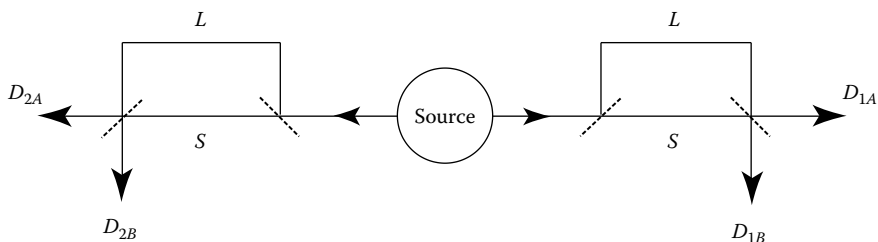


**FIGURE 12.8**

Schematic setup of a Franson interferometer.

the two interferometers,  $\Delta L_1$  and  $\Delta L_1$  are both chosen to be much greater than the coherence length,  $l_{coh}$ , of the signal-idler field, thus, there is no observable first-order interference in the single-detector counting rates of  $D_1$  and  $D_2$  when increasing or decreasing the values of  $\Delta L_1$  and  $\Delta L_1$  either individually or simultaneously. The joint-detection counting rate of  $D_1$  and  $D_2$ , however, shows  $\sim 100\%$  interference if the operation of the two interferometers satisfy the following conditions: (1) the photon pair only passes through the long-long and the short-short paths of the interferometers and (2)  $|\Delta L_1 - \Delta L_2| \ll l_{coh}$ ; (3)  $\Delta L_1 + \Delta L_1 \ll l_p$  where  $l_p$  is the coherence length of the pump for SPDC. The surprising observation is the result of a biphoton interference phenomenon.

In the following calculation, we assume condition (1) is satisfied, i.e., there are only two alternatives,  $\Psi(\tau_1^L, \tau_2^L)$  and  $\Psi(\tau_1^S, \tau_2^S)$ , contributing to a joint-photodetection event of  $D_1$  and  $D_2$ . The coincidence-counting rate of  $D_1$  and  $D_2$  is thus

$$\begin{aligned} R_c \propto & \int_T dt_1 dt_2 |\Psi(\tau_1^L, \tau_2^L) + \Psi(\tau_1^S, \tau_2^S)|^2 \\ = & \int_T dt_1 dt_2 [|\Psi(\tau_1^L, \tau_2^L)|^2 + |\Psi(\tau_1^S, \tau_2^S)|^2 \\ & + \Psi^*(\tau_1^L, \tau_2^L) \Psi(\tau_1^S, \tau_2^S) + \Psi(\tau_1^L, \tau_2^L) \Psi^*(\tau_1^S, \tau_2^S)] \end{aligned} \quad (12.21)$$

where the superscripts  $L$  and  $S$  of  $\tau$  label the long path and the short path of the  $j$ th classic interferometer,  $j = 1, 2$ . The cross term is the nontrivial term that determines the interference. Now, we further assume a biphoton wavepacket of SPDC,  $\Psi(\tau_1, \tau_2) \sim \Psi_0 v(\tau_1 + \tau_2) u(\tau_1 - \tau_2)$ , as shown in Equation 12.8. The interference term can be written as

$$\begin{aligned} & \int_T dt_1 dt_2 \Psi^*(\tau_1^L, \tau_2^L) \Psi(\tau_1^S, \tau_2^S) \\ = & e^{i\omega_p^0(\Delta L_1 + \Delta L_2)/2c} \left[ \mathcal{F}_{\tau_1^L + \tau_2^L}^* \{g(v_p)\} \otimes \mathcal{F}_{\tau_1^S + \tau_2^S} \{g(v_p)\} \right] \\ \times & e^{i(\omega_s^0 - \omega_i^0)(\Delta L_1 - \Delta L_2)/2c} \left[ \mathcal{F}_{\tau_1^L - \tau_2^L}^* \{f(v)\} \otimes \mathcal{F}_{\tau_1^S - \tau_2^S} \{f(v)\} \right]. \end{aligned} \quad (12.22)$$

It is easy to see that the two convolutions in the brackets require the satisfaction of conditions (2) and (3) for observing interference from a Franson interferometer. The interference pattern has two parts of sinusoidal modulation: the sum frequency  $\omega_s^0 + \omega_i^0 = \omega_p^0$  and the beating frequency  $\omega_s^0 - \omega_i^0$ . If degenerate SPDC is applied, and if one manipulates the optical path difference of the interferometers simultaneously with  $\Delta L_1 = \Delta L_2 = \Delta L$ , the interference pattern keeps the sum frequency only as predicated by Franson in 1989:

$$R_c \propto 1 + V \cos(\omega_p \tau) \quad (12.23)$$

where  $\tau \equiv \Delta L/c$  is the time delay between the long and short paths of the interferometer and  $V$  is the interference visibility, which is evaluated from the two convolutions in Equation 12.22.

Franson interferometer has been studied intensively in the 1990s with the use of entangled two-photon source of SPDC. Most of the interesting physics associated with Franson interferometer have been experimentally observed.

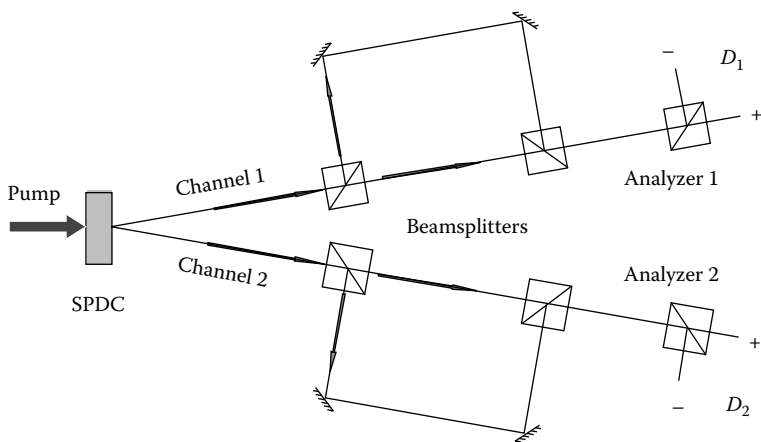
The implementation of condition (1) is not that straightforward even if we are given an entangled biphoton source of SPDC, two standard Mach-Zehnder interferometers, and proper photodetection-coincidence electronics. Naturally, there are four alternative ways in which the signal-idler photon pair may contribute to a joint-photodetection event. Besides  $\Psi(\tau_1^L, \tau_2^L)$  and  $\Psi^S(\tau_1, \tau_2^S)$ , the other two alternatives, or biphoton amplitudes,  $\Psi(\tau_1^L, \tau_2^S)$  and  $\Psi(\tau_1^S, \tau_2^L)$  do not despair automatically. The joint-photodetection-counting rate of  $D_1$  and  $D_2$  is the result of a superposition that contains four alternatives:

$$R_c \propto \int_T dt_1 dt_2 |\Psi(\tau_1^L, \tau_2^L) + \Psi(\tau_1^S, \tau_2^S) + \Psi(\tau_1^L, \tau_2^S) + \Psi(\tau_1^S, \tau_2^L)|^2.$$

Due to the operation condition of the interferometer,  $\Delta L_{1,2} > l_{coh}$ , however, only one cross term has nonzero contribution to the interference, which is the same as shown in Equation 12.22. In this case, one would observe the same interference pattern as that of Equation 12.21, except the maximum interference visibility is reduced from 100% to 50%:

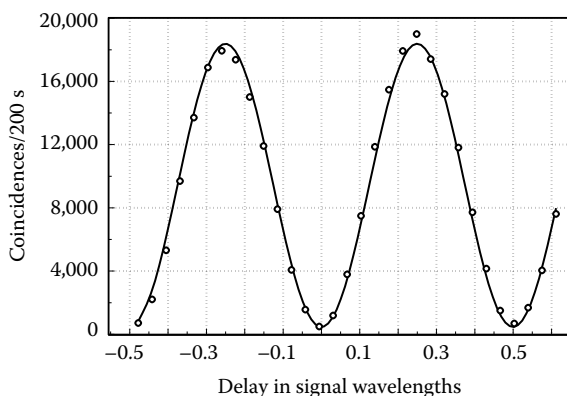
$$R_c \propto 1 + \frac{1}{2} V \cos(\omega_p \tau).$$

Figure 12.9 schematically illustrates a clever realization of Franson interference by Strekalov et al. from which ~100% interference visibility was observed. The entangled two-photon source is a non-collinear type II SPDC similar to that shown in Figure 14.5. The unbalanced Mach-Zehnder interferometer in channels 1 and 2 is implemented by a long quartz rod followed with a Pockels cell. The quartz rods delay the slow polarization component relative to the fast one due to their birefringence. The Pockels cell, by applying an adjustable DC voltage, is for “fine-tuning” of the optical path difference,  $\Delta L$ , of the interferometer. The birefringent delay of the interferometer is carefully chosen to be greater than the coherence time of the measured signal-idler field, which is mainly determined by the bandwidth of the spectral filters placed in front of  $D_1$  and  $D_2$ . The fast-slow axes of the quartz rods as well as that of the Pockels cell are both oriented carefully to provide the  $o_1 - e_2$  and  $e_1 - o_2$  amplitudes with long-long and short-short optical paths, thus satisfy condition (1) of the Franson interferometer. Following

**FIGURE 12.9**

Scheme setup of a Franson interferometer. The entangled biphoton source is a type II non-collinear SPDC. The clever use of polarization guarantees the implementation of condition (1): only  $\Psi(\tau_1^L, \tau_2^L)$  and  $\Psi(\tau_1^S, \tau_2^S)$  contribute to a joint-photodetection event.

the quartz rods and Pockels cells, in channels 1 and 2, are two polarization analyzers,  $A_1$  and  $A_2$ . The axes of the analyzers are oriented at  $45^\circ$  relative to that of the quartz rod and the Pockels cell. The joint-photodetection events are recorded as a function of the optical path difference  $\Delta L$  with the help of a coincidence circuit in nanosecond time window. A  $(95.0 \pm 1.4)\%$  visibility of interference pattern specified by Equation 12.23 was reported in an earlier publication of Strekalov et al., see Figure 12.10. Recent measurements

**FIGURE 12.10**

An earlier experimental data of Strekalov et al. reported  $(95.0 \pm 1.4)\%$  interference visibility in joint-detection counting rate. The single-detector counting rates of  $D_1$  and  $D_2$ , however, were both kept constant while tuning the optical path differences of  $\Delta L$ .

of Franson interferometer have observed  $\sim 100\%$  interference visibility with statistical errors a few orders smaller.

The high-degree two-photon coherence observed in Franson interferometer is considered as a demonstration of the nonlocal EPR inequality in energy. As we know, the loss of first-order interference in each of the Mach–Zehnder interferometer indicates a considerable large uncertainty in  $\Delta\hbar\omega_{s,i}$ , at least  $\Delta\hbar\omega_{s,i} > 2\pi\hbar c/\Delta L$ . In contrast, the two-photon interference pattern has shown quite a high degree of visibility, which indicates

$$\Delta(\hbar\omega_s + \hbar\omega_i) \ll \min(\Delta\hbar\omega_s, \Delta\hbar\omega_i).$$

In EPR's language, the energy of neither the signal photon nor the idler photon is defined in the course of their preparation and propagation; however, if one is measured with a certain value the other one must be measured with a unique value.

---

## 12.4 Two-Photon Ghost Interference

A two-photon interference experiment reported by Strekalov et al. in 1995 surprised the physics community. The experiment was named as “ghost” interference soon after the publication. The experiment itself is quite simple. The signal photon and the idler photon of SPDC are propagated to different directions to trigger two distant point-like photon-counting detectors  $D_1$  and  $D_2$ , respectively. On the way of its propagation, the signal passed a standard Young's double slit, while the idler propagated freely to reach  $D_2$ . Due to the poor spatial coherence of the signal field, there is no observable standard first-order Young's interference when scanning  $D_1$  transversely behind the double slit. A high visibility second-order double-slit interference-diffraction pattern, however, was observed in the joint-photodetection counting rate of  $D_1$  and  $D_2$  when  $D_2$  was scanned across the “empty” idler beam while  $D_1$  was placed in a fixed position behind the double slit. The name of “ghost” was given because of the surprising nonlocal feature of the phenomenon.

We now understood the observation is a two-photon interference phenomenon. The very special physics explored in the ghost interference experiment might have been its apparent nonlocal behavior: by scanning  $D_2$  across the idler beam, how could one observe the interference pattern produced by the signal beam in distance?

The schematic experimental setup of the historical ghost interference experiment is illustrated in Figure 12.11. A pair of orthogonal polarized signal–idler photon is prepared by a near-collinear degenerate type-II SPDC. The signal and the idler are separated by a polarization beamsplitter. The signal passes through a Young's double-slit (or single-slit) aperture and then

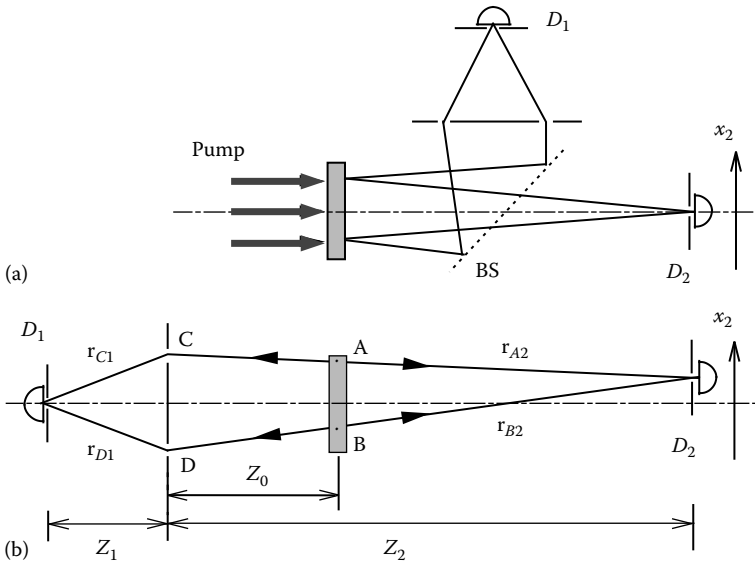


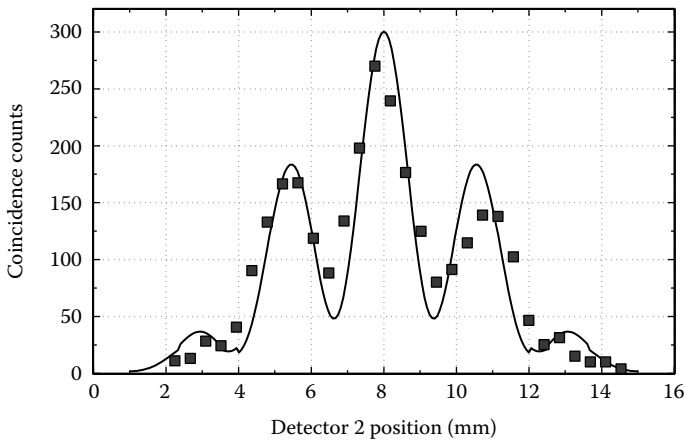
**FIGURE 12.11**  
Simplified experimental scheme (a) and the “unfolded” version (b).

travels about 1 m to meet a point-like photon counting detector  $D_1$ . The idler travels to the far-field zone to feed into an optical fiber, which is mated with a photon-counting detector  $D_2$ . During the joint-detection measurement,  $D_1$  is fixed at a point behind the double slit while the horizontal transverse coordinate,  $x_2$ , of the fiber input tip, which is equivalent to that of  $D_2$ , is scanned by a step motor.

Figure 12.12 is the ghost interference-diffraction pattern published by Strekalov et al. The coincidence counting rate is reported as a function of  $x_2$ , which is obtained by scanning  $D_2$  (the fiber tip) across the idler beam, whereas the double slit is in the signal beam. Young’s double-slit has a slit width of  $a = 0.15$  mm and slit distance of  $d = 0.47$  mm. The interference period is measured to be  $2.7 \pm 0.2$  mm and the half-width of the envelope is estimated to be about 8 mm. By curve fittings, it is easy to find that the observation is a standard Young’s interference pattern, i.e., a sinusoidal oscillation with a sinc-function envelope:

$$R_c \propto \text{sinc}^2\left(\frac{\pi ax_2}{\lambda z_2}\right) \cos^2\left(\frac{\pi dx_2}{\lambda z_2}\right). \quad (12.24)$$

The interference pattern in Figure 12.12, which is described by Equation 12.24 was taken when  $D_1$  was placed in a symmetrical point between the double slit. If  $D_1$  is moved to an asymmetrical point, which results in unequal distances to the two slits, the interference-diffraction pattern is shifted from

**FIGURE 12.12**

Typical observed interference-diffraction pattern. The solid curve is a theoretical fitting. The calculation has taken into account the finite size of  $D_1$  and  $D_2$ , resulting in less than 100% interference visibility. In this measurement,  $D_1$  was fixed in a symmetrical position behind the double slit in the signal beam, while  $D_2$  was scanned across the “empty” idler beam. If  $D_1$  is moved to an asymmetrical point, which results in unequal distance to the two slits, the interference-diffraction pattern is observed to be simply shifted to one side.

the current symmetrical position to one side of  $x_2$ . Similar to the ghost imaging experiment, the remarkable feature here is that  $z_2$  is the distance from the slits’ plane, which is in the signal beam, back through BS to the SPDC crystal and then along the idler beam to the scanning fiber tip of detector  $D_2$  (see Figure 12.11). The calculated interference period and half-width of the sinc-function from Equation 12.24 are 2.67 and 8.4 mm, respectively.

Although the interference-diffraction pattern is observed in coincidences, *the single-detector counting rates are both observed to be constant* when scanning detectors  $D_1$  and  $D_2$ . It seems reasonable not to have any interference modulation in the single counting rate of  $D_2$ , which is located in the “empty” idler beam. Of interest, however, is that the absence of the interference-diffraction structure in the single counting rate of  $D_1$ , which is behind the double slit, is mainly due to the poor spatial coherence or the considerable large divergence of the signal beam,  $\Delta\theta \gg \lambda/d$ .

To explain the ghost interference, a simple model is presented in the following. The basic concept of the model is, again, two-photon interferometry of entangled state. In Chapter 4, we have introduced two EPR  $\delta$ -functions  $\delta(\vec{p}_s - \vec{p}_i)$  and  $\delta(\vec{k}_s + \vec{k}_i)$  for near-collinear degenerate SPDC, which means (1) the signal-idler pair may come out from any point on the output plane of the SPDC, however, if the signal is measured at a certain position, the idler must be emitted from the same position; and (2) the signal and idler may propagate to any directions around the pump beam, however, if the signal

is observed in a certain direction, the idler must be emitted to the opposite direction with equal angle relative to the pump. This peculiar entanglement nature of the signal–idler two-photon system determines the only two possible two-photon amplitudes in Figure 12.11, when signal passes through the double-slit aperture while the idler triggers  $D_2$ . The coherent superposition is taken between these two-photon amplitudes.

As we have discussed in the ghost imaging experiment, the EPR  $\delta$ -functions allow us to treat SPDC as a mirror in terms of “usual” geometrical optics in the following manner: we envision the output plane as a “hinge point” and “unfold” the schematic of Figure 12.11a into that shown in Figure 12.11b. Based on the unfolded Klyshko picture of Figure 12.11b, we now give a quantitative calculation of the experiment.

The joint detection counting rate  $R_c$  is proportional to the probability of jointly detecting the signal–idler pair by detectors  $D_1$  and  $D_2$ ,

$$R_c \propto G^{(2)} = \left\langle \Psi \left| \hat{E}_1^{(-)} \hat{E}_2^{(-)} \hat{E}_2^{(+)} \hat{E}_1^{(+)} \right| \Psi \right\rangle = \left| \left\langle 0 \left| \hat{E}_2^{(+)} \hat{E}_1^{(+)} \right| \Psi \right\rangle \right|^2 \quad (12.25)$$

where  $|\Psi\rangle$  is the two-photon state of SPDC. Let us simplify the mathematics by using the following “two-mode” expression for the state, bearing in mind that the EPR  $\delta$ -functions have been taken into account based on the “straight line” picture of Figure 12.11.

$$|\Psi\rangle = \epsilon \left[ \hat{a}_s^\dagger \hat{a}_i^\dagger e^{i\varphi_A} + \hat{b}_s^\dagger \hat{b}_i^\dagger e^{i\varphi_B} \right] |0\rangle \quad (12.26)$$

where  $\epsilon$  is a normalization constant that is proportional to the pump field (classical) and the nonlinearity of the crystal,  $\varphi_A$  and  $\varphi_B$  are the phases of the pump field at A and B, and  $\hat{a}_j^\dagger$  ( $\hat{b}_j^\dagger$ ) is the photon creation operator for the upper (lower) mode in Figure 12.11 ( $j = s, i$ ). In terms of the Copenhagen interpretation, one may say that the interference is due to the uncertainty in the birthplace (A or B in Figure 12.11) of a signal–idler pair.

In Equation 12.25, the fields at the detectors are given by

$$\begin{aligned} \hat{E}_1^{(+)} &= \hat{a}_s \exp(ik r_{A1}) + \hat{b}_s \exp(ik r_{B1}) \\ \hat{E}_2^{(+)} &= \hat{a}_i \exp(ik r_{A2}) + \hat{b}_i \exp(ik r_{B2}) \end{aligned} \quad (12.27)$$

where  $r_{Ai}$  ( $r_{Bi}$ ) is the optical path length from region A (B) along the upper (lower) path to the  $i$ th detector. Substituting Equations 12.26 and 12.27 into Equation 12.25,

$$G^{(2)} \propto \left| e^{i(kr_A + \varphi_A)} + e^{i(kr_B + \varphi_B)} \right|^2 \propto 1 + \cos[k(r_A - r_B)] \quad (12.28)$$

where we have assumed  $\varphi_A = \varphi_B$  in the second line of Equation 12.34. We have also defined the overall optical path lengths between the detectors  $D_1$

and  $D_2$  along the upper and lower paths (see Figure 12.11):  $r_A \equiv r_{A1} + r_{A2} = r_{C1} + r_{C2}$ ,  $r_B \equiv r_{B1} + r_{B2} = r_{D1} + r_{D2}$ , where  $r_{Ci}$  and  $r_{Di}$  are the respective path lengths from slits C and D to the  $i$ th detector.

If the optical paths from the fixed detector  $D_1$  to the two slits are equal, i.e.,  $r_{C1} = r_{D1}$ , and if  $z_2 \gg d^2/\lambda$  (far field), then  $r_A - r_B = r_{C2} - r_{D2} \cong x_2 d/z_2$ , and Equation 12.28 can be written as

$$R_c \propto \cos^2 \left( \frac{\pi dx_2}{\lambda z_2} \right). \quad (12.29)$$

Equation 12.29 has the form of standard Young's double-slit interference pattern. Here, again,  $z_2$  is the unusual distance from the slits plane, which is in the signal beam, back through BS to the crystal and then along the idler beam to the scanning fiber tip of detector  $D_2$ .

If the optical paths from the fixed detector  $D_1$  to the two slits are unequal, i.e.,  $r_{C1} \neq r_{D1}$ , the interference pattern will be shifted from the symmetrical position of Equation 12.29 to an asymmetrical position of Equation 12.28. This interesting phenomenon has been observed and discussed following the discussion of Figure 12.12.

To calculate the "ghost" diffraction effect of a single slit, we need an integral of the effective two-photon wavefunction over the slit width (the superposition of infinite number of probability amplitudes results in a click-click coincidence detection event):

$$R_c \propto \left| \int_{-a/2}^{a/2} dx_0 \exp[-ik r(x_0, x_2)] \right|^2 \cong \text{sinc}^2 \left( \frac{\pi ax_2}{\lambda z_2} \right) \quad (12.30)$$

where  $r(x_0, x_2)$  is the distance between points  $x_0$  and  $x_2$ ,  $x_0$  belongs to the slit's plane, and the inequality  $z_2 \gg a^2/\lambda$  is applied (far-field approximation).

Repeating the above calculations, the combined interference-diffraction joint-detection counting rate for the double-slit case is given by:

$$R_c \propto \text{sinc}^2 \left( \frac{\pi ax_2}{\lambda z_2} \right) \cos^2 \left( \frac{\pi dx_2}{\lambda z_2} \right) \quad (12.31)$$

which is the same function as that of Equation 12.24 obtained from experimental data fittings. If the finite size of the detectors and the divergence of the pump are taken into account by a convolution, the interference visibility will be reduced. These factors have been considered in the theoretical plots of Figure 12.12.

Similar to the Franson interferometer, which demonstrated the nonlocal EPR inequality in energy, the ghost interference experiment has explored another nonlocal EPR inequality in momentum. As we know, the loss of first-order spatial coherence of the signal (idler) indicates a considerable large

uncertainty in the transverse component of its momentum,  $\Delta\vec{k}_{s,i}$ . In contrast, the two-photon interference pattern has shown quite a high degree of two-photon spatial coherence, which indicates

$$\Delta(\vec{k}_s + \vec{k}_i) \ll \min(\Delta\vec{k}_s, \Delta\vec{k}_i).$$

In EPR's language, the transverse momentum of neither signal photon nor idler photon is defined in the course of their preparation and propagation; however, if one is measured with a certain value, the other must be measured with a unique value despite the distance between the two measurements.

---

## 12.5 Delayed Choice Quantum Eraser

Quantum eraser, proposed by Scully and Drühl, is another thought experiment to challenge the uncertainty principle of quantum mechanics. Quantum mechanically, one can never expect to measure both precise position and momentum of a quantum at the same time. It is prohibited. We say that the quantum observable "position" and "momentum" are "complementary" because the precise knowledge of the position (momentum) implies that all possible outcomes of measuring the momentum (position) are equally probable. In 1927, Niels Bohr illustrated complementarity via the "wave-like" and "particle-like" attributes of a quantum mechanical object. Since then, complementarity has often been superficially identified with the "wave-particle duality of matter".

Over the years, Young's double-slit interferometer has been commonly used to probe, to explore, and to argue about this mystery. In this regard, the following discussion is a continuation of the history. We ask a simple question: while observing interference, can we learn which slit a photon has passed through? Quantum theory answers "no." Otherwise, there would be no interference. Complementarity forbids observing the wave behavior and particle behavior of a quantum simultaneously. It seems a photon has to make its decision to be either a wave to pass both slits or a particle to pass which slit when facing a double slit. Of course, this statement does not make any sense. Alternatively, Copenhagen taught us that it is the observer who made the decision for the photon: "no elementary quantum phenomenon is a phenomenon until it is a recorded phenomenon."<sup>\*</sup> We may translate this sentence into easier language: the photon behaves like a wave to pass both slits if the measurement device is for observing interference; the photon behaves like a particle if the measurement observes which slit the

---

<sup>\*</sup> This is a summary of Wheeler about Copenhagen's philosophical point on physical reality.

photon passes through and thus disturbing the photon enough to destroy the interference. Although most physicists were happy with this interpretation, Scully pointed out that, under certain circumstances, this common “uncertainty relation” interpretation may not be applicable. In 1982, Scully and Drühl proposed a thought experiment to show that the destroyed interference can reappear when the which-path information is “erased.” It is interesting to note that one could even erase the which-path information after the annihilation of the photon and still determine its earlier behavior to be either wave or particle.

A quantum eraser experiment similar to the original Scully–Drühl thought experiment of 1982 is illustrated in Figure 12.13. An atom labeled A or B is excited by a weak laser pulse (only one atom, either A or B, is excited). A pair of entangled quanta, photon 1 and photon 2, is then emitted from either the transition of atom A or the transition of atom B by atomic cascade decay. Photon 1, propagating to the right, is registered by detector  $D_0$ , which can be scanned by a step motor along its  $x$ -axis for the examination of interference fringes. Photon 2, propagating to the left, is injected into a beam-splitter. If the pair is generated in atom A, photon 2 will follow the A path meeting BSA with 50% chance of being reflected or transmitted. If the pair is generated in atom B, photon 2 will follow the B path meeting BSB with 50% chance of being reflected or transmitted. In view of the 50% chance of being transmitted by either BSA or BSB, photon 2 is detected by either detector  $D_3$  or  $D_4$ . The registration of  $D_3$  or  $D_4$  provides which-path information (path A or path B) on photon 2 and in turn provides which-path information for photon 1 because of the entanglement nature of the two-photon state generated by atomic cascade decay. Given a reflection at either BSA or BSB photon 2

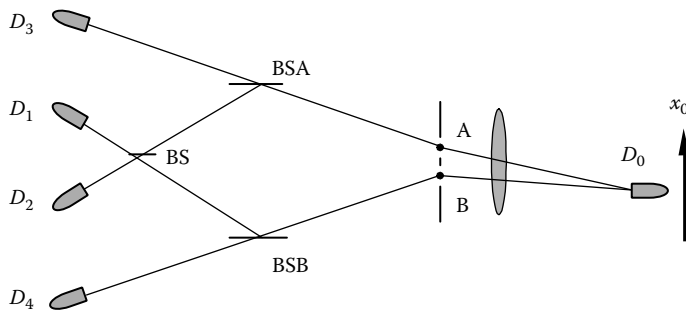


**FIGURE 12.13**

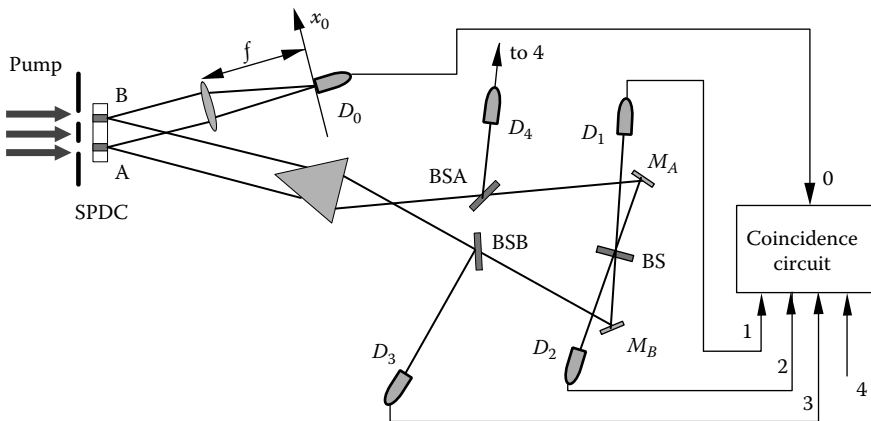
Quantum erasure: a thought experiment of Scully and Drühl. A pair of entangled photons is emitted from either atom A or atom B by atomic cascade decay. There is no observable interference fringes in the single-detector counting rate of  $D_0$ . The “clicks” at  $D_1$  or  $D_2$  erase the which-path information, thus helping to restore the interference even after the “click” of  $D_0$ . On the other hand, the “clicks” at  $D_3$  or  $D_4$  record which-slit information. Thus, no observable interference is expected with the help of these “clicks.”

will continue to follow its A or B path to meet another 50–50 beamsplitter BS and then be detected by either detectors  $D_1$  or  $D_2$ .

The experimental condition was arranged in such a way that no interference is observable in the single counting rate of  $D_0$ , i.e., the distance between A and B is large enough to be “distinguishable” for  $D_0$  to learn which-path information of photon 1. However, the “clicks” at  $D_1$  or  $D_2$  will erase the which-path information of photon 1 and help to restore the interference. On the other hand, the “clicks” at  $D_3$  or  $D_4$  record which-path information. Thus, no observable interference is expected with the help of these “clicks.” It is interesting to note that both the “erasure” and “recording” of the which-path information can be made as a “delayed choice”: the experiment is designed in such a way that  $L_0$ , the optical distance between atoms A, B, and detector  $D_0$ , is much shorter than  $L_A$  ( $L_B$ ), which is the optical distance between atoms A, B, and the beamsplitter BSA (BSB) where the “which-path” or “both-paths” “choice” is made randomly by photon 2. Thus, after the annihilation of photon 1 at  $D_0$ , photon 2 is still on its way to BSA (BSB), i.e., “which-path” or “both-path” choice is “delayed” compared to the detection of photon 1. After the annihilation of photon 1, we look at these “delayed” detection events of  $D_1$ ,  $D_2$ ,  $D_3$ , and  $D_4$  which have constant time delays,  $\tau_i \simeq (L_i - L_0)/c$ , relative to the triggering time of  $D_0$ .  $L_i$  is the optical distance between atoms A, B and detectors  $D_1$ ,  $D_2$ ,  $D_3$ , and  $D_4$ , respectively. It was predicted that the “joint-detection” counting rates  $R_{01}$  (joint-detection rate between  $D_0$  and  $D_1$ ) and  $R_{02}$  will show an interference pattern as a function of the position of  $D_0$  on its  $x$ -axis. This reflects the wave nature (both-path) of photon 1. However, no interference fringes will be observable in the joint-detection counting events  $R_{03}$  and  $R_{04}$  when scanning detector  $D_0$  along its  $x$ -axis. This is as would be expected because we have now inferred the particle (which-path) property of photon 1. It is important to emphasize that all four joint-detection rates  $R_{01}$ ,  $R_{02}$ ,  $R_{03}$ , and  $R_{04}$  are recorded at the same time during one scanning of  $D_0$ . That is, in the present experiment, we “see” both wave (interference) and which-path (particle-like) with the same measurement apparatus.

It should be mentioned that (1) the “choice” in this experiment is not actively switched by the experimentalist during the measurement. The “delayed choice” associated with either the wave or particle behavior of photon 1 is “randomly” made by photon 2. The experimentalist simply looks at which detector,  $D_1$ ,  $D_2$ ,  $D_3$ , or  $D_4$ , is triggered by photon 2 to determine either wave or particle properties of photon 1 after the annihilation of photon 1; (2) the photodetection event of photon 1 at  $D_0$  and the delayed choice event of photon 2 at BSA (BSB) are space-like separated events. The “coincidence” time window is chosen to be much shorter than the distance between  $D_0$  and BSA (BSB). Within the joint-detection time window, it is impossible to have the two events “communicating.”

In the following, we analyze a random delayed choice quantum eraser experiment by Kim et al. The schematic diagram of the experimental setup

**FIGURE 12.14**

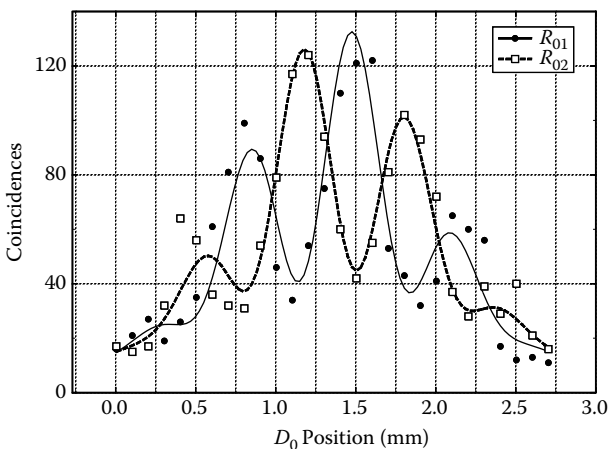
Delayed choice quantum eraser: Schematic of an actual experimental setup of Kim et al. Pump laser beam is divided by a double slit and makes two regions A and B inside the SPDC crystal. A pair of signal–idler photons is generated either from the A or the B region. The “delayed choice” to observe either wave or particle behavior of the signal photon is made randomly by the idler photon about 7.7 ns after the detection of the signal photon.

of Kim et al. is shown in Figure 12.14. Instead of atomic cascade decay, spontaneous parametric down-conversion is used to prepare the entangled two-photon state. In the experiment, a 351.1 nm Argon ion pump laser beam is divided by a double slit and directed onto a type-II phase-matching nonlinear crystal BBO at regions A and B. A pair of 702.2 nm orthogonally polarized signal–idler photon is generated either from region A or region B. The width of the region is about  $a = 0.3$  mm and the distance between the center of A and B is about  $d = 0.7$  mm. A Glen–Thompson prism is used to split the orthogonally polarized signal and idler. The signal photon (photon 1, coming from either A or B) propagates through lens  $LS$  to detector  $D_0$ , which is placed on the Fourier transform plane of the lens. The use of lens  $LS$  is to achieve the “far-field” condition, but still keep a short distance between the slit and the detector  $D_0$ . Detector  $D_0$  can be scanned along its  $x$ -axis by a step motor for the observation of interference fringes. The idler photon (photon 2) is sent to an interferometer with equal-path optical arms. The interferometer includes a prism  $PS$ ; two 50–50 beamsplitters  $BSA$  and  $BSB$ ; two reflecting mirrors  $M_A$  and  $M_B$ ; and a 50–50 beamsplitter  $BS$ . Detectors  $D_1$  and  $D_2$  are placed at the two output ports of the  $BS$ , respectively, for erasing the which-path information. The triggering of detectors  $D_3$  and  $D_4$  provides which-path information for the idler (photon 2) and, in turn, which-path information for the signal (photon 1). The detectors are fast avalanche photodiodes with less than 1 ns rise time and about 100 ps jitter. A constant fractional discriminator is used with each of the detectors to register a single photon whenever the leading edge of the detector output pulse is above

the threshold. Coincidences between  $D_0$  and  $D_j$  ( $j = 1, 2, 3, 4$ ) are recorded, yielding the joint-detection counting rates  $R_{01}$ ,  $R_{02}$ ,  $R_{03}$ , and  $R_{04}$ .

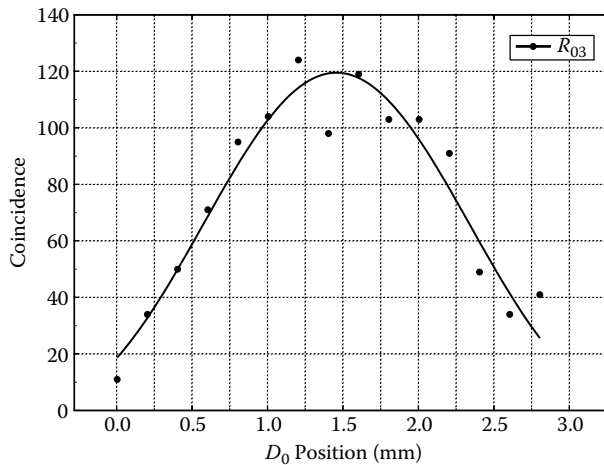
In the experiment, the optical delay ( $L_{A,B} - L_0$ ) is chosen to be  $\simeq 2.3$  m, where  $L_0$  is the optical distance between the output surface of BBO and detector  $D_0$ , and  $L_A$  ( $L_B$ ) is the optical distance between the output surface of the BBO and the beamsplitter BSA (BSB). This means that any information (which-path or both-path) one can infer from photon 2 must be at least 7.7 ns later than the registration of photon 1. Compared to the 1 ns response time of the detectors, 2.3 m delay is thus enough for "delayed erasure." Although there is an arbitrariness about when a photon is detected, it is safe to say that the "choice" of photon 2 is delayed with respect to the detection of photon 1 at  $D_0$  since the entangled photon pair is created simultaneously.

Figure 12.15, reports the joint detection rates  $R_{01}$  and  $R_{02}$ , indicating the regaining of standard Young's double-slit interference pattern. An expected  $\pi$  phase shift between the two interference patterns is clearly shown in the measurement. The single-detector counting rates of  $D_0$  and  $D_1$  are recorded simultaneously. Although interference is observed in the joint-detection counting rate, there is no significant modulation in any of the single-detector counting rate during the scanning of  $D_0$ .  $R_0$  is a constant during the scanning of  $D_0$ . The absence of interference in the single-detector counting rate of  $D_0$  is due to the chosen experimental condition  $\Delta\theta > \lambda_s/d$ , where  $\Delta\theta$  is the diverging angle of the signal field at its central wavelength  $\lambda_s$ . In the language of complementarity, it is the narrow width of the slit (the width of A and B) that disturbs the signal photon enough to destroy the



**FIGURE 12.15**

Joint-detection rates  $R_{01}$  and  $R_{02}$  against the  $x$  coordinates of detector  $D_0$ . Standard Young's double-slit interference patterns are observed. Note the  $\pi$  phase shift between  $R_{01}$  and  $R_{02}$ . The solid line and the dashed line are theoretical fits to the data.

**FIGURE 12.16**

Joint detection counting rate of  $R_{03}$ . Absence of interference is clearly demonstrated. The solid line is a sinc-function fit.

interference. The narrower the width of the slit ( $\Delta x$ ), the greater uncertainty of the transverse momentum ( $\Delta p_x$ ) will be and thus result in  $\Delta\theta > \lambda_s/d$ .

Figure 12.16 reports a typical  $R_{03}$  ( $R_{04}$ ), joint-detection counting rate between  $D_0$  and “which-path detector”  $D_3$  ( $D_4$ ). An absence of interference is clearly demonstrated. The fitting curve of the experimental data indicates a sinc-function-like envelope of the standard Young’s double slit interference-diffraction pattern. Two features should bring to our attention that (1) there is no observable interference modulation as expected and (2) the curve is different from the constant single-detector counting rate of  $D_0$ .

The experimental result is surprising from a classical point of view. The result, however, is easily explained in the contents of quantum theory. In this experiment, there are two kinds of very different interference phenomena: single-photon interference and two-photon interference. As we have discussed earlier, single-photon interference is the result of the superposition between single-photon amplitudes, and two-photon interference is the results of the superposition between two-photon amplitudes. Quantum mechanically, single-photon amplitude and two-photon amplitude represent very different measurements and, thus, very different physics.

In this regard, we analyze the experiment by answering the following questions:

(1) Why is there no observable interference in the single-detector counting rate of  $D_0$ ?

This question belongs to single-photon interferometry. In fact, the ghost interference experiment was facing a similar question: what causes the loss

of interference behind Young's double slit? The absence of interference in single-detector counting rate of  $D_0$  is due to the angular uncertainty, or uncertainty in transverse momentum, of the signal photon. Although the pump laser beam of SPDC is well collimated, i.e., the pump beam can be considered coming from a point source at distance of infinity, the signal beam (idler beam as well), under typical experimental conditions, always suffers with considerably large angular uncertainty. In connection with what we have learned in Chapter 1, this is equivalent to having the signal beam come from a distant star of finite angular size. We have learned in Chapter 5 that there would be no observable interference when the angular separation,  $\Delta\theta$ , between the double-slit of an young's interferometer is greater than  $\lambda/d$  ( $\Delta\theta > \lambda/d$ ).

(2) Why is there observable interference in the joint-detection counting rate of  $D_{01}$  and  $D_{02}$ ?

This question belongs to two-photon interferometry. Two-photon interference is very different from single-photon interference. Two-photon interference involves the addition of different yet indistinguishable two-photon amplitudes. In the following, we present a simple model to calculate the two-photon interference in the joint-detection counting rate of  $R_{01}$ . The calculation is similar to that of the ghost interference, except the "ghost" effect. The calculated two-photon interference pattern is observed by scanning the photodetector placed behind the double slit.

The coincidence-counting rate  $R_{01}$ , again, is proportional to the probability  $P_{01}$  of joint detecting the signal-idler pair by detectors  $D_0$  and  $D_1$ :

$$R_{01} \propto P_{01} = \left\langle \Psi \left| \hat{E}_0^{(-)} \hat{E}_1^{(-)} \hat{E}_1^{(+)} \hat{E}_0^{(+)} \right| \Psi \right\rangle = \left| \left\langle 0 \left| \hat{E}_1^{(+)} \hat{E}_0^{(+)} \right| \Psi \right\rangle \right|^2 \quad (12.32)$$

where  $|\Psi\rangle$  is the biphoton state of SPDC. Let us simplify the mathematics by using the following "two-mode" expression for the state, bearing in mind that the transverse momentum  $\delta$ -function will be taken into account by using the "unfold" Klyshko picture, similar to that in the "ghost" image.

$$|\Psi\rangle = \epsilon [\hat{a}_s^\dagger \hat{a}_i^\dagger e^{i\varphi_A} + \hat{b}_s^\dagger \hat{b}_i^\dagger e^{i\varphi_B}] |0\rangle$$

where  $\epsilon$  is a normalization constant that is proportional to the pump field (classical) and the nonlinearity of the SPDC crystal,  $\varphi_A$  and  $\varphi_B$  are the phases of the pump field at A and B, and  $\hat{a}_j^\dagger$  ( $\hat{b}_j^\dagger$ ),  $j = s, i$ , are the photon-creation operators for the lower (upper) mode in Figure 12.14.

In Equation 12.32, the fields at the detectors  $D_0$  and  $D_1$  are given by

$$\begin{aligned} \hat{E}_0^{(+)} &= \hat{a}_s e^{ikr_{A0}} + \hat{b}_s e^{ikr_{B0}} \\ \hat{E}_1^{(+)} &= \hat{a}_i e^{ikr_{A1}} + \hat{b}_i e^{ikr_{B1}} \end{aligned} \quad (12.33)$$

where  $r_{Aj}$  ( $r_{Bj}$ ),  $j = 0, 1$ , are the optical path lengths from region A (B) to the  $j$ th detector. Substituting the biphoton state and the field operators into Equation 12.32

$$R_{01} \propto |e^{i(kr_A + \varphi_A)} + e^{i(kr_B + \varphi_B)}|^2 \propto 1 + \cos [k(r_A - r_B)] \quad (12.34)$$

where, again, we have assumed  $\varphi_A = \varphi_B$  in the second line of Equation 12.34.

If the optical paths from detector  $D_1$  to the two slits are equal, and  $D_0$  in the far-field,  $r_A - r_B \cong x_0 d / z_0$ , and Equation 12.34 can be written as

$$R_{(01)} \propto \cos^2 \left( \frac{x_0 \pi d}{\lambda z_0} \right). \quad (12.35)$$

Equation 12.35 has the form of standard Young's double-slit interference pattern.

Similar to ghost interference, if the optical paths from detector  $D_1$  to the two slits are unequal, the interference pattern will be shifted from the symmetrical position to an asymmetrical position depending on how much phase delay is introduced by the unequal paths.

To calculate the diffraction effect of a single slit, again, we need an integral of the effective two-photon wavefunction over the slit width (the superposition of infinite number of probability amplitudes results in a click-click joint-detection event):

$$R_{01} \propto \left| \int_{-a/2}^{a/2} dx_{AB} e^{-ikr(x_0, x_{AB})} \right|^2 \cong \text{sinc}^2 \left( \frac{x_0 \pi a}{\lambda z_0} \right) \quad (12.36)$$

where  $r(x_0, x_{AB})$  is the distance between points  $x_0$  and  $x_{AB}$ ,  $x_{AB}$  belongs to the slit's plane, and the far-field condition is applied.

Repeating the above calculations, the combined interference-diffraction joint-detection counting rate for the double slit case is given by

$$R_{01} \propto \text{sinc}^2 \left( \frac{x_0 \pi a}{\lambda z_0} \right) \cos^2 \left( \frac{x_0 \pi d}{\lambda z_0} \right). \quad (12.37)$$

If the finite size of the detectors are taken into account, the interference visibility will be reduced. These factors have been observed in the joint-detection counting rate of  $R_{01}$  and  $R_{02}$ .

(3) Why is there no observable interference in the joint detection counting rate of  $R_{03}$  and  $R_{04}$ ?

This question belongs to two-photon interferometry. From the view of two-photon physics, the absence of interference in the joint-detection

counting rate of  $R_{03}$  and  $R_{04}$  is obvious: only one two-photon amplitude contributes to the joint detection events.

(4) What have we learned from this experiment?

(1) The phenomenon of two-photon interference, observed in the joint-detection events of two photodetectors, is different from that of single-photon interference. Thus, the wave-particle behavior of a single photon may not be learned from the two-photon interference measurement. If one insists on interpreting the two-photon phenomena into the physics of a single photon, nonphysical conclusions may not be avoidable.

(2) Through this experiment, we have learned, once again, that two-photon physics must be distinguished from that of two single photons. In the past two decays, this point was emphasized with a cartoon-like statement:  $2 \neq 1 + 1$ .

---

## Summary

In this chapter, we discussed the physics of biphoton interferometry. Two decades ago, based on the discovery of biphoton interference, Dirac was criticized to be mistaken because he stated that "... photon ... only interferes with itself." The debate on whether biphoton interference is the interference between two photons began since that time. This chapter started from the question: Is two-photon interference the interference of two photons? Through the analysis of a few biphoton interference experiments, we concluded that two-photon interference is not the interference of two photons. Two-photon interference involves the superposition of two-photon amplitudes. In the language of Dirac, two-photon interference is a pair of photon interfering with the pair itself.

In this chapter, we analyzed a few typical biphoton interference experiments, including Bell-type polarization correlation measurement of biphoton pairs, biphoton interference in Franson interferometer, biphoton ghost interference, and random delayed choice quantum eraser. Through these analyses, we demonstrated the details on the superposition of biphoton amplitudes, or the overlapping-convolution of the 2D nonfactorizable biphoton wavepackets along its  $(\tau_1 - \tau_2)$  or  $(\tau_1 + \tau_2)$  axes.

---

## Suggested Reading

Alley, C.O. and Y.H. Shih, *Foundations of Quantum Mechanics in the Light of New Technology*, M. Namiki (ed.), Physical Society of Japan, Tokyo, Japan, p. 47 (1986); Shih, Y.H. and C.O. Alley, *Phys. Rev. Lett.* 61, 2921 (1988).

- Dirac, P.A., *The Principle of Quantum Mechanics*, Oxford University Press, New York, 1982.
- Franson, J.D., *Phys. Rev. Lett.* 62, 2205 (1989).
- Hong, C.K., Z.Y. Ou, and L. Mandel, *Phys. Rev. Lett.* 59, 2044 (1987); Ou, Z.Y. and L. Mandel, *Phys. Rev. Lett.* 62, 50 (1988).
- Kiess, T.E., Y.H. Shih, A.V. Sergienko, and C.O. Alley, *Phys. Rev. Lett.* 71, 3893 (1993).
- Kim, Y.H., R. Yu, S.P. Kulic, Y.H. Shih, and M.O. Scully, *Phys. Rev. Lett.* 84, 1 (2000).
- Kwiat, P.G. et al., *Phys. Rev. Lett.* 75, 4337 (1995).
- Kwiat, P.G., A.M. Steinberg, and R.Y. Chiao, *Phys. Rev. A* 45, 7729 (1992).
- Kwiat, P.G., A.M. Steinberg, and R.Y. Chiao, *Phys. Rev. A* 47, 2472 (1993).
- Magyar, G. and L. Mandel, *Nature* 198, 255 (1963); Pfleegor, R.L. and L. Mandel, *Phys. Rev.* 159, 1084 (1967).
- Pittman, T.B. et al., *Phys. Rev. Lett.* 77, 1917 (1996).
- Rubin, M.H., D.N. Klyshko, Y.H. Shih, and A.V. Sergienko, *Phys. Rev. A* 50, 5122 (1994).
- Scully, M.O. and K. Drühl, *Phys. Rev. A* 25, 2208 (1982).
- Sergienko, A.V., Y.H. Shih, and M.H. Rubin, *JOSAB* 12, 859 (1995).
- Shih, Y.H., Two-photon entanglement and quantum reality, in: *Advances in Atomic, Molecular, and Optical Physics*, B. Bederson and H. Walther (eds.), Academic Press, Cambridge, New York, 1997.
- Shih, Y.H. and A.V. Sergienko, *Phys. Rev. A* 50, 2564 (1994).
- Strelkov, D.V., A.V. Sergienko, D.N. Klyshko, and Y.H. Shih, *Phys. Rev. Lett.* 74, 3600 (1995).
- Strelkov, D.V. et al., *Phys. Rev. A* 54, R1 (1996).
- Strelkov, D.V., T.B. Pittman, and Y.H. Shih, *Phys. Rev. A* 57, 567 (1998).
- Tapster, P.R., J.G. Rarity, and P.C.M. Owens, *Phys. Rev. Lett.* 73, 1923 (1994).



# 13

---

## *Two-Photon Interferometry—II: Quantum Interference of Chaotic-Thermal Light*

---

The study of entangled states greatly advanced our understanding of two-photon interferometry. Two-photon interference is not the interference between two photons; it is about a pair of photon interfering with the pair itself. In the language of quantum theory, two-photon interference is the result of superposition between indistinguishable two-photon amplitudes. Is the concept of two-photon amplitude applicable only to the entangled states? Does two-photon interference occur only with entangled photon pairs? The answer is negative. In this chapter, we study two-photon interference of chaotic-thermal light. Thermal light is traditionally defined as “classical” light.\* It is not the aim of this book to classify light into quantum or classical. Our interests are to (1) generalize the quantum theory of two-photon interferometry to chaotic light and (2) distinguish the quantum mechanical concept of two-photon interference from classical statistical correlation of intensity fluctuations.

Under certain conditions, the observed second-order interference can be factorized into a product of two individual classic first-order interferences. In this case, the interference is not only observable in the coincidences of two photodetectors, but also observable in the counting rate of each individual photodetector. We consider these factorizable two-photon interferences as trivial second-order phenomena. We will avoid this type of second-order interference in this chapter by arranging the experimental conditions in such a way note that no classic first-order interferences are observable.

It is interesting to see that the quantum concept of two-photon interference is applicable to “classical” thermal radiation. In fact, this is not the first time in the history of physics we apply quantum mechanical concepts to “classical” thermal light. We should not forget that it was Planck’s theory of blackbody radiation that originated the theory of quantum physics. The radiation Planck dealt with was “classical” thermal light.

---

\* There exist a number of definitions to classify classical light and quantum light. One of the commonly used definitions considers thermal light classical because of its positive  $P$ -function.

### 13.1 Two-Photon Young's Interference

We start from a simple Young's double-pinhole interference experiment, which is schematically illustrated in Figure 13.1. The experimental setup is the same as the classic Young's double-pinhole interferometer, except (1) the radiation at pinhole  $A$  and at pinhole  $B$  are first-order incoherent, and (2) two point-like scannable photon-counting detectors  $D_1$  and  $D_2$  are employed for monitoring the first-order interference in their individual counting rates, respectively, and for monitoring the second-order interference in their coincidence counting rate, jointly. The single-detector counting rate monitors the first-order interference, which is the result of superposition between single-photon amplitudes. The joint photodetection-counting rate observes the second-order interference, which is the result of superposition between two-photon amplitudes. In this experiment, fields  $A$  and  $B$  are first-order incoherent, i.e., the first-order mutual coherence function  $G^{(1)}(\mathbf{r}_A, t_A; \mathbf{r}_B, t_B) = 0$ . This condition is achieved by either using two independent light sources with random relative phase or by separating the double pinholes beyond the transverse spatial coherence area of a thermal field. Under this experimental condition, obviously, there is no observable first-order interference. The counting rates of  $D_1$  and  $D_2$  are both constants during their scanning. Do we expect to observe interference modulation in the joint photodetection-counting rate of the two photon-counting detectors  $D_1$  and  $D_2$  when  $G^{(1)}(\mathbf{r}_A, t_A; \mathbf{r}_B, t_B) = 0$ ?

In the following, we calculate the coincidence-counting rate of the joint photodetection between  $D_1$  and  $D_2$ , starting from modeling the quantum state of the above monochromatic chaotic-thermal field. To simplify the

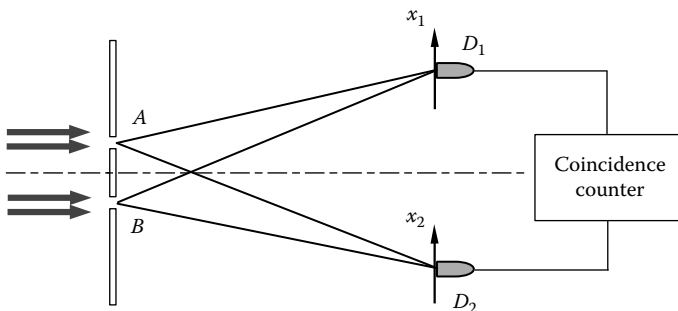


**FIGURE 13.1**

Schematic of a simple Young's double-pinhole type interference experiment. Two transversely scannable point-like photon counting detectors  $D_1$  and  $D_2$  are facing two independent monochromatic point-like weak thermal sources  $A$  and  $B$  in the far-field with  $G^{(1)}(\mathbf{r}_A, t_A; \mathbf{r}_B, t_B) = 0$ . The single-detector-counting rate and the joint photodetection-counting rates of  $D_1$  and  $D_2$  are monitored, respectively, during the scanning of the two fiber tips.

calculation, we model the sources  $A$  and  $B$  as two point-like independent sources, and each source contributes to a joint photodetection event from  $N$  possible independent and randomly radiated two-level atomic transitions, labeled as  $a_m$  and  $b_m$ ,  $m = 1 \dots N$ , respectively, with  $\Delta E_2 \simeq 0$ . Following the same analysis in Section 8.8, the states of the subfield  $A$ , which is created from source  $A$ , and the state of the subfield  $B$ , which is created from source  $B$ , are formally written as

$$\begin{aligned} |\Psi\rangle_A &\simeq \prod_m \left( |0\rangle + \epsilon c_m \hat{a}_m^\dagger |0\rangle \right) \\ &\simeq |0\rangle + \epsilon \sum_m c_m \hat{a}_m^\dagger |0\rangle + \epsilon^2 \sum_{m < n} c_m c_n \hat{a}_m^\dagger \hat{a}_n^\dagger |0\rangle + \dots \\ |\Psi\rangle_B &\simeq \prod_m \left( |0\rangle + \epsilon c_m \hat{b}_m^\dagger |0\rangle \right) \\ &\simeq |0\rangle + \epsilon \sum_m c_m \hat{b}_m^\dagger |0\rangle + \epsilon^2 \sum_{m < n} c_m c_n \hat{b}_m^\dagger \hat{b}_n^\dagger |0\rangle + \dots \end{aligned} \quad (13.1)$$

Under weak light condition, we may keep the necessary lowest-order terms of Equation 13.1 for calculating the counting rates of  $D_1$  and  $D_2$ , respectively, and the coincidence-counting rates of  $D_1$  and  $D_2$ , jointly. Similar to Section 8.8, the lowest-order approximation of the state that contributes to the joint photodetection of  $D_1$  and  $D_2$  is a mixed two-photon state, including all terms in the order of  $\epsilon^2$ . The joint photodetection-counting rate is proportional to the second-order coherence  $G^{(2)}(\mathbf{r}_1, t_1; \mathbf{r}_2, t_2)$  that is calculated from

$$\begin{aligned} G_{12}^{(2)} &= \left\langle \left\langle \hat{E}_1^{(-)} \hat{E}_2^{(-)} \hat{E}_2^{(+)} \hat{E}_1^{(+)} \right\rangle \right\rangle_{\text{QM}}_{\text{ensemble}} \\ &\simeq \text{tr} \left[ (\hat{\rho}_{AA} + \hat{\rho}_{BB} + \hat{\rho}_{AB} + \hat{\rho}_{BA}) \hat{E}_1^{(-)} \hat{E}_2^{(-)} \hat{E}_2^{(+)} \hat{E}_1^{(+)} \right] \\ &= G_{AA}^{(2)} + G_{BB}^{(2)} + G_{AB}^{(2)} + G_{BA}^{(2)}, \end{aligned} \quad (13.2)$$

where we have written the mixed two-photon state in four parts:

$$\begin{aligned} \hat{\rho}_{AA} &= \sum_{m < n} |c_m|^2 |c_n|^2 \hat{a}_m^\dagger \hat{a}_n^\dagger |0\rangle \langle 0| \hat{a}_n^\dagger \hat{a}_m^\dagger \\ \hat{\rho}_{BB} &= \sum_{m < n} |c_m|^2 |c_n|^2 \hat{b}_m^\dagger \hat{b}_n^\dagger |0\rangle \langle 0| \hat{b}_n^\dagger \hat{b}_m^\dagger \\ \hat{\rho}_{AB} &= \sum_{m < n} |c_m|^2 |c_n|^2 \hat{a}_m^\dagger \hat{b}_n^\dagger |0\rangle \langle 0| \hat{b}_n^\dagger \hat{a}_m^\dagger \\ \hat{\rho}_{BA} &= \sum_{m < n} |c_m|^2 |c_n|^2 \hat{b}_m^\dagger \hat{a}_n^\dagger |0\rangle \langle 0| \hat{a}_n^\dagger \hat{b}_m^\dagger, \end{aligned} \quad (13.3)$$

where  $|c_m|^2|c_n|^2$  represents the renormalized probability for all four density operators. In order to have a consistent renormalization for all density operators, we have broken the cross term of the mixed two-photon state  $\sum_{m,n} c_m c_n \hat{a}_m^\dagger \hat{b}_n^\dagger |0\rangle$  of Equation 13.1 into two parts:

$$\sum_{m,n} |c_m|^2 |c_n|^2 \hat{a}_m^\dagger \hat{b}_n^\dagger |0\rangle \simeq \sum_{m < n} |c_m|^2 |c_n|^2 \hat{a}_m^\dagger \hat{b}_n^\dagger |0\rangle + \sum_{m > n} |c_m|^2 |c_n|^2 \hat{a}_m^\dagger \hat{b}_n^\dagger |0\rangle.$$

In the above approximation we have ignored  $m = n$  from the sum as usual, which is valid for a large number of atomic transitions.

The 1-D second-order spatial coherence functions  $G_{AA}^{(2)}$ ,  $G_{BB}^{(2)}$ ,  $G_{AB}^{(2)}$ , and  $G_{BA}^{(2)}$  are defined and calculated from

$$\begin{aligned} G_{AA}^{(2)} &= \sum_{m < n} |c_m|^2 |c_n|^2 \left| \langle 0 | \hat{E}_2^{(+)} \hat{E}_1^{(+)} \hat{a}_m^\dagger \hat{a}_n^\dagger | 0 \rangle \right|^2 \\ &= \sum_{m < n} |c_m|^2 |c_n|^2 \left| \Psi_{mn}^{(AA)}(x_1, x_2) \right|^2 \\ G_{BB}^{(2)} &= \sum_{m < n} |c_m|^2 |c_n|^2 \left| \langle 0 | \hat{E}_2^{(+)} \hat{E}_1^{(+)} \hat{b}_m^\dagger \hat{b}_n^\dagger | 0 \rangle \right|^2 \\ &= \sum_{m < n} |c_m|^2 |c_n|^2 \left| \Psi_{mn}^{(BB)}(x_1, x_2) \right|^2 \\ G_{AB}^{(2)} &= \sum_{m < n} |c_m|^2 |c_n|^2 \left| \langle 0 | \hat{E}_2^{(+)} \hat{E}_1^{(+)} \hat{a}_m^\dagger \hat{b}_n^\dagger | 0 \rangle \right|^2 \\ &= \sum_{m < n} |c_m|^2 |c_n|^2 \left| \Psi_{mn}^{(AB)}(x_1, x_2) \right|^2 \\ G_{BA}^{(2)} &= \sum_{m < n} |c_m|^2 |c_n|^2 \left| \langle 0 | \hat{E}_2^{(+)} \hat{E}_1^{(+)} \hat{b}_m^\dagger \hat{a}_n^\dagger | 0 \rangle \right|^2 \\ &= \sum_{m < n} |c_m|^2 |c_n|^2 \left| \Psi_{mn}^{(BA)}(x_1, x_2) \right|^2, \end{aligned} \quad (13.4)$$

by substituting the spatial part of the field operators in far-field approximation:

$$\begin{aligned} \hat{E}_1^{(+)} &\simeq \sum_p \hat{a}_p e^{ikr_{A1}} + \sum_q \hat{b}_q e^{ikr_{B1}} \\ \hat{E}_2^{(+)} &\simeq \sum_{p'} \hat{a}_{p'} e^{ikr_{A2}} + \sum_{q'} \hat{b}_{q'} e^{ikr_{B2}} \end{aligned} \quad (13.5)$$

into Equation 13.4. In Equation 13.4,  $\Psi_{mn}^{(AA)}(x_1, x_2)$ ,  $\Psi_{mn}^{(BB)}(x_1, x_2)$ ,  $\Psi_{mn}^{(AB)}(x_1, x_2)$ , and  $\Psi_{mn}^{(BA)}(x_1, x_2)$  are the spatial part of the effective two-photon wavefunctions, representing the probability amplitudes for the randomly paired  $m-n$  photons, either from the same source or from different sources, to produce a joint photodetection event of  $D_1$  and  $D_2$ . The four second-order coherence functions in Equation 13.4 indicate three alternative ways to produce a joint photodetection event of  $D_1$  and  $D_2$ : (1) the event is produced by two photons both from source  $A$ , (2) the event is produced by two photons both from source  $B$ , (3)–(4) the event is produced by one photon from source  $A$  and another photon from source  $B$ . Since sources  $A$  and  $B$  are radiated independently and randomly, these four contributions are incoherent and can be calculated independently. It is easy to see that the contributions from (1) and (2) can be measured independently too by blocking the other source i.e., blocking source- $A$  to measure  $G_{BB}^{(2)}$ , or blocking source- $B$  to measure  $G_{AA}^{(2)}$ . Although contribution (3)–(4) cannot be measured directly from the joint photodetection of  $D_1$  and  $D_2$ , after learning the contributions of (1) and (2), the net contribution of (3)–(4), in principle, can be isolated and estimated by subtracting the contributions (1) and (2) from the total.

Substituting the field operators into Equation 13.4, the effective two-photon wavefunctions  $\Psi_{mn}^{(AA)}(x_1, x_2)$  and  $\Psi_{mn}^{(BB)}(x_1, x_2)$  are calculated as

$$\begin{aligned}\Psi_{mn}^{(AA)}(x_1, x_2) &= \langle 0 | \left[ \sum_p \hat{a}_p e^{ikr_{A2}} \sum_{p'} \hat{a}_{p'} e^{ikr_{A1}} \right] \hat{a}_m^\dagger \hat{a}_n^\dagger | 0 \rangle \\ &= \mathcal{A}_{a_{m2}a_{n1}}(x_1, x_2) + \mathcal{A}_{a_{n2}a_{m1}}(x_1, x_2) \\ \Psi_{mn}^{(BB)}(x_1, x_2) &= \langle 0 | \left[ \sum_q \hat{b}_q e^{ikr_{B2}} \sum_{q'} \hat{b}_{q'} e^{ikr_{B1}} \right] \hat{b}_m^\dagger \hat{b}_n^\dagger | 0 \rangle \\ &= \mathcal{A}_{b_{m2}b_{n1}}(x_1, x_2) + \mathcal{A}_{b_{n2}b_{m1}}(x_1, x_2)\end{aligned}\quad (13.6)$$

where

$$\mathcal{A}_{a_{m2}a_{n1}}(x_1, x_2) = \mathcal{A}_{a_{n2}a_{m1}}(x_1, x_2) = e^{ik(r_{A2}+r_{A1})}$$

$$\mathcal{A}_{b_{m2}b_{n1}}(x_1, x_2) = \mathcal{A}_{b_{n2}b_{m1}}(x_1, x_2) = e^{ik(r_{B2}+r_{B1})}.$$

We have used the notation  $\mathcal{A}_{a_{m2}a_{n1}}(x_1, x_2)$  to indicate the two-photon amplitude in which photon  $m$  is annihilated at  $D_2$  and photon  $n$  is annihilated at  $D_1$ , and the notation  $\mathcal{A}_{b_{m2}b_{n1}}(x_1, x_2)$  to indicate the two-photon amplitude in which photon  $n$  is annihilated at  $D_2$  and photon  $m$  is annihilated at  $D_1$ . The two amplitudes are different yet indistinguishable to a joint photodetection event produced by the randomly paired  $m-n$  photons. The superposition of

$\mathcal{A}_{a_{m2}a_{n1}}(x_1, x_2)$  and  $\mathcal{A}_{a_{n2}a_{m1}}(x_1, x_2)$  results in the effective two-photon wavefunction of the  $m-n$  photon pair, which determines the probability for the  $m-n$  photon pair to produce a joint photodetection event at spatial coordinates  $x_1$  and  $x_2$ . Obviously, the calculated effective wavefunctions of Equation 13.6 yield  $G_{AA}^{(2)} = G_{BB}^{(2)} = \text{constant}$ :

$$\begin{aligned} G_{AA}^{(2)} &\propto \sum_{m < n} |c_m|^2 |c_n|^2 \left| e^{ik(r_{A2} + r_{A1})} \right|^2 = G_0 \\ G_{BB}^{(2)} &\propto \sum_{m < n} |c_m|^2 |c_n|^2 \left| e^{ik(r_{B2} + r_{B1})} \right|^2 = G_0, \end{aligned} \quad (13.7)$$

under the assumption of a symmetrical designed interferometer.

The effective wavefunctions  $\Psi_{mn}^{(AB)}(x_1, x_2)$  and  $\Psi_{mn}^{(BA)}(x_1, x_2)$  are calculated in a similar way:

$$\begin{aligned} \Psi_{mn}^{(AB)}(x_1, x_2) &= \langle 0 | \left[ \sum_{p'} \hat{a}_{p'} e^{ikr_{A2}} + \sum_{q'} \hat{b}_{q'} e^{ikr_{B2}} \right] \\ &\quad \left[ \sum_p \hat{a}_p e^{ikr_{A1}} + \sum_q \hat{b}_q e^{ikr_{B1}} \right] \hat{a}_m^\dagger \hat{b}_n^\dagger | 0 \rangle \\ &= \mathcal{A}_{a_{m2}b_{n1}}(x_1, x_2) + \mathcal{A}_{a_{m1}b_{n2}}(x_1, x_2) \\ \Psi_{mn}^{(BA)}(x_1, x_2) &= \langle 0 | \left[ \sum_{p'} \hat{a}_{p'} e^{ikr_{A2}} + \sum_{q'} \hat{b}_{q'} e^{ikr_{B2}} \right] \\ &\quad \left[ \sum_p \hat{a}_p e^{ikr_{A1}} + \sum_q \hat{b}_q e^{ikr_{B1}} \right] \hat{b}_m^\dagger \hat{a}_n^\dagger | 0 \rangle \\ &= \mathcal{A}_{b_{m2}a_{n1}}(x_1, x_2) + \mathcal{A}_{b_{m1}a_{n2}}(x_1, x_2) \end{aligned} \quad (13.8)$$

where

$$\begin{aligned} \mathcal{A}_{a_{m2}b_{n1}}(x_1, x_2) &= \mathcal{A}_{b_{m1}a_{n2}}(x_1, x_2) = e^{ik(r_{A2} + r_{B1})} \\ \mathcal{A}_{a_{m1}b_{n2}}(x_1, x_2) &= \mathcal{A}_{b_{m2}a_{n1}}(x_1, x_2) = e^{ik(r_{B2} + r_{A1})}. \end{aligned}$$

It is not difficult to see that the superposition of these two-photon amplitudes yields the following interference pattern during the scanning of  $D_1$  and  $D_2$ :

$$\begin{aligned} G_{AB}^{(2)} &\propto \sum_{m < n} |c_m|^2 |c_n|^2 \left| e^{ik(r_{A2}+r_{B1})} + e^{ik(r_{A1}+r_{B2})} \right|^2 \\ &\simeq G_0 \cos^2 \frac{\pi d(x_1 - x_2)}{\lambda(z - z_0)} \\ G_{BA}^{(2)} &\propto \sum_{m < n} |c_m|^2 |c_n|^2 \left| e^{ik(r_{B2}+r_{A1})} + e^{ik(r_{B1}+r_{A2})} \right|^2 \\ &\simeq G_0 \cos^2 \frac{\pi d(x_1 - x_2)}{\lambda(z - z_0)}, \end{aligned} \quad (13.9)$$

where

$d$  is the transverse separation distance between the incoherent light sources  $A$  and  $B$

$z_0$  and  $z$  are the longitudinal coordinates of the double-pinholes and the photodetectors, respectively

$z - z_0$  is the longitudinal distance between the double-pinholes and the photodetectors, as usual

The normalized second-order spatial correlation function is therefore a two-photon interference pattern with 50% contrast:

$$g^{(2)} \simeq 1 + \cos^2 \left[ \frac{\pi d(x_1 - x_2)}{\lambda(z - z_0)} \right] \quad (13.10)$$

Taking into account the finite size of the sources, the interference-diffraction pattern is expected to be

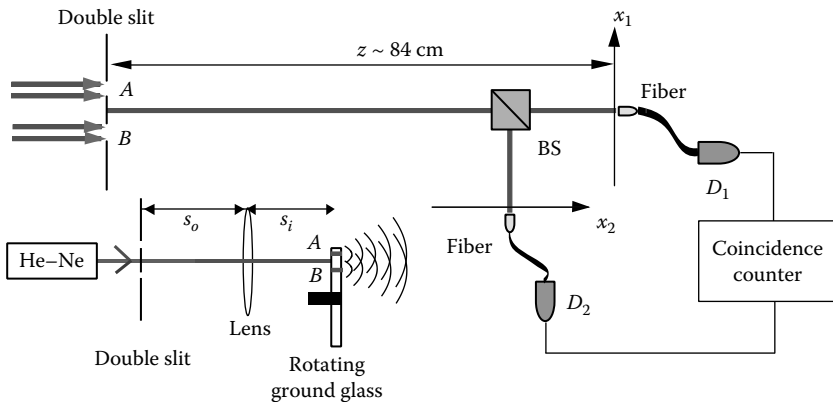
$$g^{(2)} = 1 + \text{sinc}^2 \left[ \frac{\pi b(x_1 - x_2)}{\lambda(z - z_0)} \right] \cos^2 \left[ \frac{\pi d(x_1 - x_2)}{\lambda(z - z_0)} \right], \quad (13.11)$$

where

$b$  is the 1-D width of the light sources  $A$  and  $B$

$d$  is the separation distance between the light sources  $A$  and  $B$

The above expectation has been confirmed experimentally. In 2004, Scarcelli et al. successfully observed the two-photon interference from two independent chaotic-thermal light sources. Their experimental setup is shown in Figure 13.2. The incoherent light sources  $A$  and  $B$  are simulated by a rotating ground glass and a CW He–Ne laser beam of 632 nm. The He–Ne laser

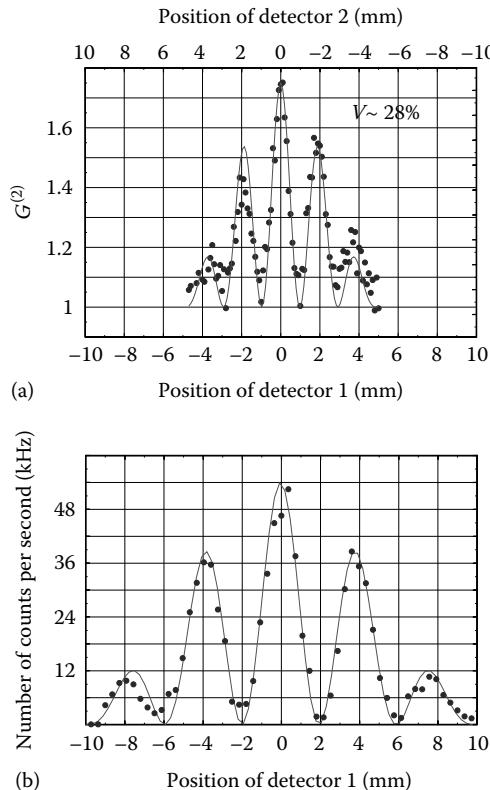
**FIGURE 13.2**

Schematic setup of a two-photon interference experiment of Scarelli et al. (2004). The experiment is prepared in such a way that no first-order interference is observable in the single-detector-counting rates of  $D_1$  and  $D_2$ , i.e., the fields from A and B are mutually incoherent with  $G^{(1)}(\mathbf{r}_A, t_A; \mathbf{r}_B, t_B) = 0$ . Do we expect to observe interference in the coincidence-counting rate of  $D_1$  and  $D_2$ ?

beam was first impinging on a double slit. A converging lens was followed to image the double slit onto the rotating ground glass. Two transversely scannable optical fibers, each coupled with a photon-counting detector, are facing two independent, point-like weak thermal sources A and B in the far-field. The single-detector-counting rate and the joint photodetection-counting rate of  $D_1$  and  $D_2$  are monitored, respectively, during the scanning of the two fiber tips. In their measurement,  $x_1$  and  $x_2$  are scanned with equal value but moved to opposite directions, i.e.,  $x_1 = -x_2$ . Under this chosen experimental condition, it is interesting to note that the interference-diffraction pattern is twice as narrow as the standard interference-diffraction pattern of He-Ne light and with interference modulation twice faster as that of the standard pattern, as if it were produced by a source of light with half the wavelength of the He-Ne laser. The measured two-photon interference-diffraction pattern is shown in the upper plot of Figure 13.3.

For comparison, a first-order interference-diffraction pattern of a He-Ne laser beam is also shown in the lower plot of Figure 13.3. In Figure 13.3, the solid line represents a fitting curve of Equation 13.11. The visibility of the pattern is about  $\sim (28 \pm 1)\%$ . During the measurement, the single-detector-counting rates of  $D_1$  and  $D_2$  were both observed as constants over the entire scanning range; see Figure 13.4, which demonstrates the absence of any first-order mutual-coherence between fields A and B.

The observed interference has four contributions:  $G_{AA}^{(2)}$ ,  $G_{BB}^{(2)}$ ,  $G_{AB}^{(2)}$ , and  $G_{BA}^{(2)}$ . The contributions of  $G_{AA}^{(2)}$  and  $G_{BB}^{(2)}$  can be calculated independently and can be measured separately by blocking the other source, i.e., blocking source-A to measure  $G_{BB}^{(2)}$ , or blocking source-B to measure  $G_{AA}^{(2)}$ . The net

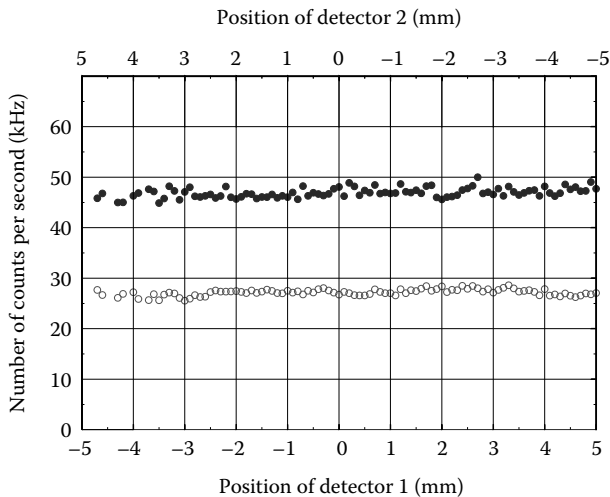
**FIGURE 13.3**

(a) Normalized second-order interference-diffraction pattern vs. position of the detectors. In this measurement,  $x_1$  and  $x_2$  were chosen with equal value but opposite direction. (b) Equivalent first-order interference-diffraction pattern of a 632 nm He-Ne laser.

contribution of  $G_{AB}^{(2)} + G_{BA}^{(2)}$ , i.e., the two-photon interference effect between incoherent sources  $A$  and  $B$ , can be isolated by subtracting the two separate measurements of  $G_{AA}^{(2)}$  and  $G_{BB}^{(2)}$  from the total. In fact, the interference visibility became  $\sim 100\%$  in the experiment of Scarcelli et al. after the subtraction of  $G_{AA}^{(2)}$  and  $G_{BB}^{(2)}$ .

In the view of quantum theory, the observed interference is the result of a superposition between two different yet indistinguishable two-photon amplitudes, corresponding to two alternative ways of producing a joint photodetection event at  $(\mathbf{r}_1, t_1)$  and  $(\mathbf{r}_2, t_2)$ . In classical theory, the nontrivial second-order correlation is considered as the statistical correlation of measured intensity fluctuations,

$$\langle I_1 I_2 \rangle = \langle I_1 \rangle \langle I_2 \rangle + \langle \Delta I_1 \Delta I_2 \rangle.$$

**FIGURE 13.4**

The counting rate of single detectors.

Although the constant background of the coincidence-counting rate of  $D_1$  and  $D_2$  can be interpreted as the product of the two measured intensities  $\langle I_1 \rangle \langle I_2 \rangle$ , the interference modulation of  $\cos^2[\pi d(x_1-x_2)/\lambda(z-z_0)]$  is obviously not  $\langle \Delta I_1 \Delta I_2 \rangle$ . The individual intensities were monitored in the experiment of Scarelli et al. by means of the single-detector-counting rate of  $D_1$  and  $D_2$ , respectively, which are shown in Figure 13.4. Can we expect to observe an interference pattern from these measured intensity fluctuations?

### 13.2 Two-Photon Anti-Correlation of Incoherent Chaotic-Thermal Light

In a temporal HBT interferometer, the temporal randomly distributed chaotic-thermal light has a twice greater chance of being measured within its coherence time by the joint photodetection of two independent photodetectors. In a spatial HBT interferometer, the spatial randomly distributed chaotic-thermal light exhibits a twice greater chance of being captured within a small transverse area that equals the spatial coherence of the thermal radiation by two-point photodetectors. Thermal light is identified with the following nontrivial temporal correlation:

$$G^{(2)}(\tau_A, \tau_B) \sim I_0^2 \left\{ 1 + \operatorname{sinc}^2 \left[ \frac{\Delta\omega(\tau_A - \tau_B)}{2} \right] \right\} \quad (13.12)$$

and the following nontrivial spatial correlation

$$G^{(2)}(\vec{\rho}_A, \vec{\rho}_B) \sim I_0^2 \left\{ 1 + \text{somb}^2 \left[ \frac{\pi \Delta\theta |\vec{\rho}_A - \vec{\rho}_B|}{\lambda} \right] \right\}. \quad (13.13)$$

The sinc-function and the sombrero-like function are defined as

$$\text{sinc}(x) = \frac{\sin(x)}{x} \quad \text{and} \quad \text{somb}(x) = \frac{2J_1(x)}{x},$$

where

$J_1(x)$  is the first-order Bessel function

$\tau_A = t_A - z_A/c$  and  $\tau_B = t_B - z_B/c$  are the temporal coordinates of the two photodetection events ( $t_j$  and  $z_j$  with  $j=A, B$  are the registration time and longitudinal coordinate of the photodetection event)

$\Delta\omega$  is the spectral bandwidth of the thermal radiation

$\vec{\rho}_A$  and  $\vec{\rho}_B$  are the transverse coordinates of the two photodetectors

$\Delta\theta$  is the angular size of the far-field thermal source and

$\lambda$  is the wavelength of the radiation

Figure 13.5 illustrates a schematic setup of a HBT interferometer, which measures the second-order spatial coherence or correlation of thermal light. When  $d = x_A - x_B$  is chosen to be greater than  $\lambda/\Delta\theta$ , the A-field and the B-field become first-order incoherent and the second-order correction become a trivial constant. Figure 13.6 schematically illustrated another modern HBT type interferometer, which measures both the temporal and spatial correlation of thermal radiation by scanning the optical fiber tips longitudinally or transversely. Equations 13.12 and 13.13 can be easily examined with this modern HBT interferometer. Similar to the setup of Figure 13.5, when  $|\vec{P}_A - \vec{P}_B|$  is chosen to be greater than  $\lambda/\Delta\theta$ , the A-field at the fiber tip A and the B-field at the fiber tip B become first-order incoherent and the second-order correlation of Equation 13.13 turns to be a trivial constant.

It was recently found that for a large angular-sized near-field thermal source, the spatial correlation is effectively within a physical “point,”

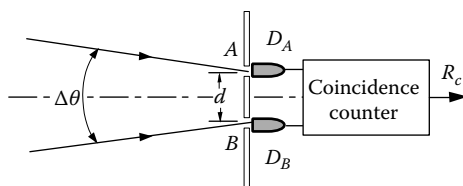


FIGURE 13.5

Schematic of a modern spatial HBT interferometer for measuring the second-order correlation of thermal light. The nontrivial HBT correlation becomes trivial when  $d > \lambda/\Delta\theta$ . Under this condition  $\Gamma^{(2)}(\mathbf{r}_A, t_A; \mathbf{r}_B, t_B) = \langle I(\mathbf{r}_A, t_A) \rangle \langle I(\mathbf{r}_B, t_B) \rangle$ . The joint photodetection-counting rate  $R_c$  turns to be constant for either CW or pulsed thermal radiations.

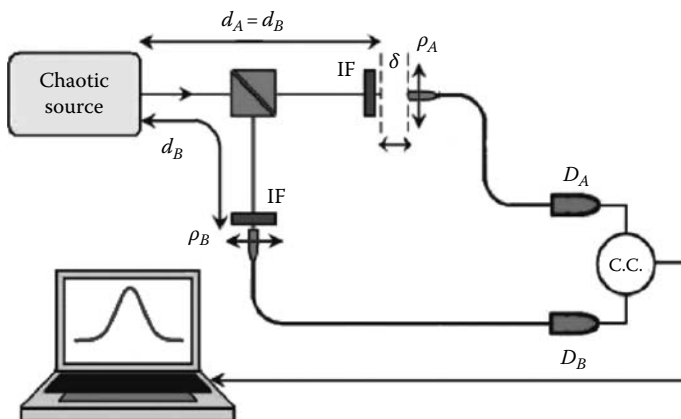


FIGURE 13.6

Schematic of a modern HBT interferometer, which measures both temporal and spatial correlation of thermal light by scanning the optical fiber tips longitudinally or transversely. Two optical fiber-coupled photon-counting detectors,  $D_A$  and  $D_B$ , and a coincidence-circuit (C.C.) are employed to form a coincidence counter. The spectral bandwidth of the radiation, which is determined by IF (interference filter), is  $\Delta\omega$ . The angular diameter of the thermal source is  $\Delta\theta$ .

indicating a typical nonlocal point-to-point-position correlation of randomly paired photons. In the language of Einstein, Podolsky, and Rosen (EPR): in a joint-detection of two photons, neither photon one nor photon two knows precisely where to go when they are created at the thermal source; however, if one of them is observed at a certain space-time point, the other one must have a twice greater probability to be found at the same space-time point. The point-to-point correlation of thermal light has been utilized for reproducing ghost images in a lensless configuration. Thermal light is also named Gaussian light due to its stochastic character. In a thermal source, the radiations created from a large number of atomic transitions are all independent. Each atomic transition creates its photon independently and randomly. There is no doubt that thermal radiations propagate in space-time in a completely random manner.\* How could the randomly distributed photons have such a correlation? Remember, unlike the entangled photon pair, the jointly measured photons from a thermal source are just two independent photons that fall into the coincidence time window only by chance.

Historically, the HBT phenomenon was interpreted as the statistical correlation of intensity fluctuations. In classical theory, a joint photodetection between two independent point-like photodetectors  $D_A$  and  $D_B$  measures the statistical correlation of intensities at space-time coordinates  $(\mathbf{r}_A, t_A)$  and  $(\mathbf{r}_B, t_B)$

\* One should not confuse this observation with the propagation of a laser beam. Laser beam propagates coherently. After propagating a distance, a large transverse sized laser beam may keep a slightly enlarged beam size due to diffraction. Thermal light propagates incoherently, which is very different from laser beam.

$$\begin{aligned}
\Gamma^{(2)}(\mathbf{r}_A, t_A; \mathbf{r}_B, t_B) &= \langle I(\mathbf{r}_A, t_A) I(\mathbf{r}_B, t_B) \rangle \\
&= \langle E^*(\mathbf{r}_A, t_A) E(\mathbf{r}_A, t_A) E^*(\mathbf{r}_B, t_B) E(\mathbf{r}_B, t_B) \rangle \\
&= \Gamma_{AA}^{(1)} \Gamma_{BB}^{(1)} + \Gamma_{AB}^{(1)} \Gamma_{BA}^{(1)} \\
&= \langle I(\mathbf{r}_A, t_A) \rangle \langle I(\mathbf{r}_B, t_B) \rangle + \langle \Delta I(\mathbf{r}_A, t_A) \Delta I(\mathbf{r}_B, t_B) \rangle. \quad (13.14)
\end{aligned}$$

where

$$\begin{aligned}
\Gamma_{AA}^{(1)} &= \langle E^*(\mathbf{r}_A, t_A) E(\mathbf{r}_A, t_A) \rangle, \\
\Gamma_{BB}^{(1)} &= \langle E^*(\mathbf{r}_B, t_B) E(\mathbf{r}_B, t_B) \rangle, \\
\Gamma_{AB}^{(1)} &= \Gamma_{BA}^{(1)} = \langle E^*(\mathbf{r}_A, t_A) E(\mathbf{r}_B, t_B) \rangle.
\end{aligned}$$

In Equation 13.14, we have applied statistical property of Gaussian light:

$$\langle X_1 X_2 X_3 X_4 \rangle = \langle X_1 X_2 \rangle \langle X_3 X_4 \rangle + \langle X_1 X_3 \rangle \langle X_2 X_4 \rangle + \langle X_1 X_4 \rangle \langle X_2 X_3 \rangle.$$

The nontrivial HBT correlation comes from the second term of Equation 13.14, which is considered as the statistical correlation of intensity fluctuations  $\langle \Delta I(\mathbf{r}_A, t_A) \Delta I(\mathbf{r}_B, t_B) \rangle$ .

Quantum mechanics, however, has a different point of view. In the quantum theory of light, a joint photodetection between two independent point-like photodetectors  $D_A$  and  $D_B$  measures the probability of observing two photons jointly at space-time coordinates  $(\mathbf{r}_A, t_A)$  and  $(\mathbf{r}_B, t_B)$ . If there exists more than one alternative way for a pair of photons, either entangled photons or randomly paired photons that fall into the coincidence time window by chance, to produce a joint photo-detection event, these probability amplitudes must be linearly superposed in the probability calculation. The observed nontrivial correlation of “peak” from thermal light is the result of the constructive superposition between these quantum amplitudes:

$$\begin{aligned}
G^{(2)}(\mathbf{r}_1, t_1; \mathbf{r}_2, t_2) &\simeq \sum_j P_j |\Psi_j(\mathbf{r}_1, t_1; \mathbf{r}_2, t_2)|^2 \\
&= \sum_{m,n} P_{mn} |\mathcal{A}_{m_1 n_2}(\mathbf{r}_1, t_1; \mathbf{r}_2, t_2) + \mathcal{A}_{n_1 m_2}(\mathbf{r}_1, t_1; \mathbf{r}_2, t_2)|^2, \quad (13.15)
\end{aligned}$$

where  $\Psi_j(\mathbf{r}_1, t_1; \mathbf{r}_2, t_2)$  is the effective two-photon wavefunction of the  $j$ th-measured photon pair.  $\Psi_j(\mathbf{r}_1, t_1; \mathbf{r}_2, t_2)$  has two amplitudes  $\mathcal{A}_{m_1 n_2}(\mathbf{r}_1, t_1; \mathbf{r}_2, t_2)$

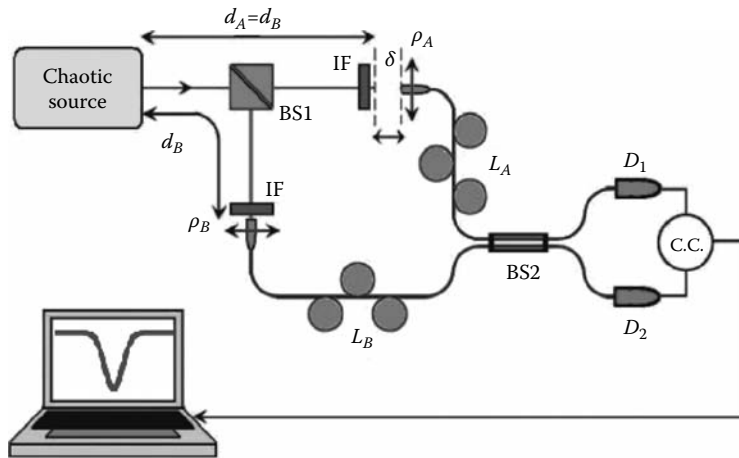
and  $\mathcal{A}_{n_1 m_2}(\mathbf{r}_1, t_1; \mathbf{r}_2, t_2)$ , corresponding to two different yet indistinguishable alternative ways for the randomly paired photon  $m$ , which is created from the  $m$ th atomic transition, and the photon  $n$ , which is created from the  $m$ th atomic transition, to produce the  $j$ th joint photodetection event.

In the view of quantum theory of light, in fact, the measurement is not restricted to a “correlation” function of “peak,” but it is also possible to observe an anti-correlation function of “dip” if a destructive superposition between the two amplitudes is achievable:

$$\begin{aligned} G^{(2)}(\mathbf{r}_1, t_1; \mathbf{r}_2, t_2) \\ \simeq \sum_j P_j |\Psi_j(\mathbf{r}_1, t_1; \mathbf{r}_2, t_2)|^2 \\ = \sum_{m,n} P_{mn} |\mathcal{A}_{m_1 n_2}(\mathbf{r}_1, t_1; \mathbf{r}_2, t_2) - \mathcal{A}_{n_1 m_2}(\mathbf{r}_1, t_1; \mathbf{r}_2, t_2)|^2. \end{aligned} \quad (13.16)$$

Mathematically, it only requires a simple change of sign, which can be easily done with the help of a unitary transformation. As we know, this kind of unitary transformation is achievable by an optical beamsplitter. Unfortunately, it took us more than half a century to demonstrate experimentally. For 50 years, we have been believing the nontrivial correlation of thermal light is a statistical correlation of intensity fluctuations.

In a set of recent experiments, Chen et al. observed the anti-correlation “dip” from the measurement of first-order and second-order incoherent chaotic-thermal light. The experimental setup of Chen et al. is schematically shown in Figure 13.7. Instead of directly measuring the intensity correlation of  $\langle I(\mathbf{r}_A, t_A)I(\mathbf{r}_B, t_B) \rangle$ , this setup measures  $\langle I(\mathbf{r}_1, t_1)I(\mathbf{r}_2, t_2) \rangle$  at the output ports of a 50/50 optical fiber beamsplitter BS2. It is BS2 in Figure 13.7 that introduces a “−” sign between the two amplitudes and produces a destructive superposition that is shown in Equation 13.16. If the two input fiber tips  $A$  and  $B$  are placed within the longitudinal coherence time and the transverse coherence area of the thermal field, i.e.,  $G^{(1)}(\mathbf{r}_A, t_A; \mathbf{r}_B, t_B) \neq 0$ , this setup is equivalent to a Mach-Zehnder interferometer.  $D_1$  and  $D_2$  will each observe first-order interference as a function of the optical delay  $\delta$  when scanning the fiber tip  $A$  along its longitudinal axis. Consequently, the joint photodetection of  $D_1$  and  $D_2$  produces an interference that is factorizable into two first-order interferences. However, in this experiment we decided to move the fiber tip  $A$  outside the transverse coherence area to force  $G^{(1)}(\mathbf{r}_A, t_A; \mathbf{r}_B, t_B) = 0$ . Under this condition, radiation  $A$  and  $B$  are first-order and second-order incoherent; there would be no observable first-order interference even in the case of “single-exposure” or instantaneous measurement. Moreover, if we measure the second-order correlation  $G^{(2)}(\mathbf{r}_A, t_A; \mathbf{r}_B, t_B)$  outside the transverse coherence area to achieve

**FIGURE 13.7**

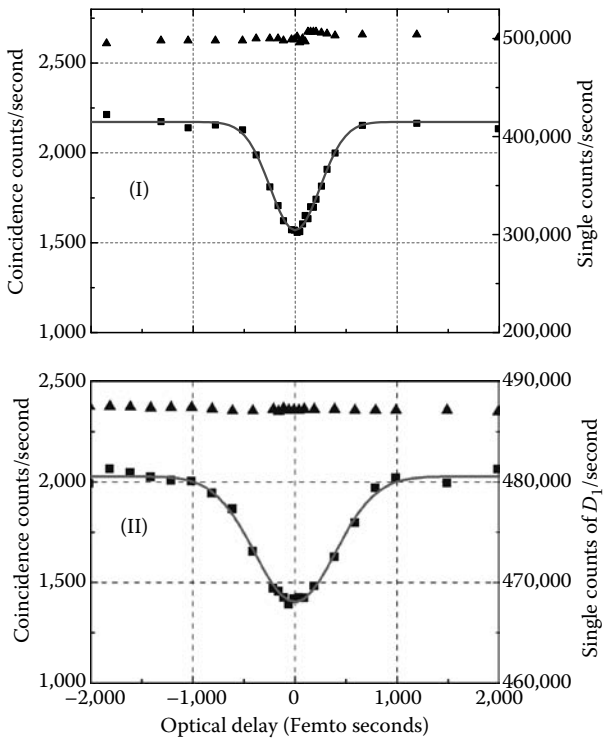
Schematic setup of an anti-correlation measurement from first-order and second-order incoherent chaotic-thermal light by Chen et al. (2009).

$G^{(1)}(\mathbf{r}_A, t_A; \mathbf{r}_B, t_B) = 0$ , the observed second-order correlation will be a trivial constant  $G^{(2)}(\mathbf{r}_A, t_A; \mathbf{r}_B, t_B) = G^{(1)}(\mathbf{r}_A, t_A; \mathbf{r}_A, t_A)G^{(1)}(\mathbf{r}_B, t_B; \mathbf{r}_B, t_B)$ . From the classical theory of statistical correlation of intensity fluctuations, the above condition means  $\langle \Delta I_A \Delta I_B \rangle = 0$ . In this regard, can we expect any nontrivial correlation by passing the incoherent radiations  $A$  and  $B$  through a simple optical beamsplitter BS2? From the classical point of view, a nontrivial second-order correlation measured by the joint photodetection of  $D_1$  and  $D_2$  means  $\langle \Delta I_{A_1} \Delta I_{B_2} \rangle \neq 0$ , where the notation  $I_{A_1}$  ( $I_{B_2}$ ) indicates the measured intensity of radiation  $A$  ( $B$ ) at  $D_1$  ( $D_2$ ). Remember a simple optical beam-splitter cannot change the intensity fluctuation correlation of the input fields from “no-correlation” to “anti-correlation.”

The measurement produces quite a surprise. An anti-correlation “dip” was observed in the joint photodetection-counting rate of  $D_1$  and  $D_2$  as functions of the optical delay  $\delta$  and the bandwidth of the spectral filters IF, while the counting rate of  $D_1$  and  $D_2$  both kept constants. Figure 13.8 reports two typical measured anti-correlation functions with different spectrum bandwidths of the chaotic-thermal field.

The experimental detail is described as follows.

1. *The source:* The light source is a standard pseudo-thermal source that was developed in the 1960s and used widely in HBT correlation measurements. The source consists of a 780 nm CW mode-locked Ti:Sapphire laser beam with  $\sim 200$  fs pulses at a 78 MHz repetition rate and a fast-rotating diffusing ground glass. The linearly polarized laser beam is enlarged transversely onto the ground glass with a diameter of 4.5 mm. The enlarged laser radiation is scattered

**FIGURE 13.8**

Typical observed anti-correlation functions with different special bandwidth:  $\tau_c \sim 345$  fs for (I),  $\tau_c \sim 541$  fs for (II). The temporal width of the “dip” is determined by the bandwidth of the spectral filters (IF). The counting rate of  $D_1$  and  $D_2$  both kept constants during the scanning of  $\delta$ .

and diffused by the rotating ground glass to simulate a near-field, chaotic-thermal radiation source: a large number of independent point sub-sources with randomly distributed relative phases.

2. *The interferometer:* A 50/50 beamsplitter (BS1) is used to split the chaotic-thermal light into transmitted and reflected radiations, which are then coupled into two identical polarization-controlled single-mode fibers  $A$  and  $B$ , respectively. The fiber tips are located  $\sim 200$  mm from the ground glass, i.e.,  $d_A = d_B \sim 200$  mm. At this distance, the angular size  $\Delta\theta$  is  $\sim 22.5$  mrad ( $1.29^\circ$ ) with respect to each input fiber tip, which satisfies the Fresnel near-field condition. Two identical narrowband spectral filters (IF) are placed in front of the two fiber tips  $A$  and  $B$ . The transverse and longitudinal coordinates of the input fiber tips are both scannable by step motors. The output ends of the two fibers can be directly coupled into the photon-counting detectors  $D_A$  and  $D_B$ , respectively, for near-field HBT correlation measurements, or coupled into the two

input ports of a 50/50 single-mode optical fiber beamsplitter (BS2) for the anti-correlation measurement.

3. *The measurement:* Two steps of measurements were made. The purpose of step one is to confirm that the light source produces chaotic-thermal field. We measured the HBT temporal and spatial correlations by scanning the input fiber tips longitudinally and transversely. In this measurement, the output ends of the fibers are coupled into  $D_A$  and  $D_B$  directly, as shown in Figure 13.5. Chaotic-thermal radiation can easily be distinguished from a laser beam by examining its second-order coherence function  $G^{(2)}(\mathbf{r}_A, t_A; \mathbf{r}_B, t_B)$ , which is characterized experimentally by the coincidence-counting rate that counts the joint photodetection events at space-time points  $(\mathbf{r}_A, t_A)$  and  $(\mathbf{r}_B, t_B)$ . Figure 13.9 reports two measured second-order correlations at 0 and at 1000 revolutions per minute (rpm) of the rotating ground glass. This measurement guarantees a typical HBT correlation of chaotic-thermal light at rotation speeds greater than 1000 rpm of the ground glass, indicating the thermal nature of the light source. In this measurement, we have also located experimentally the longitudinal and transverse coordinates of the fiber tips A and B for achieving the maximum coincidence-counting rate, corresponding to the maximum second-order correlation. In step two, we couple the 50/50 fiber beamsplitter (BS2) into the setup, as shown in Figure 13.7. This measurement was done in two steps. We first measured the first-order interference at  $\vec{\rho}_A = \vec{\rho}_B$  by scanning the input fiber tip A longitudinally in the neighborhood of  $d_A \sim 200$  mm. There is no surprise to have the first-order interference in the counting rates of  $D_1$  and  $D_2$ , respectively. When choosing  $\vec{\rho}_A = \vec{\rho}_B$ , the two

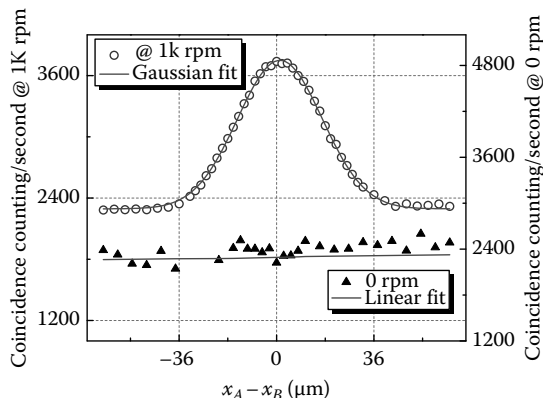


**FIGURE 13.9**

Measurement of  $G^{(2)}(x_A - x_B)$  at no rotation (0 rpm) and at 1000 rpm. Here,  $x_A$  and  $x_B$  are the  $x$ -components of  $\vec{\rho}_A$  and  $\vec{\rho}_B$ , and correspondingly  $y$  components are kept  $y_A = y_B$ .

input fiber tips are coupled within the spatial coherence area of the radiation field; we have effectively built a Mach–Zehnder interferometer. We then move the input fiber tip  $A$  transversely from  $\vec{\rho}_A = \vec{\rho}_B$  to  $|\vec{\rho}_A - \vec{\rho}_B| \gg l_c$ , where  $l_c$  is the transverse coherence length of the thermal field. (In most of the measurements,  $|\vec{\rho}_A - \vec{\rho}_B|$  was chosen to be  $|\vec{\rho}_A - \vec{\rho}_B| \geq 40l_c$ .) Then, we scan the input fiber tip  $A$  again longitudinally in the neighborhood of  $d_A \sim 200\text{mm}$ . The optical delay between the plane  $z = d_A \sim 200\text{mm}$  and the scanning input fiber tip  $A$  is labeled as  $\delta$  in Figure 13.7. Under the experimental condition of  $G^{(1)}(\mathbf{r}_A, t_A; \mathbf{r}_B, t_B) = 0$  and  $G^{(2)}(\mathbf{r}_A, t_A; \mathbf{r}_B, t_B) = \text{constant}$ , there is no surprise we lose any first-order interference. However, it is indeed a surprise that an anti-correlation is observed in terms of the joint photodetection of  $D_1$  and  $D_2$  as a function of the optical delay  $\delta$  that is reported in Figure 13.8. In these measurements,  $|\vec{\rho}_A - \vec{\rho}_B| \sim 40l_c$ .

In the following, we provide a simple analysis for the observation, which may help us to understand the two-photon interference nature of the phenomenon. This calculation is based on the same model of independent thermal light sources  $A$  and  $B$  presented in the previous section. Similar to the double-pinhole experiment, we treat  $A$  and  $B$  as two independent point-like mutually incoherent sources, exciting two groups of independent wavepackets at the fiber tips  $A$  and  $B$ :

$$\begin{aligned} |\Psi_m\rangle_A &= \int d\omega f(\omega) e^{i\omega t_{0A}} \hat{a}_m^\dagger(\omega) |0\rangle \\ |\Psi_n\rangle_B &= \int d\omega f(\omega) e^{i\omega t_{0B}} \hat{b}_n^\dagger(\omega) |0\rangle, \end{aligned} \quad (13.17)$$

where

$f(\omega)$  is the spectral function that is mainly determined by the spectral filters (IF) in the experimental setup  
 $t_{0A}$  and  $t_{0B}$  represent the creation times of the wavepackets

Following a similar analysis as that in the previous section, using the same notations  $G_{AA}^{(2)}$ ,  $G_{BB}^{(2)}$ ,  $G_{AB}^{(2)}$ , and  $G_{BA}^{(2)}$  defined in Section 13.1, we evaluate the nontrivial second-order temporal correlation functions  $G_{AB}^{(2)}(z_1, t_1; z_2, t_2)$  and  $G_{BA}^{(2)}(z_1, t_1; z_2, t_2)$ . Each  $G_{AA}^{(2)}(z_1, t_1; z_2, t_2)$  and  $G_{BB}^{(2)}(z_1, t_1; z_2, t_2)$  contributes to the joint photodetection constant, and each constant can be easily measured by blocking the other source. The following calculation is for the

second-order temporal correlation function  $G_{AB}^{(2)}(z_1, t_1; z_2, t_2)$ , which is produced by two wavepackets, one from source  $A$  and the other from source  $B$ :

$$\begin{aligned} G_{AB}^{(2)}(z_1, t_1; z_2, t_2) &\propto \langle \hat{E}^{(-)}(z_1, t_1) \hat{E}^{(-)}(z_2, t_2) \hat{E}^{(+)}(z_2, t_2) \hat{E}^{(+)}(z_1, t_1) \rangle_{\text{QM}} \Big|_{\text{Ensemble}} \\ &\simeq \sum_{m < n} \left| \Psi_{mn}^{(AB)}(z_1, t_1; z, t_2) \right|^2. \end{aligned} \quad (13.18)$$

Following a similar analysis of previous sections, the field operators are written as

$$\begin{aligned} \hat{E}^{(+)}(z_1, t_1) &= \frac{1}{\sqrt{2}} [\hat{E}^{(+)}(\tau_{A1}) + \hat{E}^{(+)}(\tau_{B1})] \\ \hat{E}^{(+)}(z_2, t_2) &= \frac{1}{\sqrt{2}} [\hat{E}^{(+)}(\tau_{A2}) - \hat{E}^{(+)}(\tau_{B2})], \end{aligned} \quad (13.19)$$

where

$\tau_{Aj} \equiv t_j - n(z_j - z_A)/c$ ,  $\tau_{Bl} \equiv t_j - n(z_j - z_B)/c$ ,  $j = 1, 2$ , are the optical delay from the detector  $D_j$  to the input planes  $A$  and  $B$ , respectively  
 $n$  is the index of refraction of the fiber

The “–” sign in  $\hat{E}^{(+)}(z_2, t_2)$  is introduced by the beamsplitter BS2.

The effective wavefunction  $\Psi_{mn}^{(AB)}(z_1, t_1; z, t_2)$  has two amplitudes that are superposed destructively:

$$\Psi_{mn}^{(AB)}(z_1, t_1; z_2, t_2) = \mathcal{A}_{m_1 n_2} \left( \tau_{A1}^R, \tau_{B2}^R \right) - \mathcal{A}_{n_1 m_2} \left( \tau_{B1}^T, \tau_{A2}^T \right).$$

Repeating the same calculation shown in the previous section, the two-photon amplitudes  $\mathcal{A}_{m_1 n_2} \left( \tau_{A1}^T, \tau_{B2}^T \right)$  and  $\mathcal{A}_{n_1 m_2} \left( \tau_{B1}^R, \tau_{A2}^R \right)$  are easily obtainable. Similarly, we now turn the sum into the integral of  $t_{0A}$  and  $t_{0B}$ ,

$$\begin{aligned} G_{AB}^{(2)}(z_1, t_1; z_2, t_2) &= G_{BA}^{(2)}(z_1, t_1; z_2, t_2) \\ &\simeq R_0 \int dt_{0A} dt_{0B} \left| \mathcal{A}_{m_1 n_2} \left( \tau_{A1}^R, \tau_{B2}^R \right) - \mathcal{A}_{n_1 m_2} \left( \tau_{B1}^T, \tau_{A2}^T \right) \right|^2. \end{aligned} \quad (13.20)$$

Examining Equation 13.20, we found an interesting solution: when taking  $t_{0A_j} \simeq t_{0B_k}$ , the cross-interference term turns into the normal square of the

Fourier transform of the spectrum

$$\int d\omega |f(\omega)|^2 e^{i\omega\delta} \int d\omega' |f(\omega')|^2 e^{-i\omega'\delta} = |\mathcal{F}_\delta\{|f(v)|^2\}|^2.$$

The coincidence-counting rate takes the form of a “dip” function of the optical delay  $\delta$

$$R_{AB} \simeq R_0 \int dt_1 dt_2 S(t_1 - t_2) G_{AB}^{(2)}(z_1, t_1; z_2, t_2) = R_0 \left[ 1 - e^{-\delta^2/\tau_c^2} \right], \quad (13.21)$$

where we have assumed a Gaussian spectrum function of  $|f(v)|^2$ . Equation 13.21 has been verified in the experiment of Chen et al. In that experiment, Chen et al. used a fast-pulsed laser to simulate the condition of  $t_{0A_j} \simeq t_{0B_k}$ .

The contributions of  $G_{AA}^{(2)}$  and  $G_{BB}^{(2)}$  are easily measured experimentally by blocking the other source. Subtracting these two contributions from the total joint photodetection-counting rate of  $D_1$  and  $D_2$ , we found the visibility of the anti-correlation function of “dip” shown in Figure 13.8 become  $\sim 100\%$ . Figure 13.10 is an observed anti-correlation “dip” from the experimental demonstration of Chen et al. After the subtraction of  $G_{AA}^{(2)}$  and  $G_{BB}^{(2)}$ ,  $G_{AB}^{(2)} + G_{BA}^{(2)}$  is recognized as the anti-correlation function in terms of the optical delay  $\delta$  with a visibility  $\sim 93\%$ .

It is interesting that the classical statistical correlation fails to explain the experimental observation. In the following, we give a simple estimation starting from

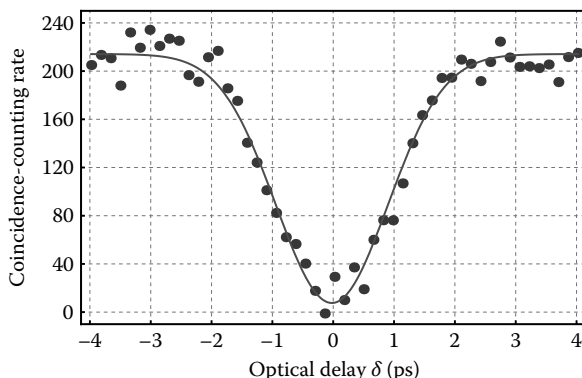


**FIGURE 13.10**

Typical measured temporal anti-correlation  $G_{AB}^{(2)}(\delta) + G_{BA}^{(2)}(\delta)$ . The visibility is  $(93.2 \pm 5.1)\%$ . In this measurement,  $G_{AA}^{(2)}$  and  $G_{BB}^{(2)}$  were subtracted from the total contribution of  $G_{AA}^{(2)} + G_{BB}^{(2)} + G_{AB}^{(2)} + G_{BA}^{(2)}$ .

$$\begin{aligned}\Gamma^{(2)}(\mathbf{r}_1, t_1; \mathbf{r}_2, t_2) &= \langle I(\mathbf{r}_1, t_1)I(\mathbf{r}_2, t_2) \rangle \\ &= \langle (E_{A1}^* + E_{B1}^*) (E_{A1} + E_{B1}) (E_{A2}^* - E_{B2}^*) (E_{A2} - E_{B2}) \rangle, \quad (13.22)\end{aligned}$$

where  $E_{Aj}$  and  $E_{Bk}$  label the radiation fields from sources  $A$  and  $B$  at photodetection event  $(\mathbf{r}_j, t_j)$  and  $(\mathbf{r}_k, t_k)$ , respectively. We have 16 expectations to evaluate:

$$\begin{aligned}&\langle I(\mathbf{r}_1, t_1)I(\mathbf{r}_2, t_2) \rangle \\ &= \langle E_{A1}^* E_{A1} E_{A2}^* E_{A2} \rangle + \langle E_{A1}^* E_{A1} E_{B2}^* E_{B2} \rangle \\ &\quad - \langle E_{A1}^* E_{A1} E_{A2}^* E_{B2} \rangle - \langle E_{A1}^* E_{A1} E_{B2}^* E_{A2} \rangle \\ &\quad + \langle E_{B1}^* E_{B1} E_{A2}^* E_{A2} \rangle + \langle E_{B1}^* E_{B1} E_{B2}^* E_{B2} \rangle \\ &\quad - \langle E_{B1}^* E_{B1} E_{A2}^* E_{B2} \rangle - \langle E_{B1}^* E_{B1} E_{B2}^* E_{A2} \rangle \\ &\quad + \langle E_{A1}^* E_{B1} E_{A2}^* E_{A2} \rangle + \langle E_{A1}^* E_{B1} E_{B2}^* E_{B2} \rangle \\ &\quad - \langle E_{A1}^* E_{B1} E_{A2}^* E_{B2} \rangle - \langle E_{A1}^* E_{B1} E_{B2}^* E_{A2} \rangle \\ &\quad + \langle E_{B1}^* E_{A1} E_{A2}^* E_{A2} \rangle + \langle E_{B1}^* E_{A1} E_{B2}^* E_{B2} \rangle \\ &\quad - \langle E_{B1}^* E_{A1} E_{A2}^* E_{B2} \rangle - \langle E_{B1}^* E_{A1} E_{B2}^* E_{A2} \rangle. \quad (13.23)\end{aligned}$$

Applying the property of Gaussian field and taking the result of  $\langle E_A^* E_B \rangle = 0$ , it is not too difficult to find that 10 terms in Equation 13.23 take zero value, and the remaining 6 terms may have nonzero contribution to  $\langle I_1 I_2 \rangle$ :

$$\begin{aligned}&\langle I(\mathbf{r}_1, t_1)I(\mathbf{r}_2, t_2) \rangle \\ &= \langle E_{A1}^* E_{A1} E_{A2}^* E_{A2} \rangle + \langle E_{B1}^* E_{B1} E_{B2}^* E_{B2} \rangle \\ &\quad + \langle E_{A1}^* E_{A1} E_{B2}^* E_{B2} \rangle + \langle E_{B1}^* E_{B1} E_{A2}^* E_{A2} \rangle \\ &\quad - \langle E_{A1}^* E_{B1} E_{B2}^* E_{A2} \rangle - \langle E_{B1}^* E_{A1} E_{A2}^* E_{B2} \rangle. \quad (13.24)\end{aligned}$$

The first two terms in Equation 13.24 correspond to the two sets of HBT correlations, similar to that in analysis one:

$$\begin{aligned}
& \langle E_{A1}^* E_{A1} E_{A2}^* E_{A2} \rangle \\
&= \langle E_{A1}^* E_{A1} \rangle \langle E_{A2}^* E_{A2} \rangle + \langle E_{A1}^* E_{A2} \rangle \langle E_{A2}^* E_{A1} \rangle \\
&= \Gamma_{A11}^{(1)} \Gamma_{A22}^{(1)} + \Gamma_{A12}^{(1)} \Gamma_{A21}^{(1)}
\end{aligned} \tag{13.25}$$

$$\begin{aligned}
& \langle E_{B1}^* E_{B1} E_{B2}^* E_{B2} \rangle \\
&= \langle E_{B1}^* E_{B1} \rangle \langle E_{B2}^* E_{B2} \rangle + \langle E_{B1}^* E_{B2} \rangle \langle E_{B2}^* E_{B1} \rangle \\
&= \Gamma_{B11}^{(1)} \Gamma_{B22}^{(1)} + \Gamma_{B12}^{(1)} \Gamma_{B21}^{(1)}.
\end{aligned} \tag{13.26}$$

It is clear that these two terms cannot produce the anti-correlation as a function of  $\delta$ .

The next two terms in Equation 13.24 are the products of mean intensities, which cannot produce the anti-correlation function of  $\delta$  either:

$$\begin{aligned}
& \langle E_{A1}^* E_{A1} E_{B2}^* E_{B2} \rangle \\
&= \langle E_{A1}^* E_{A1} \rangle \langle E_{B2}^* E_{B2} \rangle = \Gamma_{A11}^{(1)} \Gamma_{B22}^{(1)}
\end{aligned} \tag{13.27}$$

$$\begin{aligned}
& \langle E_{B1}^* E_{B1} E_{A2}^* E_{A2} \rangle \\
&= \langle E_{B1}^* E_{B1} \rangle \langle E_{A2}^* E_{A2} \rangle = \Gamma_{B11}^{(1)} \Gamma_{A22}^{(1)}
\end{aligned} \tag{13.28}$$

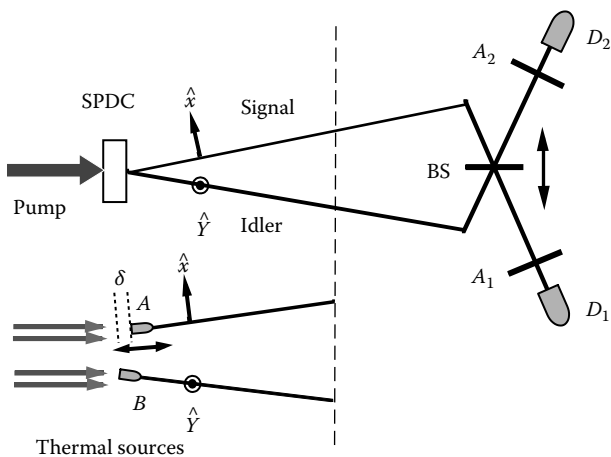
The last two “cross terms” may contribute nonzero values to produce an “anti-correlation;” however, neither of them is a function of the optical delay  $\delta$ .

$$\begin{aligned}
& \langle E_{A1}^* E_{B1} E_{B2}^* E_{A2} \rangle \\
&= \langle E_{A1}^* E_{A2} \rangle \langle E_{B2}^* E_{B1} \rangle = \Gamma_{A12}^{(1)} \Gamma_{B21}^{(1)}
\end{aligned} \tag{13.29}$$

$$\begin{aligned}
& \langle E_{B1}^* E_{A1} E_{A2}^* E_{B2} \rangle \\
&= \langle E_{B1}^* E_{B2} \rangle \langle E_{A2}^* E_{A1} \rangle = \Gamma_{B12}^{(1)} \Gamma_{A21}^{(1)}.
\end{aligned} \tag{13.30}$$

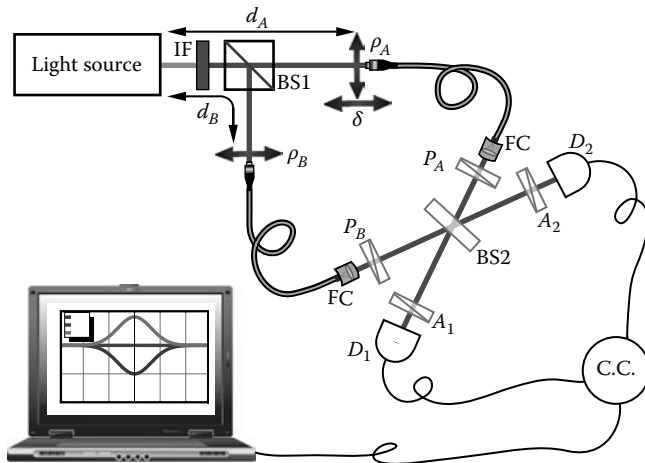
### 13.3 Two-Photon Interference with Incoherent Orthogonal Polarized Chaotic-Thermal Light

In this section, we discuss two-photon interference with orthogonal polarized incoherent chaotic-thermal light through the analysis of a simple experiment, which is schematically shown in Figure 13.11. The experimental

**FIGURE 13.11**

Schematic of a typical two-photon interferometer with orthogonal polarized incoherent chaotic-thermal light. The setup is the same as the historical two-photon polarization interferometer of Alley–Shih, except for the use of chaotic-thermal light instead of entangled photon pair. The incoherent chaotic-thermal radiations  $A$  and  $B$  are prepared in the same way as that in Section 13.2.

setup is similar to that of the historical two-photon polarization interferometer of Alley–Shih, except for the use of orthogonal polarized incoherent chaotic-thermal light instead of entangled photon pair. If the input radiation at points  $A$  and  $B$  are first-order coherent, this setup is equivalent to a polarization Mach–Zehnder interferometer.  $D_1$  and  $D_2$  will each observe first-order interference and, consequently, the joint photodetection of  $D_1$  and  $D_2$  outputs an interference pattern that is the product of the two first-order interferences. To avoid this trivial effect,  $A$  and  $B$  have to be mutually incoherent. The incoherent chaotic-thermal radiations  $A$  and  $B$  are prepared in the same way as that in the previous experiment of Chen et al. by moving the fiber tip  $A$  transversely outside of the coherence area of the near-field chaotic-thermal field, which has been described in detail in the previous section. In this experiment, most of the measurements were performed under the condition of  $|\bar{\rho}_A - \bar{\rho}_B| \geq 40l_c$ . There is no question that we will lose any first-order temporal interference. In the view of classical optics, the measurement of polarization should be trivial too. The independent  $\hat{x}$  and  $\hat{y}$  polarization will pass  $A_1$  and  $A_2$  randomly according to Malus' law. The total intensity measured by  $D_1$  and  $D_2$ , respectively, should be  $\sin^2\theta_j + \cos^2\theta_j = 1$ ,  $j = 1, 2$  in any chosen orientation of the polarizer. Again, the question is in the second-order correlation measurement. Under the condition of  $\Gamma^{(2)}(\mathbf{r}_A, t_A; \mathbf{r}_B, t_B) = \text{constant}$ , there should be no observable HBT-type correlation of intensity fluctuations, i.e.,  $\langle \Delta I_A \Delta I_B \rangle = 0$ . What can

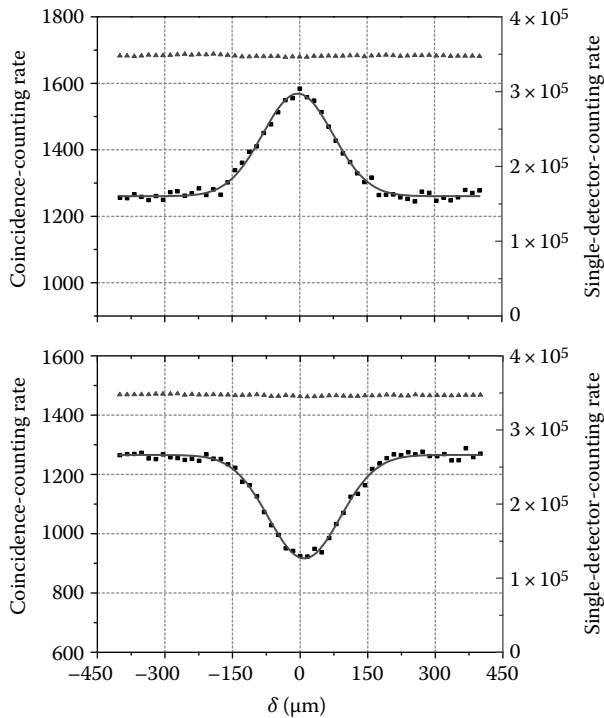
**FIGURE 13.12**

Schematic experimental setup of Chen et al. in which two surprises were observed from first-order and second-order incoherent orthogonal polarized chaotic-thermal light sources: (1) anti-correlation “dip” and correlation “peak”; (2) Bell-type polarization correlation. The experimental condition of first-order and second-order incoherence between radiations  $A$  and  $B$  is achieved by moving fiber tip  $A$  transversely outside the transverse coherence area. In this experiment, most of the measurements were performed at  $|\bar{\rho}_A - \bar{\rho}_B| \geq 40l_c$ .

we expect from the joint photodetection of  $D_1$  and  $D_2$ ? Can we expect to observe either temporal correlation or polarization correlation?

The measurement of Chen et al., however, produces two surprises in one experimental setup.

1. “Unexpected” anti-correlation “dip” and correlation “peak” were observed in the joint photodetection-counting rate of  $D_1$  and  $D_2$  as a function of the optical delay  $\delta$ , which is defined in Figure 13.12, when the orientation of  $A_1$  and  $A_2$  were chosen to be  $\theta_1 = \theta_2 = 45^\circ$ , and  $\theta_1 = 45^\circ$  with  $\theta_2 = 135^\circ$ , respectively. Figure 13.13 reports a typical anti-correlation “dip” and a typical correlation “peak” measured by Chen et al. Similar to the “anti-correlation” experiment of the previous section, if we subtract the contributions of  $G_{AA}^{(2)}$  and  $G_{BB}^{(2)}$  from the total contribution of  $G_{AA}^{(2)} + G_{BB}^{(2)} + G_{AB}^{(2)} + G_{BA}^{(2)}$ , which are experimentally measurable, the net contribution from  $G_{AB}^{(2)} + G_{BA}^{(2)}$  gives a  $\sim 100\%$  “dip” as a function of the optical delay  $\delta$ . Note, in the above statement, that we have employed the same notations  $G_{AA}^{(2)}$ ,  $G_{BB}^{(2)}$ ,  $G_{AB}^{(2)}$ , and  $G_{BA}^{(2)}$  defined in Sections 13.1 and 13.2.
2. Bell-type polarization correlation was observed as a function of the relative angle  $(\theta_1 - \theta_2)$  of the two polarization analyzers under the

**FIGURE 13.13**

Typical observed anti-correlation and correlation as the functions of the optical delay  $\delta$ , which is realized by scanning the fiber tip  $A$  along its longitudinal axis. The anti-correlation “dip” is observed when  $P_1$  and  $P_2$  were oriented at  $\theta_1 = \theta_2 = 45^\circ$ . The correlation “peak” is obtained when  $P_1$  and  $P_2$  were oriented at  $\theta_1 = 45^\circ$  with  $\theta_2 = 135^\circ$ .

condition of  $\delta = 0$ ,

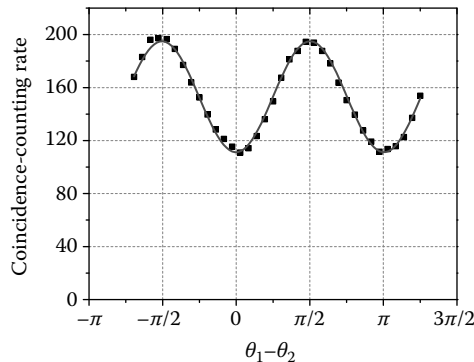
$$R_c(\theta_1, \theta_2) = R_0 [1 + V \sin^2(\theta_1 - \theta_2)], \quad (13.31)$$

where

$V$  is the contrast of the sinusoidal modulation

$R_c(\theta_1, \theta_2)$  is the coincidence-counting rate of  $D_1$  and  $D_2$ , which is obtained by manipulating the relative orientation of  $A_1$  and  $A_2$

Figure 13.14 is a typical observed polarization correlation reported by Chen et al. Furthermore, if we subtract the contributions of  $G_{AA}^{(2)}$  and  $G_{BB}^{(2)}$ , which are experimentally measurable, from the total contribution of  $G_{AA}^{(2)} + G_{BB}^{(2)} + G_{AB}^{(2)} + G_{BA}^{(2)}$ , the net contribution of  $G_{AB}^{(2)} + G_{BA}^{(2)}$  gives a Bell-type polarization correlation function of  $(\theta_1 - \theta_2)$  with  $\sim 100\%$  contrast.

**FIGURE 13.14**

Typical observed polarization correlation as a function of  $\theta_1 - \theta_2$ . In this measurement,  $\theta_2$  was fixed at  $45^\circ$  relative to  $\hat{x}$  and  $\hat{y}$ ,  $\theta_1$  was rotated at each chosen angle  $\theta_1$ . Subtracting  $G_{AA}^{(2)}$  and  $G_{BB}^{(2)}$  from the total contributions of  $G_{AA}^{(2)} + G_{BB}^{(2)} + G_{AB}^{(2)} + G_{BA}^{(2)}$ , the contrast of the sinusoidal Bell-type correlation becomes  $\sim 100\%$ .

The schematic setup of Chen et al. is shown in Figure 13.12. Some of the experimental details are described as follows:

1. The source: The incoherent chaotic-thermal source is the same as that in the anti-correlation experiment of Chen et al.
2. The polarization state: A set of polarization axis of  $\hat{x}$  and  $\hat{y}$  is defined by two Glen-Thompson polarizers, which are coupled with fiber *A* and fiber *B*, respectively. The  $\hat{x}$  polarized radiation *A* and the  $\hat{y}$  polarized radiation *B* are injected onto a 50/50 beamsplitter from its opposite input ports in a near-normal incidence configuration.\* The beamsplitter is measured with 50% reflection and 50% transmission for both  $\hat{x}$  and  $\hat{y}$  polarization.
3. The polarization analyzers: Two Glen-Thompson polarizers are coupled into the two output ports of the 50/50 beamsplitter, each followed by a photon-counting detector,  $D_1$  and  $D_2$ , for the

---

\* To achieve 50%-50% for both  $\hat{x}$  and  $\hat{y}$  polarization, near-normal incidence configuration is a better choice. This configuration is the same as that of the historical experiment of Alley and Shih, which observed Bell-type polarization correlation from an orthogonal polarized photon pair of SPDC. The first few historical “dip” experiments adopted this near-normal incidence configuration from the two-photon interferometer of Alley and Shih. In fact, it is unnecessary to choose near-normal incidence beamsplitter for an interferometer that uses only one polarization for “dip” measurement. For instance, Chen et al., using a simple 50%-50% optical fiber beamsplitter, successfully observed anti-correlation “dip” from incoherent chaotic-thermal light of one polarization, see Section 13.2.

polarization correlation measurement. The polarization analyzer can be set at any angle  $\theta$  relative to  $\hat{x}$ . The  $\hat{x}$  direction is defined as  $0^\circ$  in the above analysis.

Quantum theory gives a reasonable interpretation to the observation: the observation is a two-photon interference phenomenon, the result of a superposition between indistinguishable two-photon amplitudes. Figure 13.15 describes the four alternative ways of triggering a joint detection event of  $D_1$  and  $D_2$ . Parts (a) and (b) of Figure 13.15 represent the Bell-type correlation of  $G_{AB}^{(2)} + G_{BA}^{(2)}$ : a joint photodetection is produced by two photons, one coming from  $A$  and the other coming from  $B$ . There exists two alternative ways for the  $A$  photon and the  $B$  photon to produce a joint photodetection event: (a) The  $\hat{X}$ -polarized photon  $A$  is delayed with  $\delta$  and then is transmitted onto  $D_1$ , while the  $\hat{Y}$ -polarized photon  $B$  is transmitted onto  $D_2$ . (b) The  $\hat{X}$ -polarized photon  $A$  is delayed by  $\delta$  and then reflected onto  $D_2$ , while the

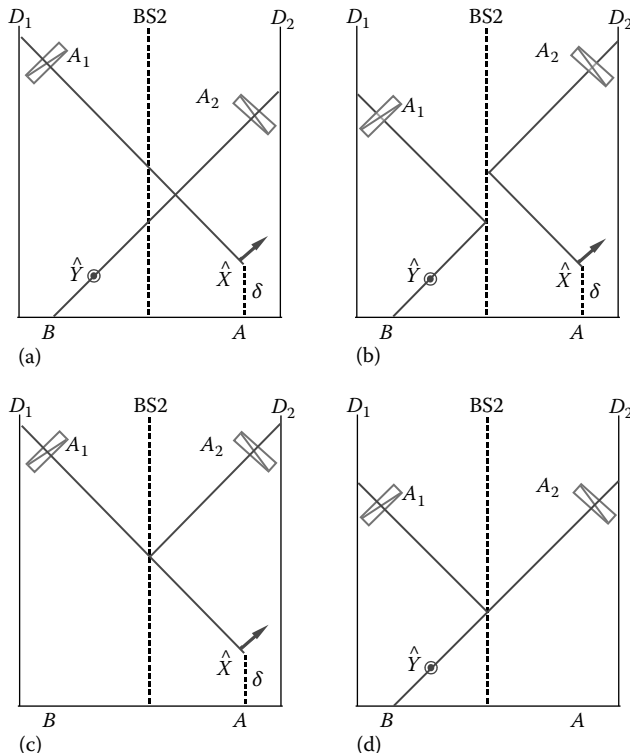


**FIGURE 13.15**

Feynman diagram of the experiment.

$\hat{Y}$ -polarized photon  $B$  is reflected onto  $D_1$ . These two amplitudes are usually called transmitted-transmitted (T-T) amplitude and reflected-reflected (R-R) amplitude. If the optical delay  $\delta$  is within the coherence time, the two alternative ways are indistinguishable. The other two alternatives are indicated by parts (c) and (d) of Figure 13.15, respectively, representing the measurements of  $G_{AA}^{(2)}$  and  $G_{BB}^{(2)}$ . (c) The two photons both come from  $A$ : one is transmitted and the other is reflected at the beamsplitter, resulting in a joint photodetection event of  $D_1$  and  $D_2$ . (d) The two photons both come from  $B$ : one is reflected and the other is transmitted at the beamsplitter, resulting in a joint photodetection event of  $D_1$  and  $D_2$ . It is not difficult to see that the joint photodetection-counting rates are merely constants in these two cases. Therefore in the following calculation we only consider the situation of (a) and (b).

The following calculation is partially adapted from the historical treatment for the Bell-type polarization correlation measurement and is partially adapted from our earlier analysis for the two-photon anti-correlation of thermal light. Taking the result of previous sections, the state of the subfields that is created by the  $m$ th and the  $n$ th atomic transition, resulting in the nontrivial correlation  $G_{AB}^{(2)} + G_{BA}^{(2)}$  is

$$\begin{aligned}
 & |\Psi_{m,n}(t_1, t_2)\rangle \\
 &= \int d\omega f(\omega) e^{-i\omega\tau_{A_{m1}}^T} \hat{x} \hat{a}_m^\dagger(\omega) |0\rangle \int d\omega' f(\omega') e^{-i\omega'\tau_{B_{n2}}^T} \hat{y} \hat{b}_n^\dagger(\omega') |0\rangle \\
 &\quad - \int d\omega' f(\omega') e^{-i\omega'\tau_{B_1}^R} \hat{y} \hat{b}_n^\dagger(\omega') |0\rangle \int d\omega f(\omega) e^{-i\omega\tau_{A_2}^R} \hat{x} \hat{a}_m^\dagger(\omega) |0\rangle \\
 &= |\hat{x} \Psi_{A_m}(t_1)\rangle |\hat{y} \Psi_{B_n}(t_2)\rangle - |\hat{y} \Psi_{B_n}(t_1)\rangle |\hat{x} \Psi_{A_m}(t_2)\rangle \tag{13.32}
 \end{aligned}$$

where we have written the state in Schrödinger representation  $\tau_{A_{m1}}^T = (t_1 - t_{0A_m}) - r_{A1}/c$ ,  $\tau_{B_{n1}}^R = (t_1 - t_{0B_n}) - r_{B1}/c$ ,  $\tau_{A_{m2}}^R = (t_2 - t_{0A_m}) - r_{A2}/c$ , and  $\tau_{B_{n2}}^R = (t_2 - t_{0B_n}) - r_{B2}/c$ ,  $t_{0A_m}$  and  $t_{0B_n}$  label the initial time of the  $m$ th and  $n$ th atomic transitions. The final state represents a coherent superposition of two-photon states, corresponding to two different yet indistinguishable probabilities of jointly observing the  $\hat{x}$ -polarized photon  $A_m$  and the  $\hat{y}$ -polarized photon  $B_n$  at space-time coordinates  $(\mathbf{r}_1, t_1)$  and  $(\mathbf{r}_2, t_2)$ : (1) the  $\hat{x}$ -polarized photon  $A_m$  is observed at  $(\mathbf{r}_1, t_1)$  and the  $\hat{y}$ -polarized photon  $B_n$  is observed at  $(\mathbf{r}_2, t_2)$ ; (2) the  $\hat{y}$ -polarized photon  $B_n$  is observed at  $(\mathbf{r}_1, t_1)$  and the  $\hat{x}$ -polarized photon  $A_m$  is observed at  $(\mathbf{r}_2, t_2)$ . The two-photon states are superposed with a relative phase delay of  $\pi$ . In terms of the concept of effective two-photon wavefunction, in the following we calculate  $G_{AB}^{(2)}$  as a function of the optical delay  $\delta$  as well as the angles  $\theta_1$  and  $\theta_2$  of the two

polarization analyzers:

$$G_{AB}^{(2)}(\theta_1, \theta_2; \delta) \propto \sum_{m < n} \left| (\hat{\theta}_1 \cdot \hat{y})(\hat{\theta}_2 \cdot \hat{x}) \mathcal{A}_{mn} \left( \tau_{A_{m1}}^T, \tau_{B_{n2}}^T \right) - (\hat{\theta}_1 \cdot \hat{x})(\hat{\theta}_2 \cdot \hat{y}) \mathcal{A}_{nm} \left( \tau_{B_{n1}}^R, \tau_{A_{m2}}^R \right) \right|^2, \quad (13.33)$$

where  $\mathcal{A}_{mn} \left( \tau_{A_{m1}}^T, \tau_{B_{n2}}^T \right)$  and  $\mathcal{A}_{nm} \left( \tau_{B_{n1}}^R, \tau_{A_{m2}}^R \right)$  have been defined in Sections 13.1 and 13.2.

According to Equation 13.33, in a two-photon interferometer with orthogonal polarized incoherent chaotic-thermal light, we will be able to observe two types of two-photon interference effects:

(I) Anti-correlation “dip” and correlation “peak.”

In the measurement of anti-correlation “dip,” we choose  $\theta_1 = 45^\circ$  and  $\theta_2 = 45^\circ$ ; Equation 13.33 can then be written as

$$G_{AB}^{(2)}(\delta) \propto \sum_{m < n} \left| \mathcal{A}_{mn} \left( \tau_{A_{m1}}^T, \tau_{B_{n2}}^T \right) - \mathcal{A}_{nm} \left( \tau_{B_{n1}}^R, \tau_{A_{m2}}^R \right) \right|^2, \quad (13.34)$$

The anti-correlation “dip” as a function of the optical delay  $\delta$  is thus expected in the coincidence counting rate  $R_{AB}$ . The calculation is the same as that in Section 13.2.

In the measurement of correlation “peak,” we choose  $\theta_1 = 45^\circ$  and  $\theta_2 = -45^\circ$ ; Equation 13.33 can then be written as

$$G_{AB}^{(2)}(\delta) \propto \sum_{m < n} \left| \mathcal{A}_{mn} \left( \tau_{A_{m1}}^T, \tau_{B_{n2}}^T \right) + \mathcal{A}_{nm} \left( \tau_{B_{n1}}^R, \tau_{A_{m2}}^R \right) \right|^2, \quad (13.35)$$

which is the same as Equation 13.34, except with a “+” sign. It is straightforward to calculate from Equation 13.35 to obtain a correlation “peak” in the coincidence-counting rate  $R_{AB}$ . The calculation is similar to that of the anti-correlation “dip.”

The observed anti-correlation “dip” and correlation “peak” of Chen et al. have been shown in Figure 13.13.

(II) Polarization correlation.

In this measurement, we make  $\delta = 0$  to achieve complete overlapping between  $\mathcal{A}_{mn} \left( \tau_{A_{m1}}^T, \tau_{B_{n2}}^T \right)$  and  $\mathcal{A}_{nm} \left( \tau_{B_{n1}}^R, \tau_{A_{m2}}^R \right)$ ; Equation 13.33 can then be

written as

$$\begin{aligned} G_{AB}^{(2)}(\theta_1, \theta_2) &\propto |(\hat{\theta}_1 \cdot \hat{y})(\hat{\theta}_2 \cdot \hat{x}) - (\hat{\theta}_1 \cdot \hat{x})(\hat{\theta}_2 \cdot \hat{y})|^2 \\ &\propto \sin^2(\theta_1 - \theta_2), \end{aligned} \quad (13.36)$$

representing the measurement of the Bell state:

$$|\Psi^{(-)}\rangle = \frac{1}{\sqrt{2}}[|X_1\rangle|Y_2\rangle - |Y_1\rangle|X_2\rangle].$$

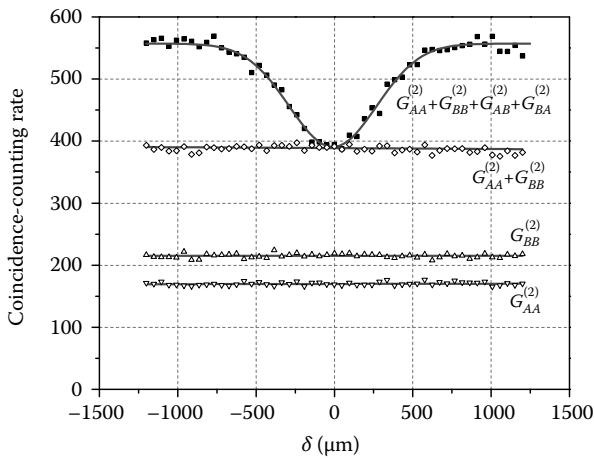
Considering the trivial contributions from the other two terms  $G_{AA}^{(2)}$  and  $G_{BB}^{(2)}$ , the contrast of the Bell-type correlation is reduced from 100% to 50%,

$$G_{AB}^{(2)}(\theta_1, \theta_2) \propto [1 + \sin^2(\theta_1 - \theta_2)]. \quad (13.37)$$

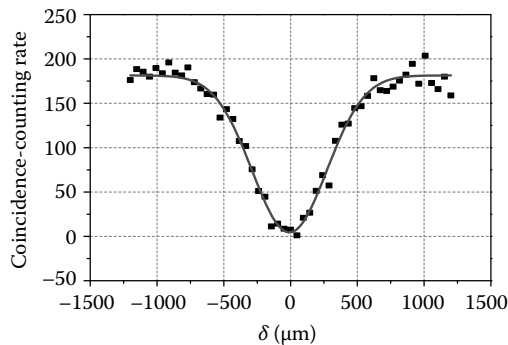
Since the contributions of  $G_{AA}^{(2)}$  and  $G_{BB}^{(2)}$  can be measured experimentally by blocking the other source, i.e., blocking source-A to measure  $G_{BB}^{(2)}$  or blocking source-B to measure  $G_{AA}^{(2)}$ , in principle, the contribution of  $G_{AB}^{(2)} + G_{BA}^{(2)}$  can be isolated from  $G_{AA}^{(2)}$  and  $G_{BB}^{(2)}$ . It is interesting to find that after subtracting the contributions of  $R_{AA}$  and  $R_{BB}$  from the total joint photodetection-counting rate  $R_c$ , the visibilities of the “dip” and the Bell-type polarization correlation resume to  $\sim 100\%$  in the experiment of Chen et al. (see Figures 13.16 through 13.18).

In summary, we may say that two wavepackets created from independent chaotic-thermal sub-sources can simulate the behavior of an entangled pair of photons by means of two-photon constructive and destructive interferences and by means of Bell-type polarization correlation. In fact, it is not too difficult to construct the complete set of Bell states by modifying the experimental setup of Chen et al. slightly. Of course, the randomly distributed chaotic-thermal light can never simulate the behavior of entangled photon pairs without the achievement of a few important experimental conditions, which may stimulate our basic understanding on the physics behind entangled EPR states.

In the experiment of Chen et al., a pair of identical wavepackets at single-photon level is prepared simultaneously with  $t_{0A_m} = t_{0B_n}$ . From pair to pair, the temporal and spatial distribution of the field may still be random, resulting in two mixed states for the subsystems of A and B. In each  $m$ - $n$ th pair, the  $\hat{x}$ -polarized photon A and the  $\hat{y}$ -polarized photon B, prepared together as a pair, interfere with the pair itself through the superposition of two different yet indistinguishable two-photon amplitudes, corresponding to two alternative ways for the pair to produce a joint photodetection event of  $D_1$  and

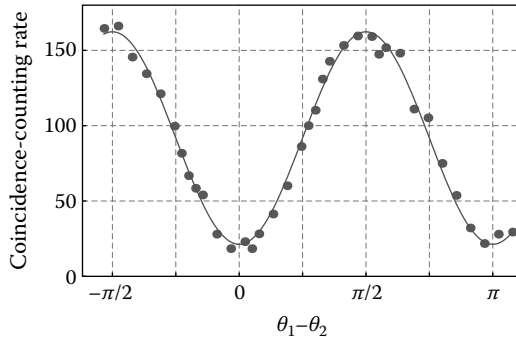
**FIGURE 13.16**

The observed  $G_{AA}^{(2)} + G_{BB}^{(2)} + G_{AB}^{(2)} + G_{BA}^{(2)}$ , and  $G_{AA}^{(2)}, G_{BB}^{(2)}$ ,  $G_{AA}^{(2)}$  and  $G_{BB}^{(2)}$  are measured by blocking the other source. Subtracting the contributions of  $G_{AA}^{(2)}$  and  $G_{BB}^{(2)}$ , the contrast of the observed anti-correlation function becomes  $\sim 100\%$ . The anti-correction “dip” is observed when  $A_1$  and  $A_2$  were oriented at  $\theta_1 = \theta_2 = 45^\circ$ .

**FIGURE 13.17**

In this measurement,  $G_{AA}^{(2)}$  and  $G_{BB}^{(2)}$  are subtracted from the direct measurement of the total contributions of  $G_{AA}^{(2)} + G_{BB}^{(2)} + G_{AB}^{(2)} + G_{BA}^{(2)}$  during the data collection. The contrast of the anti-correlation is close to 100%.

$D_2$  associated with the polarization analyzers  $A_1$  and  $A_2$ . The temporal correlation and the polarization correlation measured in each of the  $m$ - $n$ th pair will be added statistically in a homogeneous manner under the experimental condition of  $t_{0A_m} = t_{0B_n}$ . It is this condition that made it possible to observe the temporal correlation functions of “dip” and “peak,” and the Bell-type correlation of polarization.

**FIGURE 13.18**

Subtracting the contributions of  $G_{AA}^{(2)}$  and  $G_{BB}^{(2)}$ , which are measured by blocking the other source, the visibility of the observed polarization correlation as a function of  $\theta_1 - \theta_2$  becomes  $> 71\%$ , indicating the behavior of a two-photon Bell state  $\Psi^{(-)}$ . (The border between “quantum” and “classical”, in some theoretical concerns, is considered to be 71%). In this measurement,  $\theta_2$  was fixed at  $45^\circ$  relative to  $\hat{x}$  and  $\hat{y}$ , and  $\theta_1$  was rotated at each chosen angle  $\theta_1$ .

It is necessary to emphasize again that the correlation of  $G_{AB}^{(2)} + G_{BA}^{(2)}$  cannot be separated from the contributions of  $G_{AA}^{(2)}$  and  $G_{BB}^{(2)}$  in a direct coincidence measurement of  $D_1$  and  $D_2$ . Fortunately,  $G_{AA}^{(2)}$  and  $G_{BB}^{(2)}$  can be identified and measured independently by blocking the other source, i.e., blocking source-A to measure  $G_{BB}^{(2)}$ , or blocking source-B to measure  $G_{AA}^{(2)}$ . Due to the incoherent nature of the subfields  $A$  and  $B$ , it is possible, in principle, to subtract these two trivial contributions from the total joint photodetection-counting rate and isolate the measured correlation of  $G_{AB}^{(2)} + G_{BA}^{(2)}$ . The two-photon correlation explored from the measurement of  $G_{AB}^{(2)} + G_{BA}^{(2)}$  is identical with that of an entangled EPR–Bohm–Bell state (see Figure 13.18).

Now, it is time to ask ourselves: How could a chaotic-thermal state produce the same correlation of an entangled state? From the analysis of the anti-correlation experiment and the Bell-type polarization measurement, we may find the following points helpful for answering this question:

1. There is no difference in terms of the interference of a measured photon pair, or about “a photon pair that interferes with the pair itself.” The superposition of two-photon amplitudes, corresponding to different yet indistinguishable alternative ways for a pair of photons to produce a joint photodetection event, in the chaotic-thermal state and in the entangled state have the same mathematical form and imply the same physics (Figure 13.18).
2. The measurement of a chaotic-thermal state and the measurement of an entangled state are different in terms of the inhomogeneous and

homogeneous ensemble average. Entangled states are pure states. All measured photon pairs are in the same two-photon state and the joint measurement statistics is based on a homogeneous ensemble. In the case of chaotic-thermal radiation, the states of measured photon pairs may be different from pair to pair and the joint measurement statistics is based on an inhomogeneous ensemble. If we can make the ensemble average of a chaotic-thermal state close enough to that of an entangled state in certain experimental situations, a chaotic-thermal state may produce the same nontrivial correlation as that of an entangled state. Examining the second-order correlation for the above two experiments,

$$G^{(2)}(\mathbf{r}_1, t_1; \mathbf{r}_2, t_2) = \langle \langle \hat{E}^{(-)}(\mathbf{r}_1, t_1) \hat{E}^{(-)}(\mathbf{r}_2, t_2) \hat{E}^{(+)}(\mathbf{r}_2, t_2) \hat{E}^{(+)}(\mathbf{r}_1, t_1) \rangle \rangle_{\text{QM}}|_{\text{Ensemble}},$$

we found that the ensemble average on chaotic-thermal state gives the same anti-correlation function or Bell-type polarization correlation function as that of entangled state, if the following two experimental conditions are achievable: (a) the photon pair can be created simultaneously at  $t_{0A} = t_{0B}$ ; (b) the contributions of  $G_{AA}^{(2)}$  and  $G_{BB}^{(2)}$  are measurable independently, and thus are distinguishable from  $G_{AB}^{(2)} + G_{BA}^{(2)}$ .

In fact, the single-photon state of a subsystem in the two-photon EPR state is very close to that of a chaotic-thermal radiation, although the state of the measured photon pairs are very different in the two cases. In the above two experiments, Chen et al. have found a way to simulate two important properties of entangled photon pairs: (a) the pair is always created simultaneously; (b) the pair always appears at  $A$  and at  $B$ , respectively, but never both at  $A$  or both at  $B$ . For an entangled two-photon state, we can easily achieve  $G_{AA}^{(2)} = 0$ ,  $G_{BB}^{(2)} = 0$ . In the case of chaotic-thermal light, although we have not been able to make  $G_{AA}^{(2)} = 0$ ,  $G_{BB}^{(2)} = 0$ , these two contributions are independently measurable, and can be legally subtracted from the total contributions of  $G_{AA}^{(2)} + G_{BB}^{(2)} + G_{AB}^{(2)} + G_{BA}^{(2)}$ .

This simulation might be useful for quantum information processing in terms of the superposition among a large number of quantum amplitudes of a large number of photons. Following the same principle shown above, we may be able to simulate the behavior of a large number of entangled photons by utilizing the mechanism of multi-photon superposition in the measurement of the  $N$ th-order correlation  $G^{(N)}(\mathbf{r}_1, t_1; \dots; \mathbf{r}_N, t_N)$  of incoherent thermal fields.

---

## Summary

In this chapter, we generalized the concept of two-photon interference to chaotic-thermal light. The superposition of two-photon amplitudes is not restricted with entangled biphoton states. Two-photon interference may occur in the joint photodetection of chaotic-thermal light, if there exists two or more than two different yet indistinguishable alternative ways for a measured pair of photons to produce a joint photodetection event between two individual photodetectors, although the jointly detected photon pair are just two randomly distributed photons that fall into the coincidence time window of the joint photodetection by chance.

In this chapter, we analyzed three typical two-photon interference experiments of chaotic-thermal light, including a two-photon Young's double-slit experiment, a two-photon anti-correlation measurement, and a two-photon interference and polarization correlation experiment with first-order and second-order incoherent orthogonal polarized input chaotic-thermal light. These experiments provided us a solid background on the theory of two-photon interferometry of chaotic-thermal light.

It is interesting to see the concept of two-photon interference applicable to "classical" thermal radiation. Chaotic-thermal light is traditionally considered as classical radiation. The second-order and higher-order correlations of thermal radiation have been widely accepted as the statistical correlation of intensity fluctuations. It is clear that the classical statistical correlation theory of intensity fluctuations cannot give an adequate explanation to the experiments of the two-photon anti-correlation and two-photon polarization correlation and anti-correlation of Chen et al. The quantum theory of light, however, provided us a reasonable explanation. In the view of quantum optics, the nontrivial second-order and higher-order correlation or coherence of thermal light is the result of two-photon or N-photon interference, i.e., a pair of photons that interfere with the pair itself or a group of photons that interfere with the group itself, through the joint photodetection of two or more independent photodetectors.

---

## Suggested Reading

- Alley, C.O. and Y.H. Shih, *Foundations of Quantum Mechanics in the Light of New Technology*, ed. M. Namiki, Physical Society of Japan, Tokyo, Japan, p. 47, 1986.
- Chen, H., S. Karmakar, Z. Xie, and Y.H. Shih, Two-photon anti-correlation with incoherent chaotic light, to be published.
- Chen, H., T. Peng, S. Karmaker, and Y.H. Shih, Two-photon interference with incoherent orthogonal polarized chaotic light, to be published.
- Scarelli, G., A. Valencia, and Y.H. Shih, *Europhys. Lett.* 68, 618 (2004).
- Shih, Y.H. and C.O. Alley, *Phys. Rev. Lett.* 61, 2921 (1988).

# 14

---

## *Bell's Theorem and Bell's Inequality Measurement*

---

In the early 1950s, Bohm simplified the 1935 EPR state to discrete spin state by introducing a singlet state of two spin 1/2 particles:

$$|\Psi\rangle = \frac{1}{\sqrt{2}} \left[ |\uparrow\rangle_1 |\downarrow\rangle_2 - |\downarrow\rangle_1 |\uparrow\rangle_2 \right] \quad (14.1)$$

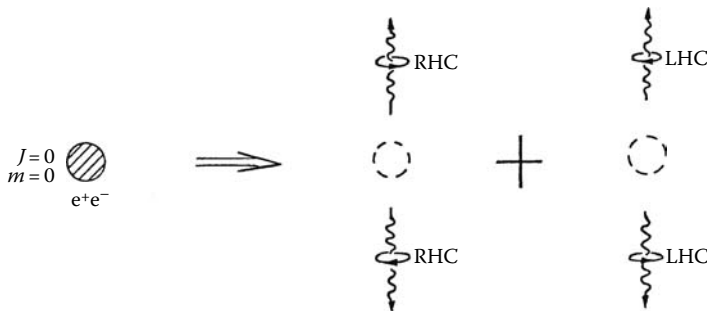
where the kets  $|\uparrow\rangle$  and  $|\downarrow\rangle$  represent states of spin “up” and spin “down,” respectively, along an *arbitrary* direction. For the EPR–Bohm state, the spin of neither particle is determined; however, if one particle is measured to be spin up along a certain direction, the other one must be spin down along that direction, despite the distance between the two spin 1/2 particles. We have shown in Chapter 9, Equation 14.1 is independent of the choice of the spin directions. The introduction of the EPR–Bohm state simplified the physical picture and the discussion about quantum entanglement dramatically.\*

A more practical example of the EPR–Bohm state concerns the polarization states of photon pairs, such as the spin-zero state of a high-energy photon pair disintegrated from the annihilation of positronium. Suppose initially we have a positron and an electron in the spin-zero state with antiparallel spins. The positronium cannot exist very long: it disintegrates into two  $\gamma$ -ray photons within  $\sim 10^{-10}$  s of its lifetime. The spin zero state is symmetric under all rotations. Therefore, the photon pair may be disintegrated into any direction in space with equal probability. The conservation of linear momentum, however, guarantees that if one of the photon is observed in a certain direction, its twin must be found in the opposite direction (with finite uncertainty  $\Delta(\mathbf{p}_1 + \mathbf{p}_1) \neq 0$ ). The conservation of angular momentum will decide the polarization state of the photon pair. As shown in Figure 14.1, in order to keep spin-zero, if photon 1 is right-hand circular polarized (RHC), photon 2 must also be RHC polarized. The same argument shows that if photon 1 is left-hand circular (LHC) polarized, then photon 2 has to be LHC polarized too. Therefore, the positronium may decay into two RHC photons or two LHC photons with equal probability.

What is the relationship between these two alternatives? If it is just two different ways of disintegration with equal probability, the two-photon system may be described by a density matrix

---

\* But, one should keep in mind that it is not a necessary to have two “terms” in an entangled state. In fact, the first entangled state suggested by EPR in 1935 has infinite number of “terms.”

**FIGURE 14.1**

Annihilation of positronium. Due to the conservation of angular momentum, if photon 1 is right-hand circular (RHC) polarized, photon 2 must also be RHC polarized. If photon 1 is left-hand circular (LHC) polarized, then photon 2 has to be LHC polarized.

$$\hat{\rho} = \frac{1}{2} [ |R_1 R_2\rangle\langle R_1 R_2| + |L_1 L_2\rangle\langle L_1 L_2| ], \quad (14.2)$$

where  $|R_j\rangle$  and  $|L_j\rangle$  indicate the RHC and LHC states for photon  $j$ , respectively. The density matrix specifies only the statistics: within  $N$   $\gamma$ -ray photon pairs, 50% of them have RHC–RHC polarization and another 50% have LHC–LHC polarization. The physical process of positronium annihilation, however, is not that simple. The law of parity conservation must be satisfied in the disintegration: the spin-zero ground state of positronium holds an odd parity. Thus, the state of the photon pair must keep its parity odd:

$$|\Psi\rangle = \frac{1}{\sqrt{2}} [ |R_1\rangle|R_2\rangle - |L_1\rangle|L_2\rangle ]. \quad (14.3)$$

It is the conservation of parity made the two-photon state very special. The two-photon state is a nonfactorizable pure state of a special superposition between the RHC and LHC states specified with a relative phase of  $\pi$ . Mathematically, “nonfactorizable” means that the state cannot be written as a product state of photon 1 and photon 2. Physically, it means that photon 1 and photon 2 are not independent anymore. The two  $\gamma$ -ray photons are in an entangled polarization state, or spin state.

The physics behind Equation 14.3 is very interesting. To describe the interesting physics of the state, however, is not an easy job. One may easily find the following popular statement about this state: the polarization state of photon 1 and photon 2 are both undefined: each has 50%–50% chance to be RHC or LHC; however, the polarization state of photon 1 can be predicted with certainty through the measurement of photon 2: whichever circular polarization state photon 2 is observed, photon 1 must be in the same state, despite the distance between them. In other words, one would always observe two RHC or two LHC polarized photons in a joint-detection event:

$$\begin{aligned} |\langle R_1 R_2 | \Psi \rangle|^2 &= |\langle L_1 L_2 | \Psi \rangle|^2 = 50\% \\ |\langle R_1 L_2 | \Psi \rangle|^2 &= |\langle L_1 R_2 | \Psi \rangle|^2 = 0. \end{aligned} \quad (14.4)$$

The result of Equation 14.4 is interesting, but may not be surprising. In fact, a statistical ensemble of photons characterized by the density matrix of Equation 14.2 would give the same result. The above statement, which is based on the correlation of circular polarization, has not explored the real interesting physics behind the *pure state* of Equation 14.3.

Can we distinguish the pure state of Equation 14.3 from the statistical mixture of Equation 14.2 through a simple polarization correlation measurement? The answer is positive. Instead of measuring circular polarization, we measure linear polarization correlation. Figure 14.2 schematically illustrates an experimental setup which will serve the purpose. The two-photon state is prepared as that in Equation 14.3 and the measurement is for linear polarization correlation. Each linear polarization analyzer has two orthogonal output channels. Four photodetectors are placed at the four output ports of the two linear polarization analyzers for twofold joint detections. There

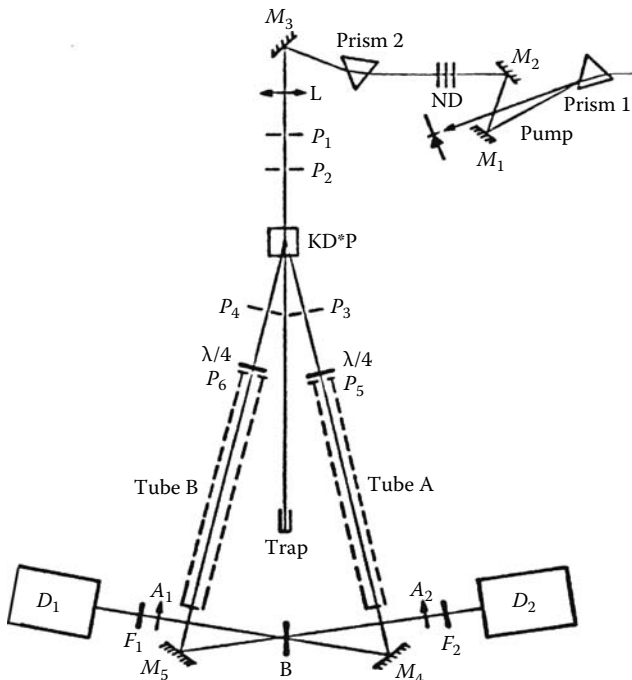


**FIGURE 14.2**

The historical two-photon polarization correlation measurement of Alley and Shih (1986). The state is prepared as that in Equation 14.3 and the measurement is for linear polarization correlation.

are four possible combinations:  $D_1$  with  $D_2$ ,  $D_1$  with  $D'_2$ ,  $D'_1$  with  $D_2$ , and  $D'_1$  with  $D'_2$ . To calculate the outcomes, it is convenient to use the conventional right-hand coordinate system, as shown in Figure 14.2. Suppose we choose the polarization analyzers along  $|X\rangle$  and  $|Y\rangle$ , the measurement on the two-photon pure state of Equation 14.3 yields

$$\begin{aligned} |\langle X_1 Y_2 | \Psi \rangle|^2 &= |\langle Y_1 X_2 | \Psi \rangle|^2 = 50\% \\ |\langle X_1 X_2 | \Psi \rangle|^2 &= |\langle Y_1 Y_2 | \Psi \rangle|^2 = 0, \end{aligned} \quad (14.5)$$

i.e., one would always observe two orthogonal polarized photons in a joint-detection event. The measurement on the statistical mixture of Equation 14.2, however, gives a completely random result:

$$\begin{aligned} \text{tr } \hat{\rho} |Y_2 X_1\rangle \langle X_1 Y_2| &= \text{tr } \hat{\rho} |X_2 Y_1\rangle \langle Y_1 X_2| = 25\% \\ \text{tr } \hat{\rho} |X_2 X_1\rangle \langle X_1 X_2| &= \text{tr } \hat{\rho} |Y_2 Y_1\rangle \langle Y_1 Y_2| = 25\%. \end{aligned} \quad (14.6)$$

Furthermore, we may rotate the linear polarization analyzers to any direction in the XY plane, such as  $\theta_1$  ( $\bar{\theta}_1 = \pi/2 - \theta$  in its orthogonal channel) and  $\theta_2$  ( $\bar{\theta}_2 = \pi/2 - \theta$  in its orthogonal channel) for the measurement of polarization correlation, where  $\theta_j$  is the angle between the polarization analyzer and the X axis. The measurement on the two-photon pure state of Equation 14.3 yields

$$|\langle \theta_1 \theta_2 | \Psi \rangle|^2 = \frac{1}{2} \sin^2(\theta_1 + \theta_2) = \frac{1}{2} \sin^2 \varphi \quad (14.7)$$

where  $\varphi = \theta_1 + \theta_2$ . Equation 14.7 indicates that the pair must be always orthogonally polarized, independent of the choice of  $\theta_j$  for each individual polarization analyzer. Considering the other three possible joint detections, we have the following polarization correlation functions in terms of  $\varphi = \theta_1 + \theta_2$ :

$$\begin{aligned} |\langle \theta_1 \theta_2 | \Psi \rangle|^2 &= |\langle \bar{\theta}_1 \bar{\theta}_2 | \Psi \rangle|^2 = \frac{1}{2} \sin^2 \varphi \\ |\langle \theta_1 \bar{\theta}_2 | \Psi \rangle|^2 &= |\langle \bar{\theta}_1 \theta_2 | \Psi \rangle|^2 = \frac{1}{2} \cos^2 \varphi \end{aligned} \quad (14.8)$$

On the other hand, the measurement on the statistical mixture of Equation 14.2 gives, again, a completely random result:

$$\begin{aligned} \text{tr } \hat{\rho} |\theta_2 \theta_1\rangle \langle \theta_1 \theta_2| &= \text{tr } \hat{\rho} |\bar{\theta}_2 \bar{\theta}_1\rangle \langle \bar{\theta}_1 \bar{\theta}_2| = 25\% \\ \text{tr } \hat{\rho} |\bar{\theta}_2 \theta_1\rangle \langle \theta_1 \bar{\theta}_2| &= \text{tr } \hat{\rho} |\theta_2 \bar{\theta}_1\rangle \langle \bar{\theta}_1 \theta_2| = 25\%. \end{aligned} \quad (14.9)$$

Now we are ready to describe the interesting physics behind Equation 14.3 with a better statement: the entangled two-photon polarization state of Equation 14.3 has specified a peculiar two-photon system, in this system, the polarization of neither photon is defined during the course of its propagation; however, if one of the photon is measured to be in a defined polarization state, the polarization state of the other photon is determined with certainty, despite the distance between the pair and *despite the choice of the polarization vector base*.

This statement is similar to the statement we have used for the original EPR state: in an EPR two-particle system, neither *position* nor *momentum* for neither particle is defined during the course of its propagation; however, if one of the particle is measured to be in a defined *position* or *momentum*, the *position* and *momentum* of the other particle is determined with certainty, despite the distance between the two particles.

The independence of the choice for polarization vector base in Equation 14.3 is equivalent to the independence of the choice of position and momentum coordinate for the original EPR state.

Regardless of whether we measure it or not, does a free propagating particle have a defined spin in the Bohm state of Equation 14.1? Does a free propagating photon have a defined polarization, either circular or linear, in the state of Equation 14.3? On one hand, the spin of neither independent particle is specified in the Bohm state of Equation 14.1, and the polarization of neither independent photon is specified in the state of Equation 14.3, we may have to believe that the particles do not have any defined spin, and the photons do not have any defined polarization, during the course of their propagation. On the other hand, if the spin of one particle, or the polarization of one photon, uniquely determines the spin of the other distant particle, or the polarization of the other photon, it would be hard for anyone who believes no action-at-a-distance to imagine that the spin of the two particles, or the polarization of the two photons, are not predetermined with defined values before the measurement. The Bohm state thus puts us into a paradoxical situation. It seems reasonable for us to ask the same question that EPR had asked in 1935: "Can quantum-mechanical description of physical reality be considered complete?"

Is it possible to have a realistic theory that provides correct predictions of the behavior of a particle similar to quantum theory and, at the same time, respects the description of physical reality by EPR as "complete?" Bohm and his followers have attempted a "hidden variable theory" to formulate the physical reality into the wavefunction of a particle or a pair of particles. The theory seemed to be consistent with quantum mechanics and satisfied the requirements of EPR. The hidden variable theory was successfully applied to many different quantum phenomena until 1964, when Bell proved a theorem to show that an inequality, which is violated by certain quantum-mechanical statistical predictions, can be used to distinguish local hidden variable statistics from quantum superpositions. Since then, the

testing of Bell's inequalities became a standard instrument for the study of fundamental problems of quantum theory. The experimental testing of Bell's inequality started from the early 1970s. Most of the historical experiments concluded the violation of Bell's inequalities and thus disproved the local hidden variable theory.\*

### 14.1 Hidden Variable Theory and Quantum Calculation for the Measurement of Spin 1/2 Bohm State

Consider two spin 1/2 particles, in the Bohm state of Equation 14.1. The particles are well separated at distance. Two groups of observers decide to measure their spins by using Stern-Gerlach analyzers. Three sets of Stern-Gerlach apparatus whose z-directions are defined by unit vectors  $\hat{\mathbf{a}}$ ,  $\hat{\mathbf{b}}$ , and  $\hat{\mathbf{c}}$ , as shown in Figure 14.3. What is the probability to find the spin of particle-1 to be +1/2 in the direction  $\hat{\mathbf{a}}$  and the spin of particle-2 to be +1/2 in the direction of  $\hat{\mathbf{b}}$ ? The following is a simple classical hidden variable model

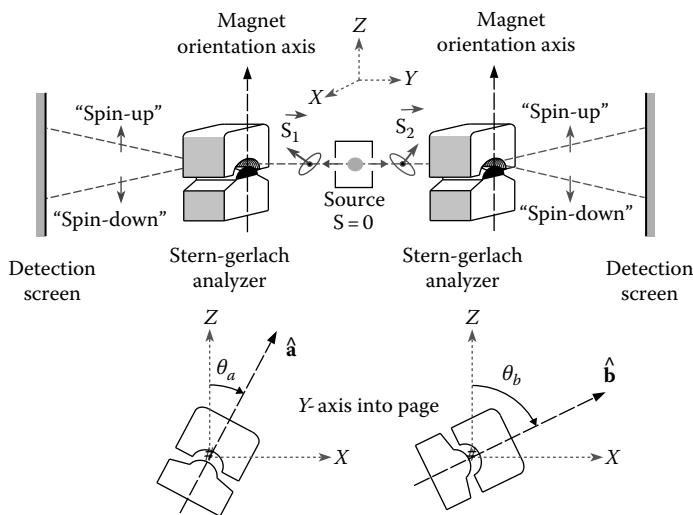


**FIGURE 14.3**

Bohm's version of the EPR *gedankenexperiment*.

\* Although Bell's theorem and Bell's inequality involve deep philosophical concerns in general, we should keep in mind that the testing of Bell's inequality in terms of the physical measurement on a physical system is essentially a physical problem. Any proposed statistical model of classical correlation, either local or nonlocal, must obey the basic physical laws of classical theory. One cannot assume a classical correlation that is never allowed in classical theory.

addressing this question. Before giving the details, we first introduce the following notation  $P_{ab}$  to specify the classical probability

$$P_{ab} = P(+_a d_b d_c | d_a +_b d_c). \quad (14.10)$$

In this notation, we chose six-elements to specify the observation. The left-side of the partition refers particle one (in channel 1) and the right-side to particle two (in channel 2). Each element represents whether a measurement of the component of the spin of the  $j$ th particle,  $j = 1, 2$ , gives + or - in the corresponding direction  $\hat{a}$ ,  $\hat{b}$ , or  $\hat{c}$ .  $d_a$ ,  $d_b$  and  $d_c$  indicate no determination in the direction  $\hat{a}$ ,  $\hat{b}$ , and  $\hat{c}$ , respectively. Note,  $P_{ab}$  is defined as to have + in direction  $\hat{a}$ , which is observed in channel 1 (left side), and to have + in direction  $\hat{b}$ , which is observed in channel 2 (right side).

In a classical hidden variable theory, if the spin component of particle-1 is measured with + in direction  $\hat{a}$ , then a measurement of the spin of particle-2 in direction  $\hat{a}$  must be - with certainty. The probability  $P_{ab}$  in which particle-1 is measured with + in the direction  $\hat{a}$  (in channel 1), and particle-2 is measured with - in the direction  $\hat{b}$  (in channel 2) is written as

$$P_{ab} = P(+ - d_c | - + d_c). \quad (14.11)$$

Similarly, we have

$$\begin{aligned} P_{bc} &= P(d_a + - | d_a - +) \\ P_{ac} &= P(+ d_b - | - d_b +). \end{aligned} \quad (14.12)$$

In a classical probability theory, the undetermined spin components of particle-1 and particle-2,  $d_a$ ,  $d_b$ , or  $d_c$ , must have specific values, either + or - in any direction. Consequently, we may write  $P_{ab}$  as a sum of probabilities for these two possibilities

$$\begin{aligned} P_{ab} &= P(+ - + | - + -) + P(+ - - | - + +) \\ &\equiv P(+ - +) + P(+ - -), \end{aligned} \quad (14.13)$$

where on the second line we have dropped the redundant information involving the second particle by writing  $P(+ - +)$  for  $P(+ - + | - + -)$ . Thus, we write Equations 14.11 and 14.12 as

$$\begin{aligned} P_{ab} &= P(+ - +) + P(+ - -), \\ P_{bc} &= P(+ + -) + P(- + -), \\ P_{ac} &= P(+ + -) + P(+ - -). \end{aligned} \quad (14.14)$$

It should be emphasized that the left-side quantities in Equation 14.14,  $P_{ab}$ , etc., are measurable probabilities, but we have no procedure for measuring the separate classical probabilities  $P(+ - +)$ ,  $P(+ - -)$ , etc. on the right side of Equation 14.14. Adding  $P_{ab}$  and  $P_{bc}$  and comparing with  $P_{ac}$ , it is easy to see that

$$P_{ab} + P_{bc} = P_{ac} + P(+ - +) + P(- + -). \quad (14.15)$$

Assuming the classical probabilities  $P(+ - +)$  and  $P(- + -)$  are positive, which is true in any classical probability theory, we then obtain the Bell–Wigner inequality

$$P_{ab} + P_{bc} \geq P_{ac}. \quad (14.16)$$

The seemingly obvious inequality of Equation 14.16 has been experimentally violated.

We next present a simple quantum-mechanical calculation for the same measurement. Let us rewrite the state vector of Equation 14.1 into the following form

$$|\psi\rangle = \frac{1}{\sqrt{2}} \left[ \begin{pmatrix} 1 \\ 0 \end{pmatrix}_1 \begin{pmatrix} 0 \\ 1 \end{pmatrix}_2 - \begin{pmatrix} 0 \\ 1 \end{pmatrix}_1 \begin{pmatrix} 1 \\ 0 \end{pmatrix}_2 \right]. \quad (14.17)$$

Recalling that for a spin 1/2 particle in a state  $|\psi\rangle$  the probability of observing spin up in a direction at angle  $\theta$  to the  $z$ -axis is

$$|\langle \theta | \Psi \rangle|^2 = \langle \Psi | \theta \rangle \langle \theta | \Psi \rangle = \langle \Psi | \hat{\pi}_\theta | \Psi \rangle, \quad (14.18)$$

where  $\hat{\pi}_\theta = |\theta\rangle \langle \theta|$  is the projection operator, and  $|\theta\rangle = e^{-(i/2)\sigma_y\theta} |\uparrow\rangle$ . The projection operator for spin up in the direction of a unit vector  $\hat{\mathbf{r}}$  at angle  $\theta$  to the  $z$ -axis is

$$\hat{\pi}_\theta = |\theta\rangle \langle \theta| = \frac{1}{2}(1 + \sigma_z \cos \theta + \sigma_x \sin \theta) \equiv \frac{1}{2}(\mathbf{I} + \vec{\sigma} \cdot \hat{\mathbf{r}}), \quad (14.19)$$

where

$\vec{\sigma} = (\sigma_x, \sigma_y, \sigma_z)$  are the Pauli matrices

$\mathbf{I}$  is the identity matrix.

We can also explicitly rewrite  $\hat{\pi}_\theta$  as a matrix,

$$\hat{\pi}_\theta = \frac{1}{2} \begin{pmatrix} 1 + \cos \theta & \sin \theta \\ \sin \theta & 1 - \cos \theta \end{pmatrix} \quad (14.20)$$

The physical observable  $P_{ab}$  is defined as the joint probability for particle-1 to be spin up along an SGA oriented in direction  $\hat{\mathbf{a}}$  and particle-2 to be spin up along another SGA oriented in direction  $\hat{\mathbf{b}}$

$$P_{ab} = \langle \Psi | \hat{\pi}_{1\hat{\mathbf{a}}} \hat{\pi}_{2\hat{\mathbf{b}}} | \Psi \rangle, \quad (14.21)$$

where each projector has two subscripts defining the particles (and channel) and the measurement direction in the  $x - z$  plane. Similarly,

$$\begin{aligned} P_{bc} &= \langle \Psi | \hat{\pi}_{1\hat{\mathbf{b}}} \hat{\pi}_{2\hat{\mathbf{c}}} | \Psi \rangle, \\ P_{ac} &= \langle \Psi | \hat{\pi}_{1\hat{\mathbf{a}}} \hat{\pi}_{2\hat{\mathbf{c}}} | \Psi \rangle. \end{aligned} \quad (14.22)$$

Evaluation of  $P_{ab}$ ,  $P_{bc}$ , and  $P_{ac}$  using the operator in Equation 14.20 and the state in Equation 14.17 gives

$$\begin{aligned} P_{ab} &= \frac{1}{4}[1 - \cos(\theta_a - \theta_b)] = \frac{1}{4}[1 - \hat{\mathbf{a}} \cdot \hat{\mathbf{b}}], \\ P_{bc} &= \frac{1}{4}[1 - \cos(\theta_b - \theta_c)] = \frac{1}{4}[1 - \hat{\mathbf{b}} \cdot \hat{\mathbf{c}}], \\ P_{ac} &= \frac{1}{4}[1 - \cos(\theta_a - \theta_c)] = \frac{1}{4}[1 - \hat{\mathbf{a}} \cdot \hat{\mathbf{c}}]. \end{aligned} \quad (14.23)$$

It is easy to find that the Bell–Wigner inequality in Equation 14.16 achieves its maximum violation when  $\theta_a = 0$ ,  $\theta_b = \pi/3$ , and  $\theta_c = 2\pi/3$ . The experimental observations have confirmed the violation.

## 14.2 Bell's Theorem and Bell's Inequality

In his 1964 paper, based on the EPR–Bohm state of Equation 14.1 and a hidden parameter  $\lambda$ , Bell derived an inequality to distinguish quantum mechanics from local realistic probability theory of hidden variable. In his pioneering work, Bell introduced a “more complete specification effected by means of parameter  $\lambda$ ” with probability distribution  $\rho(\lambda)$  for the classical statistical estimation of the expectation value of the joint measurement  $\langle \Psi | (\vec{\sigma}_1 \cdot \hat{\mathbf{a}})(\vec{\sigma}_2 \cdot \hat{\mathbf{b}}) | \Psi \rangle$  of particle-1 and particle-2 in directions  $\hat{\mathbf{a}}$  and  $\hat{\mathbf{b}}$ , simultaneously and respectively. The quantum-mechanical result of this measurement gives

$$E_{ab} = \langle \Psi | (\vec{\sigma}_1 \cdot \hat{\mathbf{a}})(\vec{\sigma}_2 \cdot \hat{\mathbf{b}}) | \Psi \rangle = -\hat{\mathbf{a}} \cdot \hat{\mathbf{b}}. \quad (14.24)$$

A special case of this result contains the determinism implicit in this idealized system. When the SGA analyzers are parallel, we have

$$E_{ab} = \langle \Psi | (\vec{\sigma}_1 \cdot \hat{\mathbf{a}}) (\vec{\sigma}_2 \cdot \hat{\mathbf{a}}) | \Psi \rangle = -1 \quad (14.25)$$

for all  $\lambda$  and all  $\hat{\mathbf{a}}$ . Thus, we can predict the result of B with certainty by obtaining the result of A. Since the quantum-mechanical state  $|\Psi\rangle$  does not determine the result of an individual measurement, this fact (via EPR's argument) suggests that there exists a more complete specification of the state by a single symbol  $\lambda$  it may have many dimensions, discrete and/or continuous parts, and different parts of it interacting with either apparatus, etc. Let  $\Lambda$  be the space of  $\lambda$  for an ensemble composed of a very large number of the particle systems. Bell represented the distribution function for the state  $\lambda$  on the space  $\Lambda$  by the symbol  $\rho(\lambda)$  and take  $\rho(\lambda)$  to be normalized

$$\int_{\Lambda} \rho(\lambda) d\lambda = 1. \quad (14.26)$$

In a deterministic hidden-variable theory, the observable  $[A(\hat{\mathbf{a}})B(\hat{\mathbf{b}})]$  has a defined value  $[A(\hat{\mathbf{a}})B(\hat{\mathbf{b}})](\lambda)$  for the state  $\lambda$ .

The locality is defined as follows: a deterministic hidden-variable theory is local if for all  $\hat{\mathbf{a}}$  and  $\hat{\mathbf{b}}$  and all  $\lambda \in \Lambda$

$$[A(\hat{\mathbf{a}})B(\hat{\mathbf{b}})](\lambda) = A(\hat{\mathbf{a}}, \lambda) B(\hat{\mathbf{b}}, \lambda). \quad (14.27)$$

This is, once  $\lambda$  is specified and the particles have separated, measurements of A can depend only upon  $\lambda$  and  $\hat{\mathbf{a}}$  but not  $\hat{\mathbf{b}}$ . Likewise measurements of B depend only upon  $\lambda$  and  $\hat{\mathbf{b}}$ . Any reasonable physical theory that is realistic and deterministic and that denies action-at-a-distance is local in this sense. For such theories, the expectation value of  $[A(\hat{\mathbf{a}})B(\hat{\mathbf{b}})]$  is given by

$$\begin{aligned} E(\hat{\mathbf{a}}, \hat{\mathbf{b}}) &= \int_{\Lambda} d\lambda \rho(\lambda) [A(\hat{\mathbf{a}})B(\hat{\mathbf{b}})](\lambda) \\ &= \int_{\Lambda} d\lambda \rho(\lambda) A(\hat{\mathbf{a}}, \lambda) B(\hat{\mathbf{b}}, \lambda), \end{aligned} \quad (14.28)$$

where  $E(\hat{\mathbf{a}}, \hat{\mathbf{b}}) \equiv E_{ab}$ , corresponding to our previous notation. It is clear that Equation 14.25 can hold if and only if

$$A(\hat{\mathbf{a}}, \lambda) = -B(\hat{\mathbf{b}}, \lambda) \quad (14.29)$$

holds for all  $\lambda \in \Lambda$ .

Using Equation 14.29, we calculate the following expectation values, which involves three different orientations of the SGA analyzers:

$$\begin{aligned}
 E(\hat{\mathbf{a}}, \hat{\mathbf{b}}) - E(\hat{\mathbf{a}}, \hat{\mathbf{c}}) &= \int_{\Lambda} d\lambda \rho(\lambda) [A(\hat{\mathbf{a}}, \lambda) B(\hat{\mathbf{b}}, \lambda) - A(\hat{\mathbf{a}}, \lambda) B(\hat{\mathbf{c}})] \\
 &= - \int_{\Lambda} d\lambda \rho(\lambda) [A(\hat{\mathbf{a}}, \lambda) A(\hat{\mathbf{b}}, \lambda) - A(\hat{\mathbf{a}}, \lambda) A(\hat{\mathbf{c}}, \lambda)] \\
 &= - \int_{\Lambda} d\lambda \rho(\lambda) A(\hat{\mathbf{a}}, \lambda) A(\hat{\mathbf{b}}, \lambda) [1 - A(\hat{\mathbf{b}}, \lambda) A(\hat{\mathbf{c}}, \lambda)]. \tag{14.30}
 \end{aligned}$$

Since  $A(\hat{\mathbf{a}}, \lambda) = \pm 1$ ,  $A(\hat{\mathbf{b}}, \lambda) = \pm 1$ , this expression can be written as

$$|E(\hat{\mathbf{a}}, \hat{\mathbf{b}}) - E(\hat{\mathbf{a}}, \hat{\mathbf{c}})| \leq \int_{\Lambda} d\lambda \rho(\lambda) [1 - A(\hat{\mathbf{b}}, \lambda) A(\hat{\mathbf{c}}, \lambda)], \tag{14.31}$$

and consequently,

$$|E(\hat{\mathbf{a}}, \hat{\mathbf{b}}) - E(\hat{\mathbf{a}}, \hat{\mathbf{c}})| \leq 1 + E(\hat{\mathbf{b}}, \hat{\mathbf{c}}). \tag{14.32}$$

This inequality is the first of a family of inequalities, which are collectively called "Bell's inequalities."

It is easy to find a disagreement between the quantum mechanics prediction of Equation 14.24 and the inequality of Equation 14.32. When we choose  $\hat{\mathbf{a}}$ ,  $\hat{\mathbf{b}}$ , and  $\hat{\mathbf{c}}$  to be coplanar with  $\hat{\mathbf{c}}$  making an angle of  $2\pi/3$  with  $\hat{\mathbf{a}}$ , and  $\hat{\mathbf{b}}$  making an angle of  $\pi/3$  with both  $\hat{\mathbf{a}}$  and  $\hat{\mathbf{c}}$ , the quantum prediction gives

$$\left| \left[ E(\hat{\mathbf{a}}, \hat{\mathbf{b}}) - E(\hat{\mathbf{a}}, \hat{\mathbf{c}}) \right]_{QM} \right| = 1, \tag{14.33}$$

while

$$1 + \left[ E(\hat{\mathbf{b}}, \hat{\mathbf{c}}) \right]_{QM} = \frac{1}{2}. \tag{14.34}$$

It does not satisfy inequality of Equation 14.32.

In summary, Bell's theorem has proved that no deterministic hidden variable theory satisfying Equation 14.25 and Equation 14.27 can agree with all of the predictions of quantum mechanics concerning the spin of a pair of spin-1/2 particles in the singlet state of Equation 14.1.

Since the space of  $\Lambda$  in Equation 14.28 is spanned into four regions with classical probabilities  $P_{ab}$ ,  $P_{-ab}$ ,  $P_{a-b}$ ,  $P_{-a-b}$  in which A and B have

values  $\pm 1$ , the expectation value evaluation of Equation 14.28 can be explicitly calculated as

$$\begin{aligned} E_{ab} &= (+1)(+1)P_{ab} + (-1)(+1)P_{-ab} + (+1)(-1)P_{a-b} + (-1)(-1)P_{-a-b} \\ &= P_{ab} - P_{-ab} - P_{a-b} + P_{-a-b}. \end{aligned} \quad (14.35)$$

Consider three directions,  $\hat{\mathbf{a}}$ ,  $\hat{\mathbf{b}}$ ,  $\hat{\mathbf{c}}$ , using the results of Equation 14.14, Equation 14.35 gives

$$\begin{aligned} E_{ab} &= P(+ - +) + P(+ - -) - P(- - +) - P(- - -) \\ &\quad - P(+) + +) - P(+) + -) + P(-) + +) + P(-) + -). \end{aligned}$$

Together with the normalization condition

$$\sum P(\pm \pm \pm) = 1,$$

$E_{ab}$  becomes

$$E_{ab} = 2[P(+ - +) + P(+ - -) + P(- + +) + P(- + -)] - 1.$$

Similarly, we have

$$E_{bc} = 2[P(+) + -) + P(-) + -) + P(+ - +) + P(- - +)] - 1.$$

$$E_{ac} = 2[P(+) + -) + P(+ - -) + P(- + +) + P(- - +)] - 1.$$

From the above three equations, it is not difficult to find that

$$\begin{aligned} E_{ab} - E_{ac} &= 1 + E_{bc} - 4P(+) + -) - 4P(- - +) \\ E_{ac} - E_{ab} &= 1 + E_{bc} - 4P(-) + -) - 4P(+ - +). \end{aligned} \quad (14.36)$$

Considering the positive values of the probabilities, Equation 14.36 implies

$$\begin{aligned} E_{ab} - E_{ac} &\leq 1 + E_{bc} \\ E_{ac} - E_{ab} &\leq 1 + E_{bc}, \end{aligned} \quad (14.37)$$

and consequently we obtain the original Bell's inequality

$$|E_{ab} - E_{ac}| \leq 1 + E_{bc}. \quad (14.38)$$

It was soon realized that Bell's inequality of Equation 14.32 cannot be tested in a real experiment, because Equation 14.25 cannot hold exactly in a realistic measurement. Any real detector cannot have a perfect quantum

efficiency of 100%, and any real analyzer cannot have a perfect distinction between orthogonal channels. In 1971, Bell proved a new inequality, which includes these concerns by assuming the outcomes of measurement A or B may take one of the following possible results

$$A(\hat{\mathbf{a}}, \lambda) \text{ or } B(\hat{\mathbf{b}}, \lambda) = \begin{cases} +1 & \text{"spin-up"} \\ -1 & \text{"spin-down"} \\ 0 & \text{particle not detected} \end{cases} \quad (14.39)$$

For a given state  $\lambda$ , we define the measured values for these quantities by the symbols  $\bar{A}(\hat{\mathbf{a}}, \lambda)$  and  $\bar{B}(\hat{\mathbf{b}}, \lambda)$ , which satisfy

$$|\bar{A}(\hat{\mathbf{a}}, \lambda)| \leq 1 \quad \text{and} \quad |\bar{B}(\hat{\mathbf{b}}, \lambda)| \leq 1. \quad (14.40)$$

Following the same definition of locality, the expectation value of  $A(\hat{\mathbf{a}})B(\hat{\mathbf{b}})$  is calculated as

$$E(\hat{\mathbf{a}}, \hat{\mathbf{b}}) = \int_{\Lambda} d\lambda \rho(\lambda) \bar{A}(\hat{\mathbf{a}}, \lambda) \bar{B}(\hat{\mathbf{b}}, \lambda). \quad (14.41)$$

Consider a measurement that involves  $E(\hat{\mathbf{a}}, \hat{\mathbf{b}})$  and  $E(\hat{\mathbf{a}}, \hat{\mathbf{b}}')$

$$E(\hat{\mathbf{a}}, \hat{\mathbf{b}}) - E(\hat{\mathbf{a}}, \hat{\mathbf{b}}') = \int_{\Lambda} d\lambda \rho(\lambda) [\bar{A}(\hat{\mathbf{a}}, \lambda) \bar{B}(\hat{\mathbf{b}}, \lambda) - \bar{A}(\hat{\mathbf{a}}, \lambda) \bar{B}(\hat{\mathbf{b}}', \lambda)], \quad (14.42)$$

which can be written in the following form:

$$\begin{aligned} E(\hat{\mathbf{a}}, \hat{\mathbf{b}}) - E(\hat{\mathbf{a}}, \hat{\mathbf{b}}') &= \int_{\Lambda} d\lambda \rho(\lambda) \bar{A}(\hat{\mathbf{a}}, \lambda) \bar{B}(\hat{\mathbf{b}}, \lambda) [1 \pm \bar{A}(\hat{\mathbf{a}}', \lambda) \bar{B}(\hat{\mathbf{b}}', \lambda)] \\ &\quad - \int_{\Lambda} d\lambda \rho(\lambda) \bar{A}(\hat{\mathbf{a}}, \lambda) \bar{B}(\hat{\mathbf{b}}', \lambda) [1 \pm \bar{A}(\hat{\mathbf{a}}', \lambda) \bar{B}(\hat{\mathbf{b}}, \lambda)]. \end{aligned} \quad (14.43)$$

Using inequality in Equation 14.40, we then have

$$\begin{aligned} |E(\hat{\mathbf{a}}, \hat{\mathbf{b}}) - E(\hat{\mathbf{a}}, \hat{\mathbf{b}}')| &\leq \int_{\Lambda} d\lambda \rho(\lambda) [1 \pm \bar{A}(\hat{\mathbf{a}}', \lambda) \bar{B}(\hat{\mathbf{b}}', \lambda)] \\ &\quad + \int_{\Lambda} d\lambda \rho(\lambda) [1 \pm \bar{A}(\hat{\mathbf{a}}', \lambda) \bar{B}(\hat{\mathbf{b}}, \lambda)], \end{aligned} \quad (14.44)$$

or

$$|E(\hat{\mathbf{a}}, \hat{\mathbf{b}}) - E(\hat{\mathbf{a}}, \hat{\mathbf{b}}')| \leq \pm [E(\hat{\mathbf{a}}', \hat{\mathbf{b}}') + E(\hat{\mathbf{a}}', \hat{\mathbf{b}})] + 2 \int_{\Lambda} d\lambda \rho(\lambda). \quad (14.45)$$

We thus derive a measurable inequality

$$-2 \leq E(\hat{\mathbf{a}}, \hat{\mathbf{b}}) - E(\hat{\mathbf{a}}, \hat{\mathbf{b}}') + E(\hat{\mathbf{a}}', \hat{\mathbf{b}}) + E(\hat{\mathbf{a}}', \hat{\mathbf{b}}') \leq 2. \quad (14.46)$$

The quantum mechanical prediction of the Bohm state in a realistic measurement with imperfect detectors, analyzers etc., can be written as

$$[E(\hat{\mathbf{a}}, \hat{\mathbf{b}})]_{QM} = C \hat{\mathbf{a}} \cdot \hat{\mathbf{b}} \quad (14.47)$$

where  $|C| \leq 1$ . Suppose we take  $\hat{\mathbf{a}}, \hat{\mathbf{a}}', \hat{\mathbf{b}}, \hat{\mathbf{b}}'$  to be coplanar with  $\phi = \pi/4$ , we can easily find a disagreement between the quantum mechanics prediction and the inequality of Equation 14.46:

$$[E(\hat{\mathbf{a}}, \hat{\mathbf{b}}) - E(\hat{\mathbf{a}}, \hat{\mathbf{b}}') + E(\hat{\mathbf{a}}', \hat{\mathbf{b}}) + E(\hat{\mathbf{a}}', \hat{\mathbf{b}}')]_{QM} = 2\sqrt{2}C. \quad (14.48)$$

Although Bell derived his inequalities based on the measurement of EPR–Bohm state of Equations 14.1, 14.32, and 14.46 are not restricted to the measurement of spin 1/2 particle pairs. In fact, most of the historical experimental testing have been the polarization measurements of photon pairs. The photon pairs are prepared in similar states, which have been called EPR–Bohm–Bell states, or Bell states in short. Most of the experimental observations violated Bell’s inequalities, which may have different forms and have their violation occur at different orientations of the polarization analyzers. However, the physics behind the violations are all similar to that of Bell’s theorem.

### 14.3 Bell States

We have given an example of EPR–Bohm state in earlier discussions. The high-energy  $\gamma$ -ray photon pair disintegrated from the annihilation of positronium is a good example to explore the physics of the EPR–Bohm state, however, the  $\gamma$ -ray photon pairs are difficult to handle experimentally: (1) There is no effective polarization analyzers available for the high energy  $\gamma$ -rays and, (2) The uncertainty in momentum correlation,  $\Delta(\mathbf{p}_1 + \mathbf{p}_2)$ , has considerable large value, resulting in a “pair collection efficiency loophole” in Bell’s inequality measurements, i.e., one may never have  $\sim 100\%$  chance to “collect” a pair for joint-photodetection measurement. Fortunately, the

two-photon state of Equation 14.3 is also observed in atomic cascade decay with visible-ultraviolet wavelengths and we have plenty of high-efficiency polarization analyzers available in those wavelengths. Thus, most of the early EPR–Bohm–Bell experiments demonstrated in the 1970s and early 1980s used two-photon source of atomic cascade decay. These experiments, unfortunately, still experienced the difficulties in the momentum uncertainty. The “pair collection” efficiency is as low as that of the annihilation of positronium. It was in the mid-1980s that, Alley and Shih introduced the nonlinear spontaneous parametric down-conversion to the preparation of entangled states. The entangled signal–idler photon pair can be easily prepared in visible-infrared wavelengths, and very importantly, the uncertainty in momentum correlation was improved significantly. The “pair collection efficiency loophole” was finally removed.

The following set of four two-photon spin states can be generated by manipulating the signal–idler pair of SPDC with beam splitters, half and/or quarter waveplates:

$$\begin{aligned} |\Psi_{RL}^{\pm}\rangle &= \frac{1}{\sqrt{2}}[|R_1\rangle|R_2\rangle \pm |L_1\rangle|L_2\rangle] \\ |\Phi_{RL}^{\pm}\rangle &= \frac{1}{\sqrt{2}}[|R_1\rangle|L_2\rangle \pm |L_1\rangle|R_2\rangle]. \end{aligned} \quad (14.49)$$

The four states in Equation 14.49, named as EPR–Bohm–Bell states, or simply “Bell states,” form a complete orthonormal basis in two-particle vector space. In principle, any arbitrary two-photon polarization state can be expressed as an appropriate superposition of Bell states. Bell states have been extensively involved in studying fundamental issues of quantum theory as well as in practical applications of quantum entanglement. In the field of quantum information, Bell states are usually represented in the following form of “qubit”:

$$\begin{aligned} |\Psi_{01}^{(\pm)}\rangle &= \frac{1}{\sqrt{2}}[|0_1 1_2\rangle \pm |1_1 0_2\rangle] \\ |\Phi_{01}^{(\pm)}\rangle &= \frac{1}{\sqrt{2}}[|0_1 0_2\rangle \pm |1_1 1_2\rangle] \end{aligned} \quad (14.50)$$

where  $|0\rangle$  and  $|1\rangle$  represent two arbitrary orthogonal polarization bases. The most popular Bell states are prepared from SPDC in linear polarization representation:

$$\begin{aligned} |\Psi_{XY}^{\pm}\rangle &= \frac{1}{\sqrt{2}}[|X_1\rangle|Y_2\rangle \pm |Y_1\rangle|X_2\rangle] \\ |\Phi_{XY}^{\pm}\rangle &= \frac{1}{\sqrt{2}}[|X_1\rangle|X_2\rangle \pm |Y_1\rangle|Y_2\rangle] \end{aligned} \quad (14.51)$$

where  $|X\rangle$  and  $|Y\rangle$ , respectively, are defined by the polarization of the *o*-ray and the *e*-ray of the nonlinear crystal of SPDC. Treating the circular polarization state as the superposition of the linear polarization states,

$$\begin{aligned} |R\rangle &= |X\rangle + i|Y\rangle \\ |L\rangle &= -|X\rangle + i|Y\rangle, \end{aligned} \quad (14.52)$$

we may find the following states exchangeable between the linear polarization representation and the circular polarization representation:

$$\begin{aligned} |\Psi_{XY}^+\rangle &= |\Psi_{RL}^-\rangle, \quad |\Psi_{XY}^-\rangle = |\Phi_{RL}^-\rangle; \\ |\Phi_{XY}^+\rangle &= |\Phi_{RL}^+\rangle, \quad |\Phi_{XY}^-\rangle = |\Psi_{RL}^+\rangle. \end{aligned} \quad (14.53)$$

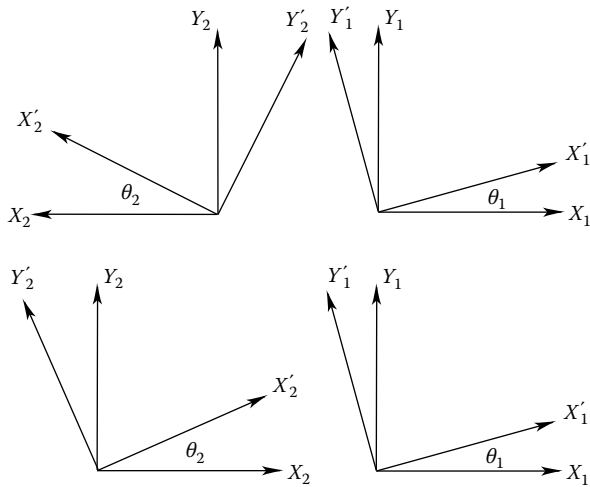
To simplify the notation, we will ignore the subscription for the linear polarization representation to replace  $|\Psi_{XY}^\pm\rangle$  and  $|\Phi_{XY}^\pm\rangle$  with  $|\Psi^\pm\rangle$  and  $|\Phi^\pm\rangle$ , respectively. The polarization correlation functions, in terms of the chosen orientations of the polarization analyzers,  $\theta_1$  and  $\theta_2$ , for the Bell states of Equation 14.51 can be easily calculated:

$$\begin{aligned} |\langle\theta_1\theta_2|\Psi^\pm\rangle|^2 &= \frac{1}{2}\sin^2(\theta_1 \pm \theta_2) \\ |\langle\theta_1\theta_2|\Phi^\pm\rangle|^2 &= \frac{1}{2}\cos^2(\theta_1 \mp \theta_2). \end{aligned} \quad (14.54)$$

The other correlation functions in terms of  $\bar{\theta}$ s or in terms of  $\theta$  and  $\bar{\theta}$  can be derived accordingly based on Equation 14.54.

It is noticed that the condition for achieving maximum correlation, in terms of  $\theta_1$  and  $\theta_2$ , in  $|\Psi^+\rangle$  ( $|\Psi^-\rangle$ ) and in  $|\Phi^+\rangle$  ( $|\Phi^-\rangle$ ) are different:  $\theta_1 + \theta_2 = \pi/2$  against  $\theta_1 - \theta_2 = \pi/2$  ( $\theta_1 - \theta_2 = 0$  against  $\theta_1 + \theta_2 = 0$ ). Thus, if one of them implies orthogonal (parallel) polarization of the photon pair, the other one must imply a different geometrical relationship between the two polarizations.

Now, we are ready to discuss the rotation symmetry of Bell states. We have mentioned earlier that while preparing Bell states in SPDC, the polarization vector base of  $|X\rangle$  and  $|Y\rangle$  are usually defined by the chosen orientation of the nonlinear crystal and the associated waveplates. What will happen if we rotate  $|X\rangle$ - $|Y\rangle$  vector base to  $|X'\rangle$ - $|Y'\rangle$  with angle  $\theta$ ? It is easy to find that in each set of Equation 14.49 and Equation 14.51, only two of the states reserve the symmetry of rotation. In a right-hand coordinate system with antiparallel propagation, i.e., the pair propagate to opposite directions, which is illustrated in the upper part of Figure 14.4, the two Bell states that reserve rotation symmetry are

**FIGURE 14.4**

Upper: right-hand coordinate system with antiparallel propagation. The  $Z_1$  ( $Z_2$ ) axis is point out from (into) the paper. The relative angle between  $X_1-Y_1$  and  $X_2-Y_2$  are  $\theta_2+\theta_1$  after the rotation. Lower: right-hand coordinate system with collinear or near-collinear propagation. Both  $Z_1$  and  $Z_2$  axes are point out the paper. The relative angle between  $X_1-Y_1$  and  $X_2-Y_2$  are  $\theta_2-\theta_1$  after the rotation.

$$\begin{aligned} |\Psi^+\rangle &= \frac{1}{\sqrt{2}}[|X'_1\rangle|Y'_2\rangle + |Y'_1\rangle|X'_2\rangle] \\ |\Phi^-\rangle &= \frac{1}{\sqrt{2}}[|X'_1\rangle|X'_2\rangle - |Y'_1\rangle|Y'_2\rangle]. \end{aligned} \quad (14.55)$$

In a right-hand coordinate system with collinear or near-collinear propagation, i.e., the pair propagate to the same direction, which is illustrated in the lower part of Figure 14.4, the two Bell states that reserve rotation symmetry are:

$$\begin{aligned} |\Psi^-\rangle &= \frac{1}{\sqrt{2}}[|X'_1\rangle|Y'_2\rangle - |Y'_1\rangle|X'_2\rangle] \\ |\Phi^+\rangle &= \frac{1}{\sqrt{2}}[|X'_1\rangle|X'_2\rangle + |Y'_1\rangle|Y'_2\rangle]. \end{aligned} \quad (14.56)$$

It might be easier to figure out the results in Equations 14.55 and 14.56 from the circular polarization-based states of Equation 14.49. If the rotation from  $X-Y$  to  $X'-Y'$  means a rotation of  $\theta_1=\theta$  in arm-1 and  $\theta_2=-\theta$  in arm-2, which is illustrated in the upper part of Figure 14.4,  $|\Psi_{RL}^\pm\rangle$  will reserve rotation symmetry:

$$\begin{aligned}
 |\Psi_{RL}^{\pm}\rangle &= \frac{1}{\sqrt{2}}[|R_1\rangle|R_2\rangle \pm |L_1\rangle|L_2\rangle] \\
 &= \frac{1}{\sqrt{2}}[e^{i(\theta_1+\theta_2)}|R'_1\rangle|R'_2\rangle \pm e^{-i(\theta_1+\theta_2)}|L'_1\rangle|L'_2\rangle] \\
 &= \frac{1}{\sqrt{2}}[|R'_1\rangle|R'_2\rangle \pm |L'_1\rangle|L'_2\rangle],
 \end{aligned} \tag{14.57}$$

corresponding to Equation 14.55. However, if the rotation from X-Y to X'-Y' means a rotation of  $\theta_1 = \theta_2 = \theta$  in both arm-1 and arm-2, which is illustrated in the lower part of Figure 14.4,  $|\Phi_{RL}^{\pm}\rangle$  will reserve rotation symmetry:

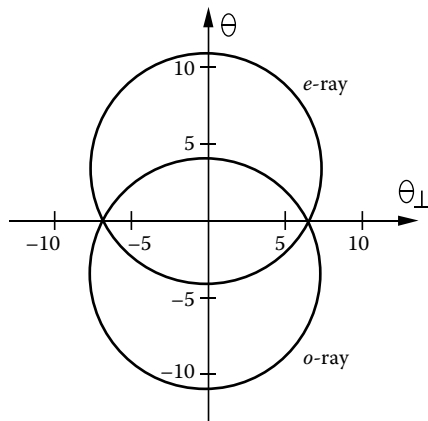
$$\begin{aligned}
 |\Phi_{RL}^{\pm}\rangle &= \frac{1}{\sqrt{2}}[|R_1\rangle|L_2\rangle \pm |L_1\rangle|R_2\rangle] \\
 &= \frac{1}{\sqrt{2}}[e^{i(\theta_1-\theta_2)}|R'_1\rangle|L'_2\rangle \pm e^{-i(\theta_1-\theta_2)}|L'_1\rangle|R'_2\rangle] \\
 &= \frac{1}{\sqrt{2}}[|R'_1\rangle|L'_2\rangle \pm |L'_1\rangle|R'_2\rangle],
 \end{aligned} \tag{14.58}$$

corresponding to Equation 14.56.

#### 14.4 Bell State Preparation

SPDC has been one of the most convenient two-photon sources for the preparation of Bell state since the early 1980s. Although Bell state is for polarization (or spin), the space-time part of the state cannot be ignored. One important “preparation” is to make the two biphoton wavepackets, corresponding to the first and the second terms in the Bell state, completely “overlap” in space-time, or indistinguishable for the joint-detection event. This is especially important for type-II SPDC. Type-II SPDC seems easier to use for the preparation of Bell state due to the orthogonal polarization of the signal and idler.

A very interesting situation for type-II SPDC is that of “noncollinear phase matching.” The signal-idler pair are emitted from an SPDC crystal, such as BBO, cut in type-II phase matching, into two cones, one ordinarily polarized, the other extraordinarily polarized, see Figure 14.5. Along the intersection, where the cones overlap, two pinholes numbered 1 and 2 are used for defining the direction of the  $\mathbf{k}$  vectors of the signal-idler pair. It is very reasonable to consider the polarization state of the signal-idler pair as

**FIGURE 14.5**

Type-II noncollinear phase matching: a cross section view of the degenerate 702.2 nm cones. The 351.1 nm pump beam is in the center. The numbers along the axes are in degrees.

$$|\Psi\rangle = \frac{1}{\sqrt{2}} (|o_1 e_2\rangle + |e_1 o_2\rangle) = |\Psi_{XY}^+\rangle \quad (14.59)$$

where  $o_j$  and  $e_j, j = 1, 2$ , are ordinarily and extraordinarily polarized, respectively. It seems straightforward to realize an EPR–Bohm–Bell measurement by simply setting up a polarization analyzer in series with a photon-counting detector behind pinholes 1 and 2, respectively, and to expect to observe the polarization correlation of Equation 14.54. This is, however, *incorrect!* One can never observe the EPR–Bohm–Bell polarization correlation unless a “compensator” is applied. The compensator is a piece of birefringent material. For example, one may place another piece of nonlinear crystal behind the SPDC. It could be the same type of crystal as that of the SPDC, with the same cutting angle, except having half the length and a  $90^\circ$  rotation in respect to that of the SPDC crystal.

What is the role of the “compensator”? There have been naive explanations about the compensator. One suggestion was that the problem comes from the longitudinal “walk-off” of the type-II SPDC. For example, if one uses a type II BBO, which is a negative uni axis crystal, the extraordinary ray propagates faster than the ordinary ray inside the BBO. Suppose the  $o - e \leftrightarrow e - o$  pair is generated in the *middle* of the crystal, the  $e$ -polarization will trigger the detector earlier than the  $o$ -polarization by a time  $\Delta t = (n_o - n_e)L/2c$ . This implies that  $D_2$  would be fired first in  $|o_1 e_2\rangle$  term; but  $D_1$  would be fired first in  $|e_1 o_2\rangle$  term. If  $\Delta t$  is greater than the coherence length of the signal–idler field, one would be able to distinguish which amplitude gave rise to the “click-click” coincidence event. One may compensate the “walk-off” by introducing an additional piece of birefringent material, like the compensator we have suggested above, to delay the  $e$ -ray relative to the  $o$ -ray by the

same amount of time,  $\Delta t$ . If, however, the signal–idler pair is generated in the *front face* or the *back face* of the SPDC, the delay time would be very different:  $\Delta t = (n_o - n_e)L/c$  for the *front face* and  $\Delta t = 0$  for the *back face*. One can never satisfy all the pairs that are generated at different places along the SPDC crystal. Nevertheless, since SPDC is a *coherent* process, the signal–idler pair is generated in such a way that it is impossible to know the birthplace of the pair. So, how is the delay time  $\Delta t$  determined?

Quantum mechanics has provided the correct answer. It is the overlap or indistinguishability of the biphoton wavepackets in space-time.

The Bell state of Equation 14.59 as well as Equations 14.49 and 14.51 are written in the simplified Schrödinger representation. It is sufficient for certain types of discussions of physics. The simplified form, however, has ignored the space-time aspect of the state, which is important here.

Adopting our earlier result, we may rewrite the state of the signal–idler pair of Figure 14.5 in the following form:

$$|\Psi\rangle = \sum_{\mathbf{k}_o, \mathbf{k}_e} \delta(\omega_o + \omega_e - \omega_p) \Phi(\Delta_k L) \hat{\mathbf{o}} a_o^\dagger(\omega(\mathbf{k}_o)) \hat{\mathbf{e}} a_e^\dagger(\omega(\mathbf{k}_e)) |0\rangle \quad (14.60)$$

where  $\hat{\mathbf{o}}$  and  $\hat{\mathbf{e}}$  are unit vectors along the o-ray and the e-ray polarization direction of the SPDC crystal, and  $\Delta_k = k_o + k_e - k_p$ . In  $\Phi(\Delta_k L)$ , the finite length of the nonlinear crystal has been taken into account. Suppose the polarizers of the detectors  $D_1$  and  $D_2$  are set at angles  $\theta_1$  and  $\theta_2$ , relative to the polarization direction of the o-ray of the SPDC crystal, respectively, the field operators can be written as

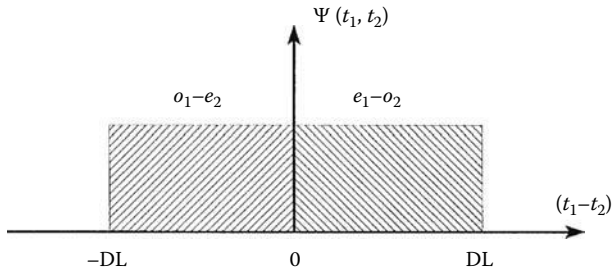
$$E_j^{(+)}(t_j, r_j) = \int d\omega \hat{\theta}_j a(\omega) e^{-i[\omega t_j - k(\omega)r_j]}$$

where  $j = 1, 2$ ,  $\hat{\theta}_j$  is the unit vector along the  $i$ th analyzer direction. Following the standard Glauber formula, the joint-detection-counting rate of  $D_1$  and  $D_2$  is thus

$$\begin{aligned} R_c &\propto \int_T dt_1 dt_2 \left| (\hat{\theta}_1 \cdot \hat{\mathbf{o}}) (\hat{\theta}_2 \cdot \hat{\mathbf{e}}) \Psi(\tau_1^o, \tau_2^e) + (\hat{\theta}_1 \cdot \hat{\mathbf{e}}) (\hat{\theta}_2 \cdot \hat{\mathbf{o}}) \Psi(\tau_1^e, \tau_2^o) \right|^2 \\ &= \cos^2 \theta_1 \sin^2 \theta_2 + \sin^2 \theta_1 \cos^2 \theta_2 \\ &\quad + \cos \theta_1 \sin \theta_2 \sin \theta_1 \cos \theta_2 \int_T dt_1 dt_2 \Psi^*(\tau_1^o, \tau_2^e) \Psi(\tau_1^e, \tau_2^o) \end{aligned} \quad (14.61)$$

where  $\Psi(\tau_1^o, \tau_2^e)$  and  $\Psi(\tau_1^e, \tau_2^o)$  are the effective two-photon wavefunctions with the following normalization:

$$\int_T dt_1 dt_2 |\Psi(\tau_1, \tau_2)|^2 = 1.$$

**FIGURE 14.6**

Without “compensator,” the two-dimensional wavepackets of  $\Psi(\tau_1^o, \tau_2^e)$  and  $\Psi(\tau_1^e, \tau_2^o)$  do not overlap along  $\tau_1 - \tau_2$  axis.

The third term of Equation 14.61 determines the degree of two-photon coherence. Considering degenerate CW laser-pumped SPDC, the biphoton wavepacket of Equation 12.8 can be simplified as

$$\Psi(\tau_1, \tau_2) = \Psi_0 e^{-i\omega_p(\tau_1 + \tau_2)/2} \mathcal{F}_{\tau_-} \{f(\Omega)\}.$$

The coefficient of  $\cos \theta_1 \sin \theta_2 \sin \theta_1 \cos \theta_2$  in the third term of Equation 14.61 is thus

$$e^{-i\omega_p(\Delta\tau_1 - \Delta\tau_2)/2} \mathcal{F}_{\tau_1^o - \tau_2^e} \{f(\Omega)\} \otimes \mathcal{F}_{\tau_1^e - \tau_2^o} \{f(\Omega)\}.$$

Therefore, two important factors will determine the result of the polarization correlation measurement: (1) the phase of  $e^{-i\omega_p(\Delta\tau_1 - \Delta\tau_2)/2}$  and (2) the value of the convolution between biphoton wavepackets  $\Psi^*(\tau_1^o, \tau_2^e)$  and  $\Psi(\tau_1^e, \tau_2^o)$ . Examining the two wavepackets associated with the  $o_1 - e_2$  and  $e_1 - o_2$  terms, we found that the convolution of the two-dimensional biphoton wavepackets of type II SPDC gives a null result due to the *asymmetrical* rectangular function of  $\Pi(\tau_1 - \tau_2)$  as indicated in Figure 14.6. In order to make the two wavepackets overlap, we may either (1) move both wavepackets a distance of  $DL/2$  (case I) or (2) move one of the wavepackets a distance of  $DL$  (case II). In both case I and case II, the convolution obtains its maximum value of one. The use of “compensator” is for this purpose. After compensating the two asymmetrical function of  $\Pi(\tau_1 - \tau_2)$ , we need to further manipulate the phase of  $e^{-i\omega_p(\Delta\tau_1 - \Delta\tau_2)/2}$  to finalize the desired Bell states. This can be done by means of a retardation plate to introduce phase delay of  $2\pi$  (+1) or  $\pi$  (-1) between the o-ray and the e-ray in either arm-1 or arm-2. The EPR-Bohm-Bell polarization correlation

$$R_c \propto \sin^2(\theta_1 \pm \theta_2)$$

is expected only when the above two conditions are satisfied. We can simplify the polarization state of the signal–idler photon pair in the form of Bell states  $|\Psi_{XY}^{(\pm)}\rangle$  in this situation only.

The biphoton wavepacket looks very different in the case of femtosecond laser–pumped SPDC. As an example, a calculation of type-II biphoton wavepacket is given in the following.

We start with the quantum state of type-II SPDC in the following format without losing generality:

$$|\psi\rangle = \int dk_o \int dk_e \int d\omega_p \int_0^L dz e^{-4\ln 2 \left[ \frac{\omega_p - \Omega_p}{\sigma_p} \right]^2} \times e^{i\Delta z} \delta(\omega_o + \omega_e - \omega_p) a_o^\dagger a_e^\dagger |0\rangle \quad (14.62)$$

where

$$\Delta = k_p - k_o - k_e$$

$L$  is the length of the nonlinear crystal

We have considered a Gaussian-like pump pulse with bandwidth  $\sigma_p$ .

To generalize the result to a realistic experimental setup, we consider placing a Gaussian-like spectral filter in front of the detector  $D_j, j = 1, 2$ . The field operator is written as

$$E_j^{(+)}(t_j, r_j) = \int d\omega e^{-4\ln 2 \left[ \frac{\omega - \Omega_j}{\sigma_j} \right]^2} a_o(\omega) e^{-i[\omega t_j - k(\omega)r_j]} \quad (14.63)$$

Define

$$\begin{aligned} \omega_o &= \Omega_o + v_o, \\ \omega_e &= \Omega_e + v_e, \\ \omega_p &= \Omega_p + v_p, \end{aligned}$$

where  $\Omega_o \equiv \Omega_1$  and  $\Omega_e \equiv \Omega_2$ .  $v_j$  is the detuning from the central frequency  $\Omega_j$ . Note that  $\Omega_o + \Omega_e = \Omega_p$  and  $v_o + v_e = v_p$ . The type-II phase mismatch  $\Delta$  is now expanded to the first leading order. Assume  $k(v) = [\Omega + v]n(\Omega + v)/c$ , where  $n(\Omega + v)$  is the index of refraction of the crystal at frequency  $\Omega + v$ .  $k(v)$  can then be expanded to

$$k_j = K_j + \frac{v_j}{u_j(\Omega_j)} \quad (14.64)$$

where the subscripts  $j = o, e, p$  and  $K_j = n_j \Omega_j / c$ , and where  $n_j$  is the index of refraction inside the nonlinear crystal. Therefore,  $\Delta$  can now be written as

$$\begin{aligned}\Delta &= k_p - k_o - k_e \\ &= \frac{v_p}{u_p(\Omega_p)} - \frac{v_o}{u_o(\Omega_o)} - \frac{v_e}{u_e(\Omega_e)} \\ &= -v_p D_+ - \frac{1}{2} v_- D,\end{aligned}\quad (14.65)$$

where  $v_- = v_o - v_e$ ,  $D_+ \equiv \frac{1}{2} \left[ \frac{1}{u_o(\Omega_o)} + \frac{1}{u_e(\Omega_e)} \right] - \frac{1}{u_p(\Omega_p)}$ , and  $D \equiv \frac{1}{u_o(\Omega_o)} - \frac{1}{u_e(\Omega_e)}$ . To make the calculation easier, we assume  $\sigma_1 = \sigma_2 = \sigma$ ; i.e., the same bandwidths for both filters. This assumption makes the  $v_-$  and  $v_+$  integrals uncoupled. We also define  $\Omega_o = \Omega_p/2 + \Omega_d$  and  $\Omega_e = \Omega_p/2 - \Omega_d$ . Note that in the case of degenerate type-II,  $\Omega_d = 0$ .

By combining Equations 14.63, 14.62, and 14.65, the biphoton wavefunction  $\Psi(\tau_+, \tau_-)$  is given by

$$\Psi(\tau_+, \tau_-) = e^{-i\Omega_p \tau_+} e^{-i\Omega_d \tau_-} \Pi(\tau_+, \tau_-) \quad (14.66)$$

where

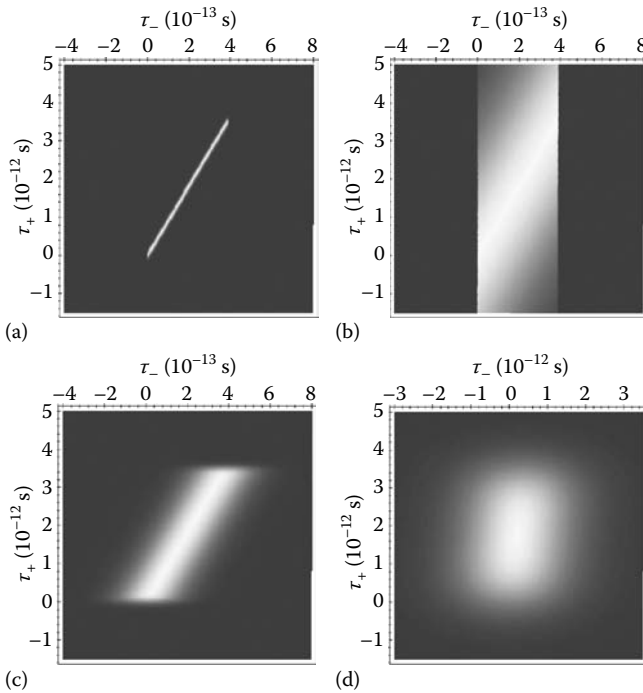
$$\begin{aligned}\Pi(\tau_+, \tau_-) &= \int dv_p \int dv_- \int_0^L dz e^{-[v_p/\delta]^2} e^{-2 \ln 2 [v_-/\sigma]^2} \\ &\quad \times e^{-iv_p \tau_+} e^{-\frac{i v_- \tau_-}{2}} e^{-i[v_p D_+ + \frac{v_-}{2} D] z}\end{aligned}\quad (14.67)$$

with  $1/\delta^2 = 2 \ln 2/\sigma^2 + 4 \ln 2/\sigma_p^2$ . If the bandwidths of the filters are taken to be infinite, Equation 14.67 can be simplified as

$$\Pi(\tau_+, \tau_-) = \begin{cases} e^{-\sigma_p^2 [\tau_+ - [D_+/D]\tau_-]^2 / 16 \ln 2} & 0 < \tau_- < DL \\ 0 & \text{otherwise.} \end{cases}$$

The  $\Pi$  function for pulsed type-II SPDC looks quite different from a CW-pumped type-II SPDC. In a CW-pumped type-II SPDC, the  $\Pi$  function is approximately independent of  $\tau_+$ . However, in short pulse-pumped type-II SPDC, it must be treated as a function of both  $\tau_-$  and  $\tau_+$ .

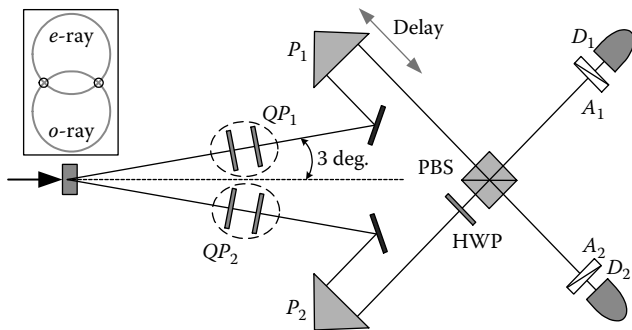
As an example, we consider a type-II BBO crystal with 2 mm thickness pumped by a laser pulse, which has a 400 nm central wavelength, and for the degenerate case,  $\lambda_o = \lambda_e = 800$  nm. Figure 14.7a shows the biphoton wavepacket generated by an 80 fs pump pulse with no spectral filtering. Strong dependence on  $\tau_+$  is observed. The  $\Pi$  function is “tilted” on the  $\tau_- - \tau_+$  plane. In Figure 14.7b, the biphoton wavepacket is generated by

**FIGURE 14.7**

Type-II biphoton as a function of the pump bandwidth and the filter bandwidth.  $\Pi(\tau_+, \tau_-)$  is shown in a density plot. (a) With no spectral filters, pump pulse duration  $\delta t_p = 80 \text{ fs}$ . (b) With no spectral filters,  $\delta t_p = 3 \text{ ps}$ . (c) With 10 nm FWHM spectral filters,  $\delta t_p = 80 \text{ fs}$ . (d) With 1 nm FWHM spectral filters,  $\delta t_p = 80 \text{ fs}$ .

3 ps pump pulse with no spectral filtering. Note that the biphoton is now stretched in  $\tau_+$  direction and starts to resemble the CW-pumped type-II biphoton. In Figure 14.7c and d, we show the effects of spectral filtering. The pump pulse duration is fixed at 80 fs, but the bandwidth of the spectral filters are varied. In Figure 14.7c, we use 10 nm FWHM spectral filters and in Figure 14.7d, a 1 nm FWHM spectral filter is applied. As expected, spectral filtering broadens the biphoton in both  $\tau_+$  and  $\tau_-$  directions. The effects in  $\tau_-$  is greater than that in  $\tau_+$ .

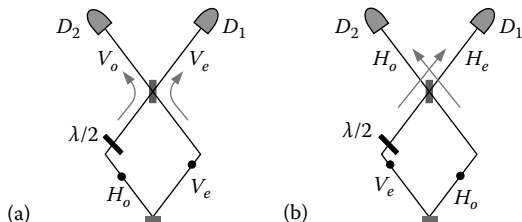
Femtosecond pulse-pumped type-II SPDC has a very peculiar space-time structure. The “tilted” biphoton wavepacket requires special efforts for preparing Bell states. Differing from CW-pumped SPDC, applying a “compensator” in this situation is not enough. Although we could shift the  $e - o$  and  $o - e$  terms to make them approach each other, the “tilted” wavepackets cannot be overlapped due to the different orientation. To overcome this problem, basically, we need to either (1) use a narrow band spectral filter to broaden the wavepacket as we have learned in Figure 14.7d; or (2) prepare the two wavepackets in the same “tilted” orientation, i.e., making

**FIGURE 14.8**

Bell states generation by ultrashort laser pulse. The nonoverlapping  $o_1 - e_2$  and  $e_1 - o_2$  amplitudes are generated via noncollinear type-II SPDC. The use of half-waveplate (HWP) and polarization beamsplitter (PBS) make the reflection–reflection and transmission–transmission two-photon wavepackets “tilted” in the same orientation.  $QP_1$  and  $QP_2$  are quartz plates for fine tuning of the relative phase between the biphoton amplitudes.

*e*-ray reach detector  $D_1$  and *o*-ray reach detector  $D_2$ , or vice versa, for both amplitudes.

A clever experimental scheme developed by Kim et al. is shown in Figure 14.8. This design uses a noncollinear type-II SPDC. The use of half-waveplate (HWP) and polarization beamsplitter (PBS) makes both reflection–reflection and transmission–transmission two-photon wavepackets “tilted” in the same orientation (see Figure 14.9). The *e*-rays and *o*-rays, respectively, always go to detectors  $D_1$  and  $D_2$ . The Bell state measurements have been tested for both CW and Femtosecond pumps. In both cases, high visibilities of interferences were achieved, indicating high-degree overlapping of the reflection–reflection and transmission–transmission two-photon amplitudes.

**FIGURE 14.9**

Two alternative ways for a photon pair triggering a joint-detection event; (a) r-r path and (b) t-t path. This figure further clarifies the role of the half-waveplate (HWP) and the polarization beamsplitter (PBS): how to make the reflection–reflection and transmission–transmission two-photon wavepackets “tilted” in the same orientation. The *e*-rays and *o*-rays always go to detectors  $D_1$  and  $D_2$ , respectively. Bell state measurements were tested for CW and femtosecond pump. In both cases, high interference visibilities were observed.

---

## Summary

In this chapter, we introduced Bell's theorem and Bell's inequality. Bell's theorem addresses two fundamental problems on quantum mechanics: *reality* and *locality*, both originated from the 1935 article of Einstein, Podolsky, and Rosen. In that paper, EPR formally raised a question: "Can quantum-mechanical description of physical reality be considered complete?" After giving a simple, yet carefully stated, criterion that defines their locality and reality: "If, without in any way disturbing a system, we can predict with certainty the value of a physical quantity, then there exist an element of physical reality corresponding to this quantity," EPR proposed an entangled two-particle state in a *gedankenexperiment* to show that it is possible to determine the position and momentum of a particle with certainty through the distant measurement of the position and momentum of its twin. They are confident on their beliefs of locality that the measurement of one particle does not disturb its twin at distance.

Does a particle in the EPR state, or in the EPR–Bohm state, have a defined position and momentum, or polarization, during the course of its propagation whether it is measured or not? Quantum theory answers NO. In the view of quantum mechanics, a particle or a pair of particles may take any or all possible values of position and momentum or polarization if the particle or the pair of particles is in the state of a superposition. It is also an experimental evidence that even if each photon in a pair is prepared with a defined polarization, an appropriate two-photon superposition may result in a state in which no polarization is specified anymore for either photon as a subsystem of the two-photon state. As a realistic physicist, Einstein felt very uncomfortable about the quantum superposition. Einstein insisted that the quantum mechanical wavefunction should be and must be able to specify physical reality that was defined in their 1935 paper. It was Bohm and his followers who attempted a hidden variable theory and formulated the physical reality into the wavefunction of a particle or a pair of particles. Bohm's theory demonstrated its success and consistency with quantum mechanics in almost every aspect of physics until Bell proved a theorem and derived an inequality to show a quantitative difference between the local hidden variable theory and quantum mechanics. In 1964, Bell constructed a general statistical model in a hidden variable parameter space with his mathematically formulated "locality" to show that an inequality can be used to distinguish quantum superposition from classical statistics. Although concerns and criticisms about Bell's theorem and Bell's inequality still exist, a large number of experimental violations of a variety of Bell's inequalities have been reported in favor of quantum superposition.

It should be emphasized that although Bell's theorem and Bell's inequality address locality and reality, it does not mean that all nonlocal problems must be associated with the violation of Bell's inequality. For instance,

the EPR correlation in position and in momentum are considered nonlocal by EPR. Their consideration was based on their believing that a measurement of one particle does not affect the observation of its twin at distance. Although classical statistical correlation may give a position–position correlation or a momentum–momentum correlation, individually, classical statistical correlation can never produce a position–position correlation and a momentum–momentum correlation simultaneously in the measurement of particle pairs. Similar to EPR correlation, we consider a two-photon interference nonlocal if the two-photon superposition involves space-like separated photodetection events. A classical statistical correlation of intensity fluctuations may simulate some aspects of two-photon interference, however, two-photon interference is always distinguishable from statistical intensity fluctuation correlation by examining the physics and/or the consequences of the physics, such as the mechanism of light propagation, the physics of beamsplitting, and/or the physical effects of local turbulence on local intensity fluctuations, as we have done in previous chapters. A proposed classical correlation must obey the basic physical laws of classical theory. One cannot assume a classical correlation that is never allowed in classical theory. Although locality and reality involve deep philosophical concerns in general, we should not forget that both problems are essentially physical problems in physics.

---

## Suggested Reading

- Alley, C.O. and Y.H. Shih, *Foundations of Quantum Mechanics in the Light of New Technology*, M. Namiki (ed.), Physical Society of Japan, Tokyo, Japan, p. 47 (1986).
- Aspect, A. et al., *Phys. Rev. Lett.* 47, 460 (1981).
- Aspect, A. et al., *Phys. Rev. Lett.* 49, 91 (1982a).
- Aspect, A. et al., *Phys. Rev. Lett.* 49, 1804 (1982b).
- Bell, J.S., *Physics*, 1, 195 (1964).
- Bell, J.S., *Speakable and Unspeakable in Quantum Mechanics*, Cambridge University Press, Cambridge, U.K. 1993.
- Bohm, D., *Quantum Theory*, Prentice Hall Inc., New York, 1951.
- Clauzer, J.F. and M.A. Horne, *Phys. Rev. D* 10, 526 (1974).
- Clauzer, J.F. and A. Shimony, *Rep. Prog. Phys.* 41, 1881 (1978).
- Clauzer, J.F., M.A. Horne, A. Shimony, and R.A. Holt, *Phys. Rev. Lett.*, 23, 880 (1969).
- Greenberger, D.M., M. Horne, and A. Zeilinger, *Bell's Theorem, Quantum Theory, and Conceptions of the Universe*, M. Kafatos (ed.), Kluwer Academic, Dordrecht, the Netherlands, 1989.
- Greenberger, D.M., M. Horne, A. Shimony, and A. Zeilinger, *Am. J. Phys.* 58, 1131 (1990).
- Kim, Y.-H., M.V. Chekhova, S.P. Kulik, M.H. Rubin, and Y.H. Shih, *Phys. Rev. A* 63, 062301 (2001a).

- Kim, Y.-H., S.P. Kulik, and Y.H. Shih, *Phys. Rev. A* 63, 060301(R) (2001b).  
Kim, Y.-H., S.P. Kulik, and Y.H. Shih, *Phys. Rev. Lett.* 86, 1370 (2001c).  
Kim, Y.-H., M.V. Chekhova, S.P. Kulik, and Y.H. Shih, *Phys. Rev. A* 67, 010301(R) (2003).  
Kwiat, P.G. et al., *Phys. Rev. A* 60, R773 (1999).  
Ou, Z.Y. and L. Mandel, *Phys. Rev. Lett.* 62, 50 (1988).  
Pittman, T.B., Y.H. Shih, A.V. Sergienko, and M.H. Rubin, *Phys. Rev. A* 51, 3495 (1995).  
Scully, M.O., N. Erez, and E.S. Fry, *Phys Lett. A* 347, 56 (2005).  
Shih, Y.H., Two-photon entanglement and quantum reality, *Advances in Atomic, Molecular, and Optical Physics*, B. Bederson and H. Walther (eds.), Academic Press, Cambridge, U.K., 1997.  
Shih, Y.H., *IEEE J. Selected Top. Quantum Electron.* 9(6), 1541 (2003).  
Shih, Y.H. and C.O. Allay, *Phys. Rev. Lett.* 61, 2921 (1988).  
Strelkalov, D.V., T.B. Pittman, A.V. Sergienko, Y.H. Shih, and P.G. Kwiat, *Phys. Rev. A* 54, R1 (1996).  
Tapster, P.R., J.G. Rarity, and P.C.M. Owens, *Phys. Rev. Lett.* 73, 1923 (1994).

**SERIES IN OPTICS AND OPTOELECTRONICS**

SERIES EDITORS: E. ROY PIKE AND ROBERT G. W. BROWN

# An Introduction to Quantum Optics

## Photon and Biphoton Physics

Authored by a highly regarded international researcher and pioneer in the field, **An Introduction to Quantum Optics: Photon and Biphoton Physics** is a straightforward overview of basic principles and experimental evidence for the quantum theory of light. This book introduces and analyzes some of the most exciting experimental research to date in the field of quantum optics and quantum information, helping readers understand the revolutionary changes occurring in optical science.

*Paints a picture of light in terms of general quantum interference, to reflect the physical truth behind all optical observations*

Unlike most traditional books on the subject, this one introduces fundamental classical and quantum concepts and measurement techniques naturally and gradually as it explores the process of analyzing typical experimental observations. Separating itself from other books with this uncommon focus on the experimental part of analysis, this volume

- Provides a general overview of the optical coherence of light without quantization
- Introduces concepts and tools of field quantization and quantum optics based on the principles and rules of quantum mechanics
- Analyzes similarities and differences between classical and quantum coherence
- Concentrates on key research topics in quantum optics
- Explains photon and biphoton physics by examining the devices and experimental procedures used to test theories

This book is basic enough for students, but it also covers a broad range of higher-level concepts that will benefit scientists and other professionals seeking to enhance their understanding of practical and theoretical aspects and new experimental methods of measurement. This material summarizes exciting developments and observations and then helps readers of all levels apply presented concepts and tools to summarize, analyze, and resolve quantum optical problems in their own work. It is a great aid to improve methods of discovering new physics and better understand and apply nontraditional concepts and interpretations in both new and historical experimental discoveries.

IP833



**CRC Press**

Taylor & Francis Group  
an informa business  
[www.crcpress.com](http://www.crcpress.com)

6000 Broken Sound Parkway, NW  
Suite 300, Boca Raton, FL 33487  
270 Madison Avenue  
New York, NY 10016  
2 Park Square, Milton Park  
Abingdon, Oxon OX14 4RN, UK

ISBN: 978-0-7503-0887-8  
9 780750 308878  
  
[www.crcpress.com](http://www.crcpress.com)